THE UNIVERSITY *of* EDINBURGH

A Co-transcriptional Mechanism for Tightly Controlling RNA Homeostasis in Yeast

Sofía Esteban Serna

THE UNIVERSITY *of* EDINBURGH

Thesis submitted for the degree of Doctor of Philosophy in Cell and Molecular Biology

University of Edinburgh

September 2024

A mis padres y a mi hermana

Declaration

I declare that this thesis was composed by myself, that the work contained herein is my own except where explicitly stated otherwise in the text and that this work has not been submitted for any other degree or professional qualification except as specified. Parts of this work have been published in:

Esteban-Serna, S., Widén, T., Gwynne, M., Farquhar, I., Duchen, M. R., Swain, P. S. and Granneman, S., 2024. A co-transcriptional mechanism for tightly controlling RNA homeostasis in yeast.
https://doi.org/10.1101/2024.10.29.620883

Esteban-Serna, S., Chu, L.C., Chauhan, M., Raja, P., Granneman, S., 2024. Defining Bacterial RNA-RNA Interactomes Using CLASH. Methods Mol Biol 2741, 307–345. https://doi.org/10.1007/978-1-0716-3565-0_17

Esteban-Serna, S., McCaughan, H., Granneman, S., 2023. Advantages and limitations of UV cross-linking analysis of protein-RNA interactomes in microbes. Mol Microbiol. https://doi.org/10.1111/MMI.15073

Sofía Esteban Serna

Edinburgh, 22nd of September 2024

Acknowledgements

I am grateful to my supervisors, Prof Sander Granneman and Prof Peter Swain, for giving me the unique opportunity to work on this project as part of two research teams and for their support, guidance, trust and patience throughout the past four years. I am also grateful to Prof Michael Duchen for helping me with the mitochondrial work; Prof Ramon Grima for building a mathematical model validating the observations presented in this thesis; and my thesis committee chair, Dr Chris Sibley, for his feedback and for, together with Dr Fiona Haward, teaching me how to do CLIP in his lab. I thank Dr Ola Helwak and Dr Lori Koch for generously making time to discuss my mammalian cell cloning and yeast mating assay experiments, respectively, as well as Dr Tessa Moses for helping me with the metabolomics experiment, and all other staff members of EdinOmics, the Centre for Optical Instrumentation Laboratory (COIL) and the Flow Cytometry Facility for the School of Biological Sciences at the University of Edinburgh, and the Medical Sciences Building Confocal Imaging Facility at University College London, for training and technical assistance.

I would like to acknowledge Tove Widén and Isabeil Faqhuar, who engineered some of the strains I used for this study. I thank Mags Gwynne for helping me with the characterisation of the synthetic constructs and for, together with Dr Hugh McCaughan, unknowingly providing me with great psychological support by giving me a chance to speak to someone in person before our building abandoned the shift working system after the pandemic in late July 2021. I would especially like to thank Dr Ivan Clark and Dr Julien Hurbain for patiently and kindly helping me with all the things that can go wrong during microscopy, and Dr Liangcui Chu and Dr Alán Muñoz González for teaching me some of their fantastic coding skills for proteomics and microfluidics analyses as well as for our hiking trips around Scotland, book exchanges and, in general, some of the best memories I will take from Edinburgh. I am also wholeheartedly thankful to my PhD mate Mehak Chauhan, from whom I have received an undeserved amount of emotional support in the lab and over many coffees at Greggs.

I am very grateful to the Wellcome Trust for an incredibly generous studentship and research grant that has allowed me to explore different aspects of the project and complete this work. I would also like to thank the Microbiology Society for awarding me a Research Visit Grant to perform some of this work at the Duchen lab, and the RNA Society for funding my attendance at the RNA 2023 conference, where I presented some of the findings of this thesis.

I am enormously thankful to my friends Anne O'Donnell, Rupali Dabas and Javier Lantero Mora for having accompanied me through this journey and supported me throughout its challenges; Carolina Vigil Hernández, who has also helped a lot despite being a few time zones away; and Ana López González and María Toro del Dedo, who have been having my back since school. I would also like to thank and partly dedicate this work to three remarkable mentors with whom I am fortunate to have crossed paths: Coach Rod Hartzog, whose friendship and wisdom have been greatly missed and remembered since 2018; Dr Alfredo Santana Rodríguez, on whom I can always rely for scientific, professional and life tips; and Dr Nisa Buset Ríos, who has been expecting this thesis since I left her class and whose influence is part of every little step I have given afterwards.

Finally, I would like to thank and dedicate this thesis to my family, as I would not have been able to complete it without their love and support. I thank my dad for always giving me sensible advice and unreservedly supporting my decisions. I thank my mum for her affection and optimism and for always encouraging me to be true to myself. Lastly, I would like to thank my sister Celia - I have no words to describe how lucky I am to have you or to thank you for tolerating and forgiving my grumpiness and always trying to help me while dealing with your own doctoral training and research.

Abstract

Transcription termination by the Nrd1-Nab3-Sen1 (NNS) complex plays a pivotal role in repressing pervasive transcription in *Saccharomyces cerevisiae*. Intriguingly, many upregulated protein-coding RNAs are also increasingly bound by the NNS complex during starvation. This implies that a subset of mRNAs encoding stress-responsive proteins are targeted for degradation shortly after transcription initiation. However, the biological significance of this observation has hitherto remained unclear. Premature termination of stress-responsive mRNAs has been proposed as a putative beneficial cellular mechanism to keep the expression of such genes low and tightly regulated during nutrient deprivation. To test this, I focused on the effect that NNS regulation exerted on one of its stress-specific targets, *PIC2*, which encodes a mitochondrial phosphate and copper importer.

Using strains lacking Nab3 and Nrd1 RNA-binding sites in *PIC2* RNA, I have demonstrated that this NNS-mediated attenuation is important for fine-tuning the expression of an evolutionarily conserved mitochondrial transporter, Pic2, when cells rely on respiration to produce ATP. Remarkably, single-cell microfluidic analyses showed that NNS regulation of *PIC2* not only reduced Pic2 protein levels but also decreased cell-to-cell variability in Pic2 expression, revealing a novel role for NNS as a transcriptional noise suppressor. Using GFP reporters, I show that this attenuation mechanism is generally applicable.

To investigate whether impairing NNS regulation of *PIC2* affected cellular physiology, I characterised the mutants and compared their phenotype to that of the parental strain. My results prove that specifically disrupting Nab3 binding to *PIC2* disturbs energy homeostasis, decreases cell fitness and leads to severe cell size increases and cell cycle delays. To determine whether these phenotypes solely emerged from the increase in activity of Pic2, I generated and inspected a *PIC2* overexpression mutant, which only exhibited defective growth and energy homeostasis. Despite proving that maintaining an optimal expression of *PIC2* is critical to enhancing microbial fitness during adaptation, this evidence also illustrated that larger levels of Pic2 did not underlie all the observed anomalies.

Combining multi-omics profiling and transcriptome-wide NNS-RNA binding footprinting, I demonstrate that disrupting Nab3 binding to *PIC2* leads to redistribution of Nrd1 among its targets and changes levels of many other NNS-regulated transcripts. Given that depleting Nab3 from the nucleus causes an enlargement of cell size and a prolongation of the cell cycle, I posit that alterations in Nrd1 transcriptome occupancy underlie the cell volume and cycle anomalies observed upon abrogation of Nab3 binding to *PIC2*. Collectively, my findings illustrate that even subtle changes in how RNA-binding proteins interact with their RNA substrates can drive significant system-wide defects and emphasise the crucial role of the NNS complex in preserving microbial fitness during stress.

Lay Summary

Like people, cells need to adapt in order to survive hostile environments. For this reason, when exposed to an adverse situation, cells change the expression of their genes to prepare them for the stress they will suffer. Genetic information is stored in cells' DNA. Still, before such information can actually be used for any purpose, it needs to be copied into RNA, which is the molecule on which I have focused throughout this work. DNA, RNA and the need to regulate the making of RNA from DNA during stress are common to all cells. However, the machinery that controls the latter is specific to each cell type. In baker's yeast, many of the changes in the making of RNA are directed by the NNS complex, which is an RNA eater that chops many RNAs. The NNS complex is formed by three members: Nrd1, Nab3 and Sen1. During stress, the whole complex goes after a set of RNAs that must be removed in adverse conditions. Mysteriously, when facing a challenge, cells make more of some of these persecuted RNAs. In other words, when they become stressed, cells begin making a bunch of RNAs that are immediately chopped by NNS. But why would the cell invest any energy in making these RNAs only to remove them right afterwards?

Making and removing those RNAs could be a strategy to tightly control their expression during stress. To check this, I looked at what happened to one of those RNAs when the NNS complex could not chop it. The chosen target RNA was *PIC2*, which carries the information to make tunnels through which copper and phosphorus can move into the mitochondria, the cell's powerhouses. In a mutant yeast in which I changed the sequence that Nab3 uses to recognise *PIC2*, I saw that Nab3 was not able to chase the *PIC2* RNAs and, so, the NNS could not chop them. Therefore, *PIC2* RNAs accumulated in these mutants. In addition to that, the amounts of Pic2 became more different across the cells of the same population. This implied that, among the mutants, there were fewer cells with the best possible quantity of *PIC2* RNAs. Of course, this variability made the mutant cells weaker than the normal ones: preventing NNS from getting rid of *PIC2* RNAs in adverse conditions made cells grow slower, delayed their life cycle, made them way larger (almost double their normal size!) and more stressed, and messed up their metabolism.

At first, I thought that all these defects were occurring because the cell was essentially flooding its powerhouses (mitochondria) with the copper and phosphorus that came into them through the Pic2 tunnels. But, when I looked at yeast and human cells with loads of Pic2 tunnels, I saw that only some of these aberrations were caused by more Pic2 tunnels as such cells did not have cell size, life cycle and stress problems. However, too many Pic2 tunnels did cause respiratory issues which damaged cells' metabolism and made them more sensitive. Strikingly, I saw that removing all Pic2 tunnels from the cells' powerhouses caused the same respiratory problems. In essence, having too many or too few *PIC2* RNAs is equally bad for the cells, and so, yeast and human cells have developed machinery which, like NNS in yeast, carries out a 'Goldilocks' regulation of the *PIC2* RNA and ensures that its levels are kept at a level that is 'just right'.

Since the larger size, life cycle and stress in yeast where NNS was not chopping *PIC2* RNAs were not caused by more Pic2 tunnels, the defects must come from the reduced capacity of NNS to eat *PIC2* RNAs. Surprisingly, in yeast cells in which neither Nab3 nor Nrd1 were able to stick to *PIC2* RNAs, such aberrations went away. Thus, I reasoned that they occurred because Nab3 was not able to join Nrd1 in *PIC2* RNAs. Basically, Nrd1 and/or Sen1 would remain stuck to *PIC2* RNAs that could not be chopped without Nab3. In turn, this would reduce the Nrd1s and Sen1s available to chop other NNS RNA targets, which would accumulate and end up causing size, life cycle, and stress problems in cells in which Nab3 cannot recognise *PIC2* RNAs. I confirmed this by seeing that the amounts of many other NNS RNA targets were also different in those cells.

In summary, my thesis has identified a machinery (NNS) that keeps the levels of *PIC2* RNAs 'just right'. This is especially important in hostile environments, as cells need to be as tough as possible to survive. When this Goldilocks regulation cannot happen, cells are more likely to perish as they would have too many or too few *PIC2* RNAs. Additionally, my work has shown that making a small change to the RNA-eating capabilities of a regulator (Nab3) can have large effects on those of the colleagues with whom it works (Nrd1). Therefore, I have characterised a principle by which any type of cell could become sick.

Resumen para Legos (Spanish)

Al igual que las personas, las células necesitan adaptarse para sobrevivir en ambientes hostiles. Por ello, cuando se encuentran en condiciones adversas, las células cambian la expresión de sus genes para prepararse para el estrés que viene. La información genética se almacena en el ADN de las células, pero, antes de que dicha información pueda utilizarse para cualquier fin, es necesario copiarla en formato ARN, que es la molécula en la que me centro a lo largo de este trabajo. El ADN, el ARN y la necesidad de regular la producción de ARN a partir del ADN en condiciones estresantes son comunes a todas las células. Pero la maquinaria que controla esta última es específica a cada tipo celular. En la levadura de pan, muchos de los cambios en la fabricación de ARN están dirigidos por el complejo NNS, que es un comecocos de ARN que devora muchos ARNs. El complejo NNS está formado por tres miembros: Nrd1, Nab3 y Sen1. Para adaptarse al estrés, todo el complejo va tras un conjunto de ARNs que necesitan ser eliminados en condiciones adversas. Misteriosamente, cuando se enfrentan a un desafío ambiental, las células empiezan a fabricar más cantidad de algunos de los ARNs que son perseguidos por el NNS. O sea, que cuando se estresan, las células empiezan a fabricar un montón de ARNs que el NNS se zampa acto seguido. Pero ¿por qué invertiría la célula energía en fabricar estos ARNs para eliminarlos inmediatamente después?

Elaborar y eliminar estos ARNs bien podía ser una estrategia para mantener un control férreo en la cantidad de ARNs que se expresan mientras la célula está estresada. Para comprobar si éste era el caso, indagué en qué le ocurría a uno de esos ARNs cuando el NNS no era capaz de comérselo. Para ello, elegí el ARN de *PIC2*, que contiene información para hacer túneles a través de los que el cobre y el fósforo pueden entrar a las mitocondrias, las centrales energéticas de la célula. Después de mutar la secuencia que Nab3 utiliza para reconocer el ARN de *PIC2*, observé que Nab3 dejaba de ser capaz de perseguir a los ARN de *PIC2* y, por tanto, el NNS dejaba de poder tragarse los ARNs de *PIC2*. Por consiguiente, los ARNs de *PIC2* se acaban acumulando en estos mutantes. Pero, además de eso, descubrí que cuando el NNS no podía eliminar los ARNs de *PIC2*, las cantidades de Pic2 entre las células de una misma población se hacían más dispares. Es decir, que, entre los

mutantes, había menos células con la cantidad óptima de ARNs de *PIC2*. Por supuesto, esta variabilidad debilita a los mutantes con respecto a las células normales: mis resultados muestran que impedir que NNS se deshiciera de los ARNs de *PIC2* en condiciones adversas ralentiza el crecimiento de las células, retrasa su ciclo vital, incrementa su tamaño (¡a casi el doble!), las estresa y altera su metabolismo.

Al principio, pensé que estos defectos se producían porque la célula estaba esencialmente inundando sus centrales energéticas (mitocondrias) con el cobre y el fósforo que les llegaban a través de los túneles Pic2. Pero, resultó que las células (de levadura y humanas) con montones de túneles Pic2 no tenían problemas con su tamaño celular, ciclo vital y estrés. No obstante, demasiados túneles Pic2 causan problemas respiratorios que dañan el metabolismo de las células y las hacen más sensibles. Sorprendentemente, vi que eliminar todos los túneles Pic2 de las centrales eléctricas de las células causaba esos mismos problemas respiratorios. Vamos, que, para las células, tener demasiados ARNs de *PIC2* es igual de malo que tener muy pocos. En consecuencia, las células han desarrollado maquinarias que, como el NNS en la levadura, regulan el número de ARNs de *PIC2* de forma parecida a como se cuece el arroz, que tiene que estar “en su punto”: ni pasado ni sin hacer.

Dado que los problemas relativos al tamaño, el ciclo vital y el estrés de las células no dependían del número de túneles Pic2, deduje que tales anomalías en las células en que NNS no eliminaba los ARNs de *PIC2* debían proceder del hecho de que NNS no podía regular a *PIC2* en esas células. Sorprendentemente, las células de levadura en las que ni Nab3 ni Nrd1 eran capaces de adherirse a los ARNs *PIC2*, dichos defectos desaparecían. Así las cosas, razoné que estos defectos ocurrían porque Nab3 no era capaz de unirse a Nrd1 en ARNs de *PIC2*. Consecuentemente, Nrd1 y/o Sen1 podían permanecer pegados a ARNs *PIC2* que no podían ser eliminados sin Nab3. Al no poder ser engullidos, los ARNs de *PIC2* estarían limitando la disponibilidad de Nrd1 y Sen1 para comerse otros ARN dianas del NNS. Estos otros ARNs se acumularían y acabarían causando problemas de tamaño, ciclo vital y estrés en las células en las que Nab3 no pueda reconocer ARNs *PIC2*. Pude confirmar que esto era cierto ya que las cantidades de muchos otros ARN dianas de NNS también eran diferentes en los mutantes en que Nab3 no reconocía los ARNs de *PIC2*.

En pocas palabras, en esta tesis he identificado una maquinaria (NNS) que mantiene los niveles de ARN de *PIC2* “en su punto”. Esto es particularmente crítico en entornos adversos, en los que células necesitan ser lo más resistentes posible para sobrevivir. Cuando esta regulación se rompe, las células perecen más fácilmente, ya que tendrían demasiados o muy pocos ARNs de *PIC2*. Asimismo, mi trabajo ha demostrado que un pequeño cambio en la capacidad que un regulador (Nab3) tiene de reconocer a uno de sus ARN diana puede tener grandes efectos en la de los compañeros con los que trabaja (Nrd1). Por tanto, he caracterizado un principio por el que cualquier otro tipo de célula podría enfermar.

Table of Contents

Abbreviations

All abbreviations used throughout this work are listed below in alphabetical order.

$^1[O_2]$: singlet oxygen
ABC: ammonium bicarbonate
Acetyl-CoA: acetyl coenzyme A
ACN: acetonitrile
ADH: alcohol dehydrogenase
ALD: aldolase
ANT: adenine nucleotide translocator
AOX: cyanide-insensitive alternative oxidase
ATCC: American Type Culture Collection
ATP: adenine triphosphate
BABY: birth annotator for budding yeast
cDNA: complementary DNA
CID: carboxyl-terminal domain-interacting domain
COX: cytochrome *c* oxidase
CPF-CF: cleavage and polyadenylation factor cleavage factor
Cq: quantification cycle
CRAC: cross-linking and analysis of cDNAs
Ct: cycle threshold
CTD: C-terminal domain of Pol II
CuL: non-proteinaceous copper ligand
CUT: cryptic unstable transcript
dCLIP: denaturing CLIP
DE: differentially expressed
DEPC: diethylpyrocarbonate
DHODH: dihydroorotate dehydrogenase
DMEM: Dulbecco's modified eagle medium
Dox: doxycycline
dsDNA: double-stranded DNA
DTT: dithiothreitol
ECL: enhanced chemoluminsecence
EDTA: ethylenediaminetetraacetic acid
ETC: electron transport chain
FAD: flavin adenine dinucleotide

FASP: filter-aided sample preparation columns
FBS: foetal bovine serum
FCCP: carbonyl cyanide-p-trifluoromethoxyphenylhydrazone
FDR: false discovery rate
FLASH: fast ligation of RNA after some sort of affinity purification for high-throughput sequencing
FRB: FKBP12-rapamycin-binding
FRT: Flp recombination target
FSC: forward scatter
GAPDH: glyceraldehyde 3-phosphate dehydrogenase
GAPDH: glyceraldehyde 3-phosphate dehydrogenase
GPx: glutathione peroxidases
gRNA: guide RNA
GSH: reduced gluthathione
GSSG: oxidised glutathione disulfide
GTP: guanosine triphosphate
Gu-HCl: guanidinium chloride
H_2O_2: hydrogen peroxide
HEK 293: 293 human embryonic kidney cells
His: histidine
HPLC: high performance liquid chromatography
HTF: His_6-TEV-3xFLAG
IMM: inner mitochondrial membrane
LB: Luria-Bertani broth
lncRNA: long non-coding RNA
MATa: mating type a
MATα: mating type α
MCF/SLC25: mitochondrial carrier family
MoClo: modular cloning
MOPS: 3-(N-morpholino)propanesulfonic acid
mRNA: messenger RNA
MS/MS: tandem mass spectrometry
MT: metallothionein
NaCN: sodium cyanide
NAD: oxidised nicotinamide adenine dinucleotide
NIM: Nrd1-interacting motif
Ni-NTA: nickel-nitrilotriacetic
NNS: Nrd1–Nab3–Sen1 complex

$O2^{-}$: superoxide anion radical
OCR: oxygen consumption rate
OD_{600}: optical density
$OH^{\cdot}$: hydroxyl radical
OMM: outer mitochondrial membrane
PAGE: polyacrylamide gel electrophoresis
PAM: protospacer adjacent motif
PDC: pyruvate decarboxylase
PDH: pyruvate dehydrogenase
PE: paired-end
PFK: phosphofructokinase
PFS: perfect focus system
PGI: glucose 6-phosphate isomerase
PGK: phosphoglycerate kinase
PGM: phosphoglycerate mutase
PI: propidium iodide
PIC: pre-initiation complex
PK: pyruvate kinase
Pol II: RNA Polymerase II
pre-mRNA: precursor messenger RNA
PSM: peptide spectrum match
PTM: post-translational modification
qWB: quantitative western blot
Rap: rapamycin
RBP: RNA-binding proteins
RISC: RNA-induced silencing complex
RNA-BS: RNA-binding site
ROI: region of interest
ROS: reactive oxygen species
RPM: reads per million
rpm: revolutions per minute
rcf: relative centrifugal force
rRNA: ribosomal RNA
RT-qPCR: Real-time quantitative reverse transcription PCR
SC: synthetic complete medium
SD: standard deviation
SDS: sodium dodecyl sulphate
SELEX: systematic evolution of ligands by exponential enrichment

SEM: standard error of the mean

Ser5P: phosphorylation at the fifth serine residue of the CTD of Pol II

sfGFP: superfolder green fluorescence protein

SGD: *Saccharomyces* Genome Database

snoRNA: small nucleolar RNA

snRNA: small nuclear RNA

SOC: catabolite repression medium

SPO: sporulation medium

SSC: side scatter

SUT: stable unannotated transcript

TBE: Tris-borate-EDTA buffer

TCA: tricarboxylic acid

Tet: Tn10-encoding

TetO2: Tet operator

TFA: trifluoroacetic acid

TMM: trimmed mean of M-values

TMRM: tetramethylrhodamine, methyl ester

TOR: target of rapamycin

TPI: triosephosphate isomerase

T-PMT: transmitted photomultiplier

TRAMP: Trf4-Air2-Mtr4 polyadenylation complex

TRC: transcription-replication conflict

tRNA: transfer RNA

TSS: transcription start site

Ura: uracil

UTR: untranslated region

uvCLAP: ultraviolet crosslinking and affinity purification

WT: wild type

YIp: yeast integrating plasmid

YPDA: yeast peptone dextrose adenine medium

List of Figures

List of Tables

I. Introduction

I.1. Transcription termination in *Saccharomyces cerevisiae*

Originally, gene expression was thought to be dictated by the central dogma of molecular biology, which postulated two sequential steps that ultimately turn the information encoded in a gene into a cellular function. The two stages of the central dogma are transcription, which entails the production of RNA from DNA, and translation, which involves the synthesis of proteins from transcripts. However, the latter process was only applicable to protein-coding genes, and consequently, gene expression was conceptually appended to include the synthesis of a final gene product, which could be, for instance, a non-coding RNA (ncRNA). Regardless of the nature of the gene product, the transcription of DNA into RNA is the key step that modulates the 'on and off' states of genes and, accordingly, underlies the identity and temporary states of cellular systems (Lee and Young, 2013).

Transcription encompasses three phases: initiation, elongation, and termination. Transcriptional initiation commences when general transcription factors bind accessible promoters and enrol the pertinent RNA polymerase to assemble the pre-initiation complex (PIC). Aided by the recruited transcription factors, the polymerase melts the double-stranded (ds)DNA to form a transcription bubble and begin RNA synthesis. Having escaped the promoter region (i.e., after having transcribed around 10 ribonucleotides), the polymerase enters the transcriptional elongation stage. During elongation, the polymerase extends the nascent RNA by adding ribonucleotides to the short nascent transcript while concurrently undergoing processive single-base translocation along the transcribed gene. Transcription elongation necessarily concludes with transcriptional termination, which occurs when the polymerase ceases to incorporate any further nucleotides into the transcript and the RNA product is released. Transcription termination is a pivotal process for gene expression; it not only yields functional and non-functional independent RNA entities but also partly dictates their fate by shaping their subsequent properties (i.e., maturation, splicing, nuclear export, localisation, stability, translatability, and degradation). Nonetheless, the

molecular events propelling timely and efficient dissociation of the polymerase from the DNA are still poorly understood.

The RNA polymerase II transcription complex (Pol II) is primordially occupied with the transcription messenger RNAs (mRNA) that are subsequently translated into proteins. Yet, in addition to protein-coding transcripts, Pol II is also responsible for producing micro-RNA precursors as well as a wealth of small nuclear (snRNAs) and small nucleolar RNAs (snoRNAs) (Houseley and Tollervey, 2009; Kuehner et al., 2011; Porrua and Libri, 2015). While exerting its role, Pol II frequently engages in pervasive transcription, thereby synthesising multiple putatively non-functional or, frequently, deleterious non-coding RNA species. Such pervasive transcripts originate from either futile bidirectional transcription arising divergently from the promoters of protein-coding genes or promiscuous binding of Pol II to genomic regions that are not transcription start sites (TSS) (Preker et al., 2008; Wyers et al., 2005). These non-productive transcriptional events result in the generation of long non-coding RNAs, such as cryptic unstable transcripts (CUTs) and stable unannotated transcripts (SUTs) in yeast and promoter-proximal transcripts (PROMPTs) in humans (Preker et al., 2008; Wyers et al., 2005; Xu et al., 2009), which ought to be degraded to prevent downstream interference with the metabolism of functional RNAs (Porrua and Libri, 2015).

Hence, the decade following the discovery of pervasive RNAs witnessed an emerging interest in RNA turnover (Rambout and Maquat, 2024). To date, the main RNA decay machinery for this class of transcripts is the exosome, which is an evolutionarily conserved eukaryotic processing complex which combines 3’ exonuclease and endonuclease enzymatic activity (Preker et al., 2008; Wyers et al., 2005). Even though there is some evidence supporting that the mammalian 5'-3' exoribonuclease 2 XRN2 can also degrade intergenic non-productive transcripts (Agostini et al., 2021; Brannan et al., 2012; Mitchell et al., 1997), such capacity has not been characterised in its yeast homologue Rat1.

Apart from shielding the cell against pervasive transcription, RNA degradation or turnover is essential for gene expression regulation (Houseley and Tollervey, 2009). In budding yeast, different systems of RNA turnover surveil all precursor mRNAs (pre-mRNAs) as well as non-coding transcripts to modulate their expression in response to changes in the environment (Bresson et al., 2017; van Nues et al., 2017). Protein-

coding RNAs, as well as functional ncRNAs and CUTs, undergo transcriptional termination. But it is not surprising that, owing to the divergent nature of these transcriptional units, Pol II uses two distinct mechanisms for transcription termination: the cleavage and polyadenylation factor (CPF)–cleavage factor (CF) pathway and Nrd1–Nab3–Sen1 (NNS) pathway. In both cases, the assembly of the multiprotein complex is contingent on the presence of sequentially encoded termination elements and the interaction with the C-terminal domain (CTD) of Pol II, which acts as a binding platform (Houseley and Tollervey, 2009; Kuehner et al., 2011; Porrua and Libri, 2015).

I.2. Transcription termination of protein-coding genes

Transcription termination of protein-coding genes is executed by three evolutionarily conserved CPF-CF complexes, namely CPF, CFIA and CFIB, which convene in the 3′ untranslated region (UTR) of the nascent transcript (Figure I.1). While various factors of the assembly, such as Cft1, Cft2, Hrp1/Nab4, Mpe1, Rna15 and Yth1, recognise the termination and processing consensus sites of the poly(A) signal in the nascent RNA, Pcf11 detects the phosphorylated Ser2 residue of the CTD and associates with Clp1 to tether to the flap loop of Rpb2, which is the second largest subunit of the polymerase (Mischo and Proudfoot, 2013; Xiang et al., 2014). Upon recruitment of the endoribonuclease Ysh1, cleavage of the transcript ensues, and a free hydroxyl group emerges on the 3’ end (3’-OH). This moiety is recognised by the poly(A) polymerase Pap1, which then adds adenine nucleotides to that end of the cleaved transcript (Figure I.1). The poly(A)-binding protein underlays the resulting poly(A) tail to putatively (i) determine its length, (ii) shelter it from 3′ end degradation and (iii) export it to the cytoplasm. Some studies have posited that this role could be shared with Pab1 and Nab2, which have been proposed to be, respectively, cytoplasmic and nuclear escorting factors that also bind and protect the poly(A) tail of the transcript and mediate the shipment of the RNA to the cytoplasm (Dunn et al., 2005; Hector et al., 2002). The nuclear export of transcripts terminated by the CPF–CF complexes is typically non-limiting, as it has been speculated that the rapid removal of terminated transcripts is a molecular strategy for not restricting the availability of the nuclear degradation machinery (Schmid et al., 2012). However, the molecular processes by which CPF-CF-terminated transcripts are transported to the cytoplasm remain uncharacterised.

Following the cleavage of the newly formed RNA, Pol II proceeds with the transcription of approximately 150 nucleotides downstream of the endonuclease acting site before releasing the RNA and DNA substrates (Creamer et al., 2011). Nevertheless, the exact details of how this process unfolds are still unclear. It is likely that the CPF-CF complex is required for transcriptional processing and Pol II dismantling, as studies have reported that altering the comprising units of the CPF–CF complex causes defects in both steps (Sadowski et al., 2003). Indeed, CPF-CF 3′ processing and RNA Pol II transcription are coupled via a direct interaction between the termination and transcription machineries (Amberg et al., 1992; Carminati et al., 2023; Hammell et al., 2002). In line with this notion, a footprint analysis of Pol II revealed that upon nuclear depletion of the Ysh1 endonuclease, protein-coding genes widely displayed termination anomalies (Schaughency et al., 2014).

Two models have been postulated for CPF–CF-dependent termination: the anti-terminator/allosteric model and the torpedo model (Figure I.1). The anti-terminator or allosteric model proposes that transcription of the polyadenylation site of the pre-mRNA induces allosteric changes in the elongation complex that ultimately prompt the dislodgement of the elongation or anti-termination factors as well as the attachment of termination factors which diminish the enzymatic processivity and eventually lead to transcription termination (Ahn et al., 2004; Kim et al., 2004a) (Figure I.1). Consistent with this hypothesis, the elongation complex loses various processing factors prior to Pol II dissociation (Ahn et al., 2004; Kim et al., 2004a). Moreover, *in vitro* elongation complexes can be undermined by supplementing the reaction with Pcf11 (Zhang et al., 2005), although the *in vivo* applicability of this finding has yet to be ascertained.

The torpedo model postulates that the 3′ end cleavage at the polyadenylation site of the precursor mRNA by the CPF-CF complex concomitantly generates a new 5’ end for the nascent pre-mRNA (Kim et al., 2004b; West et al., 2004) (Figure I.1). Contrary to the 5’ end of authentic mRNAs, the remaining 5’ end of the nascent transcript is uncapped and, thus, susceptible to degradation by Rat1, a 5′-3′ exonuclease that degrades the released RNA up to the active Pol II. Afterwards, Rat1, individually or synergistically with the co-factor Rai1, dismantles the elongation complex (Kim et al., 2004b; West et al., 2004). This hypothesis is supported by evidence showing that

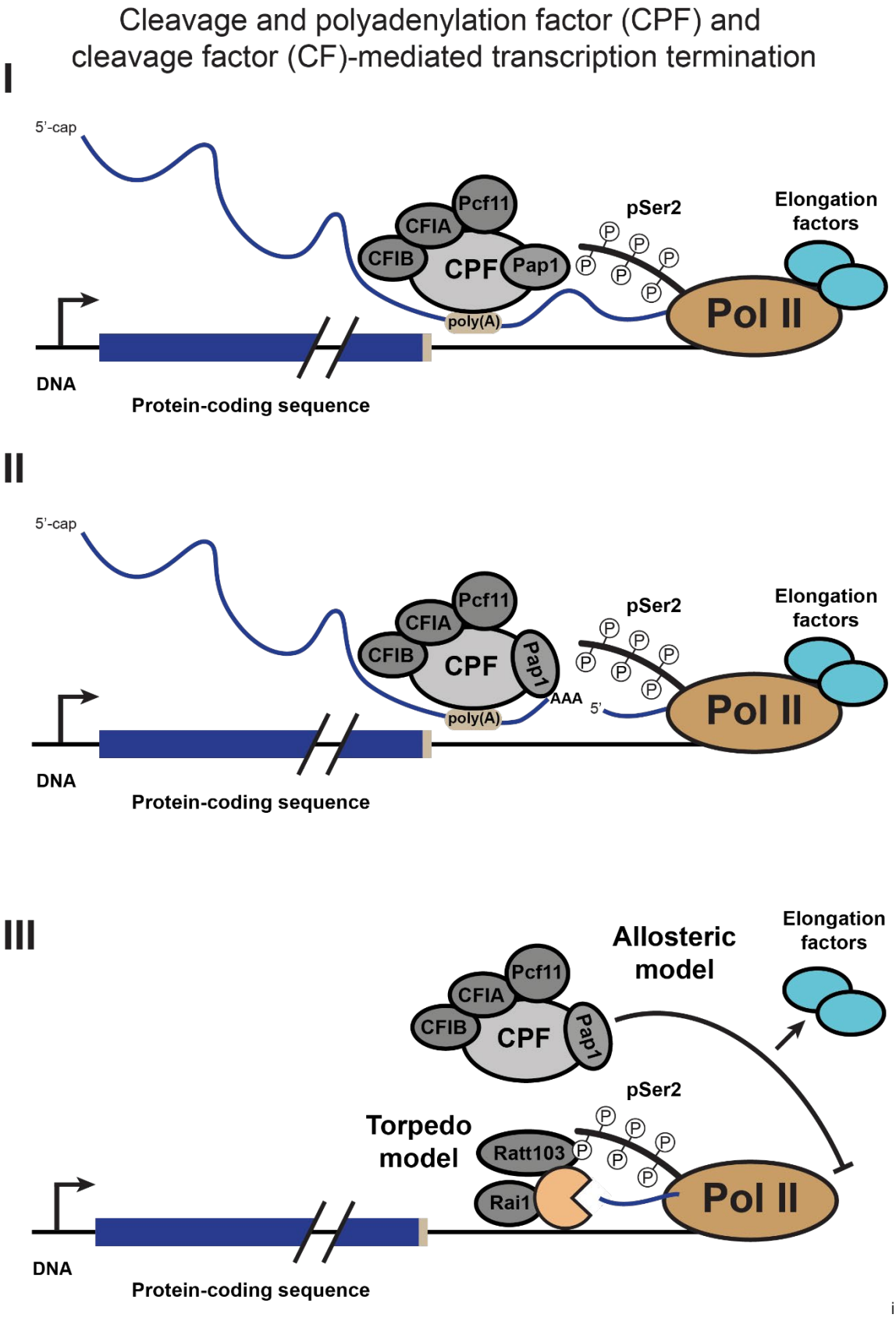

Figure I.1. Schematic representation of the CPF-CF transcriptional termination pathway. Sequential changes are shown in chronological order throughout vignettes I, II and III.

cleavage and termination are indeed coupled and that, when Rat1 action is impaired, readthrough transcription increases (Kim et al., 2004b). Nonetheless, it is not clear how the exonuclease promotes the destabilisation of the complex. On the one hand, a previous report claimed that Rat1 and Rai1-mediated degradation of the nascent RNA cannot induce termination *in vitro* (Dengl and Cramer, 2009). On the other hand, a different study stated that, in partially purified whole-cell lysates, the addition of Rat1–Rai1 could dislodge stalled elongation complexes (Pearson and Moore, 2013). Hence, such work suggested that the Rat-Rai1 complex requires additional factors to elicit termination.

Since, ultimately, there is evidence bolstering both modes of action, it is plausible that the actual termination mechanism incorporates principles from both scenarios. In other words, the unified allosteric–torpedo model is substantiated by the fact that both Rat1 and Pcf11 are recruited to the CPF-CF machinery congregating at the poly(A) site. There, a conformational change will allow them to partake in the cleavage of the newly synthesised mRNA, degradation of the remaining nascent RNA and transcription termination (Luo et al., 2006).

I.3. The Nrd1-Nab3-Sen1 complex

As indicated above, Pol II does not only transcribe protein-coding genes but also various non-coding RNAs (Houseley and Tollervey, 2009; Kuehner et al., 2011; Porrua and Libri, 2015). To terminate transcription of the latter, yeast possess a pathway that does not rely on the presence of a polyadenine signal. This mechanism is exerted by the nuclear pre-mRNA downregulation 1 (Nrd1) and the nuclear polyadenylated RNA-binding 3 (Nab3) proteins alongside Sen1, an RNA helicase (Porrua and Libri, 2015) (Figure I.2). Together, these proteins comprise the Nrd1-Nab3-Sen1 (NNS) transcription termination complex which is the canonical terminator of non-coding RNAs and simultaneously serves as a guardian of the transcriptome against pervasive transcription (Porrua and Libri, 2013). The NNS complex is unique to budding yeast and, thus, not conserved in higher eukaryotes (Bresson and Tollervey, 2018). Although the three constituent proteins possess a human homologue - SCAF8/RBM16 for Nrd1, HNRNPC for Nab3 and senataxin for Sen1 -, these are not known to form a complex in mammalian cells (Bresson and Tollervey, 2018). Interestingly, the only component

of the NNS complex with a partially conserved function in humans is Sen1, which is an ATP-dependent helicase involved in the disentanglement of transcription-replication conflicts (TRCs) such as (i) the removal of stalled transcription apparatus to allow progression of the replisome and (ii) the resolution of genotoxic R loops arising from spurious annealing of the nascent RNA to its complementary DNA locus (Aiello et al., 2022; Hasanova et al., 2023).

The NNS transcription termination complex is involved in the maturation of small nuclear RNAs (snRNAs), contributing to splicing, and small nucleolar transcripts (snoRNAs), required for ribosomal RNA (rRNA) modifications, as well as the degradation of a plethora of long non-coding (lncRNAs), such as CUTs and SUTs, stemming from pervasive transcription. Furthermore, the NNS complex has also been shown to prematurely terminate some mRNAs, namely *NRD1*, on which the complex exerts an autoregulatory negative feedback loop (Arigo et al., 2006; Steinmetz et al., 2001), *ADE12*, *IMD2*, *URA2*, *URA8* (Kuehner and Brow, 2008; Thiebaut et al., 2008), and *FKS2* (Kim and Levin, 2011). In addition to these fully characterised regulatory activities, Nrd1 and Nab3 bind many other protein-coding transcripts (Creamer et al., 2011; Schulz et al., 2013; van Nues et al., 2017; Webb et al., 2014), but the physiological implications of these interactions have remained unclear.

Despite being independent of a poly(A) site, nascent transcript recognition by Nrd1 and Nab3 is sequential. The RNA-binding motifs for Nrd1 and Nab3 are known as terminator elements and have been previously defined as GUAA/G and UCUU for each of them, respectively (Carroll et al., 2007; Creamer et al., 2011; Wlotzka et al., 2011) (Figure I.2). Even though such sequence determinants display a wide diversity in their disposition among targets, an *in vivo* systematic evolution of ligands by exponential enrichment (SELEX) screen identified the motif arrangement driving optimal NNS attenuation of transcription and dubbed it ‘supermotif’ (Porrua et al., 2012). That sequential combination encompassed one Nrd1 RNA-binding site (RNA-BS), and two Nab3 RNA-BSs embedded within an AT-rich motif that enhances transcriptional termination (Porrua et al., 2012).

Detection of cognate sequences is favoured by the preceding interaction of the Nrd1-Nab3 heterodimer with the CTD of Pol II (Kubicek et al., 2012; Vasiljeva et al., 2008), which comprises 26 repeats of the sequence Tyr^{1}-Ser^{2}-Pro^{3}-Thr^{4}-Ser^{5}-Pro^{6}-

Ser[7] (Cramer et al., 2008). This occurs when the carboxyl-terminal domain-interacting domain (CID) of Nrd1 binds to the phosphorylated fifth serine residue (Ser5P) of the CTD of Pol II (Heo et al., 2013; Kubicek et al., 2012; Tudek et al., 2014; Vasiljeva et al., 2008) (Figure I.2). Given that Ser5 phosphorylation primarily occurs during early transcription (Kim et al., 2010; Mayer et al., 2010; Tietjen et al., 2010), it facilitates recognition of consensus sites by Nrd1 and tethered Nab3, and subsequently enables immediate recognition of the nascent RNA as transcription elongation takes place (Heo et al., 2013; Tudek et al., 2014).

Although cleavage of the primary transcript has never been characterised in this termination mode, it is known that the released transcript is rapidly targeted by the nuclear exosome (Allmang et al., 1999; Gudipati et al., 2012; Thiebaut et al., 2008, 2006; Vasiljeva and Buratowski, 2006). The coordination between NNS-dependent transcription termination and partial or complete digestion of the product transcript relies on a physical interplay between the NNS machinery and the Trf4-Air2-Mtr4 polyadenylation (TRAMP) complex to recruit the exosome (Tudek et al., 2014; Vasiljeva and Buratowski, 2006) (Figure I.2). Having attached to the phosphorylated serine residue of Pol II's CTD, Nrd1 engages the TRAMP complex through the Nrd1-interacting motif (NIM) of Trf4, one of the TRAMP constitutive factors. Since the NIM region of Trf4 mimics the CTD of Pol II to which Nrd1 was initially bound, the interaction of Nrd1 with Trf4 necessarily implies a conclusion of the precedent contact. The consecutiveness and exclusiveness of both interactions provide a basis for the synchronisation of transcription termination and exoribonucleolytic activity of the exosome (Tudek et al., 2014).

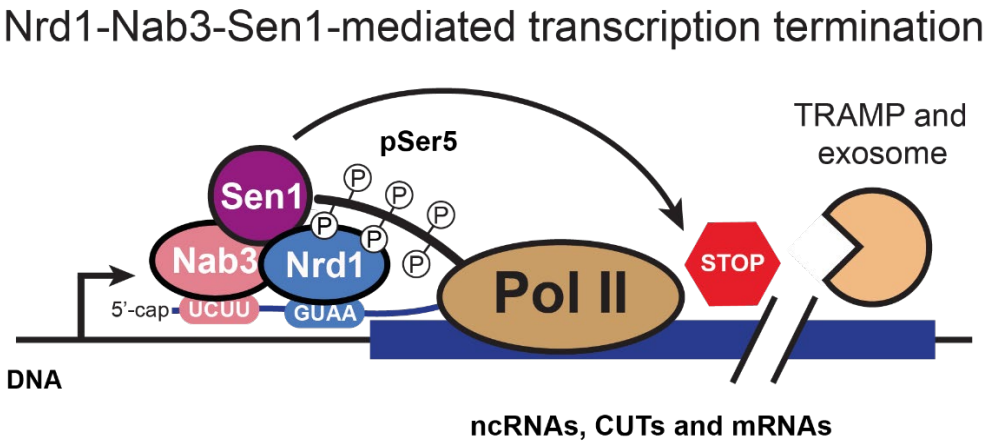

Figure I.2. Schematic representation of the NNS transcriptional termination pathway.

The TRAMP complex then introduces a short polyadenylation signal downstream of the released transcripts and labels the transcript for degradation by the exosome (LaCava et al., 2005; Vaňáčová et al., 2005; Wyers et al., 2005). The exosome is composed of 10-12 factors that are involved in the 3′ end digestion of non-coding RNA transcripts (Arigo et al., 2006; Mitchell et al., 1997; Thiebaut et al., 2006; Vasiljeva and Buratowski, 2006). Among these, two nucleases named Rrp6 and Dis3, are responsible for (i) trimming of the 3′ end of snRNA and snoRNA precursors to convert them into the mature species (Allmang et al., 1999; Gudipati et al., 2012; Hoof et al., 2000), and (ii) digesting CUTs (Arigo et al., 2006; Gudipati et al., 2012; Thiebaut et al., 2006; Wyers et al., 2005). Later studies also showed that premature truncation of protein-coding targets was also mediated by the combined action of the TRAMP complex and the exosome (Thiebaut et al., 2008; Tudek et al., 2014).

Although the cleavage mechanism and the release of Pol II in this pathway have not been fully described, work by the Libri and Buratowski groups suggests that Sen1 could direct both phenomena. *In vitro* experiments demonstrated that Sen1 is sufficient to dislodge the Pol II elongation complex from the DNA template (Porrua and Libri, 2013). Furthermore, the same study showed that cleavage of the nascent transcripts not only required the binding of Sen1 but also adenine triphosphate (ATP) and predominantly took place at Pol II pausing sites (Porrua and Libri, 2013). Subsequent *in vivo* assays proved that lowering the processivity of the polymerase elongation complex enhances NNS-dependent termination, whereas increasing its catalytic rate hampered NNS activity (Hazelbaker et al., 2013). Overall, both studies imply that Sen1 translocates to the nascent RNA to overtake Pol II and terminate transcription upon displacement of the transcript from the enzymatic active site. According to this model, Nrd1 would interact with the CTD of the polymerase and recruit Nab3. Together, the resulting Nrd1-Nab3 heterodimer would recognise their specific cognate sequences within the RNA target and serve as a structural platform for Sen1, which is a lowly expressed protein (i.e., 2549 +/- 843 molecules per cell (Ho et al., 2018)) and binds RNA in a seemingly non-specific manner (Jamonnak et al., 2011; Porrua and Libri, 2013). Sen1 would then hijack the elongation complex to release the polymerase. Nonetheless, it is also plausible that Nrd1 and Nab3 exert a more direct role in dismantling Pol II from its DNA template.

Even though the NNS-dependent pathway predominantly targets non-coding species, high-throughput studies have indicated that many protein-coding genes harbour Nrd1 and Nab3 binding sequences. Accordingly, UV cross-linking studies have illustrated that approximately 20-30% of all mRNAs in the transcriptome are bound by Nrd1 and Nab3 at those motifs (Creamer et al., 2011; Jamonnak et al., 2011; Wlotzka et al., 2011). Interestingly, previous works by the Tollervey and Granneman groups noted that, to orchestrate the changes in gene expression that cells require to endure glucose starvation, the NNS complex significantly changes its occupancy, and Nab3 binds differentially to around 25% of protein-coding transcripts (Bresson et al., 2017; van Nues et al., 2017). Comparison of Nab3 binding profiles in cells grown in media with and without glucose revealed that some of those Nab3-bound mRNAs encode stress-responsive proteins such as heat-shock factors, transmembrane sugar transporters, metabolic enzymes, antioxidant agents or mitochondrial proteins (van Nues et al., 2017) (Figure I.3). As a result of NNS-mediated transcriptional pausing during glucose starvation, RNA polymerase II accumulated in the upstream region of these genes (van Nues et al., 2017) (Figure I.3). Nonetheless, when Nab3 was conditionally sequestered in the cytoplasm using a previously reported methodology (Haruki et al., 2008), the NNS assembly onto mRNAs was impaired in the nucleus during glucose starvation, and, in turn, the RNA polymerase II could be mapped throughout these stress-specific NNS target genes (van Nues et al., 2017) (Figure I.3). Expression quantitation verified that the stress-specific NNS target genes were upregulated during glucose deprivation. In other words, during adaptation, Pol II might rapidly start transcribing a set of stress-responsive protein-coding genes shortly before the NNS complex prematurely terminates at least a fraction of its transcription complexes.

Most of these NNS mRNA targets contain CUTs or other pervasive RNAs whose transcription is initiated from a separate TSS laying distally, within or proximally to the transcribed region of the pertinent protein-coding gene (an example can be seen in Figure I.3). A holistic analysis of CUTs and SUTs concluded that they predominantly initiate from nucleosome-free regions (NFRs) enclosing the promoter of a protein-coding gene or succeeding its 3’ end (Xu et al., 2009). Therefore, divergent and overlapping transcription of pervasive RNAs was conjectured to serve as a mechanism coupling the transcriptional regulation of adjacent genes through transcriptional interference or chromatin remodelling (Xu et al., 2009). Consistent with this theory,

earlier work proposed that the nascent ribonucleotide sequence transcribed from the region in between some combinations of protein-coding and non-coding TSSs could work as a platform capturing Pol II molecules or enrolling histone-modifying enzymes (Berretta et al., 2008; Camblong et al., 2007; Thiebaut et al., 2008). Constant non-productive transcription starting from the CUT initiation site negatively correlates with transcription initiation from the mRNA TSS (Thiebaut et al., 2008). Although this regulatory mechanism and its preceding activation event remain unidentified, previous studies have suggested that the transcription of NNS mRNA targets may be dictated by nucleotide availability. For instance, lower concentrations of GTP, UTP and CTP have been reported to induce the expression of *IMD2*, *URA2* and *URA8*, which encode enzymes catalysing the rate-limiting steps of several nucleotide biosynthesis pathways (Ajazi et al., 2022; Kuehner and Brow, 2008; Thiebaut et al., 2008).

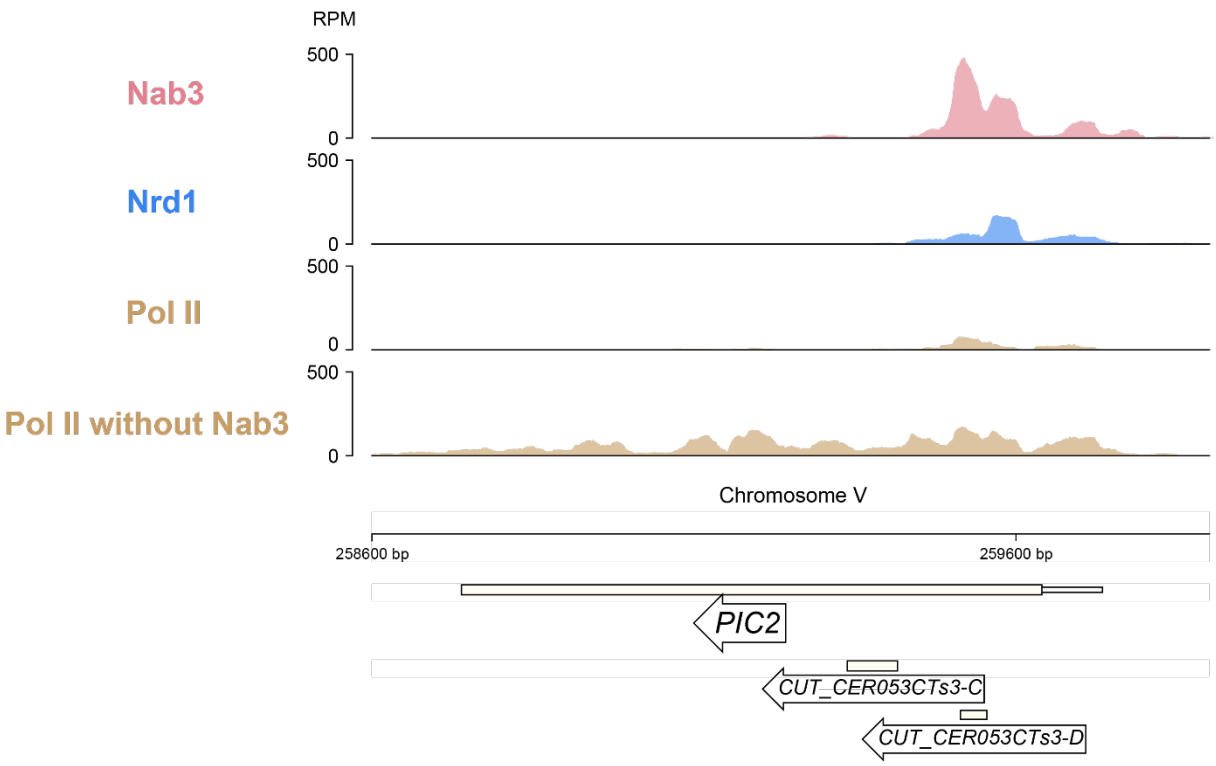

Figure I.3. RNA-binding footprints for Nab3, Nrd1 and Pol II in the locus of *PIC2*, a stress-responsive protein-coding target of the NNS complex which is upregulated during glucose depletion. Profiles show the reads per million (RPM) of bound RNA sequences for each RBP and were obtained from published sequencing data (GEO accession: GSE85545; van Nues et al., 2017).

Indeed, earlier work has speculated that the polymerase senses the nutritional shortages to which the NNS complex responds (Kwapisz et al., 2008). Mutational analyses in Pol II unveiled that amino acid substitutions modifying its switch 1 loop, which is a known sensor for inhibitors (Mukhopadhyay et al., 2008), favoured downstream mRNA TSS selection (Kwapisz et al., 2008). In combination, prior knowledge is consistent with the existence of an underlying common transcriptional regulation exerted by the NNS complex, subject to nutrient availability and directed to genes whose expression needs to be readjusted during nutrient shortages. On this basis, I hypothesised that specifically targeting this set of stress-responsive genes for transcription and termination could have evolved as a strategy to fine-tune their expression to a low, optimal level during sugar scarcity.

I.4. Investigating gene expression reprogramming during adaptation

From their synthesis to their degradation, RNAs are escorted by proteins that dictate their fate. In addition to transcription, interactions between RNA and proteins underlie co- and post-transcriptional processes, including RNA maturation, splicing, nuclear export, localisation, stability, translatability, and degradation. RNA-binding proteins (RBPs) fine-tune gene expression profiles which are essential to maintain cellular homeostasis.

Methodological developments during the last decade have vastly increased the technical repertoire to explore RNA-protein interactions *in vivo*. We recently wrote a comprehensive review discussing the advantages and pitfalls of many of these approaches (Esteban-Serna et al., 2023). Most methods to detect RNA-protein interactions are based on UV cross-linking, which entails irradiating cells with short wavelength (254 or 365 nm) UV light to induce the formation of covalent bonds between RBPs and directly bound transcripts (‘zero distance’; reviewed in (Urdaneta and Beckmann, 2020)). This property makes it possible to isolate RBP-bound RNAs under very stringent and denaturing conditions, significantly reducing noise. Although UV cross-linking is notoriously inefficient and biased towards coupling pyrimidines to a select number of amino acids (Urdaneta and Beckmann, 2020), it has become a hugely popular tool to study protein-nucleic acid interactions in living systems.

The most widely used techniques for globally identifying the RNAs bound to RBPs are cross-linking and immunoprecipitation (CLIP) and related protocols, such as CRAC, eCLIP, iCLIP and PAR-CLIP (Granneman et al., 2009; Hafner et al., 2010; Huppertz et al., 2014; Ule et al., 2003; van Nostrand et al., 2016) (Figure I.4). Like RBPome capture, these approaches rely on UV cross-linking of RBPs to their target transcripts (Figure I.4). To enrich for the cross-linked protein (and, therefore, the RNAs to which it is likely to bind directly), immunoprecipitations are generally performed under (semi-)denaturing conditions (Granneman et al., 2009; Hafner et al., 2010; Ule et al., 2003; van Nostrand et al., 2016) (Figure I.4). Following RNase trimming of unshielded ribonucleotide sequences, adapter ligation and proteinase K digestion of the cross-linked RNPs, the captured transcripts can be purified and reverse transcribed into complementary DNA (cDNA) (Figure I.4). Subsequently, high-throughput sequencing of the resulting cDNA library allows transcriptome-wide mapping of the sites to which the tested RBP was binding (Figure I.4).

The applicability of CLIP-derived procedures is contingent on the extent of their background. A general assumption of these protocols is that random binding is hampered by the harsh washing steps succeeding immunoprecipitation. Moreover, electrophoretic resolution of the RNPs under fully denaturing conditions ensures an additional enrichment step, as only cross-linked RNAs will co-migrate with the RBP in the gel. Preferred negative control samples are typically CLIP experiments with cells where the RBP is knocked out or untagged or which have not been UV treated (Granneman et al., 2009; König et al., 2010; Lee and Ule, 2018; Ule et al., 2003). In principle, these samples are not expected to produce noticeable signals upon sodium dodecyl sulphate polyacrylamide gel electrophoresis (SDS-PAGE) visualisation. Based on our experiences with CRAC, libraries emerging from the sequences in the areas corresponding to the expected migration of the RNP under study should contain 100-fold fewer unique cDNAs than those resulting from fully treated samples (Chu et al., 2022; König et al., 2010). Nonetheless, a meta-analysis of 30 published PAR-CLIP datasets derived from various human RBPs identified widespread and replicable background reads across most of them (Friedersdorf and Keene, 2014). To quantify technical background, prior work sequenced libraries proceeding from RNA-protein adducts that did not migrate with the duplexes of interest (Friedersdorf and Keene, 2014). Adjusting output signals to those originated by background characterisation was shown to dramatically improve the identification of RNA recognition sequences

(Friedersdorf and Keene, 2014). Based on relevant control samples, background correction can indeed statistically disregard binding events resulting from non-specific transcript cross-linking to incidentally proximal RBPs of interest and co-purified RNPs.

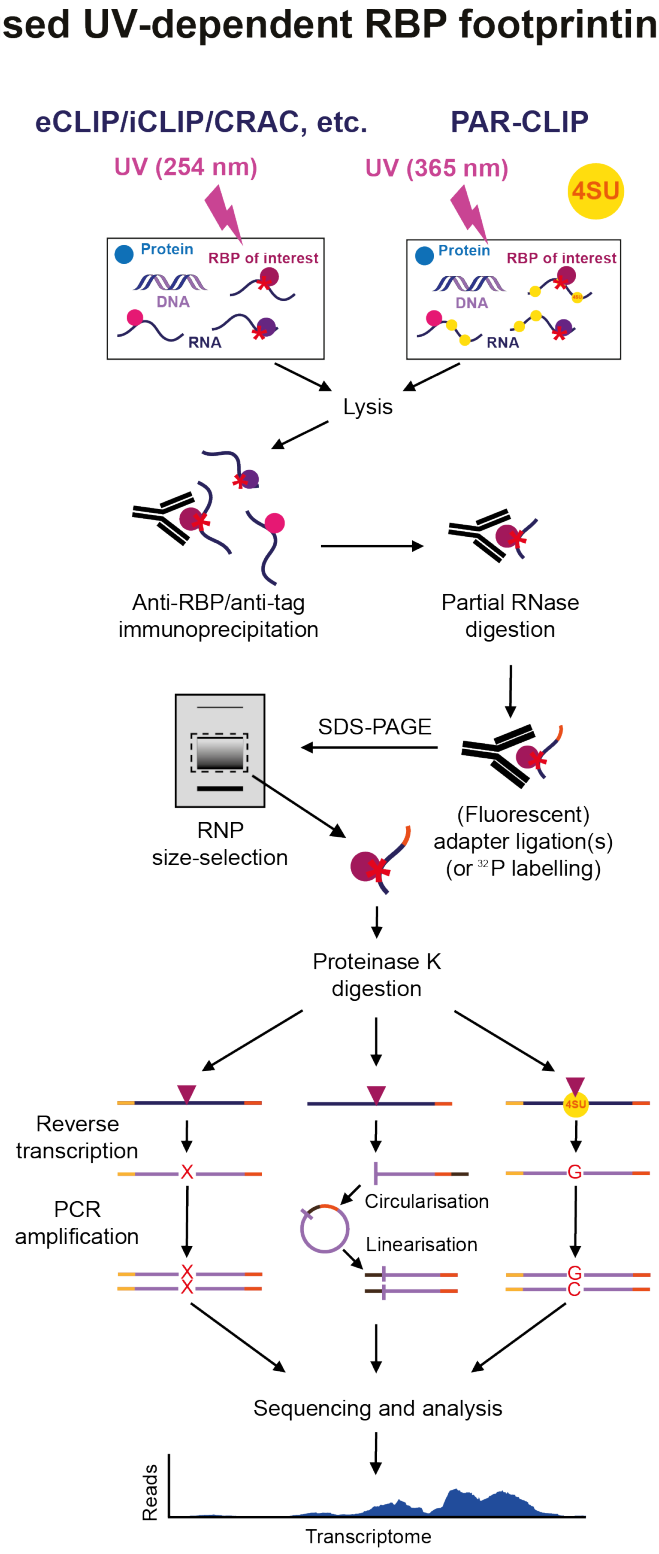

Figure I.4. Diagrammatic overview of some of the most prominent UV-dependent RBP footprinting techniques (e.g., CLIP, CRAC, iCLIP and PAR-CLIP) adapted from

Esteban-Serna et al., 2023. These protein-centric approaches use stringent affinity purification methods to isolate the protein of interest and to enrich the cross-linked RNAs. PAR-CLIP also employs uracil/uridine analogues (e.g., 4-thiouracil) for protein-RNA cross-linking. Together, these procedures allow the detection and functional characterisation of RNA binders in many organisms.

Several CLIP-related approaches have been specifically designed to further improve signal-to-noise ratios. These methods take full advantage of the fact that cross-linked RNPs can withstand highly denaturing purification conditions. These techniques include cross-linking and analysis of cDNAs (CRAC), ultraviolet crosslinking and affinity purification (uvCLAP), denaturing CLIP (dCLIP) and 'Fast Ligation of RNA After Some sort of affinity purification for High-throughput sequencing' (FLASH) (Granneman et al., 2009; Ilik et al., 2019; Maticzka et al., 2018; Rosenberg et al., 2017). All these protocols employ (tandem) affinity-based purification to recognise specific epitope tags that are compatible with denaturing purification conditions and/or strong detergents (e.g., HIS-tag and streptavidin-binding peptides sequences; Fig. 1) (Granneman et al., 2009; Maticzka et al., 2018; Rosenberg et al., 2017). Admittedly, epitope tagging can alter the stability, expression, and RNA-binding capacity of the RBP of interest. Advantageously, however, specific tag recognition-based partition spares the need for high-quality antibodies, which are not readily available for less well-studied model organisms. Accordingly, these approaches can considerably reduce background reads in resulting cDNA libraries. This property also makes them good alternatives to inspect scarcer RNPs, namely yeast pre-ribosomal complexes or those encompassing non-professional RBPs (Chu et al., 2022; Granneman et al., 2009).

To identify the transcriptomic sites comprising the RNA-binding footprint of the RBP under study, previous works have developed several tools to analyse the sequencing outputs of CLIP-seq libraries (De and Gorospe, 2017). Such process is widely referred to as 'peak calling' and broadly encompasses two steps (Uhl et al., 2017). First, peak callers determine the transcriptomic regions where reads are more prevalent in a pre-set threshold or background. Secondly, they calculate the statistical significance of the pre-selected enrichments, incorporating additional meta-data such as biological replicates, negative controls, and transcriptomic abundance to increase the signal-to-noise ratio.

I.4.1. Bioinformatics approaches for analysing CLIP/CRAC datasets

Despite displaying a wealth of features that make them suitable for different contexts, the applicability of available peak-calling options depends on the data's signature and technical implications. Some of the most widely used options have been iCount (König et al., 2010), Pyicoclip (Althammer et al., 2011), Piranha (Uren et al., 2012), ASPeak (Kucukural et al., 2013), CLIPper (Lovci et al., 2013), pyCRAC (Webb et al., 2014), PureCLIP (Krakau et al., 2017) and PEAKachu (Bischler et al., 2021), although more programs have been created - and reviewed (Chen et al., 2019) - in previous works. An essential drawback of the current software offer is that, having been developed to target specific experimental setups, technical outputs and biological questions, its usage is context-limited. For instance, while biological replicates cannot be considered by Piranha, a minimum of two independent experiments is required for PEAKachu, which uses the DESeq2 package to identify enriched clusters, which it will then render as peaks (Love et al., 2014). Overall, this heterogeneity has resulted in a lack of reproducibility in the analyses of CLIP-seq data. Later efforts to overcome this challenge have been PIPE-CLIP (Chen et al., 2014), CLIPSeqTools (Maragkakis et al., 2016), CLIP-Explorer (Heyl et al., 2020), which have compiled existing tools into streamlined pipelines and/or web servers that ease the analysis of eCLIP, FLASH, uvCLAP, and iCLIP sequencing outputs.

Statistical approaches to defining and filtering peaks also depend on the technique that was applied to generate the libraries. CLIP-seq methods typically use zero-truncated negative binomial regression to model read counts, as it was previously shown that this approach was the best fit for reads proceeding from 100 CLIP-seq datasets (Chen et al., 2019). Briefly, these tools compute the probability that a given bin is also present in the size-match input or control library and assign a p-value to each group. However, modelling genomic background inevitably reduces the sensitivity of peak calling in lowly expressed genes. To overcome this limitation, Pyicoclip (Althammer et al., 2011), iCount (König et al., 2010), ASPeak (Kucukural et al., 2013), CLIPper (Lovci et al., 2013) and pyCRAC (Webb et al., 2014) generate background controls by randomly shuffling the read counts of the experimental library in user-defined genomic regions. Notably, however, this strategy requires an annotation file in which intergenic regions are marked since peaks falling in undefined loci will be discarded otherwise. In turn, this approach is more computationally

demanding as the number of calculations to be performed scales up with the number of features in the annotation file.

Regardless, from our own tests, we have learned that many of the available workflows were difficult to implement on our servers or were not reliable enough to query whether the binding of one given protein decreased for a single gene in the transcriptome or whether its occupancy on a set of sites became somewhat abated or redistributed in a different condition or mutant. Having identified this necessity, Prof Sander Granneman developed a new package called DBPeaks, that makes use of the pyCRAC suite (Webb et al., 2014). If the binding of Nrd1 and Nab3 was, as anticipated, visibly abrogated in the strains encoding mutated versions of their cognate sequences in *PIC2*, the peak caller used should identify those sites as differentially bound. More widely, the aim of the newly developed set of functions was to detect differentially bound peaks in the occupancy profile of the NNS complex and the polymerase in different conditions and mutants.

I.5. Gene expression noise: definition, causes, impact on fitness and mechanisms to suppress it.

Gene expression comprises all biochemical processes involved in regulating the quantity of gene products (Raser and O'Shea, 2005). These reactions include, for instance, the maintenance and replication of the genome, the transcription of the DNA into RNA, the processing of the resulting transcript and the translation of such RNAs into proteins. Each of these steps introduces a variability that ultimately adds a variation in the theoretical outcome of the gene expression profile of any given cell.

In addition to that inherent source of variation, gene expression can also be modified by the internal state of a cell and the subsequent impact that such a status will have on the concentration of the substrate for each reaction. For example, the number of copies of DNA, RNA and proteins for a given gene is subject to preordained physiological processes, such as cell cycle progression and to the unpredictability of the stimuli to which that system will have to respond, such as nutrient deprivation. In the latter case, the accompanying gene expression changes will depend on the magnitude of the environmental challenge being faced and the inherent variability of

all the molecular events leading to the communication of the extracellular insult to the machinery controlling gene expression. Moreover, the constant occurrence of genetic alterations represents an additional layer of variability in the gene expression output of any cell of an initially isogenic population. Thus, in summary, gene expression variation among an identical population of cells can stem from (i) intrinsic stochasticity in the reactions preceding the synthesis of the gene product, (ii) the intracellular condition of the cell, (iii) the extracellular circumstances affecting that cell and (iv) the persistent influx of genetic mutations in every cell (Wang and Zhang, 2011).

The resulting stochasticity in the output of gene expression across an isogenic cell population is referred to as 'noise'. While the inherent variability in the biochemical process leading to variations in the production of a gene product is considered 'intrinsic' noise, all other sources of stochasticity are deemed 'extrinsic' noise (Elowitz et al., 2002; Swain et al., 2002). Cell-to-cell variation in the expression of a single gene can then be considered a measure of the overall noise for that gene resulting from the intrinsic and extrinsic factors contributing to it (Swain et al., 2002). Broadly, noise can be described as the relative deviation from the mean gene expression levels. Mathematically, noise can thus be defined as the standard deviation in the expression of a given gene divided by the average expression of that same gene ($\eta = \sigma/N$). In other words, noise can be calculated as the coefficient of variation in gene expression. In this study, I have used said mathematical definition of noise to quantify cell-to-cell variations in gene expression. Nevertheless, some reports measure cell-to-cell variability using the concept of 'noise strength', which applies the relative variance (i.e., σ^2, which corresponds to the squared standard deviation) measure divided by the mean expression of that gene in the population ($\phi = \sigma^2/N$) (Thattai and van Oudenaarden, 2001).

Suppose the average expression for a given gene within a population corresponds to the theoretical optimal levels for the expression of that gene. In that case, the immediate consequence of stochasticity in gene expression is that, necessarily, it brings on a suboptimal level of the gene product. For this reason, gene expression noise poses an efficient strategy to provide phenotypic heterogeneity. In microorganisms, this capacity is theoretically beneficial for a population to rapidly switch between phenotypic states and, accordingly, adapt to abrupt changes or fluctuating environments (Thattai and van Oudenaarden, 2004). Examples illustrating

this principle have been provided in persistent bacterial infections amidst antibiotic treatment (Balaban et al., 2004) or, more loosely, in the galactose consumption network of yeast (Acar et al., 2005). Yet, inadequate expression of a gene is disadvantageous for the population in most scenarios. With the aim of assessing the detrimental effect that 'noisy' expression of a given gene will have in a population, previous work has modelled and tested the impact that a range of suboptimal enzymatic expressions have in the adaptation and adaptability of an identical cell population (Wang and Zhang, 2011). Experimental quantification and modelling predictions revealed that stochasticity in gene expression lowered fitness by no less than 25% and that this fitness penalisation was greater when the noise increased in essential genes compared to non-essential ones (Wang and Zhang, 2011). Moreover, the same study illustrated that increased cell-to-cell variation in gene expression hindered natural selection and ultimately led to population shrinkage during environmental changes (Wang and Zhang, 2011).

Different cellular systems have developed distinct noise-suppressing strategies throughout evolution to reduce the consequences of stochasticity in gene expression. Theoretically, microRNAs have emerged as the best possible linear noise filter in eukaryotic cells (Ilker and Hinczewski, 2024). These non-coding transcripts lay at the heart of the RNA-induced silencing complex (RISC), which hybridises to a target mRNA and degrades it to fine-tune the noise in the encoded protein census (Ilker and Hinczewski, 2024). In doing so, miRNAs diminish cell-to-cell variation in protein concentration and enhance the robustness of cellular processes (Siciliano et al., 2013). Despite lacking miRNAs, budding yeast may possess alternative mechanisms to suppress stochasticity (Ilker and Hinczewski, 2024). In principle, provided a constant level of gene expression, protein noise can be reduced by enhancing transcription and either repressing translation rates or increasing RNA degradation (Ilker and Hinczewski, 2024). Still, to my knowledge, no natural noise-suppressing mechanisms have been identified in *S. cerevisiae*.

As described in I.2, while profiling Nab3 binding footprint during glucose deprivation, our group observed that the NNS complex dampened the transcription of several stress-responsive genes to ensure that they were expressed lowly and stably throughout the duration of the environmental challenge (van Nues et al., 2017) (Figure I.5). Therefore, we proposed that Nab3 could be suppressing transcriptional noise by

preventing abnormally high expression levels of stress-specific target genes during adaptive responses. Accordingly, Nab3 could modulate the delay between exposure to a given environmental challenge and the beginning of adapting gene expression or allow a rapid increase in transcription levels when the stress signal reaches a particular threshold. If so, NNS-mediated noise suppression would prevent the induction of adaptive gene expression patterns by spurious signals. To test this hypothesis, I selected one of the identified stress-specific NNS target genes, *PIC2*, which codes for a mitochondrial transporter and could, thus, be potentially related to energy homeostasis during starvation.

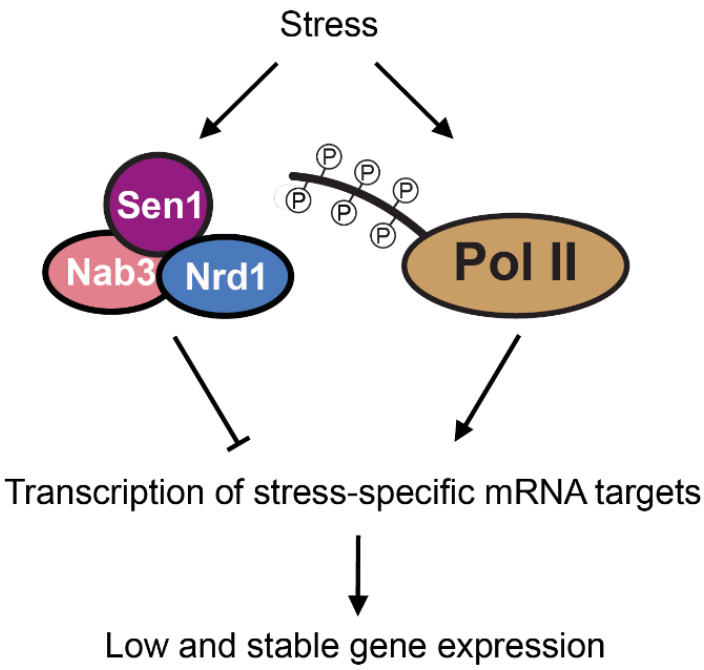

Figure I.5. Graphical summary of the main hypothesis: initiating and terminating transcription of key protein-coding genes during adaptation is a mechanism for tightly controlling their expression and maximising chances of surviving a given stress.

Intriguingly, my meta-analysis of published single-cell RNA-sequencing (scRNA-seq) data from nineteen human fibroblasts demonstrated that transcriptional noise of *SLC25A3*, the functionally conserved mammalian homologue of *PIC2*, was comparable to those of constitutively expressed genes such as *ACTB*, *GAPDH*, *RPL39A and ALDOA* (Padovan-Merhar et al., 2015) (Figure I.6). Therefore, its yeast equivalent seemed like a particularly suitable target to investigate whether NNS regulation would have any role in tightly controlling its expression noise. Moreover, interestingly, in mammalians, repression of *SLC25A3* is undertaken by the miR-141

micro-RNA (Baseler et al., 2012). Since this noise-suppressing mechanism was unavailable in yeast, I embarked on assessing whether the NNS assumed that noise-suppressing role in *PIC2* and, generally, with its other mRNA targets.

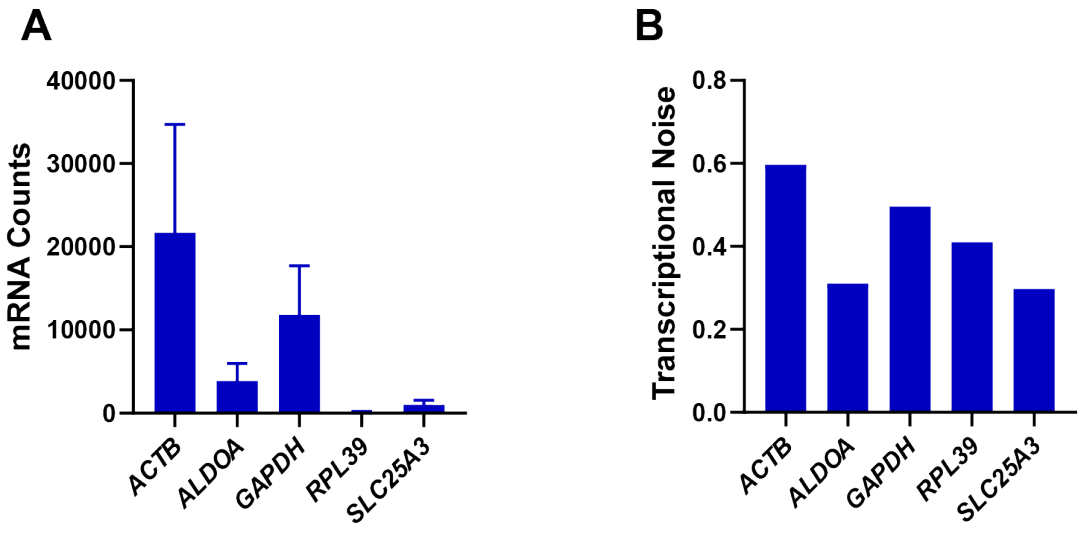

Figure I.6. *SLC25A3,* the mammalian homologue of *PIC2*, is a stably expressed gene. **A**. mRNA counts for *SLC25A3* and four housekeeping genes, namely *ACTB*, *ALDOA*, *GAPDH* and *RPL39,* widely used as standards in gene expression analyses. **B**. The transcriptional noise of *SLC25A3*, which is defined as the coefficient of variation of gene expression (i.e., mRNA counts), is lower than any of the tested reference genes.

I.6. Pic2, a eukaryotic mitochondrial phosphate and copper carrier conserved in mammalian cells.

Pic2 is a mitochondrial copper uniporter and phosphate/proton symporter of the inner mitochondrial membrane (IMM), which belongs to the evolutionarily conserved mitochondrial carrier family (MCF/SLC25). MCFs represent the most prominent family of mitochondrial proteins, encompassing around 35 factors in yeast and more than 50 carriers in humans and plants (Palmieri et al., 2000; Picault et al., 2004; Wohlrab, 2006). Altogether, this family of transporters constitutes the primary machinery for the transit of substrates, such as copper, iron, phosphate, or Krebs cycle intermediates for energy production; nucleoside phosphates for respiration and mitochondrial DNA replication; or amino acids for their metabolism and the preservation of the urea cycle.

Typically, MCF carriers are composed of three conserved sets of two membrane-spanning helices enclosed between N and C termini exposed to the intermembrane space (Figure I.7). The arrangement of the transmembrane segments displays a three-fold symmetry and allows sequential motifs to mediate the establishment of salt bridges (Robinson et al., 2008). Interspacing the transmembrane domains, these proteins display short α-helices that are essential for solute transport (Ruprecht and Kunji, 2020) (Figure I.7). Despite having arisen from phylogenetic duplication of a generalist ancestor gene and sharing an obvious structural resemblance, the members of this family have evolved different solute selectivity to supply the mitochondria with substrates for different functions. Yet, the molecular details of how this specificity is executed remain mostly uncharacterised. Some recent works have shown that single-residue mutations can be sufficient to elicit deficient transport of only one substrate in a transporter which shuttles more than one solute (King et al., 2020; Knight et al., 2019). But, ultimately, only one study has reported that the same transporter, Pic2, employs a different set of amino acids from its conserved structural arrangement to effectuate phosphate and copper transport (Runswick et al., 1987).

Embedded in their helical structures, MCFs display PX(D/E)XX(R/K) motifs that are thought to mediate the narrowing of the pore within the transporter and form salt bridges which ultimately lock the carrier in a closed state when facing the matrix (Kunji and Robinson, 2006; Pebay-Peyroula et al., 2003; Robinson et al., 2008). These non-covalent interactions succumb to substrate binding and trigger a conformational change in which the pore opens to the intermembrane space, permitting translocation of the solute into the mitochondrial matrix. Although the structure of many of these MCFs remains unresolved, sequential analyses have been applied to generate predictions determining whether individual members of the family can act as uniporters or exchangers (Robinson et al., 2008). Such analyses have suggested that the salt bridge network within Pic2's intermembrane space-facing configuration is expected to be more robust than the one established during its matrix-facing conformation. On this basis, Pic2 is consensually thought to behave as a copper uniporter (Robinson et al., 2008). Mechanistically, the greater relative strength of the intermembrane space-facing conformation would, in turn, revert the protein to its original configuration upon substrate translocation (Robinson et al., 2008).

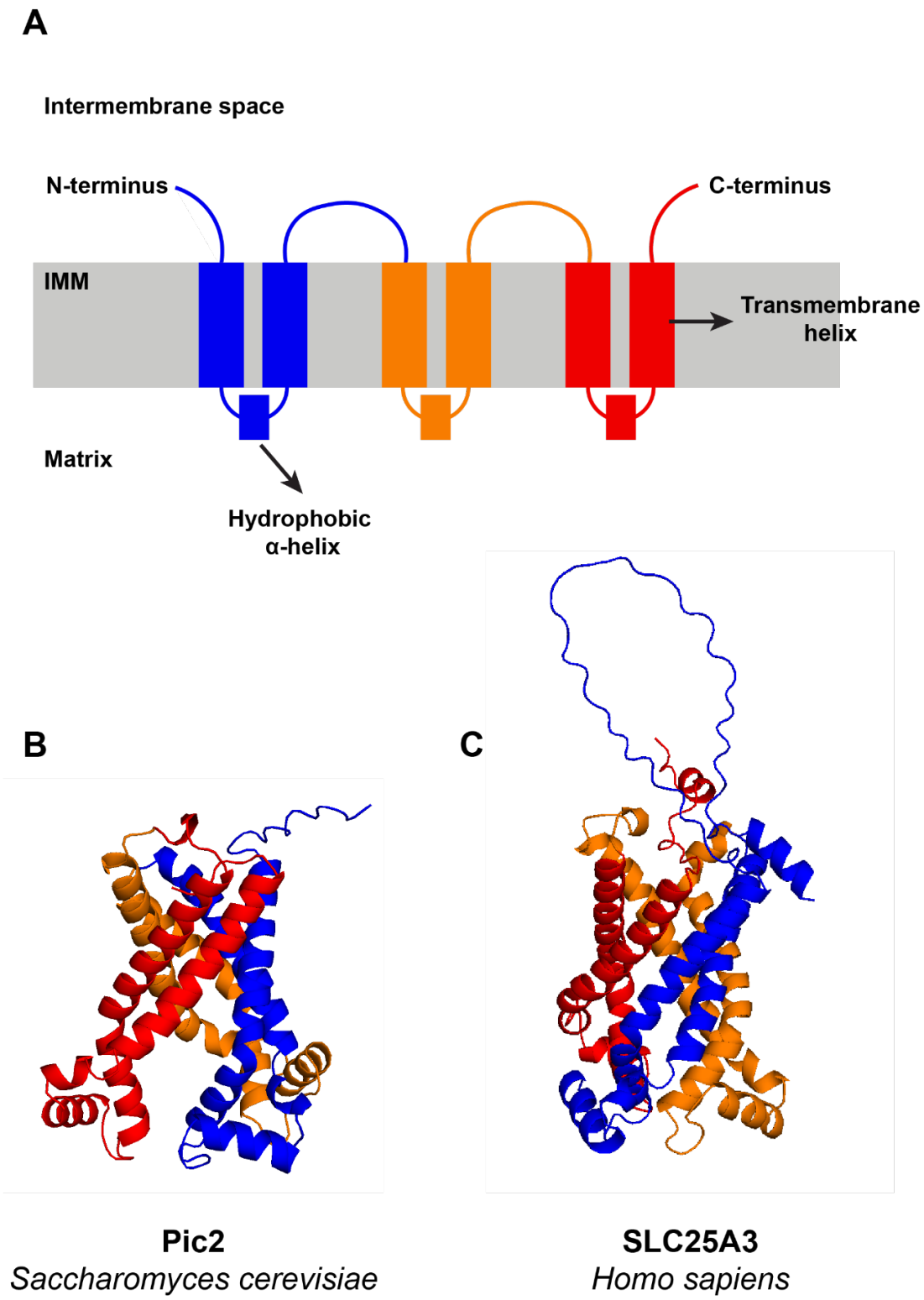

Figure I.7. Schematic representation of a typical MCF structure (**A**) and models of the structural predictions for Pic2 (**B**) and its mammalian homologue SLC25A3 (**C**). The N-terminal and C-terminal pairs of transmembrane helices are displayed in blue and red, respectively. The central helices are coloured orange. The structures of both proteins were predicted by AlphaFold and visualised with PyMOL (Jumper et al., 2021; Schrödinger, 2020).

Due to its potential toxicity, freely available copper is seldom available in intracellular contexts. Thus, the trafficking of copper into the mitochondria is undertaken by a complex including factors such as COX17, COX11 or SCO1/2 in mammalians or a non-proteinaceous copper ligand (CuL) in yeast. In yeast and humans, Pic2 oversees the maintenance of the copper reservoir within the mitochondrial matrix (Baker et al., 2017). The copper pool of the mitochondrial matrix serves a dual role. On the one hand, it buffers the concentration of copper in the cytosol. On the other hand, it feeds the synthesis of the active sites of (i) the cytochrome *c* oxidase (COX), the terminal enzyme complex of the electron transport chain (ETC; Balamurugan and Schaffner, 2006; Leary et al., 2004; Morgada et al., 2015), which is ingrained in the inner mitochondrial membrane, and (ii) the superoxide dismutase, an antioxidant catalyst that scavenges reactive oxygen species through oxidation or reduction.

Previous work has established that Pic2 is the primary Cu transporter in *Saccharomyces cerevisiae* (Vest et al., 2013). Accordingly, yeast mutants lacking *PIC2* (*pic2*∆) exhibit reduced mitochondrial copper concentrations and deficient COX synthesis. As a result, such knock-out strains display severe growth defects when grown in non-fermentable carbon sources such as glycerol (Hamel et al., 2004; Vest et al., 2013). In addition to copper, Pic2 is also able to mediate the simultaneous transport of a phosphate ion – i.e., $H_2PO_4^-$, often denoted as Pi (Wohlrab, 2006) - and an accompanying proton across the inner mitochondrial membrane (Fiermonte et al., 1998; Hamel et al., 2004; Kolbe et al., 1984). Once in the mitochondrial matrix, phosphate groups are incorporated into ADP molecules to generate ATP via oxidative phosphorylation.

In yeast, the main portion of the mitochondrial phosphate pool, however, is preserved by *MIR1* (Phelps et al., 1991; Takabatake et al., 2001), the primary phosphate-transporting MCF. Overall, Mir1 and Pic2 display considerable sequential resemblance as 40% of their amino acids are identical (Hamel et al., 2004). Furthermore, of the 22 residues known to participate in phosphate/proton transport in Mir1, 18 are also present in Pic2 (Hamel et al., 2004). Importantly, the five amino acids which are essential for phosphate transport, particularly the lysine 63 (K63) residue, were conserved in Pic2 (Briggs et al., 1999; Hamel et al., 2004). Albeit consistent with a phosphate-carrying function of Pic2, this evidence was initially contradicted by the

fact that *in vitro* reconstitution and heterologous expression of Pic2 failed to display phosphate transport activity (Takabatake et al., 2001; Wohlrab et al., 2002). In combination, these findings cast doubt on whether Pic2 was indeed a mitochondrial phosphate import in yeast. Nonetheless, it was later discovered that Pic2 expression can rescue *mir1*Δ mutants, and its overexpression can restore phosphate transit in the *mir1*Δ*pic2*Δ double mutant (Hamel et al., 2004). Yet, since depletion of *PIC2* did not yield a visible phosphate deficiency phenotypic signature in yeast (Zhu et al., 2021), Pic2 is widely accepted to be a secondary transporter of phosphate into the matrix of *S. cerevisiae*.

The mammalian homologue of *PIC2* is referred to as *SLC25A3*. Sequence homology comparisons have determined that the human mitochondrial phosphate transporter encoded by *SLC25A3* has 48% identity to the yeast Pic2 (Seifert et al., 2015). Consistent with this notion, AlphaFold predicted a high structural resemblance between both orthologues (Jumper et al., 2021) (Figure I.7). As in yeast, phosphate import to the mammalian mitochondrial matrix is known to be electroneutral. In other words, phosphate can be symported with a proton or antiported with a hydroxyl group (OH^-) (Wohlrab, 2006); however, to my knowledge, the latter exchanging role has not been documented in *S. cerevisiae* yet. Mammals lack an equivalent of Mir1, and thus, SLC25A3 assumes the role of major mitochondrial carrier of phosphate and copper (Boulet et al., 2017; Kwong et al., 2014). SLC25A3 can be present in two different isoforms stemming from alternative splicing of exon three and, hence, possess a differing sequence between amino acids 54 and 80. Each of these SLC25A3 subtypes is expressed in different tissues: whilst cardiac and skeletal myocytes produce SLC25A3-A, all other cell types synthesise SLC25A3-B (Dolce et al., 1996, 1994; Fiermonte et al., 1998). To compare the functional features of these transporters, both isoforms were heterologously expressed in liposomes from *Escherichia coli*. Following purification and biochemical characterisation, it was determined that while SLC25A3-A displayed a higher affinity for phosphate substrate, SLC25A3-B had a ~3-fold higher maximal transport rate for phosphate substrates (Fiermonte et al., 1998).

Experimental evidence strongly suggests that the principal activity of SLC25A3 is to supply Pi for oxidative phosphorylation (Fiermonte et al., 1998; Kwong et al., 2014; Wohlrab et al., 1986). Consequently, altering the amino acid sequence of such transporter has been observed to cause insufficient phosphate transit and, ultimately,

defective muscle function and development. For example, mutations in SLC25A3-A have been linked to lactic acidosis, hypertrophic cardiomyopathy, and muscular hypotonia (Oehler et al., 2009b; Peoples et al., 2021b). Some other studies attributed such multisystem disorders to a muscle-specific deficiency in ATP synthesis (Boulet et al., 2017; Mayr et al., 2007; Mayr et al., 2011).

Indeed, myocytes have a higher demand for ATP production, but to meet such energetic requirements, these cells contain larger mitochondrial populations to withstand increased metabolic demands (Moyes et al., 1997; Remels et al., 2010). Unavoidably, increased mitochondrial biogenesis needs to be partially sustained by enhanced synthesis of the electron transport chain enzymes embedded in the inner mitochondrial membrane, such as cytochrome *c* oxidase (COX), which, as its yeast counterpart, encloses copper in its catalytic site. Moreover, apart from the intrinsically higher demand for copper in skeletal muscle, primary myoblasts, which are muscle cell precursor cells, enhance their copper uptake during proliferation and differentiation (Vest et al., 2018). This increase in intracellular copper concentration is orchestrated by a defined expression pattern of CTR1, ATP7A, and ATP7B during differentiation (Vest et al., 2018). Once inside the cell, in addition to its mentioned implication in energetic supply, copper is sufficient to activate the metal-sensing MTF1 transcription factor, which subsequently prompts myogenesis (Vest et al., 2018).

Recent work established that one of the genes which MTF1 upregulates during skeletal muscle differentiation progression is *SLC25A3* (McCann et al., 2022). Consistent with the notion that SLC25A3 is required for the proliferation and differentiation of skeletal muscle cell precursors, deleting *SLC25A3* in primary myoblasts resulted in slower growth and delayed myogenesis (McCann et al., 2022). Given that these defects were overcome upon the addition of copper into the growth medium, it has been inferred that the contribution of SLC25A3 during differentiation arises from its role as a mitochondrial copper transporter (McCann et al., 2022).

In contrast to its yeast counterpart, the mammalian SLC25A3 is a well-characterised phosphate carrier with a minor copper-importing function (Boulet et al., 2017). Apart from exerting such roles in myocytes, SLC25A3 is also critical for other cell types, as knocking out *SLC25A3* or depleting copper in the mitochondrial matrix results in defective COX activity in non-muscular cell types (Boulet et al., 2017). To

further substantiate this broader role as a copper importer, the same study reported that SLC25A3-A physically interacted with COX, suggesting a major role of the mentioned transporter in the copper supplies needed for COX assembly (Boulet et al., 2017). At a molecular level, the copper-transporting capacity of SLC25A3 has been tested by heterologously expressing it in reconstituted liposomes and Lactobacillus *lactis* (Boulet et al., 2017).

I.7. Carbon metabolism in yeast

Having colonised a wide diversity of environments and adapted to their changes, yeast have developed metabolic pathways that enable them to uptake and process a wide range of available nutrients. However, despite being able to sustain growth in several carbon sources such as alcohols, organic acids and amino acids, yeast favours sugar metabolism (Rodrigues et al., 2006). The latter compounds are catalysed by metabolic networks that ultimately break down hexoses, which include fructose, galactose, glucose and mannose; disaccharides, namely maltose or sucrose; or trisaccharides, as raffinose, for instance, into pyruvate. Raffinose is a trisaccharide formed by galactose, glucose and fructose linked by an α and β glycosidic bond, respectively (Zhou et al., 2017b, 2017a). Considering its enzymatic asset, *S. cerevisiae* can only hydrolyse the latter bond using invertase. This digestion yields fructose (Figure I.8), which is an input for glycolysis, and melibiose, which, in the used yeast species, cannot be metabolised any further (Zhou et al., 2017b, 2017a). Melibiose could be further broken down into constitutive glucose and galactose molecules using the enzyme Mel1 which, albeit present in other yeast such as *Saccharomyces pastorianus*, is absent in *S. cerevisiae* (Turakainen et al., 1993).

Disaccharides are hydrolysed into hexoses which are typically modified by hexokinases (Hxk1 and Hxk2) and isomerases, such as the glucose 6-phosphate isomerase (GPI), to enter glycolysis as fructose 6-phosphate moieties (Dickinson and Schweizer, 2004) (Figure I.8). Subsequently, phosphofructokinase (PFK), phosphorylates fructose 6-phosphate to fructose 1,6-bisphosphate consuming ATP (Figure I.8). However, the cumulative action of aldolase (ALD), triosephosphate isomerase (TPI), glyceraldehyde 3-phosphate dehydrogenase (GAPDH), phosphoglycerate kinase (PGK), phosphoglycerate mutase (PGM), enolase and

pyruvate kinase (PK) throughout the remaining steps of glycolysis ultimately yields pyruvate alongside ATP and NADH (Figure I.8). At this point, pyruvate can enter fermentation or respiration. For fermentative growth, pyruvate is transformed into acetaldehyde by the pyruvate decarboxylase (PDC) and lastly reduced to ethanol by the alcohol dehydrogenase (ADH) (Dickinson and Schweizer, 2004; Pronk et al., 1996) (Figure I.8). Alternatively, pyruvate can be used as a substrate for pyruvate dehydrogenase (PDH) to proceed with downstream respiration (Figure I.8). PDH is a mitochondrial-based multi-enzymatic complex formed by pyruvate decarboxylase, lipoate acetyltransferase and lipoamide dehydrogenase, as well as the coenzymes thiamine pyrophosphate, lipoic acid, coenzyme A (CoA), oxidised flavin adenine dinucleotide (FAD) and oxidised nicotinamide adenine dinucleotide (NAD^+), which collectively catalyses the conversion of pyruvate to acetyl coenzyme A (acetyl-CoA) (Dickinson and Schweizer, 2004; Pronk et al., 1996) (Figure I.8). Such product can then enter the tricarboxylic acid (TCA) or Krebs cycle to generate reducing agents that fuel ATP production via oxidative phosphorylation (Dickinson and Schweizer, 2004; Pronk et al., 1996) (Figure I.8).

Since pyruvate can be assimilated by yeast via its membrane permease Jen1 (Figure I.8), it is possible for yeast to grow in medium containing pyruvate as a carbon source (Pronk et al., 1996). Nevertheless, since pyruvate fermentation is solely able to regenerate the oxidised NAD pool required for the preceding ATP-producing glycolysis, cultures supplemented with pyruvate as the main carbon source will have to undergo respiration to meet the energetic demands to sustain cellular functions (Pronk et al., 1996) (Figure I.8). Throughout this study, I exploited this principle to ensure that respiration would be equally activated in all tested cultures.

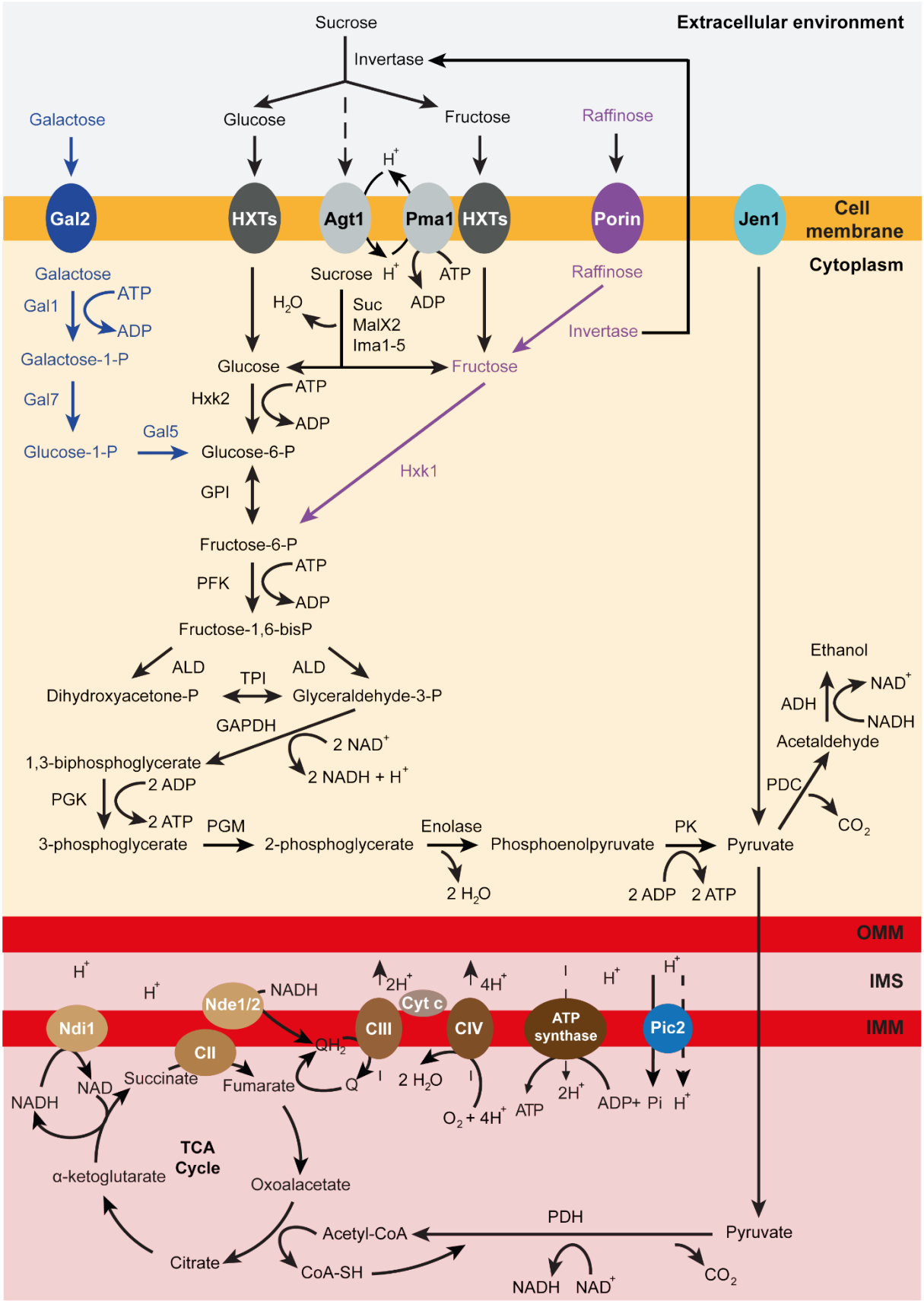

Figure I.8. Diagrammatic overview of the metabolic pathways breaking down the sugars used throughout this study. Abbreviations for the enzymes shown in the

schematic are defined in the preceding paragraph. OMM, IMS, and IMM stand for outer mitochondrial membrane, intermembrane space, and inner mitochondrial membrane.

Glucose is the preferred carbon source for yeast (Kayikci and Nielsen, 2015). Being a facultative anaerobe, *S. cerevisiae,* will ferment available glucose to ethanol if the former exceeds a concentration of 150 mg/L independently from the presence of oxygen (Verduyn et al., 1984). This phenomenon is referred to as the Crabtree effect and encompasses aerobic fermentation and glucose-mediated repression of respiratory catabolism (Herbert Grace Crabtree, 1929; Swanson and Clifton, 1948; Vemuri et al., 2007). Consequently, when grown in medium simultaneously containing glucose and any other carbon source, yeast will consume glucose first; only once it exhausts the available glucose reserve will it start catalysing the second sugar (Monod, 1949). Naturally, the rate at which both sugars will support the growth of a given microbial population will differ, and such occurrence will give rise to two distinct growth phases. This phenomenon is known as diauxie (van Dijken et al., 1993). Before a given yeast population reaches the second growth phase, glucose-induced repression of respiration remains in place.

Several known mechanisms execute glucose-mediated inhibition of respiration. On the one hand, glucose induces the expression of Hxk2, which is typically found in its inactive phosphorylated dimeric form during consumption of poorly fermentable carbon sources. When active, Hxk2 represses glucokinases that are typically expressed during the exposure to non-fermentable carbon sources (Randez-Gil et al., 1998). On the other hand, glucose inhibits the AMP-activated kinase Snf1, which orchestrates transcriptional responses to glucose shortage, heat shock, sporulation, and peroxisome biogenesis (Kayikci and Nielsen, 2015).

Given that Pic2 is a mitochondrial carrier, I expected it to impact respiration (Figure I.8). Accordingly, the expression of Pic2 has been observed to be repressed by the presence of glucose in the growth medium (Belenkiy et al., 2000; DeRisi et al., 1997; Takabatake et al., 2001). These findings implied that, to examine the phenotypic repercussion of altering the physiological expression of Pic2 in high or low sugar availability, glucose ought to be avoided. Conversely, being a poorly fermentable carbon source, raffinose was chosen as the supplementary sugar for the medium of all the experiments destined to assess NNS-mediated regulation of *PIC2*. On the other

hand, galactose was employed to assess the synthetic reporter systems as these were engineered downstream of a galactose-inducible promoter. Exposure to glucose, in this case, was also avoided as it precludes galactose from activating downstream transcription. Being respirable sugars, raffinose and galactose are converted to pyruvate and, at least partly, fed into the TCA cycle to produce NADH that can be used as reducing power for ATP generation.

I.8. Oxidative phosphorylation in yeast

Mitochondrial oxidative phosphorylation is a complex and highly controlled network through which ATP synthesis must be continuously adapted to changes in the cell energy demand to sustain growth and/or homeostasis. During respiratory metabolism, the respiratory chain re-oxidises both cytosolic and mitochondrial NADH. However, the respiratory chain of *S. cerevisiae* possesses several features that differentiate it from other eukaryotes, including higher ones and other yeast species. Firstly, the complexes III (i.e., cytochrome *b*, cytochrome *c1* and Rieske protein) and IV (i.e., cytochrome *c* oxidase) are compacted into supracomplexes (Schägger and Pfeiffer, 2000). Secondly, *S. cerevisiae* does not encode the multimeric complex-I-type NADH dehydrogenase, which is characteristic of other eukaryotes (Nosek and Fukuhara, 1994). Instead, it contains three NADH:ubiquinone oxidoreductases: while Ndi1 is internal and faces the matrix, Nde1 and Nde2 are considered external and enclose catalytic sites which are projected into the intermembrane space (Figure I.8). Collectively, these enzymes couple the oxidation of cytosolic NADH to the respiratory chain. In all cases, the transfer of two electrons from an NADH molecule to ubiquinone is mediated directly and thus, no protons are pumped into the matrix throughout this process (Luttik et al., 1998). Thirdly, it lacks a cyanide-insensitive alternative oxidase (AOX) catalysing the direct transfer of electrons from ubiquinone to molecular oxygen without generating a proton motive force (Vanlerberghe and McIntosh, 1997). Altogether, these particularities of the *S. cerevisiae* oxidative phosphorylation have rendered the ATP stoichiometry of the process lower than that of other eukaryotic systems.

Notwithstanding the low stoichiometry of oxidative phosphorylation in yeast, complete respiratory dissimilation of a glucose molecule yields approximately 16

molecules of ATP: 4 of them proceed from substrate-level phosphorylation, 2 originate from glycolysis, 2 correspond to the guanosine triphosphate (GTP) generated in the TCA cycle, and the remaining 12 molecules are derived from oxidative phosphorylation. Overall, the ATP yield of sugar respiration is eight-fold greater than that procured by fermentative catabolism. In addition to the respiration process itself, most cellular functions entail redox reactions, which, in turn, rely on the maintenance of redox homeostasis. The balance between different redox states of the pyridine nucleotide cofactors is coordinated by a set of proteins, which will be outlined in I.9.

I.9. Redox homeostasis in yeast

Pyridine nucleotides NAD and NADP are cofactors that act as electron carriers and donors for metabolic reactions when found in their reduced state. While NADPH is generally engaged in anabolic networks, NADH is required for catabolic purposes (Dijken and Scheffers, 1986). Given that yeast lacks a transhydrogenase able to convert NAD^+ and NADPH into $NADP^+$ and NADH, respectively, these reservoirs remain independent from each other, and thus reoxidation of these species must be executed separately (Bruinenberg et al., 1983). Moreover, the inner membrane of the mitochondrion is impermeable to nicotinamide adenine coenzymes and, consequently, the transit of NAD^+ and reduced and its phosphorylated derivatives NADP and NADPH between the cytoplasm and the mitochondria is not possible. Accordingly, yeast has evolved several enzymes that allow interconversion reactions among the discrete nicotinamide adenine coenzyme pools in each cellular compartment and, hence, the electron supply required for the metabolic reactions occurring in each of these.

Cytosolic NADPH is mainly provided by the glucose-6-phosphate dehydrogenase Zwf1, which catalyses the earliest reaction of the pentose phosphate pathway (Grabowska and Chelstowska, 2003; Minard and McAlister-Henn, 2001; Nogae and Johnston, 1990). A second major source of cytoplasmic NADPH is provided by the cytosolic acetaldehyde dehydrogenase Ald6 (Meaden et al., 1997; Wang et al., 1998). Finally, NADPH can also be restored by the cytosolic NADP-dependent isocitrate dehydrogenase Idp2 (Contreras-Shannon et al., 2005; Loftus et al., 1994).

If needed, oxidised NADP pools can be restored by cytoplasmic NAD kinases, which phosphorylate NAD into NADP. The main catalysts of such conversion are Utr1 and, to a lesser degree, Yef1 (Bieganowski et al., 2006; Kawai et al., 2001; Shi et al., 2005). In the mitochondria, this reaction can be catalysed by Pos5, which can also act as an NADH kinase (Outten and Culotta, 2003; Strand et al., 2003). Therefore, mitochondrial Pos5 can contribute to the preservation of NADP(H) mitochondrial reservoir regardless of its redox state (Miyagi et al., 2009; Tessier et al., 1998; Wang et al., 1997). Importantly, replenishment of $NADP^+$ and NADPH by phosphorylation of NAD^+ and NADH is quantitatively possible given that the intracellular NADP(H) pool is much smaller than the NAD(H) one (Yang and Sauve, 2016).

Yeast also displays various mechanisms to maintain the redox homeostasis of its NAD pool. NAD reduction is linked to glycolysis in the cytosol and to the PDH complex and TCA cycle in the mitochondria (Bakker et al., 2001). The reoxidation of resulting cytoplasmic and mitochondrial NADH pools can be catalysed by oxidoreductases involved in the electron transport chain and ultimately conveying their electron to molecular oxygen as a terminal acceptor (Bakker et al., 2001; de Vries and Grivell, 1988; Luttik et al., 1998; Overkamp et al., 2000). The three systems by which this occurs are the external NADH dehydrogenase (i.e., Nde1/Nde2; see I.3) (Luttik et al., 1998; Small and McAlister-Henn, 1998), the internal NADH hydrogenase (i.e., Ndi1; see I.3) and the glycerol 3-phosphate shuttle Gut2 (Larsson et al., 1998). Even though Nde1/Nde2 have been proposed as the main system for oxidating cytosolic NADH, the principles underlying the biological importance of both oxidisers at different conditions remain largely uncharacterised.

Despite being more energetically efficient, Gut2 leads to slower ATP production than that channelled through Nde1/Nde2 (Larsson et al., 1998; Påhlman et al., 2001). In turn, the latter is predominantly used in most conditions. Consistent with this observation, electrons transferred by Nde1 have higher priority to enter the electron chain than those proceeding from Gut2 or Ndi1 (Bunoust et al., 2005). Ultimately, all NADH oxidation pathways converge at the point at which donated electrons reduce ubiquinone, making its availability a limiting factor for the rate at which the electron transport chain proceeds. Accordingly, while in knockout mutants, the remaining enzyme has been observed to increase its activity and compensate for the absence of

the other dehydrogenase, overexpression of the main Nde1/Nde2 NADH dehydrogenase indirectly inhibits Gut2 (Påhlman et al., 2001).

Apart from their role in metabolism, NAD(H) and NADP(H) are pivotal in controlling the intracellular redox balance. Cellular physiology is incessantly yielding oxidants and antioxidants that must remain in balance for the successful completion of processes like cell cycle progression. Moreover, environmental perturbations can trigger ROS overproduction, an accompanying excess of oxidants and, ultimately, oxidative stress. In turn, oxidative stress is harmful to the integrity of macromolecules such as proteins, lipids, RNA and DNA, and when this damage becomes incompatible with the maintenance of healthy cellular processes, it leads to cell death (Sies et al., 2017; Tan et al., 2018) . To counterbalance the detrimental effects of increased oxidative stress, cells switch their pyridine nucleotide pools into their reduced status and, in doing so, enhance the cellular concentration of NADH and NADPH (Blacker et al., 2014). Therefore, in addition to their role as electron carriers in metabolism, $NAD(P)^+$/NAD(P)H exert an integral control of the oxidant-antioxidant homeostasis and acts as a safeguard of cellular redox biology.

I.10. Sources and effectors of the oxidative stress response

Reactive oxygen species (ROS) are unstable and highly reactive molecules derived from molecular oxygen. ROS include the superoxide anion radical ($O2^-$), hydrogen peroxide (H_2O_2), singlet oxygen $^1[O_2]$, and hydroxyl radical ($OH^\cdot$). Importantly, the superoxide and hydroxyl possess an unpaired electron and are so, more reactive than the hydrogen peroxide and singlet oxygen species, which hold paired electrons (Vahalová et al., 2021).

ROS are routinely generated by cellular physiology (e.g., mitochondrial respiration) or as a byproduct of oxidase activity (Jamieson, 1998). Their generation can also be triggered environmentally with exposure to pro-oxidants, namely hydrogen peroxide, menadione or paraquat; by enhancing the oxygen concentration in the medium or by ionizing radiation (Jamieson, 1998). Considering that metabolism yields ROS, it is not surprising that cells have developed antioxidant defences that can neutralise them if present within a physiological concentration.

Being moderately reactive and short-lived, the superoxide anion is not extensively pernicious on its own. Nevertheless, it can turn into more reactive and toxic hydroxyl and singlet radicals causing membrane lipid peroxidation (Perrone et al., 2008). For this reason, the superoxide anions must be immediately reduced to molecules lacking the ability to undergo such transformation. On the one hand, the copper-zinc (CuZn) cytoplasmic superoxide dismutase, Sod1, and its manganese (Mn) mitochondrial equivalent, Sod2, function as scavengers of superoxide anion radicals and reduce them to hydrogen peroxide and oxygen (Bermingham-McDonogh et al., 1988; Steinman, 1980). On the other hand, the peroxisomal catalase A, Cta1 (Cohen et al., 1985), and its cytosolic counterpart, Ctt1 (Petrova et al., 2004), dismutate two H_2O_2 molecules and convert them into two molecules of water, yielding an O_2 molecule as a byproduct. Similarly, the cytochrome *c* peroxidase (CcP) is also able to catalyse the conversion of hydrogen peroxide to water (Charizanis et al., 1999; Martins et al., 2013). In this case, however, the reaction is mediated by the haem compound at the active site of CcP (Charizanis et al., 1999; Martins et al., 2013). Given that such a haem group encloses a Fe^{2+} molecule at the core of a heterocyclic organic ring called a porphyrin, the ferrous iron can convey the electrons which are needed to complete the reduction reaction (Charizanis et al., 1999; Martins et al., 2013).

Among the ROS species, the hydroxyl radical ($OH^{\bullet}$) is the most reactive and harmful one. At neutral pH, it is generated by the Fenton reaction, during which transition metals like iron (i.e., Fe^{2+}, Fe^{3+}) catalyse the reduction of $O^{\bullet-}_2$ by H_2O_2. Importantly, $OH^{\bullet}$ can damage membrane-enclosed cellular components by lipid peroxidation, and as yeast lacks a scavenger for this toxic radical, the build-up of hydroxyl radicals ultimately results in cellular death (Perrone et al., 2008).

The resulting link between metal-ion homeostasis and antioxidant defences is further underscored by metallothionein (MTs), which are a group of small cysteine-rich proteins harbouring conserved motifs across microbes, plants, and mammals (de Miranda et al., 1990; Ecker et al., 1986; Kojima et al., 1976; Olafson et al., 1988). Primordially, MTs bind to heavy metals such as zinc, cadmium, and copper via their conserved cysteine-rich motifs to detoxify them (Frank et al., 1991; Kagi and Valee, 1960). Upon adopting a complex configuration with transition metal ions like zinc and cadmium, MTs subsequently release these metals in reactions with a dual outcome, namely the neutralisation of ROS and metal ion balance (Misra et al., 1996; Ruttkay-

Nedecky et al., 2013; Thornalley and Vašák, 1985). In yeast, Cup1 exerts a metallothionein role by promoting the detoxification of metal ions such as copper or cadmium (Ecker et al., 1986; Wegner et al., 2011). Following exposure to oxidative stress, *CUP1* becomes upregulated and contributes to enduring the insult (Liu and Thiele, 1996).

Similarly to metallothioneins, enzymes catalysing glutathione metabolism, also multitask in ROS and cadmium scavenger activities in *Schizosaccharomyces pombe* and *Saccharomyces cerevisiae* (Coblenz and Wolf, 1994; Smith et al., 2007). The family of glutathione peroxidases (GPx) is constituted by eight sequentially numbered isoenzymes that reduce hydrogen peroxide and organic hydroperoxides to water and alcohols by oxidising glutathione (GSH) into its oxidised disulphide state (GSSG). Then, glutathione reductase (GLR1) reduces oxidised glutathione disulfide (GSSG) back to glutathione (GSH) using the electrons donated by NADPH, which consequently becomes oxidised to $NADP^+$. Since NADPH is required to maintain intracellular gluthathione redox balance, the main supply of NADPH necessarily becomes a buffer for these series of reactions. As described in I.9., the glucose 6-phosphate dehydrogenase, encoded by *ZWF1*, catalyses the first step in the pentose phosphate pathway to re-generate NADPH. Therefore, indirectly, the pentose phosphate pathway is a fundamental factor in peroxide decomposition.

Many of these guardians against ROS are typically repressed by glucose and, in turn, become selectively upregulated during the respiratory adaptation succeeding glucose exhaustion in an aerobic fermentation batch-growth context (Krems et al., 1995). Indeed, endogenous synthesis of ROS is enhanced during respiratory growth compared to fermentative one, thereby obliging cells to express a higher concentration of such antioxidant defences. Accordingly, the upregulation of this functional set of genes can be referred to as an adaptative response. The principle of acquired stress resistance in yeast resides in the observation that when yeast cells are treated with low concentrations of hydrogen peroxide or menadione, a potent inducer or oxidative stress, cells display higher concentrations of such antioxidant enzymes and, as a result, increase their tolerance to subsequent stresses (Collinson and Dawes, 1992; Jamieson, 1992; Steels et al., 1994). Further evidence substantiating this crosstalk between varying adaptive responses is found in the fact that heat, ethanol or osmotic stresses drive the upregulation of the outlined antioxidant enzymes (Flattery-O'Brien

et al., 1993; Jamieson, 1992; Mager and Moradas Ferreira, 1993; Steels et al., 1994). Likewise, sources of intracellular stress (e.g., cytoplasmic dilution) highly relevant to this work have been observed to onset an environmental adaptive response which, in turn, is characterised by the upregulation of some of the mentioned antioxidants (Neurohr et al., 2019).

I.11. Cell size control in yeast

Heterogeneity in gene expression is often accompanied by a certain range of phenotypic variation across the cells of a population. One of the features which can greatly differ across isogenic cells is volume. While cell size can be affected by the step of the cell cycle at which a given cell finds itself, variations in volume often occur irrespectively of cell cycle progression (Bryan et al., 2014; Crissman and Steinkamp, 1973; Tzur et al., 2009).

Although variations in cell size may, in principle, seem directly innocuous to cell physiology, they can have a major effect on cellular functions as volume underpins the surface-to-volume ratio, the dimension of subcellular compartments and, most importantly, its metabolic and biosynthetic topology. The latter encompasses biochemical reaction rates, which are, in turn, sustained by a range of substrates and catalysts. Accordingly, such molecules must remain present in a constant concentration. This implication led to the theoretical expectation and, eventually, the empirical observation that the absolute count of reactants and enzymes scaled approximately linearly with cell volume (Marguerat and Bähler, 2012). Importantly, this scaling implies that global transcription rates are larger in bigger cells (Basier and Nurse, 2023; Berry et al., 2022; Elliott, 1983a, 1983b; Fraser and Nurse, 1979, 1978; Padovan-Merhar et al., 2015; Sun et al., 2020; Zhurinsky et al., 2010). Therefore, the cell-wide number of mRNAs, rRNAs, and transfer RNAs (tRNAs) will be enhanced in such cells and, consequently, will enable increased protein synthesis with cell size. Yet, biosynthetic scaling is only applicable within a physiological scope of cell volume; when the maximum limit of this phenotypic range is reached, the transcriptome and proteome fail to remain consistent with the expanding cell size. At this point, RNA and protein concentrations decline, and the cytoplasm becomes progressively diluted (Neurohr et al., 2019; Zhurinsky et al., 2010). Ultimately, the collapse of biosynthesis

proportionality triggers the disintegration of various cell functions, sparks an intracellular stress response and onsets ageing and senescence (Lanz et al., 2022; Lengefeld et al., 2021; Neurohr et al., 2019; Xie et al., 2022).

Although biosynthetic scaling is easily applicable to proteins and RNA, DNA comprises a critical exception to this principle. During the cell cycle, a single cell duplicates its DNA content, and even among cells with the same amount of DNA, cell volume still varies greatly. Conceptually, the fact that DNA does not scale with cell size entailed that the same set of genes must be expressed differently to yield the appropriate number of RNA and proteins. Indeed, whole-population measurements of mutants with aberrant volumes confirmed that the transcriptome and the proteome scaled with volume and ploidy (Marguerat et al., 2012; Marguerat and Bähler, 2012; Schmidt and Schibler, 1995; Watanabe et al., 2007; Wu et al., 2010; Zhurinsky et al., 2010). Despite having identified accompanying transcriptional changes in such mutants, prior work has not established causality between volume variations and transcriptomic abundance (Fraser and Nurse, 1979; Schmidt and Schibler, 1995; Zhurinsky et al., 2010). An additional layer of complexity has been introduced by transcriptional ‘noise’ which, similarly to how it introduces phenotypic stochasticity, is able to yield isogenic cells with different volumes across a population (Chubb et al., 2006; Golding et al., 2005; Raj et al., 2006; Raj and van Oudenaarden, 2009, 2008; Sanchez and Golding, 2013; Suter et al., 2011; Zenklusen et al., 2008).

To shed light on the homeostasis of such scaling, a previous study performed heterokaryon fusion experiments (Padovan-Merhar et al., 2015). Upon merging a small cell with a large one, this work observed that the expression of the GFP reporter system encoded in the small cell became adjusted to compensate for the overall volume of the newly formed heterokaryon. In doing so, this study confirmed that volume can directly prompt changes in transcription and, ultimately, shape gene expression (Padovan-Merhar et al., 2015). Subsequent single-molecule RNA imaging and accompanying quantitative analysis revealed that the mechanism underlying this regulation does not merely depend on the size of the cell but also on its DNA content to adjust the appropriate levels of RNA production (Padovan-Merhar et al., 2015). This transcriptional modulation is compatible with a scenario in which a limiting factor for transcription is titrated to the DNA, by either direct sequestration or biochemical compartmentalisation.

Theoretical extrapolation of the mentioned hypothesis proposed that, in such scenario, the driving force yielding changes in the transcription rate would be the abundance – and not the concentration – of the hypothetical limiting factor (Lin and Amir, 2018; Sun et al., 2020). Accordingly, as cells expand, they would increase the synthesis of such limiting factor and, consequently, cause the perceived size-induced increase in transcription (Lin and Amir, 2018; Sun et al., 2020). Since this mechanism would not depend on the ploidy, haploid and diploid cells with approximately the same volume would be expected to show a similar rate of transcription (Lin and Amir, 2018; Sun et al., 2020). Based on these criteria, transcriptional machinery, such as RNA polymerases, has been proposed as a putative limiting factor (Lin and Amir, 2018; Marguerat and Bähler, 2012; Padovan-Merhar et al., 2015; Sun et al., 2020; Zhurinsky et al., 2010).

Recent work confirmed that, indeed, RNA polymerase II acts as a limiting factor for the increasing number of transcriptional ensembles that are bound to the genome in large cells (Swaffer et al., 2023). Other constitutive factors of the transcriptional machinery do not impose a restriction on the number of transcription initiation events that can be fired in oversized cells (Swaffer et al., 2023). Crucially, despite proving the existence of a limiting factor, the same study demonstrated that the adjustment of the transcriptional rate to cell volume was not dependent on the titration of the limiting factor to the genome but rather on the recruitment dynamics of the available RNA polymerase II molecules in the nucleus (Swaffer et al., 2023). Nevertheless, the increase in transcription did not directly scale with cell volume and, hence, solely RNA polymerase II recruitment kinetics could not compensate for the scaling of mRNA concentrations as cells expand (Swaffer et al., 2023). This finding primed the identification of an additional regulatory layer at the level of mRNA stability: in large cells, the transcriptome is stabilised to preserve constant mRNA concentrations (Swaffer et al., 2023). Therefore, mRNA scaling is driven by the combined action of the RNA polymerase II dynamic equilibrium and mRNA turnover.

II. Materials and Methods

II.1. Growth and maintenance of yeast strains

All strains used in this project are derived from the BY4741 strain. BY4741 belongs to a collection of auxotrophs descending from the S288C prototrophic ancestor. Since *HIS3*, *LEU2*, *MET15* and *URA3* are knocked out in BY4741, this strain cannot grow in medium lacking histidine, leucine, methionine, and uracil. In this study, I have used *URA3* as the selection marker for all genetic modifications performed in BY4741. Genetic manipulation of the parental BY4741 strain, to which I will refer as the non-fluorescent wild type (WT), was accomplished by either CRISPR/Cas9 (see II.7.1), modular cloning (MoClo, see II.7.2), yeast integration plasmids (see II.7.3 and II.7.5) or expression vectors (see II.7.4) and gave rise to all other segregants used in this study.

BY4741-derived strains are haploids belonging to the mating type a. Thus, to perform mating assays (see II.8), I backcrossed some of the BY4741-derived strains with BY4742, which possesses identical genetic background to BY4741 but instead encodes a MATα allele in its mating-type locus. Furthermore, to examine the distribution of BY4741-derived populations among the various stages of the cell cycle and investigate the presence of polyploids within them, I conducted a cell cycle analysis (see II.14) which included the BY4743 strain as a diploid control. As BY4741, BY4743 is a reference strain emerging from the S288C prototrophic precursor and, hence, shares a common genetic background with BY4741. However, BY4743 is a diploid strain encoding two copies for all the referred alleles. A list of all the yeast strains used in this study is provided in Table II.1.

Name	Background	Source	Application
WT	BY4741	Tollervey Lab	All experiments
WT (BY4742)	BY4742	Marston Lab	Mating assay
BY4743	BY4743	Swain Lab	Cell cycle analysis
PIC2-GFP			
Δ Nab3 RNA-BSs			
Δ Nab3 RNA-BSs (SG1135)		This study (Tove Widén and Iseabail Farquhar)	
Partial Δ NNS RNA-BSs (SG1138)			

Δ NNS RNA-BSs	BY4741	This study	All experiments
*pic2*Δ*::HIS3*			
PIC2-GFP Nab3-HTF			
PIC2-GFP Nrd1-HTF			
PIC2-GFP Rpo21-HTF			
PIC2-GFP Sen1-HTF			
Δ Nab3 RNA-BSs Nab3-HTF			CRAC
Δ Nab3 RNA-BSs Nrd1-HTF			
Δ Nab3 RNA-BSs Rpo21-HTF			
Δ Nab3 RNA-BSs Sen1-HTF			
Δ NNS RNA-BSs Nab3-HTF			
Δ NNS RNA-BSs Nrd1-HTF			
Δ NNS RNA-BSs Rpo21-HTF			
Δ NNS RNA-BSs Sen1-HTF			
PIC2-GFP x BY4742 Spore 1	BY4741		Mating assay
PIC2-GFP x BY4742 Spore 2	BY4742		
PIC2-GFP x BY4742 Spore 3	BY4742		
PIC2-GFP x BY4742 Spore 4	BY4741		
Δ Nab3 RNA-BSs x BY4742 Spore 1	BY4741		
Δ Nab3 RNA-BSs x BY4742 Spore 2	BY4742		
Δ Nab3 RNA-BSs x BY4742 Spore 3	BY4741		
Δ Nab3 RNA-BSs x BY4742 Spore 4	BY4742		
Δ NNS RNA-BSs x BY4742 Spore 1	BY4742		
Δ NNS RNA-BSs x BY4742 Spore 2	BY4742		
Δ NNS RNA-BSs x BY4742 Spore 3	BY4741		
Δ NNS RNA-BSs x BY4742 Spore 4	BY4741		
BSWT	BY4741	This study (Tove Widén and Iseabail Farquhar)	Synthetic GFP expression system
BS1			
BS2			
BS3			
BS4			
BS5			

Table II.1. Summary of strains used in this study outlining their genetic background, source, and research application.

Synthetic complete (SC) medium containing or lacking uracil (SC -Ura) or histidine (SC -His) was used to grow all yeast strains. SC medium consists of yeast nitrogen base with ammonium sulphate and without amino acids (YNB w/o AA, 6.7 g/L, Formedium) and complete supplement mixture (0.79 g/L, Formedium, see composition in Table II.2). Yeast strains encoding an auxotrophic marker were selected by growth in SC medium lacking uracil or L-histidine.

Component	Concentration
Adenine	10 mg/L
L-arginine HCl	50 mg/L
L-aspartic acid	80 mg/L
L-histidine HCl	20 mg/L
L-isoleucine	50 mg/L
L-leucine	100 mg/L
L-lysine HCl	50mg/L
L-methionine	20 mg/L
L-phenylalanine	50 mg/L
DL-Homoserine	80 mg/L
L-threonine	100 mg/L
L-tryptophan	50 mg/L
Uracil	20 mg/L
L-tyrosine	50 mg/L
Valine	140 mg/L

Table II.2. Composition of complete supplement mixture for yeast synthetic complete medium.

SC or SC -Ura media were supplemented with the appropriate concentration (i.e., 2% (w/v) or 1 % (w/v)) of a carbon source like glucose, galactose, pyruvate, raffinose or sucrose (Formedium). While a concentration of 2% (w/v) of a given sugar is generally considered standard for rich media, a 1 % (w/v) concentration poses a nutritional deprivation challenge to which cells in culture must adapt. Most experiments in this study were performed in raffinose, but glucose was also used in some instances. The sugar employed for each experiment is individually specified for all experiments reported. For assessing the differences in superfolder (sf) GFP levels among the synthetic expression systems, a mixture of 1% (w/v) sucrose and 1% (w/v) galactose was used to induce expression of the reporter gene from the *pGAL1* promoter (see III.6 and III.7). All strains were pre-cultured in medium containing 2% (w/v) pyruvate for 48 hours before the start of the experiment (Fernando Montaño-Gutierrez et al., 2022). This pre-growth stage ensures that the protein expression profiles of the different strains have a homogeneous starting point.

Yeast peptone dextrose adenine (YPDA) rich medium comprising yeast extract (10 g/L), peptone (20 g/L), dextrose (20 g/L) and adenine hemisulphate (40 mg/L) was used for growing cells before transformation and freezing. Glycerol stocks for storage

of the engineered strains were prepared by mixing 0.5 mL of sterile 50% (w/v) glycerol with 0.5 mL of a YPDA-based culture containing the strain of interest grown overnight. All liquid cultures were incubated at 30ºC with shaking at 190 rpm. To facilitate growth in plates, medium for these was prepared using 2% (w/v) glucose as a carbon source and solidified upon the addition of agar to a final concentration of 1% (w/v). Cells grown in Petri dishes were incubated at 30ºC in a static incubator for 48 hours and kept at 4ºC afterwards. For the selection of transformants during the CRISPR/Cas9 genetic modification procedure (see II.7.1), cells were plated in YPDA medium supplemented with 1% (w/v) agar and nourseothricin (100 µg/mL).

II.2. Growth and maintenance of mammalian cell lines

A mammalian cell model with inducible expression of the *PIC2* homologue in humans, *SLC25A3*, was generated using the the Flp-In™ T-REx™ system (see II.3.6). This system employs the Flp-In™ parental cell line, which is derived from 293 human embryonic kidney (HEK 293) cells obtained from the American Type Culture Collection (ATCC). I received the vial containing my initial Flp-In™ parental cell line stock from the Tollervey group.

Cells were grown in the Dulbecco's Modified Eagle Medium (DMEM) containing 10% (v/v) foetal bovine serum (FBS), 2 mM L-glutamine, potassium penicillin (100 units/mL) and streptomycin sulphate (100 µg/mL). Zeocin™ (15 µg/mL) was added to the cultures of unmodified parental cell line. Cells in which the pcDNA5/FRT plasmid encoding *SLC25A3-HTF* had been integrated into the genome using the Flp-In™ system, were grown in medium containing blasticidin (15 µg/mL) and hygromycin B (100 µg/mL). Expression of the inserted *SLC25A3-HTF* was induced with doxycycline (0.2 µg/mL) 36 hours prior to downstream experiments.

To prepare frozen stocks for long-term storage at -80ºC, cells were cultured to a confluence of approximately 80-90%. After removing the medium and rinsing with PBS, cells were incubated for 1 minute with a minimum volume of StableCell™ trypsin solution (Sigma-Aldrich) at 37ºC. DMEM was then added to the detached cells to neutralise the enzyme, and the resulting volume was centrifuged at 200 rcf for 5 minutes in an Eppendorf 5804 R centrifuge. Upon disposal of the supernatant, the cell

pellet was resuspended in a solution of 90% (v/v) DMEM and 10% (v/v) of dimethyl sulfoxide (DMSO), which acts as a cryoprotective agent. The volume of DMEM-DMSO mix added to the pellet was that necessary to yield a concentration of 2 to 4 million cells per mL. Cells were stored in cryovials containing 1 mL of the suspended cell solution and frozen at -80ºC inside of a Mr. Frosty™ freezing container (Thermo Fisher Scientific) which cools the samples at a rate of -1 K/minute thereby maximising cell preservation and viability.

II.3. Bacterial growth and maintenance

The *Escherichia coli* DH5α strain (New England Biolabs) was used fornvector propagation throughout this study. A list and a brief outline of the main features of the vectors used in this study is provided in Table II.3.

Vector	Resistance Marker	Source	Application
pFA6a-GFP(S65T)-His3MX6	Ampicillin	(Longtine et al., 1998)	*GFP* fusion to *PIC2*
pFA6a His3MX6	Ampicillin	(Longtine et al., 1998)	*PIC2* knock-out
PTEF1-PIC2-pRS406	Ampicillin	This study	*PIC2* overexpression
PTEF1-yEGFPCLN2PEST-pRS406	Ampicillin	(Williams et al., 2015)	Parental plasmid for vector used for *PIC2* overexpression.
pRS426	Ampicillin	(Christianson et al., 1992)	Standardisation of *URA3* selection marker in all strains
pBS1539::HIS6-TEV-3xFLAG URA3	Ampicillin	(Granneman et al., 2009)	Fusion of HTF epitope to the NNS complex and Rpo21
pcDNA5/FRT *SLC25A3-HTF*	Ampicillin	This study	Integration of *SLC25A3-HTF* into the Flp-In™ HEK 293 cell line
pcDNA5 FRT TO	Ampicillin	Commercial (Thermo Fisher Scientific)	Original vector for integration of a gene of interest into the Flp-In™ HEK 293 cell line
pOG44	Ampicillin		Flipase-encoding vector for integration of a gene of interest into the Flp-In™ HEK 293 cell line
pcDNA6/TR	Ampicillin		Production of the tetracycline repressor
pEGFP-N2	Kanamycin	Commerical (Clontech)	Control for plasmid transfection into mammalian cells
AMP1278	Ampicillin	Swain Lab	gRNA-encoding plasmid in CRISPR/Cas9 procedure

AMP1284	Kanamycin	Swain Lab	Vector coding for endonuclease in CRISPR/Cas9 procedure
PGAL1_BSWT_sfGFP	Ampicillin	This study (Tove Widén and the Edinburgh Genome Foundry)	Integration into the 5' UTR of *RPL20A* to generate synthetic GFP expression systems
PGAL1_BS1_sfGFP			
PGAL1_BS2_sfGFP			
PGAL1_BS3_sfGFP			
PGAL1_BS4_sfGFP			
PGAL1_BS5_sfGFP			

Table II.3. Summary of the vectors used in this study indicating their antibiotic resistance markers, source, and research application.

Bacterial cultures used as inputs for plasmid DNA extractions were cultured in Luria-Bertani broth (LB) containing tryptone (10 g/L), yeast extract (5 g/L), NaCl (10 g/L) and ampicillin (100 µg/mL) or kanamycin (50 µg/mL) depending on the resistance marker enclosed within the plasmid of interest (Table II.3). In all cases, bacterial growth in liquid culture took place at 37ºC with shaking at 200 rpm. When grown in plates, LB medium was supplemented with 1% (w/v) agar and ampicillin or kanamycin to a final concentration of 100 µg/mL or 50 µg/mL, respectively. To recover them from heat-shock induced transformation, cells were incubated in super optimal broth with catabolite repression (SOC) medium comprising tryptone (20 g/L), yeast extract (5 g/L) and NaCl (0.5 g/L).

II.4. Bacterial transformation and plasmid extraction

An aliquot of competent *Escherichia coli* DH5α (New England Biolabs) were thawed on ice for 10 minutes before transferring 25 µL into a sterile 1.5 mL microcentrifuge tube containing 50 ng of the relevant plasmid. Cells were incubated on ice with the DNA for 30 minutes prior to a 30-second heat shock in a thermoblock previously set to 42°C. Immediately after this heating period, cells were transferred back to ice and left there for 1 minute. To facilitate the cells' recovery, 800 µL of SOC medium were added to each transformation tube and subsequently incubated at 37°C for 1 hour with shaking at 200-300 rpm. Finally, 200 µL of each transformation were pipetted onto their corresponding Petri dishes containing luria broth (LB) medium with 50 µg/mL of ampicillin and spread with a sterilised spreader. Inoculated plates were then incubated at 37°C overnight.

Individual bacterial colonies were inoculated in 5 mL of LB with 50 µg/mL ampicillin and incubated at 37°C for 12-18 hours with shaking at 200-300 rpm. Overnight cultures were harvested (6797 rcf, 2 minutes) in an Eppendorf 5804 R centrifuge for plasmid purification using the GeneJET plasmid miniprep kit (Thermo Fisher Scientific) according to the manufacturer's procedure. The DNA concentration of the resulting samples was measured using a DeNovix DS-11 spectrophotometer.

II.5. Yeast transformation

Five mL YPDA cultures were inoculated with a single yeast colony and incubated at 30ºC until they reached an optical density (OD_{600}) of between 1 and 1.5. The cultures were then transferred to 50 mL centrifuge tubes and spun down at 1801 rcf for 5 minutes in an Eppendorf 5810 R centrifuge. After discarding their supernatant, the cell pellets were resuspended in 1 mL of 100 mM lithium acetate (LiOAc) and pipetted into sterile 1.5 mL microcentrifuge tubes. Following another centrifugation step (604 rcf, 5 minutes, Eppendorf MiniSpin), the resulting supernatants were removed, and cells were resuspended in a volume of 500 µL of 100 mM LiOAc and incubated at room temperature for 10 minutes. During this time, cells were permeabilised by LiOAc to increase DNA transformation efficiency. Meanwhile, an appropriate volume of a solution containing 40% (w/v) PEG 4000 and 100 mM LiOAc was prepared using sterile water. Approximately 300 µL of PEG-LiOAc solution were to be allocated to each transformation after the permeabilisation treatment with LiOAc. Five µL of single-stranded salmon sperm DNA (10 mg/mL, Thermo Fisher Scientific), which acted as a carrier DNA, and 1 µg of the pertinent plasmid were added to each sample. Having been vortexed at maximum speed for 10 seconds, the mixtures were incubated at 42ºC for 25 minutes, and cells were subsequently spun down (604 rcf, 5 minutes, Eppendorf MiniSpin). Cell pellets were resuspended in 200 µL of sterile water and pipetted onto agar plates containing the adequate selective medium.

II.6. Mammalian cell transfection

On the day preceding the transfection, Flp-In™ HEK 293 cells were seeded on a 10-cm dish, aiming for 50-80% confluence on the day of the experiment. One hour

before transfection, the standard growth medium recommended for the maintenance of this cell line (see II.2) was replaced by 10 mL of DMEM supplemented with 10% (v/v) FBS and lacking antibiotics. In the meantime, a volume corresponding to 5 µg of the DNA fragment to be transfected into a single plate was dissolved in OptiMEM medium (Thermo Fisher Scientific) to a final volume of 1250 µL. Similarly, for each sample plate to be transfected, 15 µL of lipofectamine 2000 (Thermo Fisher Scientific) were mixed with 1235 µL of OptiMEM. Both mixtures were then combined, mixed by pipetting, and incubated at room temperature for at least 20 minutes to allow the formation of DNA-lipofectamine complexes that can penetrate the mammalian plasma membrane of the cells in a single plate. The transfection mixture was added in drops, trying to spread them evenly across the plate. Afterwards, the medium was mixed with the transfection solution by rocking the dish gently. Cells were then kept at 37°C for 1 hour before exposing them to a final concentration of 15 µg/mL blasticidin within their growth medium.

II.7. Genetic engineering of yeast strains and mammalian cell lines

II.7.1. Introduction of single-nucleotide mutations in *PIC2* NNS RNA-binding sites using CRISPR/Cas9.

Using a parental strain in which *GFP* had been fused to the 3' of *PIC2* (BY4741 Yeast GFP clone collection, Thermo Fisher Scientific), Tove Widén and Iseabail Farquhar used CRISPR/Cas9 gene editing to induce mutations in the 5' UTR and coding sequence of *PIC2*. The pertinent parental yeast strain was transformed with (i) a homology template, (ii) a Cas9-encoding vector and a suitable gRNA complementary to the locus at which the nucleotide substitutions were desired.

The homology templates spanned 1431 bp, delimiting approximately 500 bp-wide windows upstream and downstream of the start of the *PIC2* coding region. Homology fragments containing the wanted mutations were ordered as gBlocks™ from Integrated DNA Technologies. Five µg of the homology templates were amplified by PCR using Q5® high-fidelity DNA polymerase (New England Biolabs) and the oligonucleotides shown in Table II.4.

Oligonucleotide Type	Name	Sequence
Amplification of homology template	PIC2_HR_F	5'- CCCTTAACTTGCCTTTCCAGTTCTT - 3'
	PIC2_HR_R	5'- ACTGACTGATATTTGCTGTAATGCG - 3'
gRNAs	Nrd1_1_F	5'- ATTCTAAAAAAATAAAGTAA - 3'
	Nrd1_1_R	5'- TTACTTTATTTTTTTAGAAT - 3'
	Nrd1_3_F	5'- CTGAATTCCTCGCTGATATC - 3'
	Nrd1_3_R	5'- GATATCAGCGAGGAATTCAG - 3'
	Nab3_1_F	5'- CATGTACCTTAGGTGGTATA - 3'
	Nab3_1_R	5'- TATACCACCTAAGGTACATG - 3'
	Nab3_2_F	5'- AGTTGTATACTTCAAACTTA - 3'
	Nab3_2_R	5'- TAAGTTTGAAGTATACAACT - 3'
Amplification of gRNA-encoding region from AMP1278	F_6663	5'- CAACGATGTGCTTCAGTATTAC - 3'
	R_6664	5'- GCTGTAGATATCCTGCACTC - 3'
Amplification of Cas9-encoding fragment from AMP1284	F_6723	5'- CTGCGTTTATACGTCTCAGTTTTAGAGC - 3'
	R_6724	5'- GTTTCACTTTCCGTCTCAAGTC - 3'

Table II.4. Summary of the oligonucleotides used throughout the CRISPR/Cas9 procedure to mutate NNS RNA-BSs in *PIC2*.

The resulting amplicons were resolved by electrophoresis in 1% (w/v) agarose gels ran in Tris-borate-ethylenediaminetetraacetic acid (EDTA) buffer (TBE) at 120 V for approximately 20 minutes. The migration pattern of the samples was assessed using a Visi-Blue™ transilluminator (UVP), which emits a blue light that excites the SYBR™ Safe DNA gel stain (Thermo Fisher Scientific). After slicing the regions of the gel containing the amplicon bands at the expected size, DNA was extracted using the QIAquick Gel Extraction Kit (QIAGEN). Briefly, each gel slice was mixed with a volume of the QG buffer corresponding to three times its mass (e.g., 300 µL of buffer were added to 100 mg of gel) and subsequently melted at 50°C for 10 minutes. Samples were then vortexed vigorously to ensure complete solubilisation of the gel matrix and mixed with one volume of isopropanol. The solution was purified through a QIAquick spin column containing a DNA-binding membrane. A maximum of 800 µL were pipetted into the column at once before centrifugation (8117 rcf, 1 minute, Eppendorf MiniSpin) and disposal of the flow through. After filtering the whole sample through the column, the membrane was washed with 500 µL buffer QG. Following removal of the wash buffer by centrifugation (8117 rcf, 1 minute, Eppendorf MiniSpin), 750 µL of buffer PE were added to the membrane and incubated for 3 minutes before spun down at 8117 rcf for 1 minute in the same instrument. Finally, DNA was eluted from the membrane after a 1-minute incubation with 10 µL of buffer EB, which was gathered by centrifugation (8117 rcf, 1 minute, Eppendorf MiniSpin). DNA concentration was measured using a DS-11 series NanoDrop previously blanked with the same elution buffer.

The gRNAs comprised a sequence of 20 nucleotides which would be complementary to the CRISPR target region. To design and analyse gRNAs, the genomic sequence of *PIC2* alongside a 1000 bp-window upstream and downstream of its coding region was downloaded from the Saccharomyces Genome Database (SGD) and imported to Benchling (Benchling). Based on the Saccharomyces_cerevisiae.R64-1-1.75 reference genome, the CRISPR tool of this platform computed putative sgRNA designs with a length of 20 bp and immediately proximal to a 5′-NGG-3′ PAM sequence. Candidate gRNA designs were then classified according to their off-target score, which indicates the priority with which the gRNA engages in non-specific hybridisation. Once selected, the forward and reverse strands of the region coding for the chosen gRNAs were ordered from Integrated DNA Technologies as separate single-stranded DNA oligonucleotides.

Prior to their amplification, gRNAs needed to be incorporated into a plasmid. To do this, 10 µL of the forward and reverse sequences comprising the gRNA encoding fragment were mixed to a final concentration of 50 µM and annealed using a gradient thermocycler. The samples were denatured by heating at 100°C for 5 minutes and subsequently cooled at a rate of 0.1 K/s for 750 seconds until they reached a final temperature of 25°C. A 1:100 dilution of the annealed product was then used as a substrate for Golden Gate assembly. To apply such a technique, digestion and ligation reactions were set in a 10 µL volume containing 33 ng of the AMP1278 entry vector, 10 nM of the DNA sequence encoding the gRNA of interest, 5 units of Esp3I, 400 units of T4 DNA ligase, 1X of T4 ligase buffer and 0.1 µg/µL of bovine serum albumin (BSA). The mix underwent thirty cycles comprising a 5-minute incubation at 37°C, which is the optimal temperature for digestion and one that can be tolerated by the ligase, followed by another 5-minute incubation at 16°C, which is the condition at which the ligation occurs most efficiently. The reaction was then stopped by heating denaturation at 50°C for 2.5 minutes and 80°C for 10 minutes. Afterwards, 2 µL of Golden Gate assembly product and 200 ng of the original AMP1278 were transformed into two separate batches of *E. coli* DH5α. Transformed bacteria were selected by overnight growth in LB plates supplemented with ampicillin.

The AMP1278 plasmid displayed two Esp3I restriction sites flanking a region encoding sfGFP which should have, consequently, be excised in the assembled version of the plasmid. Accordingly, colonies transformed with a sgRNA-encoding

vector should lack green fluorescence when imaged in a UV transilluminator and they can be visually selected for downstream plasmid purification as described in II.6. The gRNA-encoding sequence of the plasmid was amplified by PCR using the Phusion® high-fidelity DNA polymerase (New England Biolabs).

The Cas9-encoding construct was amplified from the AMP1284 standard plasmid, which also contains a nourseothricin-resistance selection marker for yeast. To restrict the vector with BaeI (New England Biolabs), a digestion reaction was set in a 50 µL volume containing 1 µg of plasmid encoding the endonuclease, 5 units of BaeI, 1X rCutSmart buffer (New England Biolabs) and 20 µM of S-adenosyl methionine (32 mM, New England Biolabs), and subsequently incubated at 25°C for 15 minutes. The enzyme was inactivated by heating at 65°C for 20 minutes, and 658 ng of the linearised substrate was used as a substrate for amplification by PCR using Q5® high-fidelity DNA polymerase, and the oligonucleotides shown in Table II.4. Resulting amplicons were resolved by electrophoresis and purified by gel extraction as detailed above.

Five µg of the homology template, 2 µg of the pertinent sgRNA-encoding fragment and 1.5 µg of the purified Cas9 amplicons were transformed into four different batches of the *PIC2-GFP* parental strain as outlined in II.4. Transformants were selected in plates containing YPDA with 100 µg/mL of nourseothricin. Genomic DNA was extracted from resulting colonies by suspending them in 100 µL of 200mM LiOAc supplemented with 1% (w/v) SDS. Samples were incubated at 70°C for 5 minutes prior to the addition of 300µL of 96% (v/v) ethanol. Following vigorous vortexing, lysates were spun down at 9660 rcf for 3 minutes in an Eppendorf MiniSpin centrifuge before discarding the supernatant. After resuspending the pellets containing precipitated DNA in combination with cell debris using 100 µL of 75 % (v/v) ethanol, these were again spun down at 9660 rcf for 3 minutes in an Eppendorf MiniSpin centrifuge. Upon removal of the supernatant, the DNA in the pellet was selectively solubilised in 100 µL of sterile water. DNA in solution was partitioned from unwanted lysis byproducts by centrifugation at 9660 rcf for 15 seconds. The DNA concentration in each sample was measured using a DS-11 spectrophotometer (DeNovix) and adjusted to the one specified by the sequencing provider. In this case, samples were submitted for Sanger sequencing to Eurofins Scientific.

II.7.2. Engineering synthetic NNS-regulated GFP expression systems using MoClo.

Tove Widén designed six constructs encompassing different versions of the previously defined NNS 'supermotif' (Porrua et al., 2012). These combinations of Nab3 and Nrd1 cognate sites were embedded in the 5' UTR of *RPL20A* which, in turn, was introduced upstream of the coding region of sfGFP (Table II.5). Expression of sfGFP was driven from the strong inducible promoter *pGAL1*. Such expression systems were engineered as six separate integration plasmids by the Edinburgh Genome Foundry using Modular Cloning (MoClo). The plasmids were assembled using DNA blocks containing the *pGAL1* promoter, the Nab3 and Nrd1 binding region, the sfGFP coding sequence, its terminator, the *URA3* auxotrophic marker, yeast integration overhangs, a kanMX6 resistance cassette, a bacterial replication origin and connector sequences, which encircle the construction elements. These parts are devised so that after digestion with BsaI, the emerging sticky ends are exclusively compatible with the next part in the intended assembly. The resulting plasmids were transformed into *E. coli* as described in II.4. After being isolated, vectors were integrated into the genome by replacing the *GAL2* gene of the BY4741 strain employing the homologous recombination primers shown in Table II.6.

Construct	Sequence
BSWT	5'- GCTTGTTCCCTCCTGTACCAAAATCTGACCGTGGCAAGGTATCGCCAAATTTCATTTTAAACATTGAGGT TGAAGAATTTGGACAATCATAAGCATCTATATAGTTCCTCAAGTCTGTTAAGGAAAAACAGTGCGGAAAA - 3'
BS1	5'- GCTTGTTCCCTCCTGTACCAAAATCTGACGTAAAGAATTAAGTCTTGATATATAACAATTAGCTTGAGGTT GAAGAATTTGGACAATCATAAGCATCTATATAGTTCCTCAAGTCTGTTAAGGAAAAACAGTGCGGAAAA - 3'
BS2	5'- GCTTGTTCCCTCCTGTACCAAAATCTGACCGTGGCAAGGTATCGCCAAATTTCATTTTAAACATTGAGGT TGAAGAATTGTAACAATCATAATCTTGTATATAGTTCCTCAAGTCTTGTAAGGAAAAACAGTGCGGAAAA - 3'
BS*3*	5'- GCTTGTTCCCTCCTGTACCAAAATCTGACTCTTGGAATTAAGGTAATATATATAACAATTAGCTTGAGGTT GAAGAATTTGGACAATCATAAGCATCTATATAGTTCCTCAAGTCTGTTAAGGAAAAACAGTGCGGAAAA - 3'
BS4	5'- GCTTGTTCCCTCCTGTAAAGAATTAAGTCTTGATATATAACAATTAGCTTGTCATTTTAAACATTGAGGTT GAAGAATTTGTAAAGAATTAAGTCTTGATATATAACAATTAGCTTGTTAAGGAAAAACAGTGCGGAAAA - 3'
BS5	5'- GCTTGTTCCCTCTTGTACCAAAATCTGACCGTGGCAAGTAGAAATTTCATTCTTGAAAATTGAGGTTGTA AGAATTTGTAAATAATCATAAGCTTCTTGATATATAAGTTCTAGTCTTGTAAGAAAAACAGTGCGGAAAA - 3'

Table II.5. Sequences encoding the GFP synthetic expression systems that were transformed into BY4741.

Oligonucleotide	Sequence
BS_F	5'- TAGTTAAGTAAACACAAGATTAACATAATAAAAAAAATAATTCTTTCATA CCAGATGTCAACACAGCTAC-3'
BS_R	5'- GTCATGAAAAATTAAGAGAGATGATGGAGCGTCTCACTTCAAACGCATTA GCACGTGATACTCGGGTAAT - 3'

Table II.6. Oligonucleotides priming the amplification of the synthetic constructs in Table II.5. The blue text corresponds to sequences homologous to the *GAL2* locus in the genome, and the grey font indicates nucleotides homologous to the engineered sfGFP expression systems.

II.7.3. Knocking-out *PIC2* with a yeast integrating plasmid (Ylp).

A *PIC2* knockout mutant (*pic2Δ::HIS3)* was assembled by integration of the *Saccharomyces kluyveri HIS3* gene in the genomic sequence of *PIC2*. The PCR to generate the *HIS3MX6* amplicons that were transformed into the WT strain for integration was performed using the Q5® high-fidelity DNA polymerase and the oligonucleotides specified in Table II.7. Amplification of the auxotrophic marker from the pFA6a-His3MX6 plasmid (Addgene) was performed using forward and reverse primers coding for the 50 bp upstream and downstream the *PIC2* coding sequence (blue) followed by the 5' and 3' ends of the *HIS3MX6* sequences (grey) respectively. Transformants were grown on agar plates containing histidine-depleted synthetic defined (SC -His) medium and resulting colonies were checked for the presence of the cassette by performing PCR with Taq DNA Polymerase (New England Biolabs) with its standard Taq buffer (New England Biolabs) as well as forward and reverse primers coding for a sequence in *PIC2* 5'UTR (Table II.7, blue) and *HIS3MX6* coding region (Table II.7, grey) respectively.

Oligonucleotide	Sequence
KO_F	5'- AAAAATAAAGTAAGGGAAAAAGAGAACGGACTCATTGACAGTTGTAAAGC CGGATCCCCGGGTTAATTAA - 3'
KO_R	5'- TCCTCTAGCACAGAGTGTTTACGATAAACCTTGCCGATTGAATCGATCAG GAATTCGAGCTCGTTTAAAC - 3'
KO_Check_F	5'- CAGGCAGTCAATGACACATTG - 3'
KO_Check_R	5'- CCGACAAGTCAACTACGCTTC - 3'

Table II.7. Oligonucleotides used for replacement of the *PIC2* coding sequence by the *HIS3MX6* cassette in the *pic2Δ::HIS3* strain. KO_F and KO_R were used for amplification of such marker prior to transformation and KO_Check_F and KO_Check_R were used to amplify genomic DNA and confirm the integration of *HIS3MX6* into the targeted locus of the strain's genome.

II.7.4. Overexpression of *PIC2* from a *TEF1* promoter applying restriction enzyme-based insertion into an expression vector.

A *PIC2*-overexpressing vector was created by transforming the WT strain with a recombinant version of the PTEF1-yEGFPCLN2PEST-pRS406 plasmid (Addgene) encoding *PIC2* downstream the *TEF1* constitutive promoter. To engineer this vector, the genomic sequence between the TSS and the stop codon of *PIC2* was amplified using the Q5® high-fidelity DNA polymerase and the oligonucleotides defined in Table II.8. As shown in this table, the forward and reverse primers contained respectively MfeI (in blue) and AscI (in orange) restriction sites upstream the sequences which were complementary to *PIC2*. Digestion of 1 µg of insert occurred in a volume of 50 µL containing 10 units of MfeI (New England Biolabs), 10 units of AscI (New England Biolabs) and 1X of the rCutSmart Buffer (New England Biolabs). The reaction was incubated at 25°C for 15 minutes before the enzymes were heat inactivated at 65°C for 20 minutes. The vector backbone was cleaved by EcoRI (New England Biolabs) and AscI (New England Biolabs) following an identical procedure. Both products were purified by applying electrophoresis in 1% (w/v) agarose and subsequently purifying the bands by gel extraction (see II.7.1 for details). The two fragments were then combined at a molar 4:1 insert-to-vector ratio with 400 units of T4 DNA ligase (New England Biolabs) and 1X T4 DNA ligase buffer in a final volume of 20 µL. The reaction occurred at 16ºC overnight and was stopped by denaturing the ligase at 65ºC for 10 minutes.

The recombinant plasmid was then transformed into the BY4741 strain as described in II.5. Successfully transformed colonies were selected in SC -Ura medium. To ensure medium uniformity across samples and experiments, all other strains used in this study were transformed with the unaltered pRS426 plasmid (Addgene), which also codes for the same selectable marker.

Oligonucleotides	Sequence
TEF1-PIC2_F	5'- GATCAATTGCATTTTGCTTGTGTTTTATAG - 3'
TEF1-PIC2_R	5'- AGTGGCGCGCCCTAACCGGTGGTTGGTAAGC - 3'

Table II.8. Primers used to amplify *PIC2* coding sequence for integration downstream *pTEF1* of the PTEF1-yEGFPCLN2PEST-pRS406 plasmid. The blue and orange text indicate MfeI and AscI restriction sites, respectively.

II.7.5. Generation of a stable Flp-In™ HEK 293 cell line with inducible expression of *SLC25A3* applying the T-REx system.

Genetic assembly of a human cell model with inducible expression of *SLC25A3* was undertaken in a Flp-In™ HEK 293 cell line. The genome of these cells encompasses a Flp recombination target (FRT) site at which a gene of interest can be integrated by the Flp recombinase (Figure II.1A). This FRT element is followed by a sequence coding for the β-galactosidase-Zeocin™ fusion protein which enables the cell line to grow whilst exposed to 15 µg/mL Zeocin™. The gene of interest is then transfected into the cells as part of a construct encoding a FRT sequence followed by a hygromycin-resistance cassette and the gene of interest with its promoter and terminator (Figure II.1B). Owing to the presence of the recombination site, the whole vector will be incorporated into the genome at the FRT site of the latter (Figure II.1B). After recombination, the gene coding for hygromycin resistance will lay under the promoter that used to drive transcription of the ß-galactosidase-Zeocin™ fusion protein (Figure II.1C). Consequently, the Zeocin™-resistance marker is relocated to the distal end of the polyadenylation signal of the gene of interest and will, thus, not be expressed in the modified cell line (Figure II.1C). Ultimately, this results in the cell line ceasing to be Zeocin™-resistant and becoming hygromycin-tolerant instead.

The T-REx™ strategy expands on these to render the expression of the gene of interest inducible. This system employs native parts of the *E. coli* Tn10-encoding (Tet) resistance operon to repress or derepress the promoter under which the expression of the gene of interest occurs (Figure II.1C). Expression of *SLC25A3* was driven by a strong CMV promoter embedded with two repeats of the TetO2 element (Figure II.1B). Accordingly, the T-REx™ system requires Flp-In™ cells to be co-transfected with three different vectors, namely one encoding *SLC25A3* with its accompanying FRT recombination site, pcDNA5/FRT *SLC25A3-HTF*; another one coding for the flipase recombinase, pOG44; and a third one containing the tetracycline repressor and a blasticidin-resistance gene for selection, pcDNA6/TR. The two latter vectors are originally from Thermo Fisher Scientific and were a gift from the Tollervey group.

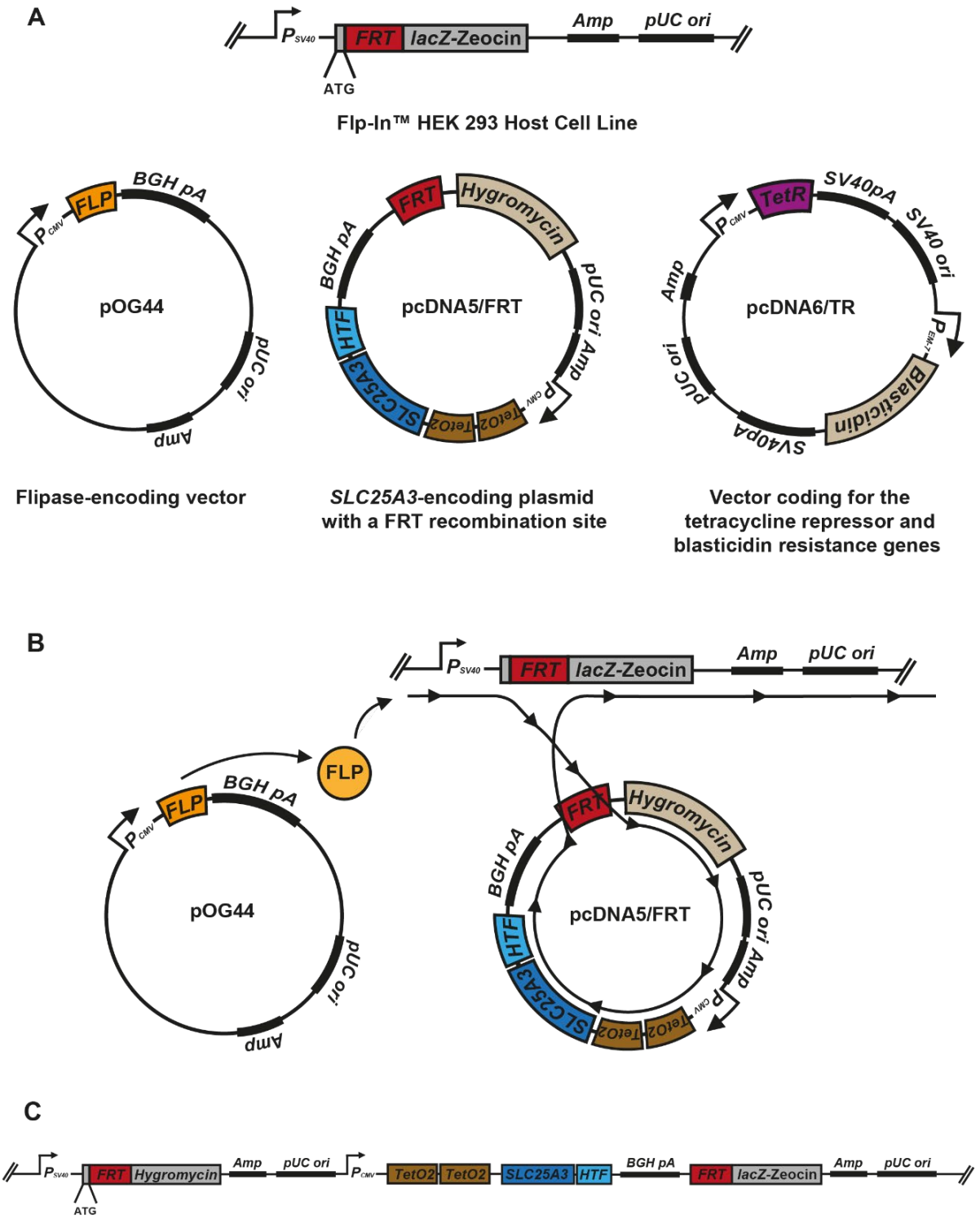

Figure II.1. Graphical summary of the Flp-In™ T-REx™ genetic engineering approach. *SLC25A3-HTF* was cloned into a vector containing a recombination site. Co-transfection with a flipase-encoding plasmid permitted the production of the recombinase, which, in turn, integrated the *SLC25A3-HTF* sequence into the cells' genome. A vector encoding for the tetracycline repressor allows inducible expression from the promoter of *SLC25A3-HTF*, which hosts two Tet operator (TetO2) sequences.

To generate the pcDNA5/FRT *SLC25A3-HTF* plasmid*, SLC25A3* was fused to a His_6-TEV-3xFLAG (HTF) tag to enable evaluation of protein expression by western blot. NotI and XhoI restriction sites were included immediately upstream and downstream of the desired construct to enable digestion and subsequent integration of the *SLC25A3-HTF* coding sequence between the CMV promoter and the BGH polyadenylation signal encoded in the pcDNA5/FRT TO vector, which was donated to me by the Tollervey group. The codon sequence of the *SLC25A3-HTF* construct was optimised for *Homo sapiens* by GeneArt (Thermo Fisher Scientific) and inserted into a standard (pMX) vector encoding a kanamycin-resistance selection marker. The designed vector was supplied as part of the GeneSyn service provided by GeneArt (Thermo Fisher Scientific).

The three plasmids were then co-transfected into Flp-In™ HEK 293 following the protocol described in II.5. The same procedure was applied to transfect the fluorescent pEGFP-N2 plasmid and only the pOG44 plasmid to two separate cell batches constituting negative controls for the transfection and plasmid (Figure II.2). Selection of transfectants was undertaken by treating the samples with 15 µg/mL blasticidin and 100 µg/mL hygromycin B. After two weeks of selection with both antibiotics, the medium was discarded, and the existent colonies were mechanically detached from the plate using PBS only. Having pelleted the cells by centrifugation at 300 rcf for 5 minutes, I resuspended the cells in DMEM supplemented with 15 µg/mL blasticidin and 100 µg/mL hygromycin B and transferred them to fresh T-25 flasks for cell line expansion at 37ºC. To induce expression of SLC25A3-HTF, transfected clones had to be treated with tetracycline or doxycycline, which is an antibiotic operating similarly to the former. I selected doxycycline (Sigma-Aldrich) as an inducing agent because its half-life, 48 hours, doubles that of tetracycline. To determine the minimum concentration of doxycycline required for significant overexpression of SLC25A3-HTF, I performed a western blot (see II.10) and quantified its expression at a range of doxycycline concentrations recommended by the cell line manufacturer.

II.7.6. Tagging *NAB3*, *NRD1*, *SEN1* and *RPO21* with a HIS6-TEV-3xFLAG epitope amplified from a yeast integrating plasmid (Ylp)

The endogenous loci coding for the proteins forming the NNS complex and Rpo21 were fused to a sequence coding for the HTF epitope. The tag sequence was amplified from the pBS1539::HIS6-TEV-3xFLAG URA3 vector (grey, Table II.9) using forward and reverse primers encoding the 50 bp preceding the stop codon of Nab3, Nrd1, Rpo21 or Sen1 (blue, Table II.9) and the 50 bp including and succeeding the stop codon for those genes respectively (blue, Table II.9). The PCR was catalysed by the Q5® high-fidelity DNA polymerase and the resulting product was treated with DpnI to degrade the parental DNA. Transformants were pipetted onto agar plates containing SC -Ura, and the correct integration of the tag in the surviving colonies was analysed using western blotting (see II.10).

Oligonucleotides	Sequence
Nab3-HTF_F	5'- CTGGCAATAATGTTCAAAGTCTATTAGATAGTTTAGCAAAACTACAAAAA GAGCACCATCACCATCACC - 3'
Nab3-HTF_R	5'- AGAATTCAAGTATAATGTACAAGAAATGGAAAAGATTGAAAAAAGGGAGT TACGACTCACTATAGG - 3'
Nrd1-HTF_F	5'- ATTCTTTGATGAATATGCTTAACCAACAGCAGCAGCAACAACAACAAAGC GAGCACCATCACCATCACC - 3'
Nrd1-HTF_R	5'- GGTAGATTAGTTTTATGTACTATGAGCAAATAAAGGGTGGAGTAAAGATC TACGACTCACTATAGGG - 3'
Rpo21-HTF_F	5'- ATTCTCCAAAGCAAGACGAACAAAAGCATAATGAAAATGAAAATTCCAGA GAGCACCATCACCATCACC - 3'
Rpo21-HTF_R	5'- AAACTATATATAATGTAATAACGTCAAATACGTAAGGATGATATACTATA TACGACTCACTATAGGG - 3'
Sen1-HTF_F	5'- GGAATGCTTCATCTAGCCCATTTATCCCAAAAAAAAGAAAGCCTAGATCA GAGCACCATCACCATCACC - 3'
Sen1-HTF_R	5'- TATACACCAATATATATGCAGGTATAATTCCTAACACTTTTACTTCAAGA TACGACTCACTATAGGG - 3'

Table II.9. Primers used for integration of the *HTF* epitope in the 3'end of the coding sequence of Nab3, Nrd1, Rpo21 and Sen1. Blue and grey fonts correspond to sequences that are homologous to the genome and the *HTF* insert, respectively.

II.8. Real-time quantitative reverse transcription PCR (RT-qPCR)

II.8.1.1. Primer design

The sequences of the yeast genes to be analysed were downloaded from the *Saccharomyces* Genome Database (SGD); namely, *PIC2* and *sfGFP* amplification

measurements were standardised to that of *ACT1*, *ALG9* and *PGK1*. The human *SLC25A3* sequence was downloaded from GenBank. FASTA files were individually inspected using SnapGene and the RNA regions of interest were copied as plain text into IDT's PrimerQuest primer design tool. A pool of putative oligonucleotides was automatically generated by the PrimerQuest software as 'qPCR 2 primers intercalating dyes'. Preliminary primers were manually curated to ensure that the ordered pairs (i) were delivered as 200 nM Primer DNA stored in 50 mM Na^{+}, 3 mM Mg^{++}, 0.8 mM dNTP, (ii) displayed a melting temperature between 59 ºC and 65ºC, (iii) possessed a GC content of around 35% and 65%, (iv) exhibited a size within a range of 17 and 30 nucleotides and (v) yielded an amplicon length of approximately 100 base pairs (with a maximum of 80 and a minimum of 120). The sequences for all the resulting working primer pairs are shown in Table II.10. Human reference primers were a kind gift from the Sibley group, and the *sfGFP* primers were designed by Mags Gwynne, who also performed the subsequent RT-qPCR in the strains coding for the synthetic expression systems.

Oligonucleotide	Sample	Sequence
ACT1_F	Yeast	5' - GCTGCTTTGGTTATTGATAACGGTTC - 3'
ACT1_R	Yeast	5' - GATGGGAAGACAGCACGAGGAG - 3'
ALG9_F	Yeast	5' - TAAGCTGGCATGTGCTGCATTC - 3'
ALG9_R	Yeast	5' - TTTGCATGATTCGGTTGATTGG - 3'
PGK1_F	Yeast	5' - GCTGCTTTGCCAACCATCAA - 3'
PGK1_R	Yeast	5' - TCGTTTCTTTCACCGTTTGGTC - 3'
PIC2_F	Yeast	5' - GGTGCTACATTCGTCGGATATT - 3'
PIC2_R	Yeast	5' - CACAGTGACACCAGGACTTAA - 3'
sfGFP_F	Yeast	5' - GGTGAGGGTGATGCTACTAATG - 3'
sfGFP_R	Yeast	5' - GCACTGGACACCATAAGTCAA - 3'
ACTB_F	Flp-In™ HEK 293	5' - CATGTACGTTGCTATCCAGGC - 3'
ACTB_R	Flp-In™ HEK 293	5' - CTCCTTAATGTCACGCACGAT - 3'
GAPDH_F	Flp-In™ HEK 293	5' - CACCATCTTCCAGGAGCGAGATC - 3'
GAPDH_R	Flp-In™ HEK 293	5' - GCAGGAGGCATTGCTGATGATC - 3'
RPL39_F	Flp-In™ HEK 293	5' - CTTCCTTTCTCCGCCATCGT - 3'
RPL39_R	Flp-In™ HEK 293	5' - TGAATCCAGCCAACCAACGT - 3'
SLC25A3_F	Flp-In™ HEK 293	5' - GATGAGGCAGATCCCTTACAC - 3'
SLC25A3_R	Flp-In™ HEK 293	5' - TGGGCACCACGAACTTATAC - 3'

Table II.10. Sequences for the oligonucleotides used for amplification of target and reference genes in yeast and Flp-In™ HEK 293 cells.

II.8.2. RNA extractions from *Saccharomyces cerevisiae*

Having been initially grown in pyruvate-containing SC cultures for 36-48 h, yeast strains were inoculated into 20 mL cultures of SC -Ura medium and incubated until they reached an OD_{600} of approximately 0.5. Cultures were then harvested by centrifugation at 3202 rcf for 7 minutes (Eppendorf 5810 R). After discarding the supernatant, cells were snap-frozen in liquid nitrogen and stored at -80ºC.

On the day of the extractions, cells were thawed on ice, washed with 5 mL of PBS, transferred to 5 mL tubes, and centrifuged at 1699 rcf for 7 minutes at 4ºC (Eppendorf 5804 R). Upon removal of PBS, cell pellets were denatured by the addition of 200 µL of guanidinium thiocyanate (GTC) acid phenol mix (Chomczynski and Sacchi, 2006). Subsequent cell lysis was performed by adding 400 µL of glass beads to each sample and vortexing all tubes at full speed for five 1-minute intervals separated by four 1-minute incubations on ice. An additional 1.5 mL of GTC phenol mix was then added to each lysate before 5 extra seconds of vortexing at maximum speed.

Samples were incubated at 65ºC for 10 minutes before being placed on ice for another 10 minutes. 800 µL of sodium acetate mix (3.3 mL 3 M NaOAc pH5.2, 0.2 mL 0.5M EDTA pH8, 1mL 1M Tris-HCl pH8, water to 100 mL) and 1.5 mL of chloroform were pipetted into each tube before vortexing each lysate at maximum speed for 5 seconds. Samples were centrifuged at 10621 rcf for 30 minutes (Eppendorf 5804 R), and the resulting aqueous phase was transferred into a new tube containing 2 mL of Phenol:Chloroform:Isoamylalcohol mix. The mixtures were vortexed vigorously and centrifuged at 10621 rcf for 5 minutes in the same instrument. Once more, the aqueous phase of each sample (approximately 1.5 mL) was mixed with 1.5 mL of Chloroform:Isoamylalcohol and vortexed at maximum speed before centrifugation at 10621 rcf for 5 minutes in an Eppendorf 5804 R centrifuge. Finally, 1mL from the aqueous phase of each sample was relocated to tubes carrying 3 mL of 96% (v/v) ethanol. The mix was vortexed vigorously and preserved at -80°C for at least 30 minutes or at -20°C overnight.

Following ethanol precipitation, samples were spun at 10621 rcf for 30 minutes at 4ºC in an Eppendorf 5804 R centrifuge. After discarding the resulting supernatants,

2 mL 70% (v/v) ethanol was pipetted into each tube. After centrifuging samples at 10621 rcf for 5 minutes at 4ºC in the same instrument, ethanol was removed, and pellets were left to air-dry for approximately 5 minutes before resuspension in 50 µL of diethylpyrocarbonate (DEPC)-treated water (Sigma-Aldrich). RNA concentrations were measured in DS-11 spectrophotometer (DeNovix).

II.8.3. RNA extractions from Flp-In™ HEK 293

Flp-In™-293 were grown in 6-well plates where each well contained 2 mL of glucose-rich DMEM medium. Once they reached approximately 90% confluence, the medium was removed, and cells were detached from the plate using trypsin (500 µL per well). Upon incubation with trypsin for 1 minute at 37ºC, DMEM was added to neutralise the enzyme and cells were transferred to a 15 mL tube and spun at 200 g for 5 minutes. The supernatant was discarded, and cells were snap-frozen by submersion in dry ice. Subsequently, cell pellets were stored at -80ºC.

On the day of the extraction, cells were collected from the freezer and placed on ice. 200 µL of GTC phenol were added immediately afterwards, and then 200 µL of zirconia beads (Thistle Scientific) to each frozen cell pellet. Each sample was vortexed at maximum speed twice for 30 seconds and incubated in a thermoblock for 5 minutes at 30º with shaking at 300 rpm. All tubes were then vortexed vigorously for another 30 seconds and subsequently placed on ice until 200 µL of chloroform and 100 µL of sodium acetate mix could be added to each of them. At this point, samples were left on a rack at room temperature for 5 minutes and centrifuged for 15 minutes at 4ºC at 10621 rcf in an Eppendorf 5804 R centrifuge. The upper aqueous phase of each sample (around 900 µL) was transferred to a 1.5 mL tube into which an equal volume of phenol:chloroform:IAA 25:24:1 was subsequently pipetted. The mixture was then vortexed at maximum speed for 5 seconds and centrifuged at 10621 rcf for 10 minutes in an Eppendorf 5804 R centrifuge. Again, the upper phase of each sample was transferred into a new tube holding approximately 800 µL of 96% (v/v) ethanol. Samples were vortexed for 5 seconds before being kept at -80ºC for 1 hour.

Following ethanol precipitation, samples were spun in an Eppendorf 5804 R centrifuge at 10621 rcf for 30 minutes at 4ºC. Once the ethanol was removed, the

pellets were washed with 1 mL of 70% (v/v) ethanol and centrifuged again at 10621 rcf for 5 minutes at 4ºC in the same instrument. After discarding the supernatants, RNA pellets were air-dried for 5 minutes at room temperature and resuspended in 11 µL of DEPC. RNA concentrations were measured in a DeNovix DS-11 spectrophotometer.

II.8.4. DNase treatment

Samples were treated with DNase to remove any contaminating DNA from the extracted RNAs. 10-20 µg of RNA were mixed with 0.9 µL of RQ1 DNase (Promega), 0.1 µL of 10X DNase buffer and 0.1 µL of RNasin® ribonuclease inhibitor (Promega) in PCR tubes. Samples were incubated in a thermocycler at 37ºC for 1 h before the reaction was stopped by adding 1 µL of RQ1 DNase stop solution (Promega) and denaturing the enzyme at 65°C for 10 minutes.

II.8.5. Reverse transcription

DNase-treated RNA extracts were split into two PCR tubes containing half of the initial sample volume; one of these tubes was reverse transcribed, whereas the other, in which no reverse transcriptase was added, served as a negative control. Two µL of SuperScript IV RT reaction buffer (Thermo Fisher Scientific), 0.75 µL of 10 mM dNTP mix (Thermo Fisher Scientific), 0.25 µL of RNasin®, 1 µL of random primer mix (New England Biolabs) and 4 µL of DEPC-treated water were added to both tubes. Finally, 0.5 µL SuperScript IV (Thermo Fisher Scientific) was pipetted into the reaction tube, and an additional 0.5 µL of nuclease-free water was added to the negative control. The reaction was started with an incubation of 5 minutes at 25ºC in a thermocycler. After that, samples were heated at 55°C for 1 h and, finally, the reaction was interrupted by denaturing the enzyme with a further increase in the temperature (80ºC, 10 minutes). A 1:10 dilution of the newly synthesised cDNA samples and their respective negative controls was performed by adding 180 µL of DEPC-treated water to all tubes.

II.8.6. Arrangement of cDNA samples in a 384-well plate

Two µL of the diluted cDNA were added to the relevant wells of a 384-well plate (Roche). Each sample was tested against four sets of primers: three sets of primers that amplified three reference genes and a primer pair that annealed to the gene of interest. Each primer pair was mixed at a final concentration of 4 µM. A further 1:5 dilution of each primer mix (i.e., one for each primer pair) was prepared using Brilliant III ultra-fast SYBR® green qPCR master mix (Agilent Technologies), and 2 µL of the resulting mix were added to every well. Every given sample was tested against each primer set in three wells, which provided technical triplicates. The negative control for the reverse transcription of each cDNA sample was added into a separate well. Finally, each oligonucleotide set was tested for primer dimerisation, which would have been detected as a fluorescence signal in wells exclusively containing the SYBR® green and primer mix with nuclease-free water. Before starting the reaction, the plate was spun in a 5810 R centrifuge (Eppendorf) at 128 rcf for 2 minutes, vortexed mildly and centrifuged again (128 rcf, 2 minutes) in the same instrument.

II.8.7. cDNA amplification and data analysis

The reaction was performed in a LightCycler® 480 qPCR device (Roche) using the default 2-step Agilent PCR programme of the LightCycler® SW 1.5 software. This PCR protocol encompasses (i) a Taq activation step (95ºC for 3 minutes), (ii) a forty-cycle amplification phase where individual cycles comprised a heating period at 95ºC for 5 seconds followed by a 10-second incubation at 60ºC and a green fluorescence reading, and (iii) a melting curve step in which 2 fluorescence recordings were acquired per second during a period at which the plate, originally incubated at 65ºC, is gradually heated at a rate of 0.29ºC/s to reach a maximum of 95ºC.

Raw data was initially processed within the machine's built-in software, which derived the cycle threshold (Ct) or quantification cycle (Cq) for each well. The cycle at which the fluorescence reading for a sample exceeds that of the background is denominated quantification cycle (Cq), and it will be lower if the concentration of the cDNA of interest is higher. The equation underlying this relationship is:

$$Cq = U - \log_E([cDNA])$$

Where U is an assay-specific unknown parameter, and E is the amplification efficiency. Since the biological definition of Cq is the cycle at which cDNA starts being exponentially amplified, its concentration will have doubled by the end of that Cq cycle. The amplification efficiency at this point is approximately 2 and thus, the previous formula can be rewritten as:

$$Cq = U - \log_2([cDNA])$$

To correct for fluctuations in *PIC2* Cq values between replicates, I also monitored the amplification of housekeeping genes, such as *ACT1*, *ALG9* and *PGK1*, whose expression remained constant across decreasing raffinose concentrations (Figures III.3, III.5 and III.6). Raw Cq values were normalised using Tidyqpcr, an R package for qPCR data analysis (Wallace and Haynes, 2021). This software uses the median Cq value of the reference genes to calculate the differential Cq (∆Cq) for the remaining ones. From the mathematical definition of Cq, I can derive that the ∆Cq for the gene of interest is the logarithmic ratio of *PIC2* cDNA concentration to that of the selected reference gene:

$$\Delta Cq_{\,PIC2} = Cq_{reference} - Cq_{PIC2}$$
$$\Delta Cq_{PIC2} = U_{reference} - \log_2([cDNA]_{reference}) - (U_{PIC2} - \log_2([cDNA]_{PIC2}))$$
$$\Delta Cq_{\,PIC2} = U_{reference} - U_{PIC2} + \log_2([cDNA]_{PIC2}) - \log_2([cDNA]_{reference})$$

Defining the difference of unknown factors as U' and applying logarithmic properties, I can rewrite the equation as:

$$\Delta Cq_{\,PIC2} = U' + \log_2([cDNA]_{PIC2}/[cDNA]_{reference})$$

From this formula, I can define the relative *PIC2* mRNA abundance as $2^{-\Delta Cq_{PIC2}}$ and subsequently use these values to compare relative cDNA concentrations of *PIC2* between samples. However, extracted *PIC2* mRNA abundances will be affected by an unknown parameter which cannot be assumed to remain constant across samples. For this reason, a second round of normalisation was performed by the median ∆Cq values of each tested gene in the reference wild-type strain (i.e., *PIC2-GFP*) to determine the differential ∆Cq (∆∆Cq) for those of the mutant strains. As shown below, this approach removes the unknown assay-specific parameter from ∆∆Cq values:

$$\Delta\Delta Cq_{\textit{PIC2 in tested strain}} = U' + \log_2([cDNA]_{\textit{PIC2 in tested strain}}/[cDNA]_{\text{reference in tested strain}}) - (U' + \log_2([cDNA]_{\textit{PIC2 in PIC2-GFP strain}}/[cDNA]_{\text{reference in }\textit{PIC2-GFP}\text{ strain}}))$$

$$\Delta\Delta Cq_{\textit{PIC2 in tested strain}} = \log_2([cDNA]_{\textit{PIC2 in tested strain}}/[cDNA]_{\text{reference in tested strain}}) - \log_2([cDNA]_{\textit{PIC2 in PIC2-GFP strain}}/[cDNA]_{\text{reference in }\textit{PIC2-GFP}\text{ strain}})$$

$$\Delta\Delta Cq_{PIC2\text{ in tested strain}} = log_2\left(\frac{\frac{[cDNA]_{PIC2\text{ in tested strain}}}{[cDNA]_{\text{reference in tested strain}}}}{\frac{[cDNA]_{PIC2\text{ in }PIC2-GFP\text{ strain}}}{[cDNA]_{\text{reference in }PIC2-GFP\text{ strain}}}}\right)$$

Finally, the fold change in mRNA abundance with respect to the reference sample can be calculated as $2^{-\Delta\Delta Cq_{PIC2}}$.

II.9. Yeast growth, oxidative stress, and fluorescence assays

Five mL of yeast cultures containing synthetic complete medium lacking uracil (SC -Ura) supplemented with 2% (w/v) pyruvate were grown at 30°C for 36 - 48 h. One hundred µL of those starter cultures were used to inoculate 2 mL of SC -Ura containing a high (i.e., 2% (w/v)) or low (i.e., 1% (w/v)) concentration of raffinose or glucose. After being incubated at 30°C for 3-4 hours, cells were harvested by centrifugation (3202 rcf, 5 minutes, Eppendorf 5810 R) and washed with 1 mL of sterile water. Upon a second round of centrifugation (3202 rcf, 5 minutes, Eppendorf 5810 R) and removal of the supernatant, cells were resuspended in 1 mL of SC -Ura medium supplemented with the applicable concentration of raffinose. During the experiments that were conducted to quantify Pic2-GFP expression, this resuspension step was performed using low fluorescence SC -Ura medium to minimise the medium's intrinsic fluorescent signal and prevent it from interfering with the one originated by the protein of interest.

Two hundred µL of each sample were then pipetted into cuvettes holding 200 µL of the relevant medium, and OD_{600} was measured. Once all cultures had been diluted to a final OD_{600} of approximately 0.1, 200 µL of each sample were transferred to three separate wells of a 96-well black non-treated polystyrene microplate (Thermo Fisher Scientific). The microplate and its accompanying lid (Grenier) were UV-treated for 5-10 minutes prior to the addition of the samples into the wells. With the aim of

detecting contamination in the media used, triplicate blank controls comprising the same volume of sterile medium were also included for each examined condition.

Absorbance was monitored in Infinite F200 (Tecan) microplate readers. Acquisitions were set to be performed at a temperature range of 29.4 and 30.4ºC throughout 300 kinetic cycles composed of (i) 535 seconds of orbital shaking at an amplitude of 6 mm, (ii) 15-flashes absorbance measurements at a wavelength of 595 nm and a bandwidth of 9 nm and (iii) a 25-flashes fluorescence top reading at an excitation wavelength of 485 nm, an excitation bandwidth of 20 nm, and an emission wavelength and bandwidth of 535 nm and 25 nm respectively. To prevent under or over-saturation of the detected fluorescence, I recorded the signal using a range of signal amplification factors. Hence, fluorescence readings were manually set to be acquired at gains of 100, 80 and 50.

The manufacturer's i-control™ software automatically recorded all absorbance and fluorescence measurements in an Excel spreadsheet. Together with an annotation CSV file specifying the strain and conditions contained within each well, this raw output file is used as an input for the Omniplate software (Montaño-Gutierrez et al., 2022), which facilitated downstream statistical analysis.

The Omniplate module is a Python package that processes time-series data raw outputs from microplate readers to analyse microbial growth and gene expression (Montaño-Gutierrez et al., 2022). Before proceeding with any estimations, optical density and fluorescence values undergo a series of corrections. Firstly, the absorbance signal for the appropriate media is discounted from the OD_{600} measurements of wells containing cultures using the `correctmedia()` tool (Montaño-Gutierrez et al., 2022). Secondly, absorbance is corrected for the non-linear relationship between OD_{600} measurements and cell count at higher absorbance values by running the `correctOD()` function (Montaño-Gutierrez et al., 2022). For all analyses, this compensation was based on a default dilution curve that is installed alongside the software and contains the measured and expected OD_{600} measurements of a BY4741 culture grown at high density and subsequently diluted by known factors.

The `correctmedia()` function can also subtract background fluorescent signals inherent to the media from the fluorescence readings of wells containing cells

(Montaño-Gutierrez et al., 2022). The resulting values were then corrected for autofluorescence by applying `correctauto()` (Montaño-Gutierrez et al., 2022). Autofluorescence was defined as the fluorescence signal emerging from an unmodified BY4741 parental strain. Final corrected fluorescence values were plotted against time using the built-in `relplot()` function of Python's seaborn package (Waskom, 2021).

Growth rates for a microbial population can be inferred as a time derivative of the logarithm of the population size. To characterise the population size, Omniplate makes assumptions about the family of latent functions that can describe it using a Gaussian-process-based algorithm (Montaño-Gutierrez et al., 2022). Since it is not defined by a single function, this method does not constrain the variety of data that can be fitted into it (Swain et al., 2016). Nonetheless, unlike non-parametric approaches, which estimate growth rates directly for the data, Omniplate allows for the prediction of errors in the estimated growth rates by fitting additional artificial replicates of the experimental data using bootstrap or iterative random re-sampling (Swain et al., 2016). Having followed this approach to process the OD values extracted from the triplicates for each sample, I could plot the average growth rate with an associated standard deviation. Similarly to the corrected fluorescence graphs, line plots for growth rate over time were generated applying seaborn's relplot() tool (Waskom, 2021).

The `getstats()` function from the Omniplate package provides a summary of the growth parameters that have been computed based on the three technical replicates that were included for each sample (Montaño-Gutierrez et al., 2022). This command outputs an estimation of maximal growth rate, time of maximal growth rate, doubling time and lag time, which is the period that a microbial population takes to reach exponential growth after inoculation into a given medium. To determine whether a strain was resistant or hypersensitive to oxidative challenges such as hydrogen peroxide, I calculated the logarithmic ratio of the maximal growth rate in medium containing 0.5 mM hydrogen peroxide to that of the medium lacking this reactive oxygen species. Resulting logarithmic fold changes could then be statistically compared to that observed in the parental strain; while strains displaying a significantly higher value than the reference strain were considered more tolerant to oxidative stress, cells with lower logarithmic ratios were deemed more susceptible to such insults. Statistical significance was determined using unpaired t-tests performed by GraphPad Prism 8.0.1, which was also used to generate the relevant bar plots.

II.10. Mammalian cell viability assay

Flp-In™ HEK 293 cells were grown in four 6-well plates to a confluence of approximately 80-90% using DMEM supplemented with blasticidin (15 µg/mL) and hygromycin B (100 µg/mL). Wells containing cell populations in which expression of *SLC25A3-HTF* was to be induced were treated with doxycycline (0.2 µg/mL) 36 hours prior to the addition of 0.5 mM of hydrogen peroxide to the wells of two of the plates and sterile water to all cell populations contained in the other pair of plates. The latter set was used as a negative control for any cell death which may have been caused by the pipetting of a liquid into the cultures.

Trypan blue (Thermo Fisher Scientific) was used to measure the viability of the cell population in three of the wells of each plate immediately after the addition of hydrogen peroxide or water. The cells were detached prior to mixing them in a 1:1 ratio with 15 µL trypan blue. The subsequent live/dead assay was performed under the premise that trypan blue would only permeate cells that did not possess intact membranes and were, therefore, either dying or dead. Cells were counted by a Countess 3 automated cell counter (Thermo Fisher Scientific), which measured unstained and stained cells in two separate samples per well. All other cultures were incubated at 37ºC for 18 hours.

On the following day, an equivalent trypan blue viability assay was executed in all remaining populations. The two technical repeats for each of the three biological replicates that were examined for uninduced and SLC25A3-overexpressing cells were grouped before performing viability calculations. The samples that had been treated with sterile water were processed identically before assessing the statistical significance of differences across wells and conditions (unpaired t-tests) and plotting their live population portions in GraphPad Prism 8.0.1.

II.11. Fitness assay

After having been growing for 48 hours on pyruvate-rich SC -Ura medium, a volume holding an equivalent to OD_{600} 0.0005 for each tested strain was transferred into a fresh 5 mL of raffinose-rich or raffinose-deprived media. An additional volume corresponding to that containing an equivalent to OD_{600} 0.0005 of the red fluorescent

wild-type strain (Ura7-mCherry) was also pipetted into the recently inoculated culture. Accordingly, the initial ratio of the strain of interest to the red-coloured reference strain was approximately 1:1. Cells were then left to compete in the medium while being incubated at 30ºC.

18 hours after inoculation, cultures had already entered the mid-exponential phase and could, thus, be sampled to test changes in population proportions. To this end, 1 mL of culture was transferred to a 1.5 mL microcentrifuge tube and centrifuged at 1073 rcf for 5 minutes in an Eppendorf MiniSpin device. Immediately afterwards, the supernatant medium was discarded and replaced with PBS. Having ensured adequate resuspension of the cells in PBS, 200 µL of this suspension were transferred to wells of a transparent 96-well plate (Thermo Fisher Scientific) where samples could be inspected by flow cytometry. A volume corresponding to OD_{600} 0.0005 of the mid-logarithmic stage culture was transferred to 5 mL of the same sterile medium to continue monitoring the competition throughout time. Additional flow cytometry samples were gathered at 18-, 36- and 60-hours post-inoculation.

Flow cytometry was performed in a BD LSR-Fortessa (BD Biosciences) machine at the Flow Cytometry Facility for the School of Biological Sciences. Following a preliminary inspection of two wells containing an untagged parental strain (i.e., BY4741) and the Ura7-mCherry fluorescent control, I programmed the voltage of the PE-Texas Red detector to be 600 PnV. A minimum of 20,000 events were recorded per well. Upon export and analysis of the resulting FCS files in FlowJo 10.8.1, all events were visualised in a dot plot displaying FSC-A against SSC-A values. A loose gate was introduced to exclude any debris that could contribute to the red fluorescence signal that I aimed to dissect. Following previously described criteria (see II.14), I inserted an additional gate to impose that the FSC-W reading did not surpass that of a single cell. Cells falling under both gates were then plotted in histograms showing PE-Texas Red distributions. Based on the profiles of the non-red wild type (i.e., BY4741) and the red reference (Ura7-mCherry) populations within the X axis of the histogram, a fluorescence gate was established between the base of both peaks. The percentage of non-red and red cells within a sample was used to calculate a ratio of non-fluorescent to fluorescent events. Each competition was performed in three independent repeats, and a mean and standard deviation were determined for said non-fluorescent:fluorescent cell ratio. The average and errors for all strains were

subsequently normalised to the mean ratio calculated for the pertinent parental reference. The statistical significance of population differences compared to the control strain was assessed by applying unpaired t-tests. These statistical tests, as well as the bar plots displaying the mean and standard deviation for each strain, were completed in GraphPad Prism 8.1.

II.12. Western blot

Following growth in SC -Ura supplemented with 2% (w/v) pyruvate, cells were transferred to 25 mL SC -Ura medium with the fitting concentration of raffinose or glucose. During the experiments aiming to assess differences in Pic2-GFP abundance, samples were collected at OD_{600} 0.25, OD_{600} 0.5 and OD_{600} 1 from cultures containing standard (i.e., 2% (w/v)) or reduced (i.e., 1% (w/v)) raffinose concentrations. For the western blots destined to compare the typical expression levels of the NNS complex and the RNA polymerase to those at which I performed CRAC, I gathered cells grown up to an OD_{600} 1 in glucose-abundant or raffinose-limiting cultures.

Once they reached the desired growth phase, the volume corresponding to a cell population equivalent to OD_{600} 5 was transferred into a 50 mL centrifuge tube and harvested by a 5-minute centrifugation step at 3202 rcf in an Eppendorf 5810 R centrifuge. Having discarded the supernatant, samples were flash-frozen in liquid nitrogen and stored at -80ºC. Flp-In™ cells were cultured in 6-well plates and, once they reached confluency, they were rinsed with PBS, detached from the plate with an incubation in trypsin as outlined in II.2. 1.2 million cells were spun down (200 rcf, 5 minutes, Eppendorf 5804 R) and identically flash-frozen upon disposal of the supernatant.

On the day of the lysis, yeast cells were retrieved on ice, resuspended in 30 mL of PBS and spun down (3202 rcf, 5 minutes, Eppendorf 5810 R). After discarding the supernatant, cell pellets were homogenised by pipetting in 2 volumes of lysis buffer (50 mM Tris-HCl pH 7.8, 150 mM NaCl, 0.1% (v/v) Nonidet P-40, 1 cOmplete™, EDTA-free Protease Inhibitor Cocktail (Roche) per 50 mL and 5 mM β-mercaptoethanol). For example, 1 mL of lysis buffer would have been added to a pellet weighing 0.5 g. Since Flp-In™ cells had already been washed with PBS, frozen pellets were completely

dissolved immediately after being exposed to the lysis buffer while being kept on ice, and no mechanical force was required. Upon addition of 3 volumes of 0.5 mm zirconia beads, yeast samples, however, were vortexed at full speed for five 1-minute intervals separated by four 1-minute incubations on ice. The beads and cell debris were then spun down by centrifugation at 10621 rcf for 20 minutes in an Eppendorf 5804 R, and the supernatants were transferred to 1.5 mL tubes.

The protein concentration of each lysate was quantified using the Qubit™ fluorometer and its accompanying protein assay kit (Thermo Fisher Scientific). After preparing a working solution consisting of a 1:200 dilution of the protein reagent solution into a protein buffer solution, I calibrated the device using 1:20 dilution of three standards containing 0 ng/µL, 200 ng/µL and 400 ng/µL BSA, respectively. The protein abundance in all lysates was measured from 1:200 dilution of each sample into the same working solution. Lysates were then diluted to the concentration of the least concentrated sample within its experimental set. Fifteen µL containing 10 µg of each protein sample were transferred into a fresh 1.5 mL tube and mixed with 5 µL of 4X NuPAGE™ LDS sample buffer (Thremo Fisher Scientific) containing 5 mM β-mercaptoethanol (Sigma-Aldrich). Samples were then heated in a thermoblock at 95ºC for 5 minutes to denature the proteins.

After heating, tubes were spun, and 20 µL of the sample were pipetted into NuPAGE™ (Thermo Fisher Scientific) precast polyacrylamide gels. Whilst lysates assigned to Pic2-GFP, Nrd1-HTF and Nab3-HTF detection were separated in 4% to 12% gradient Bis-Tris gels with 3-(N-morpholino)propanesulfonic acid (MOPS) running buffer (Thermo Fisher Scientific), samples designated to the inspection of Rpo21-HTF and Sen1-HTF were fractionated on 3% to 8% gradient Tris-acetate gels with Tris-acetate running buffer (Thermo Fisher Scientific). All electrophoreses ran for 1.5 hours at 150 V. Proteins were transferred onto a 0.2 µm nitrocellulose membrane by wet transfer in NuPAGE transfer buffer (Thermo Fisher Scientific) supplemented with 10% (v/v) methanol. The tank blotting system was placed within an ice box throughout all transfers, which ran at 100 V for 1 hour for medium-sized proteins and 3 hours for larger proteins.

Membranes were subsequently rinsed with ultrapure water and blocked using 10 mL of PBS containing 0.1% (v/v) of Tween (PBS-T) and 5% (w/v) of skimmed milk.

Blocking took place with slow shaking at room temperature for 30 minutes. Having discarded the blocking solution, immunoblotting was performed by incubating the membrane in the same solution containing the appropriate concentration of the relevant primary antibodies. To examine Pic2-GFP expression, membranes were incubated in a 1:500 dilution of anti-GFP (Invitrogen, C163) and 1:1000 dilution of anti-GAPDH (Thermo Fisher Scientific, RM114) and, to assess the expression of the NNS complex and Rpo21, I used a concentration of 1:5000 of a monoclonal anti-FLAG® M2-Peroxidase (HRP) antibody (Sigma-Aldrich, A8592). In all cases, incubation with the primary antibodies occurred overnight with slow shaking at 4ºC. After immunoblotting, membranes were washed three times with 5 mL of PBS-T and slow shaking.

Membranes probed with the anti-FLAG HRP antibody were prepared for protein detection by chemiluminescence. Proteins were subsequently detected employing the Pierce™ enhanced chemiluminescence (ECL) western blotting kit (Thermo Fisher Scientific). Chemiluminescence was visualised by applying the automatic chemiluminescence exposure settings in the Amersham ImageQuant™ 800 system (Cytvia Life Sciences). Membranes immunoblotted to anti-GFP and anti-GAPDH antibodies were incubated with a 1:5000 dilution of the goat anti-mouse IRDye 800CW (LI-COR Biosciences) and 1:5000 of the goat anti-rabbit IRDye® 680RD (LI-COR Biosciences) respectively. Hybridisation to the secondary antibodies took place in 2 hours with slow shaking at room temperature and was succeeded by fluorescence imaging using the IR long (775 nm) and IR short (660 nm) channels in the Amersham ImageQuant™ 800 device manually set to an exposure of 15 seconds and 5 minutes respectively.

In experiments destined to evaluate the relative abundance of Pic2 in the samples, the maximum intensity for the Pic2 or SLC5A3 bands in the membrane images was measured using ImageQuant TL 8.1 (Cytvia Life Sciences) and subsequently normalised to the maximum intensity of the GAPDH band in the same sample. The Pic2/SLC5A3 to GAPDH ratios were measured in biological triplicates for each strain and condition and statistically compared to the relevant reference with unpaired t-tests ran in GraphPad Prism 8.0.1, which was also employed to produce the bar plots.

II.13. Microfluidics and time-lapse microscopy

Following pre-culture growth in 5 mL cultures of SC -Ura with 2% (w/v) pyruvate for 36-48 hours, all yeast strains were grown in 5 mL cultures of SC -Ura with a concentration of carbon source (i.e., raffinose or galactose/sucrose) pertinent to the experiment. After 3-5 hours of incubation in this medium, cells were transferred into a sterile 10 mL syringe and covered with its accompanying needle and lid to prevent contamination. Cultures were loaded into the adequate chamber of an ALCATRAS device (Crane et al., 2014). Since I used 3- and 5-chamber chips, I was able to image two or four mutants with their applicable parental reference in one single experiment.

To reduce the formation of cell aggregates, thereby easing cell loading into the devices, throughout the experiment, I supplemented the relevant experimental medium with 0.05% (v/v) bovine serum albumin (BSA) and subsequently sterilised it by filtration (0.2 µm). Prior to the injection of cells into the device, its chambers were filled with BSA-containing medium. The remaining volume of such medium was stored in a syringe or centrifuge tube and paired to an automatic pump that was set to maintain a continuous inlet of 4 µL/h of fresh medium into the chip. This constant flow ensured that the original cells remained inside their traps throughout the entirety of the experiment, and their budded cells were washed away. The daughter cells were, consequently, prevented from obstructing the supply of nutrient-rich medium to the parent cells.

During microscopy, the device was placed inside an insulation chamber (Oko-labs) that was kept at 30ºC. Imaging was performed on a Nikon Ti-E inverted microscope (Nikon) using a 60X 1.4 NA oil-immersion objective (Nikon), an OptoLED light source (Cairn Research) and sCMOS (Prime95B, Photometrics), or EMCCD (Evolve, Photometrics) cameras controlled by a custom graphic user interface written for Micromanager (Edelstein et al., 2010). To preserve a constant focus throughout the duration of the experiment, images were captured with the Nikon Perfect Focus System (PFS). Images were then acquired every 5 minutes, and although the duration of image acquisition varied for each experiment, it was always kept to a period that allowed sufficient time for the objective to visit all manually defined positions within each chamber.

Images were captured in the brightfield and GFP channels applying Z-stacking; for both channels, five Z sections were taken with a spacing of 0.6 µm between each of them. For GFP imaging, I used a GFP-B,GFP/mCherry (59022) exciter (Nikon) and set the exposure time to 15 milliseconds. LED voltage was programmed to -9.7 V based on a previous optimisation for maximum signal intensity.

Experimental outputs were uploaded to the OMERO server, which stores the data and allows it to be accessed for downstream analysis (Allan et al., 2012). To analyse the microscopy images, I used the ALIBY pipeline (Muñoz González et al., 2024), which automates cell segmenting, tracking and post-processing of microscopy time-lapse images. This package fetched the images from Omero and tracked the tiles comprising the traps present across time-lapse images of every position that was established during the experimental set-up. In doing so, the software accounted for any spatial drifting which may have occurred while the images were captured. The pipeline then uses the Birth Annotator for Budding Yeast (BABY) algorithm to create masks encircling the outline of the cells in the previously defined traps and subsequently tracking them across time points to generate cell lineages (Pietsch et al., 2023). Cellular outlines are used to delimit the acquisitions in the brightfield and GFP channels and, consequently, extract the dimensions, budding events, and fluorescence intensity of each cell. Having computed the average fluorescence in regions laying outside cell masks, the pipeline subtracted such noise from the intensity values that it originally assigned to each cell in the same image. The single-cell values of the resulting matrix were used as an input for different plotting and statistical analysis functions of the seaborn and matplotlib Python libraries (Hunter, 2007; Waskom, 2021).

II.14. RNA secondary structure prediction

The sequence spanning the 20 nucleotides upstream and downstream of the region containing the NNS RNA-binding sites for *PIC2* was analysed to compare secondary structure predictions between the *PIC2-GFP* strain and all derived mutants. Widening the window at which the most proximal and distal single-point mutations occurred ensured that the sequence in which folding predictions were to be undertaken could assemble into structures resembling the ground truth in a native cellular

environment. The sequences were fed to the RNAfold algorithm (Lorenz et al., 2011), which simulated the folding of the input transcripts based on merely thermodynamic parameters: namely, it calculated the partition function, base-pairing probability matrix and the minimum free energy of the structure (Lorenz et al., 2011). Having obtained the thermodynamic ensemble of the RNA structures, the software outputted a mountain plot for each sequence (Lorenz et al., 2011). Finally, these graphs were overlapped for direct comparison.

II.15. Cell size measurement

After a standard pre-growth stage in SC -Ura with 2% (w/v) pyruvate, cells were transferred to 25 mL of the appropriate SC -Ura medium at a starting OD_{600} of 0.1. Cultures were incubated for 4-5 hours if they contained glucose as the carbon source and 6-8 hours if raffinose was provided as the only sugar. Once cultures entered mid-logarithmic growth (i.e., OD_{600} of 0.3-0.6), 800 µL were transferred to a 1.5 mL microcentrifuge tube and spun down (3202 rcf, 5 minutes, Eppendorf 5810 R). Upon disposal of their supernatant, cell pellets were resuspended in the same volume of PBS and pipetted 200 µL of the resulting cell suspensions into separate wells of a transparent 96-well plate (Thermo Fisher Scientific).

Flp-In™ HEK 293 cells were seeded in 6-well plates (Thermo Fisher Scientific) containing DMEM three days before the experiment. Doxycycline was added to the medium of the samples at a final concentration of 0.2 µg/mL to overexpress *SLC25A3*. On the day of the experiment, the confluence of the cultures was estimated at around 70-90%. The medium was then discarded, cells were rinsed with PBS, detached from the plate upon addition of 250 µL of 0.25% (v/v) trypsin-EDTA and incubated at 37ºC for 2-3 minutes. Immediately afterwards, trypsin was neutralised with the addition of 750 µL of DMEM and cells were centrifuged at 300 g for 5 minutes. The medium was then removed and replaced by 1 mL of PBS. Again, 200 µL of these cell suspensions were transferred to wells of a clear 96-well plate.

Acquisitions were recorded in a BD LSR-Fortessa (BD Biosciences) cytometer at the Flow Cytometry Facility for the School of Biological Sciences. For the purposes of this experiment, forward scatter (FSC) and side scatter (SSC) detector voltages were

set to 335-350 PnV and 315-325 PnV for yeast and 135 PnV and 261 PnV for mammalian cells. A lower laser voltage was required for human cells due to their larger size. The appropriate laser settings for each cell type were employed to acquire between 100,000 and 50,000 events per well.

Experimental files were exported in their native format and visualised in FlowJo 10.8.1, where the normalised distribution of ungated FSC values was plotted in histograms. The weighted average and standard deviation were calculated for the three independent biological repeats that were assessed per cell type and condition. Statistical analysis (unpaired t-tests) and visualisation were carried out in GraphPad Prism 8.0.1.

II.16. Mitochondrial membrane potential with MitoTracker™ Red

MitoTracker red staining and flow cytometry were used to preliminarily inspect the mitochondrial membrane potential of large cell populations. Yeast and mammalian cell samples were prepared as described in II.16.2. However, in this case, 70 nM of MitoTracker Red CMXRos (Thermo Fisher Scientific) were added to the medium 30 minutes before harvesting the cells for acquisitions. Cells lacking a GFP tag (i.e., non-fluorescent yeast strains and all mammalian cell lines) were simultaneously stained with 70 nM of MitoTracker Green FM (Thermo Fisher Scientific).

Data was acquired in a BD LSR-Fortessa (BD Biosciences) instrument at the Flow Cytometry Facility for the School of Biological Sciences. In these experiments, the FSC, TexasRed or Cy5 red, and FITC green detector voltages were set to 335-350 PnV, 515-553 PnV, and 525 PnV for yeast cells. Human cells were inspected using the 480 PnV and 350PnV for mammalian cells. A lower laser voltage was required for human cells due to their larger dimensions and fluorescence. The suitable laser settings for each cell type were employed to acquire between 100,000 and 50,000 events per well.

Recorded events were exported as FCS files and manually examined in FlowJo 10.8.1, where the normalised distribution of MitoTracker values was plotted in histograms. Median red fluorescence values were normalised to the median cell size

values or the median green fluorescence values in GFP-encoding strains and non-fluorescent cells, respectively. The weighted average for this normalised red fluorescence and its standard deviation were calculated for the independent biological triplicates that were assessed per cell type and condition. Statistical analysis (unpaired t-tests) and visualisation were carried out in GraphPad Prism 8.0.1.

II.17. Mating assay

Given that *PIC2-GFP*, Δ Nab3 RNA-BSs and Δ NNS RNA-BSs are mating type a (MATa) haploid strains, they could be backcrossed to the mating type α (MATα) BY4742 strain to generate diploid yeast cells. Crossings were performed by mixing each MATa strain with MATα in separate YPDA plates that were subsequently incubated at 30ºC. The following day, single colonies were re-streaked into fresh YPDA plates and stored at 30ºC to allow growth overnight.

The patches of the YPDA plate that were left to grow in the previous day were replica-plated onto fresh YPDA plates and mating tester YPDA plates, which had been previously coated with 200 µL of a or α factor. These fresh plates were incubated at 30ºC overnight, and patches which failed to grow in either of the mating tester YPDA plates were deemed haploid and excluded from downstream experiments.

The remaining candidates were considered potentially diploid cells and, thus, were tested for sporulation. To this end, putative diploids were re-streaked onto agar-based plates containing SPO medium (0.3% (w/v) potassium acetate, pH 7). Sporulation plates were then incubated at 30°C for up to 3 days. During these days, the plate was checked regularly for tetrads, and once these were identified, some cells were removed from the plate, resuspended in 20 µL of digestion solution (1 mg/mL of zymolase (AMS Biotechnology) dissolved in 1 M sorbitol) and subsequently incubated at room temperature for 8 minutes. To stop the reaction, 1 mL of sterile water was added to each sample. 20 µL of the resulting solution were pipetted on the border of a fresh YPDA plate and left to slide through its size before being air-dried. Once all the volume of the digestion solution had evaporated, a minimum of 8 tetrads were dissected onto each half of the plate.

Dissection plates were then incubated at 30°C overnight before proceeding with a mating-type check of the sister spores within each tetrad. The four spores originating from the same tetrad were re-streaked as broader patches in a new YPDA fresh and, once grown, replica-plated on mating-type tester plates spread with either pheromone. Dissections yielding an a to α ratio of 2:2 were considered as potentially successful and further examined for the *GFP* marker fused to the *PIC2* allele that two of the haploid spores would have inherited from their *PIC2-GFP*, Δ Nab3 RNA-BSs and Δ NNS RNA-BSs parental strain. Fluorescent spores were identified by microscopy and colony PCR.

II.18. Cell cycle analysis

Starting cultures of SC containing 2% (w/v) pyruvate were incubated for 48 hours before being used to inoculate fresh 25 mL media of SC -Ura with 2% or 1% (w/v) raffinose. These cultures were left to grow from a starting OD_{600} of 0.1 for 10 h until they reached the mid-logarithmic phase. 2 mL of each culture were then transferred into a separate 5 mL centrifuge tube, and cells were harvested by centrifugation at 3202 rcf for 5 minutes in an Eppendorf 5810 R centrifuge. Upon removal of the supernatant, cells were immediately fixed by the addition of ice-cold 70% (v/v) ethanol. After homogenising the cells in their fixation solution, they were stored at -20ºC overnight.

On the next day, cells were centrifuged (5000 rcf, 20 minutes, Eppendorf 5804 R) to remove the ethanol and exchange it for 800 µL of 50 mM sodium citrate buffer (pH 7.2). After fully resuspending all samples in this hypotonic solution, they were incubated at room temperature for 10 minutes. After that period, samples were centrifuged (1073 rcf, 5 minutes, Eppendorf MiniSpin), and the sodium citrate supernatant was replaced with an additional 800 µL of the same solution. Resuspension in fresh sodium citrate was followed by another 10-minute incubation at room temperature. Immersing cells in a hypotonic solution permeabilises the plasma membrane without compromising the structural integrity of the nuclei and, hence, facilitates subsequent enzymatic digestions and DNA staining.

Before commencing RNA digestion, sodium citrate was separated from the fixed cells by centrifugation (1073 rcf, 5 minutes, Eppendorf MiniSpin) and replenished by 300 µL of fresh solution. At this point, RNace-It™ ribonuclease cocktail (i.e., a mixture of RNase A and RNase T1; Agilent Technologies) was added to a final concentration of 0.1 mg/mL (i.e., 15 µL of 2 mg/mL stock) and incubated overnight at 37°C. Proteins were digested upon the addition of 10 µL of 20 mg/mL proteinase K (Roche) and subsequent incubation at 55ºC for 2 hours. Afterwards, to disrupt aggregates, cells were sonicated for 5 seconds using a microtip probe set to 25 µm. At this stage, samples could be stored for up to 1 month at 4ºC or stained with 50 µg/mL propidium iodide (PI; Sigma-Aldrich) for flow cytometry. In the latter case, 200 µL of each resulting sample were pipetted into individual wells of a clear 96-well plate (Thermo Fisher Scientific).

Flow cytometry was performed in a BD LSR-Fortessa (BD Biosciences) instrument at the Flow Cytometry Facility for the School of Biological Sciences. Due to the distinct size ranges of each set of cells, the laser parameters were customised for each experiment. As a rule of thumb, however, voltages were fine-tuned in a way in which they located the haploid G1 (i.e., n) peak at around 20% of the full linear scale and, therefore, the diploid G2 (i.e., 2n) at approximately 40% of the X axis range. Essentially, this configuration enabled the acquisition of haploid (i.e., n) to tetraploid (i.e., 4n) events, spanning haploid G1 through diploid G2.

For normally sized yeast cells, the forward scattering (FSC), side scattering (SSC) and PE-Texas Red lasers were set at 600 PnV, 400 PnV and 775 PnV, respectively. Nonetheless, for sample sets known to contain at least one strain displaying a larger cell diameter, I decreased the FSC and SSC detector voltages to 450 PnV and 350 PnV. Mildly lowering lasers is a typical strategy to inspect cells that would have otherwise been out of the size scale positively. The appropriate laser settings were employed to acquire approximately 10,000 events per well.

Experimental files were exported in their standard FCS format and analysed in FlowJo 10.8.1. To select single cells, I displayed all events in a graph illustrating their FSC-A against their FSC-W. When more than one cell is detected in a single event, the width (i.e., FSC-W) of such occurrence tends to be greater than its recorded area (i.e., FSC-A). Therefore, I set a gate excluding all events for which the FSC-W value exceeded the one to be expected for a single cell. I then plotted all events falling within

the single cell gate as a histogram of PE-Texas Red A to examine DNA content peaks. After visualising normalised PE-Texas Red-A histograms to the mode of the events within all the repeats of the appropriate control strain, I drew the gates for G0 (before the beginning of the n peak), G1 (delimiting the n peak), S (laying in between the two peaks), G2/M (outlining the 2 n peak) and polyploidy events (surpassing the red fluorescence values expected among diploid cells). These gates were defined alongside the representative histograms, which were directly exported from FlowJo. The statistical significance of any differences observed between the distribution of the population of a given strain along the cell cycle was assessed by applying unpaired t-tests computed by GraphPad Prism 8.1. Bar plots showing the mean and standard deviation for these distributions were generated using the same software.

II.19. Confocal microscopy

Cells grown in pyruvate-containing SC -Ura were transferred to fresh 5 mL cultures of SC -Ura supplemented with the appropriate concentration of raffinose for the experiment. Once the cultures entered the mid-exponential growth phase, a volume corresponding to OD_{600} 0.5 was spun down (2504 rcf, 5 minutes, Eppendorf 5702) to discard the growth medium. 2 mL of fresh SC -Ura with raffinose were then replenished to yield a culture at OD_{600} 0.25.

To measure mitochondrial membrane potential, I used tetramethylrhodamine, methyl ester (TMRM; Sigma-Aldrich), a cell-permeable, positively charged, red fluorescent dye that accumulates in mitochondria proportionally to their activity. TMRM was subsequently added to the culture to a final concentration of 50 mM, and cells were incubated for an additional 30 minutes. After staining, cells were then transferred to fresh medium lacking TMRM and pipetted 180 µL into the wells of a pre-coated black 96-well plate with bottom glass (Grenier). To coat such plate, 50 µL of 0.1% (w/v) poly-L-lysine (Sigma-Aldrich) were pipetted into each well and subsequently removed when all the wells in the plate had been coated. The wells were left to air-dry for 45 minutes at room temperature and afterwards washed two times with sterile water. The addition of poly-L-lysine allows some of the plated cells in suspension to eventually adhere to the poly-L-lysine in the bottom of each well and remain temporarily immobilised during

live imaging. During imaging, the 96-well plate containing the cells was enclosed inside the microscope's integrated insulation equipment, which was kept at 30ºC.

Flp-In™ HEK 293 cells were grown directly on the wells of the plate. Four days before imaging, around 12,000 cells were seeded on each well, and fresh DMEM was provided to attach and grow during the next 48 hours. Two days after seeding, the medium was changed, and *SLC25A3* expression was induced with doxycycline (0.2 µg/mL). On the day of the experiment, DMEM was removed, and cells were washed twice with 100 µL of PBS and finally incubated at 37ºC in recording medium (phenol red-free DMEM (Thermo Fisher Scientific) supplemented with 10 mM glucose, 1 mM glutamine and 10 mM HEPES, pH 7.4). 30 minutes before imaging a given well, 25 nM of TMRM was added to the recording medium. Mammalian cells express efflux pumps that can extrude dyes such as TMRM and, thus, bias their staining in cells expressing higher levels of these xenobiotic transporters. To avoid this, stained cells were also treated with 25 µM of verapamil (Sigma-Aldrich), an efflux pump inhibitor. Imaging was then performed inside an incubation chamber (Zeiss) that maintained the sample at 37ºC.

Imaging was performed by confocal laser scanning microscopy in an LSM 880 microscope (Zeiss) of the Medical Sciences Building Confocal Imaging Facility at University College London. For yeast acquisitions, TMRM was excited with a 561 nm argon laser with an output power of 0.2 mW, the pinhole was set at 2.67 arbitrary units (a.u.), and the detector gain was fixed at 850. Whereas red fluorescence parameters remained unaltered for all acquisitions, the detector gain for the transmitted photomultiplier (T-PMT) channel had to be adjusted to successfully view the outline of the cells in each sample. In both channels, 10 z-stacks were taken for TMRM images, with a spacing of 0.6 µm between slices. For Flp-In™ HEK 293 imaging, TMRM settings were slightly modified compared to those of yeast cells: the argon laser power was decreased to 0.1 mW to minimise radiation-induced stress in the cells, the pinhole was reduced to 1.62 a.u. to increase the resolution of the stained areas and, owing to the larger diameter of human cells, the z-stacking parameters were changed to acquire 14 regularly spaced slices spanning 13 µm. To verify that the signal captured in the red fluorescence channel emerged solely from TMRM, I acquired control images of unstained yeast cells. Additionally, to confirm that TMRM was exclusively being sequestered by *active* mitochondria, I re-imaged stained samples in which

mitochondrial membrane potential was collapsed upon the addition of carbonyl cyanide-p-trifluoromethoxyphenylhydrazone (FCCP; Sigma-Aldrich), a powerful uncoupler of oxidative phosphorylation. In these samples, the TMRM signal was expected to dissipate because of the FCCP-mediated transport of protons from the intermembrane space into the inner mitochondrial membrane.

Images were saved as CZI files and viewed with standard ImageJ in a default stack order (Schneider et al., 2012). Channels were split, and regions of interest (ROIs) were drawn and added to the transmitted photomultiplier (T-PMT) channel. Having selected the cells that will be examined, ROIs were saved as ROI files for re-evaluation. In the TMRM channel, the image's stacks were z-projected to obtain the maximal intensity. The image's threshold was then adjusted using the Otsu method for image segmentation, which is an algorithm for image analysis that converts fluorescence to grayscale, assigns an intensity value for every pixel and, thenceforth, partitions them into foreground and background based on a threshold value. All the wild-type replicates were assessed individually for Otsu's optimal threshold value, and the highest value was then imposed as a common threshold to discriminate between stained mitochondria and background TMRM fluorescence in all remaining images of the derived strains.

To correct for the varying background fluorescence of individual images, I drew an ROI in a space without cells and subsequently measured its fluorescence on the TMRM channel without introducing a minimal threshold. This background fluorescence was then subtracted from the mean fluorescence for the maximum projection of each selected ROI in the same image. Corrected fluorescence was then normalised to the mean corrected fluorescence of the corresponding replicate for the wild-type strain for direct comparison. At least 50 cells from three independent biological repeats were examined for a single condition and strain. Unpaired t-tests between each mutant and its wild-type counterpart were performed in GraphPad Prism 8.0.1. Bar plots showing the mean and standard error of the mean for each cell type were generated with the same software.

II.20. Respirometry

Having been incubated in pyruvate-containing SC -Ura medium for two days, starter cultures were used to inoculate 5 mL of fresh SC -Ura with the appropriate concentration of raffinose. When the cells reached approximately OD_{600} 0.5, a volume equivalent to OD_{600} 0.2 was spun down (2504 rcf, 5 minutes, Eppendorf 5702). After discarding the supernatant, the cell pellet was resuspended in 2 mL of fresh medium and pipetted into one chamber of an Oroboros O2k oxygraph (Oroboros). By contrast, Flp-In™ HEK 293 cells were grown inside T-25 flasks (Sigma-Aldrich) containing DMEM. *SLC25A3* overexpression was induced in the relevant cell population by exposing them to 0.2 µg/mL doxycycline 24 hours prior to the experiment. On the day of the experiment, cells were centrifuged (200 g, 5 minutes) and, after disposing of the growth medium, the pellet was resuspended in fresh DMEM containing 15 mM HEPES pH 7.4 (Thermo Fisher Scientific). In this instance, medium required buffering to ensure that cells would keep their physiological pH despite the changes in carbon dioxide concentration that cells faced during the experiment.

Respirometry was performed using an oximeter which was previously calibrated using the relevant medium (i.e., SC -Ura with 2% (w/v) or 1% (w/v) raffinose or DMEM with 15 mM HEPES pH 7.4). The instrument was deemed calibrated once the oxygen concentration measurements for sterile medium stabilised in between a range of 160 and 240 µM, depending on the composition of the medium, and the oxygen flux per volume was flattened at around 0 pmol/s*mL. Oxygen concentration recordings were performed at 30ºC or 37ºC when monitoring yeast or mammalian cultures respectively. Once cells were pipetted into the chamber, 15 minutes elapsed before the oxygen consumption signal stopped fluctuating. The value around which the signal stabilised was representative of the basal oxygen consumption rate (OCR). Having monitored their basal OCR, Flp-In™ HEK 293 cells were exposed to 2 µM oligomycin A (Sigma-Aldrich), which occludes proton import in the ATP synthase and prevents phosphorylation of ADP into ATP. Thus, upon oligomycin injection, the decline in OCR with respect to the basal measurement, will be indicative of the portion of respiration that was being effectively used for ATP production. This step was omitted during experiments examining yeast populations as oligomycin A does not permeate the cell wall and, thus, the populations under study remain largely unaffected by the drug.

The maximal respiration rate was assessed in yeast and mammalian samples following treatment with FCCP. This uncoupling agent imports protons from the intermembrane space to the mitochondrial matrix thereby collapsing mitochondrial membrane potential and driving oxygen consumption by complex IV to its maximum activity. Owing to the different sensitivity that both species displayed towards the drug, the concentration of FCCP which was injected to the chamber was different for yeast and mammalian cells: while yeast samples underwent 2-3 injections of 5 μM FCCP, human cells were treated with 2-3 additions of 1 μM FCCP.

Cells were then treated with antimycin A which inhibits complex III and so blocks the respiratory chain. Consequently, oxygen uptake is reduced to that employed in non-mitochondrial respiration. Whilst 0.5 μM of antimycin A was sufficient to elicit a visible effect in mammalian cells, 2 μM were required for yeast cells. In Flp-In™ HEK 293 cells, antimycin A injection was shortly followed by the addition of rotenone, which blocked the mammalian complex I.

Experimental traces were saved and exported in the native DLD format for analysis in the Oroboros Datlab 7 software (Oroboros). Having identified and demarcated sections on which the oxygen consumption signal remained relatively constant, I extracted the average value for these marks and used them to calculate the mean and standard deviation for the basal, non-ATP linked (in mammalians only) and maximal respiratory rates of the yeast strains and mammalian cell lines under study. Statistical significance was evaluated by unpaired t-tests performed in GraphPad 8.1, which was also used to assemble the bar plots showing the mean and standard deviation for the oxygen consumption rate of every sample across each stage.

II.21. NADH fluorescence quantification

Cells grown in pyruvate-containing SC -Ura cultures were used to inoculate 5 mL of sterile SC -Ura containing a high or low raffinose concentration. Cultures were incubated at 30ºC from a starting OD_{600} of 0.1 until they entered mid-logarithmic growth. At that point, cultures were spun down (2504 rcf, 5 minutes, Eppendorf 5702), and the medium was replenished by a fresh one to the volume necessary to dilute the

total amount of cells to an OD_{600} of approximately 0.2. Subsequently, 200 µL of the recently diluted culture were pipetted into 9 separate wells.

While the basal measurement was taken in untreated cells, another set of cells was exposed to FCCP. As detailed in II.19, FCCP elicits maximal respiration and, consequently, drives full oxidation of the NAD pool to its NAD^+ state. Therefore, any NADH signal recorded upon the addition of FCCP was assumed to correspond to a background measurement for the NADH autofluorescence acquisitions. Conversely, another set of samples was treated with sodium cyanide (NaCN; VWR International) which blocks complex IV, blocks the electron transport chain and impedes respiration. Even though NaCN-mediated inhibition of complex IV is not substrate-dependent, the physiological response of the cell to a shutdown of the electron transport chain is to increase the production of substrates that can be fed to the ETC to resume respiration. Consequently, the cell fully reduces its NAD pool, thereby yielding its maximum NADH fluorescence. Given that the nicotinamide moiety of NADH absorbs UV radiation and subsequently emits light of approximately 460 nm in wavelength, the presence of the reduced coenzyme can be monitored as blue fluorescence following exposure to UV light.

Fluorescence measurements were recorded using the OD_{600} and NADH fluorescence modes of the of the CLARIOstar Plus (BMG LABTECH) microplate reader. OD_{600} measurements were obtained to enable normalisation of the NADH fluorescence values to cell number. NADH fluorescence itself was recorded 2 minutes after the addition of the drug. Due to their different susceptibility to FCCP and NaCN, yeast cells were exposed to 15 µM and 1.25 mM of these drugs respectively whereas Flp-In™ HEK 293 cells were treated with 1 µM of FCCP and 1 mM NaCN.

Readings were exported as CSV files for further analysis. Firstly, all NADH autofluorescence signals were divided by the OD_{600} measurement in the same well to compensate for any technical disparity on the cell abundance of individual samples. Then, the average of the technical triplicates that were included for each sample was calculated and used as the only value for that biological replicate. Afterwards, NAD pools were calculated by subtracting the reading acquired when all the NAD pool was assumed to be oxidised (NAD^+) from the one at which the NAD pool was predominantly in its reduced state (NADH). Having estimated the NAD pool for each sample, I

calculated the redox ratio of each well by discounting the background NADH fluorescence from the basal NADH measurements and dividing the resulting value over that of the NAD pool. In essence, this ratio indicated which fraction of the NAD pool was in a reduced state for a given sample. This strategy was applied to obtain the redox ratios of three independent biological repeats per strain or cell line gathered in different growth conditions. Statistical analysis (unpaired t-tests) and visualisation were performed in GraphPad Prism 8.1.

II.22. Untargeted whole-cell metabolite profiling

Cells grown in SC -Ura with 2% (w/v) pyruvate for 48 hours were used to inoculate 25 mL of raffinose-limiting SC -Ura cultures at a starting OD_{600} of 0.1. Once the cultures reached an OD_{600} of approximately 0.5, 500 µL were transferred to a sterile 1.5 mL microcentrifuge tube and quenched by submersion into a dry ice/ethanol bath for 10 seconds. While being kept inside the bath, samples were mixed vigorously to avoid freezing and, potentially, undesired cell lysis. After the rapid cooling step, samples were kept on ice before being spun down at 1000 rcf for 10 minutes in a pre-cooled Eppendorf 5804 R centrifuge that was kept at 4ºC throughout the entire procedure. When the first round of centrifugation concluded, a volume of 150-450 µL was transferred to a sterile 1.5 mL microcentrifuge tube and stored on ice as a back-up. The remaining volume underwent an additional centrifugation (2500 rcf, 5 minutes, Eppendorf 5804 R) at 4ºC. Following removal of its supernatant, the cell pellet was resuspended in a 10-fold volume of ice-cold high performance liquid chromatography (HPLC)-grade chloroform:methanol:water (1:3:1) mixture. This implies that a pellet that was estimated to occupy a volume equivalent to, for example, 2 µL was dissolved in 20 µL of the mentioned chloroform:methanol:water solution.

An equivalent volume of 0.5 mm zirconia beads was added to the samples before they were vortexed at maximum speed for five 1-minute intervals spaced by four 1-minute incubations on ice. Lysates were then incubated at 4ºC for 1 hour with shaking at 1200 rpm. Samples were subsequently vortexed at maximum speed for 5 minutes on a cooled mixer before being spun down (13000 rcf, 3 min, Eppendorf 5804 R) at 4ºC to separate the cell debris from the supernatant. Supernatants were transferred to

sterile 1.5 mL microcentrifuge tubes and stored at -80ºC. Metabolite characterisation was performed by EdinOmics (untargeted metabolite profiling service).

II.23. Whole proteome profiling

After growth in SC -Ura with pyruvate (i.e., 2% (w/v)) for 36-48 hours, cells were transferred to 25 mL of fresh raffinose-rich or raffinose-deprived SC -Ura at an initial OD_{600} of 0.1. Cultures were incubated at 30ºC until they entered their mid-logarithmic growth phase. For samples that had reached an OD_{600} of exactly 0.5, 5 mL of cells were harvested by centrifugation (1699 rcf, 5 minutes, Eppendorf 5804 R). The volume that was collected for remaining cultures was adjusted to compensate for slight differences in cell count. Upon disposal of the supernatant, cells were flash frozen by immersion into liquid nitrogen and stored at -80ºC until lysis.

Cell pellets were resuspended in 20 µL of 4% (w/v) SDS dissolved in 100 mM Tris-HCl pH 8 and incubated at 95ºC for 30 minutes. Afterwards, the samples underwent three 10-second pulses of sonication alternated with 5-second pauses. During the lysis, the sonicator was set at an amplitude of 5 µm and the samples were always kept on ice. Following sonication, the SDS in solution was diluted to 1% (w/v) with the addition of 60 µL of 100 mM Tris-HCl pH 8 to each sample. Additionally, 8.5 µL of dithiothreitol (DTT) were pipetted into each sample to keep a final concentration of 10 mM and tubes were then placed at 50ºC for 30 minutes. During this incubation, the reducing agent DTT disrupted the disulphide bonds and thus enabled the suspension of the proteins as single units. To separate the proteins in solution from the cell debris, samples were spun down at 20817 rcf for 15 minutes in an Eppendorf 5804 R centrifuge and the supernatant was transferred into a new tube.

After measuring their concentration by fluorometric quantification (see II.10 for a detailed procedure), a volume holding 100 µg was aliquoted for each sample. An appropriate volume of a solution containing 8 M urea in 100 mM Tris-HCl pH 8 was added to each tube until the sample was exposed to a final concentration of 6 M urea. Upon mixing, denatured proteins were cleaned with filter-aided sample preparation columns (FASP, Microcon-30kDa centrifugal filter unit, Millipore, MRCF0R030). After centrifugation (14000 g, 40 minutes), the flow-through fraction was discarded, and the

filter membrane was further washed with 200 µL of 8 M urea in 100 mM Tris-HCl pH 8.

The proteins in the filter were then alkylated with 100 µL of 5 mM iodoacetamide (IAA, Sigma-Aldrich) dissolved in 8 M urea. Alkylation occurred at room temperature in the dark for 20 minutes. During this time, the alkylating agent IAA substituted the hydrogen in reduced cysteine residues by alkyl groups to block them from potentially interacting with other cysteine residues and re-forming disulphide bridges. Having washed the filter membrane with 100 µL of 8 M urea Tris-HCl pH 8 solution, I performed two additional 100 µL-washes with 50 mM ammonium bicarbonate (ABC, Sigma-Aldrich). Upon centrifugation and subsequent removal of the flow-through fraction (14000 g, 10 minutes), 1 µg of mass spectrometry grade trypsin protease (Thermo Fisher Scientific) was diluted into 39 µL ABC and subsequently applied to the column of each membrane. All samples were incubated at 37 °C overnight until an additional 40 µL of ABC were added to each sample and its peptides were collected by centrifugation (14000 g, 10 minutes).

The peptide concentration was measured before samples were acidified to pH≤3 with the pertinent volume of 10% (v/v) trifluoroacetic acid (TFA) and desalted in C18-StageTips. These tips were built by stacking two pieces of C18 filters (Empore, 2215) on the 200 µL microtips and activated upon addition of 15 µL methanol. Having spun down the methanol through the filters (14000 g, 10 minutes), these were equilibrated with 50 µL of 0.1% (v/v) TFA before samples were added and passed through the tips (14000 g, 10 minutes). After washing the membrane with 50 µL of 0.1% (v/v) TFA (14000 g, 10 minutes), tips could be stored at -20ºC immediately before mass spectrometry. In this case, peptides were eluted with 40 µL 80% (v/v) acetonitrile (ACN) in 0.1% (v/v) TFA and tandem mass spectrometry (MS/MS) analysis was performed on an Ultimate Ultra3000 chromatography system coupled with a Orbitrap Fusion™ Lumos™ Tribrid™ mass spectrometer (Thermo Fisher Scientific) at the Mass Spectrometry Facility of the Institute of Genetics and Molecular Medicine (IGMM).

Raw output files were subsequently analysed using MaxQuant version 1.6.5.0. This software employs a target-decoy approach to parse output files for peptide identification via the Andromeda search engine (Cox et al., 2011; Cox and Mann, 2008), which pairs tandem mass spectra to putative amino acid sequences and scores

these matches using a probabilistic score called peptide spectrum match (PSM) (Cox and Mann, 2008). The target-decoy default strategy generates a reverse database comprising the protein sequences in the original database shown from their end to their start (Cox and Mann, 2008). The software then computes the properties (length, charge, PSM Adromeda score) of these random peptides and integrates them into the dataset to calculate false discovery rates (FDRs) for the sequence entries in the original dataset (Cox and Mann, 2008). To do so, MaxQuant requires (i) a CSV file outlining the experimental design, (ii) a FASTA search reference database, namely UP000002311 559292 YEAST *Saccharomyces cerevisiae* from the European Bioinformatics Institute, and (iii) the RAW files (Cox and Mann, 2008).

Although most preset parameters could be applied for my whole-proteome profiling experiments, I still included and modified some of these specifications (Cox and Mann, 2008). For the group-specific settings, trypsin was selected as the protease of choice and the minimum peptide length was set to 7 amino acids that could encode a maximum of 2 missed cleavage sites (Cox and Mann, 2008). First search peptide tolerance was set at 20 parts per million (ppm) and reduced to 4.5 ppm for the main searches (Cox and Mann, 2008). Statistical significance at this level was determined using a peptide spectrum match (PSM) threshold of a maximum of 1% FDR (Cox and Mann, 2008).

To identify protein groups, cysteine carbamidomethylation was designated as a fixed modification whereas methionine oxidation and protein N-terminal acetylation were categorised as variable modifications (Cox and Mann, 2008). While sorting peptides into protein groups, the algorithm occasionally encounters razor peptides (i.e., the ones that could have emerged from more than one protein) and assigns them to the protein group with the highest number of detected peptides (Cox and Mann, 2008). If the number of identified peptides within the candidate groups was identical, the given razor peptide was allocated to the protein group enclosing peptides with the largest PSM scores (Cox and Mann, 2008). Peptides that were deemed contaminants by the software were set to be included at this point as they were filtered prior to the statistical analysis (Cox and Mann, 2008).

Having performed the protein identification analysis based on the programmed preferences, MaxQuant returned a proteinGroup output TXT file that was modified to

include only the intensity columns for all the samples within one comparison set (Cox and Mann, 2008). The reduced matrix was fed to Perseus, which is a platform software that allows statistical analysis of multi-dimensional omics data (Tyanova et al., 2016). The table was filtered to exclude proteins that were only identified by their post-translational modifications (PTM), reverse proteins from the decoy databased and contaminants (e.g., benzonase and trypsin). Intensities were then normalised using a logarithmic transformation (Tyanova et al., 2016). Triplicates were grouped and protein entries that were not detected in at least two replicates within each strain were excluded from the analysis. Imputation of missing values was performed by replacement with data from a downshifted (1.8) normal distribution with a width of 0.3 (Tyanova et al., 2016).

Statistical analysis of the resulting log_2-transformed dataset was performed using a likelihood ratio test with the EdgeR, a R package that performs differential expression analysis of omics profiles with biological replicates (Robinson et al., 2009). This pipeline applies trimmed mean of M-values (TMM) normalisation before performing unpaired t-tests comparing the mutants to their wild-type reference and adjusting the resulting p-values using the Benjamini–Hochberg correction (Robinson et al., 2009). The mentioned TMM strategy aims to compensate for non-identical library sizes (Robinson et al., 2009). However, the premise of this normalisation method is that inherent compositional biases result in some proteins displaying a higher count due to merely technical reasons (Robinson et al., 2009). Hence, proteins that are intrinsically overrepresented should be excluded from the total library counts that are commonly used to correct for size differences (Robinson et al., 2009). To this end, TMM trims the most variable genes and then computes a normalisation factor to adjust unequal library sizes. Significant upregulation and downregulation were established based on a threshold fold change of more than 1 and less than -1 respectively (Robinson et al., 2009). Since values had undergone a log_2-transformation, these values selected for proteins that displayed a two-fold differential expression with respect to the wild-type reference (Robinson et al., 2009). Having run the described analyses, edgeR returned a series of output CSV files that were used as an input for R's ggplot2 package, which was used to generate the volcano plots (Wickham, 2016).

II.24. Whole transcriptome sequencing

Cells were grown in 5 mL of SC -Ura with 2% (v/v) pyruvate for 36-48 hours and subsequently used to inoculate 25 mL cultures of SC -Ura with the pertinent concentration of raffinose at an initial OD_{600} of 0.1. Once cultures reached an OD_{600} of 0.5, cells were harvested by centrifugation (3202 rcf, 5 minutes, Eppendorf 5810 R). Upon disposal of the supernatant, cell pellets were snap-frozen in liquid nitrogen and stored at -80ºC until the day on which cell lysis took place.

On the day of the lysis, RNA was extracted from all samples following the procedure described in II.8.2. Traces of DNA which may have co-partitioned with the samples were degraded during a DNase treatment as the one outlined in II.8.3. The quality of the RNA samples was then inspected in an Agilent 2100 bioanalyzer (Agilent Technologies) using an RNA 6000 pico assay (Agilent Technologies) according to the manufacturer's instructions. Briefly, the gel matrix was filtered by centrifugation (1500 rcf, 10 minutes) into an RNase-free microcentrifuge tube. Having kept all reagents equilibrated at room temperature for 30 minutes before use, I added 1 µL of previously mixed dye concentrate to 65 µL of filtered gel, vortexed the mixture to ensure homogenisation, and spun it down by centrifugation at 17949 rcf for 10 minutes in an Eppendorf 5804 R centrifuge. The gel mix was then pipetted into the corresponding wells of the microchip and loaded using the supplied priming station. Afterwards, the 9 µL of RNA conditioning solution, 1 µL the ladder and 1 µL RNA samples were added to the appropriate wells. Finally, 5 µL of the marker were added to each well. The presence of the marker in all wells allowed a direct comparison of the migration patterns of each RNA extract with that of the reference ladder.

Given that around 80% of the transcriptome consists of ribosomal RNA (rRNA), yeast RNA extracts were expected to display two main bands: one corresponding to the 25S rRNA, composed of 3396 nucleotides, and a second one emerging from the 18S rRNA, which comprises around 1800 nucleotides. A uniform ratio of the ribosomal band intensity is generally indicative of suitable RNA integrity across samples. However, in addition to ribosomal ratios, the RNA integrity number (RIN) algorithm also integrates other parameters of the electropherograms that can be used as a standardised measure for RNA intactness. After checking that the RIN scores for all extracts were larger than 7, samples were submitted to Novogene for paired-end

sequencing of 150 bp-reads in a NovaSeq 6000 system (Illumina). Before sequencing, samples underwent a rRNA depletion step, and libraries were generated using the TruSeq preparation protocol (Illumina).

Raw sequencing outputs in FASTQ format were processed using the paired-end (PE) version of the pyCRAC pipeline (Webb et al., 2014). This package demultiplexes barcoded reads and removes adapter sequences by applying the previously developed Flexbar tool (Dodt et al., 2012). The resulting reads undergo two quality control steps. Firstly, sequences are filtered based on their length and nucleotide quality values (i.e., PHRED scores). Secondly, since PCR artefacts will display identical random prefixes, they can easily be pinpointed and excluded from downstream analysis (collapsed). The remaining unique reads were collated in a FASTA file and subsequently aligned to the corresponding regions of the Saccharomyces_cerevisiae.R64-1-1.75 reference genome with the Novoalign tool (version 2.07). The pyReadCounters function of the pyCRAC package (version 1.5.1) was used to compute the number of reads that map to each gene and genomic feature (Webb et al., 2014). The resulting tables for all the samples to be compared within the same condition were then merged into a single TXT file that was used to perform a differential expression analysis using the DESeq2 R package (Love et al., 2014). This pipeline corrects for size variability by computing a scaling factor for each sample (Love et al., 2014). To obtain such a normalisation factor, the software calculates the ratio of the raw count of a given gene in one of the samples to the geometric mean of the counts for that same gene across the compared samples (Love et al., 2014). The median of all the ratios calculated within a sample is defined as the scaling factor for that replicate (Love et al., 2014). Having adjusted the raw reads, the package then performs a logarithmic transformation of the data and calculates a fold change and an FDR for each entry (Love et al., 2014). Statistical significance was assessed for entries which exceeded or were lower than 1 and -1, respectively (Love et al., 2014). Volcano plots were produced using the ggplot2 R package (Wickham, 2016).

II.25. Cross-linking and analysis of cDNAs (CRAC)

5 mL cultures of pyruvate-containing SC -Ura were used to inoculate 25 mL of SC -Ura supplemented with 1% (w/v) raffinose at an initial OD_{600} of 0.1. Having been incubated at 30ºC overnight, these cultures saturated and were used to inoculate 500 mL of SC -Ura containing an identical concentration of raffinose. For cross-linking and analysis of cDNAs (CRAC) experiments in Sen1, a total volume of 1 L was cultured per sample. When the cultures reached an OD_{600} of 1, cultures were UV cross-linked (254 nm; 500 mJ/cm^2) in the Vari-X-linker (UVO3) and harvested using a 0.8 µm membrane (Merck) and a filtration device connected to a vacuum pump (McKellar et al., 2020; van Nues et al., 2017). After approximately less than 1 minute, all medium passed through the filter, and the membrane could then be folded into a 50 mL centrifuge tube, snap frozen in liquid nitrogen and stored at -80ºC (Granneman et al., 2009).

On the day of the experiment, cells were thawed on ice and detached by rinsing the filters with 30 mL of PBS. Cells were then spun down by centrifugation (3202 rcf, 7 minutes, Eppendorf 5810 R) at 4ºC. After discarding the supernatant, pellets were weighted and resuspended in a volume of lysis buffer (150 mM NaCl, 50 mM Tris pH 7.8, 0.1% (v/v) Nonidet P-40, 1 EDTA-free Protease Inhibitor Cocktail (Roche) per 50 mL and 5 mM β-mercaptoethanol) corresponding to twice their mass (i.e., 1.8 mL would be added to a 0.9 g of pellet). Lysates were then transferred to a fresh 50 mL tubes, where they were mixed with 2 volumes of 0.5 mm zirconia beads, and vortexed at maximum speed for five 1-minute intervals spaced by 1-minute incubations on ice. Upon addition of an additional volume of lysis buffer, the beads and cell debris were collected by centrifugation at 4ºC (3202 rcf, 15 minutes, Eppendorf 5810 R) and the supernatants were transferred to 1.5 mL microcentrifuge tubes. To remove any impurities that may have co-partitioned with the supernatant, an additional centrifugation step (10621 rcf, 20 minutes, Eppendorf 5804 R) was performed at 4ºC. In this case, the supernatant was transferred to a new tube containing 75 µL of anti-FLAG® M2 magnetic beads (Sigma-Aldrich, M8823-5ML) which had been previously washed three times with 1 mL TN150 buffer (150 mM NaCl, 50 mM Tris pH 7.8, 0.1% (v/v) Nonidet P-40 and 5 mM β-mercaptoethanol). Immunoprecipitation took place in a nutating platform at 4ºC and lasted 2 hours.

After pelleting the beads with a magnetic rack, the lysate was discarded and the beads were washed three times with 2 mL TN1000 buffer (50 mM Tris pH 7.8, 1 M NaCl, 0.1% (v/v) Nonidet P-40 and 5 mM β-mercaptoethanol) and three times with 2 mL TN150 buffer. Beads were rotated for 5 minutes during each of these washes. Finally, beads were resuspended in 550 µL of TN150 and incubated with 1 µL of a 1:100 diultion of RNace-It™ for exactly 5 minutes at 37 °C. After trimming all RNAs which were covalently linked to the immunoprecipitated proteins, I transferred the solution containing the beads and the RNases into a tube containing 0.4 g of guanidium hydrochloride (Gu-HCl) and the necessary volume of NaCl and imidazole (pH 8.0) concentration to reach a final concentration of 300 mM and 10 mM respectively the sample was added. Tubes were then vortexed vigorously to release the HTF-tagged protein from the beads and inactivate the RNases.

The mixture was then pipetted onto 50 µL of nickel-nitrilotriacetic (Ni-NTA) agarose resin (QIAGEN) equilibrated with wash buffer I (6 M Gu-HCl, 10 mM imidazole, 300 mM NaCl, 50 mM Tris-HCl pH 7.8, 0.1% (v/v) Nonidet P-40 and 5 mM β-mercaptoethanol) and rotated (12 rpm) at 4 °C overnight for Nab3, Nrd1 and Rpo21, and for 2 hours in the case of Sen1 CRAC. After the incubation, the Ni-NTA agarose beads were transferred to Pierce columns (Thermo Fisher Scientific) and washed twice with 500 µL of wash buffer I before undergoing three additional washes of 500 µL with NP-PNK buffer (10 mM $MgCl_2$, 50 mM Tris-HCl pH 7.8, 0.1% (v/v) Nonidet P-40, 5 mM β-mercaptoethanol).

Immunoprecipitated RNA-protein conjugates were resuspended in 80 µL of 1X PNK buffer containing 4 units of FastAP thermosensitive alkaline phosphatase (Thermo Fisher Scientific) to remove 2’ and 3’ phosphates, and 80 units of RNasin® ribonuclease inhibitor (Promega) were added to minimise RNA degradation. Alkaline phosphatase treatment required incubation at 37 °C and had a duration of 1 hour for Nab3, Nrd1 and Rpo21, and lasted only 15 minutes for Sen1. Former experimental manipulation of the latter bait revealed that Sen1 was more susceptible to degradation and, thus, the duration of all reactions was reduced to the minimum incubation time as per product recommendations.

Dephosphorylation was stopped upon addition of 500 µL of wash buffer I, which denatured the enzymes. After three washes with 500 µL of NP-PNK buffer, the beads

were resuspended in 80 µL of reaction mix containing 0.6 µM of the applicable App-PE 3′ adapter (see Table II.11), 30 units of T4 RNA ligase 2 truncated K227Q (New England Biolabs), 60 units RNasin® (Promega) and 10% (w/v) polyethylene glycol 8000 (PEG 8000). The mixture was incubated at 25 °C for 6 hours in the case of Nab3, Nrd1 and Rpo21, and for 2 hours during Sen1 CRAC.

Having been washed once with 500 µL of wash buffer I and three times with 500 µL of NP-PNK buffer, the Ni-NTA resin was incubated with 60 µL of NP-PNK buffer containing 30 µCi ^{32}P-γATP (PerkinElmer) and 30 units of T4 polynucleotide kinase (New England Biolabs) at 37 °C to radiolabel the cross-linked RNAs. After 40 minutes of incubation, ATP (Roche) was supplemented to a final concentration of 1 mM and the reaction continued for another 20 minutes.

Oligonucleotide Type	Name	Sequence
5' Adapter for Sequencing	L5Aa	5'-invddT-ACACrGrArCrGrCrUrCrUrUrCrCrGrArUrCrUrNrNrNrUrArArGrCrN-OH-3'
	L5Ab	5'-invddT-ACACrGrArCrGrCrUrCrUrUrCrCrGrArUrCrUrNrNrNrArUrUrArGrCrN-OH-3'
	L5Ac	5'-invddT-ACACrGrArCrGrCrUrCrUrUrCrCrGrArUrCrUrNrNrNrGrCrGrCrArGrCrN-OH-3'
	L5Ad	5'-invddT-ACACrGrArCrGrCrUrCrUrUrCrCrGrArUrCrUrNrNrNrCrGrCrUrUrArGrCrN-OH-3'
	L5Ba	5'-invddT-ACACrGrArCrGrCrUrCrUrUrCrCrGrArUrCrUrNrNrNrArGrArArGrCrN-OH-3'
	L5Bb	5'-invddT-ACACrGrArCrGrCrUrCrUrUrCrCrGrArUrCrUrNrNrNrGrUrGrArArGrCrN-OH-3'
	L5Bc	5'-invddT-ACACrGrArCrGrCrUrCrUrUrCrCrGrArUrCrUrNrNrNrCrArCrUrArGrCrN-OH-3'
	L5Bd	5'-invddT-ACACrGrArCrGrCrUrCrUrUrCrCrGrArUrCrUrNrNrNrUrCrUrCrUrArGrCrN-OH-3'
	L5Ca	5'-invddT-ACACrGrArCrGrCrUrCrUrUrCrCrGrArUrCrUrNrNrNrCrUrArGrCrN-OH-3'
	L5Cb	5'-invddT-ACACrGrArCrGrCrUrCrUrUrCrCrGrArUrCrUrNrNrNrUrGrGrArGrCrN-OH-3'
	L5Cc	5'-invddT-ACACrGrArCrGrCrUrCrUrUrCrCrGrArUrCrUrNrNrNrArCrUrCrArGrCrN-OH-3'
	L5Cd	5'-invddT-ACACrGrArCrGrCrUrCrUrUrCrCrGrArUrCrUrNrNrNrGrArCrUrUrArGrCrN-OH-3'
	L5Da	5'-invddT-ACACrGrArCrGrCrUrCrUrUrCrCrGrArUrCrUrNrNrNrCrGrUrGrArUrN-OH-3'
	L5Db	5'-invddT-ACACrGrArCrGrCrUrCrUrUrCrCrGrArUrCrUrNrNrNrGrCrArCrUrArN-OH-3'
	L5Dc	5'-invddT-ACACrGrArCrGrCrUrCrUrUrCrCrGrArUrCrUrNrNrNrUrArGrUrGrCrN-OH-3'
	L5Dd	5'-invddT-ACACrGrArCrGrCrUrCrUrUrCrCrGrArUrCrUrNrNrNrArUrCrArCrGrN-OH-3'
	L5Ea	5'-invddT-ACACrGrArCrGrCrUrCrUrUrCrCrGrArUrCrUrNrNrNrCrArCrUrGrUrN-OH-3'
	L5Eb	5'-invddT-ACACrGrArCrGrCrUrCrUrUrCrCrGrArUrCrUrNrNrNrGrUrGrArCrArN-OH-3'
	L5Ec	5'-invddT-ACACrGrArCrGrCrUrCrUrUrCrCrGrArUrCrUrNrNrNrUrGrUrCrArCrN-OH-3'
	L5Ed	5'-invddT-ACACrGrArCrGrCrUrCrUrUrCrCrGrArUrCrUrNrNrNrArCrArGrUrGrN-OH-3'
3' Adapter for Sequencing	App_PE	5'App-NAGATCGGAAGAGCACACGTCTG-ddC 3'
Primer for Reverse Transcription		5'-CAGACGTGTGCTCTTCCGATCT-3'
Primers for Library Amplification	P5	5'-AATGATACGGCGACCACCGAGATCTACACTCTTTCCCTACACGACGCTCTTCCGATCT-3'
	P3 BC1	5'-CAAGCAGAAGACGGCATACGAGATCGTGATGTGACTGGAGTTCAGACGTGTGCTCTTCCGATCT-3'
	P3 BC3	5'-CAAGCAGAAGACGGCATACGAGATGCCTAAGTGACTGGAGTTCAGACGTGTGCTCTTCCGATCT-3'

	P3 BC4	5'-CAAGCAGAAGACGGCATACGAGATTGGTCAGTGACTGGAGTTCAGACGTGTGCTCTTCCGATCT-3'
	P3 BC5	5'-CAAGCAGAAGACGGCATACGAGATCACTGTGTGACTGGAGTTCAGACGTGTGCTCTTCCGATCT-3'
	P3 BC6	5'-CAAGCAGAAGACGGCATACGAGATATTGGCGTGACTGGAGTTCAGACGTGTGCTCTTCCGATCT-3'
	PC3 BC13	5'-CAAGCAGAAGACGGCATACGAGATCTTGTAGTGACTGGAGTTCAGACGTGTGCTCTTCCGATCT-3'

Table II.11. Adapters and primers used during the CRAC procedure.

To stop the reaction, the Ni-NTA beads were washed three times with 500 µL of wash buffer I and three times with 500 µL washes of NP-PNK buffer followed before the addition of the 5′ linker ligation mix. The reaction took place in a volume of 80 µL of NP-PNK buffer supplemented with 1.25 µM of the fitting adapter, 40 units of T4 RNA ligase 1 (New England Biolabs), 80 units of RNasin® and 10 mM ATP. 5' adapter ligation was left to proceed overnight at 16 °C.

On the next day, the reaction was stopped by washing the Ni-NTA resin three times with 500 µL of wash buffer I and another three times with 500 µL of wash buffer II (10 mM imidazole, 50 mM NaCl, 50 mM Tris pH 7.5, 0.1% (v/v) Nonidet P-40 and 5 mM β-mercaptoethanol). RNA-protein complexes were eluted from the Ni-NTA beads using elution buffer (250 mM imidazole, 50 mM NaCl, 50 mM Tris pH 7.5, 0.1% (v/v) Nonidet P-40 and 5 mM β-mercaptoethanol). RNA-protein adducts were precipitated by the addition of trichloroacetic acid (TCA) and glycogen to a final concentration of 20% (v/v) and 0.08 µg/µL. Following vortexing and a 20-minute incubation on ice, samples were centrifuged (14600 rcf, 20 minutes, Eppendorf 5418 R) at 4°C.

Resulting pellets were resuspended in 800 µL of cold acetone and precipitated by another round of centrifugation (14600 rcf, 20 minutes, Eppendorf 5418 R) at 4ºC. After discarding the supernatant and leaving the pellets to air-dry, the latter were resuspended in 20 µL of 4X NuPAGE™ LDS sample buffer containing 5 mM β-mercaptoethanol. Samples containing the same protein bait were combined at this point and ran in one well of a NuPAGE™ precast polyacrylamide gel. Whilst complexes derived from Nab3 and Nrd1 could be separated in 4% to 12% gradient Bis-Tris gels with MOPS running buffer, pools proceeding from Rpo2 and Sen1 pull-downs were

partitioned in 3% to 8% gradient Tris-acetate gels with Tris-acetate running buffer. Electrophoresis ran at 150 V for approximately 1.5 hours. Afterwards, the gel was placed facing an Amersham Hyperfilm™ MP (Cytvia Life Sciences) inside an X-ray film cassette (Kodak) kept at -80ºC throughout exposure. Whereas the exposure times for Nab3 and Nrd1 were approximately 20 minutes, longer incubations were required to detect Rpo21 (4 hours) and Sen1 (6 hours).

Test CRAC experiments were performed to determine whether immunoprecipitated proteins were cross-linking to RNAs under the tested conditions. This set of experiments followed many of the steps of the full CRAC protocol but omitted all library preparation steps (i.e., alkaline phosphatase and adapter ligation). Moreover, during test CRAC, PAGE is followed by electroblotting of the protein of interest onto a nitrocellulose membrane using a default programme from the iBlot® dry transfer system (Thermo Fisher Scientific). Subsequently, HTF-tagged proteins were immunodetected with an anti-FLAG® M2-Peroxidase (HRP) antibody as described in II.10.

For the experiments in which samples were designated for generating sequencing libraries, the film with the band revealing the presence of the bait protein at its corresponding size was used as a footprint to cut the contour of the signal from the gel fragment which contained the RNA-protein adducts. The extracted gel slice was mechanically fragmented using a pipette tip and mixed with 160 µg of proteinase K dissolved in 600 µL of wash buffer II containing 1% (v/v) SDS and 5 mM EDTA and shook (1000 rpm) at 55ºC for 2 hours. The resulting soluble fraction (550 µL), was then transferred to a new 1.5 mL microcentrifuge tube, mixed with an equal volume of acid phenol:chloroform:IAA (25:24:1) mix, vortexed and centrifuged at 14600 rcf for 5 minutes in an Eppendorf 5418 R. The top fraction (~ 550 µL), was combined with an identical volume of chloroform:IAA (24:1) mix, vortexed and centrifuged (14600 rcf, 5 minutes, Eppendorf 5418 R). The upper fraction, which is usually 450 µL, was ultimately transferred to a new 2 mL microcentrifuge tube holding 40 µg of glycogen and 450 µL of 3 M NaOAc pH 5.2 and 900 µL of cold 96% (v/v) ethanol. Ethanol precipitation of extracted RNA occurred overnight at -20ºC.

The following day, precipitated RNA pellets were spun down at 14600 rcf for 30 minutes in a pre-cooled (4ºC) Eppendorf 5418 R centrifuge. The supernatant was

replaced by 1 mL of cold 70% (v/v) ethanol and, after 3 tube inversions, another centrifugation step (14600 rcf, 5 minutes) at 4ºC in the same instrument ensured that all pellets remained adhered to the bottom of the tube. The ethanol was then discarded and, after air-drying the resulting pellets, these were resuspended in 10 µL of nuclease-free water.

Following purification of the cross-linked RNAs, each sample was supplemented with dNTPs and the listed reverse transcription primer (Table II.11) at a final concentration of 5 mM and 10 µM respectively. Mixtures were heated at 85ºC for 3 minutes and subsequently flash chilled on ice for 5 minutes. Each sample was mixed with 6 µL of reverse transcription buffer containing 1X SuperScript™ IV buffer, 16.7 mM DTT and 40 units of RNasin® and 200 units of SuperScript™ IV reverse transcriptase. Reactions were incubated at 50ºC for 1 hour and then heated to 65ºC for 15 minutes to inactivate the enzyme.

The temperature of the samples was then brought down to 37ºC before initiating a digestion with 10 units of RNase H (New England Biolabs) at 37ºC for 30 minutes. Afterwards, the cDNA samples were diluted in 18 µL of DEPC and combined with 2.5 volumes of RNAClean XP beads (Thermo Fisher Scientific) and 1.5 volumes of isopropanol and mixed well by pipetting. After incubating the mixtures at room temperature for 15 minutes, tubes were placed on magnetic rack for 5 minutes. When the solution became clear, the supernatant was substituted with 200 µL of cold 70% (v/v) ethanol for 30 seconds. Upon two additional ethanol replacements, beads were left to air-dry for 2 minutes before eluting bound cDNA in 12 µL of nuclease-free water.

The cDNA libraries were amplified by PCR with Pfu DNA polymerase (Promega) for 24 cycles (95 °C, 20 seconds; 52 °C, 30 seconds; and 72 °C, 1 minute) using the oligonucleotides outlined in Table II.11. Amplicons were then mixed with 2 volumes of RNAClean XP beads and purified following the aforementioned procedure. Amplified cDNA libraries were eluted in 20 µL of DEPC-treated water. PCR products were then mixed with gel loading dye (New England Biolabs) and resolved in a precast 6% (w/v) agarose Novex™ TBE gel (Thermo Fisher Scientific) alongside 6µL of a 50 bp (N3236S, New England Biolabs) and 1 kb (SM0311, Thermo Fisher Scientific) ladder. Electrophoresis ran at 100 V for 1 hour before staining the gel with 10 µL of SYBR™ Safe DNA gel stain dissolved in 100 mL of TBE buffer. After 10 minutes, the gel was

transferred to a transparent film and imaged in a ImageQuant TL 8.1 (Cytvia Life Sciences). The acquired image was printed to real scale and used as a reference to cut the gel fragment containing the resolved cDNA library, which will normally lay between 200 and 400 bp. The gel slice was transferred to a 1.5 mL microcentrifuge tube and smashed before adding 400 µL of nuclease-free water.

The gel matrix was then dissolved by shaking (1100 rpm) at 37ºC for 1 hour and the resulting mixture was filtered through 2 Whatman grade GF/D glass microfiber 10 mm-prefilters (GE Healthcare) placed on a Corning™ Costar™ Spin-X™ centrifuge tube filter (Thermo Fisher Scientific). Centrifugation at 14600 rcf for 1 minute (Eppendorf 5418 R) yielded a flow through fraction from which DNA could be precipitated. 1 mL of a 70% (v/v) ethanol with 20 µg of glycogen and 40 µL 3 M NaOAc pH 5.2 was pipetted into each sample, vortexed and incubated at -80ºC for 30 minutes. Resulting pellets were spun down (14600 rcf, 30 minutes, Eppendorf 5418 R) at 4ºC and their supernatant was substituted by 1mL of cold 70% (v/v) ethanol. Upon centrifugation (14600 rcf, 5 minutes, Eppendorf 5418 R) at 4ºC, the ethanol was removed, and the pellets were air-dried before resuspension in 15 µL of DEPC-treated water.

The concentration and quality of the resulting libraries was assessed in an Agilent 2100 bioanalyzer using an Agilent high sensitivity DNA kit (Agilent Technologies). The chip preparation was performed analogously to how it was described in II.24 but following the guidelines specific to this assay. After the gel had run, acquisitions were analysed using the 2100 expert software (Agilent Technologies). Based on the electropherogram, this programme calculated the concentration and average fragment size for the region of the electropherogram at which the library was found. After pooling suitable libraries together, the samples and its corresponding traces were submitted to Novogene for sequencing (pre-made libraries partial lane sequencing service). Sequencing was performed on an Illumina NovaSeq 6000 platform using a pair-end run generating 150 bp-reads.

Sequencing outputs were returned as FASTQ files which were processed applying the paired-end version of the pyCRAC pipeline (Webb et al., 2014) as indicated in II.24. If the number of reads within a given library was deemed insufficient it was either merged with another biological replicate or discarded. Two biological

repeats were produced for each CRAC experiment. For peak calling, I used the DBPeaks of the pyCRAC suite (Webb et al., 2014). After filtering out low-quality reads following the criteria mentioned in the previous paragraph, the remaining ones were gathered into BAM outputs and fed into the newly developed DB_Peaks.py peak calling algorithm of the pyCRAC package (Webb et al., 2014). These files were scanned with `countReadsBam()`, which uses the pyReadCounters tool from the pyCRAC package to generate GTF peak files from gene counts. The `getPeaks()` tool uses the previously developed `pyCalculateFDRs()` to retrieve the peaks that are enriched in each library relative to a randomised sequence dataset. The peak GTF files are then filtered by executing the `filterPeaks()` command which removes peaks comprising less reads than the mean coverage of all the intervals in the dataset. Although I used mean, median, or mean with one standard deviation could be used as thresholds. Peak widths were then normalised to a minimum length of 10 nucleotides with the `adjustPeakWidths()` function. Afterwards, `mergeGTFintervals()` applied BEDTools to concatenate intervals or peaks that are contained in all replicates (Quinlan and Hall, 2010). Subsequently, the `numberPeaks()` function assigns a number to each filtered peak to prevent misidentification in downstream steps. The software then performs pyReadCounters analysis on the bam files using the new GTF file containing the numbered filtered peaks. I then combined the hit tables output by pyReadCounters and combined them using the `mergeHittables()` function. Finally, the `runDESeq()` command automatically performs the statistical analysis to identify differential peaks using the DESeq2 pipeline (Love et al., 2014). By default, DESeq2 returns results in a TXT file so I developed two additional functions to extract the fold change calculated and incorporate it into the original peak file. Finally, the `getSignificantPeaks()` function generates a new GTF file containing solely the peaks that were called significant by the DESeq2 (Love et al., 2014).

III. The NNS Complex Acts as a Transcriptional Noise Suppressor for Protein-coding Genes

III.1. Introduction

Although the NNS complex predominantly mediates transcription termination of non-coding RNAs, high-throughput studies have demonstrated that between 20% and 30% of protein-coding transcripts are bound by Nab3 and Nrd1 (Creamer et al., 2011; Jamonnak et al., 2011; Webb et al., 2014; Wlotzka et al., 2011). Admittedly, functional validation of such binding has solely been obtained for a selected number of mRNAs, in which NNS premature termination of the transcript has been proved to contribute to regulating the expression of the gene (Arigo et al., 2006; Creamer et al., 2011; Kim and Levin, 2011; Kuehner and Brow, 2008; Schulz et al., 2013; Steinmetz et al., 2006; Thiebaut et al., 2008; Webb et al., 2014). A notable example of a fully studied NNS mRNA target is *NRD1*, which is autoregulated by its own product protein (Arigo et al., 2006; Steinmetz et al., 2001).

Importantly, however, the biological role of NNS-dependent attenuation of other protein-coding targets remains largely unexplored. Prior work by the Granneman and Tollervey groups has shown that, upon glucose starvation, Nab3 transcriptomic occupancy is redistributed in around 25% of protein-coding RNAs (Bresson et al., 2017; van Nues et al., 2017). These results showed that NNS prematurely terminates several stress-responsive genes and suggested that the complex could be involved in fine-tuning the expression of protein-coding targets, possibly to enhance fitness during environmental stresses (van Nues et al., 2017). Such a putative regulatory mechanism would entail a novel function for NNS as a noise suppression mechanism to elicit optimal levels of expression of targeted protein-coding genes at a specific time after detecting a given threshold of the signal to which the cell must adapt.

My project aimed to test whether the NNS-mediated attenuation of previously defined mRNA targets was widely applicable to protein-coding genes displaying NNS cross-linking. More specifically, I sought to check if that NNS regulatory mode was (i)

more prominent throughout the transcriptomic reprogramming required during the nutrient stress adaptation response and (ii) coupled to the suppression of noise in the expression of stress-responsive NNS targets. To study this, I focused on one of the stress-specific protein-coding target genes that the Granneman group had identified in the referred study: *PIC2*, which encodes for a mitochondrial transporter and could, thus, be potentially related to energy homeostasis during starvation.

Before the start of my work, Tove Widén and Iseabail Farquhar, previous members of the Granneman and Swain groups, had engineered a group of mutants with single-point substitutions in the Nab3 and Nrd1 RNA-binding sites, which were located within the first 500 bp of the *PIC2* transcription start site. After sequencing the *PIC2* loci of these strains, I identified one mutant in which both Nab3 binding sites in *PIC2* had been modified and another mutant in which all Nab3 and Nrd1 cognate sites in *PIC2* had been altered (Figure III.1). Henceforth, I will refer to these strains as ∆ Nab3 RNA-BSs and ∆ NNS RNA-BSs (Figure III.2). The nucleotide substitutions introduced in those mutants were expected to impair NNS binding to the *PIC2* transcript, prevent its premature transcription termination and, ultimately, increase *PIC2* expression levels.

The work presented in this chapter concentrates on the impact that disrupting NNS regulation of *PIC2* had in the expression of the gene. Firstly, I identify a set of suitable growth conditions at which to assess the NNS regulatory role in *PIC2*. Secondly, I show that the extent of NNS-mediated mRNAs suppression in *PIC2* is greater upon sugar restriction. Thirdly, I demonstrate that the single-point substitutions introduced in Nab3 and Nrd1 recognition sequences selectively impair the recruitment of the pertinent protein to its binding site. Fourthly, I prove that such mutations increase the transcriptional and translational levels of *PIC2*. Finally, I confirm that the novel noise-suppressing role that I had identified in *PIC2* is broadly applicable to other mRNA targets irrespectively of their promoter strength.

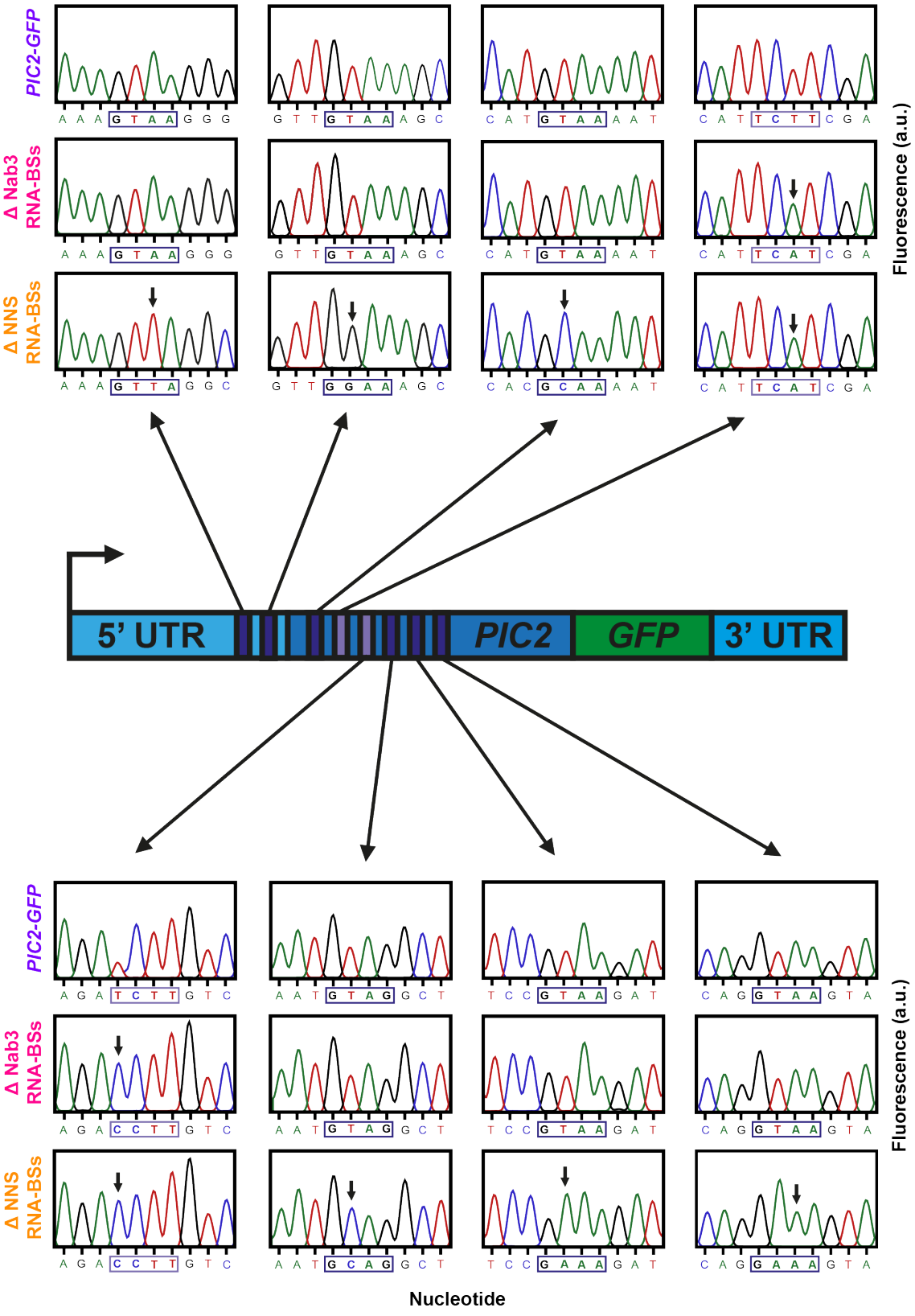

Figure III.1. Sequencing traces for the Nab3 and Nrd1 binding sites of *PIC2* in the *PIC2-GFP*, Δ Nab3 RNA-BSs and Δ NNS RNA-BSs strains. Single-point mutations are indicated with arrows.

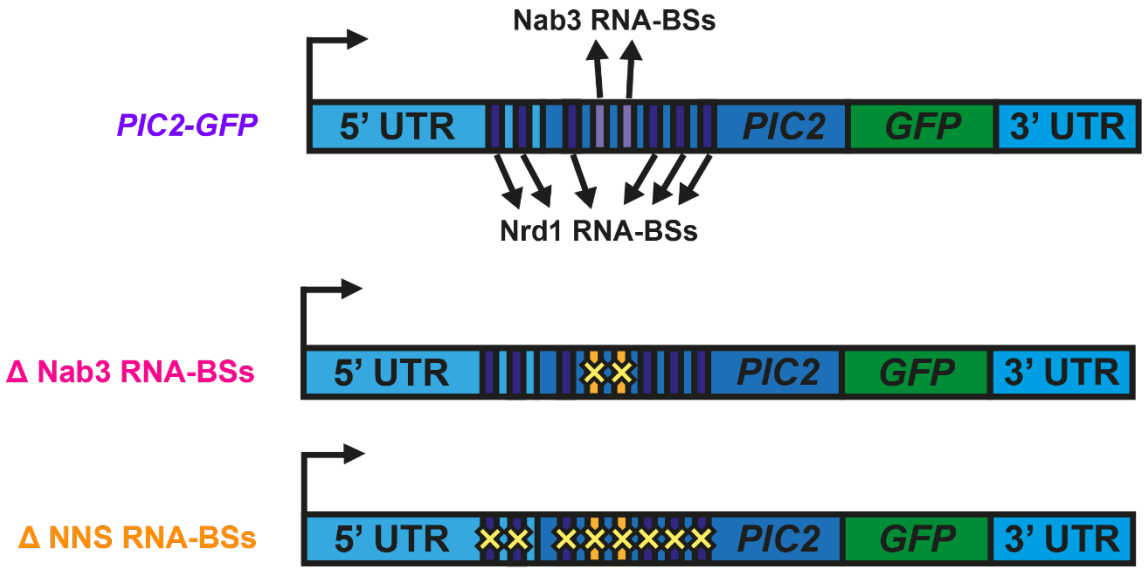

Figure III.2. Schematic summary of the mutations in the Δ Nab3 RNA-BSs and Δ NNS RNA-BSs mutants derived from the parental *PIC2-GFP* strain.

III.2. *PIC2* mRNA levels are dependent on nutrient availability.

The primordial aim of my work was to test whether NNS recruitment to *PIC2* could be disrupted by introducing single-point mutations in Nab3 or Nrd1 consensus sites, and whether, if so, that binding deregulation would have any impact on the levels of *PIC2* expression and, in turn, on downstream cellular functions. Nevertheless, before setting off to investigate any of those aspects, I needed to identify a suitable set of growth conditions at which to study them.

Firstly, I chose synthetic complete (SC) medium for my analyses. SC growth medium contains defined concentrations of mineral salts, vitamins and amino acids and, hence, enables a precise growth control, thereby reducing experimental variability (see Table II.2). Moreover, being transparent, SC would also be a suitable medium for CRAC experiments as it was expected to enhance UV cross-linking efficiency in inducing protein-RNA adducts. Secondly, I decided to formulate the medium using a uracil-depleted amino acid mix (SC -Ura). The reason for this choice is that the HTF-integration or *pTEF1*-driven overexpression plasmids encoded the *URA3* auxotrophic marker. Therefore, successfully transformed colonies could be selected in uracil-lacking medium. To ensure medium uniformity across samples and experiments,

strains lacking a functional copy of the *URA3* gene were transformed with an empty pRS426 plasmid containing said selectable marker. Thirdly, as *PIC2* encodes a mitochondrial transporter, it was likely to intervene in respiration, which is known to be downregulated by fermentable carbon sources such as glucose (Rolland et al., 2002). Thus, I used raffinose throughout the entire study as, being poorly fermentable, this sugar obliges cells to derepress respiration to be able to fully metabolise the available carbon source.

Furthermore, to confirm that premature termination of *PIC2* was, as reported (van Nues et al., 2017), specifically strengthened during adaptation, I compared the RNA abundance of *PIC2* in low (i.e., 1% (w/v)) and high (i.e., 2 % (w/v)) glucose and raffinose concentrations (Figure III.3). Transcript levels comparison was conducted applying real-time quantitative PCR (RT-qPCR), which quantified the abundance of *PIC2* and normalised it to that of three housekeeping genes, namely *ACT1*, *ALG9* and *PGK1*, within the same condition. Subsequently, I compared the normalised levels of *PIC2* in each medium to those of the reference (i.e., the ones measured in SC -Ura containing 2% (w/v) glucose) (Figure III.3). Such approach revealed that, consistent with glucose-induced repression of respiratory metabolism, *PIC2* mRNA levels increased when the strains were grown in the presence of raffinose (Figure III.3). Accordingly, all subsequent experiments were performed employing medium with raffinose as the main carbon source.

Previous work had shown that *PIC2* transcription is significantly enhanced during glucose starvation (van Nues et al., 2017). This finding implies that when cells switch to respiration to extract as much ATP as possible from every remaining glucose molecule in the medium, Pic2 is required and, therefore, *PIC2* expression is induced. Consistent with this evidence, I observed that the levels of *PIC2* mRNA in medium containing only 1% (w/v) raffinose doubled that quantified in medium with 2% (w/v) raffinose. Importantly, these results illustrated that *PIC2* expression was not only shaped by the metabolic route by which the administered sugar was assimilated but also by the concentration of said sugar.

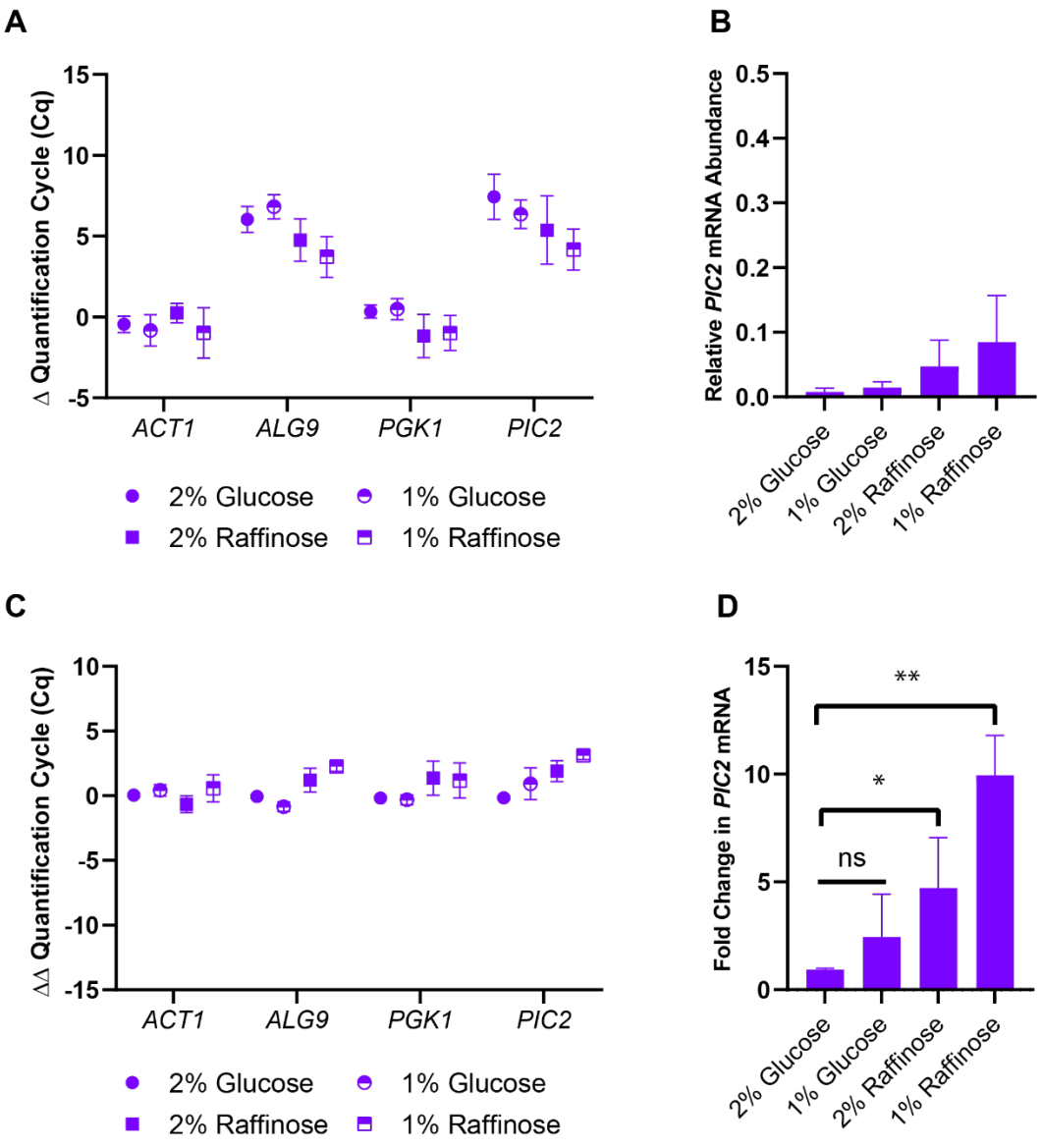

Figure III.3. RT-qPCR quantification of *PIC2* mRNA in the *PIC2-GFP* strain when grown in SC -Ura medium containing either 2% (w/v) glucose, 1% (w/v) glucose, 2% (w/v) raffinose and 1% (w/v) raffinose. **A**. Normalisation of raw quantification cycle (Cq) values to the median Cq of the reference genes within their own sample. **B**. Calculated ΔCqs for *PIC2* were used to derive a relative *PIC2* mRNA abundance within each condition. **C**. Median ΔCq values of each tested gene were normalised to those of the reference condition (i.e., 2% (w/v) glucose) to determine the differential ΔCq (ΔΔCq) values. **D**. These ΔΔCqs were exponentially transformed to find the fold change in mRNA abundance with respect to the reference sample. Data shows the mean of three biological repeats for each condition. Error bars represent standard deviation (SD). Statistical comparison of the fold change in *PIC2* mRNA across conditions was performed by unpaired t-tests: *: $p<0.05$, **: $p<0.01$ and ***: $p<0.001$ and 'ns': $p>0.05$.

III.3. Removal of Nab3 RNA-binding sites in *PIC2* increases *PIC2* RNA levels.

Having defined a set of growth conditions suitable for examining *PIC2* mRNA levels, I next determined whether the single-nucleotide mutations introduced in the Nab3 and Nrd1 recognition sequences of *PIC2* indeed impaired NNS binding in the mutant strains. To this end, I performed cross-linking and analysis of cDNAs (CRAC) (Granneman et al., 2009), a CLIP-related method that maps transcriptome-wide binding sites for RBPs at nucleotide resolution. This procedure employs two affinity-based purification steps which are based on the recognition of a His6-TEV-3xFLAG (HTF) tag. Therefore, prior to applying this technique, I engineered strains in which Nrd1, Nab3, Sen1 or Rpo21 (i.e., the largest catalytic component of the RNA polymerase II) were C-terminally fused to such epitope (Figure III.4). Given that I intended to compare the binding of NNS and Pol II in the mutants to that of the parental *PIC2-GFP* reference, these genetic modifications were separately inserted in the three strains. Furthermore, since I aimed to perform CRAC in SC -Ura containing 1% (w/v) raffinose, I first verified that the expression levels of the proteins and the intensity of the radioactive signal yielded by their adducted RNAs would be sufficient to conduct the experiments in that medium (Figures III.4 and III.5).

The full CRAC protocol is detailed in II.25 and a schematic summary is provided in Figure III.6. In summary, upon UV irradiation, cells were lysed and the RBP of interest with its cross-linked RNAs was purified with anti-FLAG magnetic beads. Following the trimming of covalently bonded RNAs using a cocktail of RNases, ribonucleoproteins were eluted from the FLAG beads using chaotropic agents. As a second enrichment step, eluates were incubated with nickel-charged affinity beads in denaturing conditions. The 5' ends of cross-linked RNAs in the immobilised complexes were subsequently radiolabelled with ^{32}P-ATP by T4 polynucleotide kinases. After elution, the complexes were TCA-precipitated and resolved on polyacrylamide gels. Autoradiography enabled the detection of radioactive signals in the region of the gel to which the ribonucleoproteins had migrated. Once the complexes had been excised from the gel, proteinase K released the cross-linked RNAs. Having isolated and reverse-transcribed purified transcripts, I then prepared the resulting cDNA libraries for sequencing.

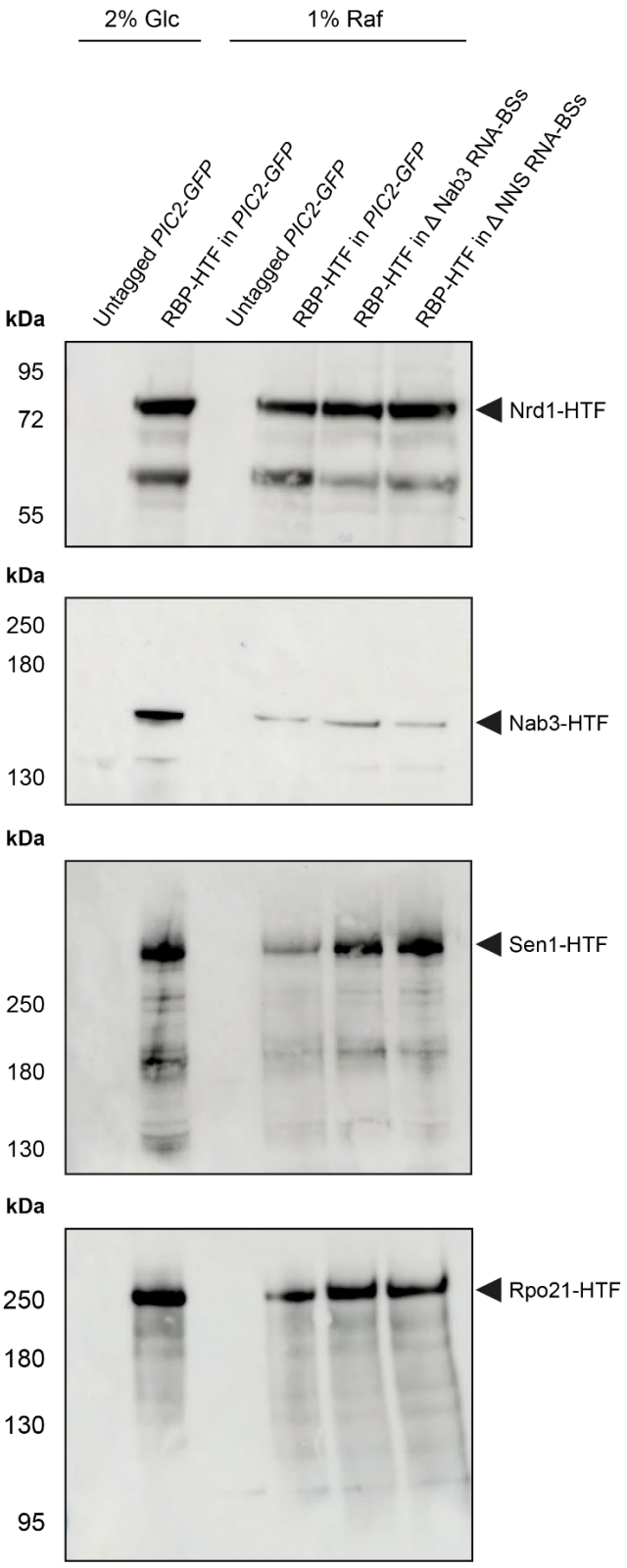

Figure III.4. Expression tests confirming the presence of Nrd1-HTF, Nab3-HTF, Sen1-HTF and Rpo21-HTF in *PIC2-GFP*, Δ Nab3 RNA-BSs and Δ NNS RNA-BSs. Although the levels of Nab3 were visibly diminished in raffinose-limiting (i.e., 1% (w/v) Raf) compared to glucose-rich (i.e., 2% (w/v) Glc), its expression was still high enough to successfully apply CRAC (see Figure III.5).

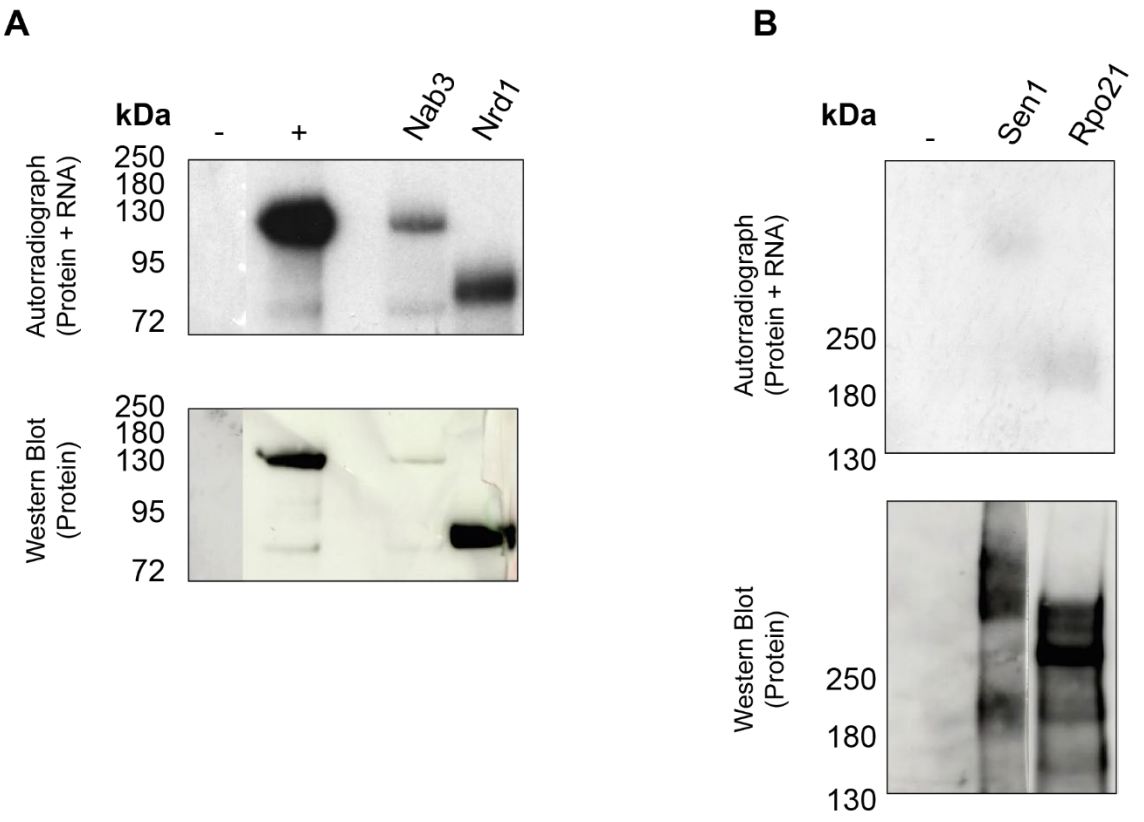

Figure III.5. Western blot and autoradiogram showing retrieved Nab3, Nrd1 and Sen1 ribonucleoprotein complexes in a *PIC2-GFP* parental strain grown in low (i.e., 1% (w/v)) raffinose medium. Exposure time for the autoradiogram in **A** was 40 minutes, the one displayed in **B** occurred overnight. Signals were compared to those of a negative control (uncross-linked sample) and a positive control (Nab3-HTF grown in medium containing 2% (w/v) glucose).

To analyse the sequencing outputs of my CRAC libraries, Prof Sander Granneman developed a peak calling algorithm capable of identifying differential RNA binding (DBPeaks; https://git.ecdf.ed.ac.uk/sgrannem/dbpeaks). Briefly, the package initially applies the pyCalculateFDRs function of the pyCRAC package to identify significantly enriched peaks across all genes of each individual replicate from the reference strain (i.e., *PIC2-GFP* encoding HTF-tagged NNS components or RNA polymerase) and the mutants (Webb et al., 2014). At this stage, only the peaks that were identified in *all* datasets were considered. The pipeline then calculated the total number of reads within the selected peaks and discarded the ones containing a number of reads that was lower than that of the mean coverage of all other peaks in the dataset. Filtered peak files were then annotated and statistically analysed using DESeq2 (Love et al., 2014). The results show that, as expected, disrupting both Nrd1

and Nab3 binding sites (∆ NNS RNA-BSs) almost completely abrogated binding of both proteins to the *PIC2* transcript (Figure III.7). As I had hypothesised, the ∆ Nab3 RNA-BSs mutations blocked Nab3 binding to *PIC2* but, importantly, Nrd1 cross-linking was predominantly still retained throughout its binding sites in the same RNA (Figure III.7). These data demonstrate that Nrd1 can still be recruited to *PIC2* even when Nab3 no longer binds the transcript (Figure III.7). I concluded that while Nrd1 binding was slightly reduced in ∆ Nab3 RNA-BSs, the mutations selectively impaired Nab3 binding in the ∆ Nab3 RNA-BSs mutant as well as Nab3 and Nrd1 binding in the ∆ NNS RNA-BSs strain (Figure III.7).

I next checked whether altering NNS binding to *PIC2* indeed increased its mRNA abundance. RT-qPCR revealed that, in high raffinose medium (i.e., 2% (w/v)), *PIC2* mRNA levels increased by 2- to 3-fold in ∆ Nab3 RNA-BSs compared with its parental counterpart (Figure III.8). This was consistent with defective NNS-mediated premature transcription termination of *PIC2*. Since *PIC2* upregulation increased to 3- to 4-fold when the same mutant was grown in lower (i.e., 1% (w/v)) raffinose concentrations (Figure III.9), I concluded that the NNS regulatory role is more prominent during nutrient scarcity.

Unexpectedly, *PIC2* mRNA levels only modestly increased in ∆ NNS RNA-BSs (Figure III.8-9), possibly because its larger number of nucleotide substitutions affected mRNA stability, overshadowing any effects from diminished NNS regulation. Given that such mutant encoded six sequence mutations more than ∆ Nab3 RNA-BSs, it was plausible that the resulting *PIC2* transcript in the former strain was less stable. To evaluate this possibility, I checked the probability of folding of the *PIC2* transcript in both mutants and their parental *PIC2-GFP* using the RNAfold web server (Lorenz et al., 2011), an algorithm computing thermodynamic structure predictions based on minimum free energy predictions (Figure III.10). As expected, the thermodynamic ensemble profile estimated for the transcript in the ∆ NNS RNA-BSs mutant displayed lower probability of folding than that of the *PIC2-GFP* reference throughout most nucleotide positions. Hence, apart from affecting the *PIC2* mRNA levels in the strain, lower mRNA stability was likely decreasing the translatability of the *PIC2* transcripts in this strain.

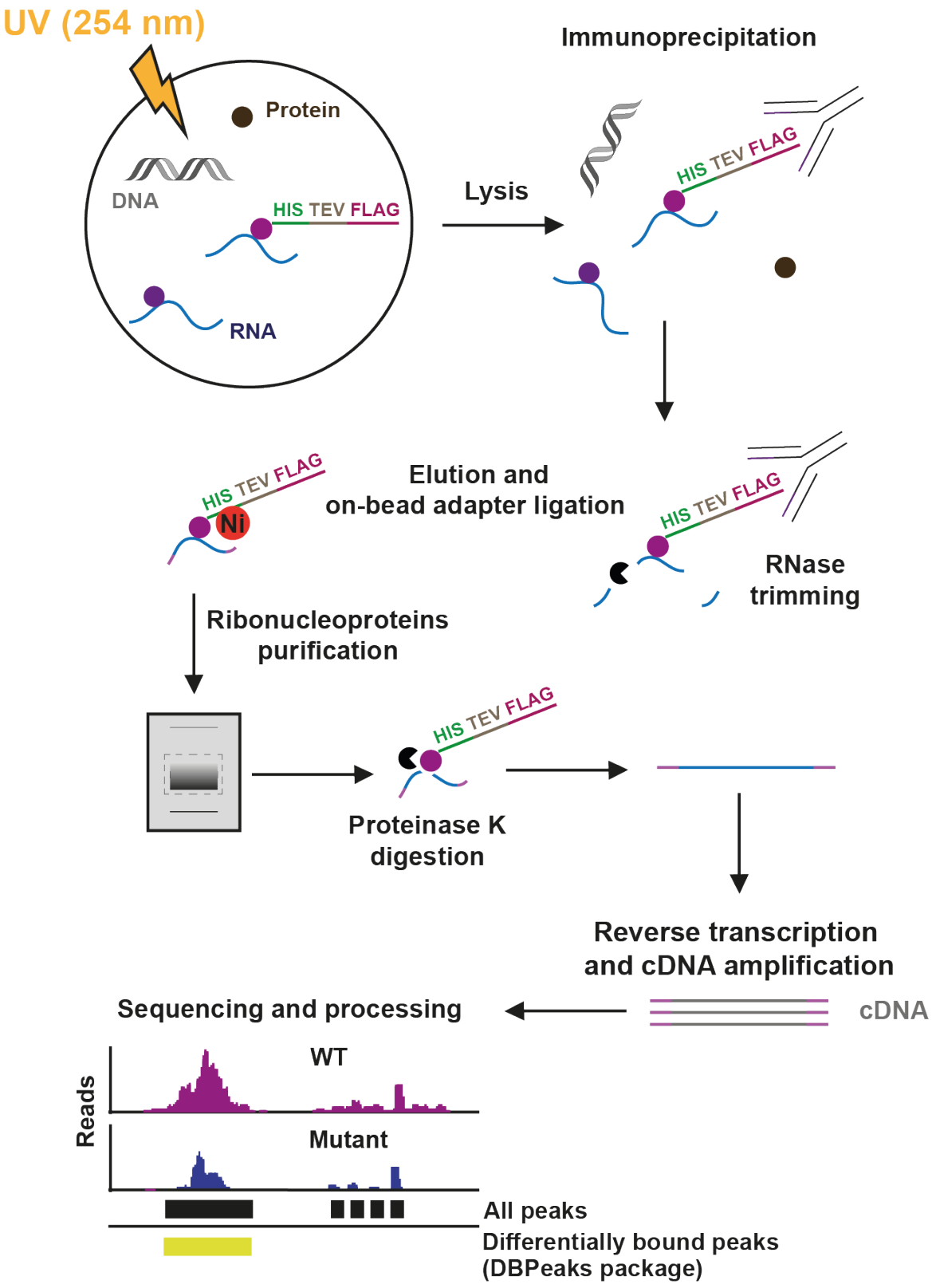

Figure III.6. Schematic outline of the CRAC protocol.

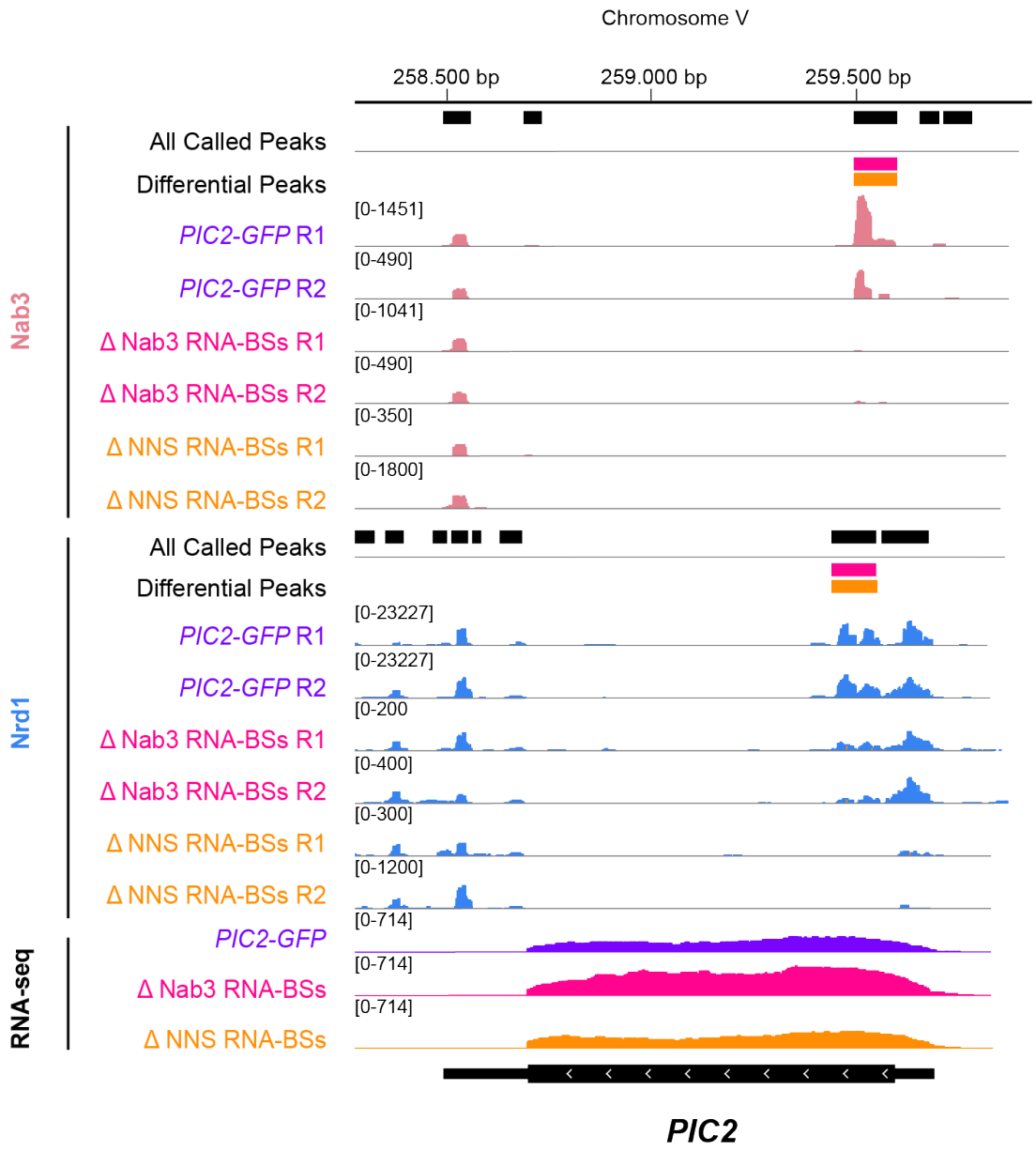

Figure III.7. CRAC and RNA-seq traces showing that removing Nab3 binding sites in *PIC2* does not prevent Nrd1 binding. Snapshots of read distributions obtained in Nab3 CRAC (top panel), Nrd1 CRAC (middle panel) and RNA-seq data (lower panel) of the parental *PIC2-GFP* strain and Δ Nab3 RNA-BSs and Δ NNS RNA-BSs mutants. CRAC datasets show two independent repeats. The RNA-seq data track was generated by merging biological triplicate datasets triplicates were merged for the RNA-seq one. All Nrd1 and Nab3 binding sites were identified using pyCalculateFDRs from the pyCRAC package (Webb et al., 2014). Differential binding sites identified by DBPeaks in Δ Nab3 RNA-BSs and Δ NNS RNA-BSs are indicated.

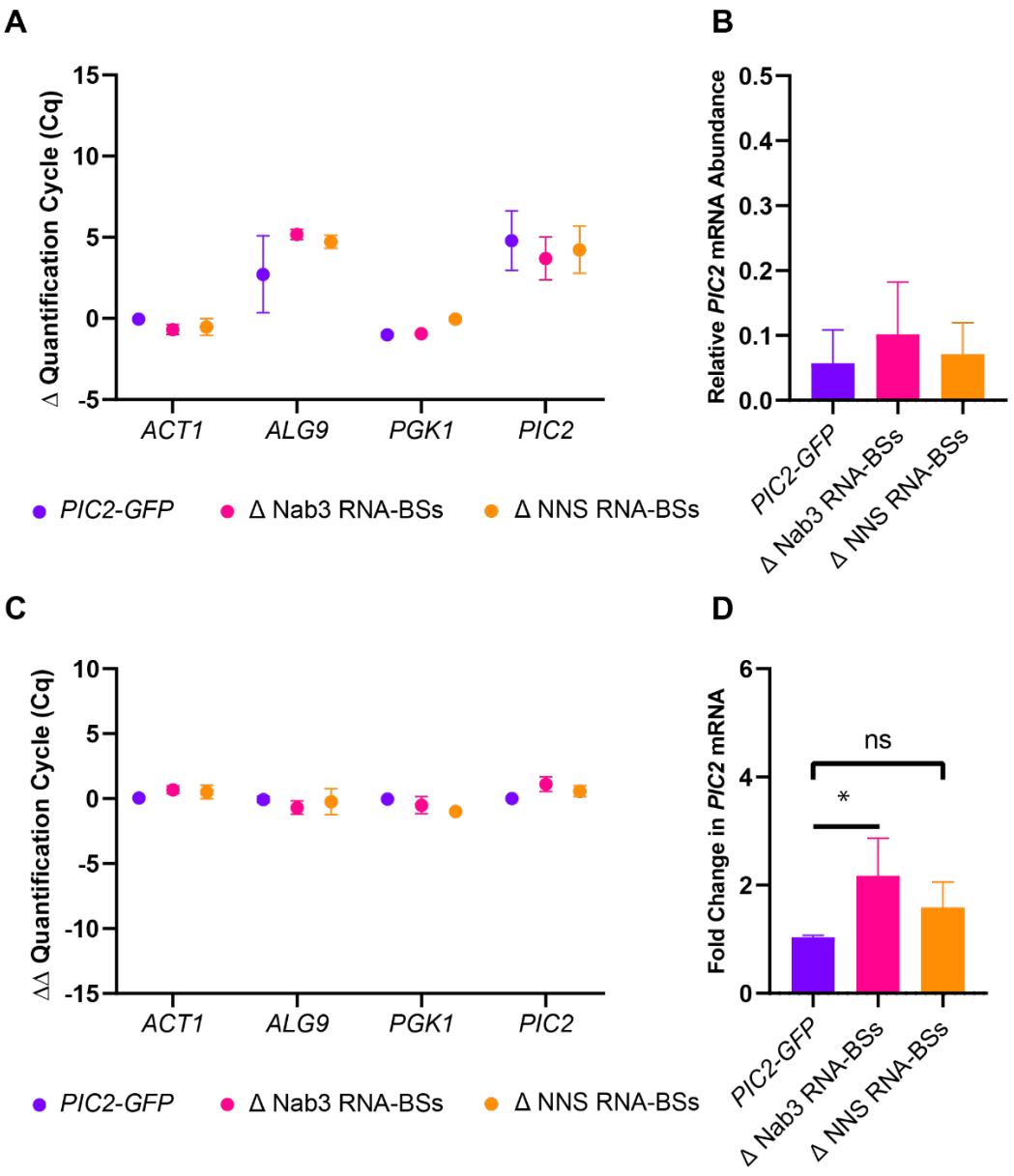

Figure III.8. RT-qPCR quantification of *PIC2* mRNA in the *PIC2-GFP*, Δ Nab3 RNA-BSs and Δ NNS RNA-BSs strains when grown in SC -Ura medium containing 2% (w/v) raffinose. **A**. Normalisation of raw quantification cycle (Cq) values to the median Cq of the reference genes within their own sample. **B**. Calculated ΔCqs for *PIC2* were used to derive a relative *PIC2* mRNA abundance within each condition. **C**. Median ΔCq values of each tested gene were normalised to those of the parental strain (i.e., *PIC2-GFP*) to determine the differential ΔCq (ΔΔCq) values. **D**. These ΔΔCqs were exponentially transformed to find the fold change in mRNA abundance with respect to the reference sample. Data shows the mean of three biological repeats for each condition. Error bars represent standard deviation (SD). Statistical comparison of the fold change in *PIC2* mRNA of both mutants with respect to the parental *PIC2-GFP* reference was performed by unpaired t-tests: *: $p<0.05$ and 'ns': $p>0.05$.

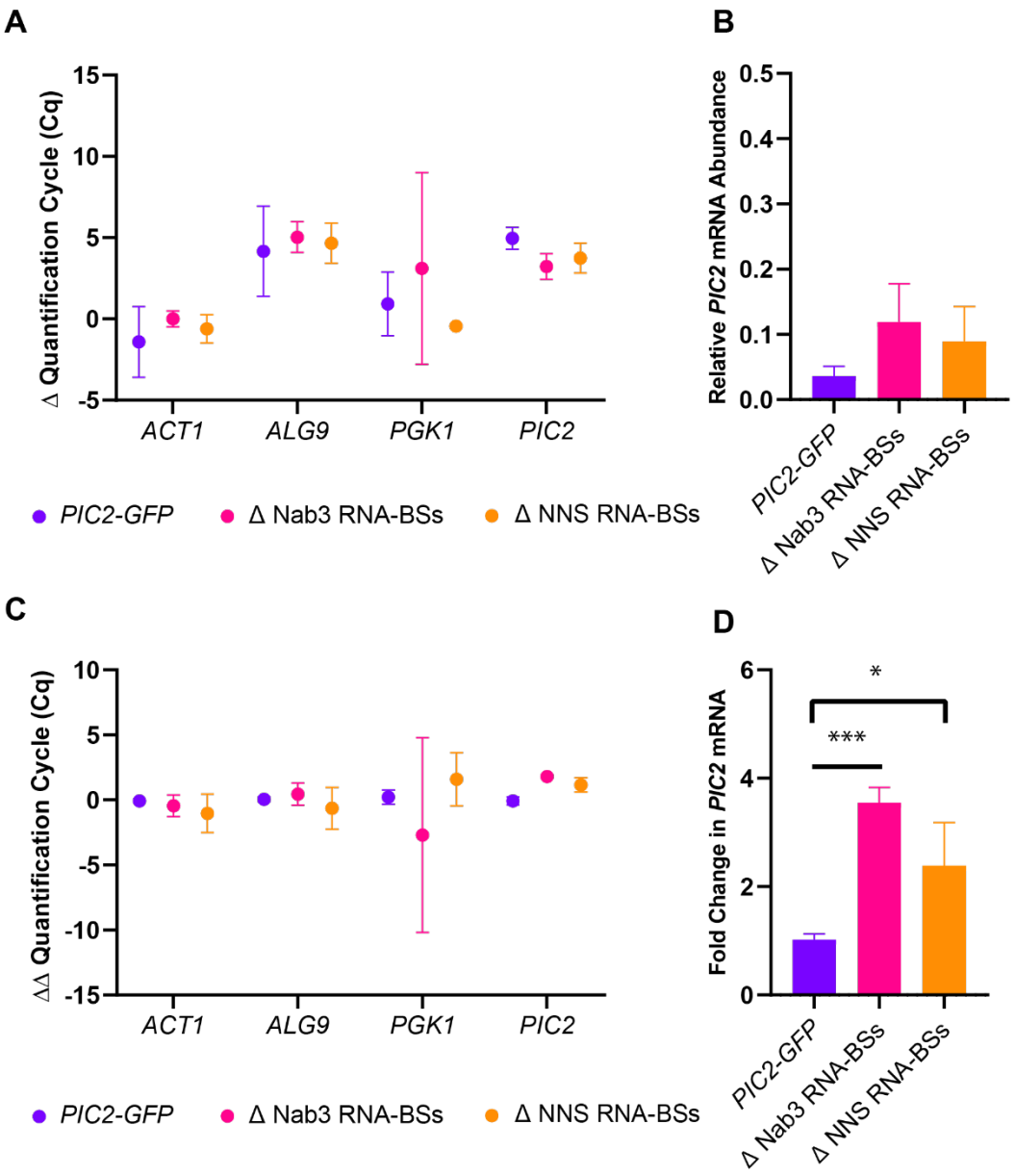

Figure III.9. RT-qPCR quantification of *PIC2* mRNA in the *PIC2-GFP*, Δ Nab3 RNA-BSs and Δ NNS RNA-BSs strains when grown in SC -Ura medium containing 1% (w/v) raffinose. **A**. Normalisation of raw quantification cycle (Cq) values to the median Cq of the reference genes within their own sample. **B**. Calculated ΔCqs for *PIC2* were used to derive a relative *PIC2* mRNA abundance within each condition. **C**. Median ΔCq values of each tested gene were normalised to those of the parental strain (i.e., *PIC2-GFP*) to determine the differential ΔCq (ΔΔCq) values. **D**. These ΔΔCqs were exponentially transformed to find the fold change in mRNA abundance with respect to the reference sample. Data shows the mean of three biological repeats for each condition. Error bars represent standard deviation (SD). Statistical comparison of the fold change in *PIC2* mRNA of both mutants with respect to the parental *PIC2-GFP* reference was performed by unpaired t-tests: *: $p<0.05$, ***: $p<0.001$ and 'ns': $p>0.05$.

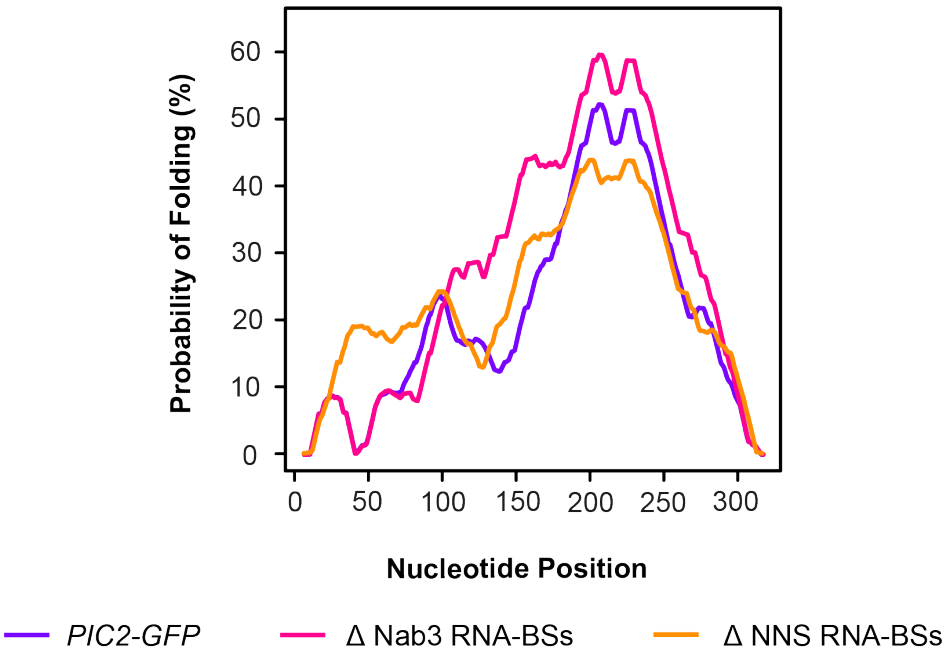

Figure III.10. Thermodynamic ensemble profiles for the *PIC2* transcripts produced by the *PIC2-GFP*, Δ Nab3 RNA-BSs and Δ NNS RNA-BSs strains. Estimates for probability of folding are based on minimum free energy predictions by the RNAfold suite (Lorenz et al., 2011).

III.4. Removal of Nab3 RNA-binding sites in *PIC2* increases Pic2 protein abundance.

To verify whether the significant increases in *PIC2* mRNA abundance that I had detected in the mutants yielded an accompanying increase in Pic2 protein levels, I proceeded to quantify Pic2-GFP levels in the three strains. Initially, I performed a preliminary semi-quantitative inspection of Pic2 protein levels by quantitative western blot. This methodology relies on the detection of a fluorescent or chemiluminescent signal proportional to the amount of protein of interest, and its normalisation to that of a housekeeping protein, such as glyceraldehyde 3-phosphate dehydrogenase (GAPDH), in the same sample. The selected housekeeping protein was expected to be constitutively expressed across conditions and, hence, the intensity of its signal could be used to correct for variability in sample preparation, loading and transfer. To ensure that the intensity of the signal remained unaffected by exposure times and the kinetics of chemiluminescent enzymatic reactions, secondary antibodies labelled with near-infrared (NIR) fluorescent dyes were used to detect α-GFP and α-GAPDH primary

antibodies (Figure III.11A). After quantifying the maximum intensity for each of the bands in the membrane, Pic2 intensity values for a given lane were normalised to those of its GAPDH ones.

To gain a general outlook of the expression profile of Pic2 throughout different growth phases, samples were gathered from three independent biological replicates harvested at OD_{600} 0.25, 0.5 and 1. Moreover, with the purpose of comparing changes in translational expression of *PIC2* based on nutrient availability, this time-resolved approach was applied to cultures containing 2% (w/v) and 1 % (w/v) raffinose. As depicted in Figure III.11B-C, the relative intensity value of Pic2-GFP compared to that of GAPDH in the same sample remained mostly constant throughout the early (i.e., 0.25 OD_{600}), mid (i.e., 0.5 OD_{600}) and late (i.e., 1 OD_{600}) exponential growth stations. Thus, to quantify the overall abundance of Pic2 in *PIC2-GFP*, ∆ Nab3 RNA-BSs, ∆ NNS RNA-BSs, the three biological replicates were grouped per strain and normalised to the mean intensity ratio calculated for the parental reference in each condition (Figure III.11D-E). Statistical comparison of the normalised intensity ratios showed that, in agreement with the *PIC2* RNA levels measured in RT-qPCR evaluation, the protein levels of Pic2 were larger for ∆ Nab3 RNA-BSs and ∆ NNS RNA-BSs in low raffinose medium. Additionally, again supporting the *PIC2* RNA quantification showcased in the previous section, while Pic2 protein abundance was significantly enhanced in ∆ Nab3 RNA-BSs in high raffinose medium, no difference in Pic2 levels was detected between ∆ NNS RNA-BSs and the *PIC2-GFP* reference at these growth conditions (Figure III.11D-E).

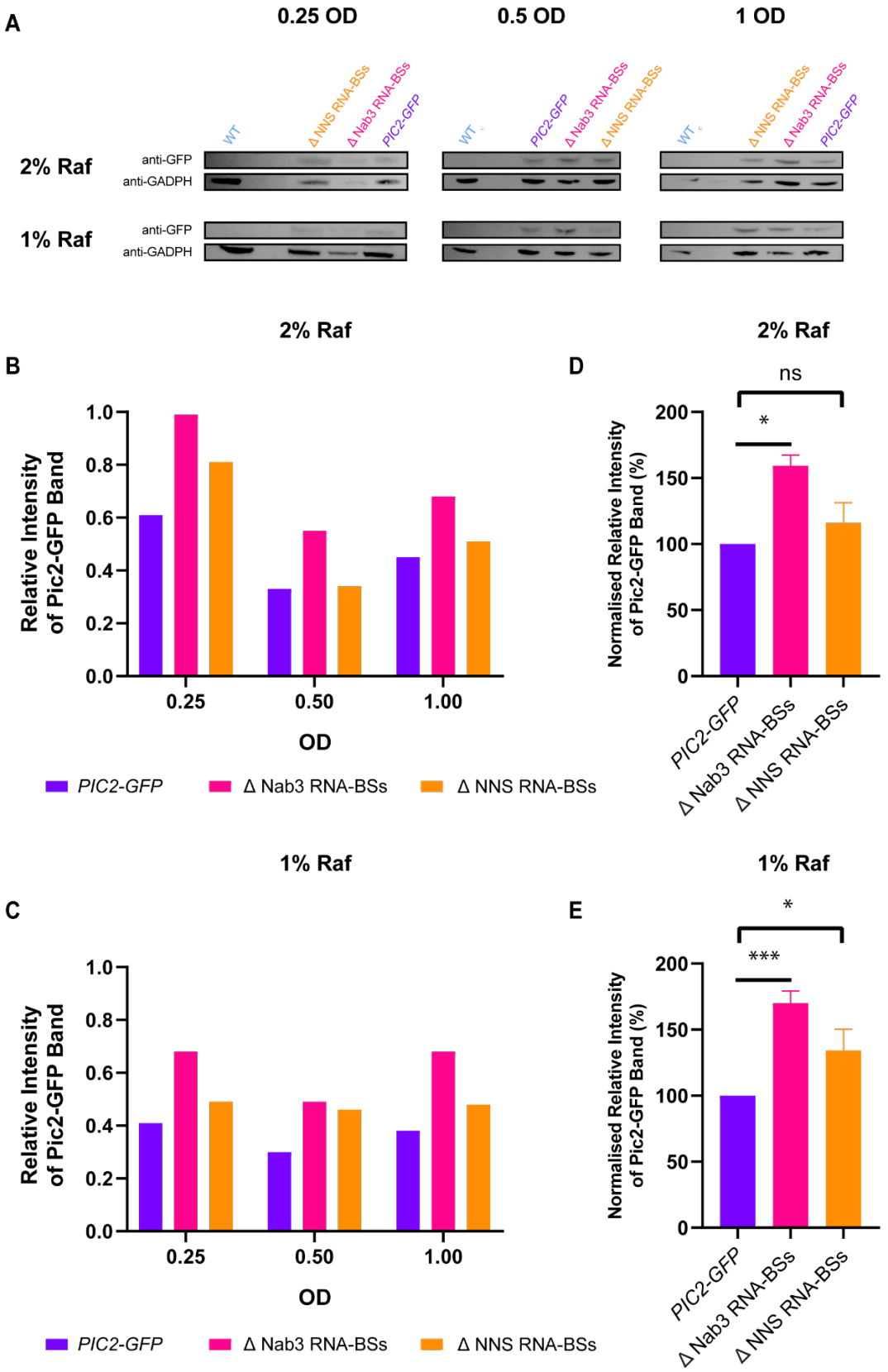

Figure III.11. qWBs show that Pic2-GFP levels are increased in accordance with *PIC2* mRNA abundance. **A**. Anti-GFP and anti-GAPDH bands for *PIC2-GFP*, Δ Nab3 RNA-BSs and Δ NNS RNA-BSs. A non-fluorescent parental strain from which the *PIC2-GFP* strain was derived was also included as a negative control. Experiments were performed on samples gathered from three independent biological replicates

harvested from cultures containing 2% (w/v) or 1% (w/v) raffinose and grown to early (i.e., 0.25 OD_{600}), mid (i.e., 0.5 OD_{600}) and late (i.e., 1 OD_{600}) exponential growth phases. **B**. Relative intensities of the Pic2-GFP band were calculated by dividing the maximum signal for the Pic2-GFP band over that of GAPDH within the same sample. **C**. ∆ Nab3 RNA-BSs and ∆ NNS RNA-BSs average Pic2 relative intensities were normalised to that of the parental strain. Data shows the normalised mean of three biological repeats for each condition. Error bars represent standard deviation (SD). Statistical comparison of the fold change in Pic2-GFP signal of each mutant with respect to the parental reference *PIC2-GFP* was performed by unpaired t-tests: *: $p<0.05$, **: $p<0.01$ and ***: $p<0.001$ and 'ns': $p>0.05$.

Having detected general Pic2 abundance increases throughout the growth phases of both mutants, I next checked whether these findings could be reproduced employing a technique that would allow me to measure Pic2-GFP levels in individual cells of a population throughout time. In addition to providing a fully quantitative method, such an approach would shed light on the variability in the expression of Pic2-GFP within the cells from isogenic populations of the mutants and the parental reference. To this end, I applied time-lapse microscopy imaging of ALCATRAS microfluidics systems (Crane et al., 2014). These devices comprise flow chambers that trap individual yeast cells in pillars or 'jails' (Crane et al., 2014). While they remained in those structures, cells were continuously exposed to a constant rate of fresh growth medium for the length of the experiment and microscopy images were acquired at regular intervals for more than 12 hours (Figure III.12).

Using the BABY and ALIBY software (Muñoz González et al., 2024; Pietsch et al., 2023), cells were identified and tracked to obtain single-cell fluorescence recordings. The mean fluorescence values for a given cell were divided over its measured area in pixels and used as a proxy for the average concentration of Pic2 molecules in that cell. After considering the data for the entire cell population, my analyses showed that Pic2-GFP fluorescence and, therefore presumably its abundance, increased when the NNS could not fully target *PIC2* (Figure III.13). Since these findings were consistent with western blotting and RT-qPCR comparisons, I concluded that whilst Pic2 levels were substantially larger in the ∆ Nab3 RNA-BSs strain, Pic2 expression was only minorly increased in ∆ NNS RNA-BSs.

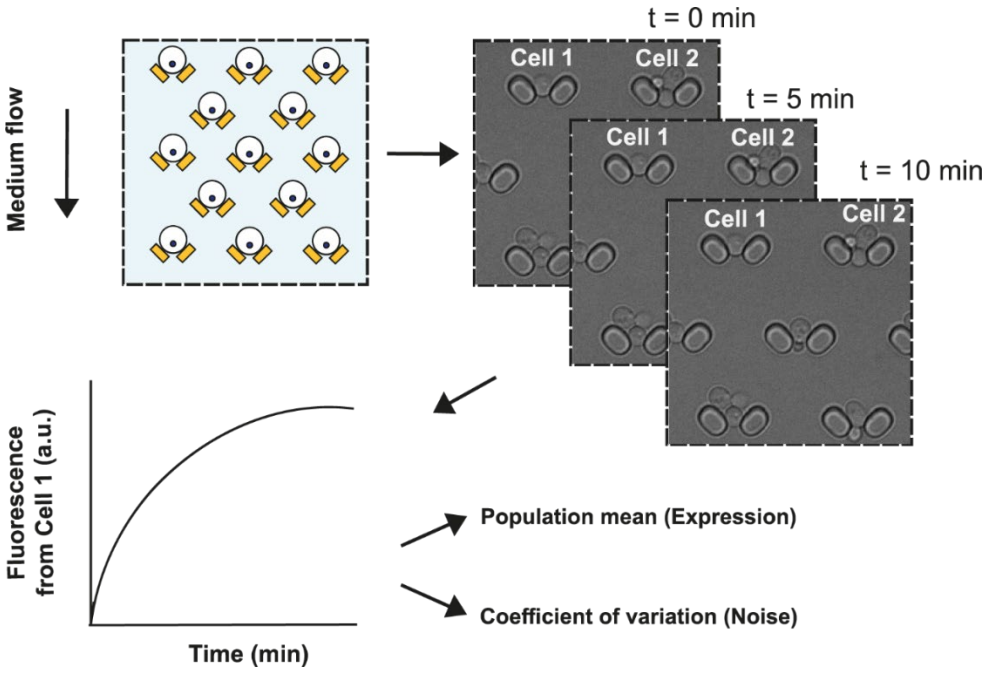

Figure III.12. Illustrative outline of the microfluidics experiments performed to generate the time-resolved Pic2 expression and noise measurements.

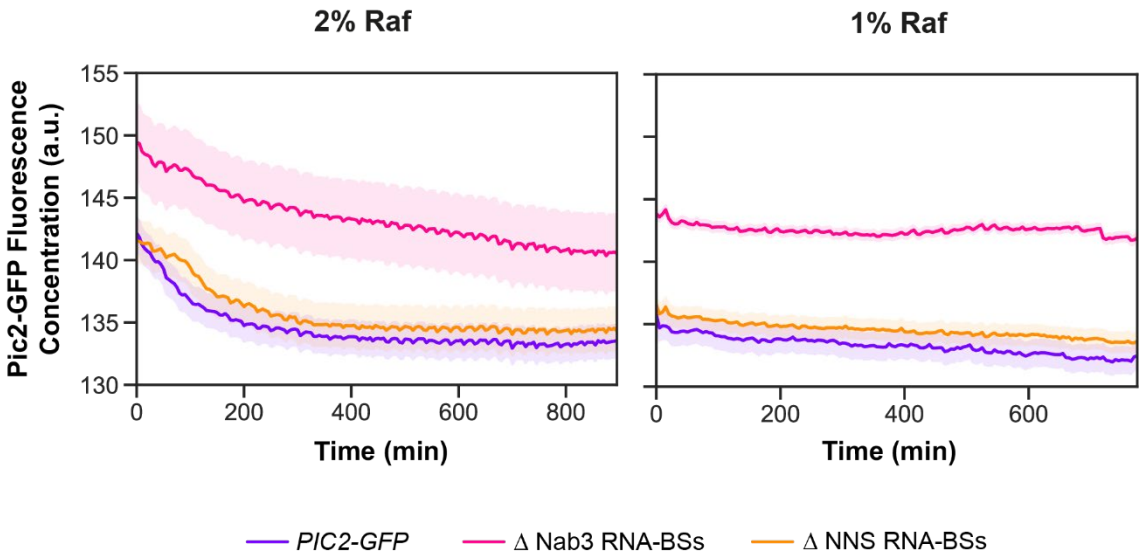

Figure III.13. Time-resolved analyses of mean fluorescence concentration of Pic2-GFP for *PIC2-GFP*, Δ Nab3 RNA-BSs and Δ NNS RNA-BSs strains grown in abundant (i.e., 2% (w/v)) and restrictive (i.e., 1% (w/v)) raffinose concentrations. At least 500 cells were analysed for each strain and condition. In the Y axis, 'a.u.' stands for arbitrary units.

III.5. Removal of NNS RNA-binding sites in *PIC2* increases Pic2 expression noise.

Nrd1 and Nab3 binding to nascent RNA transcripts depends on multiple factors, including the number and order of RNA-binding motifs in the transcript (Porrua et al., 2012), polymerase occupancy on the DNA, the phosphorylation status of the Pol II CTD (Vasiljeva et al., 2008), the processivity of the polymerase, and its elongation rate (Hazelbaker et al., 2013). High recruitment of Pol II to a gene increases the probability of Nrd1 and Nab3 binding to polymerases, which, in turn, increases their likelihood of terminating. Therefore, one plausible role of NNS could be regularising Pol II transcription of *PIC2*. If that was the case, NNS would contribute to stress-induced transcriptional remodelling by reducing fluctuations or preventing overshooting of *PIC2* expression in individual cells. This controlled transcriptional response to a new environment could, in turn, increase the cell fitness and endow it with a selective advantage.

To test this, I calculated the coefficient of variation of Pic2-GFP fluorescence concentration of all the cells in the examined *PIC2-GFP*, ∆ Nab3 RNA-BSs and ∆ NNS RNA-BSs populations (Figure III.14). As described in I.5., the noise in their Pic2 expression was calculated as the coefficient of variation in the Pic2-GFP concentrations recorded for every cell in the studied populations (Swain et al., 2002). As anticipated, I observed that the noise in Pic2 expression (i.e., the coefficient of variation of Pic2-GFP concentration) was larger in the ∆ Nab3 RNA-BSs strain regardless of the raffinose concentration in the medium (Figure III.14). Conversely, whereas the noise in Pic2 expression among ∆ NNS RNA-BSs cells was not significantly different from that of the *PIC2-GFP* population in medium containing 2% (w/v) raffinose, it did experience a modest increase when the sugar became limiting (Figure III.14).

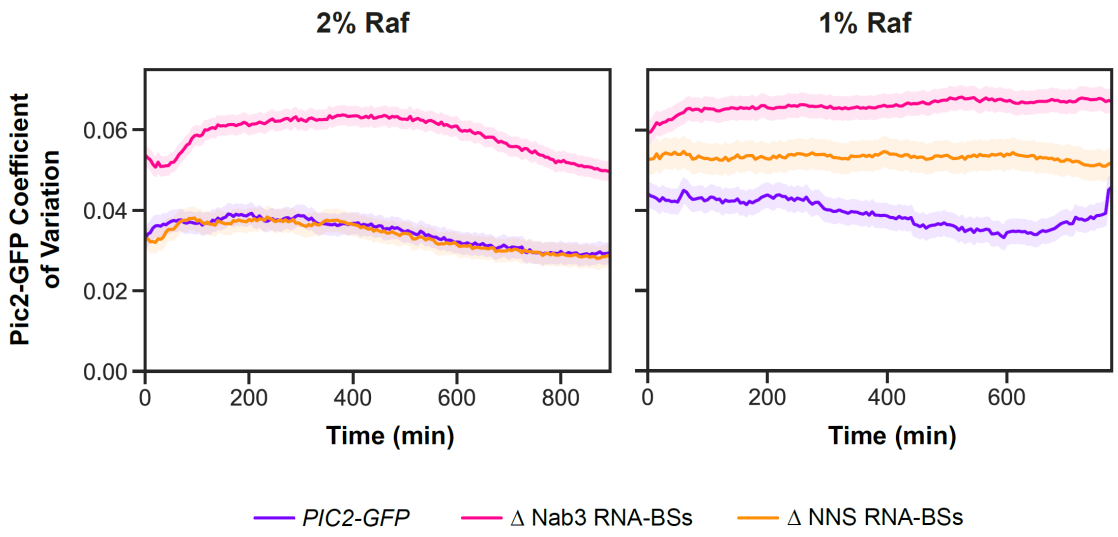

Figure III.14. Time-resolved coefficients of variation for *PIC2-GFP*, Δ Nab3 RNA-BSs and Δ NNS RNA-BSs strains grown in high (i.e., 2% (w/v)) and limiting (i.e., 1% (w/v)) raffinose abundance. Values are derived from the single-cell continuous-flow microfluidics experiments presented in Figure III.9.

Previous studies have also measured noise in protein expression using flow cytometry (Bar-Even et al., 2006; Newman et al., 2006). Using such established protocols, I was able to quantify noise in larger populations (i.e., around 2,000 cells in flow cytometry experiments compared to approximately 500 cells that I could consider during the microfluidics analyses) and restrict the analyses to cells displaying almost identical dimensions. This latter aspect also represented an advantage with respect to the original microfluidics approach, which was uniformly applied to all cells remaining in the traps for more than 80% of the duration of the experiment independently from their volume.

During cytometry, a laser emitting lights of different wavelengths is shone at single cells from various angles. Accordingly, after passing through the cells, the light waves are slightly modified. When recorded in the same direction at which light with a wavelength of 488 nm was originally radiated, the deflection recorded is proportional to the size of the cell through which the light has just traversed. This phenomenon is referred to as forward scatter or FSC and its values can be monitored by detectors sensitive to different parameters of the resulting pulse or signal, namely its area (A), width (W) or height (H). These properties can also be obtained for light at other wavelengths, which in turn excites different fluorophores. More specifically, for

detecting Pic2-GFP, it was possible to employ a cytometer equipped with an argon laser capable of emitting light at 500 nm.

Based on the outlined principles, the approach described in the work by Bar-Even and co-authors applies two filters (Bar-Even et al., 2006). Firstly, a gate selects the 50% of events that are closest to the largest peak in the FSC-W channel (Bar-Even et al., 2006). Secondly, a threshold is established to keep the 40% of events that are closest to the main peak of the FSC-A channel (Bar-Even et al., 2006). The original work also describes an extra gate that was introduced to minimise the amount of noise based on the green fluorescence values obtained. That gate entailed removing 3.5% and 4% of the events on the lowest and highest side of the distribution obtained in such pulse (Bar-Even et al., 2006). Even though the authors argued that this filter removed outliers at both ends of the distribution and would thus avoid considering dead cells or minor aggregates during the analysis, they also indicated that the inclusion of this criterion barely modified their results quantitatively and had no effects on them qualitatively (Bar-Even et al., 2006).

I decided not to execute the third gating threshold because, by imposing the first two filters, I had already reduced the examined population to less than a quarter of the original acquisition and, having selected cells which were strictly proximal to the median cell size, I considered that it was highly unlikely that remaining events would comprise cell clumps or precipitates, which would present clearly distinct cell size values. Moreover, I ensured that no dead cells were incorporated into the analysis by applying the FSC-A and FSC-W gates exclusively to the fraction of the original population displaying a green fluorescence value greater than that under which 95 % of a non-fluorescent BY4741 wild-type strain lay. Apart from averting dead or dying cells displaying decreasing levels of Pic2-GFP, this selection corrected for the background autofluorescence signal that even non-fluorescent cells would produce in the green fluorescence detectors.

I also re-analysed the cytometry data following the strategy described by Newman *et al*. (Newman et al., 2006). Similarly to the Bar-Even approach, Newman and colleagues introduced a filter which discarded the upper and lowest 5% of the events recorded based on the area of their cell size signal (i.e., FSC-A) (Newman et al., 2006). Subsequently, this work implemented a gate removing the highest and

lowest 5% of the occurrences according to the area of their granularity signal, which is measured by the side scattering of visible light (SSC-A) (Newman et al., 2006). Having determined the median value of both parameters in the remaining cells, they inserted a circular gate of a predefined optimal size centred upon both medians (Newman et al., 2006). The noise of the remaining set of cells was calculated as the coefficient of variation of green fluorescence and compared to that obtained after applying the approach defined by the Barkai group. Notably, in support of my previous microfluidics findings, both procedures detected a significant increase in the noise of Pic2-GFP expression among ∆ Nab3 RNA-BSs cells (Figure III.15). Despite identifying a mildly larger coefficient of variation among the ∆ NNS RNA-BSs mutant, cytometry-based analyses failed to identify a significant difference for this strain.

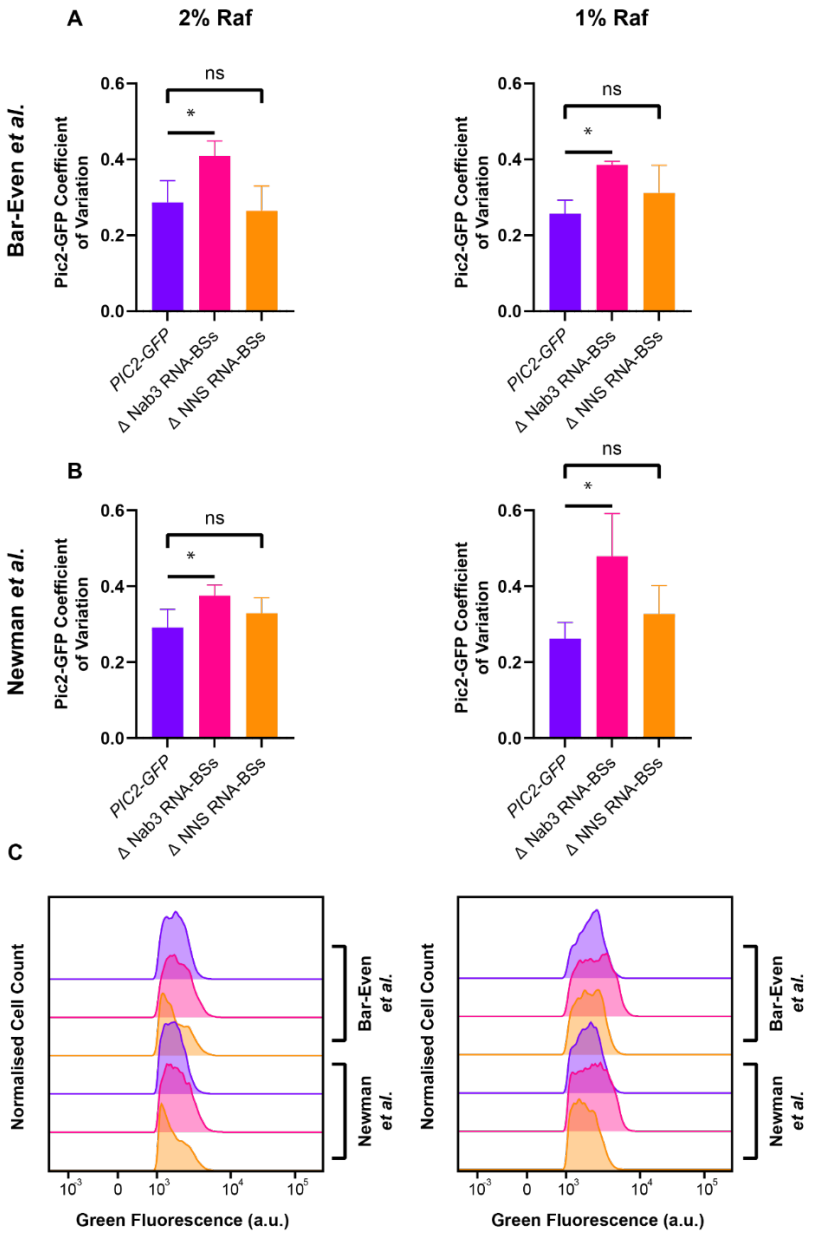

Figure III.15. Established cytometry gating strategies for noise quantification confirm that stochasticity in Pic2-GFP expression is larger in the Δ Nab3 RNA-BSs mutant. **A**. Coefficient of variation in Pic2-GFP fluorescence after following the filtering criteria described in a study by Bar-Even and colleagues. **B**. Coefficient of variation in Pic2-GFP fluorescence based on the gating imposed by Newman and co-workers. **C**. Cytometry traces displaying the green fluorescence distribution of the remaining cell population after implementing all the selection thresholds applied by either approach. Data shows the normalised mean of three biological repeats for each condition. Error bars represent standard deviation (SD). Statistical comparison coefficient of variation for Pic2-GFP in the final population of each mutant with respect to the parental reference *PIC2-GFP* was performed by unpaired t-tests: *: $p<0.05$ and 'ns': $p>0.05$.

III.6. Addition of NNS RNA-binding sites to a synthetic reporter system decreases *GFP* RNA levels.

Although *PIC2* mRNA levels in low raffinose medium were 10-fold larger than those cells grown in glucose-containing medium (Figure III.3B), the gene is still lowly expressed compared to other transcripts under these conditions (Figure III.16A). Therefore, it was possible that the described NNS attenuation mechanism is limited to genes with low transcription levels. To address this concern and generalise the role of the NNS complex as a transcriptional noise suppressor for protein-coding targets, the Edinburgh Genome Foundry applied modular cloning (MoClo) to synthesise six constructs encompassing different combinations of Nab3 and Nrd1 motifs. The design of these expression systems was inspired by an *in vivo* screen that identified a set of optimal sequence determinants for NNS-mediated transcription attenuation (i.e., the 'supermotif') (Porrua et al., 2012). By introducing NNS cognate sequences in the upstream region of sfGFP, the expression of this reporter gene could be used as an indicator of the extent to which varying the abundance and distribution of Nab3 and Nrd1 binding affected the transcriptional levels and expression noise of the distal mRNA target. Expression of sfGFP was driven from the strong inducible promoter *pGAL1* to assess whether the NNS complex could counteract high rates of transcription initiation in medium supplemented with 1% (w/v) galactose and 1% (w/v) sucrose. Importantly, the relative abundance of *GFP* transcripts in the BSWT strain was two orders of magnitude larger than that of *PIC2* mRNA in the *PIC2-GFP* parental strain (3.09 vs 0.03), demonstrating that this synthetic system generated very highly expressed transcripts (Figure III.16C).

These GFP reporter expression systems encoded the 5'UTR sequence of the *RPL20A* gene, which encodes a ribosomal protein. There were two reasons underlying this locus choice: firstly, its translation product was highly abundant as Rpl20a is present at around 54,835 copies per cell (Ho et al., 2018); accordingly, the 5' UTR of its encoding gene must be able to support very high levels of translation initiation and efficient ribosome scanning. Secondly, the 5'UTR of *RPL20A* was extensive enough to fit the longest combination of binding sites and their accompanying spacer sequences. Since *RPL20A* intrinsically encoded a Nab3 binding site, the latter was disrupted in the parental strain used as the wild-type reference in such expression

systems. The derived reporter constructs displayed identical length and underlying sequence but contained varying combinations of Nab3 and Nrd1 binding sites. While BS1, BS2 and BS3 were designed to test whether positional or sequential divergence from a canonical NNS termination sequence would increase transcriptional levels and fluctuations of the downstream target, BS4 and BS5 were devised to check whether increasing the number of NNS regulatory motifs would reduce expression and noise of the target transcript. In all cases, the reporter constructs were integrated into the genome of the same BY4741 parental strain by replacing the *GAL2* locus. Given that Gal2 is the only known galactose importer in yeast (see Figure I.8), preventing its expression ensured that the concentration of galactose in the medium remained constant throughout the duration of the experiments. Consequently, while the supplied galactose would not be catabolised by these strains, it could still drive the expression of the reporter gene through the inducible *pGAL1* promoter.

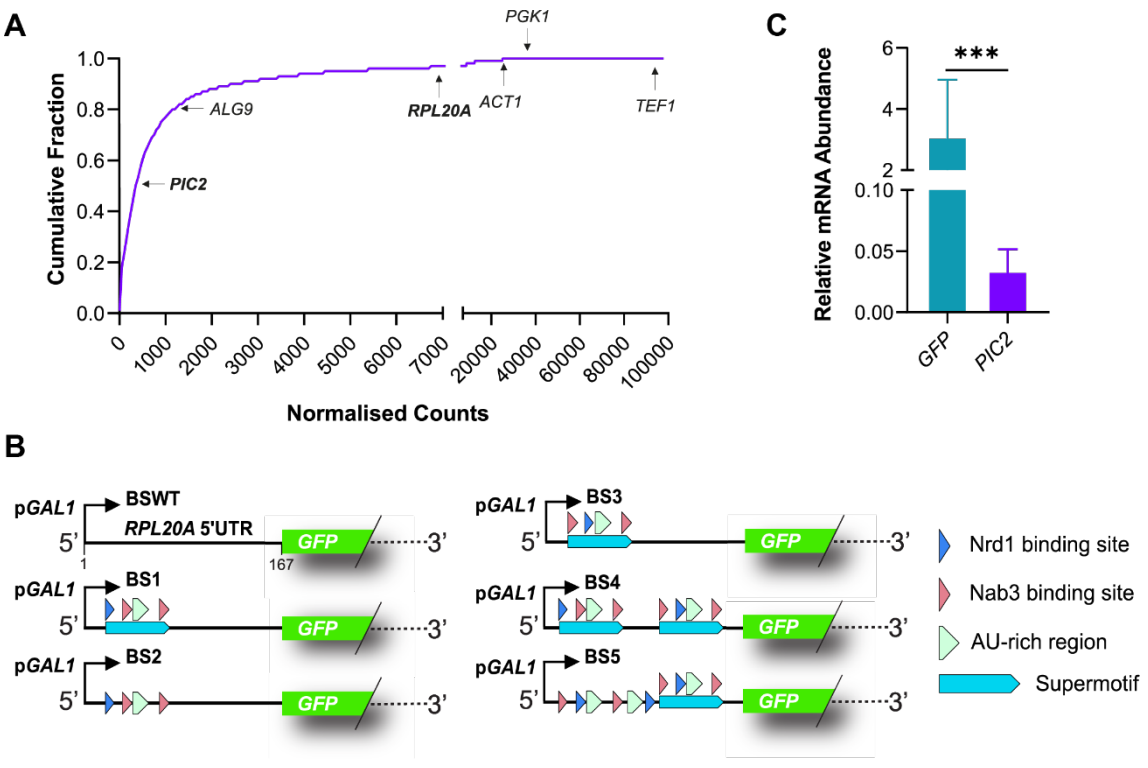

Figure III.16. Testing the role of the NNS complex as a repressor of expression and stochasticity in protein-coding genes using a library of strong, inducible synthetic constructs. **A**. Cumulative distribution of transcript abundance quantified by RNA-sequencing in the *PIC2-GFP* strain grown in low raffinose medium. In the cumulative plot, I have indicated the abundances of *PIC2*, the reference genes used in the RT-qPCR analyses (*ALG9*, *PGK1*, *ACT1* and *TEF1*), and *RPL20A* as its 5' UTR was used

to generate the synthetic constructs shown in B. **B**. Diagrammatic overview of the Nab3 and Nrd1 RNA binding sites embedded in each of the *pGAL1-GFP* synthetic reporter constructs. **C**. Relative mRNA abundance of *PIC2* and *GFP* in the *PIC2-GFP* and BSWT strains grown in 1% (w/v) sucrose and 1% (w/v) galactose medium.

On the one hand, the 5'UTR of BS1 incorporated the reported supermotif found to be sufficient to enable NNS-dependent termination in CUTs (Porrua et al., 2012). This sequence encompassed one Nrd1 binding site and two Nab3 RNA-BSs followed by an AT-rich motif that is also known to contribute to optimal transcriptional termination (Porrua et al., 2012) (Figure III.16B). On the other hand, BS2 comprised the same combination of recognition sites as BS1 but, unlike in the latter, RNA-BSs were separated by spacer regions native to the 5'UTR in *RPL20A* (Figure III.16B). Conversely, BS3 encoded a version of the supermotif construct in which the Nab3 and Nrd1 cognate sequences upstream the AT-rich element had been transposed (Figure III.16B). Importantly, the Libri group had already established that swapping the first Nab3 and Nrd1 motif in the supermotif, as in BS3, or substituting the spacer regions of the supermotif with native sequences, like in BS2, diminished NNS attenuation (Porrua et al., 2012). Hence, I expected the termination efficiency of the original BS1 construct to be larger than that of BS2 or BS3.

The reporter system assembled in BS4 and BS5 was expected to yield even lower GFP levels than BS1. The reason for this expectation is that BS4 consisted of two complete supermotif sequences, and BS5 contained four binding sites for Nab3 and three Nrd1 RNA-BSs (Figure III.16B). In this latter case, out of the seven NNS recognition sequences, three Nab3 recognition sites and one Nrd1 cognate motif were adjacent to AT-rich regions facilitating termination.

RT-qPCR analyses performed by Mags Gwynne on RNA extracts from the BS reporter strains revealed that *GFP* transcription was reduced in all variants encoding supermotif sequences or derivatives thereof. This finding was consistent with a broader role of transcriptional attenuation of the NNS complex even in highly expressed mRNAs (Figure III.17). Furthermore, the extent to which transcriptional repression occurred was greatest when several copies of the supermotif were introduced (i.e., BS4 and BS5), and lowest when the canonical termination sites encoded in BS1 underwent sequential or positional perturbations (i.e., BS2 and BS3) (Figure III.17).

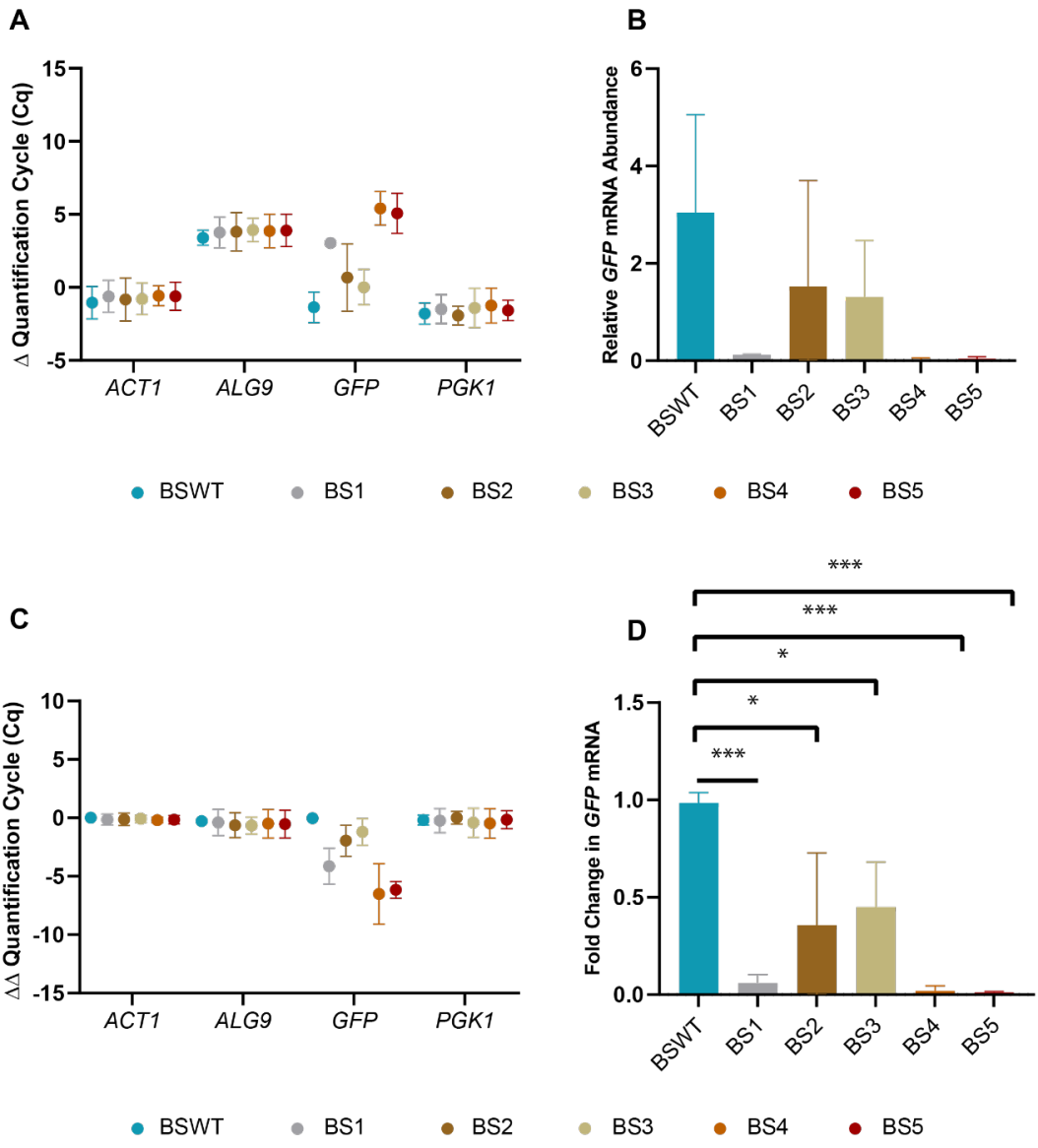

Figure III.17. RT-qPCR quantification of GFP mRNA in the synthetic reporter strains when grown in SC -Ura medium containing 1% (w/v) galactose and 1% (w/v) sucrose. **A**. Normalisation of raw quantification cycle (Cq) values to the median Cq of the reference genes within their own sample. **B**. Calculated ΔCqs for *PIC2* were used to derive a relative *PIC2* mRNA abundance within each condition. **C**. Median ΔCq values of each tested gene were normalised to those of the parental strain (i.e., BSWT) to determine the differential ΔCq (ΔΔCq) values. **D**. These ΔΔCqs were exponentially transformed to find the fold change in mRNA abundance with respect to the reference sample. Data shows the mean of three biological repeats for each condition. Error bars represent standard deviation (SD). Statistical comparison of the fold change in *PIC2* mRNA of both mutants with respect to the parental *PIC2-GFP* reference was performed by unpaired t-tests: *: p<0.05, ***: p<0.001 and 'ns': p>0.05. This experiment was conducted by Mags Gwynne and was presented in their dissertation.

III.7. Addition of NNS RNA-binding sites to a synthetic reporter system decreases GFP protein abundance and noise.

Thus far, my results demonstrated that NNS can prematurely terminate protein-coding genes with very different expression levels. Primed by this finding, I sought to investigate GFP expression in BSWT, BS1 and BS3 using microfluidics and time-lapse microscopy with the aim of ascertaining whether NNS-mediated repression and noise suppression was also active on these synthetic targets. As shown in Figure III.18A, the GFP fluorescence concentration exhibited an identical trend to that revealed by RNA quantification.

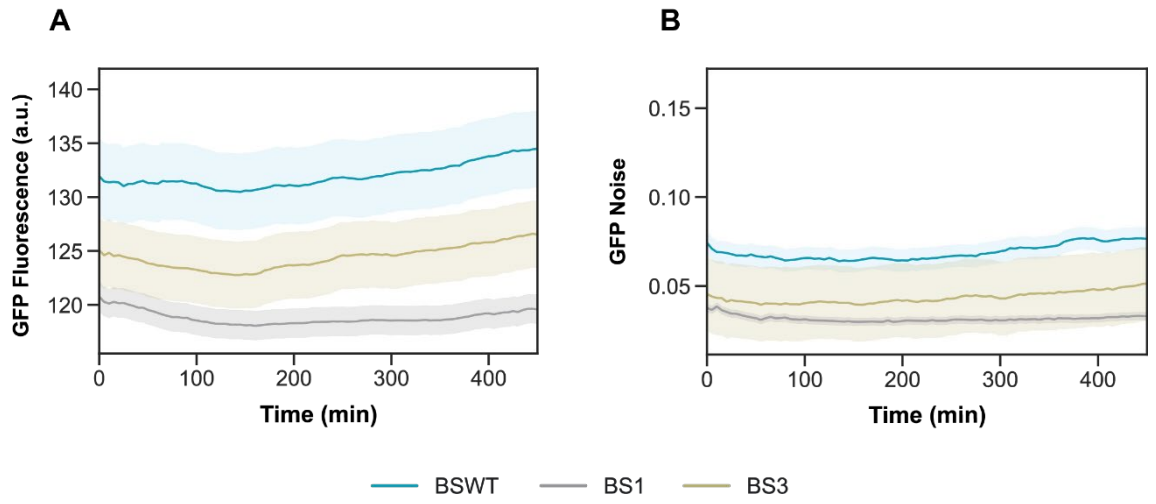

Figure III.18. Time-resolved mean fluorescence concentration of Pic2-GFP (**A**) and its coefficient of variation (**B**) for the BSWT, BS1 and BS3 reporter strains. At least 500 cells were analysed for each strain and condition. In the Y axis of A, 'a.u.' stands for arbitrary units.

Hence, the first conclusion of my microfluidics experiments was that enhanced *GFP* mRNA levels were accompanied by comparable GFP protein increases. This agreed with previous observations by Mags Gwynne, who directly compared the GFP protein levels of the six strains comprising the synthetic reporter library by performing microplate reader fluorescence assays (Figure III.19). In these experiments, raw fluorescence values were recorded for technical triplicates of each of the reporter strains throughout the duration of the experiment. After being corrected for background fluorescence by excluding the fluorescent signal of their non-fluorescent wild-type

BY4741 reference strain, fluorescence values were normalised to that of the parental BSWT from which the reporter systems were derived. Upon normalisation, graphical comparison of GFP fluorescence fully resembled the pattern of the RT-qPCR transcriptional quantification and my microfluidics experiment: insertion of a supermotif drastically reduced the protein abundance with respect to the unregulated BSWT system. In contrast, while translational levels of GFP were slightly higher in systems with poorer NNS termination efficiency, such as BS2 and BS3, GFP abundance was almost completely suppressed upon incorporation of one or more supermotifs (i.e., BS1, BS4 and BS5).

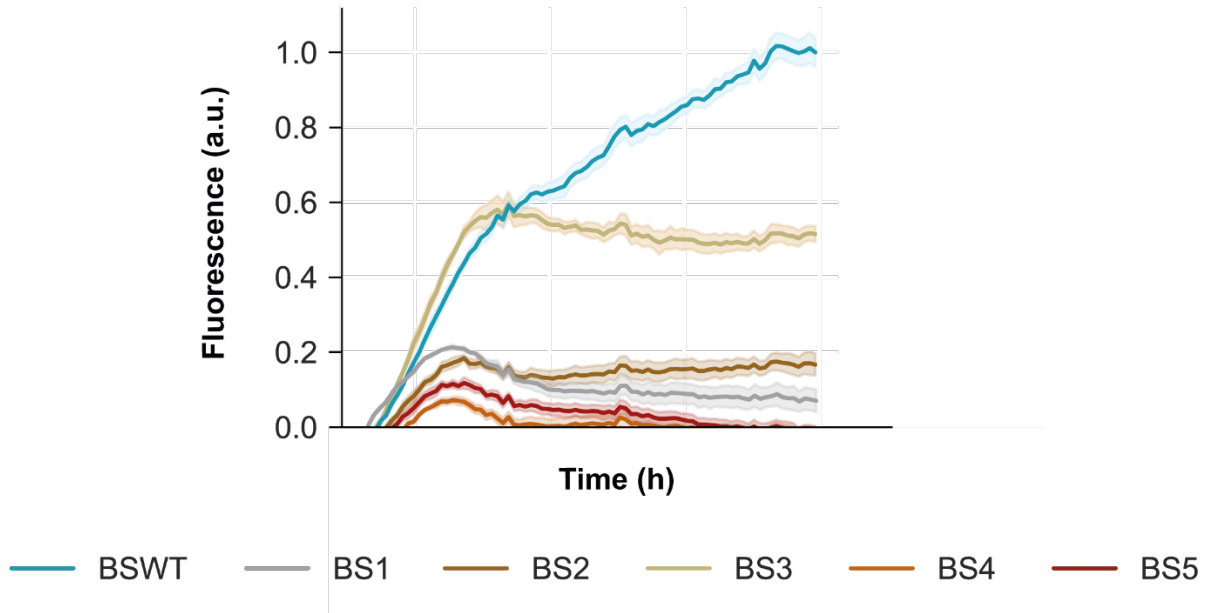

Figure III.19. Microplate reader recordings of GFP expression (in arbitrary units) in reporter strains across time. Fluorescence values were normalised to those of the parental BSWT strain. Cells were grown in SC medium containing 1% (w/v) sucrose and 1% (w/v) galactose. This experiment was conducted by Mags Gwynne and was presented in their dissertation.

As described in III.5, I employed the previously developed BABY cell segmentation algorithm and the ALIBY image processing package software (Muñoz González et al., 2024; Pietsch et al., 2023), to calculate the coefficient of variation of GFP fluorescence concentration in the microfluidics experiments which I ran on BSWT, BS1 and BS3 (Figure III.18B). BS2, BS4 and BS5 were excluded from these experiments because the microfluidics devices available at that time possessed only three chambers, thereby constraining my evaluations to three strains per experiment. In line with my predictions, the canonical set of recognition sites in BS1 essentially

halved the stochasticity detected in the GFP levels of the parental strain (i.e., BSWT). On the other hand, BS3 presented intermediate noise levels (Figure III.18B). In summary, these experiments prove that the NNS complex can act as a transcriptional repressor and noise suppressor of protein-coding genes if provided with at least one canonical termination region.

III.8. Discussion

In this chapter, I have shown that the NNS complex can suppress the expression and transcriptional noise of its protein-coding target *PIC2*. This finding is consistent with previously defined roles of mRNA attenuation by the NNS complex (Arigo et al., 2006; Creamer et al., 2011; Kim and Levin, 2011; Kuehner and Brow, 2008; Schulz et al., 2013; Steinmetz et al., 2006; Thiebaut et al., 2008; Webb et al., 2014). Although NNS-driven premature termination of protein-coding transcripts had been shown to be responsive to nucleotide availability (Ajazi et al., 2022; Kuehner and Brow, 2008; Thiebaut et al., 2008), characterisation of NNS-mediated attenuation of *PIC2* was shown to be sensitive to sugar concentration. This was showcased by the fact that impairing NNS repression of *PIC2* yielded larger expression increases in low raffinose medium.

My findings in low (i.e., 1 % (w/v)) raffinose medium alongside the fact that Nab3 was previously shown to undergo a genome-wide redistribution during glucose starvation (Bresson et al., 2017; van Nues et al., 2017), nourished a model in which the NNS complex is destined to preserve the optimal expression level of protein-coding targets in adverse environments, thereby becoming particularly consequential during nutrient deprivation. To test whether such regulation implied minimising noise in the expression of protein-coding targets to achieve an optimal abundance of the encoded protein during adaptation, I applied in-house and previously established methodologies to quantify the cell-to-cell variability in the expression of the *PIC2* model target (i.e., its noise) (Bar-Even et al., 2006; Crane et al., 2014; Newman et al., 2006). Having confirmed that the NNS complex acts as a noise inhibitor for *PIC2*, I went on to check whether this novel regulatory role of the NNS complex was applicable to other mRNA targets that, as described in previous work from the Granneman group, became

concomitantly targeted for transcription initiation and premature termination during glucose depletion (van Nues et al., 2017).

Nevertheless, within the timeframe of my PhD, it was practically inviable to individually characterise the dozens of stress-responsive protein-coding RNAs which Rob van Nues and colleagues had identified as NNS targets. Doing so, would have entailed fusing a GFP epitope to each of these genes and repeating the mRNA and protein abundance quantification that I have shown for *PIC2* throughout this chapter. Therefore, I sought to generalise the noise-suppressing role which I had characterised in *PIC2* using a library of synthetic reporter strains. Given that the expression of the employed GFP reporter system is driven by the strong and inducible *pGAL1* reporter in the presence of 1% (w/v) galactose and 1% (w/v) sucrose, I concluded that the unveiled NNS-directed repression and noise tuning role is (i) applicable to highly abundant mRNA species and (ii) not limited to stressful environments. These findings illustrate that, if provided with the motifs to which it binds in canonical targets such as CUTs (Porrua et al., 2012), the NNS complex is capable of lowering the expression and noise of protein-coding targets. Thus, my findings strongly suggest that such regulatory mode is not confined to *PIC2* or targets with similar expression profiles, but it is likely to be widespread in the transcriptome.

Despite having identified a novel regulatory role of the NNS complex. The data contained in this chapter provides no evidence for its physiological role. In other words, while this set of experiments characterised NNS regulation in a stress-specific mRNA target and generalise it to other mRNAs with different expression patterns, this set of results does not delve into the biological implications of this findings. I expected that, if *Saccharomyces cerevisiae* had developed this co-transcriptional regulatory system for stress-specific targets such as *PIC2*, the role of this regulatory mechanism was likely to be of considerable importance during adaptation. Accordingly, I next aimed to study whether compromising the tight regulation which NNS exerts on *PIC2* would result in any cellular defect and, ultimately, in reduced fitness.

IV. Abrogating Nab3 Binding to *PIC2* Decreases Fitness, Enlarges Cell Size and Prolongs Cell Cycle

IV.1. Introduction

In this chapter, I will introduce the phenotypic consequences of dismantling NNS regulation in *PIC2*. As I had illustrated that NNS repression of *PIC2* mRNA abundance was greater during nutrient deprivation, I expected that preventing NNS assembly onto *PIC2* mRNAs would not only affect the downstream expression of the gene but also have significant consequences for cellular survival amid sugar scarcity. To test this, I quantified the growth rates of the mutants and *PIC2-GFP* in different media.

However, before presenting those data, I will start by introducing a prominent and unexpected phenotype which I noticed in the same ∆ Nab3 RNA-BSs mutant. While preparing the microfluidics experiments that were presented in III.4, it became clear that said mutant was visibly larger than *PIC2-GFP* or its ∆ NNS RNA-BSs counterpart. Intriguingly, previous research had described that oversized cells experience cytoplasmic dilution and, in turn, become stressed and delayed throughout their cell cycle phases (Neurohr et al., 2019). Thus, such a striking effect in cell volume prompted me to assess the cell cycle transition and intracellular stress status of these strains.

In addition to these experiments, I examined the mitochondrial activity of the mutants and their parental strain. Given that *PIC2* is a phosphate:proton symporter and a copper uniporter in the inner mitochondrial membrane, I expected that even mild changes in its expression would likely alter the maintenance of mitochondrial functions. Mitochondrial activity is tightly linked to the balance of charges and protons in either side of the inner mitochondrial membrane. The electric gradient is referred to as the mitochondrial membrane potential, which is an optically measurable feature kept at healthy levels during physiological activity of the electron transport chain.

The results presented in this chapter show that the ∆ Nab3 RNA-BSs mutant exhibited defective growth, larger cell size, delayed cell cycle, mitochondrial hyperpolarisation and higher levels of intracellular stress. In contrast, the ∆ NNS RNA-BSs strain always displayed a much milder version, if any, of the defects studied. On this basis, in the last two sections, I demonstrate that the observed anomalies are genetically linked to impaired Nab3 regulation of *PIC2* specifically.

IV.2. Cells with partial NNS binding to *PIC2* are aberrantly larger.

Throughout the microfluidics experiments described in III.4 and III.5, it became apparent that mutant cells encoding a *PIC2* allele lacking Nab3 binding sites (i.e., the ∆ Nab3 RNA-BSs ones) were clearly larger than their parental counterparts (Figure IV.1A). Upon closer inspection of all strains in a confocal microscope (Figure IV.1B), I confirmed that indeed ∆ Nab3 RNA-BSs was visibly larger than its *PIC2-GFP* reference. To quantify this, I used the ALIBY pipeline to compute the area of each of the cells imaged during my microfluidics experiments and, subsequently, estimate their volume throughout time (Muñoz González et al., 2024). Indeed, the average volume for the ∆ Nab3 RNA-BSs population was approximately twice that of the parental *PIC2-GFP* (Figure IV.1C).

Since Pic2 has never been reported to be functionally involved in cell size control, I applied flow cytometry as a complementary method that would allow me to substantiate my findings by measuring cell size across larger populations. In this method, a laser emitting visible light is shone at single cells, and the light waves are, thus, slightly modified. When recorded in the same direction in which the light was originally radiated, the deflection recorded is proportional to the size of the cell through which the light has just traversed. This phenomenon is referred to as forward scatter or FSC, and its values were monitored for three independent populations of each strain grown in raffinose-rich or raffinose-deprived growth media. Subsequently, the average of the three population medians for each strain and condition was normalised to that obtained for the *PIC2-GFP* reference grown in a high raffinose medium. As shown in Figure IV.2, the cell size of the ∆ Nab3 RNA-BSs mutant increased by approximately 50%.

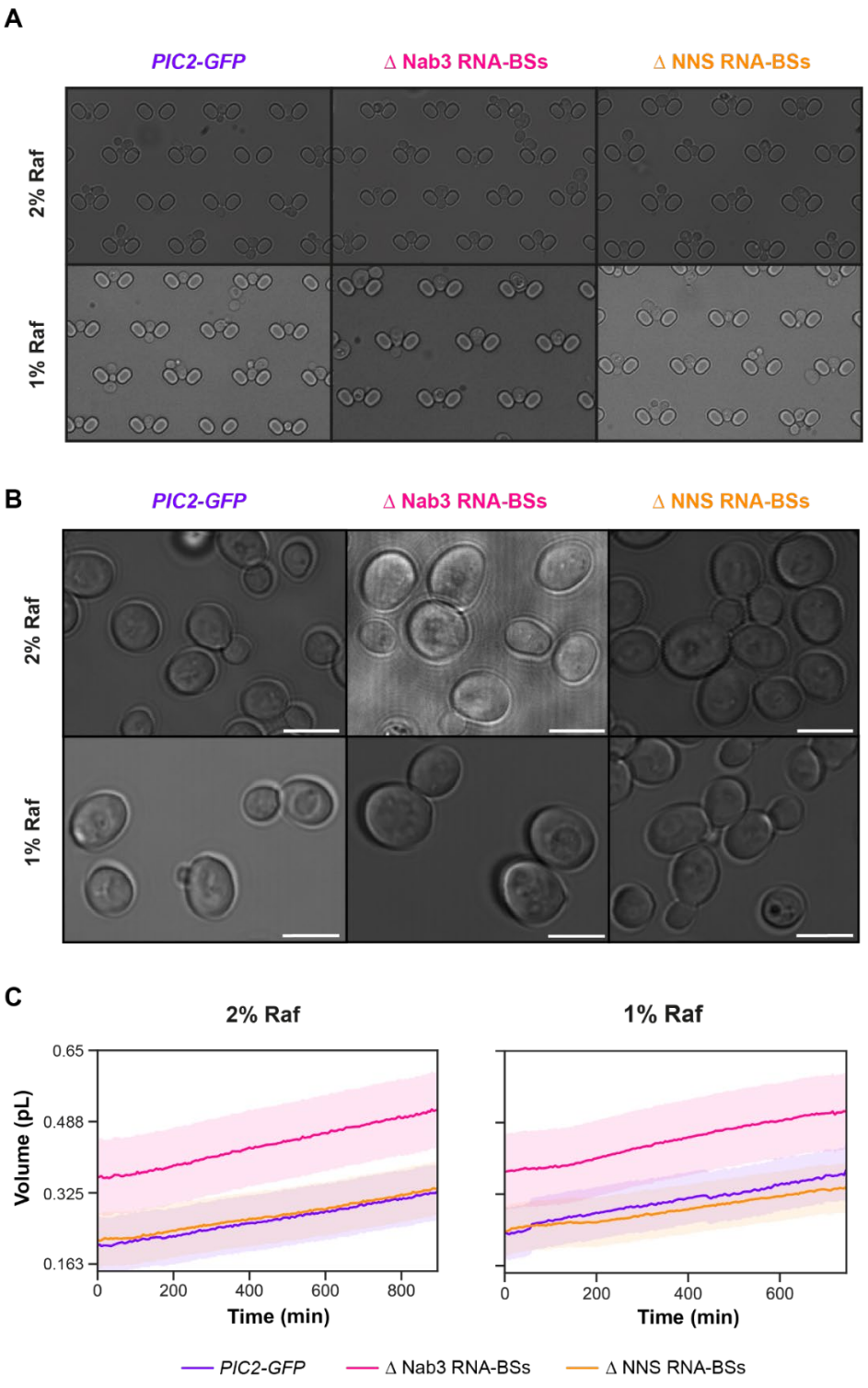

Figure IV.1. Δ Nab3 RNA-BSs cells are larger than their parental counterparts. **A**. Inverted microscopy images of *PIC2-GFP*, Δ Nab3 RNA-BSs and Δ NNS RNA-BSs cells in high (i.e., 2%(w/v)) or low (i.e., 1% (w/v)) raffinose medium whilst in the ALCATRAS devices. **B**. Confocal microscopy images of *PIC2-GFP*, Δ Nab3 RNA-BSs and Δ NNS RNA-BSs cells grown in raffinose-rich (i.e., 2%(w/v)) or raffinose-limiting (i.e., 1%(w/v)) medium. Scale bar indicates 5 µm. **C**. Time-resolved average volume estimations based on the microfluidics experiments shown in Figures III.9 and III.10.

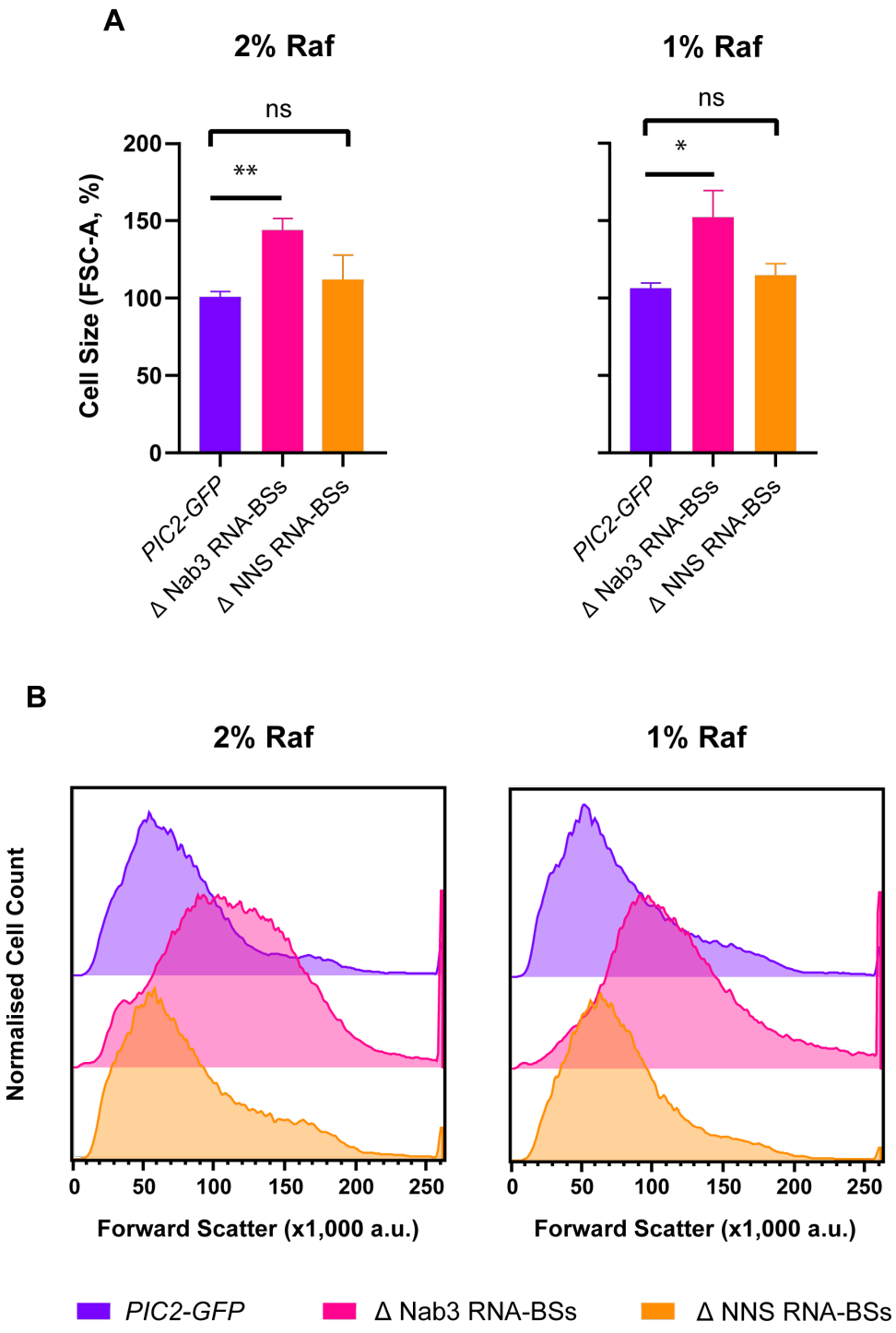

Figure IV.2. Flow cytometry confirms that the cell size of the Δ Nab3 RNA-BSs cells is greater than that of their parental counterparts. **A**. Weighted means of the median FSC values for three independent biological repeats were calculated for each strain and normalised to the parental *PIC2-GFP*. Error bars represent standard deviation. Statistical comparisons between each mutant and the *PIC2-GFP* reference were performed by an unpaired t-test. *: $p<0.05$ and 'ns': $p>0.05$. **B**. Representative traces of the cell size distribution of *PIC2-GFP* and derived mutants from flow cytometry analyses. The sizes were compared using their forward light scatter (FSC) values.

IV.3. Cells with partial NNS binding to *PIC2* undergo longer cell cycles and present larger polyploid populations.

Earlier work had established that cell cycle progression is delayed in oversized cells (Neurohr et al., 2019). Consequently, having established that the ∆ Nab3 RNA-BSs mutant displayed a reduced cell growth rate and an anomalously large cell size, I went on to assess whether these observations could stem from impaired cell cycle progression. To pursue this, I determined the cell cycle stage of the cells in three separate populations of both mutants and their parental reference. These experiments relied on DNA content quantification, which was enabled by propidium iodide (PI), a red fluorescent stain which intercalates between nitrogenous bases. Being impermeable to cell membranes and able to bind RNA as well as DNA, PI must be supplied to fixed permeabilised cells which had previously undergone an RNase treatment (detailed in II.17).

Cell cycle analyses evidenced that the fraction of ∆ Nab3 RNA-BSs mutants undergoing G1 phase was lower than that of the *PIC2-GFP* populations (Figure IV.3). Unlike the latter, mutants without Nab3 cognate sequences in *PIC2* were predominantly in S or G2/M phases, implying that they spent more time in these states and, hence, their cell cycle progression is delayed. Moreover, there were more polyploids among the cells lacking Nab3 RNA-BSs in *PIC2*, suggesting that they suffer mitotic defects more frequently than their parental counterparts. Furthermore, in line with my RT-qPCR measurements and cell size observations, no prolongation of the cell cycle was detected in the strain lacking NNS binding sites in *PIC2* (i.e., ∆ NNS RNA-BSs) (Figures III.4-5 and IV.3). Hence, specifically disrupting Nab3 binding to *PIC2* increases the expression of the gene and causes cell size anomalies and modest delays in cell cycle progression.

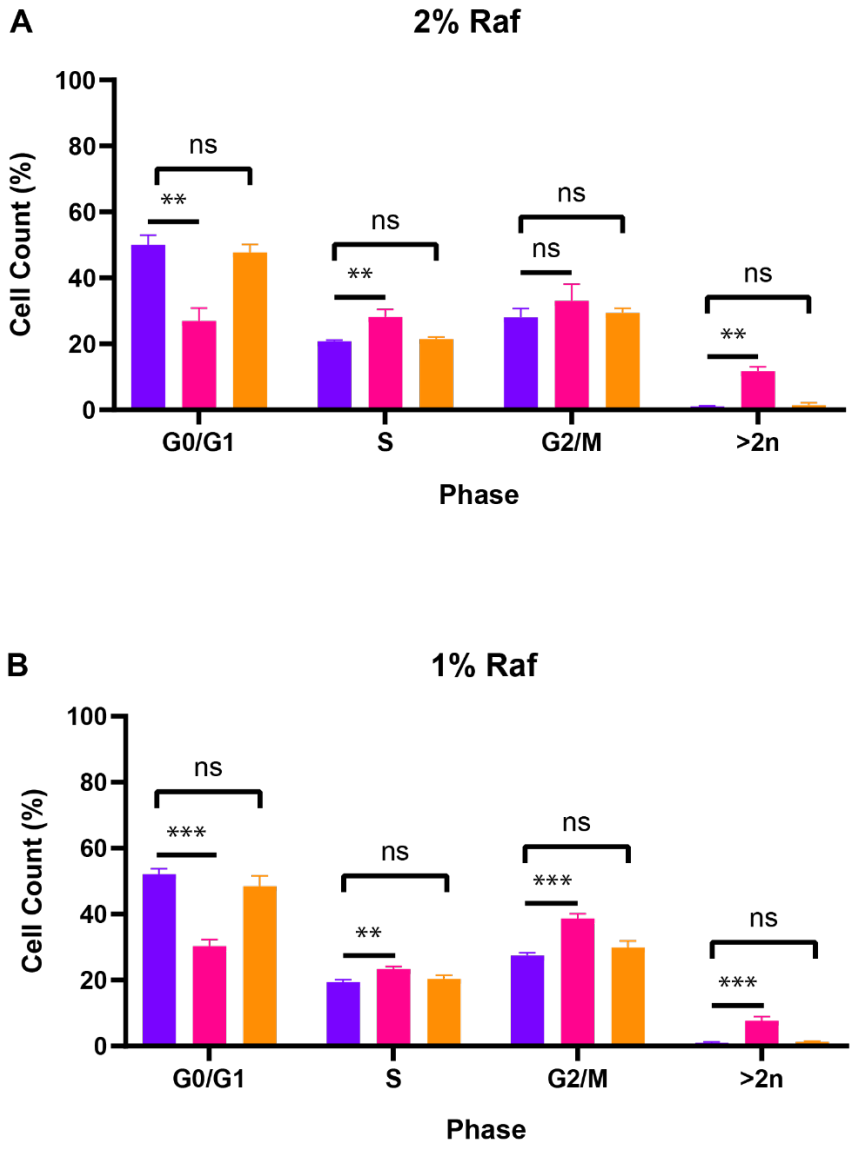

Figure IV.3. Weighted means of the population fraction of *PIC2-GFP*, Δ Nab3 RNA-BSs and Δ NNS RNA-BSs within each cell cycle phase. Values based on biological triplicates and error bars represent the standard deviation derived after considering the three repeats per strain and condition. Statistical comparisons were performed by unpaired t-tests. *: $p<0.05$, **: $p<0.01$, ***: $p<0.001$ and 'ns': $p>0.05$. While **A** shows the results obtained for cultures with medium supplemented with 2% (w/v) raffinose, **B** displays the data gathered from cells grown in the presence of 1% (w/v) raffinose.

IV.4. Preventing Nab3 binding to *PIC2* causes defects in cell growth and reduces fitness.

The abnormally large cell sizes and cell cycle delays identified in the ∆ Nab3 RNA-BSs mutant suggested that this strain may also be facing problems during cell division. To explore this possibility, I re-examined my microfluidics data to count the budding events or 'births' for every imaged cell. However, after visualising a scatter plot showing cellular volume against fluorescence and faceting it based on the number of births, I observed that there were not any significant cell division defects among larger cells (Figure IV.4A). Conversely, the budding events that each mother cell underwent did appear to be mildly negatively correlated with Pic2-GFP concentration (Figure IV.4B). In other words, cells with greater Pic2-GFP expression divided less often. These results were compatible with my cell cycle observations as elongated G2/M phases in ∆ Nab3 RNA-BSs could be a cause or a consequence of impaired cell division.

To fully evaluate the phenotypic consequences of blocking Nrd1 and Nab3 binding to *PIC2*, I assessed the growth rates of the mutants and the strain from which they were derived. With this aim, I monitored the progression of a freshly inoculated 200 µL-culture of each strain in medium containing high (i.e., 2% (w/v)) or low (i.e., 1% (w/v)) raffinose concentrations (Figure IV.4C). Given that optical density (OD_{600}) readings can be taken as measurements of microbial concentration in low density cultures, a time-resolved OD_{600} monitoring of cultures inoculated at a starting OD_{600} of 0.01 could be used to reveal the growth profiles of *PIC2-GFP* and its derived mutants (see II.9 for technical details) (Figure IV.4C). Strikingly, I discovered that deleting Nab3 binding sites in *PIC2* reduced the maximal growth rate of ∆ Nab3 RNA-BSs by a third of the one determined for its parental counterpart (Figure IV.4C). The growth defect displayed approximately the same magnitude in both tested raffinose concentrations, suggesting that it was independent of the sugar available in the growth medium (Figure IV.4C).

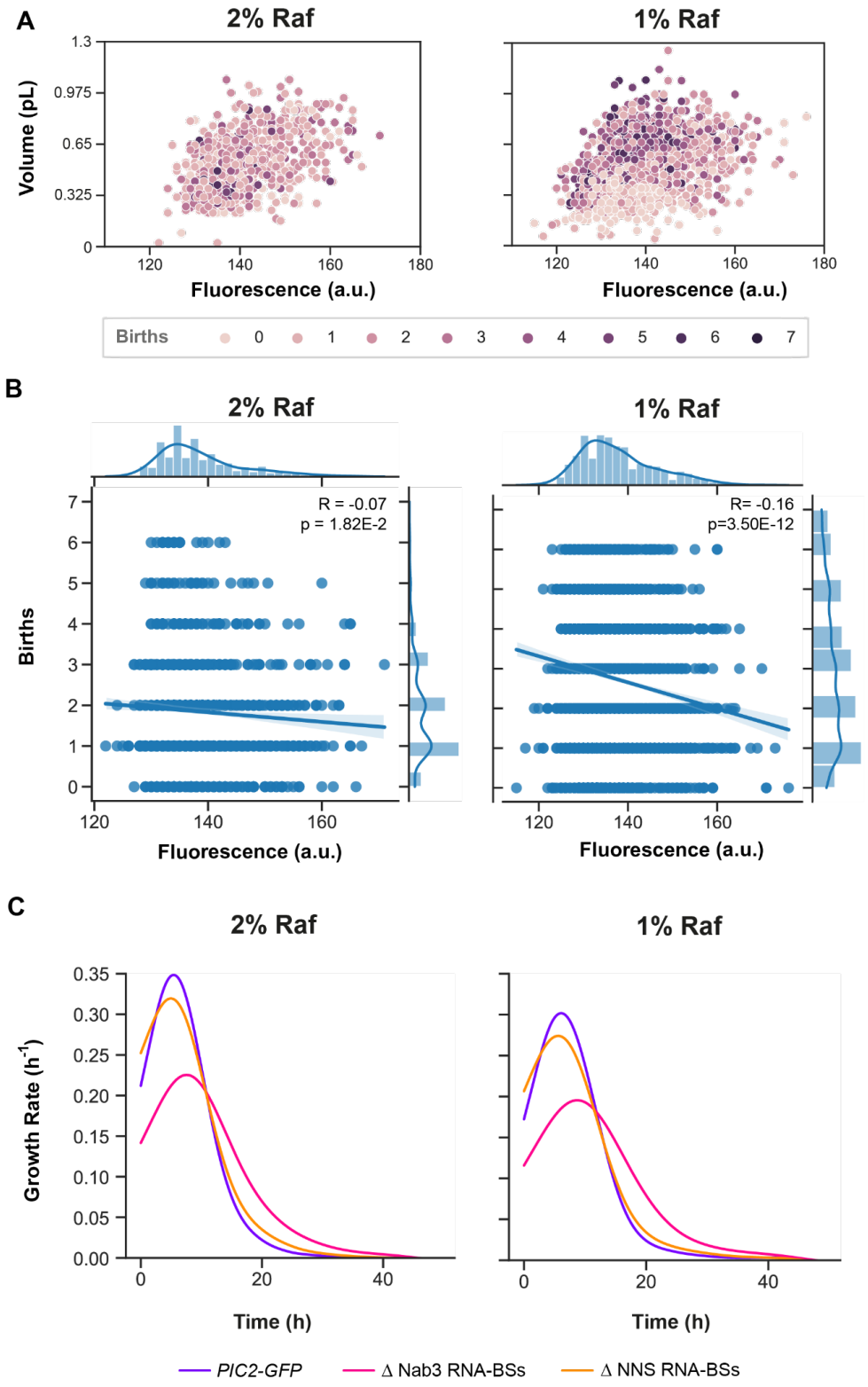

Figure IV.4. The Δ Nab3 RNA-BSs mutant displays a growth defect. **A**. Dot plot showing the estimated volume of all tracked cells regardless of the strain to which they belonged against their recorded Pic2-GFP fluorescence concentration measurement in arbitrary units. Each dot represents an individual cell and was coloured based on the number of cell divisions which it underwent throughout the duration of the experiment (i.e., around 15 hours). Results did not suggest any clear pattern between

cell volume and the number of budding events or births. **B**. Joint distribution plot showcasing the correlation of the number of births per cell with its Pic2-GFP fluorescence signal. The distributions on the X and Y axes indicate the variability across Pic2-fluorescence and the number of budding events within all examined cells. Calculated Pearson correlation coefficients and associated p-values are shown in the upper right corner of the graph. **C**. Time-resolved growth rates of the *PIC2-GFP*, ∆ Nab3 RNA-BSs and ∆ NNS RNA-BSs strains. Lines show the mean of three technical replicates.

Naturally, I expected that a 30% reduction in the maximal growth rate of the ∆ Nab3 RNA-BSs would render the strain less fit than its parental counterpart. To test this, I performed a series of fitness assays. In these experiments, the *PIC2-GFP* parental strain and both mutants competed separately against a fluorescent reference strain in which mCherry had been terminally fused to *URA8*. After inoculating the cells at the exact same OD_{600}, cultures were screened periodically every 18 hours for evolving non-fluorescent:fluorescent ratios. These ratios were calculated by determining the portion of the population that emitted a red fluorescence. The threshold or gate discriminating between fluorescent and non-fluorescent populations was derived from previous acquisitions of cultures containing the fluorescent (i.e., Ura8-mCherry) and non-red fluorescent (*PIC2-GFP*) populations only. Given that each competition was performed in three separate cultures, I extracted the average non-fluorescent:fluorescent ratio and associated standard deviation for each set of triplicates. After normalising the mean ratio to that of the parental *PIC2-GFP*, I could compare the relative fitness of each mutant to that of the strain from which they were derived.

As expected, my results demonstrated that the fitness of ∆ Nab3 RNA-BSs was already substantially diminished in the first time point regardless of the concentration of raffinose in the growth medium: in both tested media, the mutant was outcompeted by the fluorescent reference. While the mentioned fitness cost became statistically significant 36 hours post-inoculation in raffinose-rich medium, the fitness decrease was not statistically significant until the third time point of the assays (i.e., 60 hours after inoculation) performed in raffinose-deprived medium (Figure IV.5). This slight disagreement between conditions, nevertheless, is most likely due to the larger error accompanying the mean non-fluorescent:fluorescent ratio for the *PIC2-GFP* reference

at the second time point of the assay performed in medium containing 1% (w/v) raffinose (Figure IV.5A-B). In contrast to Δ Nab3 RNA-BSs, the Δ NNS RNA-BSs mutant only displayed a mild decrease in fitness after 60 hours of competition in low raffinose medium (Figure IV.5B). Therefore, the fitness differences detected in both mutants were in line with my earlier phenotypic characterisation and *PIC2* expression assessments: effects were, if any, much milder in the Δ NNS RNA-BSs strain.

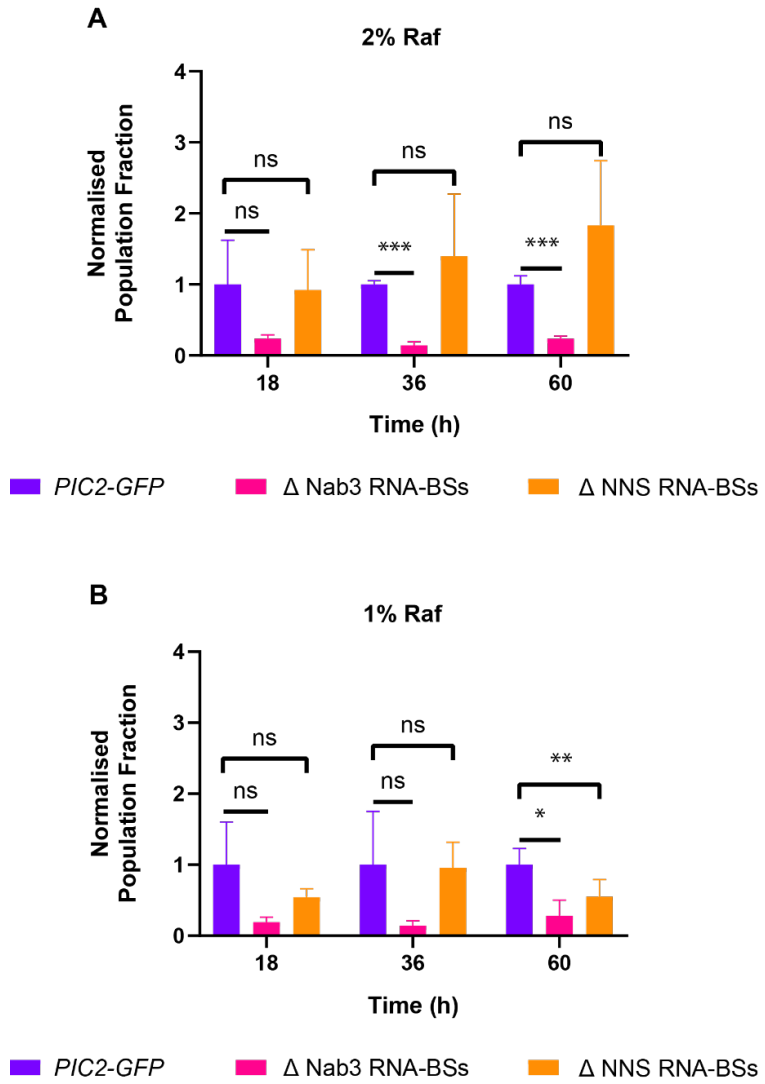

Figure IV.5. Competition assays comparing the fitness of *PIC2-GFP* with that of Δ Nab3 RNA-BSs and Δ NNS RNA-BSs. Bar plots display the log_2-transformed fold changes of the population fraction of tested strains (i.e., WT, *TEF1-PIC2*, and *pic2Δ*) against a fluorescent reference. Values shown are averages and standard deviations from biological triplicates normalised to the fold changes observed in the parental strain.

IV.5. Cells with partial NNS binding to *PIC2* display mitochondrial membrane hyperpolarisation.

Having established that enhanced *PIC2* mRNA levels and altered cell size and cell cycle were a direct consequence of preventing Nab3 binding to *PIC2*, I sought to identify a connection between these phenotypes and the cellular role of Pic2. My search began with processes directly related to the function of my model gene, which, as outlined, encoded a mitochondrial copper uniporter and phosphate symporter of the inner mitochondrial membrane (IMM). To widely inspect mitochondrial function, I looked at mitochondrial membrane potential ($\Delta\psi_m$), which is the dominant force driving ATP production and, thus, a widely used proxy for energy homeostasis (Duchen, 2004). At first, I assessed mitochondrial membrane potential in large cellular populations using MitoTracker™ Red CMXRos, a red fluorescent dye that passively diffuses throughout the plasma membrane and, once inside the cell, accumulates in active mitochondria proportionally to their membrane potential.

For this purpose, I stained mid-exponential cultures 30 minutes before inspecting them using flow cytometry. Median red fluorescence values for each of the three populations examined per strain and condition were normalised to the forward scatter medians of the same sample (Figure IV.6). This correction was performed to compensate for the fact that mitochondrial networks are known to scale with cell volume and (Miettinen and Björklund, 2016), so, the MitoTracker™ Red CMXRos staining was expected to be inherently greater in the larger ∆ Nab3 RNA-BSs mutant. Still, despite the normalisation, ∆ Nab3 RNA-BSs exhibited larger normalised red fluorescence values, which indicated that the mitochondrial membranes of this mutant were hyperpolarised with respect to those of the *PIC2-GFP* reference (Figure IV.6). Conversely, the mitochondrial membrane potential of ∆ NNS RNA-BSs cells was not significantly increased with respect to that of the parental strain (Figure IV.6).

Although this evidence supported my original predictions, this initial strategy for mitochondrial membrane potential evaluation presented various caveats. Firstly, flow cytometry did not provide information on the dye subcellular localisation and, so, it was not possible to identify or correct for background cytoplasmic staining which may modify the detected signal. Secondly, albeit certainly responsive to mitochondrial membrane potential, MitoTracker™ Red CMXRos was also reported to be less

sensitive than other dyes in detecting photoinduced potential flickering in human skin fibroblasts (Desai et al., 2024). Indeed, MitoTracker dyes are known to possess a reactive chloromethyl moiety which covalently binds to the thiol groups of the peptides in the mitochondria. Consequently, MitoTracker stains remain trapped within mitochondria some time after the potential has changed (Kholmukhamedov et al., 2013).

To overcome these limitations and consolidate my findings, I repeated the mitochondrial membrane potential measurements by staining cells with tetramethyl rhodamine ethyl ester (TMRM). Like MitoTracker™ Red CMXRos, TMRM is a red-fluorescent cationic fluorophore which is electrophoretically sequestered into the mitochondrial matrix of functional mitochondria proportionally to their membrane potential. Since these interactions are essentially charge-based, a loss or increase in mitochondrial membrane potential will immediately result in the release or further build-up of TMRM. Furthermore, to ensure that individual TMRM signals could be (i) corrected for background fluorescence and (ii) normalised to cell volume, I applied live confocal microscopy to image previously TMRM-stained cells.

Mid-exponential cultures were equilibrated with TMRM 30 minutes before being harvested for the experiment. Afterwards, cells were imaged in fresh medium (Figures IV.7-8). To achieve temporary immobilisation of the inspected yeast cells, imaging was performed on wells which had been coated with poly-L-lysine, a synthetic adherent, prior to the start of the experiment. Furthermore, to ensure that no background red fluorescence was inherently present in my samples, I imaged unstained cells (Figures IV.7-8). As an additional control, I also confirmed that TMRM was exclusively retained by functional mitochondria (Figures IV.7-8). To test this, I re-imaged each strain after chemically collapsing the mitochondrial membrane potential of the cells in the sample (Figures IV.7-8). Mitochondrial membrane potential dissipation was achieved upon addition of carbonyl cyanide-p-trifluoromethoxyphenylhydrazone (FCCP), a powerful uncoupler of oxidative phosphorylation, which permeabilises the inner mitochondrial membrane to allow the free transit of protons between the mitochondrial matrix and the intermembrane space.

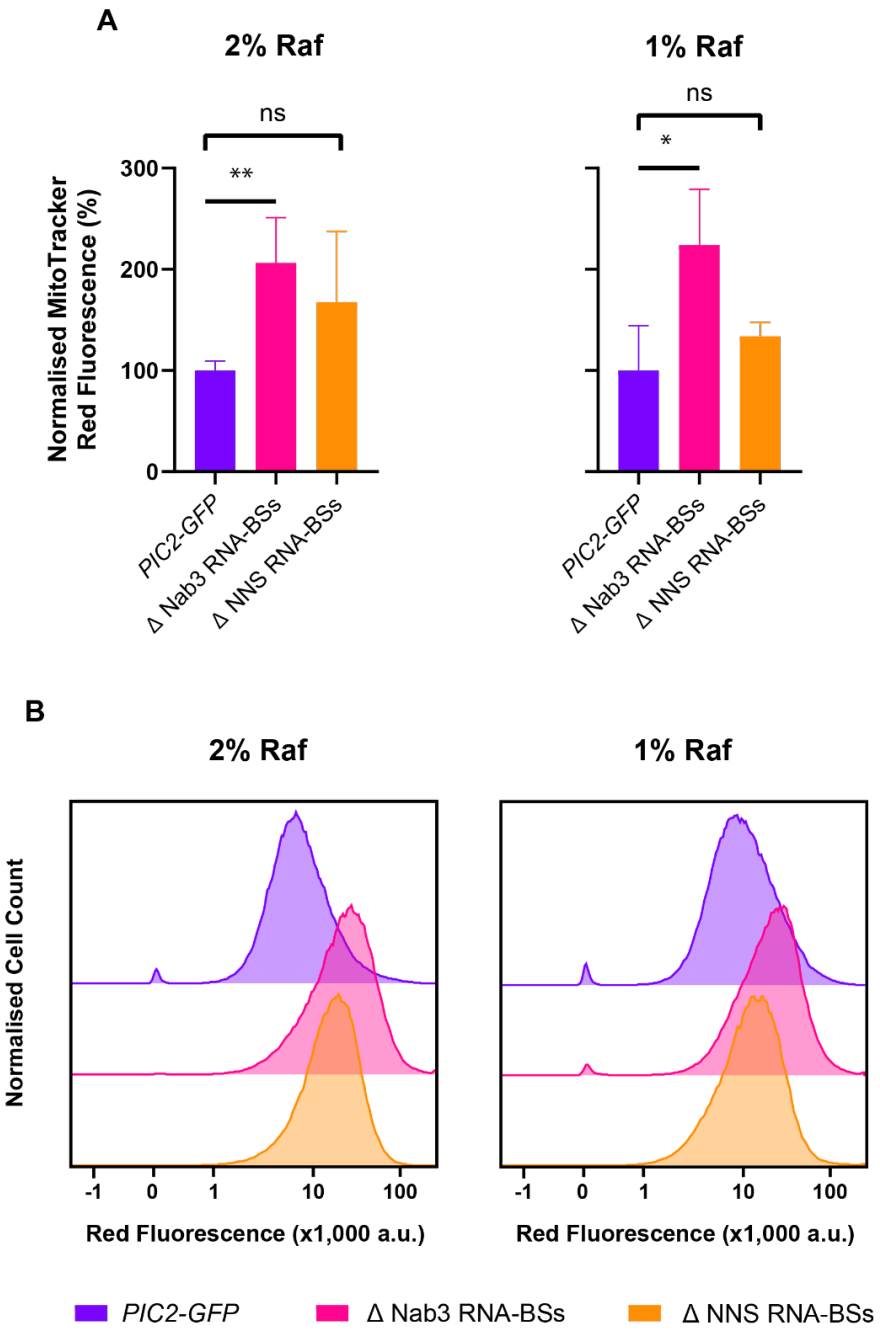

Figure IV.6. Mitochondrial membrane potential measurements of MitoTracker™ Red CMXRos by flow cytometry uncovered mitochondrial hyperpolarisation in the Δ Nab3 RNA-BSs mutant. **A**. Medians for single-cell red fluorescence emissions were normalised to the corresponding median forward scattering value. The bar graph shows the weighted average and standard deviation of the mentioned ratio across three biological batches containing more than 50,000 cells. Statistical comparisons between each mutant and the *PIC2-GFP* reference were performed by an unpaired t-test. *: $p<0.05$, **: $p<0.01$ and 'ns': $p>0.05$. **B**. Representative flow cytometry traces of the MitoTracker™ Red CMXRos staining distribution of *PIC2-GFP,* Δ Nab3 RNA-BSs Δ NNS RNA-BSs strains at mid log phase (OD_{600} ~0.5).

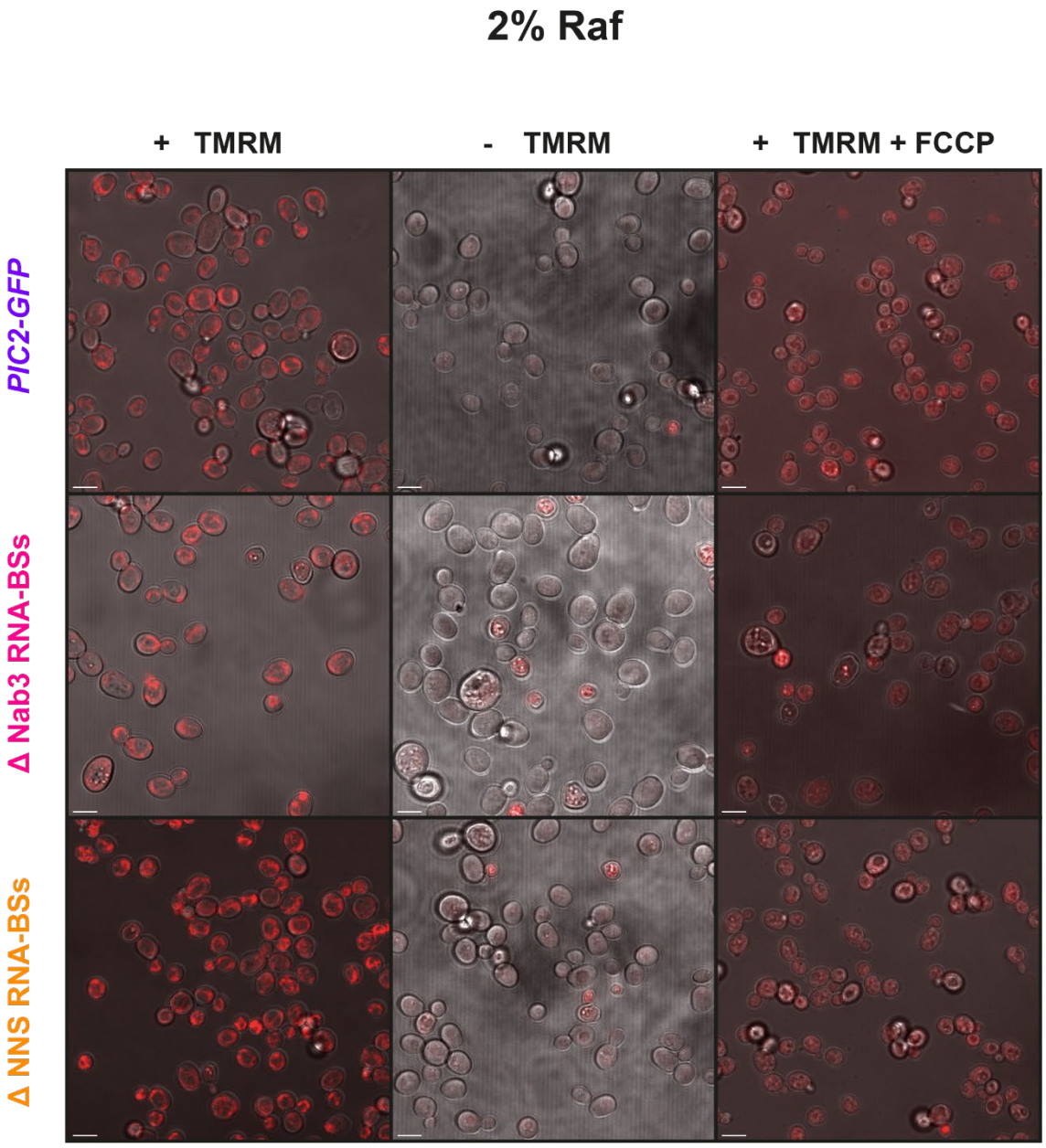

Figure IV.7. Representative confocal microscopy images of stained (+TMRM), unstained (-TMRM) and stained and depolarised (+TMRM + FCCP) *PIC2-GFP,* Δ Nab3 RNA-BSs and Δ NNS RNA-BSs cells grown in SC -Ura medium supplemented with 2% (w/v) raffinose. Whereas -TMRM and +TMRM + FCCP images constituted negative controls to test the specificity and functionality of the dye, the +TMRM images were used to calculate the normalised TMRM fluorescence measured in Figure IV.9.

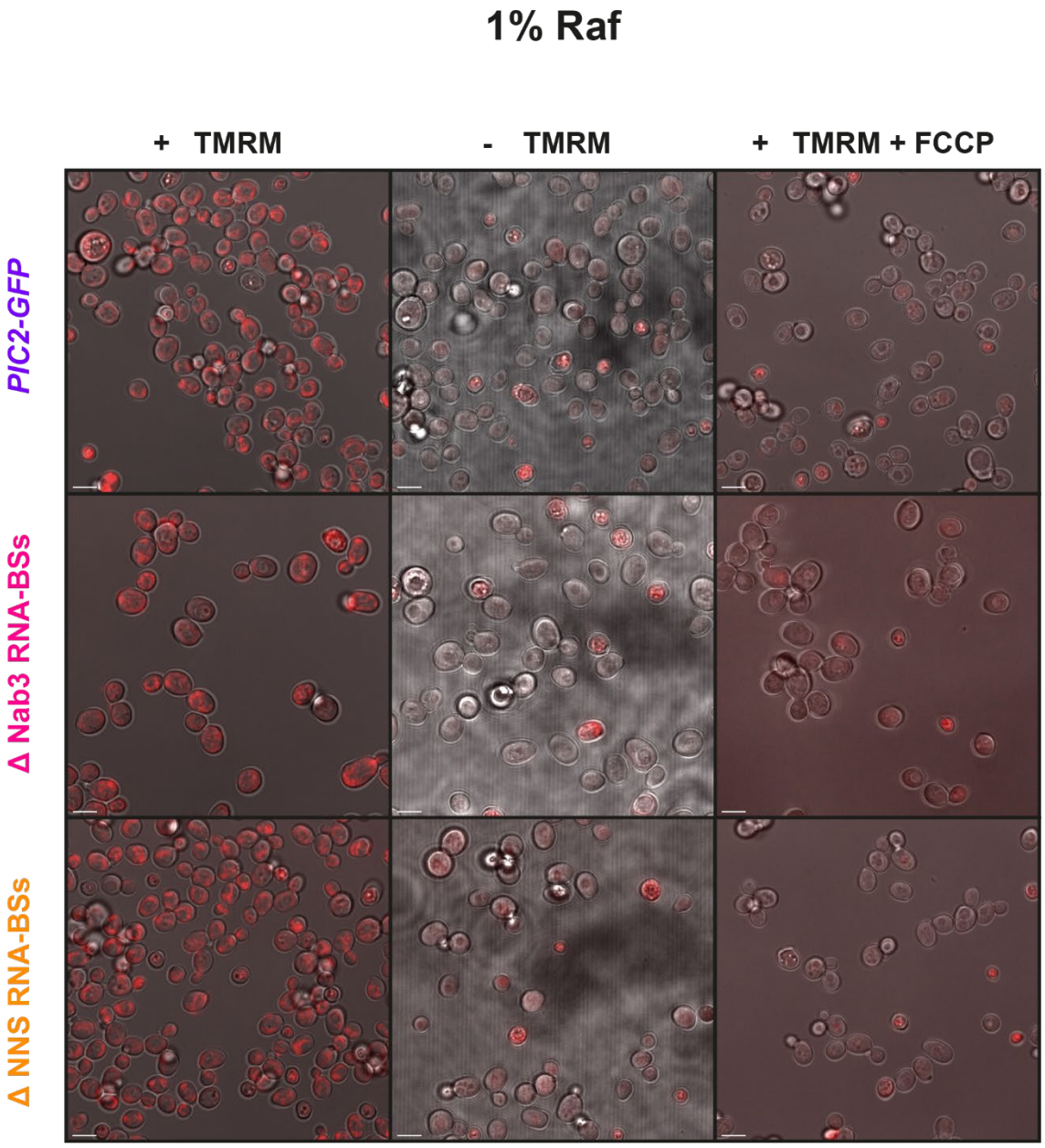

Figure IV.8. Representative confocal microscopy images of stained (+TMRM), unstained (-TMRM) and stained and depolarised (+TMRM + FCCP) *PIC2-GFP,* Δ Nab3 RNA-BSs and Δ NNS RNA-BSs cells grown in SC -Ura medium supplemented with 1% (w/v) raffinose. Whereas -TMRM and +TMRM + FCCP images constituted negative controls to test the specificity and functionality of the dye, the +TMRM images were used to calculate the normalised TMRM fluorescence measured in Figure IV.9.

In line with earlier flow cytometry experiments, live confocal microscopy detected a substantial mitochondrial membrane hyperpolarisation in the Δ Nab3 RNA-BSs mutant and a mild but significant increase in the mitochondrial membrane potential of Δ NNS RNA-BSs (Figure IV.9). This latter aspect represented a contradiction with respect to the MitoTracker™ Red CMXRos staining (Figure IV.9). However, this disagreement is likely emerging from the error associated to both techniques. Whilst the cytometry-derived fluorescence measurements displayed a greater standard deviation, the variability of the mean fluorescence in microscopy data was much smaller. This can partly be accounted for by the threshold and standardisation that this approach implements, as they considerably diminish background and non-specific signal. An additional point of dissent between both approaches was the magnitude of the mitochondrial hyperpolarisation in Δ Nab3 RNA-BSs. Nonetheless, this was not surprising considering that previous reports had already established that the numerical data obtained from MitoTracker™ dyes and TMRM differed (Desai et al., 2024).

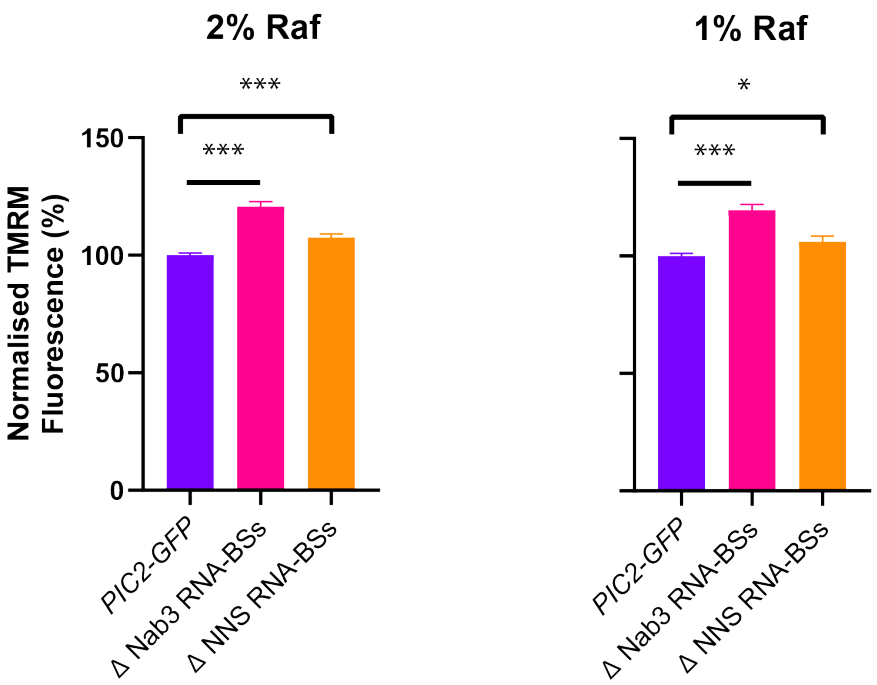

Figure IV.9. Mean normalised TMRM fluorescence values gathered from confocal imaging of more than 50 cells from three independent biological repeats for *PIC2-GFP,* Δ Nab3 RNA-BSs and Δ NNS RNA-BSs. Error bars represent the standard error of the mean (SEM). Statistical comparisons between each mutant and their parental *PIC2-GFP* were conducted by unpaired t-tests. *: $p<0.05$, ***: $p<0.001$ and 'ns': $p>0.05$.

Overall, however, the general trend of both strategies confirmed that the ∆ Nab3 RNA-BSs mutant presented a mitochondrial-related energy homeostasis defect which ultimately led to mitochondrial membrane hyperpolarisation. Additionally, consistent with prior phenotypic evaluations, the ∆ NNS RNA-BSs mutant exhibited an ambiguous phenotype oscillating between a milder version of the defects identified in ∆ Nab3 RNA-BSs and the features of the unaffected parental strain.

IV.6. Preventing Nab3 binding to *PIC2* increases basal oxygen consumption rates during nutrient deprivation.

Electron transfer between the different complexes of the electron transport chain generates a reduction potential that enables proton pumping across the inner mitochondrial membrane. The build-up of positive charges in the intermembrane space elicits an electrochemical potential comprising a pH (0.8 pH units/50 mV) and an electric (120-180 mV) gradient with respect to the basic and negatively charged mitochondrial matrix. The latter component is commonly referred to as the mitochondrial membrane potential which, in combination with the proton gradient, represents the dominant force driving ATP production and, thus, a widely used proxy for energy homeostasis (Duchen, 2004). While reductions in mitochondrial membrane potential occur due to increased ATP synthesis or mitochondrial dysfunction, larger mitochondrial membrane potential arises from downregulated ATP generation or increased proton pumping. Accordingly, an electrical charge imbalance across the inner mitochondrial membrane is often, albeit not necessarily, accompanied by differences in oxygen consumption. Previous methodological guidelines have, in fact, underscored the importance of carefully evaluating this parameter to correctly contextualise the apparent increase in mitochondrial membrane potential and identify its possible sources (Lemasters and Ramshesh, 2007; Perry et al., 2011).

To this end, I performed high-resolution respirometry. For this set of experiments, I used an oxygraph equipped with polarographic oxygen sensors, which measured oxygen concentration within a closed chamber containing the sample. Subsequently, oxygen consumption rates are extracted based on the estimated number of cells examined. On this basis, I examined cells from cultures at mid-logarithmic growth phases that were diluted to identical optical densities before the

start of the experiment. Basal oxygen consumption rates revealed that the Δ Nab3 RNA-BSs mutant sustained higher respiratory rates than the parental reference, specifically during nutrient deprivation (Figure IV.10). Reminiscent of all the other experiments showing few phenotypic differences between Δ NNS RNA-BSs and its parental strain, these results also identified no respirometric differences between that mutant and *PIC2-GFP* (Figure IV.10).

Furthermore, to assess their maximal respiration rate, samples were treated with FCCP, an uncoupling agent that imports protons from the intermembrane space to the mitochondrial matrix, thereby collapsing mitochondrial membrane potential and driving oxygen consumption by complex IV to its maximum activity. Having estimated the basal and maximal respiratory rates, I could then derive the reserve respiratory capacity for each strain, which is a measurement of the spare respiration capabilities of a given set of cells to meet an energetic demand (Figure IV.10). Despite displaying a slightly enhanced maximal respiration rate, Δ Nab3 RNA-BSs barely benefited from a larger respiratory margin since its reserve respiratory capacity was not significantly larger than that of *PIC2-GFP* (Figure IV.10).

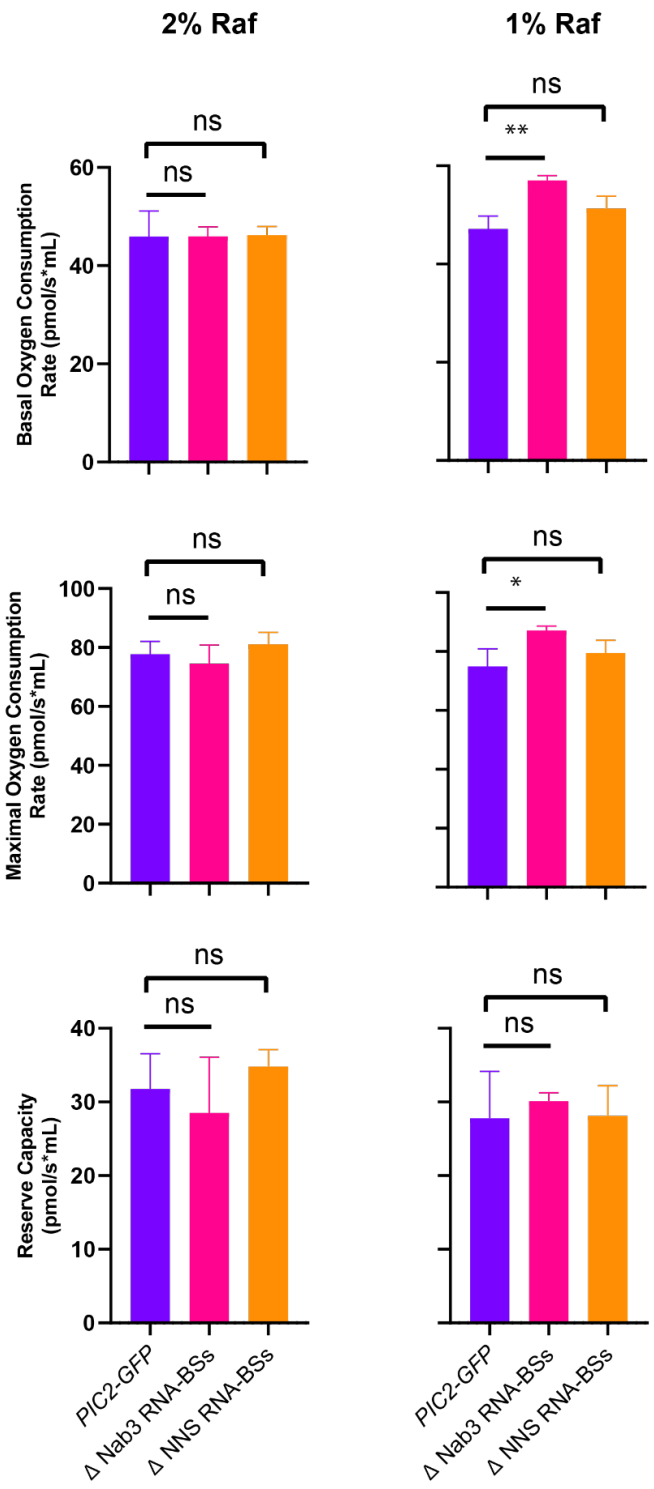

Figure IV.10. Mean for the measured basal, maximal and reserve capacity oxygen consumption rates. Three separate respiration assays were performed for independent cultures of *PIC2-GFP*, Δ Nab3 RNA-BSs and Δ NNS RNA-BSs grown in raffinose-abundant (i.e., 2% (w/v)) or raffinose-deprived (i.e., 1% (w/v)) medium. Error bars represent standard deviation. Statistical comparisons between each mutant and their parental *PIC2-GFP* were conducted by unpaired t-tests. *: $p<0.05$, **: $p<0.01$ and 'ns': $p>0.05$.

IV.7. Disrupting Nab3 binding to *PIC2* alters the cellular redox status and confers resistance to oxidative insults.

As well as driving a proton build-up and the resulting mitochondrial membrane hyperpolarisation, enhanced oxygen consumption can, as suggested by the oxidative stress theory of ageing, trigger a proportional increase in ROS production (Hulbert et al., 2007; Sohal et al., 2002; Speakman et al., 2004). Although some studies have shown that the ROS production per unit oxygen consumed in the resting state of mitochondrial respiration is larger than that during active states (Barja, 2013; Nicholls, 2004; Speakman and Garratt, 2014), recent theoretical modelling has clarified that in physiological conditions, this effect was unlikely to deflect the proportionality of both variables (Hou et al., 2021). Thus, increased oxygen consumption can indeed lead to ROS overproduction, which onsets an adaptation response. Based on this phenomenon and given that previous studies had established that oversized cells elicited adaptation responses (Neurohr et al., 2019), I hypothesised that the observed energy homeostasis defects arose from intracellular stress.

Increased mitochondrial electron transport chain activity enhances mitochondrial conversion of NADH to NAD^+ and, consequently, lowers the mitochondrial NADH/NAD^+ ratio (Yang and Sauve, 2016). In turn, reduced NADH/NAD^+ balance alters the rate at which the mitochondrial isocitrate dehydrogenase, Idh2, converts α-ketoglutarate to citrate in the TCA cycle. In doing so, ultimately, decreased NADH/NAD^+ ratios limit the entry of acetyl-CoA into the TCA cycle (McLain et al., 2011). While increased oxidative metabolism decreases NADH/NAD^+ levels, NADPH acts as an electron donor for many antioxidants, such as reduced glutathione or reduced thioredoxin (Arnér and Holmgren, 2000; Cejudo et al., 2012; Tribble and Jones, 1990), which contribute to neutralising reactive oxygen species (Agledal et al., 2010). Importantly, however, intracellular concentrations of $NADP^+$ and NADPH are significantly lower than those of NAD^+ and NADH (Yang and Sauve, 2016). Moreover, unlike the NAD pool, NADP species are predominantly maintained in their reduced form (Cejudo et al., 2012; Tribble and Jones, 1990).

Since the nicotinamide group of NADH and NADPH can be excited by UV radiation and subsequently emit light of approximately 460 nm in wavelength, the

abundance of both reduced coenzymes can be monitored as a blue, fluorescent signal following exposure to UV light. Therefore, I examined the state of the nicotinamide adenine dinucleotide (NAD(P)) pool in both strains by performing fluorescence microplate reader assays (see II.21). However, given that (i) the NADP pool is less abundant than its NAD counterpart and (ii) that the former is stably and generally kept in its reduced format, changes in NAD(P)/NAD(P)H ratios will predominantly be driven by changes in the redox balance of intracellular NAD species. Consistent with higher oxidative stress, NAD species in the Δ Nab3 RNA-BSs mutant were predominantly in their oxidised state (i.e., NAD^+) compared to those in the *PIC2-GFP* reference strain, which were primarily in a reduced state (i.e., NADH) (Figure IV.11).

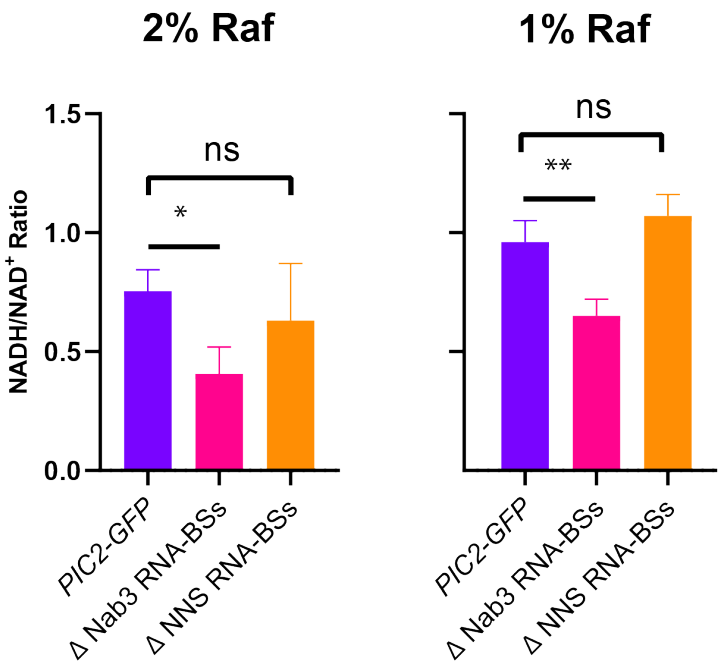

Figure IV.11. Mean NADH/NAD^+ ratios calculated based on three independent fluorescence assays of *PIC2-GFP*, Δ Nab3 RNA-BSs and Δ NNS RNA-BSs grown in media containing either 2% (w/v) or 1% (w/v) raffinose. Error bars represent the standard deviation from three biological replicates. Statistical comparisons between each mutant and their parental *PIC2-GFP* strain were conducted by unpaired t-tests. *: $p<0.05$, **: $p<0.01$ and 'ns': $p>0.05$.

To corroborate that, indeed, Δ Nab3 RNA-BSs was inherently stressed, I devised an oxidative stress assay based on acquired stress resistance: since exposure to a mild stress confers resistance to subsequent ones, stressed cells were expected to be less affected by environmental insults. Accordingly, I expected that cells which

were already stressed would be less affected by the addition of hydrogen peroxide to the medium. To assess this, I performed microplate reader growth assays monitoring the growth of *PIC2-GFP*, ∆ Nab3 RNA-BSs and ∆ NNS RNA-BSs in the presence and absence of a moderate concentration of hydrogen peroxide (i.e., 0.5 mM) which had been previously shown to be compatible with *S. cerevisiae* viability but restricted its growth (Bayliak et al., 2017) (Figure IV.12A). Indeed, whereas the growth of the parental strain was negatively affected by exposure to the exogenous hydrogen peroxide, the ∆ Nab3 RNA-BSs mutant's growth rate modestly increased following hydrogen peroxide addition (Figure IV.12B). These results prove that disrupting Nab3 RNA-BSs in *PIC2* causes energy homeostasis defects which drive greater respiratory demands and intracellular oxidative stress.

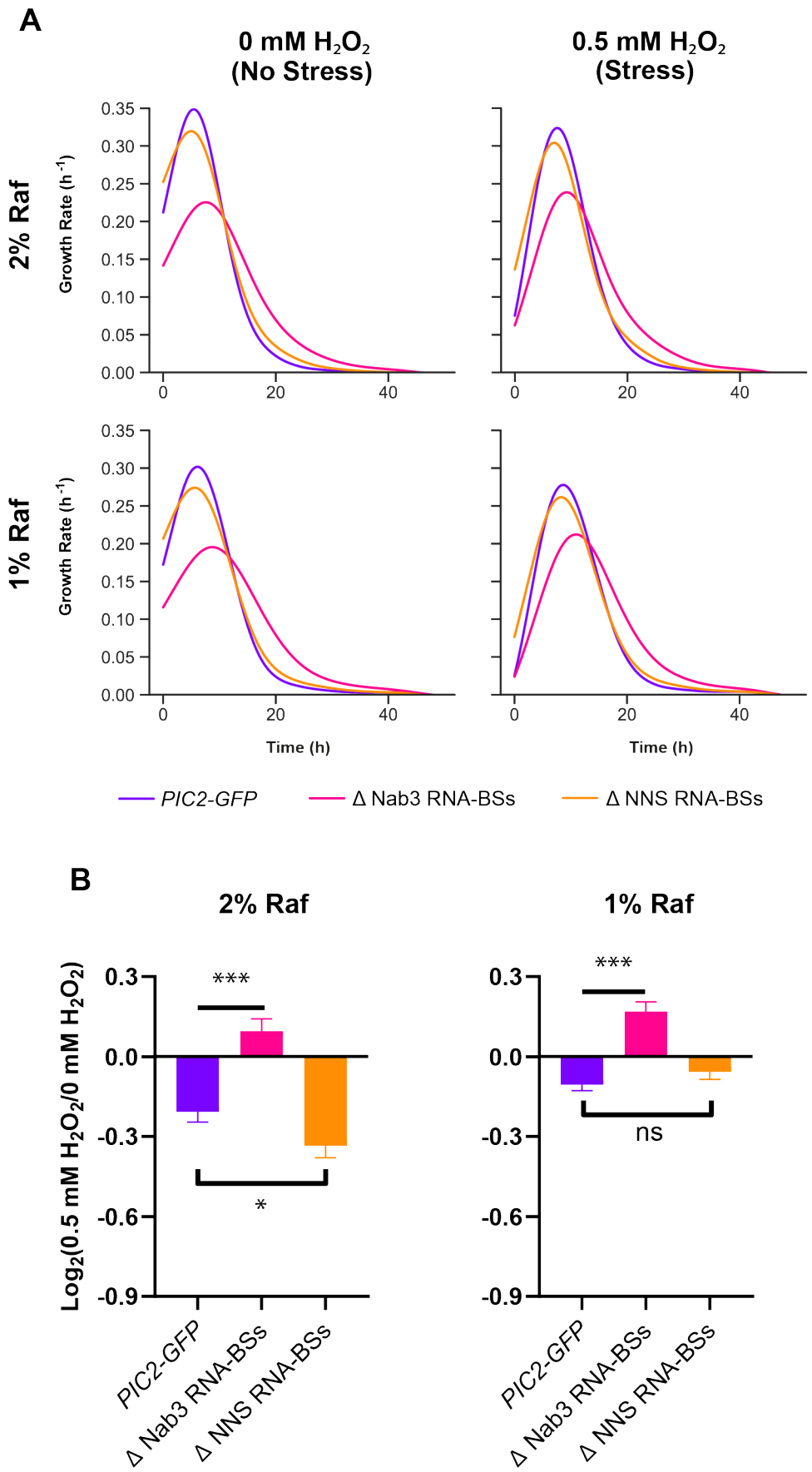

Figure IV.12. Oxidative stress assays comparing the change in the growth rate of *PIC2-GFP*, Δ Nab3 RNA-BSs and Δ NNS RNA-BSs in medium lacking hydrogen

peroxide to those which they display upon the addition of hydrogen peroxide. **A.** Time-resolved growth rate computed for *PIC2-GFP*, ∆ Nab3 RNA-BSs and ∆ NNS RNA-BSs strains in medium supplemented with high (i.e., 2% (w/v)) and low (i.e., 1% (w/v)) raffinose concentrations and containing either 0 mM or 0.5 mM of hydrogen peroxide (H_2O_2). **B**. Change in the maximum growth rate for *PIC2-GFP*, ∆ Nab3 RNA-BSs and ∆ NNS RNA-BSs strains when exposed to 0.5 mM of hydrogen peroxide (H_2O_2). Fold changes in growth rates were calculated as the binary logarithm of the ratio of the maximum growth rates recorded in the stressful medium (i.e., containing 0.5 mM H_2O_2) to the ones derived in the innocuous medium. Error bars are derived from the standard deviations of a bootstrapping iteration, which resampled the measured OD_{600} values 100 times. The standard deviations obtained from Omniplate were then accordingly propagated when calculating the ratio and applying the $\log_2$-transformation. Statistical comparisons between each mutant and their parental *PIC2-GFP* strain were conducted by unpaired t-tests. *: $p<0.05$, ***: $p<0.001$ and 'ns': $p>0.05$. The data presented in this figure is representative of two independent biological repeats of this experiment.

IV.8. Cell size and mitochondrial anomalies co-segregate with mutations in Nab3 RNA-binding sites in *PIC2*.

Before delving into the cause of this phenotype, I aimed to ascertain whether it was genetically linked to the mutations disrupting NNS regulation of *PIC2*. To this end, fluorescent strains were backcrossed with a non-fluorescent wild-type strain of the opposite mating type (i.e., BY4742). After undergoing meiosis and sporulation, the resulting diploid strain yielded tetrads enclosing four haploid daughter cells (Figure IV.13). Among these, two coded for a wild-type version of *PIC2,* and the remaining ones bore the fluorescently tagged *PIC2* locus. Upon visual identification and genetic screening of the daughter strains coding for wild-type *PIC2* and its *GFP*-encoding sisters, I employed flow cytometry to measure the cell size and the mitochondrial membrane potential of all the descendants from the *PIC2-GFP*, ∆ Nab3 RNA-BSs and ∆ NNS RNA-BSs mating assays (Figures IV.13-14).

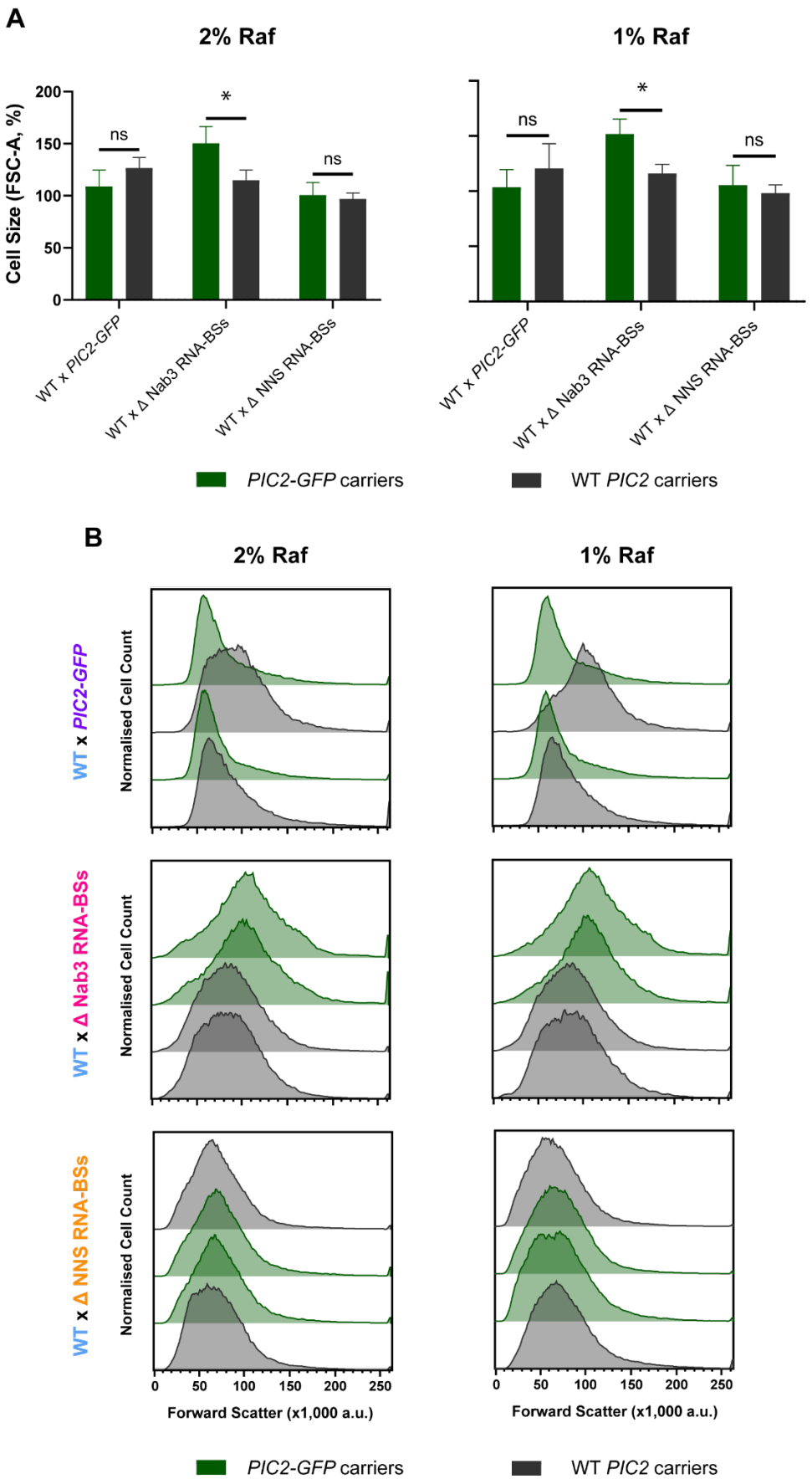

Figure IV.13. Mating assays demonstrate that excessive cell size co-segregates with Δ Nab3 RNA-BSs mutations in *PIC2*. **A.** Normalised cell size of the wild-type *PIC2* and

GFP carriers emerging from the backcrosses of *PIC2-GFP*, ∆ Nab3 RNA-BSs and ∆ NNS RNA-BSs mutants with the non-fluorescent background strain in raffinose-rich (i.e., 2% (w/v)) and raffinose-limiting (i.e., 1% (w/v)) medium. Values for each strain were obtained from the weighted mean of the median forward scatter values of three biological repeats containing more than 10,000 cells. Normalised percentages were calculated in relation to *PIC2-GFP* in the same condition. Error bars represent standard deviation. Statistical comparisons between each mutant and their parental *PIC2-GFP* strain were conducted by unpaired t-tests. *: $p<0.05$, **: $p<0.01$ and 'ns': $p>0.05$. ***B.*** Representative traces of the cell size distribution of all the daughter strains derived from each mating assay. The sizes were compared using their forward light scatter (FSC) values. My results showed that ∆ Nab3 RNA-BSs mutation carriers were also larger than their non-fluorescent counterparts (Figure IV.13). Given that there was no difference in the cell size between strains stemming from the *PIC2-GFP* and ∆ NNS RNA-BSs backcrosses, I concluded that increased cell size specifically co-segregated with defective Nab3 binding to *PIC2*.

Interestingly, the landscape was different for the mitochondrial membrane potential measurements. In this case, strains bearing mutations in Nab3 binding sites (i.e., resulting from the ∆ Nab3 RNA-BSs backcross) or all NNS recognition motifs (i.e., proceeding from the ∆ NNS RNA-BSs mating assay) displayed mitochondrial hyperpolarisation in low raffinose medium (Figure IV.14*)*. Conversely, in medium containing 2% (w/v) raffinose, mitochondrial membrane potential was only minimally higher among mutants originated from the ∆ NNS RNA-BSs backcross (Figure IV.14*)*. Although the technical limitations associated with MitoTracker™ Red CMXRos chemical nature and cytometry-based mitochondrial membrane potential quantification should be still considered in this case, these results suggest that mitochondrial membrane hyperpolarisation could be co-segregating with increased Pic2 expression. Notably, nonetheless, given that mitochondrial membrane hyperpolarisation in the ∆ NNS RNA-BSs was only detected using TMRM staining and confocal microscopy (Figure IV.9), the validity of this conclusion had to be further evaluated.

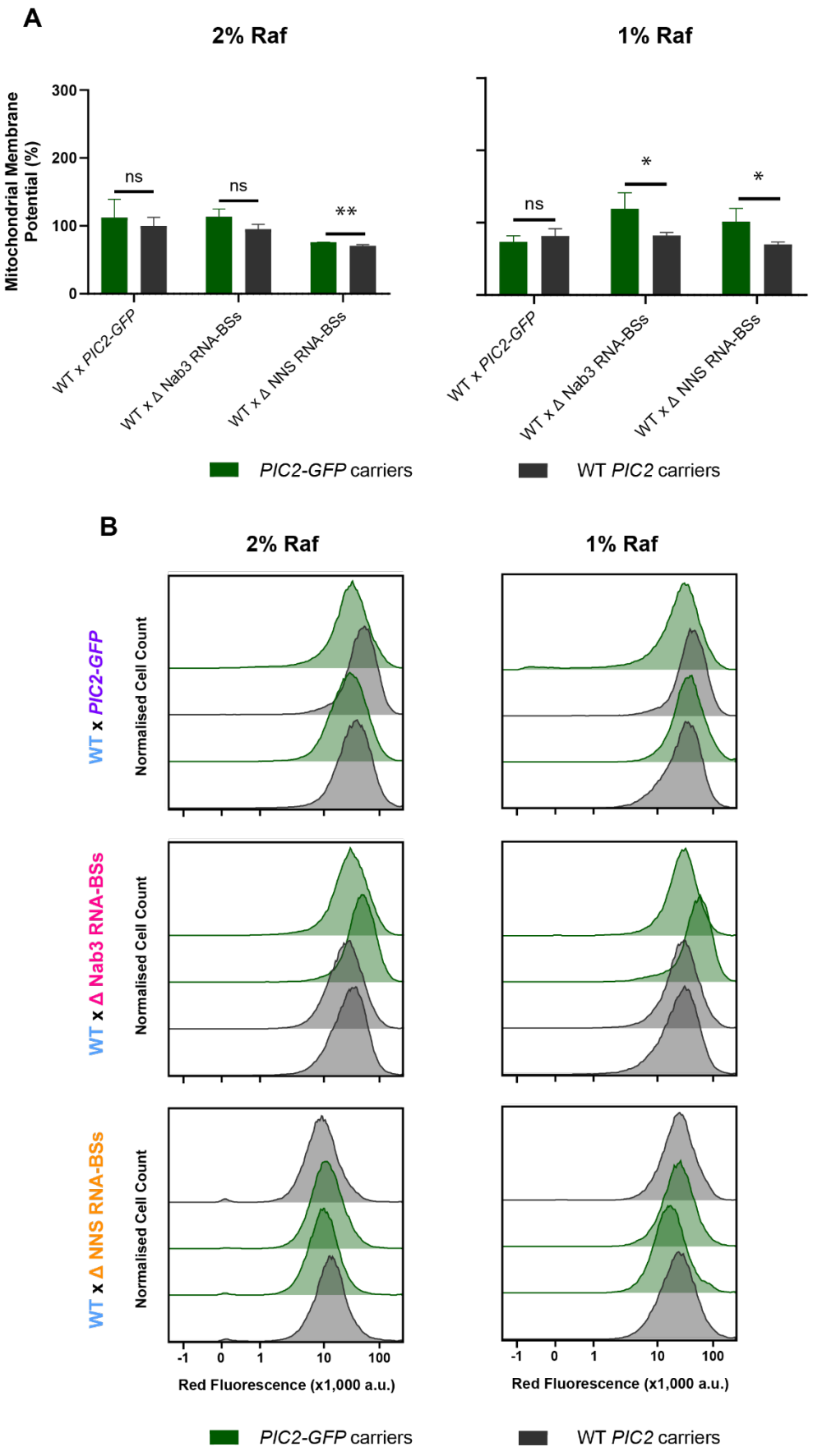

Figure IV.14. Mating assays demonstrate that mitochondrial hyperpolarisation appeared to be genetically linked to enhanced expression of *PIC2-GFP*. **A.** Normalised

mitochondrial membrane potential of the wild-type *PIC2* and *GFP* carriers emerging from the backcrosses of *PIC2-GFP*, ∆ Nab3 RNA-BSs and ∆ NNS RNA-BSs mutants with the non-fluorescent background strain in raffinose-rich (i.e., 2% (w/v)) and raffinose-limiting (i.e., 1% (w/v)) medium. Values for each strain were obtained from the weighted medians of red fluorescence emissions previously normalised to the corresponding median forward scattering value. Bar plots display averages of three biological repeats containing more than 10,000 cells. Normalised percentages were calculated in relation to *PIC2-GFP* in the same condition. Error bars represent standard deviation. Statistical comparisons between each mutant and their parental *PIC2-GFP* strain were conducted by unpaired t-tests. *: $p<0.05$, **: $p<0.01$ and 'ns': $p>0.05$. **B**. Representative flow cytometry traces of the MitoTracker™ Red CMXRos staining of all the daughter strains derived from each mating assay.

IV.9. Completely disrupting NNS binding to *PIC2* does not cause significant cell size, cell cycle and mitochondrial anomalies.

Considering that *PIC2* has never been linked to cell size homeostasis, I proceeded to test whether cell size aberrations were present in strains with a different set of mutations in the NNS recognition sites of *PIC2*. To this end, I repeated the RT-qPCRs, cell size, cell cycle and mitochondrial membrane potential evaluations in another ∆ Nab3 RNA-BSs clone (i.e., ∆ Nab3 RNA-BSs #2) and a mutant in which all Nab3 and some Nrd1 recognition sites were disrupted (i.e., partial ∆ NNS RNA-BSs) (Figures IV.15 and IV.16). The rationale of this set of experiments was that, if larger cell size was indeed caused by abrogation of Nab3 cognate sites in *PIC2*, the ∆ Nab3 RNA-BSs #2 should recapitulate the increase in cell size described in the original ∆ Nab3 RNA-BSs clone. On the other hand, the partial ∆ NNS RNA-BSs would clarify whether additionally abrogating Nrd1 cognate sites in *PIC2* would affect the extent of the described defects.

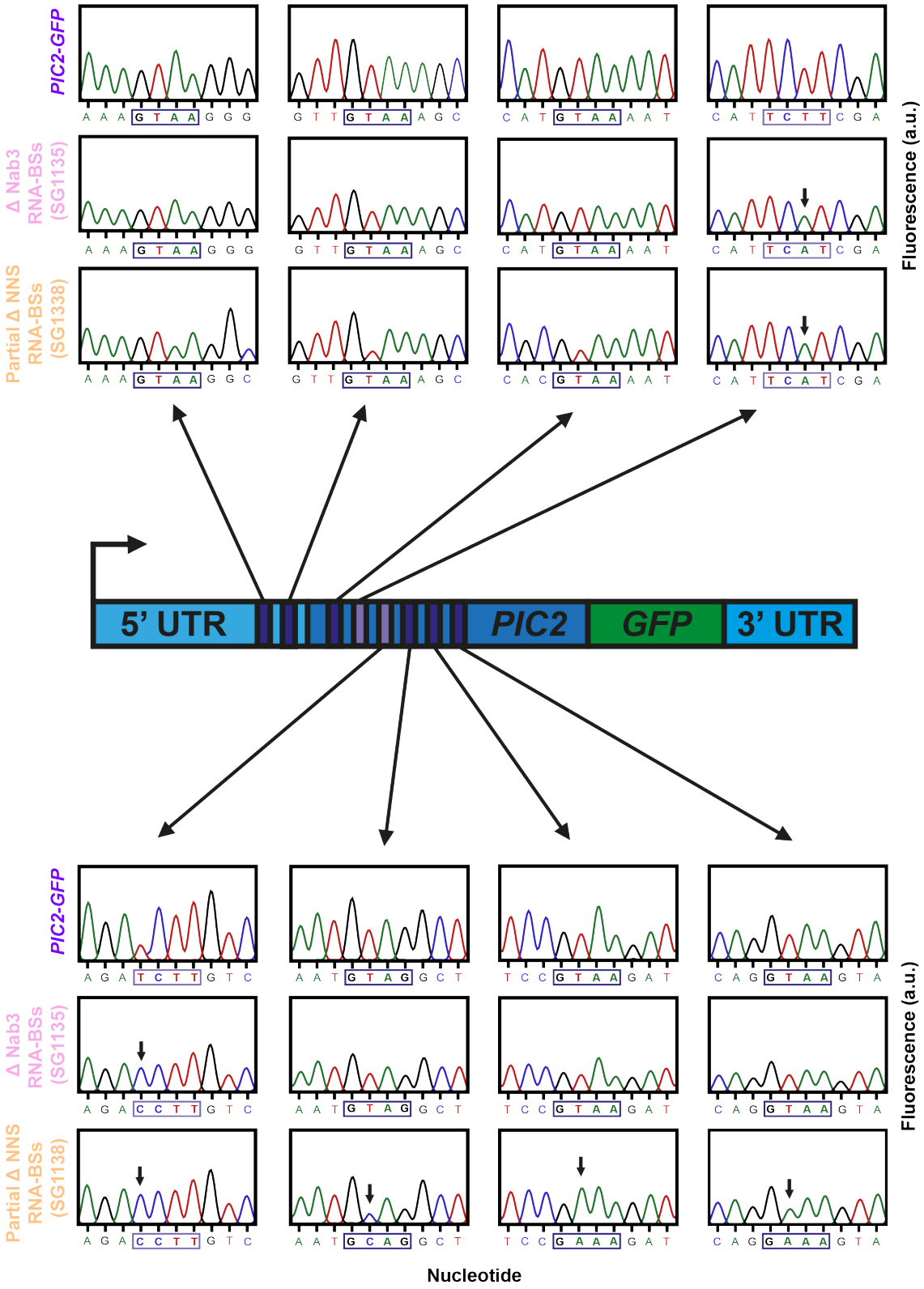

Figure IV.15. Sequencing traces for the Nab3 and Nrd1 binding sites of *PIC2* in the *PIC2-GFP*, Δ Nab3 RNA-BSs #2 and the partial Δ NNS RNA-BSs strains. Single-point mutations are indicated with arrows.

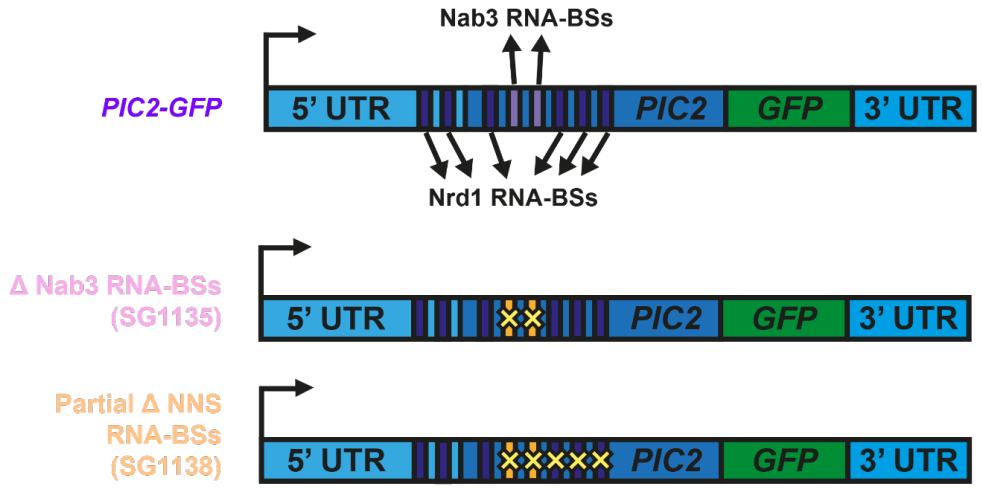

Figure IV.16. Schematic summary of the mutations in the Δ Nab3 RNA-BSs #2 and the partial Δ NNS RNA-BSs mutants derived from the parental *PIC2-GFP* strain.

Before starting with the phenotypic characterisation of the two additional mutants, I measured their *PIC2* mRNA levels and analysed them alongside my previous *PIC2-GFP*, Δ Nab3 RNA-BSs and Δ NNS RNA-BSs RT-qPCR data. In agreement with my previous findings in the original Δ Nab3 RNA-BSs mutant, Δ Nab3 RNA-BSs #2 also displayed enhanced *PIC2* mRNA levels, and the partial Δ NNS RNA-BSs strain exhibited an intermediate increase in *PIC2* transcript abundance (Figure IV.17A). Therefore, the imbalance of Nab3 and Nrd1 binding to the transcript appeared to be the factor driving overproduction of *PIC2* transcripts. However, at this point, I also considered that differences in *PIC2* upregulation could be partly attributed to the fact that *PIC2* transcripts with a higher number of mutations exhibited a lower predicted probability of folding (Figure IV.17B).

Next, I sought to establish whether the two additional clones displayed phenotypic outcomes following a similar trend to the one observed for *PIC2* RNA levels. For this purpose, I measured the cell size of Δ Nab3 RNA-BSs #2 and the partial Δ NNS RNA-BSs (Figure IV.18). As expected, the cell size aberrations observed in the Δ Nab3 RNA-BSs #2 strain were comparable to those of Δ Nab3 RNA-BSs (Figure IV.18). Moreover, cell volume anomalies were more subtle in the partial Δ NNS RNA-BSs mutant and undetectable in the mutant without NNS regulation in *PIC2* (Figure IV.18). Cumulatively, this pattern suggested that the aggravation of the cell size defects originated from an imbalance in Nab3 and Nrd1 binding to the *PIC2* transcript.

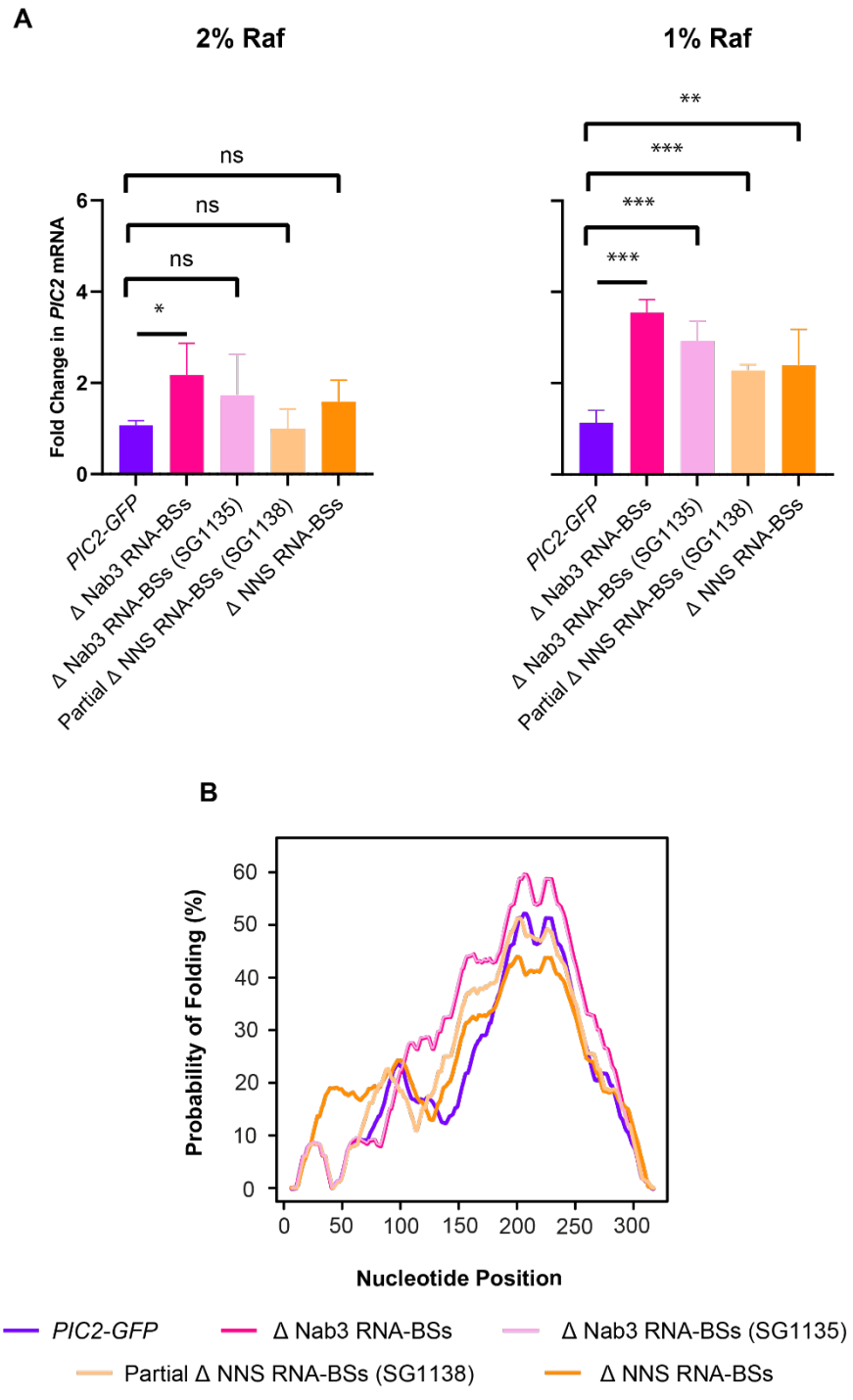

Figure IV.17. Preventing Nab3 binding while maintaining Nrd1 recruitment to the *PIC2* transcript increases *PIC2* mRNA levels. **A**. Fold changes of *PIC2-GFP* mRNA in all mutants compared to the parental reference in high (i.e., 2% (w/v)) and low (i.e., 1% (w/v)) raffinose media. Bar plots display means and standard deviations from three independent experiments. **B**. Thermodynamic ensemble profiles for the *PIC2* transcripts produced by the *PIC2-GFP* and all derived mutant strains. Estimates for the probability of folding are based on minimum free energy predictions by the RNAfold suite (Lorenz et al., 2011).

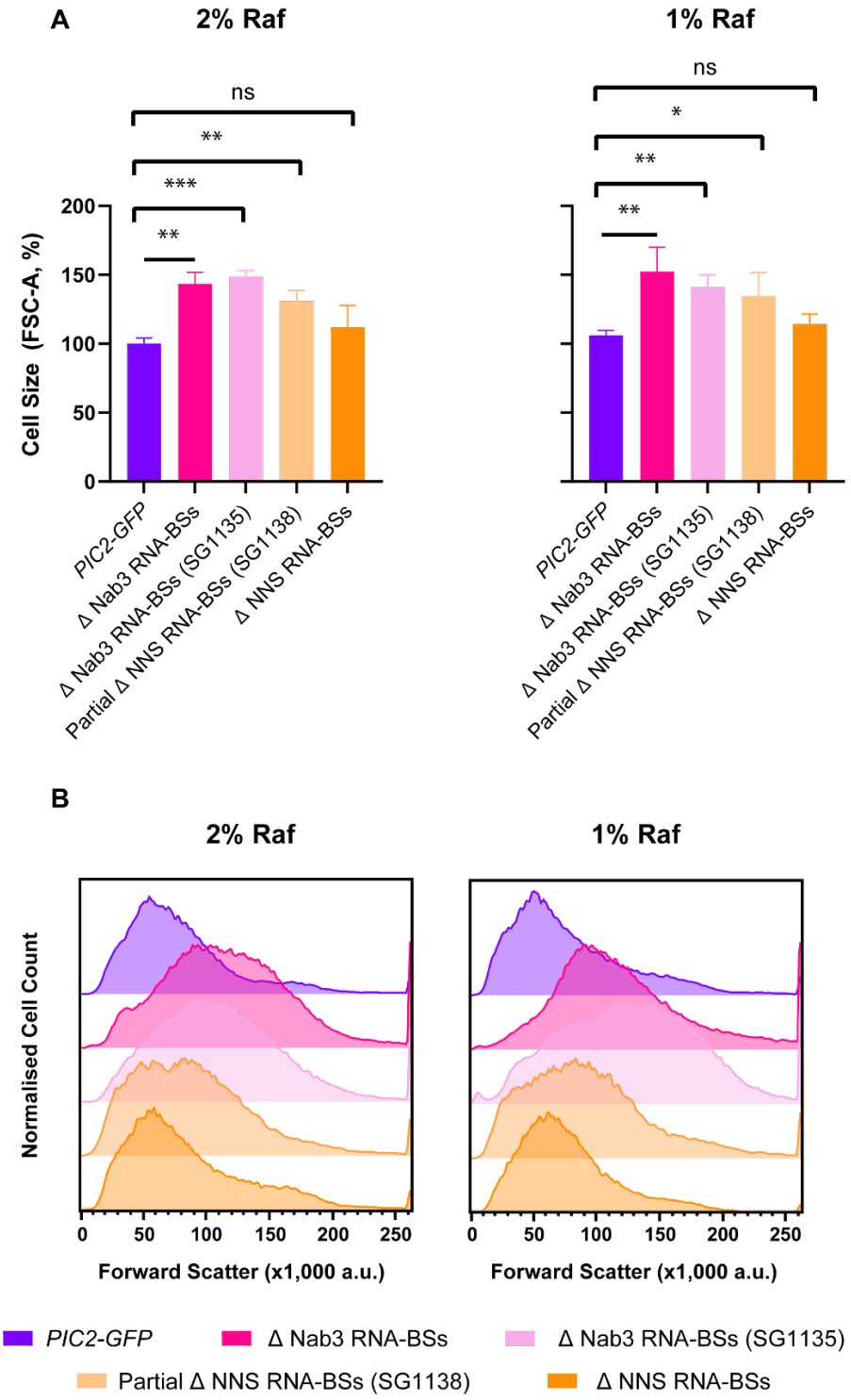

Figure IV.18. Abnormal enlargement of cell size was more severe in mutants where only Nab3 binding to *PIC2* was abrogated. **A**. Weighted means of the median FSC values for three independent biological repeats were calculated for each strain and normalised to the parental *PIC2-GFP*. Error bars represent standard deviation. Statistical comparisons between each mutant and the *PIC2-GFP* reference were performed by an unpaired t-test. *: p<0.05, **: p<0.01, ***: p<0.001 and 'ns': p>0.05. **B**. Representative traces of the cell size distribution of *PIC2-GFP* and derived mutants

from flow cytometry analyses. The sizes were compared using their forward light scatter (FSC) values.

Following the rationale that led me to identify cell cycle delays in ∆ Nab3 RNA-BSs, I tested whether the cell cycle of the ∆ Nab3 RNA-BSs #2 mutant was prolonged likewise and if cell cycle delays attenuated in the partial ∆ NNS RNA-BSs strain. After performing cell cycle analyses technically identical to the ones described in IV.4., I discovered that a lower fraction of ∆ Nab3 RNA-BSs #2 was in the G1 phase compared to the *PIC2-GFP* reference (Figure IV.19-20). Although this effect was only detected as significant in medium containing 1% (w/v) raffinose (Figure IV.20), it was already perceptible for both ∆ Nab3 RNA-BSs clones when cells were grown in the presence of 2% (w/v) raffinose. Unlike the parental *PIC2-GFP*, mutants without Nab3 binding motifs in *PIC2* were more frequently undergoing S or G2/M, suggesting extended cell cycles (Figure IV.19-20). Moreover, the two mutants lacking Nab3 RNA-BSs in *PIC2* exhibited a higher proportion of polyploids (Figure IV.19-20). Furthermore, in line with my steady-state *PIC2* mRNA measurements and cell size observations, the prolongation of the cell cycle ameliorated in the partial mutant, and no differences were detected in the strain lacking NNS binding sites in *PIC2* (∆ NNS RNA-BSs) (Figure IV.19-20). Overall, this evidence shows that disrupting Nab3 binding while maintaining Nrd1 binding to *PIC2* increases the expression of the gene and underlies the observed cell size and cell cycle aberrations.

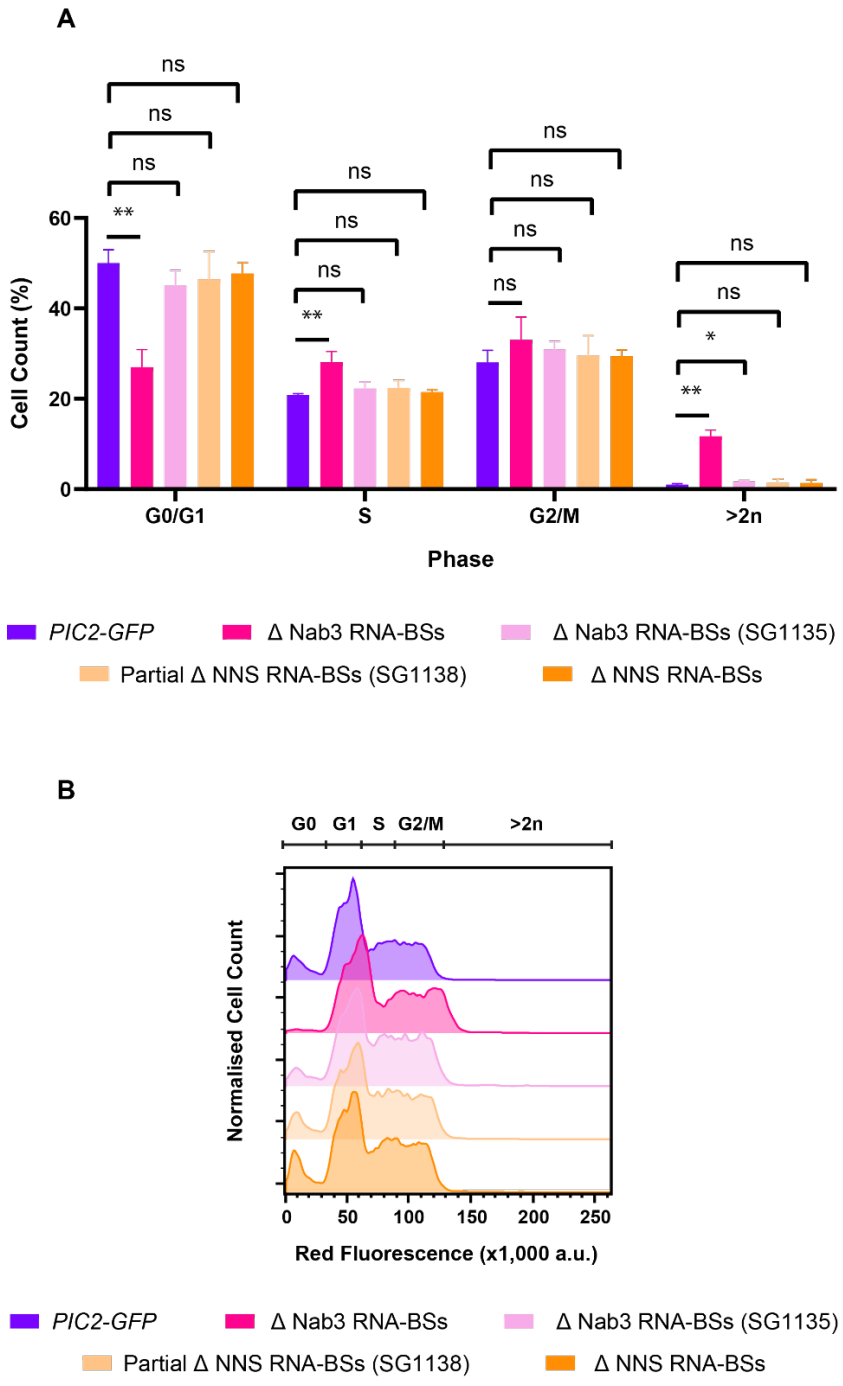

Figure IV.19. Cell cycle analysis of *PIC2-GFP* and all derived mutants grown to mid-exponential phase (OD_{600} ~0.5) in medium containing 2% (w/v) raffinose. **A**. Weighted means of the population fraction of *PIC2-GFP* and the studied mutants within each cell cycle phase. Values based on biological triplicates and error bars represent the standard deviation calculated after considering the three repeats per strain and condition. Statistical comparisons were performed by unpaired t-tests. *: $p<0.05$, **: $p<0.01$, ***: $p<0.001$ and 'ns': $p>0.05$. **B**. Representative flow cytometry traces of the DNA profiles of all strains.

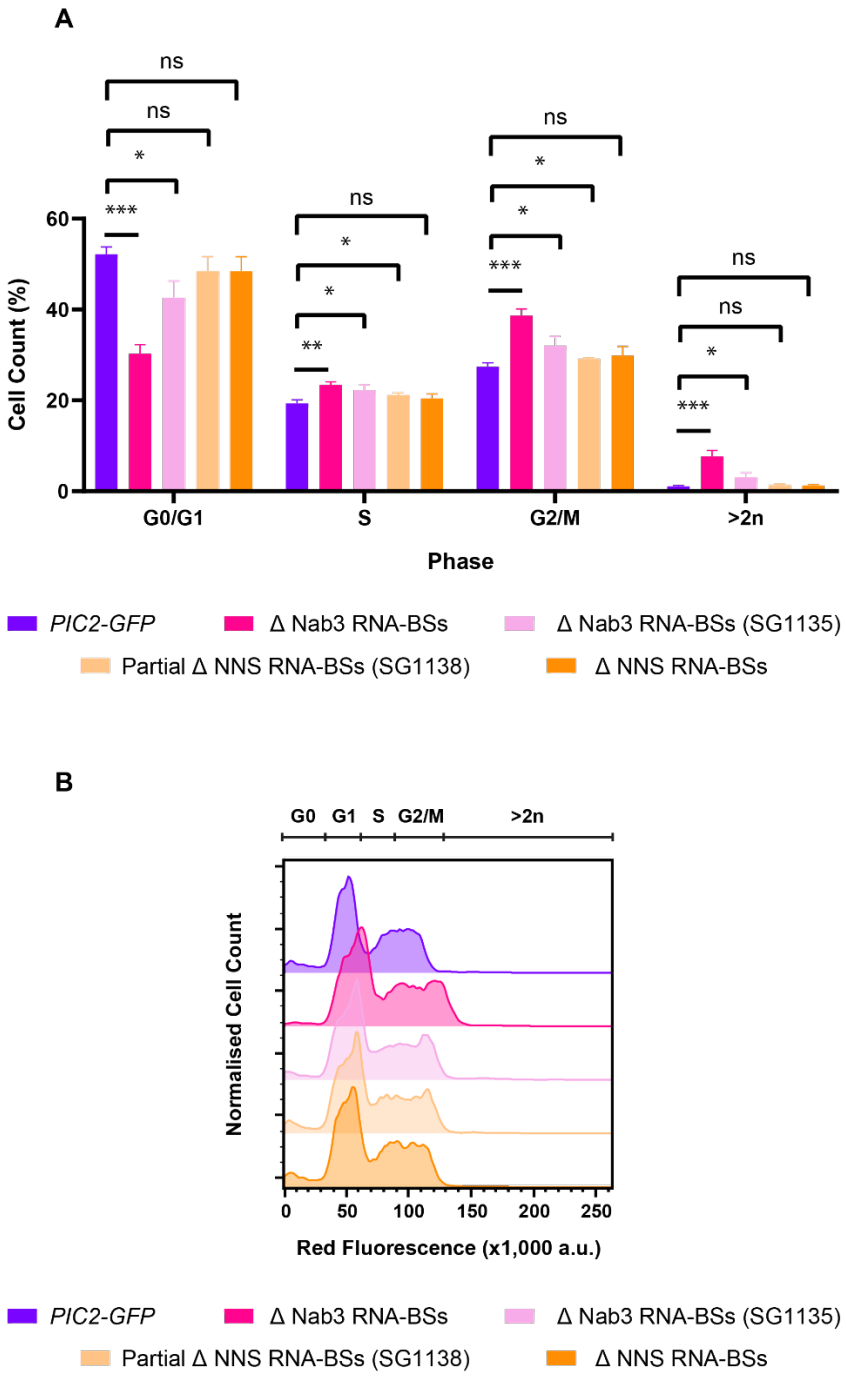

Figure IV.20. Cell cycle analysis of *PIC2-GFP* and all derived mutants grown to mid-exponential phase (OD_{600} ~0.5) in medium containing 1% (w/v) raffinose. **A**. Weighted means of the population fraction of *PIC2-GFP* and the studied mutants within each cell cycle phase. Values based on biological triplicates and error bars represent the standard deviation calculated after considering the three repeats per strain and condition. Statistical comparisons were performed by unpaired t-tests. *: $p<0.05$, **: $p<0.01$, ***: $p<0.001$ and 'ns': $p>0.05$. **B**. Representative flow cytometry traces of the DNA profiles of all strains.

To completely reiterate the phenotypic characterisation that I pursued in the original Δ Nab3 RNA-BSs clone and Δ NNS RNA-BSs, I quantified the mitochondrial membrane potential of the newly identified Δ Nab3 RNA-BSs #2 and partial Δ NNS RNA-BSs mutants by staining mid-logarithmic cultures with MitoTracker™ Red CMXRos (Figure IV.21). Upon flow cytometry inspection, my measurements displayed the same trend as the *PIC2* mRNA fold change, cell size and cell cycle evaluations: while the Δ Nab3 RNA-BSs #2 fully recapitulated prior observations on the original Δ Nab3 RNA-BSs clone, the partial Δ NNS RNA-BSs mutant yielded a milder hyperpolarisation constituting an intermediate between the one described in the mutants lacking Nab3 RNA-BSs in *PIC2* and Δ NNS RNA-BSs (Figure IV.21). Importantly, my findings show that, in line with enhanced cell volume and prolonged cell cycle phenotypes, increases in mitochondrial membrane potential were highest in the strains in which mutations were only introduced in the Nab3 binding motifs of the *PIC2* transcript.

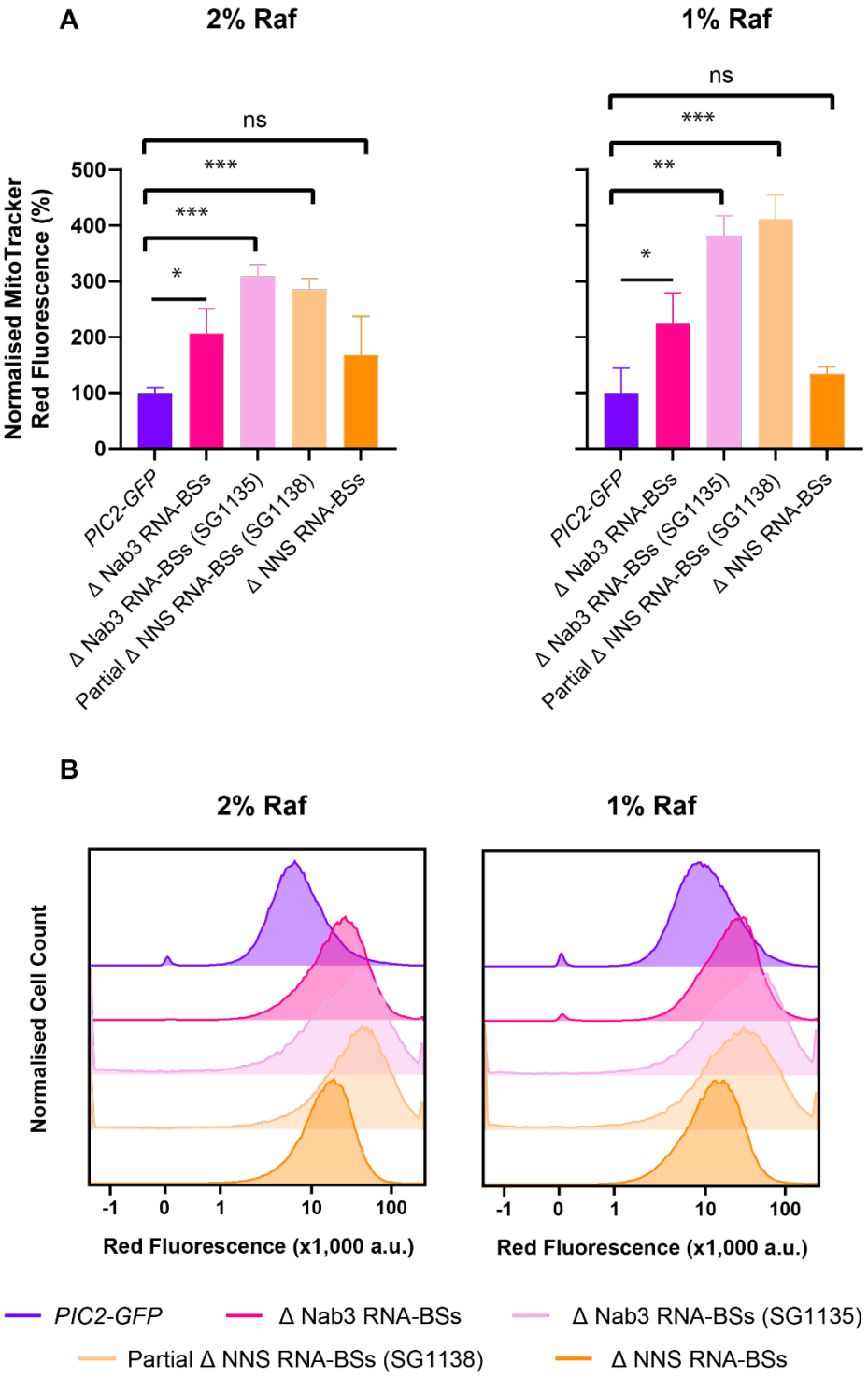

Figure IV.21. Mitochondrial membrane hyperpolarisation was highest upon disruption of Nab3 binding to *PIC2* and appeared to regress to that of the *PIC2-GFP* parental strain when Nrd1 sites were removed as well. **A**. Medians for single-cell red fluorescence emissions were normalised to the corresponding median forward scattering value. The bar graph shows the weighted average and standard deviation of the mentioned ratio across three biological batches containing more than 50,000 cells. Statistical comparisons between each mutant and the *PIC2-GFP* reference were

performed by an unpaired t-test. *: $p<0.05$, **: $p<0.01$ and 'ns': $p>0.05$. **B**. Representative flow cytometry traces of the MitoTracker™ Red CMXRos staining distribution of *PIC2-GFP,* ∆ Nab3 RNA-BSs ∆ NNS RNA-BSs strains at mid log phase (OD_{600} ~0.5).

IV.10. Discussion

The results presented in this chapter have characterised the phenotypic disadvantages of preventing Nab3 binding to *PIC2*. My growth assays have shown that the maximum growth rate of the ∆ Nab3 RNA-BSs strain is reduced by around a third compared to that of its parental *PIC2-GFP* strain. Moreover, the same mutant possesses a cell size approximately 50% larger than that of its parental counterpart. In line with previous studies, abnormally enlarged cell volume co-occurred with cell cycle prolongation and larger levels of intracellular stress. Previous oversized cellular models imply that intracellular stress may not be emerging solely from the increased expression of *PIC2* in the ∆ Nab3 RNA-BSs (Neurohr et al., 2019). Yet, aberrantly enhanced intracellular stress levels in basal conditions could potentially be exacerbated due to the physiological link between Pic2 and mitochondrial activity, which was also significantly affected in the ∆ Nab3 RNA-BSs strain.

At first, I assumed that the most likely molecular cause underlying these cellular defects was the increase in *PIC2* expression that I had detected in the ∆ Nab3 RNA-BSs strain (Figure IV.22A). Accordingly, the next section of this work will focus on testing whether the observed phenotypes indeed arose from an increase in the expression of Pic2. Despite being compatible with such a model, my results evidenced that the proportion of the increase in *PIC2* mRNA abundance and the accompanying defects specifically co-segregated with the imbalance of Nab3 and Nrd1 binding. In other words, while strains only lacking Nab3 binding sites in *PIC2* (i.e., ∆ Nab3 RNA-BSs and ∆ Nab3 RNA-BSs #2) exhibited the highest *PIC2* mRNA increases and the most discernible phenotypes, both features became slightly milder in the partial ∆ NNS RNA-BSs mutant and were almost imperceptible in the ∆ NNS RNA-BSs. Of course, it is possible that such differences reside in the effects that additional single-point nucleotide substitutions had on the stability of the *PIC2* transcripts in the mutants lacking some or all Nrd1 binding sites in *PIC2*. However, the genetic linkage between

the observed defects and the disruption of Nab3 RNA recognition sites in *PIC2* pointed towards a scenario where the imbalance in Nab3 and Nrd1 recruitment to a slightly overexpressed target (i.e., *PIC2*) was affecting how NNS binds to other RNA substrates (Figure IV.22B). In the remaining two results chapters of this work, I will present the work I did to test both models as well as my interpretation of the findings in support of or against these two hypotheses.

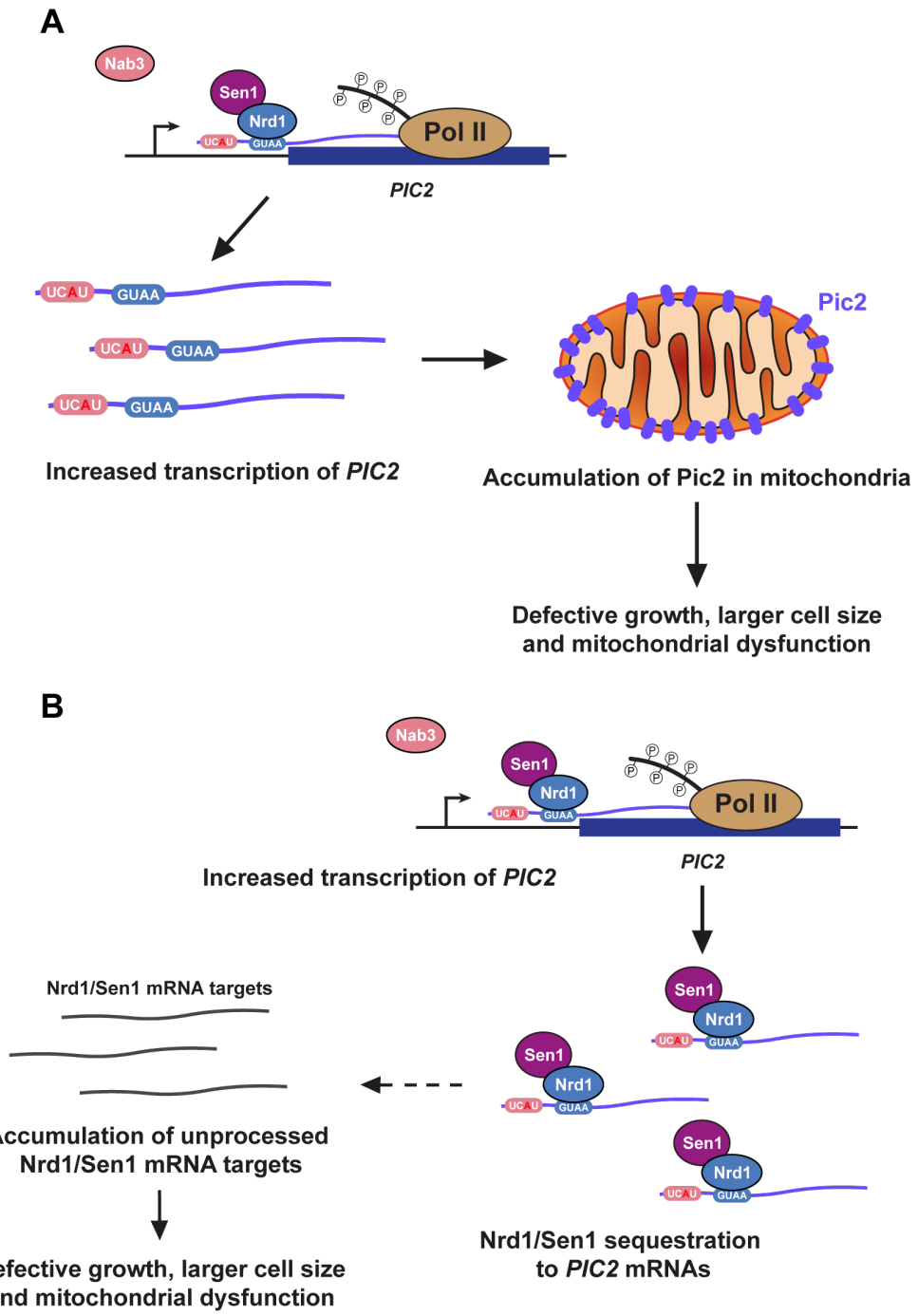

Figure IV.22. Schematic summary of the hypothesised mechanisms explaining the features and phenotypes described in chapters III and IV.

V. Deviations from Wild-type Levels of Pic2 Decrease Yeast and Mammalian Cell Fitness and Adaptability

V.1. Introduction

In the previous chapter, I presented a full phenotypic characterisation of the mutants with Nab3 and Nrd1 mutations in *PIC2*. So far, I have provided evidence showing that specifically abrogating Nab3 cognate sites while preserving those of Nrd1 caused excessive cell size, cell cycle prolongations, mitochondrial hyperpolarisation and resistance to oxidative stress. I have also proposed that the molecular basis for such defects could be either the enhanced expression of *PIC2* in strains encoding such mutations or a broader *PIC2* mRNA-driven alteration of NNS regulation of the transcriptome. Naturally, the most likely scenario was that merely increasing Pic2 levels somehow underlay the observed anomalies.

To test this hypothesis, I assembled a strain in which *PIC2* expression was driven by the promoter of *TEF1*, which was found to be the most abundant transcript in the RNA sequencing datasets that I had obtained for *PIC2-GFP* and derived mutants in medium containing 1% (w/v) raffinose (Figure III.13A). My expectation was that if the anomalies in ∆ Nab3 RNA-BSs stemmed from an abnormally high expression of *PIC2*, such features should also be present or aggravated in the *pTEF1-PIC2* mutant. However, the phenotypic characterisation of that strain illustrated that the energy homeostasis defects in the *pTEF1-PIC2* mutant were different from those of the ∆ Nab3 RNA-BSs strain.

Throughout these investigations, I also aimed to gain a deeper understanding of the evolutionary pressure which had favoured stringent mechanisms of *PIC2* expression control in eukaryotes. Firstly, to benchmark my findings against those of previous studies, I engineered and characterised a strain in which *PIC2* was knocked out (Vest et al., 2013). As previously reported, such strain displayed severe growth

defects that, according to the work presented in this chapter, are also accompanied by mitochondrial membrane hyperpolarisation and impaired basal respiration. Altogether, these results underscored the biological importance of avoiding suboptimal expression patterns of *PIC2* which, as I will show in the next few pages, was specifically disadvantageous in adverse environments.

As I explained in I.5., *PIC2* is a conserved mitochondrial phosphate and copper carrier with a mammalian homologue, *SLC25A3* (Boulet et al., 2017). As its yeast counterpart, *SLC25A3* displayed remarkably low transcriptional noise (Figure I.6). Consistent with such a tightly controlled expression pattern, which is known to be exerted by a miRNA (Baseler et al., 2012), mutations affecting the levels of expression of *SLC25A3* have been linked to cardiac and muscular diseases (Mayr et al., 2007). Considering the physiological role of Pic2/SLC25A3, the serious consequences of suboptimally expressing them and the stringent regulatory mechanisms to which their encoding genes are subject, I sought to gain further insight into the molecular steps by which increased expression of *PIC2/SLC25A3* drove cellular defects. For this purpose, I generated a SLC25A3-overexpressing mammalian model which fully recapitulated the phenotypes of the *PIC2* overexpression yeast strain.

Despite having provided insight into the mechanistic basis for the defects strictly driven by anomalous Pic2 levels, the results compiled in this chapter show that deviations from the optimal expression of *PIC2* do not cause the cell size or cell cycle aberrations that I had identified in the ∆ Nab3 RNA-BSs mutant. The source of these defects will be later reviewed in chapter VI.

V.2. Overexpression or deletion of *PIC2* delays cell growth during environmental challenges and decreases cell fitness.

Having characterised the ∆ Nab3 RNA-BSs mutant, I aimed to identify the mechanism underpinning the described growth, cell size, cell cycle and energy homeostasis defects. The simplest justification for these anomalies was that they merely emerged from an increase in the abundance and activity of Pic2. To test this, I transformed a non-fluorescent parental strain with a vector encoding *PIC2* downstream a strong *pTEF1* promoter (Figures V.1-3): if a higher expression of Pic2 was indeed

driving the described anomalies, the resulting Pic2 overexpressing strain should recapitulate or exacerbate all defects.

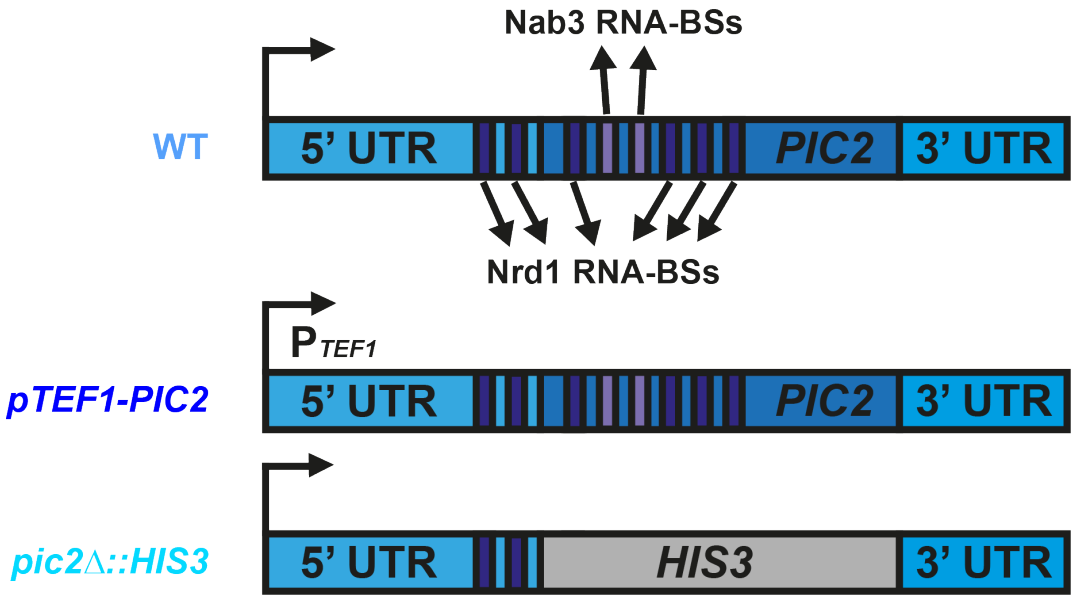

Figure V.1. Schematic summary of the mutations in the Δ Nab3 RNA-BSs and Δ NNS RNA-BSs mutants derived from the parental *PIC2-GFP* strain.

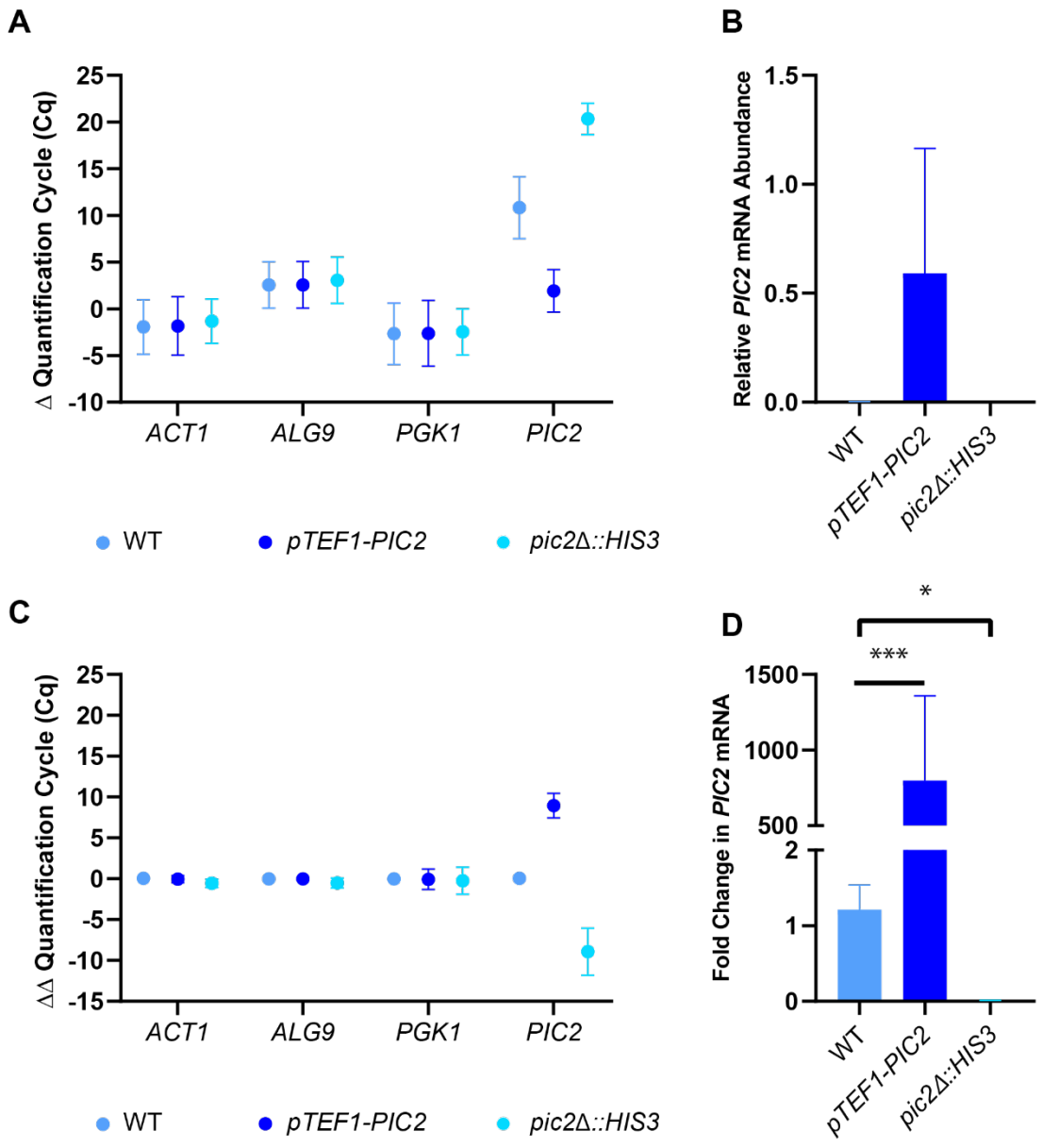

Figure V.2. RT-qPCR quantification of *PIC2* mRNA in the WT, *pTEF1-PIC2* and *pic2Δ::HIS3* strains when grown in SC -Ura medium containing 2% (w/v) raffinose. **A**. Normalisation of raw quantification cycle (Cq) values to the median Cq of the reference genes within their own sample. **B**. Calculated ΔCqs for *PIC2* were used to derive a relative *PIC2* mRNA abundance within each condition. **C**. Median ΔCq values of each tested gene were normalised to those of the parental strain (i.e., WT) to determine the differential ΔCq (ΔΔCq) values. **D**. These ΔΔCqs were exponentially transformed to find the fold change in mRNA abundance with respect to the reference sample. Data shows the mean of three biological repeats for each condition. Error bars represent standard deviation (SD). Statistical comparison of the fold change in *PIC2* mRNA of both mutants with respect to the parental WT reference was performed by unpaired t-tests: *: $p<0.05$, ***: $p<0.001$ and 'ns': $p>0.05$.

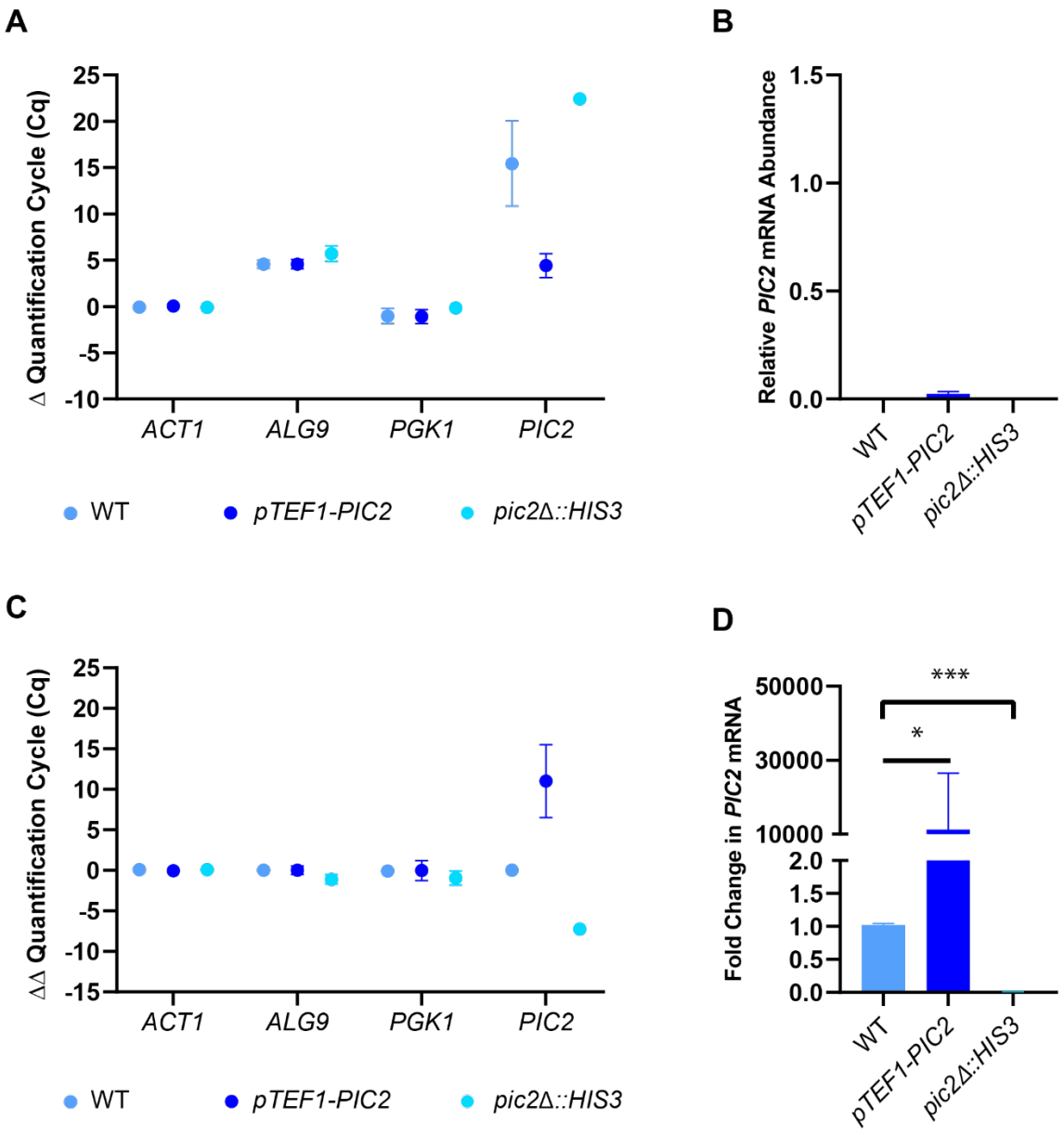

Figure V.3. RT-qPCR quantification of *PIC2* mRNA in the WT, *pTEF1-PIC2* and *pic2Δ::HIS3* strains when grown in SC -Ura medium containing 1% (w/v) raffinose. **A**. Normalisation of raw quantification cycle (Cq) values to the median Cq of the reference genes within their own sample. **B**. Calculated ΔCqs for *PIC2* were used to derive a relative *PIC2* mRNA abundance within each condition. **C**. Median ΔCq values of each tested gene were normalised to those of the parental strain (i.e., WT) to determine the differential ΔCq (ΔΔCq) values. **D**. These ΔΔCqs were exponentially transformed to find the fold change in mRNA abundance with respect to the reference sample. Data shows the mean of three biological repeats for each condition. Error bars represent standard deviation (SD). Statistical comparison of the fold change in *PIC2* mRNA of both mutants with respect to the parental WT reference was performed by unpaired t-tests: *: $p<0.05$, ***: $p<0.001$ and 'ns': $p>0.05$.

To span the scope of phenotypic consequences caused by changes in the expression of *PIC2*, I generated a *pic2Δ::HIS3* knock-out mutant (Figures V.1-3). Preventing expression of its product protein was previously shown to cause a clear growth defect (Vest et al., 2013), which I expected to reproduce before proceeding further with its characterisation. After engineering the strains, I characterised the growth of both mutants. Briefly, I tracked the progression of a freshly inoculated 200 µL-culture of each strain in raffinose-rich (i.e., 2% (w/v)) and raffinose-deprived (i.e., 1% (w/v)) media (Figure V.4). Since optical density (OD_{600}) readings mirror the microbial number or concentration in low-density cultures, a time-resolved OD_{600} monitoring of cultures inoculated at a starting OD_{600} of 0.01 could determine the growth patterns of Pic2-overexpressing and Pic2-lacking mutants (see II.9 for technical details) (Figure V.4).

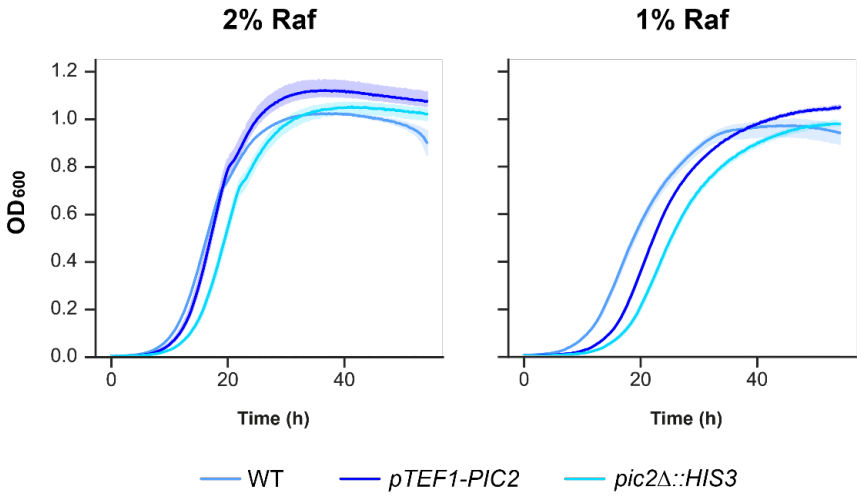

Figure V.4. Time-resolved optical density (OD_{600}) of the WT, *pTEF1-PIC2* and *pic2Δ::HIS3* strains. Lines show the mean of the three technical replicates in one of the biological duplicates performed for this experiment. Shown graphs are representative of those of the additional repeat.

In line with previous work (Vest et al., 2013), the *pic2Δ::HIS3* mutant suffered a growth defect when grown in the presence of a poorly fermentable carbon source (Figure V.4). However, unlike the Δ Nab3 RNA-BSs mutant, the *PIC2* overexpressing strain grew slightly better than its parental reference in medium containing 2% (w/v) raffinose. Intriguingly, this fitness benefit not only disappeared in low sugar concentrations (i.e., medium supplemented with 1% (w/v) raffinose) but was replaced with a significant growth delay with respect to the parental BY4741 strain (Figure V.4). Overall, my preliminary growth characterisation evoked a scenario in which Pic2

absence was always penalised in the presence of a semi-respirable sugar regardless of the concentration. On the other hand, it appeared that while Pic2 overabundance bestowed cells with a fitness advantage at optimal nutrient-rich conditions, it also constituted a liability during raffinose scarcity.

To confirm the respective fitness benefits and costs in the tested conditions, I performed competition experiments by culturing the assessed strain against a fluorescent wild-type reference (Figure V.5). As outlined in II.11 and IV. 3, strains were individually co-cultured with a fluorescent reference strain in which a mCherry epitope had been introduced downstream *URA8*. After inoculating the pertinent strain and the fluorescent reference at an identical initial OD_{600}, cultures were sampled at 18-hour intervals to monitor the progression of non-fluorescent and fluorescent populations using flow cytometry. Individual cells were classified into non-fluorescent and fluorescent populations based on the red fluorescence values; cells exceeding a previously established gate would be considered fluorescent, and those exhibiting fluorescent values lower than those of the threshold would be deemed non-fluorescent. As described in IV.4, the filter was set according to the distribution of red fluorescence values obtained from cultures containing fluorescent (i.e., Ura8-mCherry) and non-red fluorescent (*PIC2-GFP*) cells. Having extracted the average non-fluorescent:fluorescent ratio and associated standard deviation for the separate triplicates that I performed for the WT, *pTEF1-PIC2* and *pic2*Δ*::HIS3* strains (Figure V.5), I then normalised the mean ratios to that of the parental WT in the relevant condition. This enabled a direct comparison of the relative fitness of each mutant to that of the strain from which they were derived (Figure V.5).

As shown in Figure V.5, the results of the competition assays were consistent with the growth profiles that I had previously recorded in the microplate reader (Figure V.4). In raffinose-abundant (i.e., 2% (w/v)) medium, *pic2*Δ*::HIS3* consistently displayed lower mean counts than the fluorescent reference throughout the entire experiment and, ultimately, the decrease became significant with respect to WT performance in the last time point (Figure V.5A). Conversely, the *pTEF1-PIC2* mutant increased its normalised population fraction throughout the experiment and ended up significantly surpassing that of WT 60 hours after inoculation (Figure V.5A). Importantly, however, the topography of its comparative fitness in raffinose-limiting medium (i.e., 1 (w/v)) was noticeably different (Figure V.5B). In this case, *pTEF1-PIC2* became outcompeted by

the fluorescent reference and such fitness defect was already significant after 36 hours of competition (Figure V.5B). Similarly, the *pic2Δ::HIS3* mutant was also less fit than its parental WT during sugar deprivation (Figure V.5B). Nevertheless, unlike *pTEF1-PIC2*, this handicap only became significant in the third time point of the assay. Cumulatively, these findings consolidate the notion that while insufficient expression of Pic2 was pernicious in all circumstances, enhanced Pic2 levels were beneficial in raffinose-abundant conditions but represented a drawback during nutritional challenges.

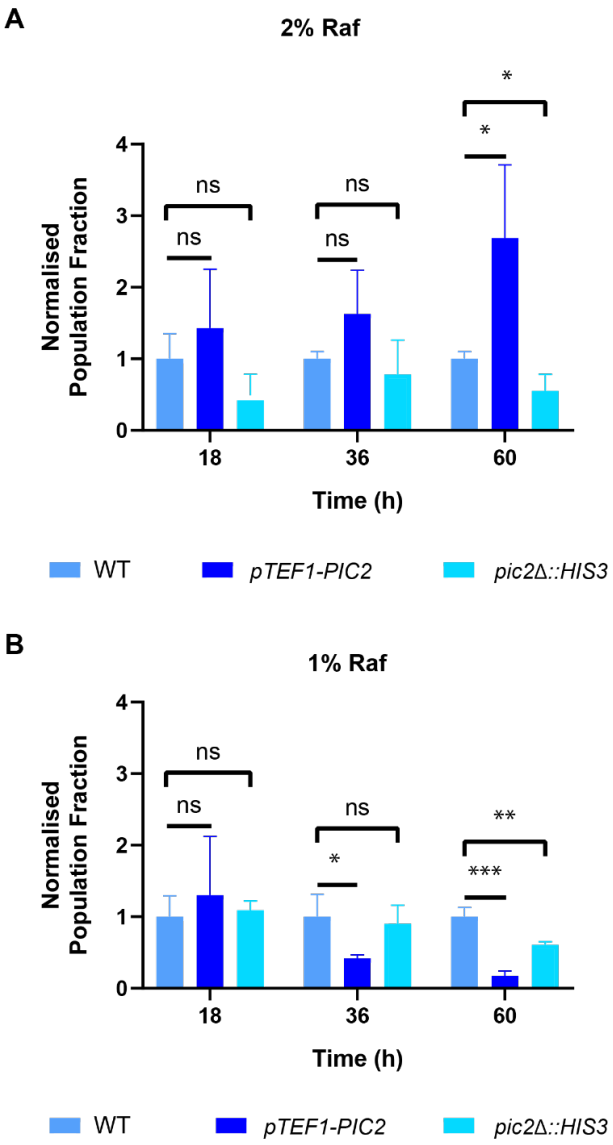

Figure V.5. Competition assays comparing the fitness of the parental strain (WT) with that of *pTEF1-PIC2* and *pic2Δ::HIS3*. Bar plots display the log_2-transformed fold changes of the population fraction of tested strains (i.e., WT, *pTEF1-PIC2*, and *pic2Δ::HIS3*) against a fluorescent reference. Values shown are averages and standard deviations from biological triplicates normalised to the fold changes observed in the parental strain.

To expand on the implications of these results, I determined whether Pic2 overexpression would also impose a fitness restriction during another type of environmental insult, namely oxidative stress. To test this, I applied the oxidative stress assays described in II.15 and previously applied in IV.7. I compared the maximal growth rate of the examined strains in cultures lacking hydrogen peroxide to the one which they exhibited upon the addition of said reactive oxygen species. Having performed microplate reader growth assays in the presence and absence of hydrogen peroxide, I demonstrated that, indeed, Pic2-overexpressing cells displayed a greater decrease in maximal growth rate when exposed to oxidative stress in medium containing 2% (w/v) raffinose (Figure V.6). In line with enhanced tolerance of stressed cells to subsequent challenges, the reduction in the growth rate in *pTEF1-PIC2* upon oxidative stress induction was not significantly lower than that of its wild-type (WT) counterparts (Figure V.6). Similarly, *pic2*Δ*::HIS3* were not differently affected by hydrogen peroxide addition at any of the two raffinose concentrations tested (Figure V.6). In summary, these assays illustrate that whereas *PIC2* overexpression was advantageous in nutrient-abundant conditions, it rendered cells significantly more vulnerable to nutritional and oxidative challenges. Again, in line with the growth and fitness assays, the *PIC2* deletion strain was equally disadvantaged in all tested conditions (Figure V.6).

This evidence provided an evolutionary explanation for why a stress-specific suppression mechanism such as NNS-mediated mRNA premature termination is required to tightly regulate the expression of such transporter during adaptation. However, these data demonstrated that the growth patterns of *pTEF1-PIC2* did not recapitulate those of the Δ Nab3 RNA-BSs mutant and, instead, presented substantially different features. Firstly, unlike Δ Nab3 RNA-BSs, the *pTEF1-PIC2* strain showed enhanced growth and fitness in medium containing 2% (w/v). Secondly, contrasting with the stress resistance that I had characterised in the Δ Nab3 RNA-BSs mutant independently from the sugar concentration tested (see IV.7), *pTEF1-PIC2* presented hypersensitivity to oxidative stress when grown in 2% (w/v) raffinose and no significant changes with respect to WT in medium supplemented with 1% (w/v) raffinose. Thus, my results also suggested that stress-derived energy homeostasis defects overpower the Pic2-driven ones in the Δ Nab3 RNA-BSs strain.

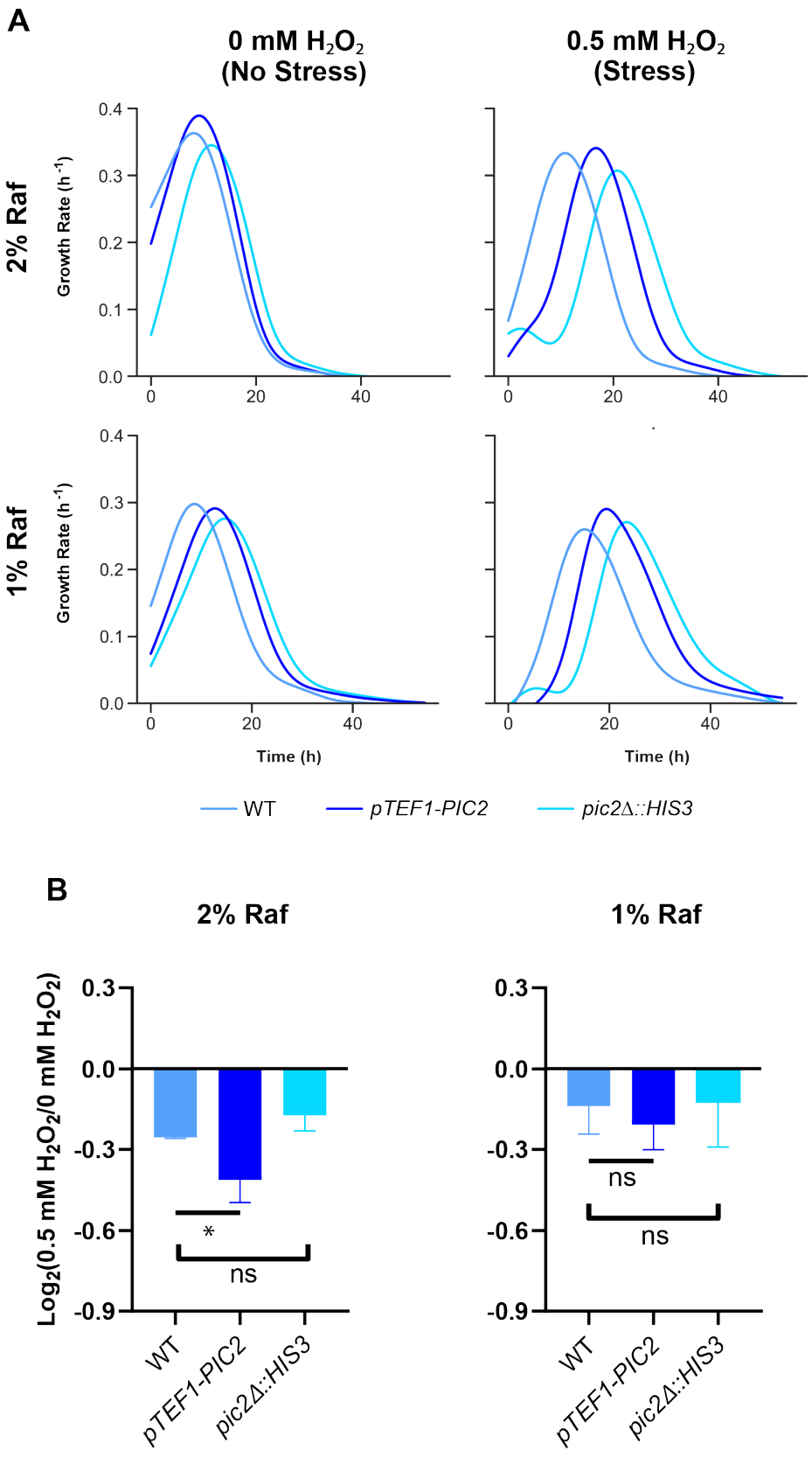

Figure V.6. Oxidative stress assays comparing the change in the growth rate of WT, *pTEF1-PIC2*, and *pic2*Δ*::HIS3* in medium lacking hydrogen peroxide to those which they display upon addition of hydrogen peroxide. **A.** Time-resolved growth rate computed for WT, *pTEF1-PIC2*, and *pic2*Δ*::HIS3* strains in medium supplemented with

high (i.e., 2% (w/v)) and low (i.e., 1% (w/v)) raffinose concentrations and containing either 0 mM or 0.5 mM of hydrogen peroxide (H_2O_2). **B**. Change in the maximum growth rate for WT, *pTEF1-PIC2*, and *pic2*Δ*::HIS3* populations when exposed to 0.5 mM of hydrogen peroxide (H_2O_2). Fold changes in growth rates were calculated as the binary logarithm of the ratio of the maximum growth rates recorded in the stressful medium (i.e., containing 0.5 mM H2O2) to the ones derived in the innocuous medium. Error bars represent standard deviations, which were accordingly propagated from the ones predicted by Omniplate. Statistical comparisons between each mutant and their parental WT strain were conducted by unpaired t-tests. *: $p<0.05$, ***: $p<0.001$ and 'ns': $p>0.05$.

To verify this hypothesis, I quantified the NADH/NAD^+ ratio of the Pic2-overexpressing and Pic2-lacking mutants and their wild-type BY4741 reference. As explained in IV.7 and technically detailed in II.21, the state of the NAD(P) pool is dictated by cellular metabolism and energy homeostasis. While decreased NADH/NAD^+ balances are generally indicative of increased oxidative metabolism and higher levels of intracellular reactive oxygen species, an enhanced NADH/NAD^+ ratio is typically reflective of reductive stress (Yang and Sauve, 2016).

Exploiting the fact that NADH and NADPH emit light of approximately 460 nm in wavelength upon excitation by UV radiation, the presence of both reduced coenzymes can be monitored as a blue fluorescent signal after exposing the examined cultures to UV light. Accordingly, I assessed the status of the nicotinamide adenine dinucleotide (NAD(P)) pool in both strains using fluorescence measurements of a microplate reader assay as detailed in II.21. Importantly, nonetheless, the NADP pool is less abundant than the NAD one and significantly less prone to oxidation changes than the latter, as it is mostly kept in its reduced state. Thus, contributions to this set of measurements are predominantly dominated by changes in the NAD pool. In line with their susceptibility to hydrogen peroxide addition, the redox state of the NAD species in *pTEF1-PIC2* and *pic2*Δ*::HIS3* did not significantly differ from that of their WT reference (Figure V.7).

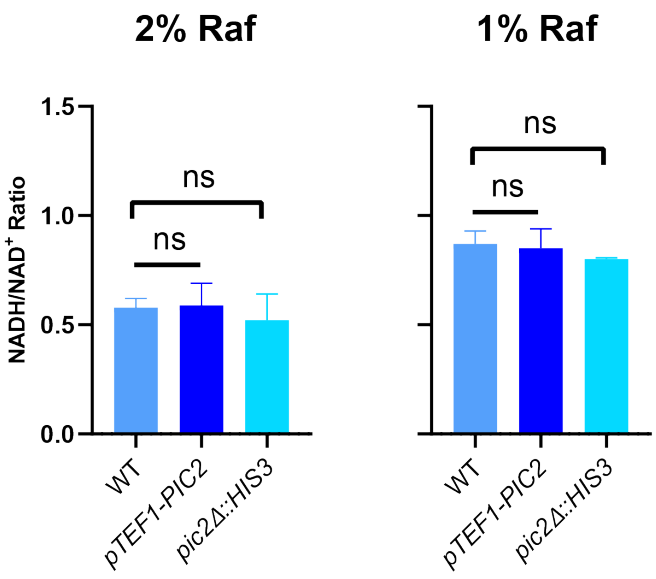

Figure V.7. Mean NADH/NAD⁺ ratios calculated based on three independent fluorescence assays of WT, *pTEF1-PIC2*, and *pic2Δ::HIS3* grown in media containing either 2% (w/v) or 1% (w/v) raffinose. Error bars represent the standard deviation of three biological repeats. Statistical comparisons between each mutant and their parental WT strain were conducted by unpaired t-tests. *: $p<0.05$, **: $p<0.01$ and 'ns': $p>0.05$.

Overall, the experiments described in this section illustrate that far from resembling or amplifying the phenotypes identified in the Δ Nab3 RNA-BSs mutant, *pTEF1-PIC2* exhibited discordant growth, fitness and stress tolerance capabilities when compared to the former. Critically, overexpressing Pic2 was detrimental for cells facing any deviation from the optimal growth conditions and so, provided an explanation for targeted NNS stress-specific repression and noise suppression of the *PIC2* gene.

V.3. Yeast cells with suboptimal levels of Pic2 display mitochondrial hyperpolarisation.

Considering the physiological role of Pic2 as a phosphate/proton symporter and a copper uniporter, I anticipated that lowering or exaggerating its abundance in the inner mitochondrial membrane would probably disturb the charge homeostasis at each of its sides and, consequently, drive alterations in the mitochondrial membrane polarisation. Moreover, I expected that gaining more insight into the mitochondrial activity of these

mutants could shed light on the discrepancies that I had detected between the *pTEF1-PIC2* mutant and ∆ Nab3 RNA-BSs and guide additional experiments to identify the underlying cause of such incongruences.

With this aim, I quantified mitochondrial membrane potential using the technical approaches which I described in the preceding chapter, namely (i) MitoTracker™ Red CMXRos staining prior to flow cytometry-based fluorescence assessment and (ii) TMRM staining before confocal microscopy imaging and evaluation of corrected and normalised dye accumulation. Firstly, I proceeded to inspect the mitochondrial activity of cells from mid-logarithmic WT, *pTEF1-PIC2* and *pic2∆::HIS3* cultures by staining them with MitoTracker™ Red CMXRos. In this case, the mitochondrial membrane potential-sensitive MitoTracker™ Red CMXRos fluorescent signal was normalised to the green fluorescent signal of MitoTracker™ Green FM, which reportedly binds to mitochondria regardless of their mitochondrial membrane potential. This normalisation is a widely used strategy to ascertain that MitoTracker™ Red CMXRos changes do not stem from differences in mitochondrial mass but from mitochondrial activity (Cottet-Rousselle et al., 2011).

After gathering the flow cytometry data, I divided the median MitoTracker™ Red CMXRos fluorescence signal by the median MitoTracker™ green fluorescence signal. By normalising mitochondrial activity by mitochondrial mass, I obtained the corrected mitochondrial membrane potential value for the parental WT and then expressed all other net mean red fluorescence values as a percentage of the one measured for the reference. Considering the errors calculated from the three biological replicates that were performed for each strain and condition, I could statistically compare the mutants to WT. Ultimately, I found that both mutants displayed mitochondrial membrane hyperpolarisation independently from the sugar concentration in the medium. Interestingly, despite lying on opposing extremes of the Pic2 expression spectrum, abnormal mitochondrial activity was common in both mutants. Moreover, in this case, it appeared that *a priori*, increased mitochondrial membrane potential could be a common defect in the ∆ Nab3 RNA-BSs and *pTEF1-PIC2* strains. Although notably, the mitochondrial membrane hyperpolarisation described in the former was 50% greater than the increase in mitochondrial membrane potential detected in the latter.

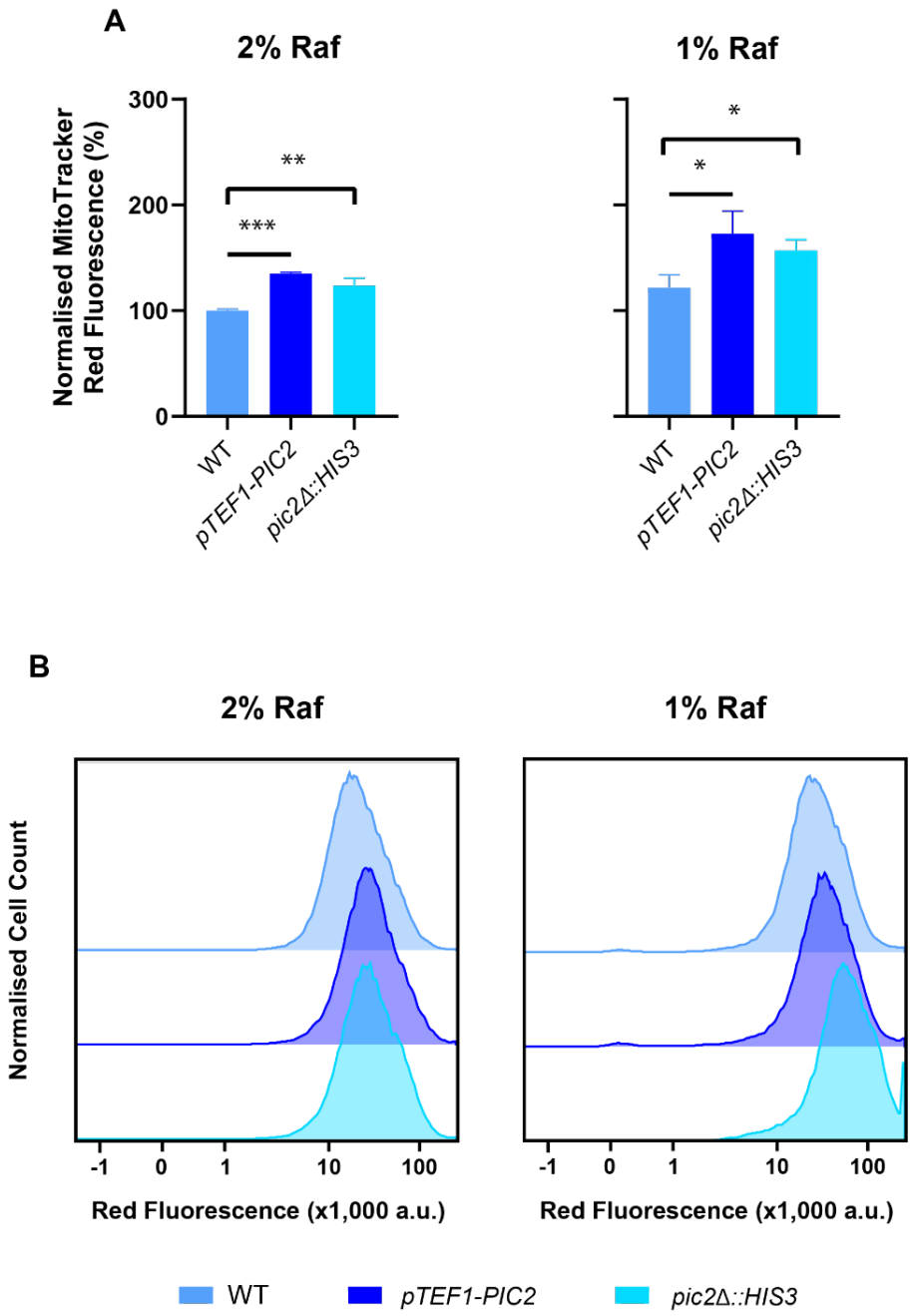

Figure V.8. Mitochondrial membrane potential measurements of MitoTracker™ Red CMXRos by flow cytometry uncovered mitochondrial hyperpolarisation in the *pTEF1-PIC2* and *pic2Δ::HIS3* mutants. **A**. Medians for single-cell red fluorescence emissions were normalised to the corresponding median forward scattering value. The bar graph shows the weighted average and standard deviation of the mentioned ratio across three biological batches containing more than 50,000 cells. Statistical comparisons between each mutant and the *PIC2-GFP* reference were performed by an unpaired t-test. *: $p<0.05$, **: $p<0.01$ and 'ns': $p>0.05$. **B**. Representative flow cytometry traces of the MitoTracker™ Red CMXRos staining distribution of WT, *pTEF1-PIC2* and *pic2Δ::HIS3* strains at mid-log phase (OD_{600} ~0.5).

Since the magnitude of the mitochondrial membrane potential increase in *pTEF1-PIC2* was lower than the one identified in the ∆ Nab3 RNA-BSs mutant, I questioned whether the hyperpolarisation measured in *pTEF1-PIC2* would be high enough to be detected by a less noisy technical approach such as TMRM quantification in confocal microscopy imaging. I imaged untreated cells to guarantee that no background red fluorescence was included in the analysis (Figures V.9-10). Furthermore, to verify that TMRM was solely retained by functional mitochondria (Figures V.9-10), I acquired images of WT, *pTEF1-PIC2* and *pic2∆::HIS3* cells in which the mitochondrial membrane potential had been previously chemically dissipated (Figures V.9-10). Mitochondrial membrane potential collapse was attained by treating cells with carbonyl cyanide-p-trifluoromethoxyphenylhydrazone (FCCP), a strong uncoupler of oxidative phosphorylation, which depolarises the inner mitochondrial membrane by enabling the free transit of protons between the mitochondrial matrix and the intermembrane space (Figures V.9-10).

Having measured the maximum filtered red fluorescence of at least 50 cells from three independent cultures of each strain in both tested conditions and subsequently normalised it to that of the parental reference, I was able to confirm that mitochondria in both mutants were hyperpolarised in low raffinose (i.e., 1% (w/v)) medium (Figure V.11). Although the increase in mitochondrial membrane potential was deemed significant by an unpaired t-test, the difference between the mitochondrial membrane potential of all strains grown in high raffinose (i.e., 2% (w/v)) medium was seldom visibly noticeable (Figure V.11). Cumulatively, these results suggest that contrary to that detected in the ∆ Nab3 RNA-BSs mutant, the mitochondrial membrane hyperpolarisation described in *pTEF1-PIC2* and *pic2∆::HIS3* cells worsened during nutrient deprivation (Figure V.11). In turn, this pattern hinted that the molecular phenomena driving an increase in the mitochondrial membrane potential of the Pic2-overexpressing and Pic2-lacking mutants was different from that of the ∆ Nab3 RNA-BSs strain.

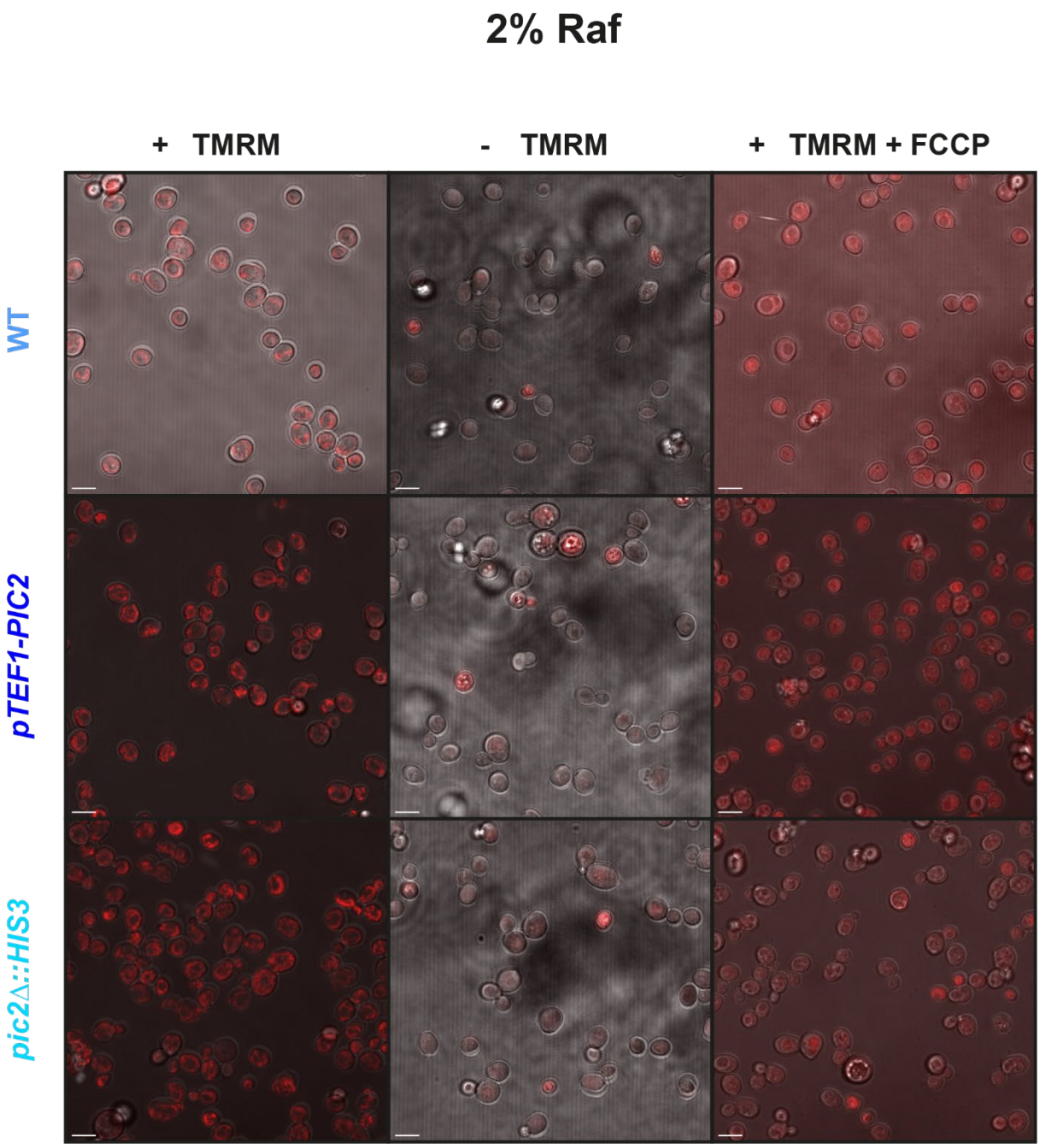

Figure V.9. Representative confocal microscopy images of stained (+TMRM), unstained (-TMRM) and stained and depolarised (+TMRM + FCCP) WT, *pTEF1-PIC2* and *pic2*Δ*::HIS3* cells grown in SC -Ura medium supplemented with 2% (w/v) raffinose. Whereas -TMRM and +TMRM + FCCP images constituted negative controls to test the specificity and functionality of the dye, the +TMRM images were used to calculate the normalised TMRM fluorescence measured in Figure V.11. Scale bar represents 5 μm.

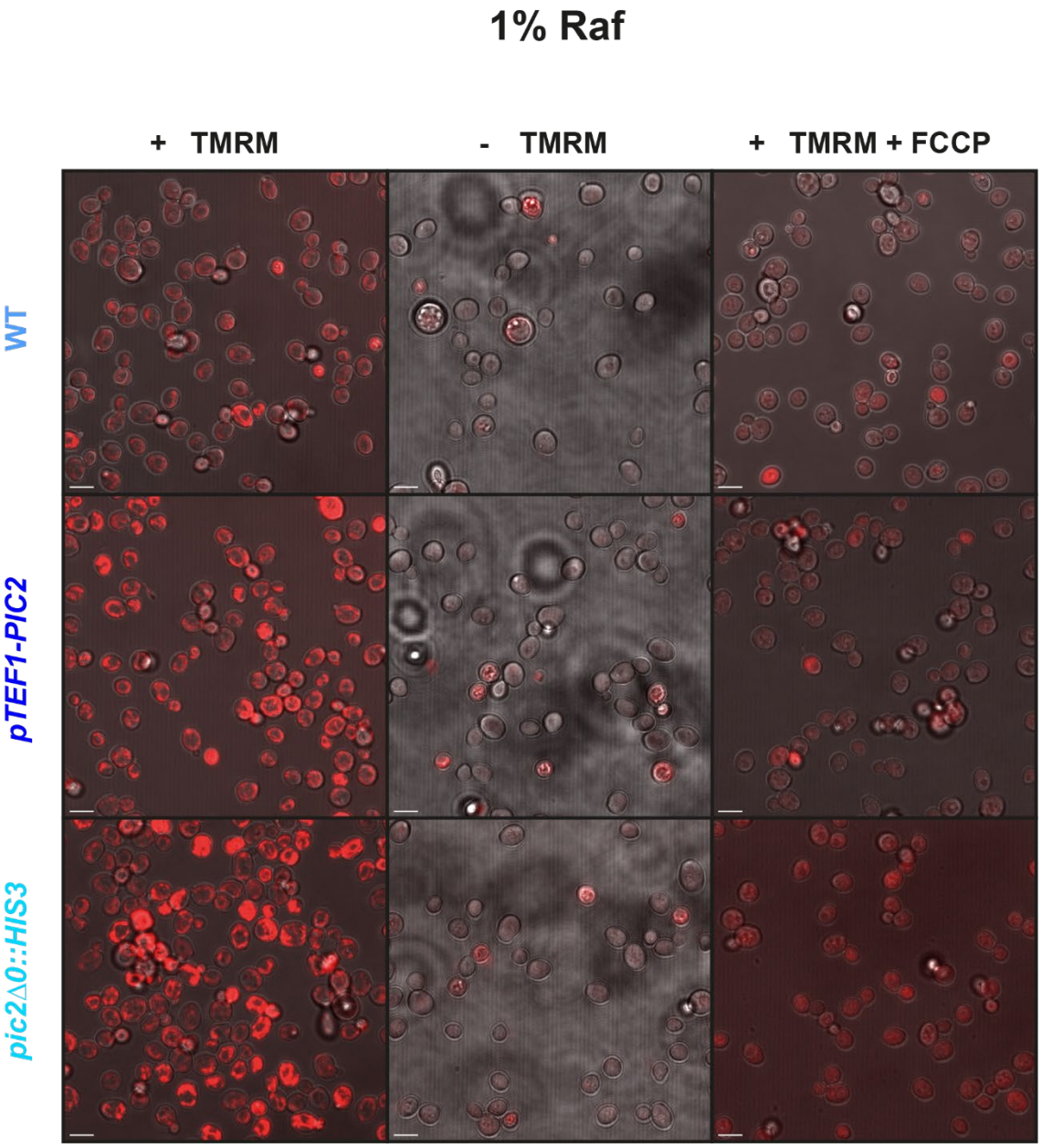

Figure V.10. Representative confocal microscopy images of stained (+TMRM), unstained (-TMRM) and stained and depolarised (+TMRM + FCCP) WT, *pTEF1-PIC2* and *pic2*Δ*::HIS3* cells grown in SC -Ura medium supplemented with 1% (w/v) raffinose. Whereas -TMRM and +TMRM + FCCP images constituted negative controls to test the specificity and functionality of the dye, the +TMRM images were used to calculate the normalised TMRM fluorescence measured in Figure V.11. Scale bar represents 5 μm.

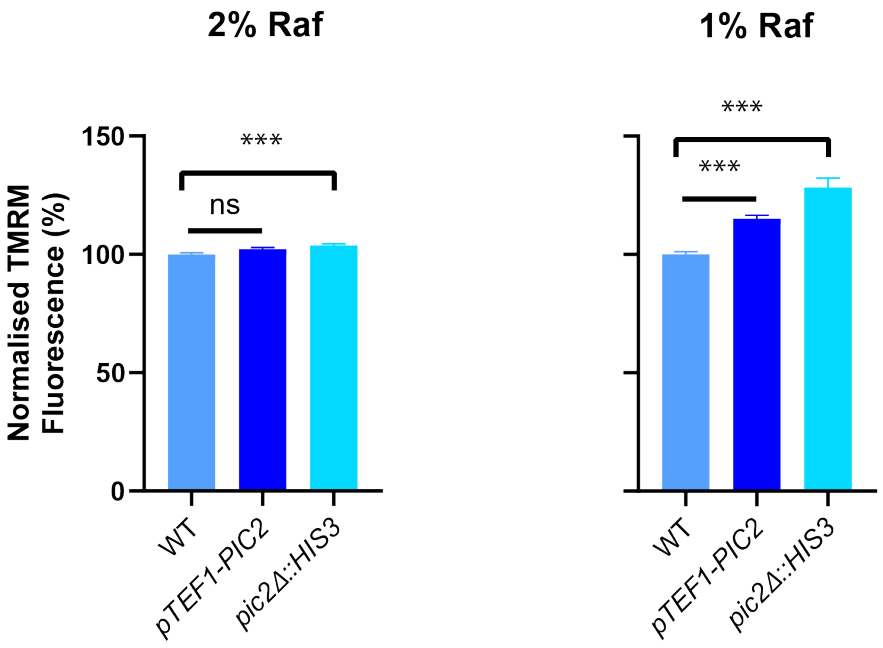

Figure V.11. Mean normalised TMRM fluorescence values gathered from confocal imaging of more than 50 cells from three independent biological repeats for WT*,* *pTEF1-PIC2* and *pic2*Δ*::HIS3.* Error bars represent the standard error of the mean (SEM). Statistical comparisons between each mutant and their parental WT were conducted by unpaired t-tests. *: p<0.05, ***: p<0.001 and 'ns': p>0.05.

To further reinforce that the energy homeostasis defect priming the mitochondrial hyperpolarisation detected in the Δ Nab3 RNA-BSs and *pTEF1-PIC2* mutants did not share a common origin, I performed mitochondrial membrane potential measurements in medium containing glucose. As demonstrated in III.2 and in line with glucose-induced repression of respiration (Rolland et al., 2002), the transcriptional abundance of *PIC2* in the presence of a fermentable sugar is much lower than in the presence of raffinose. Additionally, I conducted a microplate reader fluorescence assay to confirm that lower levels of *PIC2* mRNA abundance indeed resulted in restricted Pic2 protein levels among cells grown in glucose-containing medium (Figure V.12). Having validated this finding, I used MitoTracker™ Red CMXRos and flow cytometry to assess the mitochondrial activity of the fluorescent and non-fluroescent mutants in medium containing high and low glucose concentrations. The premise of this experiment was that if the root cause of the observed mitochondrial hyperpolarisation were an increase in the levels of Pic2, the increases in mitochondrial membrane potential would be attenuated or completely neutralised at a condition in which *PIC2* expression was kept to minimum levels. As depicted in Figure V.13, whereas the

mitochondrial membrane hyperpolarisation disappeared in the mutants with suboptimal expression of Pic2 (i.e., *pTEF1-PIC2* and *pic2Δ::HIS3*), Δ Nab3 RNA-BSs still displayed the same mitochondrial membrane potential increase in conditions in which *PIC2* was not highly expressed. Thus, these assays prove that while the energy homeostasis defects in the *pTEF1-PIC2* and *pic2Δ::HIS3* mutants were stemming from increased Pic2 abundance, those in the Δ Nab3 RNA-BSs strain were likely arising from a feature that was still affecting the strain even when *PIC2* expression was not very high. Again, this evidence supported the idea that stress-derived energy homeostasis defects in Δ Nab3 RNA-BSs appear to dominate its phenotype and, concomitantly, conceal any anomalies originating from enhanced Pic2 levels.

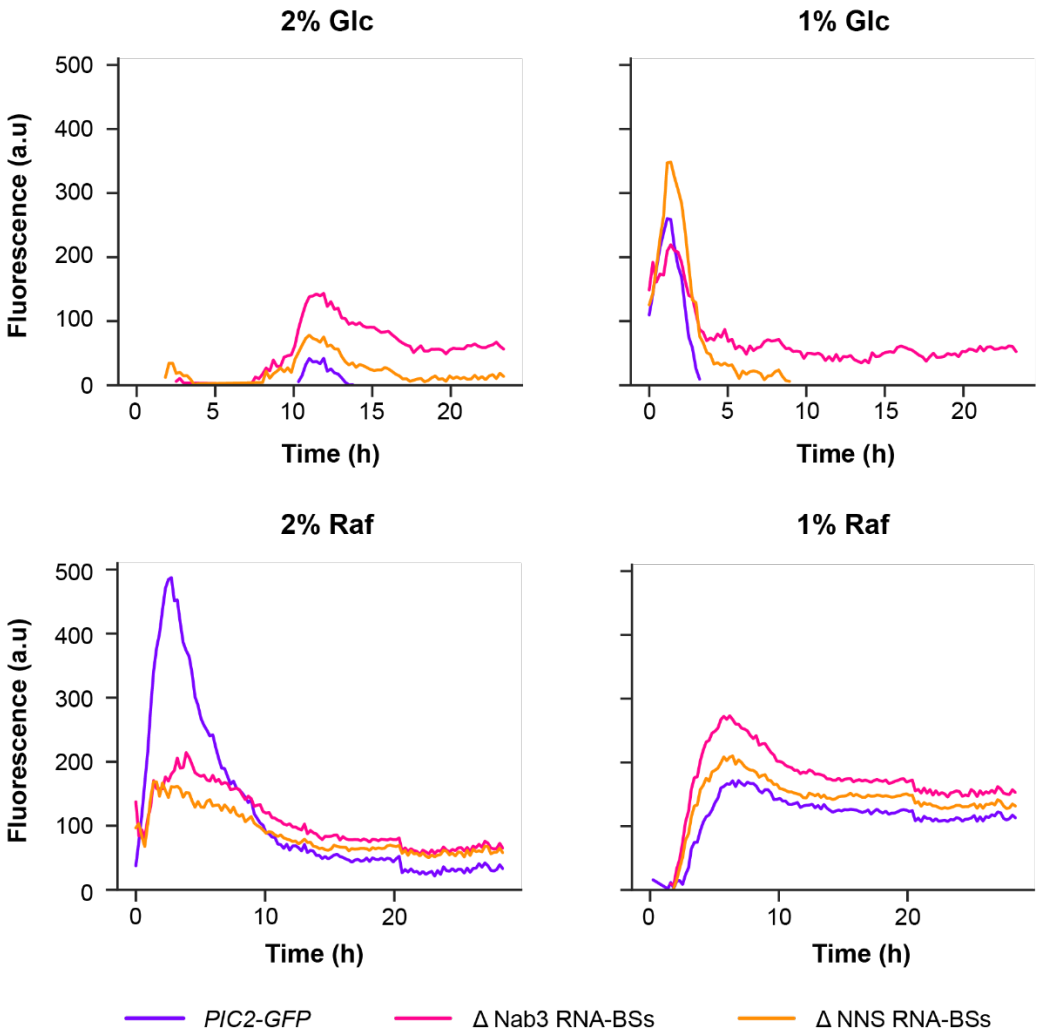

Figure V.12. Microplate reader recordings of Pic2-GFP expression (in arbitrary units) in the *PIC2-GFP*, Δ Nab3 RNA-BSs and Δ NNS RNA-BSs strains across time. Fluorescence values were normalised to those of the parental *PIC2-GFP* strain. Cells were grown in SC -Ura medium containing 2% (w/v) or 1% (w/v) of glucose or raffinose.

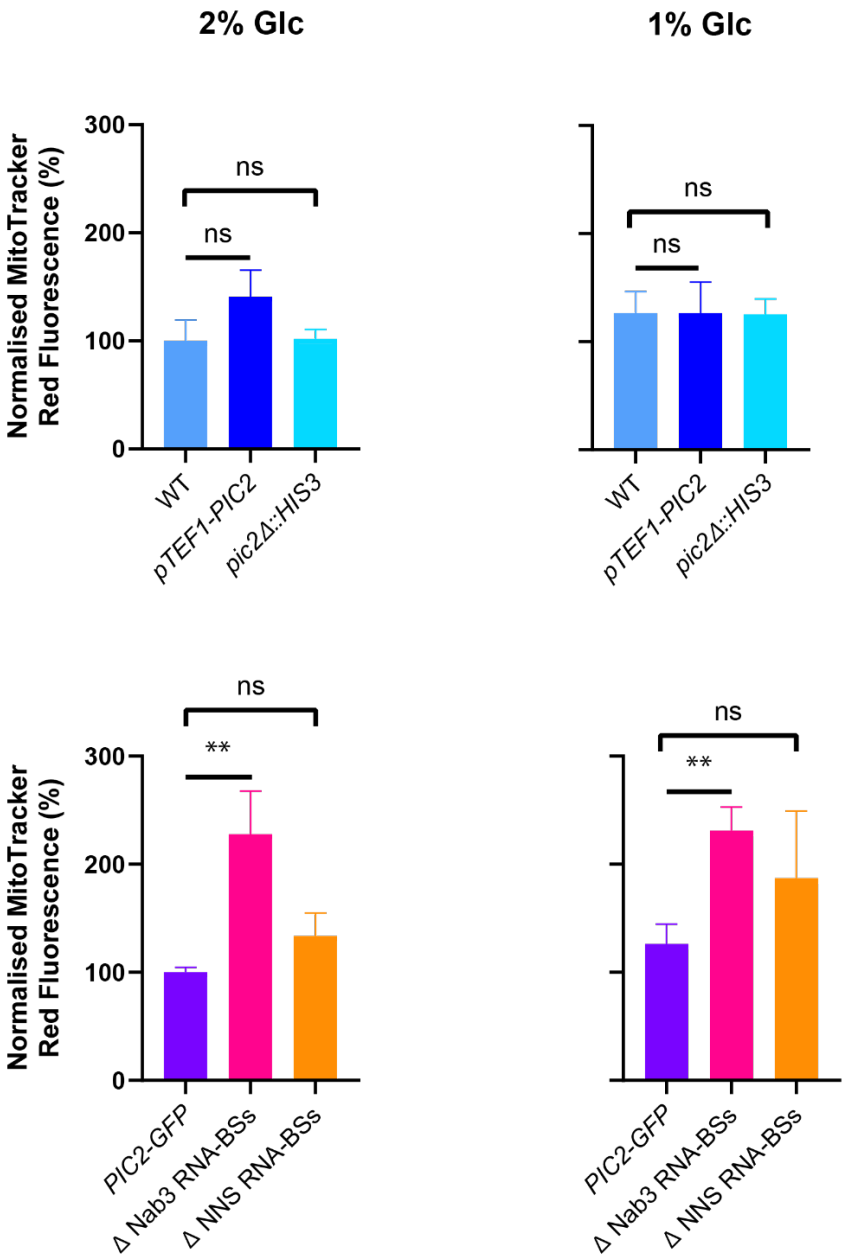

Figure V.13. Mitochondrial membrane potential measurements of MitoTracker™ Red CMXRos by flow cytometry uncovered mitochondrial hyperpolarisation in the *pTEF1-PIC2*, *pic2Δ::HIS3*, Δ Nab3 RNA-BSs and Δ NNS RNA-BSs mutants when grown in medium supplemented with 2% (w/v) or 1% (w/v) glucose. Medians for single-cell red fluorescence emissions were normalised to the corresponding median green fluorescence value. The bar graph shows the weighted average and standard deviation of the mentioned ratio across three biological batches containing more than 50,000 cells. Statistical comparisons between each mutant and the pertinent parental reference (i.e., WT for *pTEF1-PIC2* and *pic2Δ::HIS3*, and *PIC2-GFP* for , Δ Nab3 RNA-BSs and Δ NNS RNA-BSs) were performed by an unpaired t-test. *: $p<0.05$, **: $p<0.01$ and 'ns': $p>0.05$.

V.4. Suboptimal levels of Pic2 impair respiration.

Mitochondrial membrane hyperpolarisation can stem from different defects. Therefore, to explore the origin of such feature, I performed high-resolution respirometry using an oxygraph coupled to polarographic oxygen detectors. These units sense and quantify oxygen concentration in an isolated recipient enclosing the inspected solution. Before the start of the experiment, cells from cultures at mid-logarithmic growth phases were resuspended in a fresh volume of the same medium at an OD_{600} of 0.2. Oxygen consumption rates were derived by considering the estimated number of cells in the sample. Basal oxygen consumption rates evidenced that, while *pic2∆::HIS3* mutant maintained lower respiratory rates than its parental WT regardless of the sugar concentration in the medium, the *pTEF1-PIC2* strain endured decreased respiratory rates exclusively during raffinose scarcity (i.e., 1% (w/v)) (Figure V.14). Importantly, this posed an additional key difference with respect to ∆ Nab3 RNA-BSs, which accommodated higher basal respiratory rates than its parental reference at both tested raffinose concentrations (Figure V.14).

Moreover, to measure their maximal respiration rate, samples were exposed to FCCP. This uncoupling agent permeabilises the inner mitochondrial membrane and enables the transport of protons from the intermembrane space to the mitochondrial matrix, thereby disrupting mitochondrial membrane potential and stimulating oxygen consumption by complex IV activity to reach its maximum capacity. After obtaining the basal and maximal respiratory rates, I calculated the reserve respiratory capacity for each strain, which is a measurement of the spare respiration capabilities of a given set of cells to meet an energetic demand (Figure V.14). As shown in Figure V.14, none of the mutants displayed significantly different maximal respiration rates in medium containing 1% (w/v) raffinose and, consequently, did not exhibit any substantial modifications in their reserve respiratory capacity. Nonetheless, in the presence of a higher concentration of raffinose (i.e., 2% (w/v)), the maximum respiratory rate of *pTEF1-PIC2* and *pic2∆::HIS3* were slightly increased and substantially reduced compared to that of the parental WT strain, respectively. While the increase in the *pTEF1-PIC2* maximal respiratory rate was too subtle to elicit any improvements in its spare respiratory capacity, the decrease in that of *pic2∆::HIS3* was accompanied by a corresponding 10% reduction in the reserve respiratory capacity (Figure V.14).

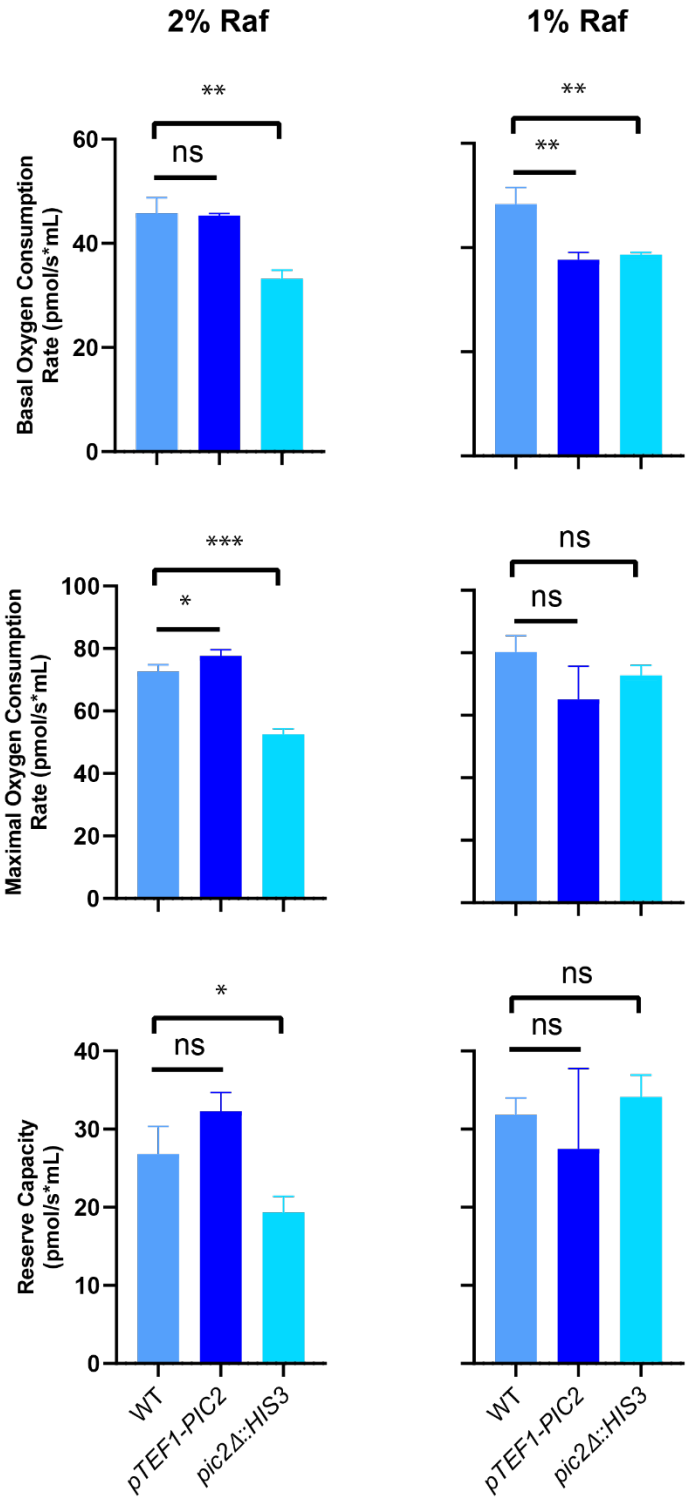

Figure V.14. Mean for the measured basal, maximal and reserve capacity oxygen consumption rates. Three separate respiration assays were performed for independent cultures of WT*, pTEF1-PIC2* and *pic2Δ::HIS3* grown in raffinose-abundant (i.e., 2% (w/v)) or raffinose-deprived (i.e., 1% (w/v)) medium. Error bars represent standard deviation of three biological replicates. Statistical comparisons between each mutant and their parental WT were conducted by unpaired t-tests. *: $p<0.05$, **: $p<0.01$ and 'ns': $p>0.05$.

Crucially, respirometry firmly established that the origin of the mitochondrial membrane hyperpolarisation in the Pic2-overexpressing strain was not the same as the one affecting the Δ Nab3 RNA-BSs mutant, as the former displayed impaired respiration at both tested raffinose concentrations, whereas the latter presented increased basal respiratory rates regardless of sugar concentration. Additionally, strains with suboptimal levels of *PIC2* displayed inhibited respiration in all the conditions at which they displayed growth defects (Figures V.4-6 and V.14). Cumulatively, these results verify that deviations from appropriate levels of Pic2 expression inhibit respiration, thereby diminishing fitness.

At a molecular level, mitochondrial hyperpolarisation and reduced oxygen consumption rates could only co-occur when fewer protons are being transported through the ATP synthase. This phenomenon could be a consequence of two plausible scenarios: either a higher number of protons were 'leaking' into the mitochondrial matrix by mechanisms that are not coupled to oxidative phosphorylation of ADP into ATP or direct inhibition of ATP synthesis. Possible ways in which to distinguish between these two possibilities were directly quantifying the 'proton leak' or comparing the change in mitochondrial membrane potential ensuing from the exposure of the sample to a blocking agent of the ATP synthase. The former assay would directly confirm or rule out the prospect of having a greater portion of basal oxygen consumption which was not destined to ATP generation. If the proton leak was found to be unaffected in both strains, the response of mitochondrial membrane potential to oligomycin treatment would allow me to determine whether the impaired ATP synthesis stemmed from a decrease in the rate at which the reaction was catalysed or a reduction in the rate at which the product molecule (i.e., ATP) was exchanged for the substrate one (i.e. ADP) in the mitochondrial matrix. In other words, while the speed of ATP synthesis is dictated chiefly by the ATP synthase, the reaction could be slowed down by the inhibition of the adenine nucleotide translocator (ANT), which imports ADP into the mitochondrial matrix by exporting product ATP molecules into the cytoplasm.

Regardless, to perform the two mentioned assays in yeast, I would have needed to inhibit the ATP synthase in the inspected cells. In *S. cerevisiae*, this has been broadly achieved using oligomycin (Nagley et al., 1986) and, more recently, bedaquiline (Luo et al., 2020). However, I found that oligomycin was unable to inhibit the ATP synthase in any of my samples. While troubleshooting, I learned that the

BY4741 parental strain had been reported to be resistant to the drug (Leadsham and Gourlay, 2010). Therefore, to assess the effects that blocking the ATP synthase would have on the mitochondrial membrane potential of these samples, I would have had to perform these experiments in mitochondrial extracts. Mitochondrial isolation in yeast is technically challenging and given that I performed all my mitochondrial characterisation experiments as part of a two-month stay at Prof Michael Duchen's laboratory at University College London, I would have had to optimise a mitochondrial extraction protocol in a short period of time. Since mammalian cells are responsive to such agents, I proceeded with characterising the human cell model. If, as I had hypothesised, overexpressing the studied mitochondrial transporter indeed elicited an identical set of defects in mammalian and yeast cells, I could also assess the impact of oligomycin exposure in the former and subsequently extrapolate my findings to the latter.

V.5. Overexpression of *SLC25A3* renders mammalian cells hypersensitive to oxidative stress.

As detailed in I.6., Pic2 is functionally conserved in higher eukaryotes. Thus, I sought to generate an equivalent mammalian model to test if my conclusions were relevant to humans, where systemic knock-out and overexpression of the gene have been associated with disease (Oehler et al., 2009; Peoples et al., 2021). Moreover, my meta-analysis of published single-cell RNA-sequencing data revealed that transcriptional noise of the mammalian homologue of *PIC2* (*SLC25A3*) was remarkably low and comparable to those of constitutively expressed genes (Padovan-Merhar et al., 2015) (Figure I.6). Altogether, these findings suggested that suboptimal levels of *PIC2* expression need to be tightly regulated across eukaryotic species and, therefore, were likely to be poorly tolerated in challenging growth scenarios. During the first four sections of this chapter, I provided evidence confirming these suspicions in *S. cerevisiae*.

My results were partially substantiated by mammalian cell models in which deleting *SLC25A3* triggered mitochondrial hyperpolarisation (Wolf et al., 2017) and decreased ATP synthesis (Peoples et al., 2021). These defects were consistent with a systemic lack of SLC25A3 transporters being deleterious to human health (Kwong et al., 2014).

Increasing SLC25A3 protein levels has also been associated with disease, but I did not find a mitochondrial or respirometric characterisation of a *SLC25A3* overexpression model to which to compare my findings in yeast. Thus, I set out to investigate whether, similarly to the *PIC2* and *SLC25A3* knockout models, a SLC25A3-overexpressing cell line would resemble the Pic2-overexpressing yeast model. To this end, I applied the Flp-In™ system to generate a HEK 293 cell line in which overexpression of *SLC25A3* could be induced using doxycycline. To be able to quantify the expression of its encoded protein, I terminally fused the sequence of *SLC25A3* to a codon-optimised HTF tag.

Applying the T-REx™ system, *SLC25A3* transcription is driven by a strong constitutive promoter (P_{CMV}) and controlled by two tetracycline/doxycycline-induced transcriptional activation elements (TetO2). According to the manufacturer, overexpression of the gene of interest usually requires doxycycline or tetracycline concentrations between 0.2 µg/mL and 1 µg/mL. However, it was preferable to minimise the concentration of antibiotic required to elicit the desired overexpression, as it would reduce the probability of causing confounding off-target cellular effects that I could mistakenly ascribe to *SLC25A3* overexpression. Hence, I next determined the lowest doxycycline concentration capable of driving overexpression of *SLC25A3*. With this aim, I quantified SLC25A3 protein levels by western blotting with anti-FLAG antibodies (Figure V.15). After normalising the maximum SLC25A3 signals to that of GAPDH in the same sample, I concluded that even the lowest recommended doxycycline concentration (i.e., 0.2 µg/mL) was already sufficient to drive high levels of SLC25A3 expression (Figure V.15). Additionally, further increasing the doxycycline concentration did not significantly increase SLC25A3 abundance any further (Figure V.15).

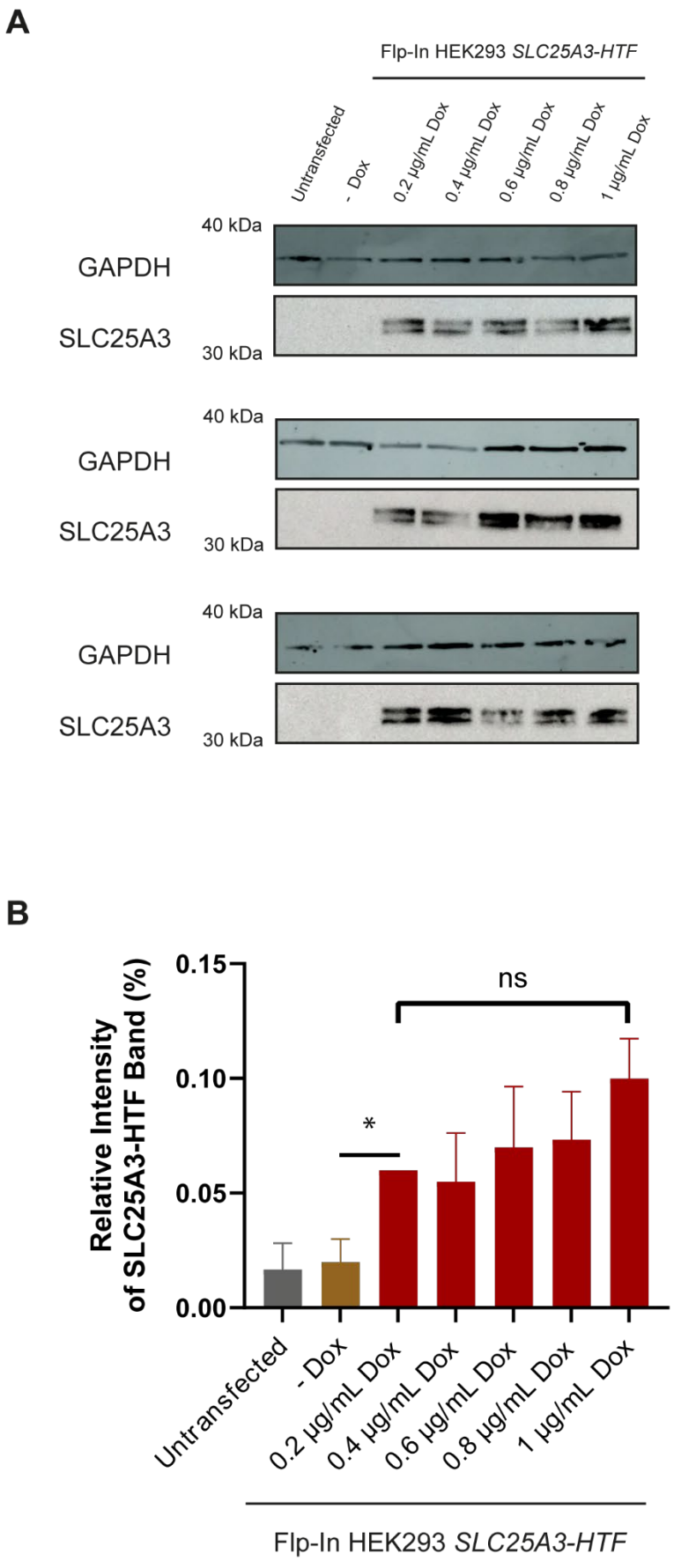

Figure V.15. qWBs shows that a significant increase in the protein levels of SLC25A3-HTF can be increased upon the addition of doxycycline. **A**. Anti-GAPDH and anti-FLAG

bands for the three biological repeats which I performed to quantify the changes in SLC25A3-HTF protein abundance induced by exposure of the cells in said cultures to the indicated doxycycline concentrations. **B**. Relative intensities of the SLC25A3-HTF band were calculated by dividing the maximum signal for such band over that of GAPDH within the same sample. Data shows the normalised mean of three biological repeats for each condition. Error bars represent standard deviation (SD). Statistical comparison of the fold change in SLC25A3-HTF signal of the doxycycline-treated samples to that of their uninduced counterparts (- Dox) was performed by unpaired t-tests: *: $p<0.05$, **: $p<0.01$ and ***: $p<0.001$ and 'ns': $p>0.05$.

To verify that I could induce *SLC25A3* overexpression with 0.2 µg/mL doxycycline, I performed RT-qPCR in untransfected, uninduced and doxycycline-treated cell cultures. The abundance of *SLC25A3* was normalised to signals from three housekeeping genes, namely *ACTB*, *GAPDH* and *RPL39*, within the same condition. Relative abundances were then normalised to the levels detected in the untreated samples (Figure V.16). Subsequent comparison revealed a ~15-fold increase of *SLC25A3* mRNA levels upon doxycycline induction (Figure V.16D).

I proceeded to characterise HEK 293 cells grown with 0.2 µg/mL doxycycline for 24 hours and compare their phenotypes with those of uninduced counterparts. Mirroring the assays that I had described earlier in yeast, I began comparing the basal growth patterns of both samples. In the case of human cells, the growth progression of examined populations was derived from time-resolved cell counts. This experiment confirmed that the growth of SLC25A3-overexpressing cells was almost indistinguishable from that of their uninduced counterparts (Figure V.17). Even though the cell count for the induced population was significantly lower at the third time point of the assay (i.e., 48 hours), the difference disappeared in subsequent time points and only re-appeared 120 hours the initial measurement (Figure V.17). Accordingly, I concluded that enhanced SLC25A3 levels did not dramatically affect the basal division rate of mammalian cells in rich medium.

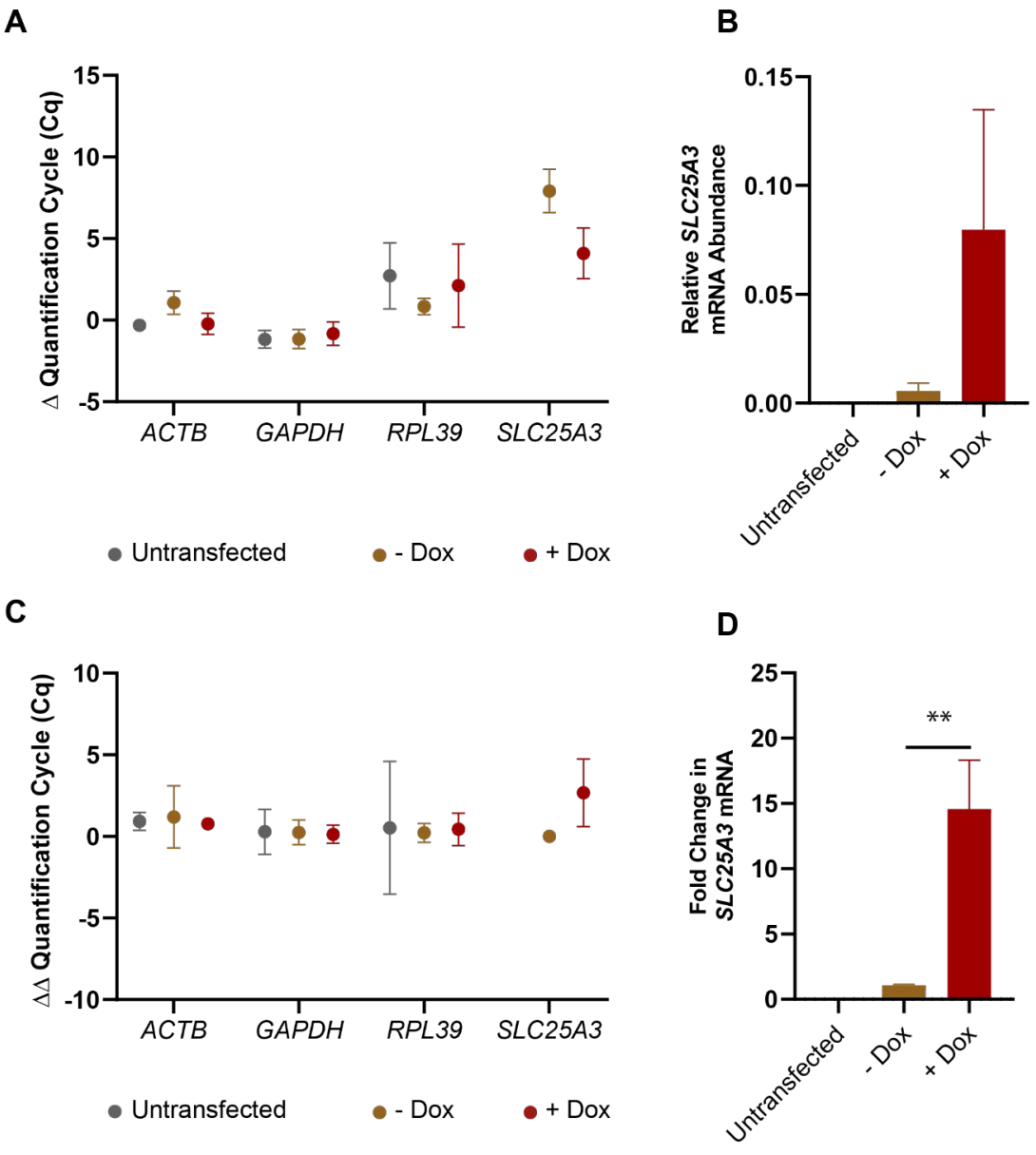

Figure V.16. RT-qPCR quantification of *SLC25A3-HTF* mRNA in uninduced (- Dox) and doxycycline-treated (+ Dox) Flp-In™ HEK 293 cells. Untransfected samples were included in the analysis as negative controls. **A**. Normalisation of raw quantification cycle (Cq) values to the median Cq of the reference genes within their own sample. **B**. Calculated ΔCqs for *SLC25A3-HTF* were used to derive a relative *SLC25A3-HTF* mRNA abundance within each condition. **C**. Median ΔCq values of each tested gene were normalised to those of the untreated cell samples to determine the differential ΔCq (ΔΔCq) values. **D**. These ΔΔCqs were exponentially transformed to find the fold change in mRNA abundance with respect to the reference sample (i.e., - Dox). Data shows the mean of three biological repeats for each condition. Error bars represent standard deviation (SD). Statistical comparison of the fold change in *SLC25A3-HTF* mRNA across conditions was performed by unpaired t-tests: **: $p<0.01$.

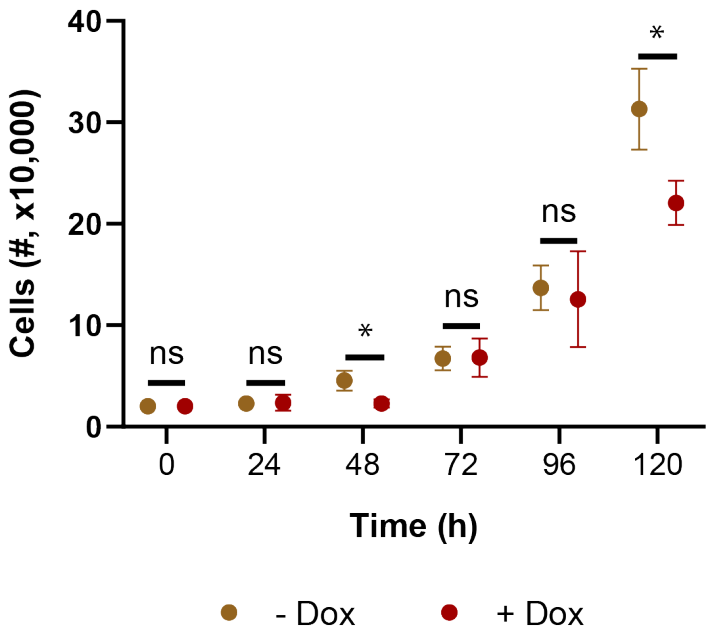

Figure V.17. Time-resolved cell counts for doxycycline-treated (+ Dox) and uninduced (- Dox) *SLC25A3-HTF* Flp-In™ HEK 293 cells seeded at the same confluency. Dots represent the mean of three biological repeats measured at the same time point. Error bars represent standard deviation (SD). Statistical comparison of the SLC25A3-overexpressing populations with their uninduced counterparts was performed by unpaired t-tests: *: $p<0.05$ and 'ns': $p>0.05$.

Next, I sought to determine whether, as in yeast, increasing the expression of *SLC25A3* lowered the tolerance of these mammalian cells to oxidative stress. Thus, applying cell counting, I went on to assess the effect of oxidative stress on cell viability. To this end, I employed a live/dead exclusion assay based on the principle that trypan blue would only penetrate cells with permeable or non-intact membranes, which were, in turn, either undergoing apoptosis or cell death. The cell counter calculated the fraction of the population which was dead or dying at the start of the assay, and I could compare those to the viability of the sample after having been exposed to 0.5 mM hydrogen peroxide for 18 hours (Figure V.18). This concentration of hydrogen peroxide was chosen because it had been successfully applied in similar experimental contexts and mammalian cell lines (Ransy et al., 2020; Saputra et al., 2024). My results show that samples overexpressing *SLC25A3* displayed a greater decrease in cell viability after facing oxidative stress (Figure V.18). Therefore, I concluded that, similarly to Pic2-overexpressing yeast, the tested HEK 293 model with increased expression of *SLC25A3* was also hypersensitive to oxidative stress.

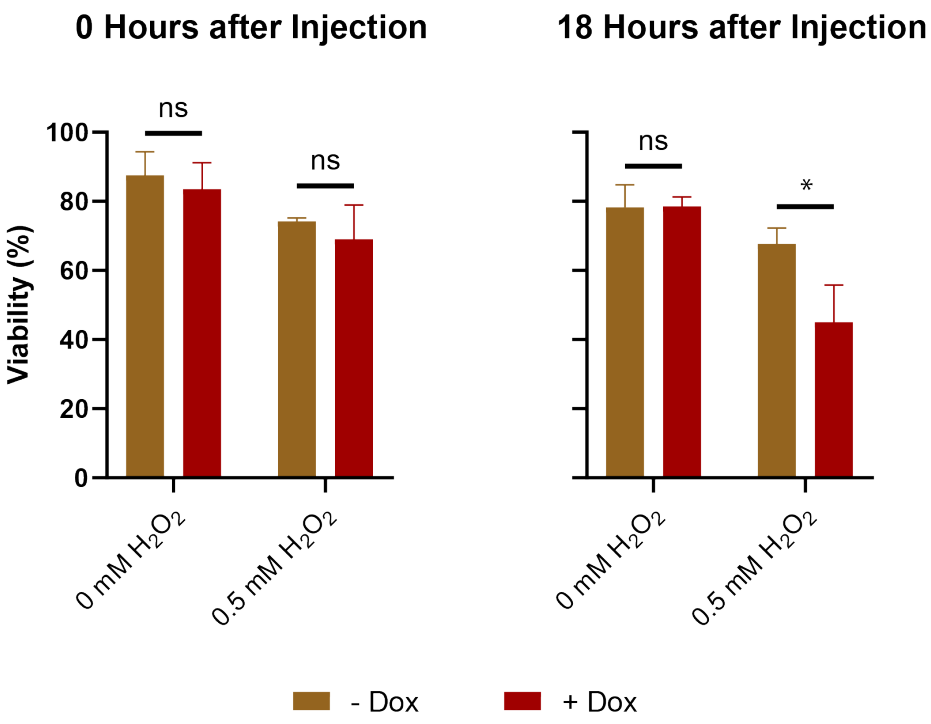

Figure V.18. Cell viability of the cell line overexpressing *SLC25A3* (+ Dox) and its uninduced reference (- Dox) at 0 hours and 18 hours after injection of 0.5 mM of hydrogen peroxide (H_2O_2) or sterile water (0 mM H_2O_2). Two technical measurements were taken for three biological repeats. The average of each set of triplicates is shown in the bar graph. Error bars represent standard deviation (SD). An identical control experiment was conducted by treating cell cultures with sterile water and assessing their viability after 18 hours. The viability of the cultures supplemented with doxycycline was compared to that of those treated with sterile water using unpaired t-tests: *: $p<0.05$ and 'ns': $p>0.05$.

To further evaluate the phenotypic similarity of the SLC25A3-overexpressing mammalian cell line and the *pTEF1-PIC2* yeast strain, I examined the redox status of the NAD pool in HEK 293 cells. In this case, I re-suspended 80% confluent cultures in HEPES-buffered DMEM, which maintained an adequate cellular pH despite the changes in carbon dioxide concentration that cells faced during the experiment. Cell solutions were prepared aiming for approximately 1.5 million cells per mL and exact counts were recorded in a cell counter for subsequent fluorescence normalisation. Upon fluorescence quantification, I was able to confirm that, reminiscent of Pic2-overexpressing yeast, human cells with increased *SLC25A3* expression presented no significant changes in NADH/NAD^+ ratio compared to the uninduced population (Figure V.19).

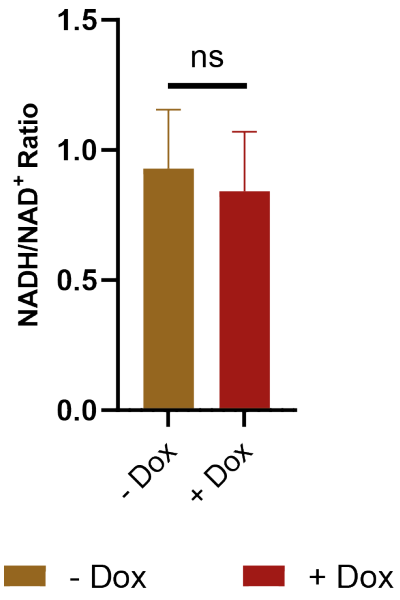

Figure V.19. Mean NADH/NAD$^+$ ratios calculated based on three independent fluorescence assays of induced (+ Dox) and uninduced (- Dox) *SLC25A3-HTF* Flp-In™ HEK 293 cells. Error bars represent standard deviation (SD). Statistical comparison between both populations were conducted by unpaired t-tests. 'ns': p>0.05.

V.6. Overexpression of *SLC25A3* reduces basal respiration of mammalian cells.

Next, I sought to characterise the oxygen consumption capabilities of the SLC25A3-overexpressing HEK 293 cells and contrast them to those of their uninduced relatives. The objective of this assay was two-fold: on the one hand, it would yield additional data to substantiate the apparent similarity between the yeast Pic2-overexpressing model and the implications of overexpressing its functionally conserved homologue in mammalian cells; on the other hand, if the respiratory patterns observed in yeast were reproduced by the HEK 293 samples, I expected to gain further insight into the molecular causes of the respiration inhibition caused by suboptimal expression of the studied mitochondrial transporter. Unlike yeast, mammalian cells are susceptible to oligomycin, which is a drug that shuts down proton import by the ATP synthase and, consequently, hinders oxidative phosphorylation of ADP into ATP. Accordingly, upon exposure to oligomycin, the oxygen consumption rate of the cells in the examined sample will diminish with respect to their basal one.

The observed reduction corresponds to the fraction of oxygen that is effectively destined for ATP production. The remaining component of respiration is, thus, not coupled to ATP production and is generally indicative of mitochondrial damage.

After performing the assays as detailed in II.20., I extracted the oxygen consumption at its basal rate, the proton leak, the maximal respiration rate and the reserve or spare capacity (Figure V.20). Importantly, consistent with my findings in Pic2-overexpressing yeast, SLC25A3-overexpressing HEK 293 cells also displayed reduced basal oxygen consumption rates (Figure V.20). Notably, this mammalian model also displayed significantly lower maximal respiratory rates, implying that enhancing SLC25A3 levels had a negative effect on the capacity of the electron transport chain to operate at its utmost efficiency (Figure V.20). Naturally, this decrease in the maximum respiration capabilities was accompanied by a significant reduction in the reserve capacity of SLC25A3-overexpresing cells, indicating that they displayed a lower respiratory margin to achieve increased oxygen consumption rates and face energetic pressures (Figure V.20). In other words, while the human model with increased SLC25A3 also exhibited impaired basal respiration, it appeared that the repercussion of that effect was more unfavourable to the mammalian cell line than to the yeast model. These subtle differences were likely underpinned by the distinct biological contributions of Pic2 and SLC25A3 as phosphate and copper transporters in their respective cell types.

Importantly, these oximetric assays in the mammalian model proved that increasing the abundance of SLC25A3 did not necessarily facilitate proton import into the mitochondrial matrix through non-ATP production mechanisms. Essentially, these experiments appeared to exclude the possibility that a higher proton leak was causing the energy homeostasis defects that this cell line and its yeast counterpart were experiencing. Unavoidably, this implied that enhancing the levels of SLC25A3 and, by extension, the ones of Pic2 resulted in diminished ATP synthesis in mammalian and yeast cells, respectively. However, to confirm this, I needed to ascertain whether the SLC25A3-overexpressing model also experienced mitochondrial hyperpolarisation.

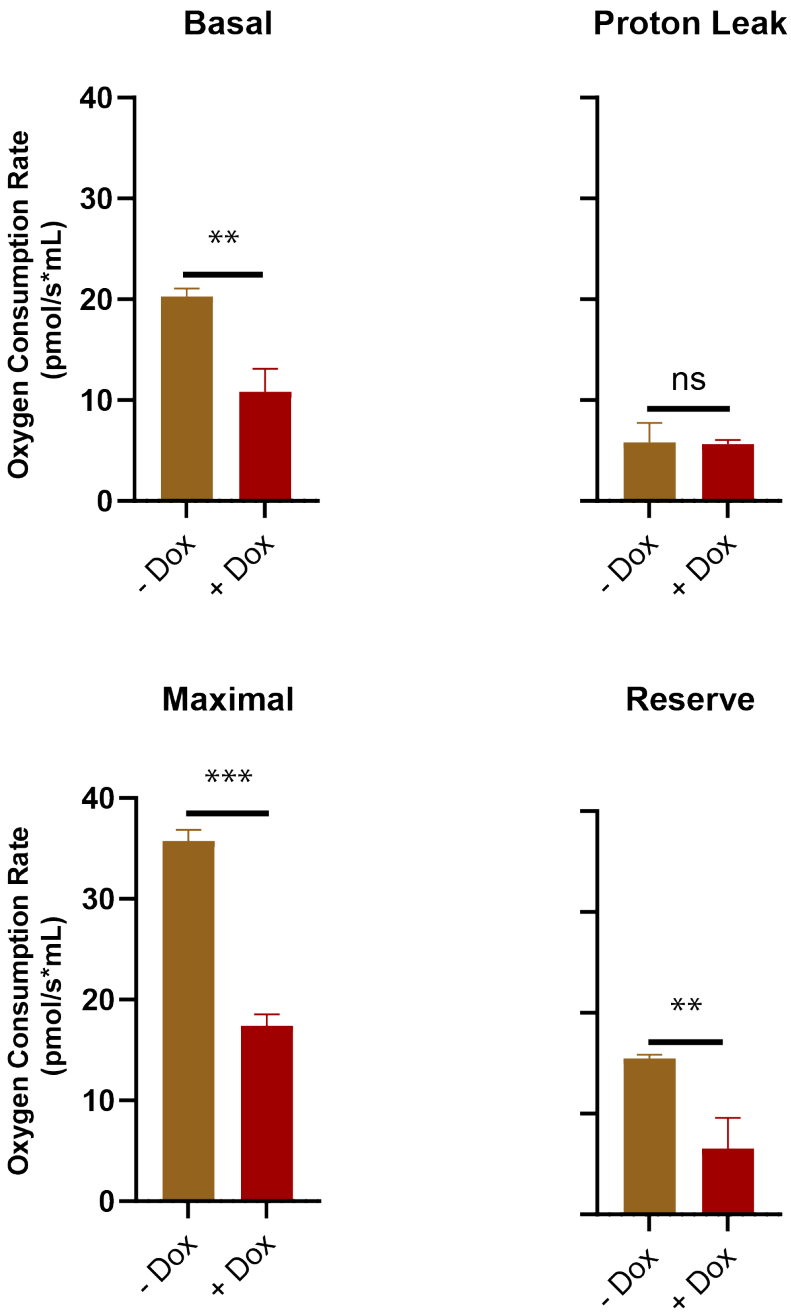

Figure V.20. Mean for the measured basal, maximal and reserve capacity oxygen consumption rates. Three separate respiration assays were performed for independent cultures of induced (+ Dox) and uninduced (- Dox) *SLC25A3-HTF* Flp-In™ HEK 293 cells. Error bars represent standard deviation. Statistical comparisons between both sets of cells were conducted by unpaired t-tests. *: $p<0.05$, **: $p<0.01$ and 'ns': $p>0.05$.

V.7. Overexpression of *SLC25A3* in human cells yields mitochondrial membrane hyperpolarisation.

As for all other mitochondrial membrane potential assessments, I started quantifying MitoTracker™ Red CMXRos accumulation using flow cytometry. The main advantage of this approach is that it allowed me to inspect larger populations, which would numerically corroborate the corrected and normalised measurement of TMRM in confocal microscopy images. Similarly to the procedure which I employed to assess mitochondrial membrane potential in the *pTEF1-PIC2* and *pic2Δ::HIS3* mutants, I also supplemented mammalian cell cultures with MitoTracker™ Green FM, whose green fluorescence signal is proportional to the mitochondrial mass in the sample. This co-staining allowed me to normalise the MitoTracker™ Red CMXRos fluorescence to the mitochondrial population in each sample. Thus, I ensured that changes in mitochondrial membrane potential signal were not just caused by an enhanced mitochondrial mass in one of the cell lines but rather by an increase in their activity.

Having examined samples with flow cytometry, I observed that, like their yeast counterparts, HEK 293 cells overexpressing *SLC25A3* displayed mitochondrial membrane hyperpolarisation with respect to their uninduced counterparts (Figure V.21). Moreover, in congruency with *pTEF1-PIC2* features, the mitochondrial mass was unaltered by *SLC25A3* expression levels (Figure V.21). These data confirmed that increasing the levels of the functionally conserved SLC25A3/Pic2 carrier drives mitochondrial membrane hyperpolarisation. Furthermore, given that both cell types exhibited decreased oxygen consumption and hypersensitivity to oxidative stress, it was likely that the mechanism underlying these energy homeostasis defects was the same in both cell types.

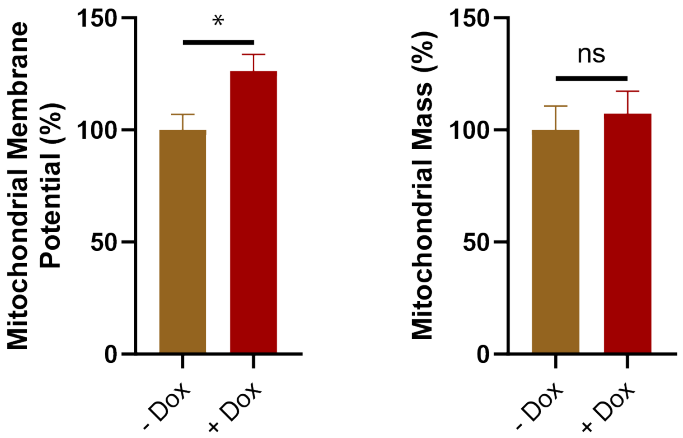

Figure V.21. Mitochondrial membrane potential measurements of MitoTracker™ Red CMXRos by flow cytometry uncovered mitochondrial hyperpolarisation in the SLC25A3-overexpressing cell line. Medians for single-cell red fluorescence emissions were normalised to the corresponding median green fluorescence value. The bar graph shows the weighted average and standard deviation of the mentioned ratio across three biological batches containing more than 50,000 cells. Statistical comparisons between doxycycline-treated (+ Dox) and the control reference (- Dox) were performed by an unpaired t-test. *: $p<0.05$, and 'ns': $p>0.05$.

Upon TMRM staining, confocal microscopy imaging and subsequent computational analysis verified that mitochondrial membrane potential was larger in mammalian cells with higher levels of SLC25A3 (Figures V.22A-B). Since my earlier oximetry assays rejected the possibility that a greater proton leak would be triggering the mitochondrial hyperpolarisation observed in cells overexpressing SLC25A3, and, by that logic, Pic2, I concluded that ATP synthesis must be inhibited in both cell types. On this basis, I continued to employ confocal microscopy to elucidate which reaction component was limiting the ATP synthesis in both cellular models: the catalytic rate or the substrate/product balance. In other words, was an excess of SLC25A3/Pic2 directly inhibiting the ATP synthase or the ADP/ATP translocase (ANT)?

To answer this question, I set out to measure the change in mitochondrial membrane potential that oligomycin could stimulate in HEK 293 cells with normal and increased levels of SLC25A3 (Figure V.22C). In principle, oligomycin treatment should hinder proton import through the ATP synthase and, in turn, prompt proton accumulation in the intermembrane space. That proton build-up maximises the charge imbalance between both sides of the inner mitochondrial membrane and, in doing so,

hyperpolarises the mitochondrial membrane. Consequently, if the observed mitochondrial membrane potential difference between SLC25A3-overexpressing cells and their uninduced counterparts was arising from inhibition of the ATP synthase, oligomycin-induced hyperpolarisation should neutralise such difference. Alternatively, if the described mitochondrial membrane hyperpolarisation in cells with more SLC25A3 originated from defective ADP/ATP translocation, the increase in its mitochondrial membrane potential with respect to the uninduced cell population should remain unaltered upon exposure to oligomycin.

Being an inhibitor of the ATP synthase, oligomycin is highly toxic to cells. Thus, after a certain period of action, the drug eventually causes cell death. For this reason, I imaged TMRM fluorescence at regular intervals following the addition of the drug. In this way, I determined the timeframe at which the mitochondrial membrane potential of the sample reached its maximum in the uninduced control population (Figures V.22C-D). This time point corresponded to the first one at which no further increase of mitochondrial membrane potential was detected (Figure V22.D, 9 minutes). I then used that time point to image at least 20 cells from both samples. During the analysis, I filtered the red fluorescence to exclude the background signal and, subsequently, normalised individual measurements to the mean of the pertinent sample. The results evidenced that, despite being treated with oligomycin, the SLC25A3-overexpressing cells still displayed larger mitochondrial membrane potential than their uninduced counterparts (Figure V.22E). Accordingly, these experiments show that enhanced levels of SLC25A3 inhibit the adenine translocase (ANT).

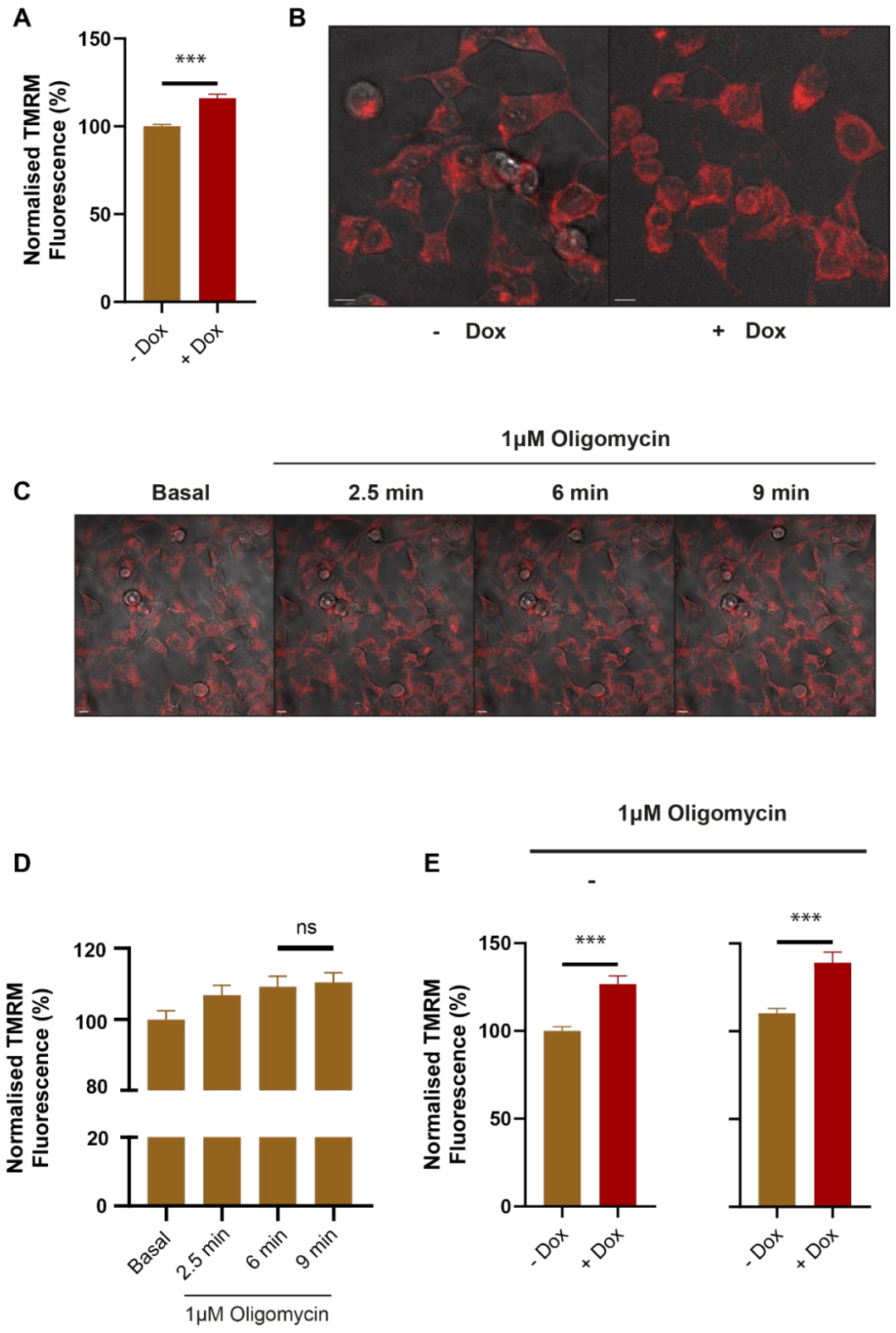

Figure V.22. TMRM staining and confocal microscopy live cell imaging confirm that mitochondria in SLC25A3-overexpressing cells are hyperpolarised and that such mitochondrial membrane potential increase persists even upon ATP synthase inhibition. **A**. Mean normalised TMRM fluorescence values gathered from confocal imaging of more than 50 cells from three independent biological repeats of

doxycycline-treated (+ Dox) and uninduced (- Dox) cells. Error bars represent the standard error of the mean (SEM). Statistical comparisons between both sets of cells were conducted by unpaired t-tests. ***: $p<0.001$ and 'ns': $p>0.05$. **B**. Representative confocal microscopy images of stained SLC25A3-overexpressing cells and their uninduced counterparts. **C**. Time-resolved confocal microscopy images of a TMRM-stained uninduced culture treated with 1 µM oligomycin. **D**. Time-resolved mean normalised TMRM fluorescence values gathered from confocal imaging of the same uninduced cell culture. **E**. Mean normalised TMRM fluorescence values gathered from confocal imaging of all shown cells from the uninduced and SLC25A3-overexpressing cultures (27 and 23 cells, respectively). Error bars represent the standard error of the mean (SEM). Statistical comparisons between both sets of cells were conducted by unpaired t-tests. ***: $p<0.001$ and 'ns': $p>0.05$.

Alongside V.5 and V.6, the data presented in this section show that the mammalian SLC25A3-overexpresing model fully recapitulated the mitochondrial hyperpolarisation, reduced respiration, and hypersensitivity to oxidative stress that I had identified in the Pic2-overexpressing yeast. Apart from having proven that the energy homeostasis defects impairing respiration and decreasing fitness in yeast are molecularly conserved in human cells, my results provide an explanation for the molecular basis of the observed energy homeostasis defects: increased abundance of SLC25A3 inhibits ADP/ATP exchange in the ANT translocase, which, in turn, limits ATP-linked oxygen consumption and, ultimately, reduces the basal oxygen consumption rate. Unsurprisingly, reduced respiration makes cells more vulnerable to unfavourable environmental conditions, thereby contributing to decreased tolerance to nutrient deprivation and oxidative insults.

V.8. *PIC2* and *SLC25A3* expression does not directly affect cell size.

The fact that the energy homeostasis defects in the Δ Nab3 RNA-BSs were dramatically different to those caused by increased Pic2/SLC25A3 protein levels prompted me to question whether any of the remaining defects discovered in the former mutant would be reproduced in the latter. For this reason, I tested whether the size of the Pic2-overexpressing yeast and SLC25A3-overexpressing mammalian cells was larger than those of their parental and uninduced counterparts, respectively (Figures V.23-24). To this end, I measured the forward light scatter (FSC) of at least three samples for each tested cell type and condition (Figures V.23-24). After calculating the weighted mean and its accompanying standard deviation, unpaired t-tests were conducted to confirm that, consistent with the dissimilarities in the mitochondrial characterisation assays, neither the *pTEF1-PIC2* strain nor the induced *SLC25A3* mammalian overexpression model exhibited larger cell size than WT or the examined uninduced populations (Figures V.23-24). Based on these results, I concluded that enhanced *PIC2* expression and activity were not driving the increase in cell volume that I had previously identified in Δ Nab3 RNA-BSs and, therefore, the cause underlying such cell volume aberrations must lay on another feature of the Δ Nab3 RNA-BSs mutant.

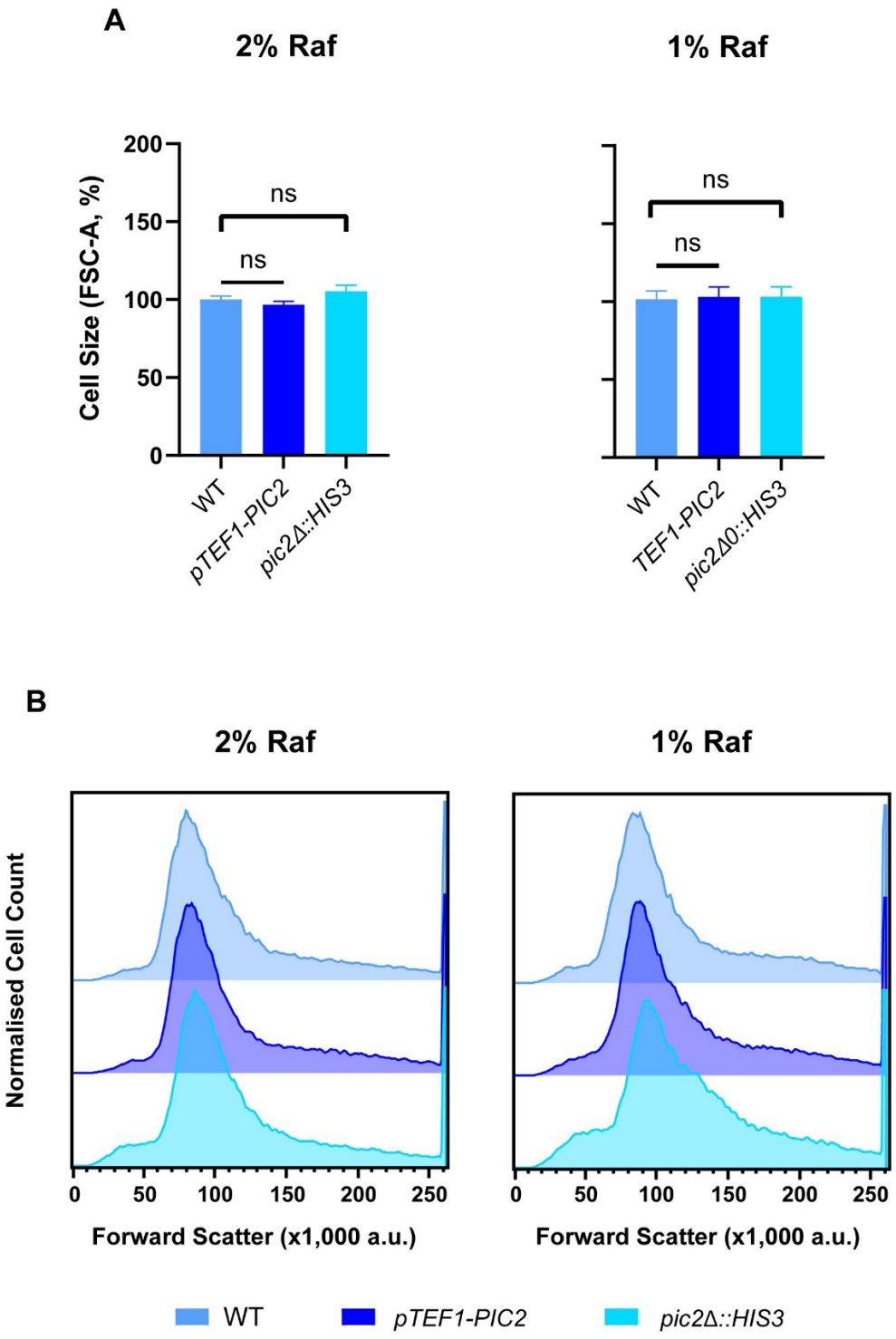

Figure V.23. Flow cytometry revealed no differences in the cell size of WT, *pTEF1-PIC2* and *pic2Δ::HIS3*. **A**. Weighted means of the median FSC values for three independent biological repeats were calculated for each strain and normalised to the parental WT. Error bars represent standard deviation. Statistical comparisons between each mutant and the WT reference were performed by an unpaired t-test. *: $p<0.05$ and 'ns': $p>0.05$. **B**. Representative traces of the cell size distribution of WT and derived mutants from flow cytometry analyses. The sizes were compared using their forward light scatter (FSC) values.

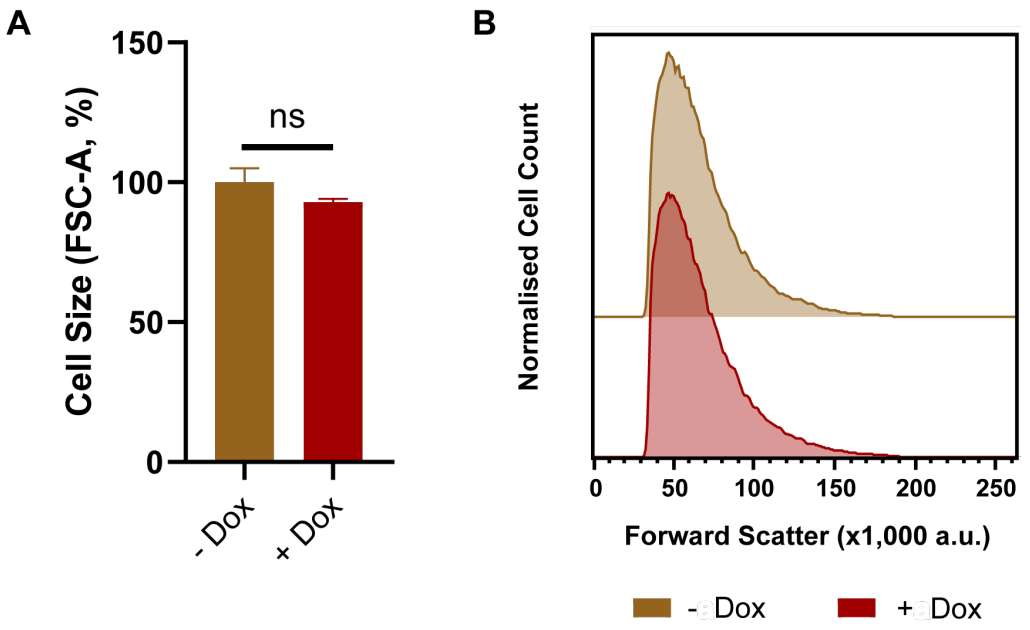

Figure V.24. Flow cytometry revealed no differences in the cell size of SLC25A3-overexpressing (+ Dox) and their uninduced (- Dox) counterparts. **A**. Weighted means of the median FSC values for three independent biological repeats were calculated for both cell lines and normalised to those of the uninduced population. Error bars represent standard deviation. Statistical comparisons between both groups of cells were performed by an unpaired t-test. *: $p<0.05$ and 'ns': $p>0.05$. **B**. Representative traces of the cell size distribution of doxycycline-treated and untreated samples according to flow cytometry analyses. The sizes were compared using their forward light scatter (FSC) values.

V.9. *PIC2* expression does not impact the cell cycle.

As mentioned before, a previous study by the Amon group uncovered cytoplasmic dilution in excessively large cells and linked such phenotype to cell cycle delays (Neurohr et al., 2019). Consequently, given that *pTEF1-PIC2* cells were not found to be oversized, I hypothesised that these mutants would have normal cell cycle progression. To examine the cell cycle of *pTEF1-PIC2* and *pic2Δ::HIS3* mutants, I stained the DNA content of previously fixed, permeabilised cells which had undergone RNA and protein depletion (Figures V.25-26). The dye used to visualise the DNA of examined cells was, as in earlier instances, propidium iodide and the DNA quantity of the single cells was assessed as a red fluorescence signal employing a flow cytometer (Figures V.25-26). As depicted in Figures V.25 and V.26, there were no differences

between the DNA profiles of the mutant populations and their parental counterparts (WT). Accordingly, I concluded that Pic2 levels did not directly affect the cell cycle. Therefore, the cell cycle prolongation observed in the Δ Nab3 RNA-BSs strain must proceed, as its cell volume increases, from a different molecular cause.

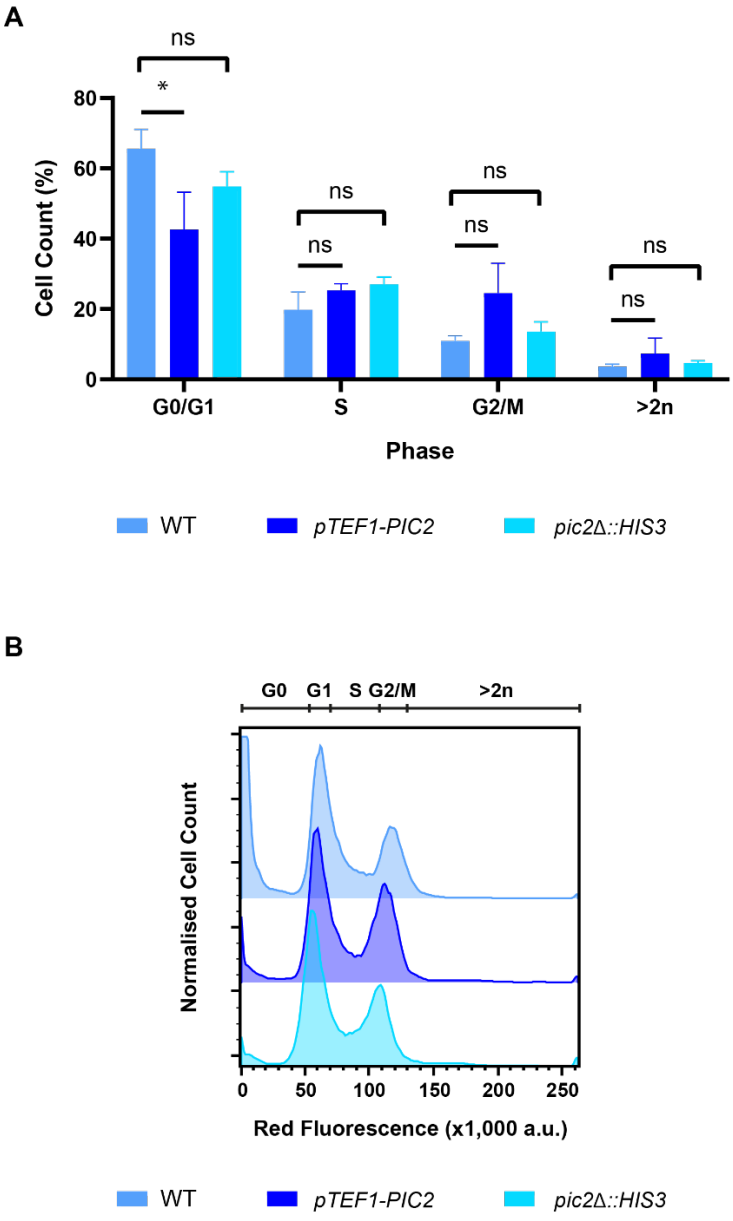

Figure V.25. Cell cycle analysis of WT, *pTEF1-PIC2* and *pic2Δ::HIS3* grown to mid-exponential phase (OD_{600} ~0.5) in medium containing 2% (w/v) raffinose. **A**. Weighted means of the population fraction of WT, *pTEF1-PIC2* and *pic2Δ::HIS3* within each cell cycle phase throughout growth in medium supplemented with 2% (w/v) raffinose. Values based on biological triplicates and error bars represent the standard deviation derived after considering the three repeats per strain and condition. Error bars represent standard deviation. Statistical comparisons were performed by unpaired t-

tests. *: p<0.05 and ‘ns’: p>0.05. **B**. Representative flow cytometry traces of the DNA profiles of all strains.

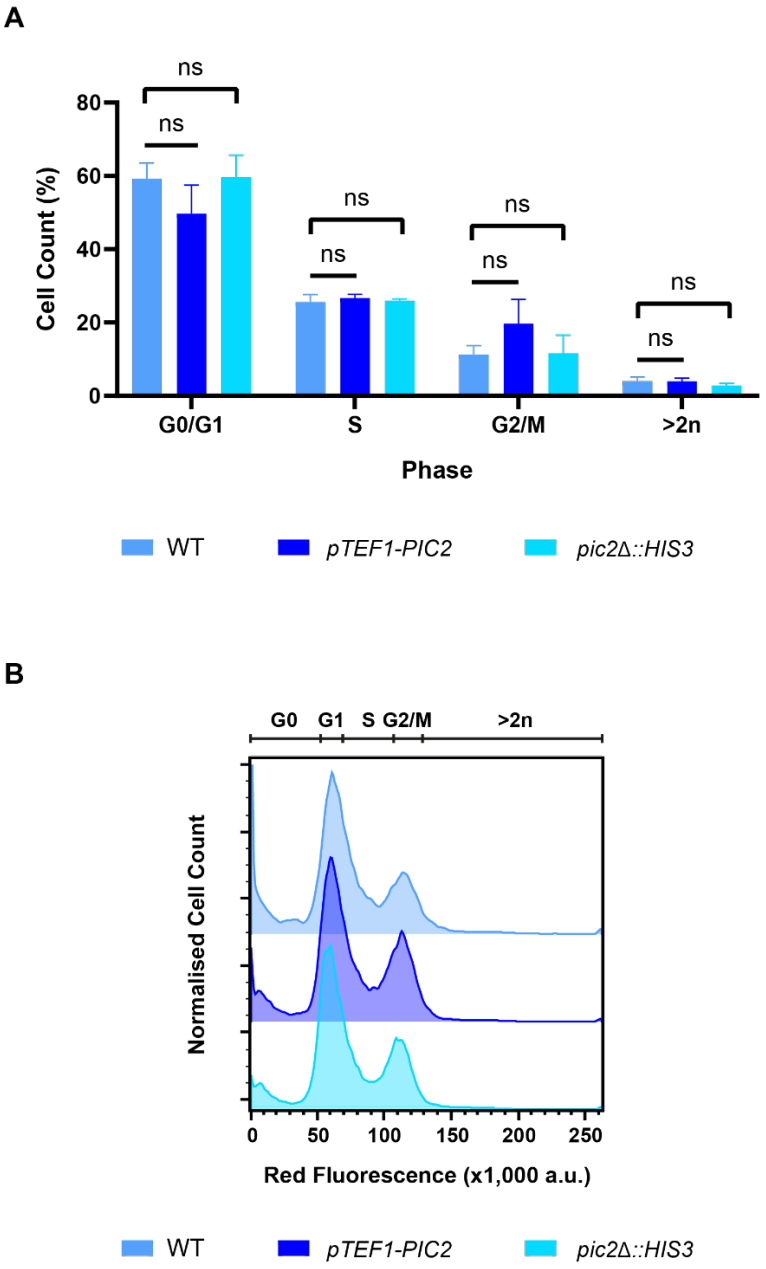

Figure V.26. Cell cycle analysis of WT, *pTEF1-PIC2* and *pic2Δ::HIS3* grown to mid-exponential phase (OD_{600} ~0.5) in medium containing 1% (w/v) raffinose. **A**. Weighted means of the population fraction of WT, *pTEF1-PIC2* and *pic2Δ::HIS3* within each cell cycle phase throughout growth in medium supplemented with 1% (w/v) raffinose. Values based on biological triplicates and error bars represent the standard deviation derived after considering the three repeats per strain and condition. Error bars represent standard deviation. Statistical comparisons were performed by unpaired t-tests. ‘ns’: p>0.05. **B**. Representative flow cytometry traces of the DNA profiles of all strains.

V.10. Discussion

My results have illustrated that the NNS complex premature termination of a model stress-specific mRNA target exerts a 'Goldilocks' regulation in the expression pattern of the encoding gene. The data presented in this chapter show that while *PIC2* overexpression bestowed increased fitness in nutrient-rich concentrations, Pic2 excess was critically penalised when cells underwent nutrient restriction or were exposed to environmental insults which demanded efficient respiration to be endured. Interestingly, respiration inhibition and enhanced susceptibility to extracellular ROS are features also present in the mutants lacking *PIC2*. Despite also displaying defects when grown in high-raffinose conditions, *PIC2* KO cells had been previously shown to be practically identical to the parental reference when cultured in rich medium containing fermentable sources (Vest et al., 2013). Comprehensively, these observations obey general microbial adaptive behaviour (Engl et al., 2020): whereas bet hedging enables the development of stochastic phenotypes that may be compatible with survival in ideal growth conditions and potentially beneficial in unforeseen scenarios, adaptation requires transcriptomic adjustments to acquire a gene expression pattern that is 'just right'. Accordingly, all departures from such optimal levels become equally disadvantageous.

Although mammalian cells lack a conserved homologue of the NNS complex, they they control the expression of target genes with alternative regulators such as micro RNAs, which reduce fluctuations in protein levels and are not present in *S. cerevisiae* (Siciliano et al., 2013). More specifically, in humans, miR-144 has been identified as a key regulator of *SLC25A3* (Baseler et al., 2012). In this study I have shown that, as in yeast, overexpressing *SLC25A3* in mammalian cells impairs respiration and increases sensitivity to oxidative stress. In turn, as in the *PIC2* KO yeast strain, human cell models lacking *SLC25A3* also decreased oxygen consumption (Seifert et al., 2016).

At a molecular level, overexpression and deletion of *PIC2* and *SLC25A3* are invariably accompanied by mitochondrial membrane hyperpolarisation in yeast and humans. Cumulatively, these phenotypes show that Pic2 and SLC25A3 decrease oxygen consumption by direct inhibition of the adenine nucleotide translocator (ANT), which replaces newly synthesised ATP with ADP in the mitochondrial matrix. Since the ANT translocase has been co-immunoprecipitated with SLC25A3 in mammalian

systems (Alcalá et al., 2008), it is indeed likely that SLC25A3 abundance and/or activity directly and physically shapes that of the ADP/ATP translocase. Furthermore, given that my *PIC2* deletion strain and previously reported *SLC25A3* knock-out models display identical mitochondrial membrane potential increases, impaired respiration and, in the case of the latter diminished ATP production (Wolf et al., 2017), I surmise that lower expression of the Pic2/SLC25A3 possibly has the same inhibitory effect in the ANT translocator. However, importantly, this is purely my interpretation of the results as I do not present evidence confirming this claim.

Despite having (i) illustrated the biological importance of NNS regulation in preventing abnormally high or low levels of a stress-induced gene such as *PIC2* and (ii) characterised the molecular basis by which increasing Pic2 abundance causes cell-wide defects, the described evidence also proves that the origin of the phenotypes described in ∆ Nab3 RNA-BSs was independent of that of Pic2 activity (Tables V.1-2). Apart from the discrepancies identified throughout the mitochondrial and energy homeostasis assays, cell size quantification and cell cycle evaluations clearly showed that the aberrantly larger cell volumes and delayed cell cycle were not recapitulated in the *pTEF1-PIC2* mutant (Tables V.1-2). Accordingly, alternative mechanisms that could be putatively accounting for the phenotypes detected in ∆ Nab3 RNA-BSs had to be tested.

	PIC2-GFP	**∆ Nab3 RNA-BSs**	**∆ NNS RNA-BSs**	**WT**	***pTEF1-PIC2***	***pic2∆::HIS3***
Fold change of *PIC2* expression with respect to parental strain	1.04 ± 0.04	2.17 ± 0.70	1.59 ± 0.47	1.21 ± 0.32	798.22 ± 560.47	0.01 ± 0.01
Growth rate (h^{-1})	0.37 ± 0.01	0.25 ± 0.01	0.35 ± 0.01	0.38 ± 0.01	0.44 ± 0.01	0.35 ± 0.01
Normalised survival ratio against a reference strain	1 ± 0.12	0.24 ± 0.03	1.83 ± 0.91	1 ± 0.1	2.69 ± 1.02	0.55 ± 0.23
Mitochondrial membrane potential (flow cytometry, MitoTracker, %)	100.00 ± 9.30	206.28 ± 44.92	167.61 ± 70.04	100.00 ± 1.39	135.14 ± 1.35	123.61 ± 6.93
Mitochondrial membrane potential (confocal microscopy, TMRM, %)	100 ± 13.71	120.71 ± 22.64	107.60 ± 17.53	100 ± 7.36	108.70 ± 6.06	107.50 ± 5.52
Logarithmic ratio of Maximal growth rate in 0.5 mM H_2O_2/maximal growth rate in innocuous medium	-0.21 ± 0.04	0.10 ± 0.05	-0.33 ± 0.05	-0.14 ± 0.10	-0.21 ± 0.09	-0.12 ± 0.17
NADH/NAD^+ ratio	0.75 ± 0.09	0.41 ± 0.11	0.63 ± 0.24	0.58 ± 0.04	0.59 ± 0.1	0.52 ± 0.12
Basal oxygen consumption (pmol/s*mL)	45.93 ± 5.22	45.98 ± 1.93	46.25 ± 1.72	45.77 ± 2.99	45.32 ± 0.43	33.23 ± 1.64
Maximal oxygen consumption (pmol/s*mL)	77.72 ± 4.35	74.51 ± 6.29	81.05 ± 4.03	72.60 ± 2.17	77.63 ± 1.97	52.58 ± 1.68
Reserve capacity (pmol/s*mL)	31.79 ± 4.76	28.53 ± 7.56	34.80 ± 2.32	26.83 ± 3.52	32.31 ± 2.36	19.35 ± 2.04
Normalised cell size (%)	100 ± 4.03	143.43 ± 8.30	111.91 ± 15.76	100 ± 2.17	96.74 ± 2.19	105.44 ± 3.81
Population fraction undergoing G0/G1 (%)	50.04 ± 2.91	27.00 ± 3.87	47.71 ± 2.43	65.57 ± 5.50	42.62 ± 10.62	54.83 ± 4.21
Population fraction undergoing S (%)	20.80 ± 0.30	28.13 ± 2.36	21.47 ± 0.58	19.80 ± 5.07	25.37 ± 1.88	27.03 ± 2.08
Population fraction undergoing G2/M (%)	28.07 ± 2.68	33.07 ± 5.03	29.40 ± 1.39	10.98 ± 1.43	24.53 ± 8.51	13.53 ± 2.83
Population fraction undergoing polyploidy (%)	1.05 ± 0.18	11.70 ± 1.35	1.37 ± 0.72	3.68 ± 0.70	7.43 ± 4.30	4.63 ± 0.65

Table V.1. Summary of the phenotypic features quantified in *PIC2-GFP*, ∆ Nab3 RNA-BSs and ∆ NNS RNA-BSs as well as WT, *pTEF1-PIC2* and *pic2∆::HIS3* grown in medium containing 2% (w/v) raffinose.

	PIC2-GFP	**∆ Nab3 RNA-BSs**	**∆ NNS RNA-BSs**	**WT**	***pTEF1-PIC2***	***pic2∆::HIS3***
Fold change of *PIC2* expression with respect to parental strain	1.02 ± 0.11	3.55 ± 0.28	2.39 ± 0.79	1.02 ± 0.02	11197.64 ± 0.12	0.00 ± 0.01
Growth rate (h^{-1})	0.37 ± 0.01	0.26 ± 0.01	0.38 ± 0.01	0.29 ± 0.01	0.32 ± 0.01	0.28 ± 0.01
Normalised survival ratio against a reference strain	1 ± 0.23	0.28 ± 0.22	1.83 ± 0.91	1 ± 0.13	0,17 ± 0.07	0.61 ± 0.04
Mitochondrial membrane potential (flow cytometry, MitoTracker, %)	100.00 ± 44.40	224.14 ± 55.03	133.98 ± 13.40	121.61 ± 12.28	172.79 ± 21.26	156.98 ± 10.21
Mitochondrial membrane potential (confocal microscopy, TMRM, %)	100.00 ± 12.46	119.49 ± 27.69	106.03 ± 28.99	100 ± 6.13	106.82 ± 6.92	107.93 ± 1.40
Maximal growth rate in 0.5 mM H_2O_2/maximal growth rate in innocuous medium logarithmic ratio	-0.11 ± 0.02	0.17 ± 0.04	-0.06 ± 0.03	-0.14 ± 0.10	-0.21 ± 0.09	-0.12 ± 0.17
$NADH/NAD^+$ ratio	0.96 ± 0.09	0.65 ± 0.07	1.07 ± 0.09	0.87 ± 0.06	0.85 ± 0.09	0.8 ± 0.01
Basal oxygen consumption (pmol/s*mL)	47.18 ± 2.58	57.04 ± 1.00	51.34 ± 2.46	48.33 ± 3.20	37.66 ± 1.43	38.60 ± 0.46
Maximal oxygen consumption (pmol/s*mL)	74.96 ± 5.95	87.16 ± 1.46	79.47 ± 4.34	80.17 ± 5.25	65.16 ± 10.55	72.73 ± 3.23
Reserve capacity (pmol/s*mL)	27.78 ± 6.37	30.12 ± 1.14	28.12 ± 4.09	31.83 ± 2.15	27.50 ± 10.25	34.12 ± 2.79
Normalised cell size (%)	100 ± 3.36	143.72 ± 16.49	107.75 ± 6.82	100 ± 5.28	101.44 ± 6.30	110.91 ± 2.26
Population fraction undergoing G0/G1 (%)	52.15 ± 1.64	30.25 ± 2.01	48.45 ± 3.20	59.23 ± 4.29	49.70 ± 7.82	59.67 ± 6.02
Population fraction undergoing S (%)	19.33 ± 0.80	23.40 ± 0.69	20.40 ± 1.04	25.53 ± 2.08	26.67 ± 1.00	25.93 ± 0.49
Population fraction undergoing G2/M (%)	27.43 ± 0.86	38.67 ± 1.46	29.87 ± 1.99	11.20 ± 2.50	19.70 ± 6.61	11.64 ± 4.94
Population fraction undergoing polyploidy (%)	1.06 ± 0.20	7.70 ± 1.28	1.26 ± 0.20	4.06 ± 1.03	3.94 ± 0.90	2.80 ± 0.67

Table V.2. Summary of the phenotypic features quantified in *PIC2-GFP*, ∆ Nab3 RNA-BSs and ∆ NNS RNA-BSs as well as WT, *pTEF1-PIC2* and *pic2∆::HIS3* grown in medium containing 1% (w/v) raffinose.

VI. Blocking Nab3 Binding to *PIC2* mRNAs Impacts Expression of Other NNS-regulated Targets

VI.1. Introduction

In the preceding chapter, I established that increases in *PIC2* mRNA and protein levels did not result in identical phenotypes observed in the ∆ Nab3 RNA-BSs mutant. More specifically, *PIC2* overexpression did not cause significant cell size enlargement or cell cycle prolongations, nor did it elicit the same set of energy homeostasis imbalances that I had detected in the strain lacking Nab3 cognate sites in *PIC2*. Therefore, although Pic2 overabundance was, as expected, detrimental for the cell, the ∆ Nab3 RNA-BSs appeared to be facing intracellular conditions driving phenotypes that were overlaying and obscuring the ones owing to enhanced Pic2 levels alone.

In chapter IV, I showed that specifically preventing Nab3 recruitment to *PIC2* transcripts yielded the most accentuated anomalies. Interestingly, however, combining mutations in Nab3 cognate sites with impaired Nrd1 binding ameliorated such defects. Cumulatively, this suggested that creating an imbalance in the RNA recognition capabilities of Nab3 and Nrd1 for *PIC2* mRNA was causing the phenotypes in the ∆ Nab3 RNA-BSs strain. Strikingly, the CRAC experiment showcased in chapter I showed that Nrd1 occupancy in *PIC2* was largely unaffected in the mutant that is unable to bind Nab3. In the same section of that chapter, I provided evidence that Nrd1 recognition on its own is not sufficient to induce premature termination of *PIC2* transcripts. Previous work established that degradation of ncRNAs by the exosome is required to release Nab3 and Nrd1 from their target after transcriptional termination (Villa et al., 2020). Therefore, I reasoned that if Nrd1 on its own was not able to prematurely terminate *PIC2* as efficiently as the whole NNS complex, some Nrd1 molecules could be remaining bound to excess *PIC2* mRNAs because they cannot be recycled rapidly enough. Thus, reduced availability of Nrd1 would impact the homeostasis of co-regulated NNS RNA targets in the ∆ Nab3 RNA-BSs mutant. Accordingly, I suspected that disrupting Nab3 binding to *PIC2* could change the levels of many other NNS-regulated transcripts and, so, ultimately drive the cell volume and

cycle anomalies as well as the increased intracellular stress detected in Δ Nab3 RNA-BSs.

Earlier literature had detected cell size increases in yeast cells undergoing induced Nab3 depletion or encoding mutations in the RNA-binding residues of Nrd1 (Ajazi et al., 2022; Darby et al., 2012). Given that Nab3 and Nrd1 are engaged in the transcriptional termination of diverse RNAs in the nucleus, both models hamper NNS complex assembly onto most of its targets. Based on these findings, I set out to investigate whether blocking transcriptome-wide NNS-mediated termination would lead to cell size and cell cycle anomalies similar to those that I had identified in the Δ Nab3 RNA-BSs.

VI.2. Conditional depletion of Nab3 increases cell size, prolongs cell cycle, and induces polyploidy.

Intriguingly, previous studies had reported cell size increases in yeast models where Nab3 or Nrd1 are prevented from binding their RNA targets (Ajazi et al., 2022; Darby et al., 2012). To establish a causal relationship between these two phenomena, I used a previously engineered anchor-away strain in which Nab3 could be conditionally depleted from the nucleus (Haruki et al., 2008; van Nues et al., 2017) (Figure VI.1). In this strain, Nab3 was fused to the FKBP12-rapamycin-binding (FRB) domain in a strain in which the ribosomal protein RPL13A had been previously tagged with the FKBP12 epitope (Figure VI.1). RPL13A-FKBP12 assembles into pre-ribosomes in the nucleus. Then, in the presence of rapamycin, the FKBP12 and FRB domains form a stable complex that effectively ties Nab3-FRB to pre-ribosomal complexes. During ribosome maturation, these highly abundant pre-ribosomes are exported to the cytoplasm, thereby titrating any bound Nab3 away from the nucleus.

Given that rapamycin is required to induce cytoplasmic sequestration of the tagged nuclear protein of interest, this experiment had to be performed in rapamycin-resistant strains encoding a genetically altered version of *TOR1* (i.e., *tor1-1*). Such gene codes for a subunit of the target of rapamycin (TOR) complex, an evolutionarily conserved protein kinase which modulates cell growth based on nutritional availability (Schmelzle and Hall, 2000). In fact, TOR was originally discovered in yeast by the resistance that

strains containing mutations in *TOR1* and its *TOR2* counterpart displayed to rapamycin-prompted growth inhibition (Heitman et al., 1991).

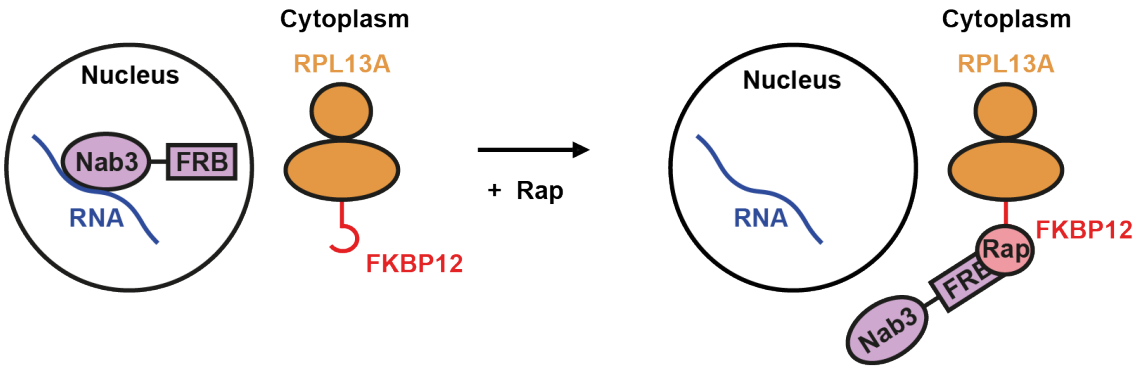

Figure VI.1. Simplified schematic overview of the anchor-away conditional depletion system.

After exposing *NAB3-FRB* and its rapamycin-resistant parental counterpart to rapamycin, I monitored changes in their cell size throughout time. To account for the differences that could have emerged from the presence of rapamycin in the medium, I performed a time-series recording of cell size in a parental strain lacking a C-terminal *FRB* (Figures VI.2-4). Using flow cytometry, I measured the forward light scatter (FSC) of *NAB3-FRB* and its parental reference when grown in medium containing 2% (w/v) or 1% (w/v) raffinose (Figures VI.2-4). To compare the dimensional changes experienced by each strain, I compared the FSC values of each time point to those of the untreated sample gathered at the first time point (Figures VI.2-4). As these assays were performed in triplicates for each strain and condition, I could plot the weighted average and standard deviations for the median FSC value obtained in each biological repeat. Upon statistical analysis, I observed that depleting Nab3 from the nucleus yielded larger cell sizes (Figures VI.2-4).

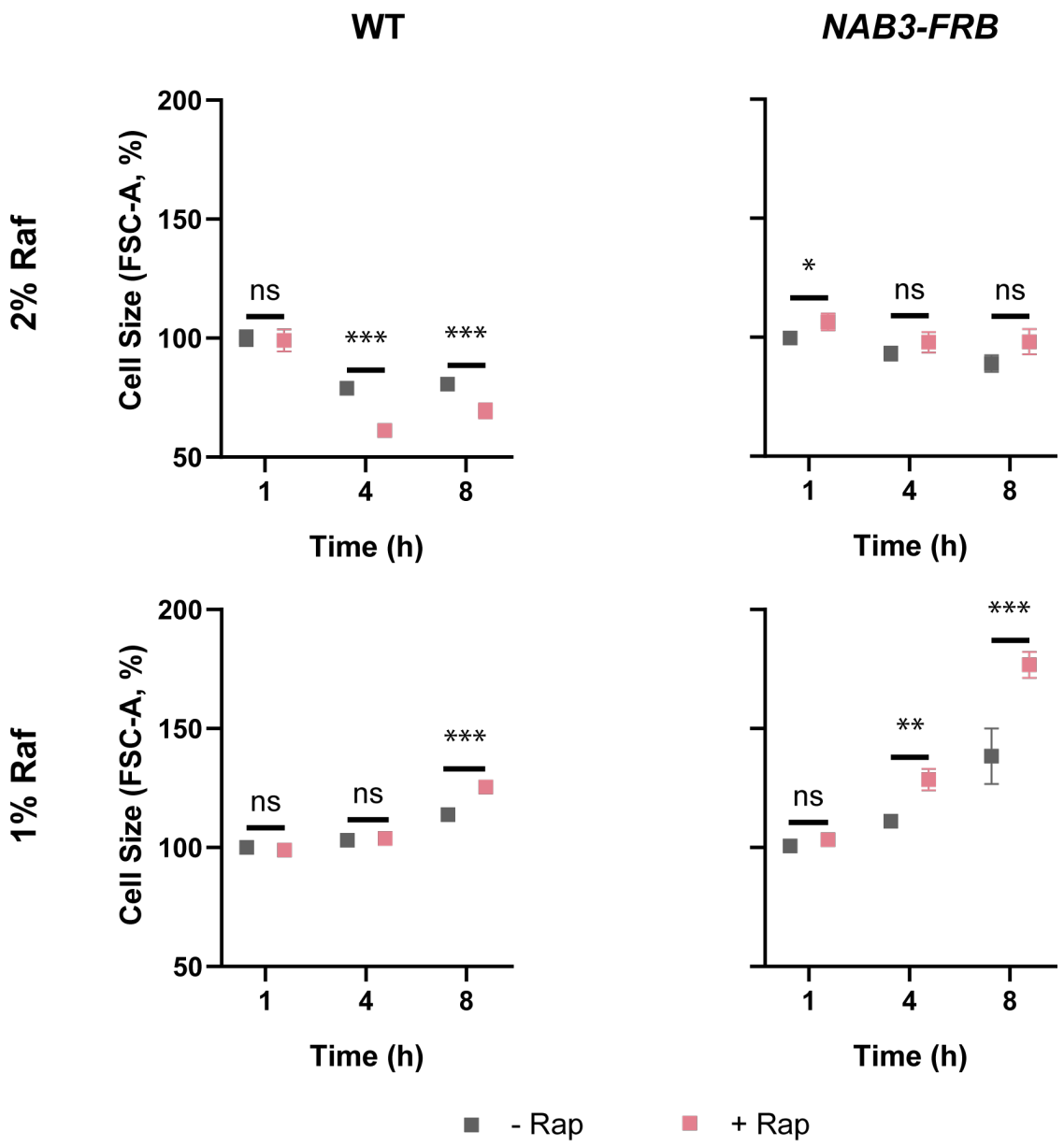

Figure VI.2. Cell sizes increase upon cytoplasmic sequestration of Nab3 in *NAB3-FRB*. Cell sizes in the parental rapamycin-resistant WT strain were monitored to identify the effect that the drug would have on exposed populations (+ Rap) compared to untreated counterparts (- Rap) when grown in medium supplemented with 2% (w/v) or 1% (w/v) raffinose. Boxes represent weighted means of the median FSC values for three independent biological repeats that were calculated for each strain and normalised to the parental WT. Error bars represent standard deviation. Statistical comparisons between each mutant and the *PIC2-GFP* reference were performed by an unpaired t-test. *: $p<0.05$, **: $p<0.01$ and ***: $p<0.001$ and 'ns': $p>0.05$.

In raffinose-abundant (i.e., 2% (w/v)) medium, rapamycin treatment significantly decreased the cell size of the parental strain after 4 hours of exposure to the drug

(Figures VI.2-3). Nonetheless, in the sample undergoing rapamycin-dependent Nab3 nuclear depletion, cell size was significantly larger at the first time point and, unlike the parental strain, exhibited no significant changes upon rapamycin exposure in succeeding time points (Figures VI.2-3). In other words, it seemed that, in raffinose-rich medium, the cell size increases driven by cytoplasmic sequestration of Nab3 neutralised the cell size decreases that rapamycin was intrinsically inducing the parental strain.

Notably, this evidence did not agree with prior findings reporting that, in the presence of rapamycin, cells become larger (Chan and Marshall, 2014). However, this incongruence may be owing to the different growth media in which the experiments were conducted: while my cultures contained synthetic complete medium supplemented with raffinose, the cells in the referred study were grown in rich YPDA medium formulated with yeast extract, peptone and glucose (Chan and Marshall, 2014). Therefore, it is plausible that rapamycin has a different effect on cell size depending on the medium as well as the nature and concentration of the sugar in suspension. In fact, in murine fibroblasts, rapamycin is known to cause cell volume decreases (Fingar et al., 2002).

On the other hand, the cell volumes measured in low (i.e., 1% (w/v)) raffinose medium evidenced a more defined impact of Nab3 cytoplasmic sequestration in cell size (Figures VI.2 and VI.4). In this growth condition, increases in the cell size of the *NAB3-FRB* strain were already detectable after 4 hours of rapamycin treatment and eventually became equivalent to those in the Δ Nab3 RNA-BSs following 8 hours of exposure to rapamycin (Figures VI.2 and VI.4). Importantly, nevertheless, exposing the parental strain to rapamycin for 8 hours resulted in minor cell size enlargements (Figures VI.2 and VI.4). Indeed, rapamycin can arrest cells in G1, thereby increasing their cell size (Barbet et al., 1996; Neurohr et al., 2019). Thus, despite having been engineered to resist the toxicity of rapamycin (Haruki et al., 2008), the parental strain does not appear to be fully insensitive to the drug. Overall, however, this surprising finding did not undermine the general conclusion of the experiment which was that preventing Nab3 from localising to its native nuclear environment led to enhanced cell size.

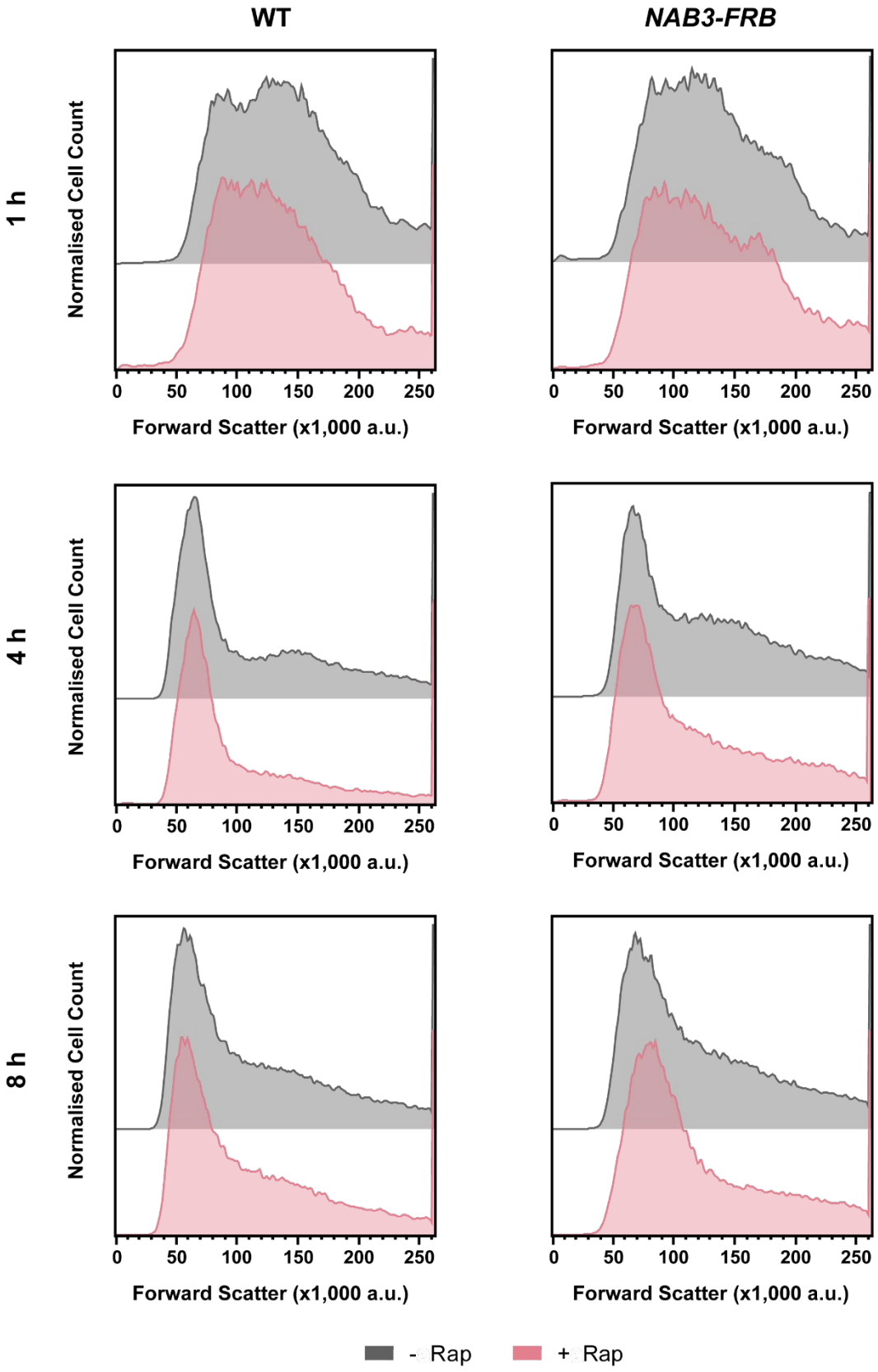

Figure VI.3. Representative flow cytometry traces of the cell size distribution of WT and *NAB3-FRB* strains when grown in medium containing 2% (w/v) raffinose and either exposed to rapamycin (+ Rap) or untreated (- Rap). The sizes were compared using their forward light scatter (FSC) values.

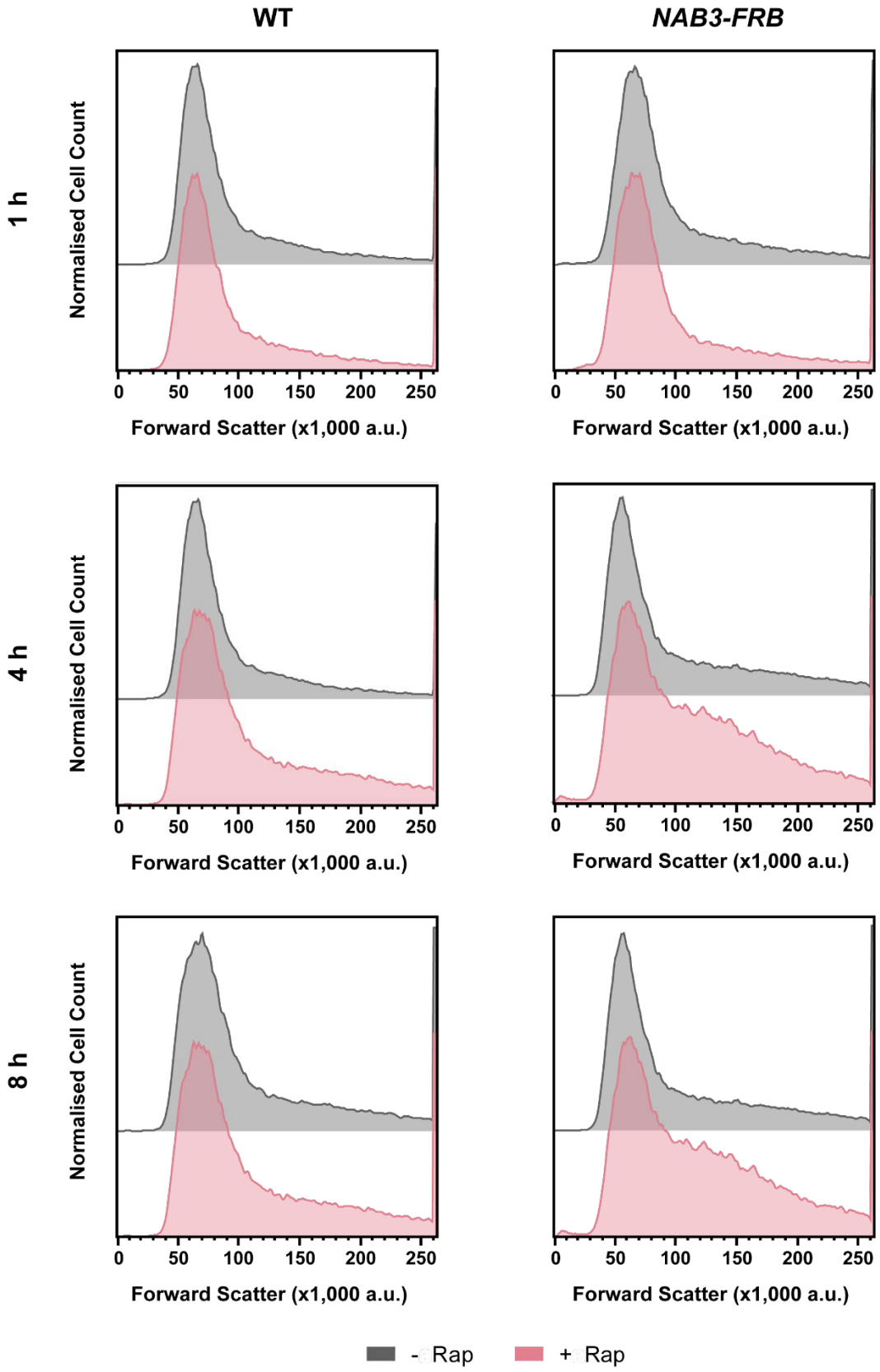

Figure VI. 4. Representative flow cytometry traces of the cell size distribution of WT and *NAB3-FRB* strains when grown in medium containing 1% (w/v) raffinose and either exposed to rapamycin (+ Rap) or untreated (- Rap). The sizes were compared using their forward light scatter (FSC) values.

Since cell size increases have been linked to cell cycle disruptions (Neurohr et al., 2019), I next tested whether the cell cycle of the *NAB3-FRB* strain became longer upon Nab3 depletion. To this end, I stained the DNA content of previously fixed, permeabilised, RNA-depleted and proteinase-treated *NAB3-FRB* anchor-away cells and their background reference counterparts (Figures VI.5-6). As in IV.4, IV.9 and V.9, I used propidium iodide to mark the DNA quantity of single cells and subsequently assessed it as a red fluorescence signal employing flow cytometry to perform time-resolved cell cycle analyses. In this case, nonetheless, I extended the timespan of the experiment (Figures VI.5-6). The reason for this choice is that, based on my microplate reader assays and on the doubling time which I had estimated in prior experiments, I expected that at least one full cell cycle would be required to observe whether the oversized strain would display cell cycle defects. Given that around 2.5 and 4 hours were required for cellular replication in medium supplemented with 2% (w/v) and 1% (w/v) raffinose, I inspected the assessed populations 4, 8, 16 and 32 hours after treating the cultures with rapamycin. These sampling times allowed cells to divide at least a few times throughout the experiment.

As expected, no differences in cell cycle were identified up to 16 hours after sequestering Nab3 in the cytoplasm, regardless of the concentration of the medium in which the cells were grown (Figures VI.5-6). Yet, after 16 hours of rapamycin treatment, *NAB3-FRB* cells spent less time in G1, underwent prolonged S phases and became polyploid more frequently than their parental counterparts (Figures VI.5-6). These effects aggravated after 32 hours when significantly longer S phases were replaced by extended G2/M phases (Figures VI.5-6). Since rapamycin is known to cause G1 arrest (Barbet et al., 1996), and the parental strain was not fully resistant to the drug, the distribution of the cells from the control strain across different cell cycle stages was expected to shift towards 1n states throughout time (Figures VI.5-6). Since this was not occurring in the strain in which Nab3 was depleted from the nucleus, I concluded that impeding NNS termination of its RNA targets impaired cell cycle progression.

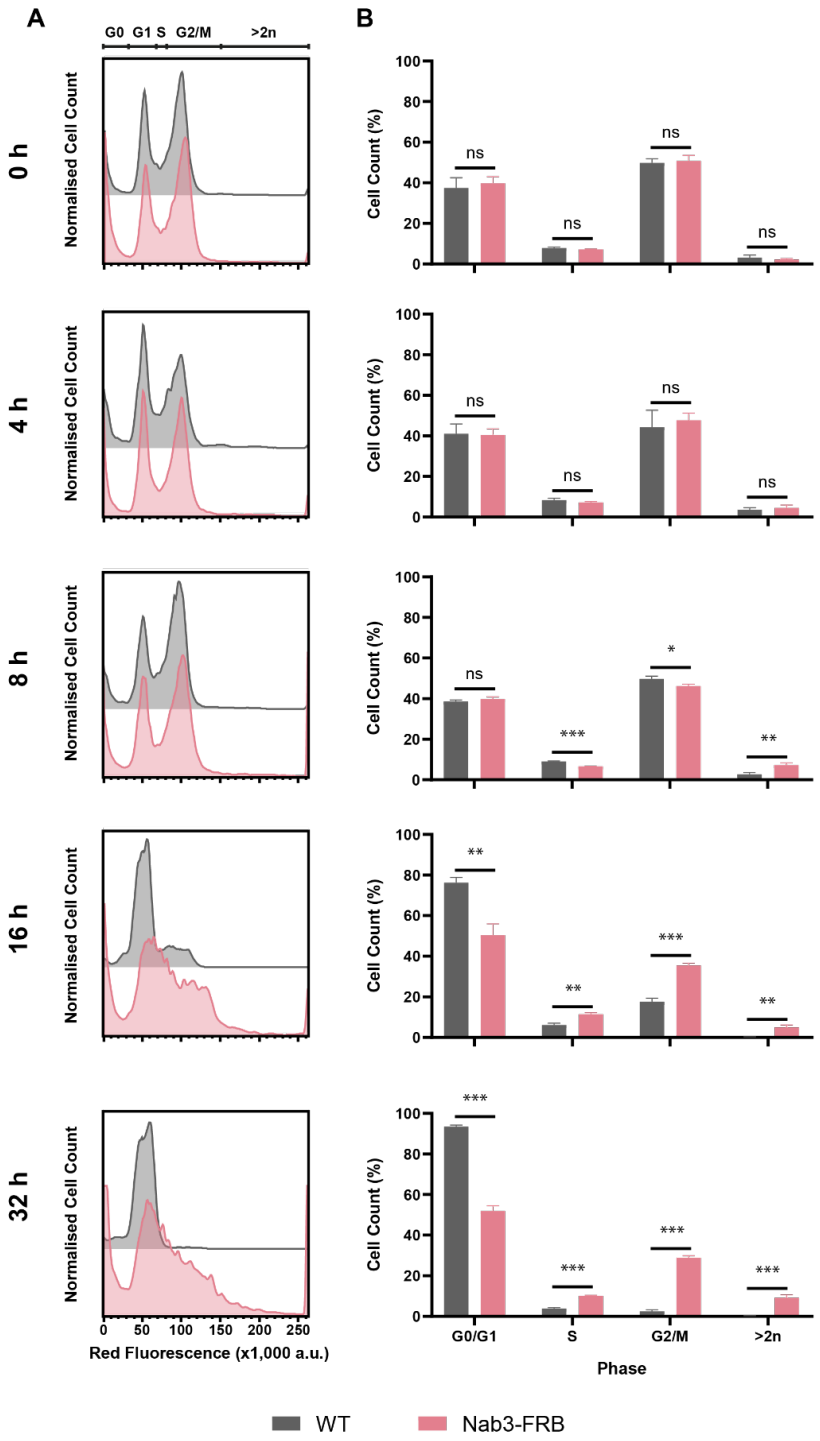

Figure VI.5. Cell cycle analysis of WT and *NAB3-FRB* and all derived mutants grown to mid-exponential phase (OD_{600} ~0.5) in medium containing 2% (w/v) raffinose. **A**. Representative flow cytometry traces of the DNA profiles of all strains. **B**. Weighted means of the population fraction of WT and *NAB3-FRB* within each cell cycle phase. Values based on biological triplicates and error bars represent the standard deviation calculated after considering the three repeats per strain. Error bars represent standard deviation. Statistical comparisons were performed by unpaired t-tests. *: $p<0.05$, **: $p<0.01$, ***: $p<0.001$ and 'ns': $p>0.05$.

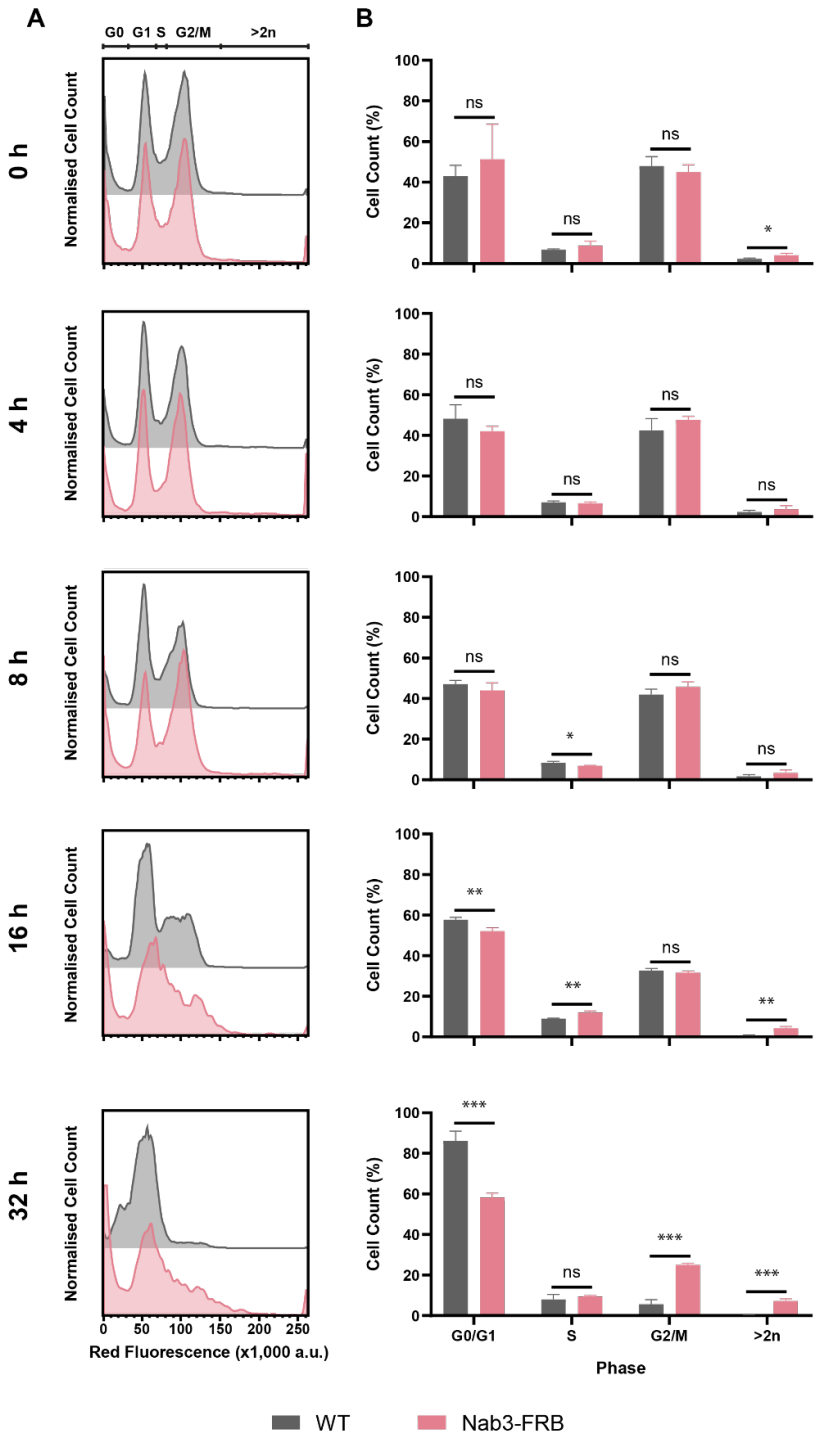

Figure VI.6. Cell cycle analysis of WT and *NAB3-FRB* and all derived mutants grown to mid-exponential phase (OD_{600} ~0.5) in medium containing 1% (w/v) raffinose. **A**. Representative flow cytometry traces of the DNA profiles of all strains. **B**. Weighted means of the population fraction of WT and *NAB3-FRB* within each cell cycle phase. Values based on biological triplicates and error bars represent the standard deviation calculated after considering the three repeats per strain. Error bars represent standard deviation. Statistical comparisons were performed by unpaired t-tests. *: $p<0.05$, **: $p<0.01$, ***: $p<0.001$ and 'ns': $p>0.05$.

VI.3. ncRNA targets of the NNS complex are more numerous in cells lacking Nab3 binding sites in *PIC2*.

One of the most remarkable findings of my PhD project was that abrogating Nab3 binding to a single mRNA species (i.e., *PIC2*) could elicit an identical set of aberrations as the one described upon Nab3 depletion. Primed by this contrast, I ideated a sequestration model that could explain the occurrence of such phenotypes in the Δ Nab3 RNA-BSs strain. In that mutant, the binding of Nab3 to *PIC2* mRNA was obstructed by two single-point mutations in the Nab3 recognition sites. Yet, my CRAC data showed that Nrd1 could still effectively cross-link to the *PIC2* transcript and, hence, could potentially recruit Sen1. Based on these observations, I devised a 'sequestration model' to explain the observed cell size and cell cycle defects in Δ Nab3 RNA-BSs. Although mutations Δ Nab3 RNA-BSs prevented Nab3 binding to *PIC2* mRNA (Figure III.4), Nrd1 continues binding to the *PIC2* transcript (Figure III.4) and might still recruit Sen1. I conjectured that because the *PIC2* transcripts in Δ Nab3 RNA-BSs could presumably no longer be terminated, Nrd1 could be sequestered to overabundant *PIC2* mRNAs by either titration or prolonged retention to the transcripts. Either scenario would reduce the availability of Nrd1, thereby altering its transcriptome-wide binding and preventing it from partaking in terminating the transcription of its targets. Ultimately, this causes a build-up of other NNS RNA targets, including those regulating cell division (Greenlaw et al., 2023), and potentially drives the cell size and cell cycle defects that I had observed in the mutant undergoing Nab3 sequestration (Figures VI.2-6). This hypothesis was based on previous work demonstrating that (i) RNA degradation is required for the effective release of Nrd1 and Nab3 from their substrates and (ii) that a degradation-resistant circular ncRNA decoy is sufficient to disrupt genome-wide NNS termination (Villa et al., 2020).

To test this idea and check whether NNS substrates accumulated in the Δ Nab3 RNA-BSs, I undertook a multi-omic comparison. Firstly, I conducted whole-transcriptome sequencing in the *PIC2-GFP* strain and its derived mutants. In these experiments, I used Δ NNS RNA-BSs as a control strain in which I did not expect to see much, if any, Nrd1 sequestration to *PIC2* transcripts. Moreover, since the excess of *PIC2* transcripts reached its highest point in the Δ Nab3 RNA-BSs cells grown in raffinose-limiting (i.e., 1% (w/v)) medium (Figures III.3 and III.8-9), I expected said

mutant to display the largest number of differentially expressed (DE) RNAs when grown in such conditions.

Applying DESeq2 (Love et al., 2014), I identified differentially expressed (DE) transcripts exhibiting at least a two-fold change in abundance in any of the two examined mutants (Figure VI.7). According to this criterion, in raffinose-rich (i.e., 2% (w/v)) medium, the ∆ Nab3 RNA-BSs mutant displayed 130 DE RNAs. In contrast, I only detected 6 differentially expressed transcripts in ∆ NNS RNA-BSs cultures grown in the same conditions (Figure VI.7A). As I had anticipated, the number of DE RNAs greatly increased in both mutants when grown in low raffinose (i.e., 1% (w/v)) medium: the number of DE RNAs in the ∆ Nab3 RNA-BSs and ∆ NNS RNA-BSs mutants went up to 488 and 41, respectively (Figure VI.7B). Therefore, these data strongly suggested that blocking Nab3 binding to *PIC2* impinges on other NNS targets and that its impact became larger in low raffinose (i.e., 1% (w/v)) medium.

Despite their vast phenotypic differences, the transcriptome of the ∆ Nab3 RNA-BSs mutant was remarkably similar to that of *PIC2-GFP,* as only 488 RNAs were differentially abundant between both strains. Strikingly, 31 (out of 131) and 98 (out of 488) of the DE transcripts detected in medium containing high (i.e., 2% (w/v)) or low (i.e., 1% (w/v)) raffinose concentrations were CUTs and other ncRNAs (Figure VI.8). Given that these transcripts are NNS targets, the observation that ncRNAs comprised more than 20% of the DE transcripts in the ∆ Nab3 RNA-BSs mutant was consistent with reduced availability of the NNS components in that strain (Figure VI.8). Admittedly, the fraction of ncRNAs in ∆ NNS RNA-BSs was more than twice that of ∆ Nab3 RNA-BSs. However, the total number of DE ncRNAs in ∆ NNS RNA-BSs in raffinose-rich and raffinose-limiting medium was only 2 and 18, respectively (Figure VI.8). Moreover, almost all those occurrences - 2 and 11 ncRNAs in medium containing 2% (w/v) or 1% (w/v) respectively - were also differentially expressed in the ∆ Nab3 RNA-BSs (Figure VI.7). Altogether, these findings suggested that alterations in the abundance of ncRNAs in ∆ Nab3 RNA-BSs were more prominent and consequential than those in the ∆ NNS RNA-BSs mutant.

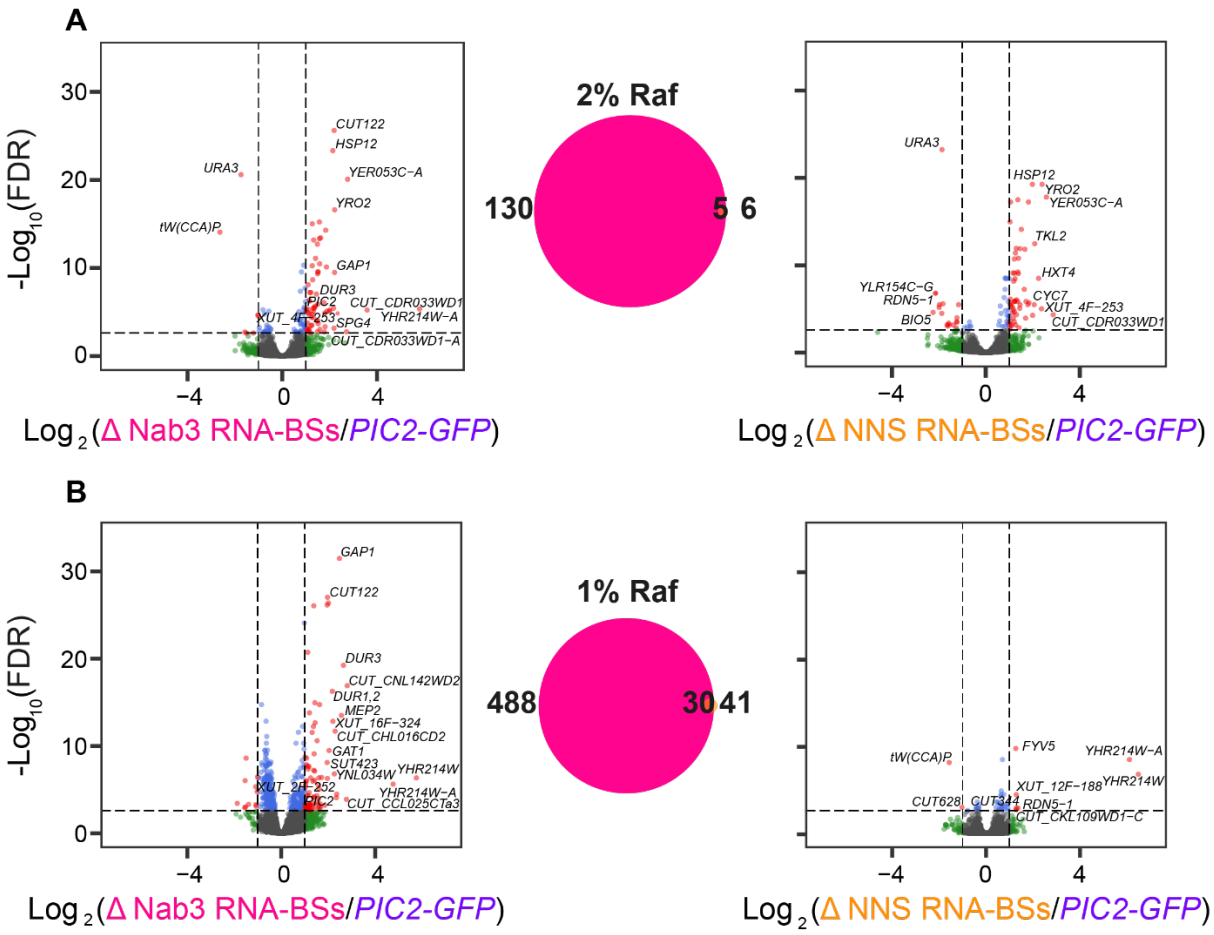

Figure VI.7. Transcriptomic comparison of Δ Nab3 RNA-BSs and Δ NNS RNA-BSs with *PIC2-GFP*. Volcano plots of transcripts with differential expression in Δ Nab3 RNA-BSs and Δ NNS RNA-BSs with respect to *PIC2-GFP* in raffinose-rich (**A**; 2% (w/v)) and raffinose-restricted (**B**; 1% (w/v)) medium. Selected RNAs presented $\log_2$(fold change)>1 (vertical dashed line) and false discovery rate (FDR)<0.05 (horizontal dashed line). Venn diagrams in **A** and **B** depict the count of differentially expressed transcripts in each mutant as well as the number of RNAs which were found to be differentially expressed in both strains at the tested conditions (i.e., 2% (w/v) Raf and 1% (w/v) Raf).

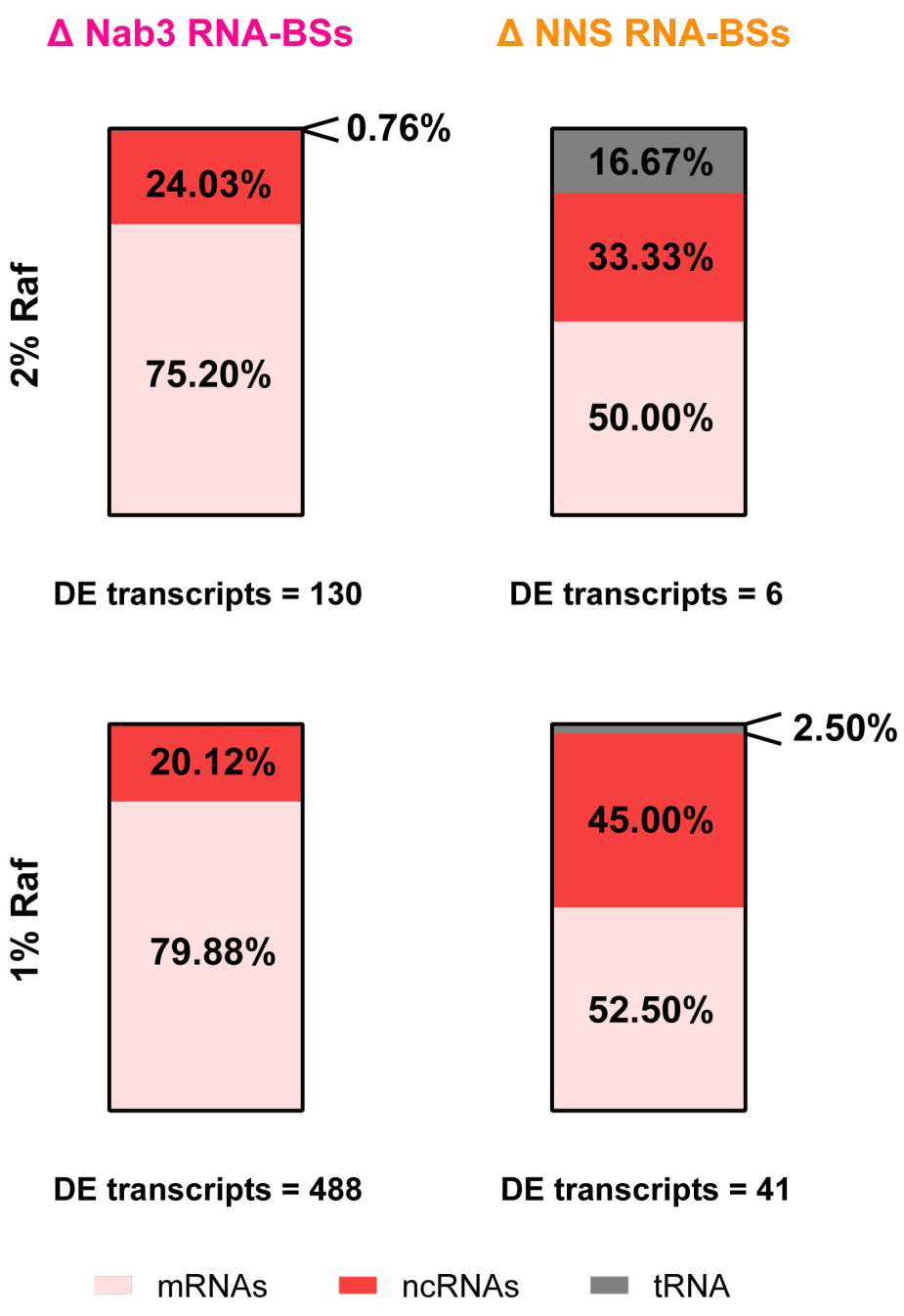

Figure VI.8. Bar charts indicating the proportion of messenger, non-coding and transfer RNAs among the transcripts that are differentially abundant in Δ Nab3 RNA-BSs and Δ NNS RNA-BSs grown in medium containing 2% (w/v) or 1% (w/v) raffinose.

With the aim of linking my transcriptomic findings with the phenotyping assays that I described in chapter IV, I performed gene ontology (GO) analyses on the differentially expressed transcripts of both mutants (Figure VI.9). Consistent with the higher levels of intracellular stress in Δ Nab3 RNA-BSs, my results detected an upregulation of genes involved in nutrient, heat, oxidative, and copper stress responses in all used growth media (Figure VI.9). In raffinose-rich (i.e., 2% (w/v)) medium, carboxylic acid

and aldehyde metabolism alongside protein deglutathionylation were enriched in Δ Nab3 RNA-BSs (Figure VI.9A). (Figure VI.9A). Interestingly, these metabolic processes were all linked to adaptive responses. For instance, carboxylic acids can be imported as nutrients or extruded in response to acid stress (Casal et al., 2016). Moreover, the upregulation of aldehyde dehydrogenase activity is a typical and evolutionarily conserved response to stress, which, in yeast, is particularly directed to alleviate stress derived from oxidative conditions or ethanol exposure (Singh et al., 2013). Finally, glutathionylation of cysteine residues is a reversible post-translational modification occurring in response to proteins being exposed to reactive oxygen species, particularly superoxide and hydrogen peroxide (Shino et al., 2022).

In raffinose-deprived medium (i.e., 1% (w/v)), there were additional GO terms that justified many of the anomalies that I had discovered in chapter IV, namely the excessive cell size and delayed cell cycle of Δ Nab3 RNA-BSs. Neurohr and colleagues discovered that, once a cell-specific volume threshold was surpassed, cellular protein and RNA content failed to scale with cell size (Neurohr et al., 2019). Ultimately, the cytoplasm of oversized cells becomes diluted, and accordingly, translation and transcription become downregulated in such populations. Consistent with this notion, ncRNA metabolism and nuclear export, as well as translation and ribosome biogenesis, were downregulated in Δ Nab3 RNA-BSs with respect to the parental *PIC2-GFP* (Figure VI.9B). Moreover, inhibition of the metabolism of non-coding transcript species was also in line with the accumulation of CUTs, SUTs, XUTs and other ncRNA targets of the NNS complex displaying differential abundant in Δ Nab3 RNA-BSs. Furthermore, the downregulation of transcripts involved in cell cycle regulation explained the delayed transition of this mutant through the G2/M phase (Figure VI.9B). Lastly, consistent with the increased respiratory rates detected in the Δ Nab3 RNA-BSs strain, energy derivation processes were also significantly enhanced in said mutant (Figure VI.9B). Conversely, the same analyses in Δ NNS RNA-BSs yielded no significant enrichments for differentially expressed transcripts.

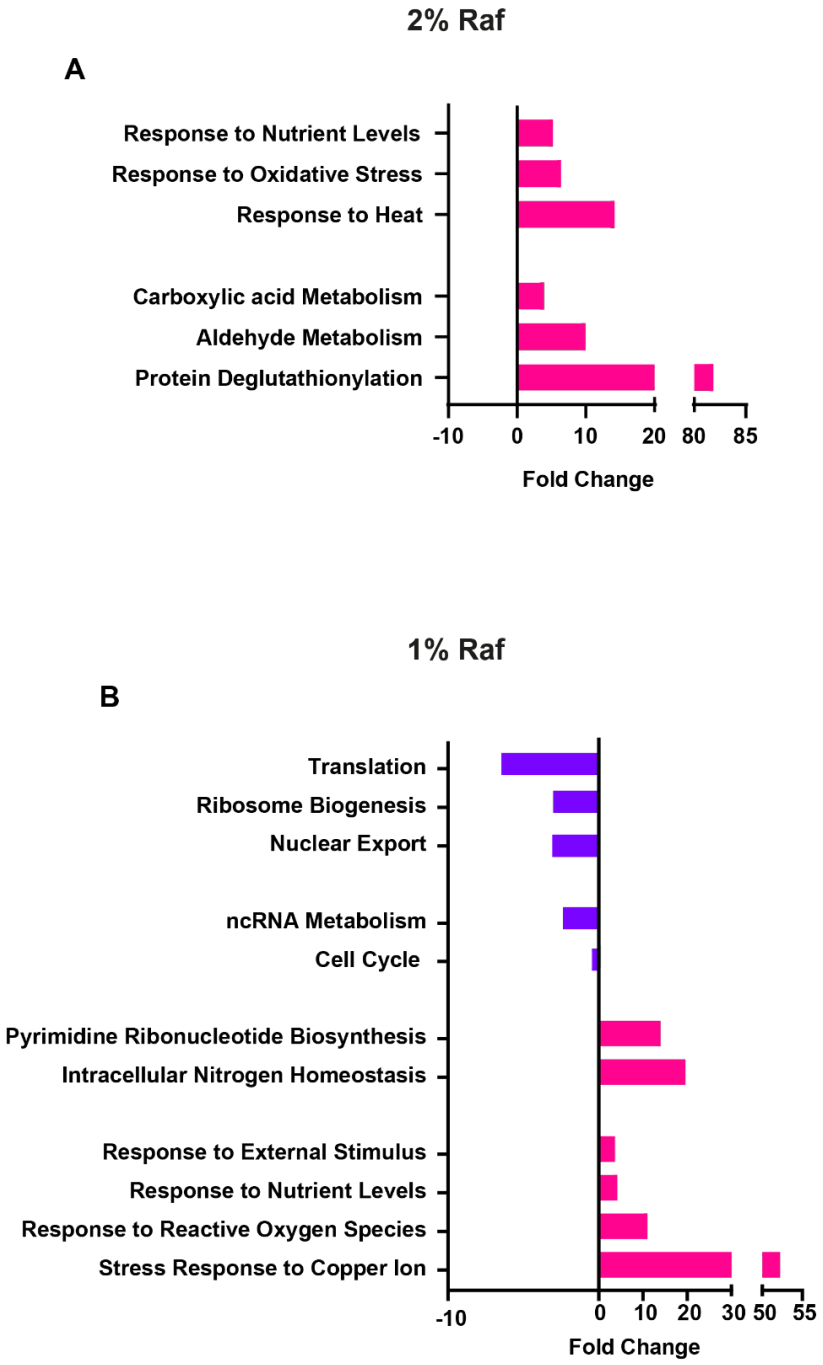

Figure VI.9. Significantly enriched biological processes identified by the PANTHER gene ontology software across the differentially expressed transcripts in Δ Nab3 RNA-BSs cells with respect to their *PIC2-GFP* reference (Thomas and Mushayahama, 2022). **A**. Biological processes that are up or downregulated in the mutant strain in medium containing 2% (w/v) raffinose, **B**. Differential biological processes found in Δ Nab3 RNA-BSs cells grown in medium supplemented with 1% (w/v) raffinose. The terms that are overrepresented in Δ Nab3 RNA-BSs and *PIC2-GFP* are shown in pink and purple, respectively. The bar plots only include significant biological processes (i.e., FDR <0.05).

VI.4. Various NNS protein-coding targets are differentially expressed in cells lacking Nab3 binding sites in *PIC2*.

To assess the impact of the transcriptomic changes in ∆ Nab3 RNA-BSs and ∆ NNS RNA-BSs on their protein profiles, I compared the proteomes of both mutants to that of their parental *PIC2-GFP* strain. Prior work has shown that quantitatively mRNA and protein abundances are weakly correlated, with overall reported Spearman or Pearson correlation coefficients, usually laying between 0.4 and 0.6 (Gan et al., 2013; Gry et al., 2009; Jüschke et al., 2013; Lan et al., 2012; Lundberg et al., 2010; O'Brien et al., 2010). Furthermore, several studies have demonstrated that there is a delay between transcriptomic remodelling and the resulting proteomic changes (Fournier et al., 2010; Kristensen et al., 2013; Lee et al., 2011; Robles et al., 2014; Waldbauer et al., 2012). Accordingly, I did not foresee a full agreement between the lists of differentially expressed RNAs and proteins.

My results showed that in raffinose-abundant medium (2%(w/v)), the number of differentially expressed proteins in ∆ NNS RNA-BSs (77) was slightly larger than that detected in the ∆ Nab3 RNA-BSs mutant (64). But, considering that the *S. cerevisiae* proteome comprises 5,858 proteins (Ho et al., 2018), the percentage of DE proteins in both mutants was relatively small (1.31% and 1.09% respectively). Interestingly, contrary to my analyses on RNA-sequencing outputs, the fraction of DE terms in the ∆ NNS RNA-BSs mutant which overlapped with those identified in ∆ Nab3 RNA-BSs was much lower (i.e., around 25% in proteomic comparisons compared to more than 75% in transcriptomic ones). However, based on previous reports, it was not unexpected to see disagreements between the mass spectrometry and the RNA-sequencing data. In fact, a similar trend was observed in low raffinose medium (i.e., 1% (w/v)), where the number of differentially abundant proteins for the ∆ Nab3 RNA-BSs and ∆ NNS RNA-BSs strains was 94 and 50 respectively (Figure VI.10). Importantly, in medium supplemented with 1% (w/v) raffinose conditions, where Pic2-GFP abundance increased, the proteome of the ∆ Nab3 RNA-BSs strain became more distinct from that of the parental strain.

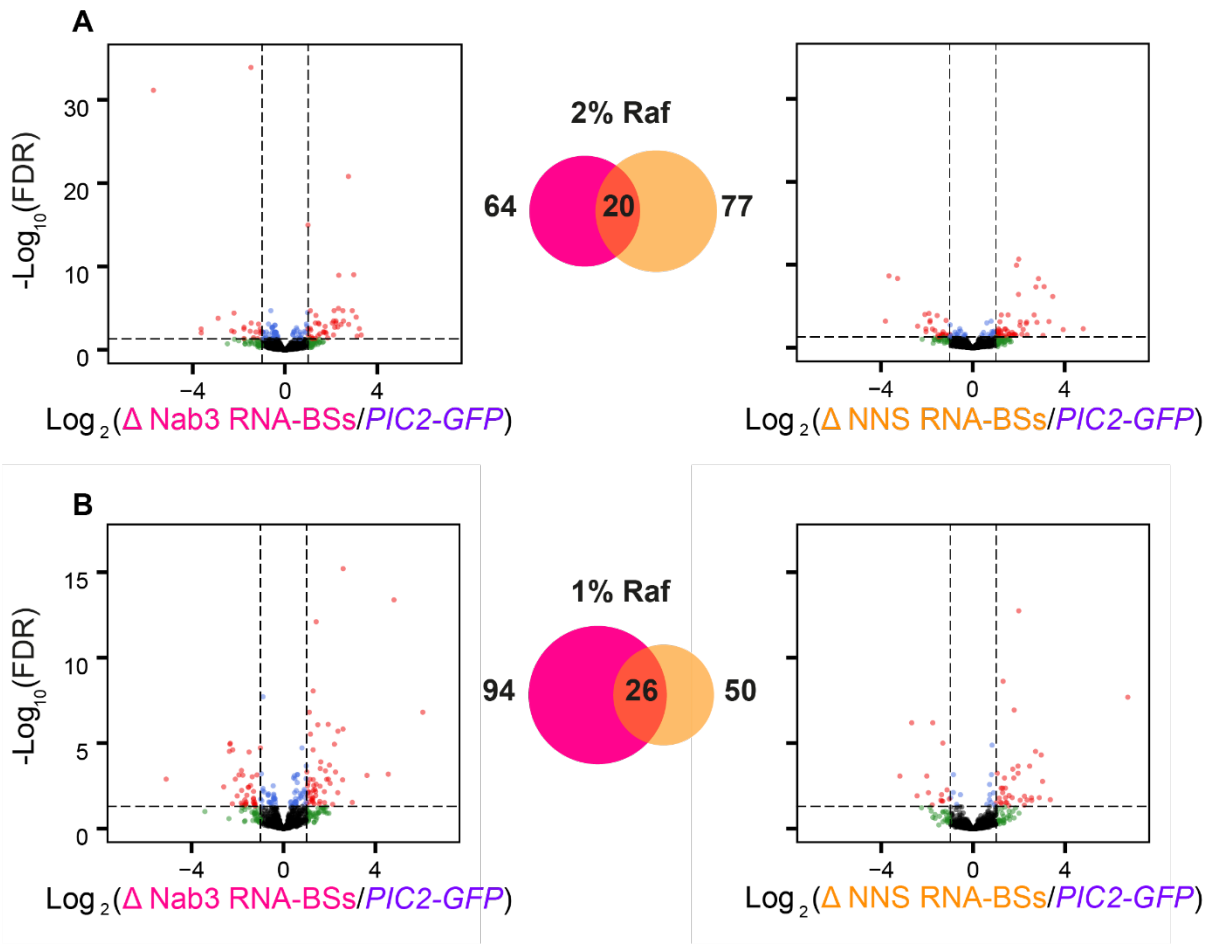

Figure VI.10. Proteomic comparison of Δ Nab3 RNA-BSs and Δ NNS RNA-BSs with *PIC2-GFP*. Volcano plots of proteins with differential expression in Δ Nab3 RNA-BSs and Δ NNS RNA-BSs with respect to *PIC2-GFP* in raffinose-rich (**A**; 2% (w/v)) and raffinose-restricted (**B**; 1% (w/v)) medium. Selected factors presented $\log_2$(fold change)>1 (vertical dashed line) and false discovery rate (FDR)<0.05 (horizontal dashed line). Venn diagrams in **A** and **B** depict the count of differentially expressed proteins in each mutant as well as the number of factors which were found to be differentially expressed in both strains at the tested conditions (i.e., 2% (w/v) Raf and 1% (w/v) Raf).

Overall, my comparative analyses suggested that the phenotypes that I had described in Δ Nab3 RNA-BSs stemmed from transcriptomic and proteomic changes which, as demonstrated by the functional enrichments among its DE transcripts, belonged to cellular pathways related to cell size, cell cycle and cellular response to stress (Figure VI.9). To test whether such processes were also prominent among differentially abundant proteins, I performed a similar GO search. Initially, I applied

identical screening criteria: I looked for functional groups strictly among statistically significant proteins (i.e., FDR<0.05) displaying a fold change in expression higher than 2 or lower than -2. Nonetheless, given that very few proteins displayed a log_2 fold-change of +/-1, this analysis did not yield any significant enrichment. To circumvent this, I decided to carry out the search in all the proteins with significantly different expression (i.e., FDR<0.05) in the mutant with respect to the parental strain (Figure VI.10).

The results revealed that in high (i.e., 2% (w/v)) raffinose medium, processes related to gene expression such as RNA (e.g., ribonucleoprotein complex biogenesis) and protein synthesis (e.g., cytoplasmic translation as well as ribosome assembly and biogenesis) were downregulated in the Δ Nab3 RNA-BSs strain (Figure VI.11A). These features agreed with earlier evidence demonstrating that transcription and translation were inhibited in cells that, like the Δ Nab3 RNA-BSs ones, were significantly larger than their wild-type yeast counterparts (Neurohr et al., 2019). Moreover, in line with the higher respiratory rates in which Δ Nab3 RNA-BSs engages, energy-derivation processes such as oxidation of organic compounds or generation of precursor metabolites and energy, were upregulated in such mutant (Figure VI.11A). Conversely, when grown in the same medium, the Δ NNS RNA-BSs strain displayed inhibited amide and amino acid metabolism (Figure VI.12A). Given the breadth and ambiguity of the two only significant gene ontology terms yielded by this analysis, it was difficult to draw any meaningful conclusion about the biological implications, if any, that these enrichments may have in the Δ NNS RNA-BSs strain.

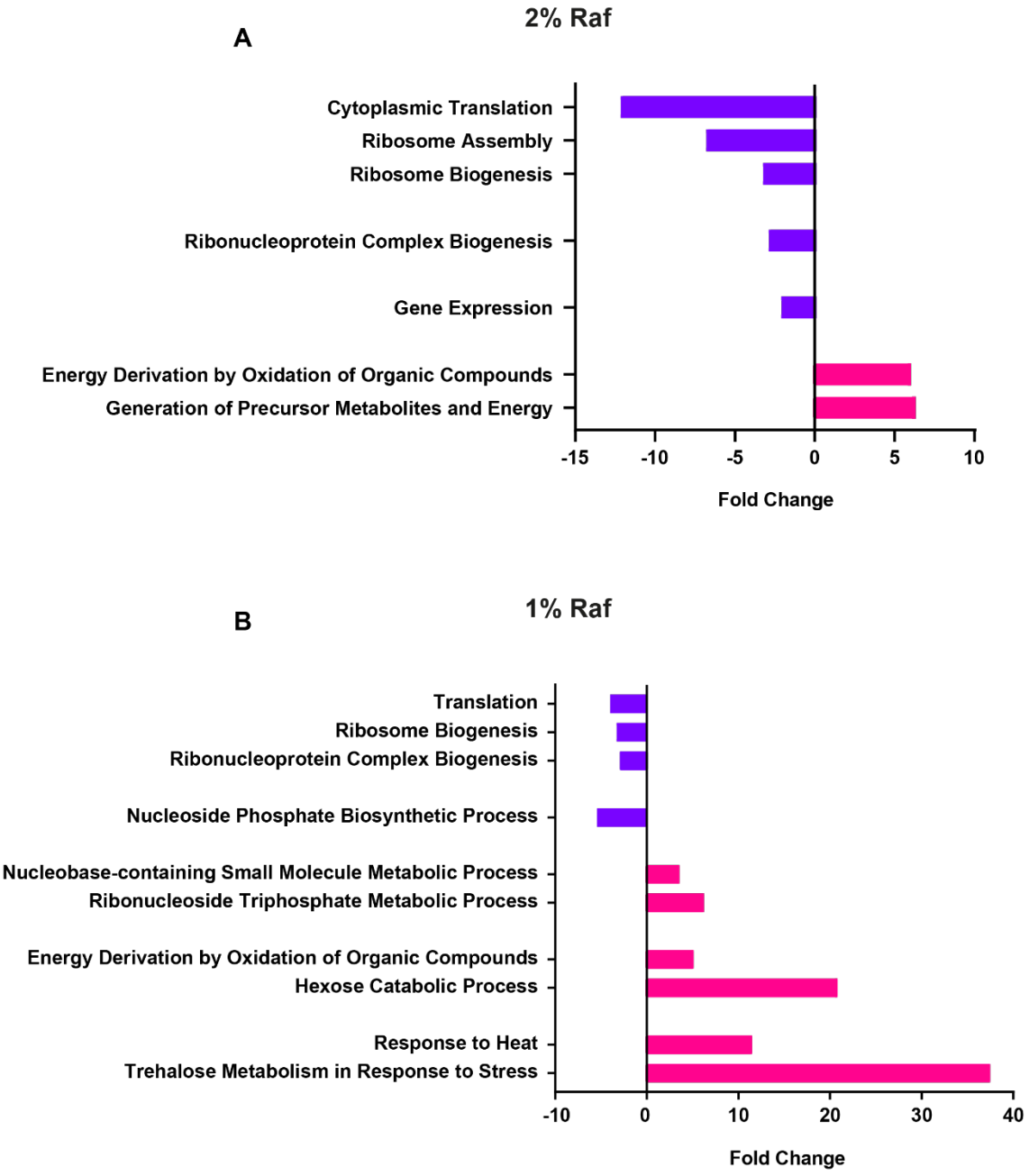

Figure VI.11. Significantly enriched biological processes identified by the PANTHER gene ontology software across the differentially expressed proteins in ∆ Nab3 RNA-BSs cells with respect to their *PIC2-GFP* reference (Thomas and Mushayahama, 2022). **A**. Biological processes that are up or downregulated in the mutant strain in medium containing 2% (w/v) raffinose, **B**. Differential biological processes found in ∆ Nab3 RNA-BSs cells grown in medium supplemented with 1% (w/v) raffinose. The terms that are overrepresented in ∆ Nab3 RNA-BSs and *PIC2-GFP* are shown in pink and purple, respectively. The bar plots only include significant biological processes (i.e., FDR <0.05).

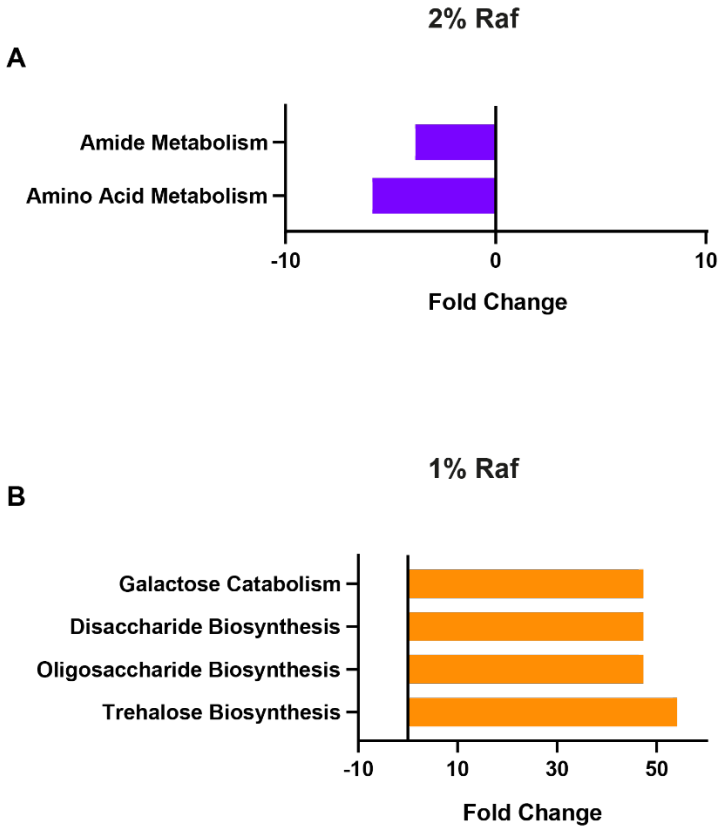

Figure VI.12. Significantly enriched biological processes identified by the PANTHER gene ontology software across the differentially expressed proteins in Δ NNS RNA-BSs cells with respect to their *PIC2-GFP* reference (Thomas and Mushayahama, 2022). **A**. Biological processes that are up or downregulated in the mutant strain in medium containing 2% (w/v) raffinose, **B**. Differential biological processes found in Δ NNS RNA-BSs cells grown in medium supplemented with 1% (w/v) raffinose. The terms that are overrepresented in Δ Nab3 RNA-BSs and *PIC2-GFP* are shown in orange and purple, respectively. The bar plots only include significant biological processes (i.e., FDR <0.05).

In low (i.e., 1% (w/v)) raffinose medium, however, the few functional enrichments detected in Δ NNS RNA-BSs were in accordance with my initial predictions: sugar metabolism proteins seemed to be more abundant in this mutant (Figure VI.12B). This was expected due to the mild increase in *PIC2* expression, which I had detected in some of my previous assays (Figures III.9 and III.11), and the accompanying subtle increase in mitochondrial membrane potential. The rationale of this prediction was that mildly enhanced assimilation of sugars could fuel small increases in mitochondrial membrane potential (Figures IV.9). Notionally, this principle would also explain the

upregulation of hexose catabolism that I observed in ∆ Nab3 RNA-BSs (Figure VI.11B). Moreover, oxidation of organic compounds, which was found to be stimulated in ∆ Nab3 RNA-BSs, could reasonably increase the intracellular concentration of reactive oxygen species and ultimately underlie the acquired resistance to oxidative stress shown in Figure IV.12. Furthermore, gene expression was, as in raffinose-rich medium, downregulated in the oversized mutant (Figure VI.11).

Nevertheless, in this instance I also found that ribonucleotide metabolic pathways, encompassing nucleoside phosphate biosynthesis, nucleobase-containing small molecule metabolism and ribonucleoside triphosphate metabolism, were altered in ∆ Nab3 RNA-BSs (Figure VI.11B). Intriguingly, several reports had collectively outlined ribonucleotide homeostasis as the main functional family to which the limited number of fully characterised protein-coding targets of the NNS complex predominantly belonged (Ajazi et al., 2022; Kuehner and Brow, 2008; Thiebaut et al., 2008). Therefore, proteomic comparisons of both examined mutants with their parental reference supported the sequestration model.

VI.5. The pyrimidine synthesis pathway, a prominent target of the NNS complex, is upregulated in cells lacking Nab3 binding sites in *PIC2* mRNA.

In the two previous sections, I showed that the functional enrichment analyses revealed a significant upregulation of RNAs and proteins involved in nucleotide biosynthesis (Figures VI.9 and VI.11). To shed light on the specific routes underpinning the alterations in ribonucleotide homeostasis, I conducted intracellular metabolite profiling. Given the elevated cost of this experiment and considering that I had only identified aberrant nucleotide metabolism in ∆ Nab3 RNA-BSs grown in medium containing 1% (w/v) raffinose, I proceeded to compare the metabolome of this mutant with that of *PIC2-GFP* in low raffinose medium. The experiments were run in triplicates, and upon computation of the average and standard deviation for the relative abundance of all detected metabolites, statistical analyses determined the set of metabolites that were differentially abundant in both strains.

My results showed that among the 7 differentially abundant metabolites, 6 of them were found to be in excess in ∆ Nab3 RNA-BSs and 1 was more highly concentrated in *PIC2-GFP* (Figure VI.13A). Subsequent functional pathway enrichment analysis established that metabolites implicated in the *de novo* pyrimidine synthesis pathway were systemically upregulated in the mutant (Figure VI.13A). The *de novo* pyrimidine synthesis encompasses the formation of uridine nucleotides from carbamoyl phosphate, aspartate, and phosphoribosyl pyrophosphate (Figure VI.13B). Incidentally, in most eukaryotic species the enzyme dihydroorotate dehydrogenase (DHODH) is embedded in the inner mitochondrial membrane and, by oxidising dihydroorotate to orotate, reduces coenzyme Q (CoQ) and flavin mononucleotide (FMN), which are key components of the electron transport chain. Consequently, in most eukaryotes, dihydroorotate dehydrogenase couples oxidative phosphorylation to the *de novo* synthesis of pyrimidines. Given that Pic2 is also (i) ingrained in the inner mitochondrial membrane and (ii) known to impact mitochondrial activity and oxygen consumption, it would have made sense to assume that upregulation of pyrimidine synthesis in the mutant originated from increased expression of Pic2. However, in this regard, *Saccharomyces cerevisiae* constitutes a notable exception with respect to other eukaryotes, as its dihydroorotate dehydrogenase, Ura1, is cytoplasmic and uses the electrons released during the oxidation of dihydroorotate to orotate to reduce fumarate to succinate (Figure VI.13B). Accordingly, I concluded the *de novo* pyrimidine synthesis in *S. cerevisiae* does not directly contribute to the electron transport chain and hence, such biochemical route remains functionally unrelated to Pic2 in *Saccharomyces cerevisiae*.

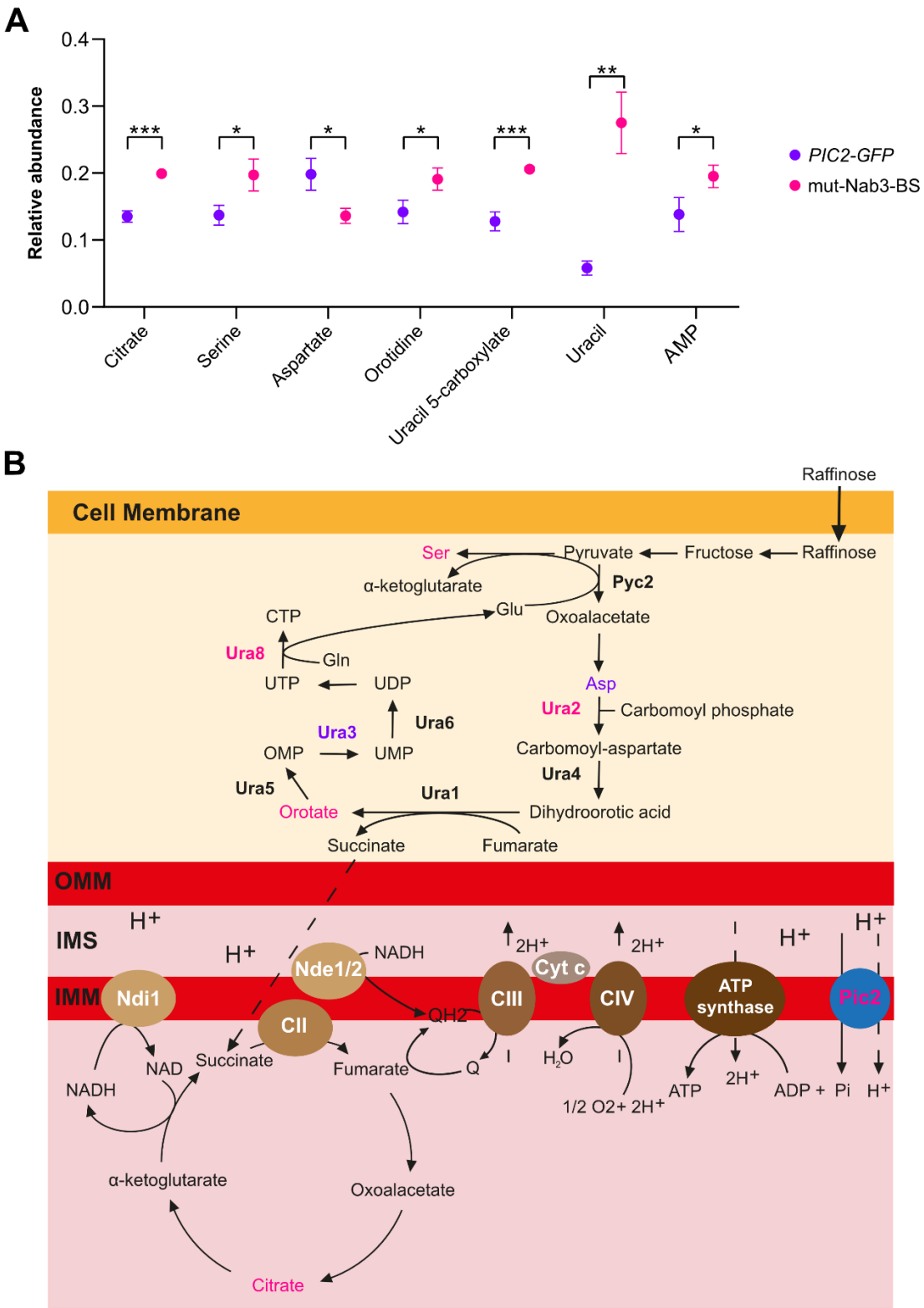

Figure VI.13. Gene expression changes in Δ Nab3 RNA-BSs are functionally linked to its metabolic alterations. **A**. Dot plot showing the average relative abundances of the metabolites identified as differentially abundant in the Δ Nab3 RNA-BSs mutant across three independent biological comparisons with *PIC2-GFP*. Error bars represent standard deviation (SD). **B**. Schematic overview of the pyrimidine synthesis pathway

and Pic2 function in transporting phosphate and copper across the inner mitochondrial membranes (IMM). Metabolites and enzymes in pink font are upregulated in ∆ Nab3 RNA-BSs; the ones shown in purple are significantly more abundant in the parental strain. IMS and OMM denote intermembrane space and outer mitochondrial membrane, respectively.

Metabolomic comparisons, thus, confirmed the findings presented in chapter V: the defects of ∆ Nab3 RNA-BSs stem from an independent molecular mechanism that was overshadowing that resulting from excessive Pic2 levels. In turn, these findings also substantiated a putative Nrd1/Sen1 sequestration to *PIC2* mRNA transcripts as 2 (i.e., Ura2 and Ura8, Figure) of the 8 enzymes catalysing the reactions comprising this pathway were well-studied targets of the NNS complex (Ajazi et al., 2022; Thiebaut et al., 2008). Consistent with a lower availability of Nrd1 and/or Sen1 for partaking in the premature termination of cognate RNAs in ∆ Nab3 RNA-BSs, Ura2 and Ura8 were upregulated in said mutant (Figure VI.13A). Accordingly, I concluded that the gene expression changes observed in ∆ Nab3 RNA-BSs significantly altered its metabolic flux. Cumulatively, this evidence bolstered the Nrd1/Sen1 out-titration model. However, I had yet to prove whether changes in the gene expression profile of the ∆ Nab3 RNA-BSs mutant could indeed be driven by altered Nrd1/Sen1 binding to NNS targets.

VI.6. Nrd1 transcriptomic distribution is altered in cells lacking Nab3 binding sites in *PIC2*.

If the Nrd1/Sen1 sequestration model was correct, changes in Nrd1 availability should also impact the expression of other NNS targets. Accordingly, I hypothesised that the NNS complex would also directly regulate many of the differentially expressed transcripts in the mutant lacking Nab3 binding sites in *PIC2* (i.e., ∆ Nab3 RNA-BSs). To preliminarily test this, I assessed whether the differentially expressed transcripts in the ∆ Nab3 RNA-BSs and ∆ NNS RNA-BSs strains generally contained a higher number of Nrd1 and Nab3 RNA-binding motifs, which would increase the chances of NNS-mediated termination.

With this aim, I scanned the sequences of all RNAs in the transcriptome for Nab3 and Nrd1 consensus sequences (i.e., UCUU and GUAA, respectively) (Carroll et al.,

2007, 2004) and computed the fraction of transcripts displaying at least one Nab3 RNA-BS or one Nrd1 recognition motif. The percentage of transcripts bearing either Nab3 or an Nrd1 site constituted the background fraction of Nab3 and Nrd1 recognition that must be significantly exceeded to consider that a given population of RNAs is significantly enriched in Nab3 or Nrd1 cognate sites. I also calculated the portion of RNAs with Nab3 and Nrd1 motifs among all the RNAs in the transcriptome; such percentage represented a positive control comprising all possible NNS targets.

Afterwards, I categorised the transcripts that were differentially expressed in the Δ Nab3 RNA-BSs and Δ NNS RNA-BSs strains into RNAs lacking or containing Nab3 or Nrd1 binding sites (Figure VI.14). As shown in Figure VI.14, the proportion of DE transcripts harbouring Nab3 and Nrd1 recognition motifs in the Δ Nab3 RNA-BSs mutant was larger than that calculated for the DE RNAs in Δ NNS RNA-BSs. Moreover, the DE RNAs of Δ Nab3 RNA-BSs encompassed a higher number of transcripts with Nab3 and Nrd1 motifs compared to the negative control (i.e., all RNAs). Conversely, the DE RNAs of Δ NNS RNA-BSs were not significantly different from those of the background control in that respect (Figure VI.14). Therefore, these findings are consistent with my hypothesis that a considerable proportion of the gene expression changes detected in the Δ Nab3 RNA-BSs mutant indeed occurred in NNS targets.

To substantiate this notion, I used the pyCalculateFDRs function from the pyCRAC package to identify significantly enriched binding peaks in my Nab3 and Nrd1 CRAC libraries (Webb et al., 2014). Firstly, I found the Nab3 and Nrd1 RNA-binding sites common to the two biological repeats which I performed in the parental reference. Then, I quantified the overlap between the genes targeted by Nab3 and Nrd1 in the CRAC datasets of *PIC2-GFP* and the DE RNAs in the Δ Nab3 RNA-BSs and Δ NNS RNA-BSs mutants (Figure VI.15). Interestingly, I observed that a significantly larger fraction of protein-coding genes in Δ Nab3 RNA-BSs were targeted by Nab3 and Nrd1 (Figure VI.15). Moreover, all the DE ncRNAs (around 100) in that mutant were bound by Nab3 and Nrd1. Admittedly, the fraction of differentially abundant non-coding transcripts containing Nab3 and Nrd1 peaks was larger in Δ NNS RNA-BSs (Figure VI.15). However, it is important to bear in mind that the total number of DE RNAs in the Δ NNS RNA-BSs strain is more than ten times lower than that of Δ Nab3 RNA-BSs (Figure VI.15). Therefore, proportionally comparing both transcript populations would tend to overrepresent any effect in the smallest dataset (i.e., DE RNAs of Δ NNS RNA-

BSs). Collectively, these analyses suggest that disrupting Nab3 binding to *PIC2* not only affects this specific transcript but also influences the abundance of other NNS target transcripts, indicating a broader co-regulation of NNS RNA targets across the transcriptome.

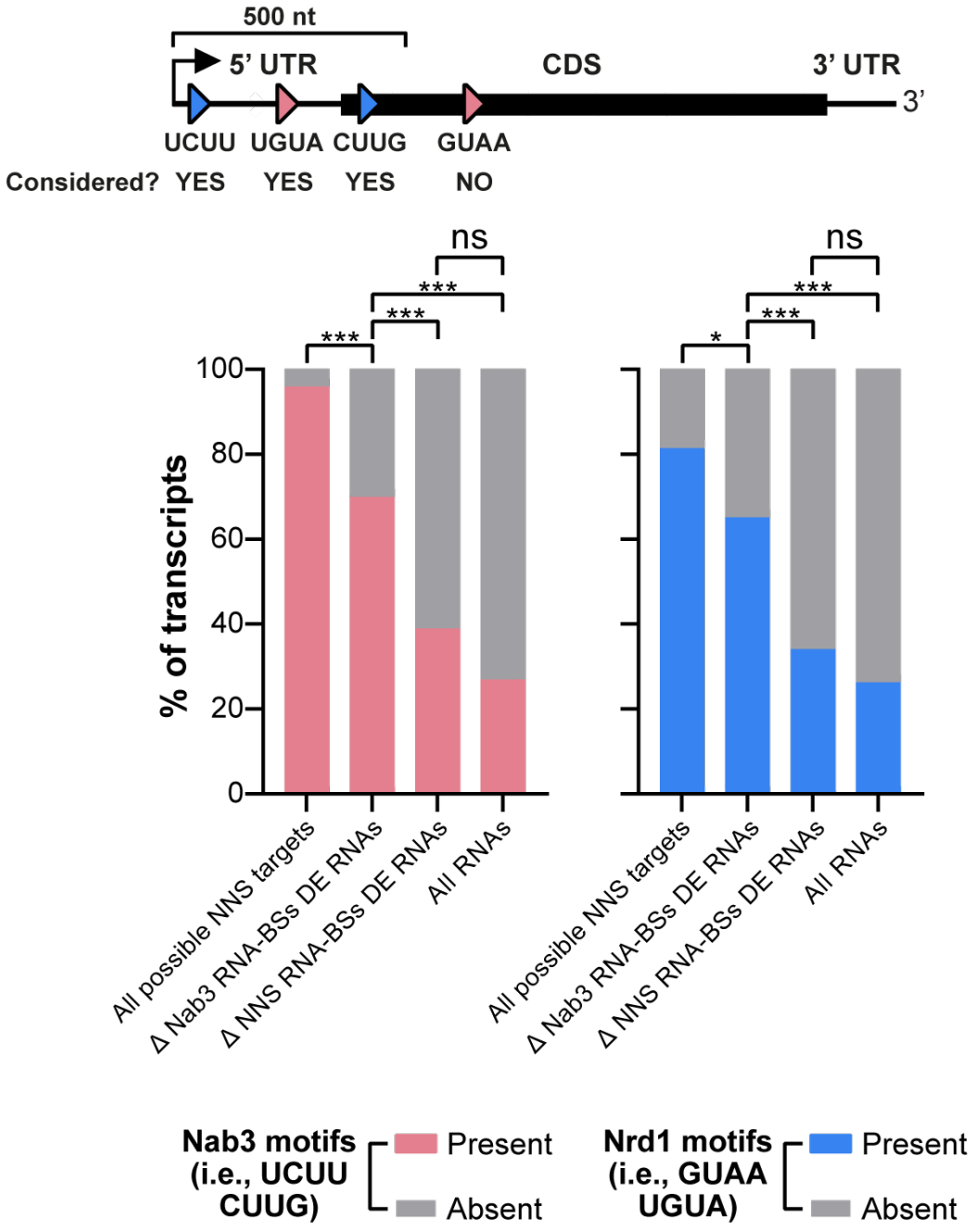

Figure VI.14. Fraction of transcripts containing Nab3 and Nrd1 binding motifs across differentially expressed transcripts of the Δ Nab3 RNA-BSs and Δ NNS RNA-BSs strains, all transcripts annotated in the genome (negative control) and all transcripts with at least one Nrd1 or Nab3 motif (positive control). Statistical comparison was performed using Fisher's exact test. *: $p<0.05$, ***: $p<0.001$ and 'ns': $p>0.05$.

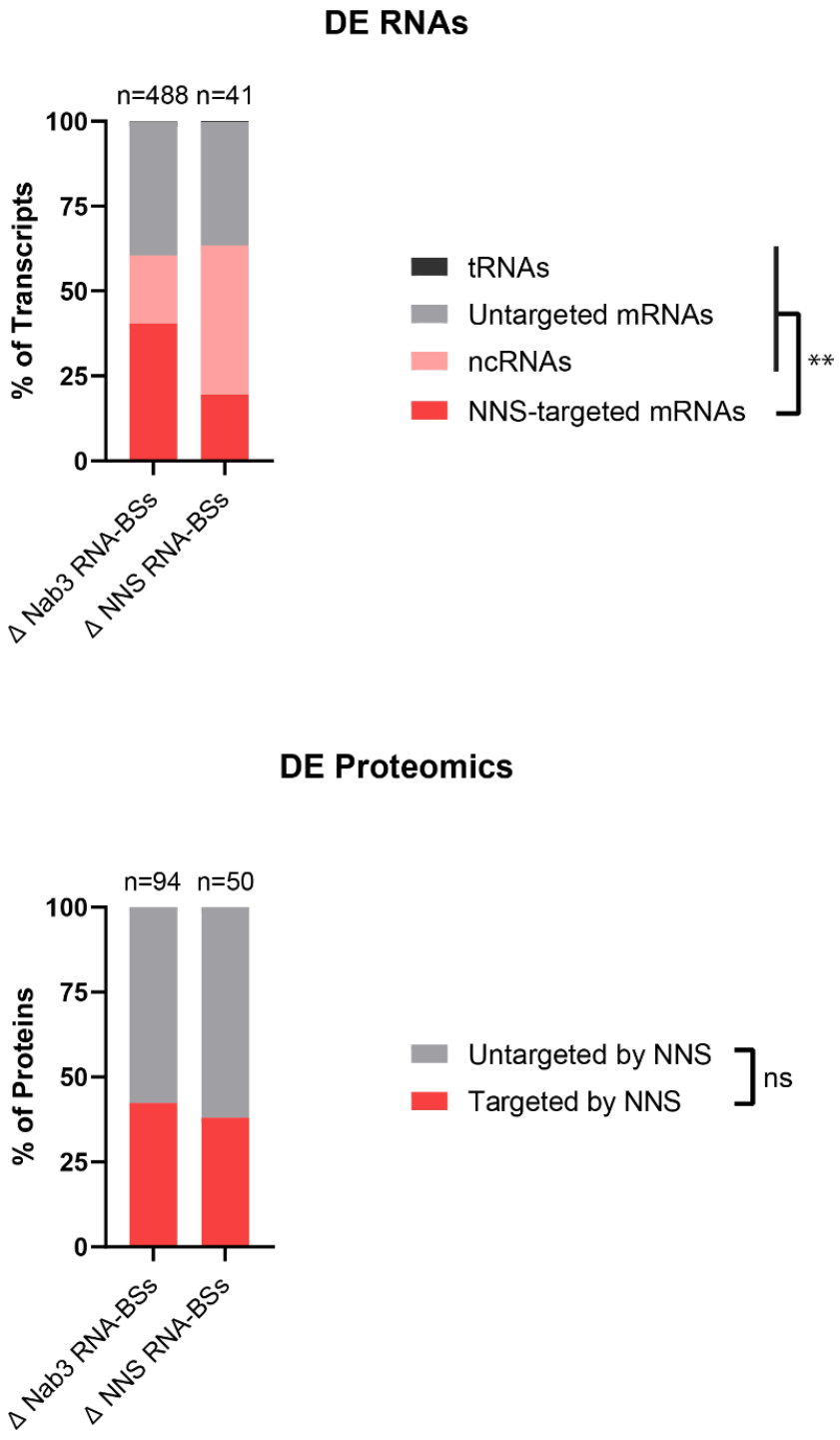

Figure VI.15. Stacked bar charts showing the proportion of differentially expressed RNAs and proteins in the Δ Nab3 RNA-BSs and Δ NNS RNA-BSs strains, which are also differentially bound by Nab3 and Nrd1 according to my CRAC data. The plot displaying DE RNAs also indicates the portion of differentially expressed transcripts comprising ncRNAs, tRNAs and mRNAs, which are not bound by Nab3 and Nrd1. Statistical comparison of the fractions of NNS targets in the Δ Nab3 RNA-BSs and Δ NNS RNA-BSs mutants was performed using Fisher's exact test. *: $p<0.05$ and 'ns': $p>0.05$.

Next, I went on to assess whether these transcriptomic differences also altered the proteome of the mutant strains. To this end, I followed the same approach to quantify the proportion of DE proteins in the Δ Nab3 RNA-BSs and Δ NNS RNA-BSs strains that were encoded by Nab3 and Nrd1 targets (Figure VI.15). As shown in Figure VI.15, more than a third of the proteins that were differentially expressed in both mutants were encoded by genes bearing Nab3 and Nrd1 binding sites. Although the fraction of Nab3 and Nrd1 targets was 4% larger among the DE proteins of Δ Nab3 RNA-BSs, it was not high enough to be considered significantly different from that of Δ NNS RNA-BSs (Figure VI.15). Nevertheless, as for the transcriptomic assessments, the number of differentially expressed proteins in Δ NNS RNA-BSs was almost half of those in the Δ Nab3 RNA-BSs mutant (Figure VI.15).

To confirm that the observed changes in the transcriptome and proteome could potentially arise due to altered Nab3 and Nrd1 binding to NNS targets, I employed the DBPeaks tool developed by Prof Sander Granneman to identify differentially bound Nab3, Nrd1, Rpo21 and Sen1 peaks within the CRAC datasets. Briefly, by applying the pyCalculateFDRs function from the pyCRAC package (Webb et al., 2014), I performed peak-calling in the two experimental replicates performed for each protein in the three tested strains. Subsequently, I excluded the peaks encompassing fewer reads than the mean coverage of all other peaks in the dataset. Afterwards, DBPeaks filtered out entries that were not found in all samples and normalised the widths of the remaining peaks to a minimum length. Finally, the software obtained the total number of reads covering those peaks in each strain and fed the resulting count tables to DESeq2 (Love et al., 2014), which identified the peaks that were differentially bound (DB) in the mutants with respect to the parental *PIC2-GFP* reference.

The results demonstrated that Nab3 occupancy across the transcriptome of the mutants barely differed from that in the parental strain (Table VI.1). Whereas Δ Nab3 RNA-BSs presented 6 DB Nab3 sites (including the one in *PIC2*), the Δ NNS RNA-BSs Nab3 only displayed one differential Nab3 peak (i.e., the one in *PIC2*). Overall, my CRAC assays revealed that, apart from disrupting its binding to *PIC2*, the Nab3 mutations did not significantly affect global Nab3 occupancy in any of the mutant strains (Table VI.1).

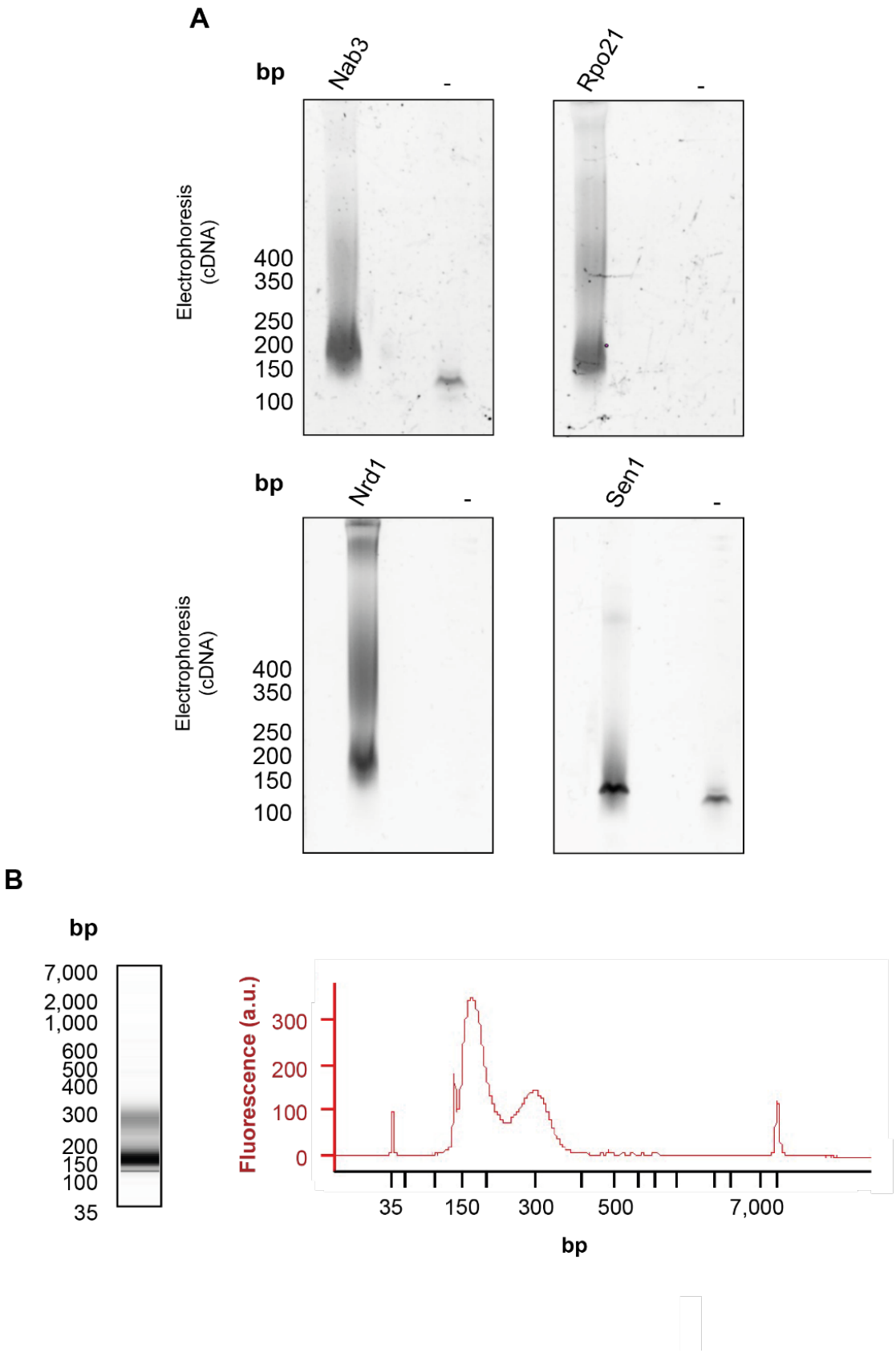

Figure VI.16. Quality check of cDNA libraries yielded after performing CRAC in Nab3, Nrd1, Sen1 and Rpo21. **A**. Electrophoretic resolution enabled isolation of all fragments between 200 and 400 bp. **B**. Bioanalyzer traces of the purified fragments (200-400 bp) of all pooled libraries.

RNA-seq	Total transcripts	Differentially expressed transcripts	Upregulated	Downregulated
∆ Nab3 RNA-BSs	12411	488 (3.9%)	196	292
∆ NNS RNA-BSs	12411	41 (0.1%)	31	10
Mass Spectrometry	**Total proteins**	**Differentially expressed proteins**	**Upregulated**	**Downregulated**
∆ Nab3 RNA-BSs	1056	94 (9%)	56	38
∆ NNS RNA-BSs	1056	50 (4.7%)	38	12
Nab3 CRAC	**Total peaks**	**Differentially bound Nab3 peaks**	**More Nab3 binding**	**Less Nab3 binding**
∆ Nab3 RNA-BSs	17643	6 (0.03%)	4	2 (including *PIC2*)
∆ NNS RNA-BSs	17270	1 (0.006%)	0	1 (only *PIC2*)
Nrd1 CRAC	**Total peaks**	**Differentially bound Nrd1 peaks**	**More Nrd1 binding**	**Less Nrd1 binding**
∆ Nab3 RNA-BSs	37368	378 (1%)	24	354
∆ NNS RNA-BSs	41492	442 (1.2%)	10	432
Sen1 CRAC	**Total peaks**	**Differentially bound Sen1 peaks**	**More Sen1 binding**	**Less Sen1 binding**
∆ Nab3 RNA-BSs	946	0 (0%)	0	0
∆ NNS RNA-BSs	1012	0 (0%)	0	0
Rpo21 CRAC	**Total peaks**	**Differentially bound Rpo21 peaks**	**More Rpo21 binding**	**Less Rpo21 binding**
∆ Nab3 RNA-BSs	28370	0 (0%)	0	0
∆ NNS RNA-BSs	33822	131 (1.2%)	91	40

Table VI.1. Summary of the key findings of the RNA-sequencing, mass spectrometry and CRAC experiments for Nab3, Nrd1, Sen1 and Rpo21.

In contrast, the Nrd1-binding profile was significantly altered in both mutants. DBPeaks analyses unveiled hundreds of differentially bound Nrd1 peaks (representing 1% of all Nrd1 peaks; Table VI.1, Figure VI.17). Although I had predicted changes in Nrd1 occupancy across the transcriptome of ∆ Nab3 RNA-BSs, I did not expect to detect so many DB Nrd1 peaks in the ∆ NNS RNA-BSs mutant. However, since the ∆ NNS RNA-BSs mutant did display a modest cell size increase and growth defect, it is conceivable that the observed alterations in Nrd1 binding could be, to some extent, underpinning these mild phenotypic changes. To investigate this further, I asked how many of the DE transcripts of both mutants also displayed DB Nab3 and Nrd1 peaks. This comparison would clarify whether the observed DB Nrd1 peaks in the ∆ Nab3 RNA-BSs and ∆ NNS RNA-BSs strains were impacting their gene expression profiles.

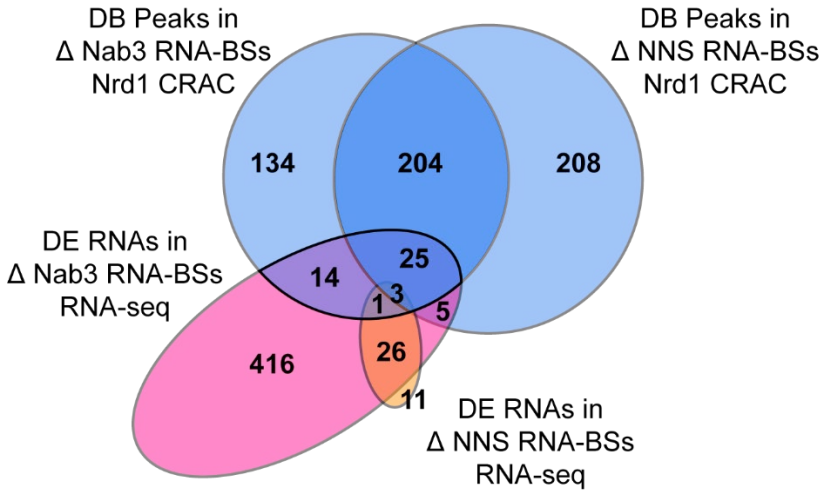

Figure VI.17. Overlaps between the differentially expressed transcripts and the differentially bound Nrd1 peaks in Δ Nab3 RNA-BSs and Δ NNS RNA-BSs. RNAs that are differentially expressed and differentially bound by Nrd1 in Δ Nab3 RNA-BSs are itemised in Figure VI.19.

My analyses revealed that while Δ NNS RNA-BSs displayed many DB peaks, these changes did not significantly impact its transcriptome and proteome. The main evidence in support of this claim is that Δ NNS RNA-BSs displayed only 3 differentially expressed genes containing Nrd1 differentially bound peaks (Figure VI.17 and Table VI.1). Additionally, its differentially expressed transcripts were not significantly enriched in Nrd1 and Nab3 motifs (Figure VI.17), suggesting that their altered expression is not linked to defective NNS regulation. Therefore, although both mutants demonstrated altered Nrd1 binding, the resulting transcriptomic and phenotypic consequences were markedly different.

In contrast, Nrd1 DB peaks in Δ Nab3 RNA-BSs seemed to have a major effect on its gene expression. Consistent with a reduction in Nrd1 availability in the Δ Nab3 RNA-BSs strain, most (94%) of its 378 differentially bound Nrd1 sites showed decreased Nrd1 binding (Table VI.1). Importantly, more than 10% of these sites (41) occurred in differentially expressed genes (Table VI.1) such as *DUR3*, a stress-specific mRNA regulated by the NNS complex (van Nues et al., 2017) (Figure VI.18). To gain further insight into how differential binding of Nrd1 to these transcripts could be driving changes in their expression, I explored whether Nrd1 binding was increased or decreased in individual genes (Figure VI.19).

Nrd1 targets functional non-coding RNAs as well as pervasive or bidirectional transcripts whose expression generally negatively correlates with that of the downstream protein-coding gene (Thiebaut et al., 2008). Reduced binding of Nrd1 to the latter group would be indicative of decreased NNS termination of pervasive or bidirectional transcripts which would increase their abundance and, in turn, lower the expression of the corresponding protein-coding gene. Conversely, mirroring the impact expected in functional ncRNA targets, I foresaw that abated Nrd1 recruitment to its protein-coding targets, such as *PIC2*, would similarly result in impaired premature termination of the encoded RNA and would ultimately increase the levels of such transcript. Increased Nrd1 binding was much less frequently detected among DB Nrd1 peaks. Whereas enhanced Nrd1 binding to direct targets was expected to lower their RNA abundance, increased recruitment of Nrd1 to pervasive or bidirectional transcripts would generally increase the levels of the distal coding gene.

To test whether these instances were prevalent among downregulated and upregulated transcripts, respectively, I sorted differentially expressed transcripts in the ∆ Nab3 RNA-BSs mutant depending on their increased or decreased abundance with respect to the parental *PIC2-GFP* (Figure VI.19). Then, I classified their differential Nrd1 peaks into those that displayed reduced or increased Nrd1 signal (Figure VI.19). As I hypothesised, while downregulated transcripts were significantly more likely to display reduced Nrd1 binding to their pervasive or bidirectional products, 60% of the upregulated RNAs in ∆ Nab3 RNA-BSs exhibited abated Nrd1 binding to their coding sequence (Figure VI.19). Collectively, these results suggest that while overexpressed RNAs increase their abundance due to defective NNS termination, the downregulated protein-coding genes were most likely affected by enhanced expression of a flanking pervasive RNAs interfering with their transcription (Thiebaut et al., 2008).

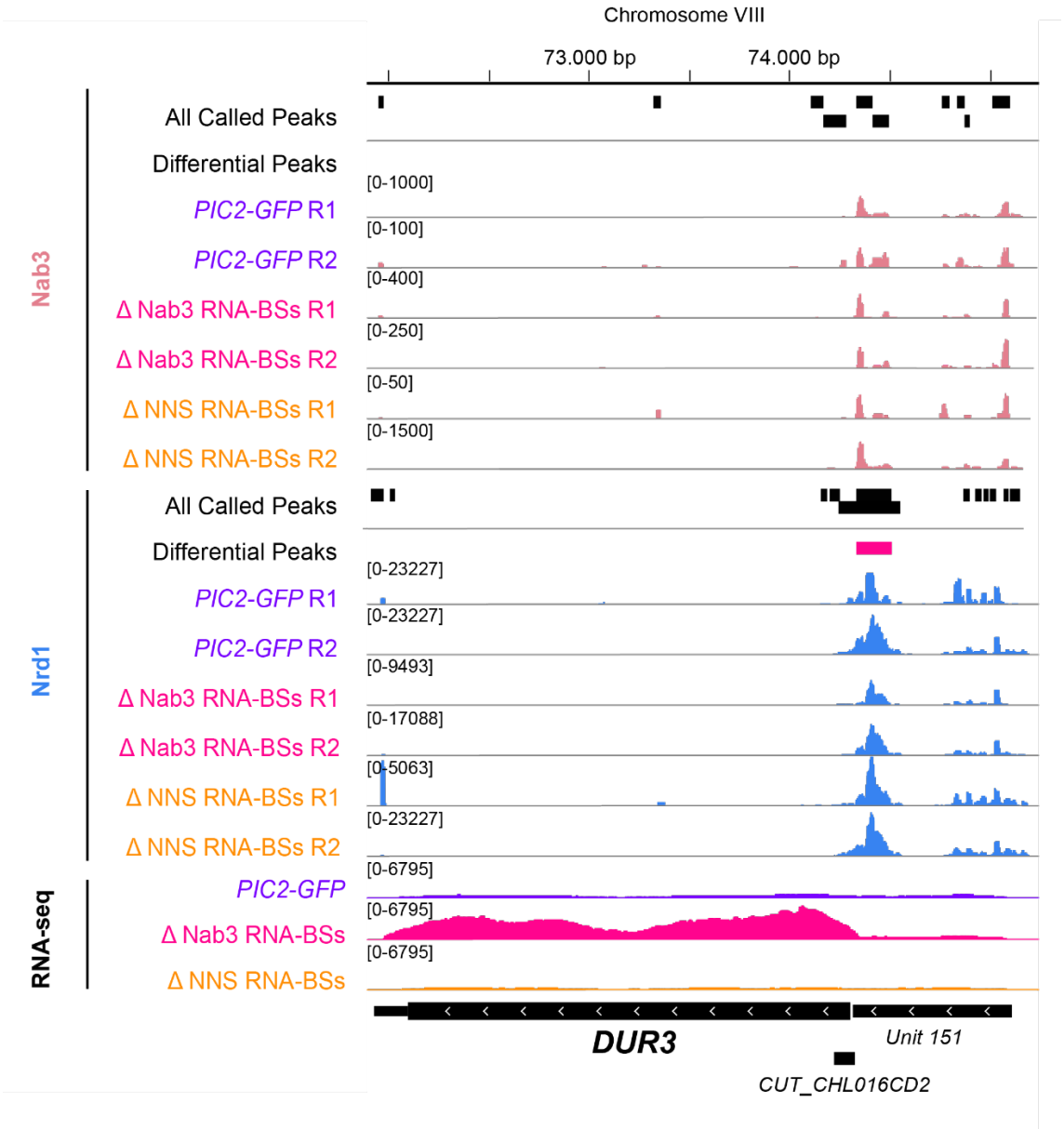

Figure VI.18. Abrogating Nab3 binding to *PIC2* dampens Nrd1 binding to differentially expressed NNS targets such as *DUR3***.** Visualisation of the raw reads obtained in Nab3 and Nrd1 CRAC and RNA-sequencing in the NNS co-regulated mRNA target *DUR3* in the *PIC2-GFP*Δ Nab3 RNA-BSs and Δ NNS RNA-BSs strains. To compensate for differences in library coverage, the raw reads shown in the Y axes were adjusted to display similar signals in neighbouring peaks which had not been deemed differentially bound by the DBPeaks package.

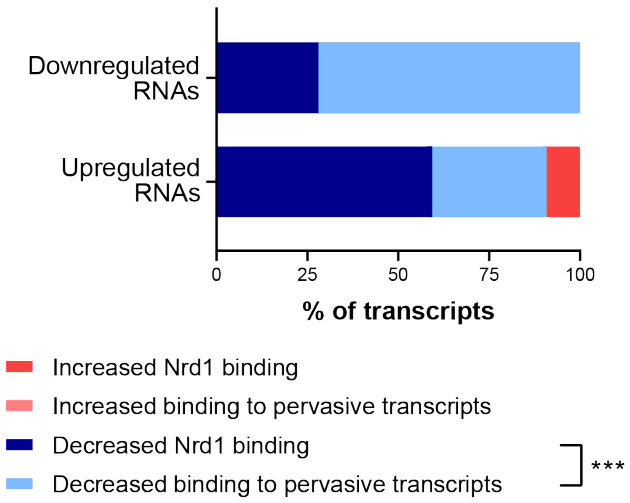

Figure VI.19. Stacked bar charts displaying the nature of the change in Nrd1 differentially bound peaks (increased or decreased) directly or pervasively affecting the Δ Nab3 RNA-BSs differentially expressed RNAs (upregulated or downregulated) in which they lay. Statistical comparison was performed by Fisher's exact test. ***: $p<0.001$.

Consistent with the trend revealed by transcriptomic effects, the extent of the impact which differential Nrd1 binding had in the translational landscape of both mutants was completely distinct: whereas only 1 of the proteins that were differentially abundant in Δ NNS RNA-BSs was encoded by a transcript with abated Nrd1 occupancy, 10 of the 94 differentially expressed factors of the Δ Nab3 RNA-BSs mutant corresponded to mRNAs with lower Nrd1 binding (Table VI.1).

To ascertain that these differences were solely arising from a difference in NNS-mediated decay rather than by changes in the rate at which the transcripts were synthesised, I sought to determine whether the RNA-binding footprint of the main subunit of the RNA polymerase II in yeast, Rpo21, displayed significant differences between the parental strain and the derived mutants. To this end, I conducted Rpo21 CRAC on two biological replicates of each tested strain. Given that my proteomic analyses uncovered that Rpo21 levels were upregulated in the Δ Nab3 RNA-BSs mutant, I had to compensate for the fact that the number of Rpo21 molecules pulled down in the CRAC libraries derived from the Δ Nab3 RNA-BSs strain was likely higher. Therefore, I could not assume that the compared libraries would have equal RNA inputs as I could potentially provoke a technically biased overrepresentation of the binding of Rpo21 to some co-immunoprecipitated species in the Δ Nab3 RNA-BSs

mutant. This also implied that I could not compare the coverage of Rpo21 targets based on the standard reads per million (RPM) to determine differential expression.

To circumvent this challenge, I applied a previously reported normalisation strategy (Cordiner et al., 2023). Briefly, to account for the varying pools of RNA-protein interactions retrieved from CRAC experiments in strains with different expression of Rpo21, I calculated a tRNA-rRNA scaling factor. I reasoned that tRNA and rRNA hits could be used as a proxy for background binding, as they should not be significantly bound by Rpo21. Accordingly, I summed the reads for both species and divided them by an arbitrary number (i.e., 30,000; Cordiner et al., 2023) to generate the scaling factor. The number of raw counts for every genomic feature was then divided by the scaling factor to normalise the reads of each experimental replicate to the depth of the library to which they belonged. Subsequent DESeq2 analyses detected no DB Rpo21 peaks in ∆ Nab3 RNA-BSs and 131 differentially bound sites across the ∆ NNS RNA-BSs libraries (Table VI.1). Hence, Rpo21 CRAC data revealed that transcriptomic differences in the ∆ Nab3 RNA-BSs strain were not caused by changes in the RNA polymerase II occupancy.

Finally, I aimed to check whether the observed changes in Nrd1 binding correlated with altered Sen1 occupancy in the same transcriptomic regions. Unfortunately, under the tested growth conditions, the expression of Sen1 was very low, and I was not able to generate good-quality cDNA libraries, as evidenced by the significantly lower number of unique cDNAs present in the sequencing data (Figure VI.20 and Table VI.2). Therefore, the ultimate proof for the Sen1 sequestration has remained elusive. Nevertheless, as I will explain in the next section and chapter, I still believe that Sen1 out-titration by *PIC2* transcripts is the most plausible factor driving genome-wide deregulation of NNS targets.

Holistically, these results demonstrate that inhibiting Nab3 binding to a single mRNA species changes Nrd1 occupancy across the transcriptome. Combined with the gene ontology enrichments outlined in Figures VI.9 and VI.11, the described CRAC analyses suggested that the affected portion of Nrd1 targetome was functionally involved in biological processes related to the severe phenotypic defects identified in the ∆ Nab3 RNA-BSs mutant, including increased cell size, reduced fitness, and defective energy homeostasis.

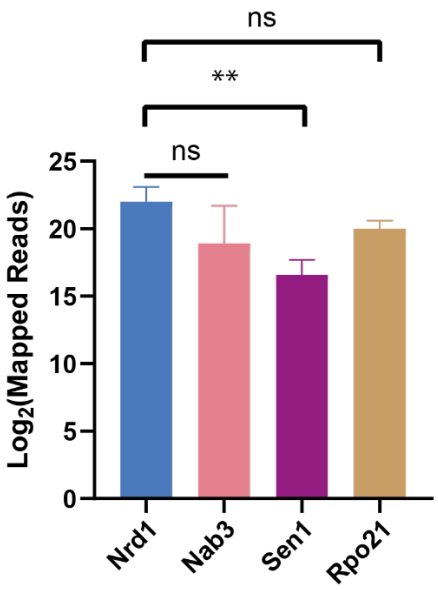

Figure VI.20. Bar graph showing the log_2-transformed average read coverage for the six CRAC experiments performed in Nrd1, Nab3, Sen1 and Rpo21 across the three tested strains. Error bars represent standard deviations (SD). Statistical comparisons were performed by unpaired t-tests. **: $p<0.01$ and 'ns': $p>0.05$.

	PIC2-GFP		Δ Nab3 RNA-BSs		Δ NNS RNA-BSs	
Nrd1	2,513,346	763,167	1,658,554	971,578	12,318	422,588
Nab3	14,170,659	5,669,733	1,657,240	3,194,419	2,147,348	6,474,116
Sen1	75,123	38,188	68,136	221,719	74,585	264,547
Rpo21	1,310,129	1,178,396	507,365	933,713	1,372,575	1,454,601

Table VI.2. Mapped reads for the two CRAC libraries obtained for Nrd1, Nab3, Sen1 and Rpo21 in *PIC2-GFP*, Δ Nab3 RNA-BSs and Δ NNS RNA-BSs.

VI.7. Discussion

In this work, I have demonstrated that global Nrd1 occupancy becomes altered in a strain in which Nab3 cannot be recruited to one of their shared transcript targets. Having identified the RNA species that become differently expressed in such mutant, I was able to determine that more than 10% of those transcripts also display significantly lower Nrd1 binding. Functional categorisation of the differentially expressed RNAs pool revealed that these were often involved in cellular pathways related to the phenotypic disadvantages which I had discovered in Δ Nab3 RNA-BSs.

These bioinformatic analyses evinced the plausibility of Nrd1 (and, potentially, Sen1) sponging to *PIC2* transcripts as the underlying cause of the defects described in chapter IV. However, importantly, I was not able to rigorously establish (i) the precise molecular cascade that results in the diminished availability of Nrd1 for its target transcripts in ∆ Nab3 RNA-BSs and (ii) the mechanism by which deregulation of hundreds of NNS targets causes the anomalous features of such mutant.

I speculate that Nrd1 titration may occur through various mechanisms. Nab3, which possesses prion-like domains (O'Rourke and Reines, 2016), partitions into nuclear granules during nutrient starvation (Loya et al., 2018). Despite also containing intrinsically disordered regions, Nrd1 has not been reported to engage in phase separation. Nevertheless, previous work has noted the presence of nucleoids in strains with mutations in the RNA-recognition motif of Nrd1 (Darby et al., 2012), suggesting that Nrd1 might form condensates in response to environmental stimuli, possibly in conjunction with target transcripts and Nab3. Additionally, Nrd1 and/or Sen1 may be sequestered to different subcellular compartments while still bound to accumulating *PIC2* transcripts in the ∆ Nab3 RNA-BSs mutant. If excess *PIC2* transcripts were translated, Nrd1 and Sen1 could be exported alongside the transcript to the cytoplasm, effectively titrating these proteins away from the nucleus. Indeed, although Nab3, Nrd1 and Sen1 localisation is predominantly nuclear, they all have been detected in ribonucleoproteins, which exhibit dynamic cellular localisation and could potentially shuttle when bound to their targets (Mitchell et al., 2013).

Since Nrd1 is an abundant protein – around 6882 +/- 1896 molecules per cell (Ho et al., 2018) – it seems improbable that a mild *PIC2* overabundance would significantly alter Nrd1's ability to bind other target transcripts. Conversely, Sen1 appears to be a limiting factor for the assembly of the complex (2549 +/- 843 molecules per cell) (Ho et al., 2018). Hence, tightly modulating its concentration is required for efficient NNS-mediated termination (Mischo et al., 2018). Accordingly, I posited that the most likely cause underlying disrupted NNS-termination in the studied system is the sequestration of Sen1 to ∆ Nab3 RNA-BSs *PIC2* transcripts through an interaction with Nrd1. To test this, I performed several Sen1 CRAC experiments in *PIC2-GFP* and derived mutants. Nonetheless, under the growth conditions used, Sen1 cross-linking to RNA was inefficient relative to the other NNS components. Despite multiple attempts, the resulting Sen1 CRAC cDNA libraries were of low complexity. This

prevented us from drawing conclusions about Sen1 recruitment to mRNA substrates in the mutant strains. Therefore, I could not confirm whether Sen1 occupancy in NNS targets was also significantly affected in ∆ Nab3 RNA-BSs.

My phenotypic analyses on a strain in which Nab3 could be depleted from its native nuclear environment show that impairing NNS termination leads to the onset of severe cell size anomalies. These findings further bolster a tentative Sen1 sequestration model as restrictions in its physiological abundance are known to cause cell cycle (Mischo et al., 2018) and cell division defects (Choudhary et al., 2023). Although no aberrant cell size was documented in these studies (Choudhary et al., 2023; Mischo et al., 2018), a mere increase in the DNA resulting from a delayed exit from the G2 phase could theoretically drive a cell size increase (Neurohr et al., 2019). Notably, the Δ Nab3 RNA-BSs mutant was not only oversized but also displayed reduced growth and fitness as well as increased intracellular stress, which coincided with the previous characterisation of other oversized models (Neurohr et al., 2019). On this basis, I hypothesise that ∆ Nab3 RNA-BSs cells are likely exceeding their critical DNA:cytoplasm ratio and undergoing cytoplasmic dilution, which was defined as a senescence trait (Neurohr et al., 2019). Consistent with this notion, recent work uncovered that the transcriptome is more heavily regulated by the NNS complex during quiescence (Greenlaw et al., 2023). Given that NNS targets are predominantly non-coding, it is possible that these operate as regulators of cell size and, by extension, affect the cell cycle. However, the functional characterisation of ncRNAs in yeast remains unexplored.

VII. Conclusion

Throughout their lifespan, RNAs are chaperoned by proteins that govern their fate: apart from driving transcription, interactions between RNA and proteins rule RNA maturation and splicing, nuclear export and localisation, stability and translatability, as well as decay. In doing so, RBPs shape the transcriptional profiles underpinning cellular homeostasis and response to the environment. Thus, upon facing extracellular pressures such as nutrient depletion, RBPs must rapidly reprogram the cellular transcriptome to produce proteins that confer cells the capacity to endure and alleviate the effects of the subsequent stress.

Transcriptomic remodelling encompasses a dynamic interplay between the RNA transcription and decay machineries, which control the extent and timing of gene expression. Earlier work by the Granneman group had pioneered time-resolved UV cross-linking approaches that allowed temporal monitoring of the interactions between the RNA transcription and decay machineries (Cordiner et al., 2023; van Nues et al., 2017). Applying those methods, former members of the group unveiled a novel and unusual role for the NNS complex in prematurely terminating dozens of protein-coding genes which were simultaneously upregulated during glucose starvation in *S. cerevisiae* (van Nues et al., 2017). Briefly, this finding implied that a subset of mRNAs encoding stress-responsive proteins are targeted for degradation shortly after transcription initiation.

Albeit intriguing, the biological relevance of that observation remained elusive. From an energetic perspective, the discovery seemed counterintuitive: why would yeast invest resources in transcribing mRNAs encoding much-needed stress-responsive proteins and subsequently target them for degradation? Given that such phenomenon appeared to be specifically accentuated during stress, the same report speculated that the NNS complex could be preventing overshooting of gene expression during adaptation, thereby propelling an optimal and homogeneous expression of stress-responsive genes among the cell population facing a given environmental challenge (van Nues et al., 2017). In line with this prediction, I have demonstrated that this NNS attenuation mechanism not only reduces mRNA levels but also minimises the cell-to-cell variability in the expression of *PIC2*, a model stress-

responsive gene encoding a mitochondrial transporter. More specifically, I have shown that NNS-mediated premature termination of *PIC2* is pivotal for the maintenance of cell fitness during nutrient depletion. Furthermore, using synthetic reporter gene systems, I have demonstrated that this NNS-dependent attenuation and noise suppression are not confined to lowly expressed genes, such as *PIC2*, but are also applicable to highly activated ones. On this basis, I propose that the mRNA-attenuating and noise-suppressing activity of the NNS complex is critical to maintaining tight expression of genes that, when transcribed at inadequate levels, would be detrimental to the cell.

VII.1. Discovery of a novel yeast co-transcriptional noise-suppression mechanism

Having established that NNS decreases *PIC2* mRNA levels, I sought to understand the biological significance of this observation. The probability of Nrd1 and Nab3 binding to nascent RNA transcripts is determined by multiple factors, namely (i) the number and order of NNS RNA-binding motifs in the transcript (Porrua et al., 2012), (ii) the polymerase occupancy near the 5' end of the gene, (iii) the phosphorylation status of the Pol II CTD (Vasiljeva et al., 2008), (iv) the processivity of the polymerase, and (v) its elongation rate (Hazelbaker et al., 2013). Accordingly, the NNS complex could be homogenising Pol II transcription of *PIC2* to minimise variability in *PIC2* expression among the cells of a population. This controlled transcriptional response to a new environment would, in turn, increase the cell fitness and provide a selective advantage to cells which were able to keep their Pic2 levels close to the optimal concentration. Such a hypothesis had been envisioned and reasoned from a purely biological framework, and so it was surprising to find that this model would be, theoretically, highly unexpected (Schnoerr et al., 2017; van Kampen, 2007).

Most classical RNA degradation simulations have been applied to mechanisms in which the decaying factor is much more abundant than the complexes to be decayed. In these scenarios, termination of the bound polymerase can be modelled as a first-order reaction, where the catalytic rate depends on the concentration of transcribing polymerases. This implies that there is little noise emerging from the decay machinery, as it has been reported for Xrn1 (Baudrimont et al., 2019), and consequently, the noise in the expression of the transcribed gene is equivalent to that

of the noise of the binding polymerases. Intrinsic noise corresponds to the stochastic variation in protein counts caused by small fluctuations (Elowitz et al., 2002; Raser and O'Shea, 2005). The effects of these fluctuations are greater for lowly expressed genes as they become proportionally larger in small mRNA and protein pools (Bar-Even et al., 2006). Accordingly, most simulations of stochasticity show that the noise (i.e., the coefficient of variation) of bound polymerases decreases with increasing gene expression (Schnoerr et al., 2017; van Kampen, 2007). Thus, considering that both Pol II transcription initiation and NNS binding to transcripts are inherently noisy, how could combining these two systems subsequently reduce noise in gene expression rather than amplify it? To help answer this question, Prof Ramon Grima generated a mathematical model that did not only explain NNS-mediated noise suppression but also suggested a mechanism which was consistent with the transcriptome-wide defects that I had characterised in the ∆ Nab3 RNA-BSs mutant (Figure VII.1).

In contrast to classical RNA degradation models, in the case of NNS transcriptional termination, Sen1 constitutes a limiting factor present in approximately 2549 +/- 843 molecules per cell (Ho et al., 2018). Being a lowly expressed protein, Sen1 is noisy (Newman et al., 2006), and its stochasticity is transferred to target mRNAs during NNS-mediated decay. Previous work demonstrated that full NNS assembly and co-transcriptional termination leads to polymerases queuing in the 5' end of the gene and that, while a fraction of them is dismantled by the NNS complex, the remaining polymerases proceed with transcription of the target gene (van Nues et al., 2017) (Figure I.3). At equilibrium, when the NNS complex can terminate a fraction of the queuing polymerases (i.e., $k<k_0$), the effect of the noise of Sen1 in gene expression would still be lower if the expression of the gene is higher, as predicted by classical noise models (Figure VII.1, Phase A). However, if the ability of NNS to terminate a fraction of the queuing polymerases is reduced any further, the complex cannot bind the polymerases fast enough, and phase B ensues (Figure VII.1, Phase B). In this regime, the size of fluctuations increases with the gene expression. This phenomenon has rarely been studied in modelling literature (Grima, 2014), but agrees with the observations presented throughout this thesis.

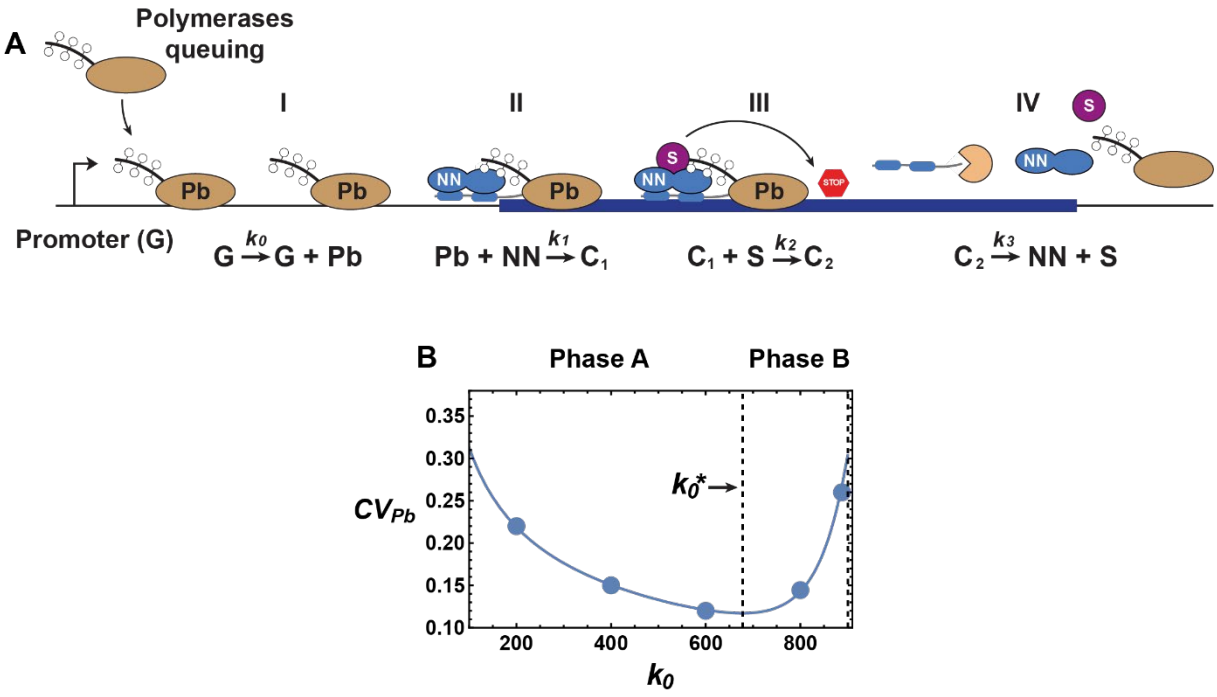

Figure VII.1. Overview of the model developed by Prof Ramon Grima to explain how the coefficient of variation of Pic2-GFP can increase with increasing expression. **A**. Cartoon of the reaction system. **B**. Plot of the coefficient of variation of the bound polymerase (Pb) versus the rate of synthesis of Pb (k_0) for an individual NNS target gene (e.g. *PIC2*). Predictions were generated by Prof Ramon Grima using two different stochastic modelling techniques.

In the model created by Prof Ramon Grima, k_0^* represents a critical value of the initial rate beyond which the queue of Pol II becomes too large; if that value is exceeded, the noise starts to increase with the mean expression. This implied that for *PIC2*, NNS would be almost saturated by the polymerases, as otherwise, phase B would not be possible. This conclusion was consistent with, Sen1 abundance constraining the ability of the NNS complex to terminate the more than 5,000 mRNA targets which the Nrd1-Nab3 heterodimer recognises according to my CRAC experiments. Based on this numerical limitation and on the vast phenotypical effects that disrupting Nab3 motifs in *PIC2* had on the Δ Nab3 RNA-BSs mutant, it was conceivable that NNS was generally operating close to saturation. However, this would also entail that efficient NNS transcriptome-wide transcriptional repression can only be achieved efficiently if transcription is terminated shortly after Sen1 is recruited to the Nrd1-Nab3 heterodimer. In other words, in Figure VII.1, k_3 needs to happen very quickly to release Sen1 back into a very limited molecular pool. Indeed, stochastic

simulations performed by Prof Ramon Grima predicted that the rate for the last reaction of the model would have to occur very quickly to make phase B possible.

How would k_0 be surpassed in the ∆ Nab3 RNA-BSs mutant? Given that Nrd1 still binds *PIC2* mRNAs lacking Nab3 RNA-binding sites, it is likely that its retention time, and that of any co-recruited Sen1 molecules, to those *PIC2* transcripts, is prolonged. Theoretically, this would reduce the number of Nrd1 and Sen1 molecules available. Further limiting the availability of Nrd1 and Sen1 would decrease the rate of binding of the Nrd1-Nab3 heterodimer to the transcript (k_1) and the amount of NNS that is fully assembled (k_2). Hence, this mathematical model does not only shed light on the kinetic basis for NNS-mediated noise suppression of *PIC2* expression but also reinforces the notion that, in the ∆ Nab3 RNA-BSs mutant, NNS is likely becoming saturated, possibly due to restrictions in the pools of NNS components or reduced complex assembly.

Importantly, to the best of my knowledge, this work provides the first evidence of a co-transcriptional gene expression noise-suppression mechanism in yeast. Earlier work in *Saccharomyces cerevisiae* has reported gene expression noise-suppression mechanisms that are either TATA-box dependent (Duveau et al., 2018), translational (e.g., Kel1; (Garcia et al., 2021)) or synthetic (Mundt et al., 2018). Notably, a similar transcriptional mechanism was recently found in *Escherichia coli* as Hfq, which is a key RNA-binding protein common to many bacterial lineages, was shown to reduce the noise in the protein products of a target operon (Kalita et al., 2024). Like Hfq (Iosub et al., 2020), NNS interacts with thousands of RNA species on which it could potentially be exerting a noise-suppressing role (van Nues et al., 2017). Using GFP reporters, I illustrate that NNS-dependent attenuation and noise suppression are generally applicable to mRNAs with an abundance more than two orders of magnitude greater than that of the tested *PIC2* mRNA model. Therefore, my results posit that this regulatory role of the NNS complex could be widespread across the transcriptome.

VII.2. A modest change in the abundance of an mRNA disturbs the homeostasis of co-regulated RNAs.

Having focused on the evolutionarily conserved mitochondrial copper and phosphate transporter, Pic2, as a model target, my work demonstrates that increasing Pic2 expression noise by preventing Nab3 binding significantly increased cell size, reduced fitness, disrupted energy homeostasis and caused cell cycle delays (Figure VII.2). Thus, these major physiological changes were caused by preventing a single RNA-binding protein (Nab3) from binding to one lowly-expressed mRNA target (*PIC2*). This not only underscores the importance of NNS in maintaining 'Goldilocks' levels of expression of stress-responsive genes but also highlights the system's high sensitivity to perturbations (Figure VII.2). Additionally, my work has shown that impairing NNS attenuation of a lowly expressed protein-coding transcript during stress is sufficient to impact the transcriptome-wide binding footprint of Nrd1. In turn, these changes in occupancy could conceivably incur considerable fitness costs (Figure VII.2).

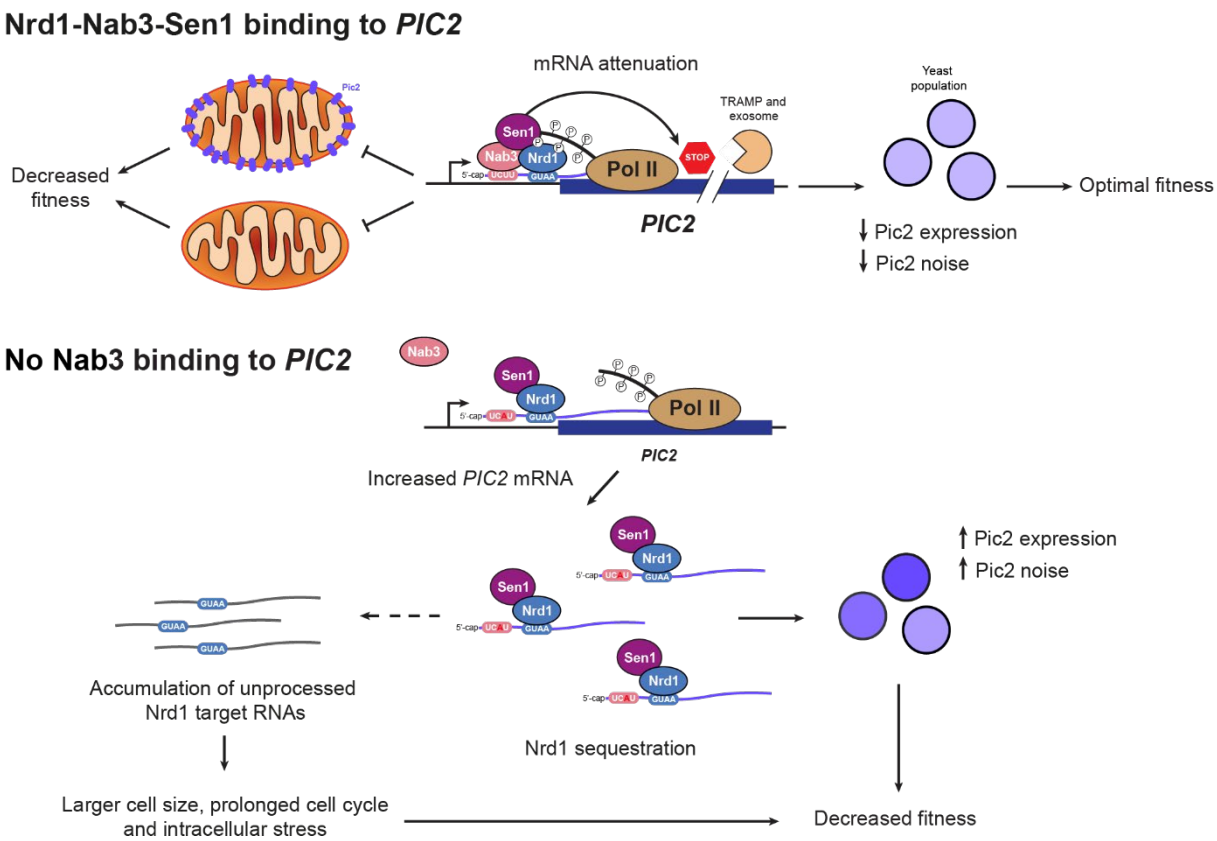

Figure VII.2. Schematic summary of the molecular and phenotypic consequences of disrupting Nab3 binding to *PIC2*.

Although phenotypic dissection and multi-omic functional analyses allowed me to establish that disruption of Nab3 binding sites in *PIC2* resulted in the observed defects, the mechanism by which the latter emerge is still missing some detail. I speculate that the fundamental molecular basis for the cell size and cell cycle anomalies relies on the temporal or spatial sequestration of components of the NNS complex to the *PIC2* transcript. Nrd1 is known to have some intrinsically disordered regions (Loya et al., 2013) which often drive phase separation in other proteins (Courchaine et al., 2016). One of these other proteins is, in fact, Nab3, which partitions into nuclear granules during glucose starvation (Loya et al., 2018). Although granule formation has not been explicitly described in Nrd1 to date, Darby and colleagues demonstrated that, upon glucose depletion, Nrd1 localises to perinuclear speckles that, despite being distinct from both stress granules and P bodies, still contained Nab3. Moreover, the same study showed that introducing mutations in the RNA-recognition motif of Nrd1 increased the number and size of Nrd1 'nucleoids' (Darby et al., 2012). Consequently, in the light of previous evidence, it is feasible that Nrd1 undergoes condensation in response to stress. Moreover, such putative Nrd1 phase separation would be likely to affect Nab3 and/or Sen1. Alternatively, spatial out-titration of Nrd1 and Sen1 could also arise from prolonged retention to the *PIC2* transcript since, by remaining bound to this mRNA population, some of the Nrd1 and/or Sen1 pool could be co-transported to the cytoplasm. Indeed, albeit eminently nuclear, Nab3, Nrd1 and Sen1 have been detected in cytoplasmic ribonucleoproteins (Mitchell et al., 2013). Therefore, these factors may be shuttling outside the nucleus more frequently than what has been predicted.

On the other hand, as discussed in the preceding section, the availability of fully assembled NNS complexes may be diminished by numerically constraining the small Sen1 pool present in cells. This situation would not only be consistent with the aforementioned model but also with prior evidence showing that Sen1 levels must be tightly fine-tuned for NNS-mediated termination to occur efficiently (Mischo et al., 2018). To obtain experimental evidence validating that transcriptome-wide Sen1 occupancy is altered in the mutant lacking Nab3 binding sites in *PIC2* (i.e., ∆ Nab3 RNA-BSs), I performed Sen1 CRAC experiments in the mutants and their parental reference. Since Sen1 cross-linking to RNA was poor in the tested conditions (Figure S1B), I tried to tailor the CRAC protocol to minimise the protein degradation and maximise input bait numbers (see II.25). However, despite multiple attempts, the

output cDNA libraries encompassed a low number of unique reads. Accordingly, differential binding analyses could not elucidate whether the Sen1 RNA-binding footprint was significantly altered in the ∆ Nab3 RNA-BSs mutant.

My work demonstrates that preventing NNS-mediated termination of one protein-coding transcript enlarges cell size and extends the cell cycle. These results further point towards a scenario in which Sen1 is sequestered, as previous studies have shown that constraining Sen1 cellular concentrations disrupts the cell cycle and cell division (Choudhary et al., 2023; Mischo et al., 2018). Even though cell size anomalies were not reported in these cases (Choudhary et al., 2023; Mischo et al., 2018), prior literature has described that enhancing the DNA content in a cell prolongs the G2 phase and, by extension, becomes larger (Neurohr et al., 2019). Remarkably, apart from increased cell volume, the ∆ Nab3 RNA-BSs mutant grew more slowly, was less fit and displayed higher intracellular stress. Given that this set of defects echoed earlier descriptions of other oversized cellular models, I propose that my mutant is likely exceeding the critical DNA:cytoplasm ratio, thereby experiencing cytoplasmic dilution and premature senescence (Neurohr et al., 2019). In line with this conclusion, a recent report has revealed that the NNS complex targets a higher number of RNAs during quiescence (Greenlaw et al., 2023).

As most NNS targets are non-coding, it is plausible that these are perhaps exerting a regulatory role in cell volume and, consequently, in cell cycle progression. Nevertheless, given that most ncRNAs in yeast remain functionally uncharacterised, it is difficult to ascertain whether this hypothesis is correct. On the other hand, these findings suggest that NNS-mediated attenuation of target mRNAs could act as a mechanism to coordinate the expression of functionally related protein-coding genes, possibly involved in cell cycle regulation, in response to environmental cues. My results imply that the levels of such targets would be subject to changes in NNS availability genes. In this respect, NNS would behave like a class-specific transcription factor, which, additionally, suppresses noise to fine-tune the expression of target genes.

VII.3. Conservation and divergence in 'Goldilocks' regulation of *PIC2* expression homeostasis in yeast and human cells

To expand the implications of my findings beyond yeast, I also explored the regulation of the highly conserved mammalian homologue of *PIC2* (*SLC25A3*), which is also tightly controlled and similarly critical for energy homeostasis (Boulet et al., 2017; Padovan-Merhar et al., 2015) (Figure I.6). Mutations causing defective or excessive expression of this gene have been linked to a variety of human diseases (Mayr et al., 2011; Oehler et al., 2009; Peoples et al., 2021). In human cells, *SLC25A3* regulation involves the microRNA machinery (Baseler et al., 2012), a system that is absent in the yeast *Saccharomyces cerevisiae*. However, intrigued by the possibility that the molecular basis of the defects that I had detected in yeast was applicable to human cells and plausibly contribute to the onset of such conditions, I sought to determine whether SLC25A3-overexpressing HEK 293 cells would show similar energy homeostasis and phenotypic profiles to those observed in yeast overproducing Pic2. Since this was indeed the case, my findings highlight how organisms have evolved distinct molecular strategies to achieve gene expression homeostasis.

My results indicate that yeast and mammalian cells displaying high Pic2 or SLC25A3 protein levels are penalised when subjected to nutrient restriction or detrimental conditions demanding efficient respiration for survival. Interestingly, respiration inhibition and increased susceptibility to extracellular ROS were also observed in mutants lacking *PIC2*. Despite also showing growth defects in the partially respirable raffinose-containing medium, *pic2*Δ cells are known to perform nearly identically to the parental strain when grown in rich medium containing fermentable sugars (Vest et al., 2013). These observations align with general microbial adaptive behaviour: while bet hedging enables the development of stochastic phenotypes that may be advantageous in ideal growth conditions and potentially beneficial in unpredictable scenarios, adaptation also requires that the expression pattern of some genes becomes 'just right'. Thus, maintaining *PIC2* expression at a 'Goldilocks' level is crucial for optimal cellular function under varying environmental stresses.

In conclusion, the data presented in this thesis has characterised and contextualised a new function of the yeast NNS complex in reducing noisy expression

of protein-coding targets. My work also underscores the biological importance of this role by showing that even modest deviations from the optimal expression levels of a model target gene reduce fitness. Finally, I have demonstrated that preventing the binding of one component of an RNA-binding complex (i.e., Nab3) to a single mRNA species is sufficient to alter the recruitment of other proteins of such complex (e.g., Nrd1) across shared transcript targets. Based on this observation as well as the presented phenotypic dissection and bioinformatic analyses of multi-omics data, I propose that that sequestration of one RNA-binding protein to a single mRNA species can elicit significant pathophysiologic changes in essential cellular features.

Bibliography

Acar, M., Becskei, A., van Oudenaarden, A., 2005. Enhancement of cellular memory by reducing stochastic transitions. Nature 2005 435:7039 435, 228–232. https://doi.org/10.1038/nature03524

Agledal, L., Niere, M., Ziegler, M., 2010. The phosphate makes a difference: cellular functions of NADP. Redox Rep 15, 2–10. https://doi.org/10.1179/174329210X12650506623122

Agostini, F., Zagalak, J., Attig, J., Ule, J., Luscombe, N.M., 2021. Intergenic RNA mainly derives from nascent transcripts of known genes. Genome Biol 22, 1–19. https://doi.org/10.1186/S13059-021-02350-X/FIGURES/5

Ahn, S.H., Kim, M., Buratowski, S., 2004. Phosphorylation of serine 2 within the RNA polymerase II C-terminal domain couples transcription and 3' end processing. Mol Cell 13, 67–76. https://doi.org/10.1016/S1097-2765(03)00492-1

Aiello, U., Challal, D., Wentzinger, G., Lengronne, A., Appanah, R., Pasero, P., Palancade, B., Libri, D., 2022. Sen1 is a key regulator of transcription-driven conflicts. Mol Cell 82, 2952-2966.e6. https://doi.org/10.1016/J.MOLCEL.2022.06.021

Ajazi, A., Choudhary, R., Tronci, L., Bachi, A., Bruhn, C., 2022. CTP sensing and Mec1 ATR-Rad53 CHK1/CHK2 mediate a two-layered response to inhibition of glutamine metabolism. PLoS Genet 18, e1010101.

Alcalá, S., Klee, M., Fernández, J., Fleischer, A., Pimentel-Muiños, F.X., 2008. A high-throughput screening for mammalian cell death effectors identifies the mitochondrial phosphate carrier as a regulator of cytochrome c release. Oncogene 27, 44–54. https://doi.org/10.1038/sj.onc.1210600

Allan, C., Burel, J.-M., Moore, J., Blackburn, C., Linkert, M., Loynton, S., MacDonald, D., Moore, W.J., Neves, C., Patterson, A., Porter, M., Tarkowska, A., Loranger, B., Avondo, J., Lagerstedt, I., Lianas, L., Leo, S., Hands, K., Hay, R.T., Patwardhan, A., Best, C., Kleywegt, G.J., Zanetti, G., Swedlow, J.R., 2012. OMERO: flexible, model-driven data management for experimental biology. Nature Methods 2012 9:3 9, 245–253. https://doi.org/10.1038/nmeth.1896

Allmang, C., Kufel, J., Chanfreau, G., Mitchell, P., Petfalski, E., Tollervey, D., 1999. Functions of the exosome in rRNA, snoRNA and snRNA synthesis. EMBO J 18, 5399–5410. https://doi.org/10.1093/EMBOJ/18.19.5399

Althammer, S., González-vallinas, J., Ballaré, C., Beato, M., Eyras, E., 2011. Pyicos: a versatile toolkit for the analysis of high-throughput sequencing data. Bioinformatics 27, 3333–3340. https://doi.org/10.1093/BIOINFORMATICS/BTR570

Amberg, D.C., Goldstein, A.L., Cole, C.N., 1992. Isolation and characterization of RAT1: an essential gene of Saccharomyces cerevisiae required for the efficient nucleocytoplasmic trafficking of mRNA. Genes Dev 6, 1173–1189. https://doi.org/10.1101/GAD.6.7.1173

Arigo, J.T., Eyler, D.E., Carroll, K.L., Corden, J.L., 2006. Termination of Cryptic Unstable Transcripts Is Directed by Yeast RNA-Binding Proteins Nrd1 and Nab3. Mol Cell 23, 841–851. https://doi.org/10.1016/j.molcel.2006.07.024

Arnér, E.S.J., Holmgren, A., 2000. Physiological functions of thioredoxin and thioredoxin reductase. Eur J Biochem 267, 6102–6109. https://doi.org/10.1046/J.1432-1327.2000.01701.X

Baker, Z.N., Cobine, P.A., Leary, S.C., 2017. The mitochondrion: a central architect of copper homeostasis. Metallomics 9, 1501–1512. https://doi.org/10.1039/C7MT00221A

Bakker, B.M., Overkamp, K.M., van Maris, A.J.A., Kötter, P., Luttik, M.A.H., van Dijken, J.P., Pronk, J.T., 2001. Stoichiometry and compartmentation of NADH metabolism in Saccharomyces cerevisiae. FEMS Microbiol Rev 25, 15–37. https://doi.org/10.1111/J.1574-6976.2001.TB00570.X

Balaban, N.Q., Merrin, J., Chait, R., Kowalik, L., Leibler, S., 2004. Bacterial persistence as a phenotypic switch. Science (1979) 305, 1622–1625. https://doi.org/10.1126/SCIENCE.1099390

Balamurugan, K., Schaffner, W., 2006. Copper homeostasis in eukaryotes: Teetering on a tightrope. Biochimica et Biophysica Acta (BBA) - Molecular Cell Research 1763, 737–746. https://doi.org/https://doi.org/10.1016/j.bbamcr.2006.05.001

Barbet, N.C., Schneider, U., Helliwell, S.B., Stansfield, I., Tuite, M.F., Hall, M.N., 1996. TOR controls translation initiation and early G1 progression in yeast. Mol Biol Cell 7, 25–42. https://doi.org/10.1091/mbc.7.1.25

Bar-Even, A., Paulsson, J., Maheshri, N., Carmi, M., O'Shea, E., Pilpel, Y., Barkai, N., 2006. Noise in protein expression scales with natural protein abundance. Nature Genetics 2006 38:6 38, 636–643. https://doi.org/10.1038/ng1807

Barja, G., 2013. Updating the mitochondrial free radical theory of aging: an integrated view, key aspects, and confounding concepts. Antioxid Redox Signal 19, 1420–1445. https://doi.org/10.1089/ARS.2012.5148

Baseler, W.A., Thapa, D., Jagannathan, R., Dabkowski, E.R., Croston, T.L., Hollander, J.M., 2012. miR-141 as a regulator of the mitochondrial phosphate carrier (Slc25a3) in the type 1 diabetic heart. American Journal of Physiology-Cell Physiology 303, C1244–C1251. https://doi.org/10.1152/ajpcell.00137.2012

Basier, C., Nurse, P., 2023. The cell cycle and cell size influence the rates of global cellular translation and transcription in fission yeast. EMBO J 42. https://doi.org/10.15252/EMBJ.2022113333/SUPPL_FILE/EMBJ2022113333-SUP-0001-EVFIGS.PDF

Baudrimont, A., Jaquet, V., Wallerich, S., Voegeli, S., Becskei, A., 2019. Contribution of RNA Degradation to Intrinsic and Extrinsic Noise in Gene Expression. Cell Rep 26, 3752-3761.e5. https://doi.org/10.1016/j.celrep.2019.03.001

Bayliak, M., Burdyliuk, N., Lushchak, V., 2017. Growth on Alpha-Ketoglutarate Increases Oxidative Stress Resistance in the Yeast Saccharomyces cerevisiae. Int J Microbiol 2017, 5792192. https://doi.org/10.1155/2017/5792192

Belenkiy, R., Haefele, A., Eisen, M.B., Wohlrab, H., 2000. The yeast mitochondrial transport proteins: new sequences and consensus residues, lack of direct relation between consensus residues and transmembrane helices, expression patterns of the transport protein genes, and protein-protein interactions with other proteins. Biochim Biophys Acta 1467, 207–218. https://doi.org/10.1016/S0005-2736(00)00222-4

Bermingham-McDonogh, O., Gralla, E.B., Valentine, J.S., 1988. The copper, zinc-superoxide dismutase gene of Saccharomyces cerevisiae: cloning, sequencing,

and biological activity. Proceedings of the National Academy of Sciences 85, 4789–4793. https://doi.org/10.1073/PNAS.85.13.4789

Berretta, J., Pinskaya, M., Morillon, A., 2008. A cryptic unstable transcript mediates transcriptional trans-silencing of the Ty1 retrotransposon in S. cerevisiae. Genes Dev 22, 615–626. https://doi.org/10.1101/GAD.458008

Berry, S., Müller, M., Rai, A., Pelkmans, L., 2022. Feedback from nuclear RNA on transcription promotes robust RNA concentration homeostasis in human cells. Cell Syst 13, 454-470.e15. https://doi.org/10.1016/J.CELS.2022.04.005/ATTACHMENT/0CE5EC77-7860-4F28-8703-258261227A51/MMC1.PDF

Bieganowski, P., Seidle, H.F., Wojcik, M., Brenner, C., 2006. Synthetic lethal and biochemical analyses of NAD and NADH kinases in Saccharomyces cerevisiae establish separation of cellular functions. J Biol Chem 281, 22439–22445. https://doi.org/10.1074/JBC.M513919200

Bischler, T., Maticzka, D., Förstner, K., Wright, P., 2021. PEAKachu.

Blacker, T.S., Mann, Z.F., Gale, J.E., Ziegler, M., Bain, A.J., Szabadkai, G., Duchen, M.R., 2014. Separating NADH and NADPH fluorescence in live cells and tissues using FLIM. Nature Communications 2014 5:1 5, 1–9. https://doi.org/10.1038/ncomms4936

Boulet, A., Vest, K.E., Maynard, M.K., Gammon, M.G., Russell, A.C., Mathews, A.T., Cole, S.E., Zhu, X., Phillips, C.B., Kwong, J.Q., Dodani, S.C., Leary, S.C., Cobine, P.A., 2017. The mammalian phosphate carrier SLC25A3 is a mitochondrial copper transporter required for cytochrome c oxidase biogenesis. Journal of Biological Chemistry 293, 1887–1896. https://doi.org/10.1074/jbc.RA117.000265

Brannan, K., Kim, H., Erickson, B., Glover-Cutter, K., Kim, S., Fong, N., Kiemele, L., Hansen, K., Davis, R., Lykke-Andersen, J., Bentley, D.L., 2012. mRNA decapping factors and the exonuclease Xrn2 function in widespread premature termination of RNA polymerase II transcription. Mol Cell 46, 311–324. https://doi.org/10.1016/J.MOLCEL.2012.03.006

Bresson, S., Tollervey, D., 2018. Surveillance-ready transcription: nuclear RNA decay as a default fate. Open Biol 8. https://doi.org/10.1098/RSOB.170270

Bresson, S., Tuck, A., Staneva, D., Tollervey, D., 2017. Nuclear RNA Decay Pathways Aid Rapid Remodeling of Gene Expression in Yeast. Mol Cell 65, 787-800.e5. https://doi.org/10.1016/j.molcel.2017.01.005

Briggs, C., Mincone, L., Wohlrab, H., 1999. Replacements of basic and hydroxyl amino acids identify structurally and functionally sensitive regions of the mitochondrial phosphate transport protein. Biochemistry 38, 5096–5102. https://doi.org/10.1021/BI982945N

Bruinenberg, P.M., van Dijken, J.P., Scheffers, W.A., 1983. A theoretical analysis of NADPH production and consumption in yeasts. J Gen Microbiol 129, 953–964. https://doi.org/10.1099/00221287-129-4-953/CITE/REFWORKS

Bryan, A.K., Hecht, V.C., Shen, W., Payer, K., Grover, W.H., Manalis, S.R., 2014. Measuring single cell mass, volume, and density with dual suspended microchannel resonators. Lab Chip 14, 569–576. https://doi.org/10.1039/C3LC51022K

Bunoust, O., Devin, A., Avéret, N., Camougrand, N., Rigoulet, M., 2005. Competition of Electrons to Enter the Respiratory Chain. Journal of Biological Chemistry 280, 3407–3413. https://doi.org/10.1074/jbc.m407746200

Camblong, J., Iglesias, N., Fickentscher, C., Dieppois, G., Stutz, F., 2007. Antisense RNA Stabilization Induces Transcriptional Gene Silencing via Histone Deacetylation in S. cerevisiae. Cell 131, 706–717. https://doi.org/10.1016/J.CELL.2007.09.014

Carminati, M., Rodríguez-Molina, J.B., Manav, M.C., Bellini, D., Passmore, L.A., 2023. A direct interaction between CPF and RNA Pol II links RNA 3′ end processing to transcription. Mol Cell 83, 4461-4478.e13. https://doi.org/10.1016/J.MOLCEL.2023.11.004/ATTACHMENT/FA230562-BC00-4D67-8324-E74125CC289F/MMC1.PDF

Carroll, K.L., Ghirlando, R., Ames, J.M., Corden, J.L., 2007. Interaction of yeast RNA-binding proteins Nrd1 and Nab3 with RNA polymerase II terminator elements. RNA 361–373.

Carroll, K.L., Pradhan, D.A., Granek, J.A., Clarke, N.D., Corden, J.L., 2004. Identification of cis Elements Directing Termination of Yeast Nonpolyadenylated

snoRNA Transcripts. Mol Cell Biol 24, 6241–6252. https://doi.org/10.1128/MCB.24.14.6241-6252.2004

Casal, M., Queirós, O., Talaia, G., Ribas, D., Paiva, S., 2016. Carboxylic acids plasma membrane transporters in saccharomyces cerevisiae. Adv Exp Med Biol 892, 229–251. https://doi.org/10.1007/978-3-319-25304-6_9/FIGURES/6

Cejudo, F.J., Ferrández, J., Cano, B., Puerto-Galán, L., Guinea, M., 2012. The function of the NADPH thioredoxin reductase C-2-Cys peroxiredoxin system in plastid redox regulation and signalling. FEBS Lett 586, 2974–2980. https://doi.org/10.1016/J.FEBSLET.2012.07.003

Chan, Y.H.M., Marshall, W.F., 2014. Organelle size scaling of the budding yeast vacuole is tuned by membrane trafficking rates. Biophys J 106, 1986–1996. https://doi.org/10.1016/j.bpj.2014.03.014

Charizanis, C., Juhnke, H., Krems, B., Entian, K.D., 1999. The mitochondrial cytochrome c peroxidase Ccp1 of Saccharomyces cerevisiae is involved in conveying an oxidative stress signal to the transcription factor Pos9 (Skn7). Mol Gen Genet 262, 437–447. https://doi.org/10.1007/S004380051103

Chen, B., Yun, J., Kim, M.S., Mendell, J.T., Xie, Y., 2014. PIPE-CLIP: a comprehensive online tool for CLIP-seq data analysis. Genome Biol 15. https://doi.org/10.1186/GB-2014-15-1-R18

Chen, X., Castro, S.A., Liu, Q., Hu, W., Zhang, S., 2019. Practical considerations on performing and analyzing CLIP-seq experiments to identify transcriptomic-wide RNA-protein interactions. Methods. https://doi.org/10.1016/j.ymeth.2018.12.002

Chomczynski, P., Sacchi, N., 2006. The single-step method of RNA isolation by acid guanidinium thiocyanate-phenol-chloroform extraction: Twenty-something years on. Nat Protoc 1, 581–585. https://doi.org/10.1038/nprot.2006.83

Choudhary, R., Niska-Blakie, J., Adhil, M., Liberi, G., Achar, Y.J., Giannattasio, M., Foiani, M., 2023. Sen1 and Rrm3 ensure permissive topological conditions for replication termination. Cell Rep 42, 112747. https://doi.org/10.1016/j.celrep.2023.112747

Christianson, T.W., Sikorski, R.S., Dante, M., Shero, J.H., Hieter, P., 1992. Multifunctional yeast high-copy-number shuttle vectors. Gene 110, 119–122. https://doi.org/10.1016/0378-1119(92)90454-W

Chu, L.C., Arede, P., Li, W., Urdaneta, E.C., Ivanova, I., McKellar, S.W., Wills, J.C., Fröhlich, T., von Kriegsheim, A., Beckmann, B.M., Granneman, S., 2022. The RNA-bound proteome of MRSA reveals post-transcriptional roles for helix-turn-helix DNA-binding and Rossmann-fold proteins. Nature Communications 2022 13:1 13, 1–18. https://doi.org/10.1038/s41467-022-30553-8

Chubb, J.R., Trcek, T., Shenoy, S.M., Singer, R.H., 2006. Transcriptional pulsing of a developmental gene. Curr Biol 16, 1018–1025. https://doi.org/10.1016/J.CUB.2006.03.092

Coblenz, A., Wolf, K., 1994. The role of glutathione biosynthesis in heavy metal resistance in the fission yeast Schizosaccharomyces pombe. FEMS Microbiol Rev 14, 303–308. https://doi.org/10.1111/J.1574-6976.1994.TB00103.X

Cohen, G., Fessl, F., Traczyk, A., Rytka, J., Ruis, H., 1985. Isolation of the catalase A gene of Saccharomyces cerevisiae by complementation of the cta1 mutation. Mol Gen Genet 200, 74–79. https://doi.org/10.1007/BF00383315

Collinson, L.P., Dawes, I.W., 1992. Inducibility of the response of yeast cells to peroxide stress. J Gen Microbiol 138, 329–335. https://doi.org/10.1099/00221287-138-2-329

Contreras-Shannon, V., Lin, A.P., McCammon, M.T., McAlister-Henn, L., 2005. Kinetic properties and metabolic contributions of yeast mitochondrial and cytosolic NADP+-specific isocitrate dehydrogenases. J Biol Chem 280, 4469–4475. https://doi.org/10.1074/JBC.M410140200

Cordiner, R.A., Dou, Y., Thomsen, R., Bugai, A., Granneman, S., Heick Jensen, T., 2023. Temporal-iCLIP captures co-transcriptional RNA-protein interactions. Nature Communications 2023 14:1 14, 1–16. https://doi.org/10.1038/s41467-023-36345-y

Cottet-Rousselle, C., Ronot, X., Leverve, X., Mayol, J.F., 2011. Cytometric assessment of mitochondria using fluorescent probes. Cytometry Part A. https://doi.org/10.1002/cyto.a.21061

Courchaine, E.M., Lu, A., Neugebauer, K.M., 2016. Droplet organelles? EMBO J 35, 1603–1612. https://doi.org/10.15252/embj.201593517

Cox, J., Mann, M., 2008. MaxQuant enables high peptide identification rates, individualized p.p.b.-range mass accuracies and proteome-wide protein quantification. Nat Biotechnol 26, 1367–1372. https://doi.org/10.1038/nbt.1511

Cox, J., Neuhauser, N., Michalski, A., Scheltema, R.A., Olsen, J. V., Mann, M., 2011. Andromeda: A peptide search engine integrated into the MaxQuant environment. J Proteome Res 10, 1794–1805. https://doi.org/10.1021/pr101065j

Cramer, P., Armache, K.J., Baumli, S., Benkert, S., Brueckner, F., Buchen, C., Damsma, G.E., Dengl, S., Geiger, S.R., Jasiak, A.J., Jawhari, A., Jennebach, S., Kamenski, T., Kettenberger, H., Kuhn, C.D., Lehmann, E., Leike, K., Sydow, J.F., Vannini, A., 2008. Structure of eukaryotic RNA polymerases. Annu Rev Biophys 37, 337–352. https://doi.org/10.1146/ANNUREV.BIOPHYS.37.032807.130008

Crane, M.M., Clark, I.B.N., Bakker, E., Smith, S., Swain, P.S., 2014. A Microfluidic System for Studying Ageing and Dynamic Single-Cell Responses in Budding Yeast. PLoS One 9, e100042. https://doi.org/10.1371/JOURNAL.PONE.0100042

Creamer, T.J., Darby, M.M., Jamonnak, N., Schaughency, P., Hao, H., Wheelan, S.J., Corden, J.L., 2011. Transcriptome-wide binding sites for components of the Saccharomyces cerevisiae non-poly(A) termination pathway: Nrd1, Nab3, and Sen1. PLoS Genet 7. https://doi.org/10.1371/journal.pgen.1002329

Crissman, H.A., Steinkamp, J.A., 1973. Rapid, simultaneous measurement of DNA, protein, and cell volume in single cells from large mammalian cell populations. J Cell Biol 59, 766–771. https://doi.org/10.1083/JCB.59.3.766

Darby, M.M., Serebreni, L., Pan, X., Boeke, J.D., Corden, J.L., 2012. The Saccharomyces cerevisiae Nrd1-Nab3 Transcription Termination Pathway Acts in Opposition to Ras Signaling and Mediates Response to Nutrient Depletion. Mol Cell Biol 32, 1762 LP – 1775. https://doi.org/10.1128/MCB.00050-12

de Miranda, J.R., Thomas, M.A., Thurman, D.A., Tomsett, A.B., 1990. Metallothionein genes from the flowering plant Mimulus guttatus. FEBS Lett 260, 277–280. https://doi.org/10.1016/0014-5793(90)80122-Y

De, S., Gorospe, M., 2017. Bioinformatic tools for analysis of CLIP ribonucleoprotein data. Wiley Interdiscip Rev RNA 8, e1404. https://doi.org/10.1002/WRNA.1404

de Vries, S., Grivell, L.A., 1988. Purification and characterization of a rotenone-insensitive NADH:Q6 oxidoreductase from mitochondria of Saccharomyces cerevisiae. Eur J Biochem 176, 377–384. https://doi.org/10.1111/J.1432-1033.1988.TB14292.X

Dengl, S., Cramer, P., 2009. Torpedo Nuclease Rat1 Is Insufficient to Terminate RNA Polymerase II in Vitro. J Biol Chem 284, 21270. https://doi.org/10.1074/JBC.M109.013847

DeRisi, J.L., Iyer, V.R., Brown, P.O., 1997. Exploring the metabolic and genetic control of gene expression on a genomic scale. Science 278, 680–686. https://doi.org/10.1126/SCIENCE.278.5338.680

Desai, S., Grefte, S., van de Westerlo, E., Lauwen, S., Paters, A., Prehn, J.H.M., Gan, Z., Keijer, J., Adjobo-Hermans, M.J.W., Koopman, W.J.H., 2024. Performance of TMRM and Mitotrackers in mitochondrial morphofunctional analysis of primary human skin fibroblasts. Biochim Biophys Acta Bioenerg 1865. https://doi.org/10.1016/J.BBABIO.2023.149027

Dickinson, J.R., Schweizer, M., 2004. Carbon metabolism 58–119. https://doi.org/10.1201/9780203503867-10

Dijken, J.P. van, Scheffers, W.A., 1986. Redox balances in the metabolism of sugars by yeasts. FEMS Microbiol Lett 32, 199–224. https://doi.org/10.1111/J.1574-6968.1986.TB01194.X

Dodt, M., Roehr, J.T., Ahmed, R., Dieterich, C., 2012. FLEXBAR—Flexible Barcode and Adapter Processing for Next-Generation Sequencing Platforms. Biology 2012, Vol. 1, Pages 895-905 1, 895–905. https://doi.org/10.3390/BIOLOGY1030895

Dolce, V., Fiermonte, G., Palmieri, F., 1996. Tissue-specific expression of the two isoforms of the mitochondrial phosphate carrier in bovine tissues. FEBS Lett 399, 95–98. https://doi.org/10.1016/S0014-5793(96)01294-X

Dolce, V., Iacobazzi, V., Palmieri, F., Walker, J.E., 1994. The sequences of human and bovine genes of the phosphate carrier from mitochondria contain evidence

of alternatively spliced forms. Journal of Biological Chemistry 269, 10451–10460. https://doi.org/10.1016/S0021-9258(17)34081-4

Duchen, M.R., 2004. Mitochondria in health and disease: perspectives on a new mitochondrial biology. Mol Aspects Med 25, 365–451. https://doi.org/10.1016/J.MAM.2004.03.001

Dunn, E.F., Hammell, C.M., Hodge, C.A., Cole, C.N., 2005. Yeast poly(A)-binding protein, Pab1, and PAN, a poly(A) nuclease complex recruited by Pab1, connect mRNA biogenesis to export. Genes Dev 19, 90–103. https://doi.org/10.1101/GAD.1267005

Duveau, F., Hodgins-Davis, A., Metzger, B.P.H., Yang, B., Tryban, S., Walker, E.A., Lybrook, T., Wittkopp, P.J., 2018. Fitness effects of altering gene expression noise in saccharomyces cerevisiae. Elife 7. https://doi.org/10.7554/ELIFE.37272

Ecker, D.J., Butt, T.R., Sternberg, E.J., Neeper, M.P., Debouck, C., Gorman, J.A., Crooke, S.T., 1986. Yeast metallothionein function in metal ion detoxification. Journal of Biological Chemistry 261, 16895–16900. https://doi.org/10.1016/s0021-9258(19)75973-0

Edelstein, A., Amodaj, N., Hoover, K., Vale, R., Stuurman, N., 2010. Computer control of microscopes using μmanager. Curr Protoc Mol Biol 1–17.

Elliott, S.G., 1983a. Coordination of growth with cell division: Regulation of synthesis of RNA during the cell cycle of the fission yeast Schizosaccharomyces pombe. MGG Molecular & General Genetics 192, 204–211. https://doi.org/10.1007/BF00327667/METRICS

Elliott, S.G., 1983b. Regulation of the maximal rate of RNA synthesis in the fission yeast Schizosaccharomyces pombe. MGG Molecular & General Genetics 192, 212–217. https://doi.org/10.1007/BF00327668/METRICS

Elowitz, M.B., Levine, A.J., Siggia, E.D., Swain, P.S., 2002. Stochastic gene expression in a single cell. Science (1979) 297, 1183–1186. https://doi.org/10.1126/SCIENCE.1070919/SUPPL_FILE/ELOWITZSOM.PDF

Engl, C., Jovanovic, G., Brackston, R.D., Kotta-Loizou, I., Buck, M., 2020. The route to transcription initiation determines the mode of transcriptional bursting in E. coli. Nat Commun 11. https://doi.org/10.1038/s41467-020-16367-6

Esteban-Serna, S., McCaughan, H., Granneman, S., 2023. Advantages and limitations of UV cross-linking analysis of protein-RNA interactomes in microbes. Mol Microbiol. https://doi.org/10.1111/MMI.15073

Fernando Montaño-Gutierrezid, L., Correiaid, K., Swainid, P.S., Montaño-Gutierrez, L.F., Correia, K., Swain, P.S., 2022. Multiple nutrient transporters enable cells to mitigate a rate-affinity tradeoff. https://doi.org/10.1371/journal.pcbi.1010060

Fiermonte, G., Dolce, V., Palmieri, F., 1998. Expression in Escherichia coli, Functional Characterization, and Tissue Distribution of Isoforms A and B of the Phosphate Carrier from Bovine Mitochondria. Journal of Biological Chemistry 273, 22782–22787. https://doi.org/10.1074/JBC.273.35.22782

Fingar, D.C., Salama, S., Tsou, C., Harlow, E., Blenis, J., 2002. Mammalian cell size is controlled by mTOR and its downstream targets S6K1 and 4EBP1/eIF4E. Genes Dev 16, 1472–1487. https://doi.org/10.1101/GAD.995802

Flattery-O'Brien, J., Collinson, L.P., Dawes, I.W., 1993. Saccharomyces cerevisiae has an inducible response to menadione which differs from that to hydrogen peroxide. J Gen Microbiol 139, 501–507. https://doi.org/10.1099/00221287-139-3-501/CITE/REFWORKS

Fournier, M.L., Paulson, A., Pavelka, N., Mosley, A.L., Gaudenz, K., Bradford, W.D., Glynn, E., Li, H., Sardiu, M.E., Fleharty, B., Seidel, C., Florens, L., Washburn, M.P., 2010. Delayed correlation of mRNA and protein expression in rapamycin-treated cells and a role for Ggc1 in cellular sensitivity to rapamycin. Mol Cell Proteomics 9, 271–284. https://doi.org/10.1074/MCP.M900415-MCP200

Frank, C., Iii, S., Savas, M.M., Petering, D.H., 1991. Ligand Substitution and Sulfhydryl Reactivity of Metallothionein. Methods Enzymol.

Fraser, R.S.S., Nurse, P., 1979. Altered patterns of ribonucleic acid synthesis during the cell cycle: a mechanism compensating for variation in gene concentration. J Cell Sci 35, 25–40. https://doi.org/10.1242/JCS.35.1.25

Fraser, R.S.S., Nurse, P., 1978. Novel cell cycle control of RNA synthesis in yeast. Nature 1978 271:5647 271, 726–730. https://doi.org/10.1038/271726a0

Friedersdorf, M.B., Keene, J.D., 2014. Advancing the functional utility of PAR-CLIP by quantifying background binding to mRNAs and lncRNAs. Genome Biol 15, R2. https://doi.org/10.1186/gb-2014-15-1-r2

Gan, H., Cai, T., Lin, X., Wu, Y., Wang, X., Yang, F., Han, C., 2013. Integrative proteomic and transcriptomic analyses reveal multiple post-transcriptional regulatory mechanisms of mouse spermatogenesis. Mol Cell Proteomics 12, 1144–1157. https://doi.org/10.1074/MCP.M112.020123

Garcia, I., Orellana-Muñoz, S., Ramos-Alonso, L., Andersen, A.N., Zimmermann, C., Eriksson, J., Bøe, S.O., Kaferle, P., Papamichos-Chronakis, M., Chymkowitch, P., Enserink, J.M., 2021. Kel1 is a phosphorylation-regulated noise suppressor of the pheromone signaling pathway. Cell Rep 37, 110186. https://doi.org/10.1016/J.CELREP.2021.110186

Golding, I., Paulsson, J., Zawilski, S.M., Cox, E.C., 2005. Real-time kinetics of gene activity in individual bacteria. Cell 123, 1025–1036. https://doi.org/10.1016/J.CELL.2005.09.031

Grabowska, D., Chelstowska, A., 2003. The ALD6 gene product is indispensable for providing NADPH in yeast cells lacking glucose-6-phosphate dehydrogenase activity. J Biol Chem 278, 13984–13988. https://doi.org/10.1074/JBC.M210076200

Granneman, S., Kudla, G., Petfalski, E., Tollervey, D., 2009. Identification of protein binding sites on U3 snoRNA and pre-rRNA by UV cross-linking and high-throughput analysis of cDNAs. Proc Natl Acad Sci U S A 106, 9613 LP – 9618. https://doi.org/10.1073/pnas.0901997106

Greenlaw, A.C., Alavattam, K.G., Tsukiyama, T., 2023. Post-transcriptional regulation shapes the transcriptome of quiescent budding yeast. Nucleic Acids Res 1–21. https://doi.org/https://doi.org/10.1093/nar/gkad1147

Grima, R., 2014. Anomalous fluctuation scaling laws in stochastic enzyme kinetics: Increase of noise strength with the mean concentration. Phys Rev E 89.1.

Gry, M., Rimini, R., Strömberg, S., Asplund, A., Pontén, F., Uhlén, M., Nilsson, P., 2009. Correlations between RNA and protein expression profiles in 23 human cell lines. BMC Genomics 10. https://doi.org/10.1186/1471-2164-10-365

Gudipati, R.K., Xu, Z., Lebreton, A., Séraphin, B., Steinmetz, L.M., Jacquier, A., Libri, D., 2012. Extensive Degradation of RNA Precursors by the Exosome in Wild-Type Cells. Mol Cell 48, 409–421. https://doi.org/10.1016/j.molcel.2012.08.018

Hafner, M., Landthaler, M., Burger, L., Khorshid, M., Hausser, J., Berninger, P., Rothballer, A., Ascano, M., Jungkamp, A.C., Munschauer, M., Ulrich, A., Wardle, G.S., Dewell, S., Zavolan, M., Tuschl, T., 2010. Transcriptome-wide Identification of RNA-Binding Protein and MicroRNA Target Sites by PAR-CLIP. Cell 141, 129–141. https://doi.org/10.1016/J.CELL.2010.03.009

Hamel, P., Saint-Georges, Y., De Pinto, B., Lachacinski, N., Altamura, N., Dujardin, G., 2004. Redundancy in the function of mitochondrial phosphate transport in Saccharomyces cerevisiae and Arabidopsis thaliana. Mol Microbiol 51, 307–317. https://doi.org/10.1046/J.1365-2958.2003.03810.X

Hammell, C.M., Gross, S., Zenklusen, D., Heath, C. V., Stutz, F., Moore, C., Cole, C.N., 2002. Coupling of termination, 3' processing, and mRNA export. Mol Cell Biol 22, 6441–6457. https://doi.org/10.1128/MCB.22.18.6441-6457.2002

Haruki, H., Nishikawa, J., Laemmli, U.K., 2008. The Anchor-Away Technique: Rapid, Conditional Establishment of Yeast Mutant Phenotypes. Mol Cell 31, 925–932. https://doi.org/10.1016/J.MOLCEL.2008.07.020

Hasanova, Z., Klapstova, V., Porrua, O., Stefl, R., Sebesta, M., 2023. Human senataxin is a bona fide R-loop resolving enzyme and transcription termination factor. Nucleic Acids Res 51, 2818–2837. https://doi.org/10.1093/NAR/GKAD092

Hazelbaker, D.Z., Marquardt, S., Wlotzka, W., Buratowski, S., 2013. Kinetic Competition between RNA Polymerase II and Sen1-Dependent Transcription Termination. Mol Cell 49, 55–66. https://doi.org/10.1016/j.molcel.2012.10.014

Hector, R.E., Nykamp, K.R., Dheur, S., Anderson, J.T., Non, P.J., Urbinati, C.R., Wilson, S.M., Minvielle-Sebastia, L., Swanson, M.S., 2002. Dual requirement for yeast hnRNP Nab2p in mRNA poly(A) tail length control and nuclear export. EMBO J 21, 1800. https://doi.org/10.1093/EMBOJ/21.7.1800

Heitman, J., Movva, N.R., Hall, M.N., 1991. Targets for cell cycle arrest by the immunosuppressant rapamycin in yeast. Science 253, 905–909. https://doi.org/10.1126/SCIENCE.1715094

Heo, D.H., Yoo, I., Kong, J., Lidschreiber, M., Mayer, A., Choi, B.Y., Hahn, Y., Cramer, P., Buratowski, S., Kim, M., 2013. The RNA polymerase 2 C-terminal domain-interacting domain of yeast Nrd1 contributes to the choice of termination pathway and couples to RNA processing by the nuclear exosome. Journal of Biological Chemistry 288, 36676–36690. https://doi.org/10.1074/jbc.M113.508267

Herbert Grace Crabtree, B., 1929. Observations on the carbohydrate metabolism of tumours. Biochemical Journal 23, 536–545. https://doi.org/10.1042/BJ0230536

Heyl, F., Maticzka, D., Uhl, M., Backofen, R., 2020. Galaxy CLIP-Explorer: A web server for CLIP-Seq data analysis. Gigascience. https://doi.org/10.1093/gigascience/giaa108

Ho, B., Baryshnikova, A., Brown, G.W., 2018. Unification of Protein Abundance Datasets Yields a Quantitative Saccharomyces cerevisiae Proteome. Cell Syst 6, 192-205.e3. https://doi.org/10.1016/J.CELS.2017.12.004

Hoof, A. van, Lennertz, P., Parker, R., 2000. Yeast Exosome Mutants Accumulate 3′-Extended Polyadenylated Forms of U4 Small Nuclear RNA and Small Nucleolar RNAs. Mol Cell Biol 20, 441–452. https://doi.org/10.1128/MCB.20.2.441-452.2000

Hou, C., Metcalfe, N.B., Salin, K., 2021. Is mitochondrial reactive oxygen species production proportional to oxygen consumption? A theoretical consideration. BioEssays 43. https://doi.org/10.1002/bies.202000165

Houseley, J., Tollervey, D., 2009. The Many Pathways of RNA Degradation. Cell 136, 763–776. https://doi.org/10.1016/J.CELL.2009.01.019

Hulbert, A.J., Pamplona, R., Buffenstein, R., Buttemer, W.A., 2007. Life and death: metabolic rate, membrane composition, and life span of animals. Physiol Rev 87, 1175–1213. https://doi.org/10.1152/PHYSREV.00047.2006

Hunter, J.D., 2007. Matplotlib: A 2D graphics environment. Comput Sci Eng 9, 90–95. https://doi.org/10.1109/MCSE.2007.55

Huppertz, I., Attig, J., D'Ambrogio, A., Easton, L.E., Sibley, C.R., Sugimoto, Y., Tajnik, M., König, J., Ule, J., 2014. iCLIP: Protein-RNA interactions at nucleotide resolution. Methods 65, 274–287. https://doi.org/10.1016/J.YMETH.2013.10.011

Ilik, I.A., Aktas, T., Maticzka, D., Backofen, R., Akhtar, A., 2019. FLASH: ultra-fast protocol to identify RNA-protein interactions in cells. Nucleic Acids Res 48, 15. https://doi.org/10.1093/nar/gkz1141

Ilker, E., Hinczewski, M., 2024. Bioenergetic costs and the evolution of noise regulation by microRNAs. Proc Natl Acad Sci U S A 121. https://doi.org/10.1073/PNAS.2308796121

Iosub, I.A., van Nues, R.W., McKellar, S.W., Nieken, K.J., Marchioretto, M., Sy, B., Tree, J.J., Viero, G., Granneman, S., 2020. Hfq CLASH uncovers sRNA-target interaction networks linked to nutrient availability adaptation. Elife 9, 1–33. https://doi.org/10.7554/eLife.54655

Jamieson, D.J., 1998. Oxidative stress responses of the yeast Saccharomyces cerevisiae. Yeast 14, 1511–1527. https://doi.org/10.1002/(SICI)1097-0061(199812)14:16<1511::AID-YEA356>3.0.CO;2-S

Jamieson, D.J., 1992. Saccharomyces cerevisiae has distinct adaptive responses to both hydrogen peroxide and menadione. J Bacteriol 174, 6678. https://doi.org/10.1128/JB.174.20.6678-6681.1992

Jamonnak, N., Creamer, T.J., Darby, M.M., Schaughency, P., Wheelan, S.J., Corden, J.L., 2011. Yeast Nrd1, Nab3, and Sen1 transcriptome-wide binding maps suggest multiple roles in post-transcriptional RNA processing. RNA 17, 2011–2025. https://doi.org/10.1261/RNA.2840711

Jumper, J., Evans, R., Pritzel, A., Green, T., Figurnov, M., Ronneberger, O., Tunyasuvunakool, K., Bates, R., Žídek, A., Potapenko, A., Bridgland, A., Meyer, C., Kohl, S.A.A., Ballard, A.J., Cowie, A., Romera-Paredes, B., Nikolov, S., Jain, R., Adler, J., Back, T., Petersen, S., Reiman, D., Clancy, E., Zielinski, M., Steinegger, M., Pacholska, M., Berghammer, T., Bodenstein, S., Silver, D., Vinyals, O., Senior, A.W., Kavukcuoglu, K., Kohli, P., Hassabis, D., 2021. Highly accurate protein structure prediction with AlphaFold. Nature 2021 596:7873 596, 583–589. https://doi.org/10.1038/s41586-021-03819-2

Jüschke, C., Dohnal, I., Pichler, P., Harzer, H., Swart, R., Ammerer, G., Mechtler, K., Knoblich, J.A., 2013. Transcriptome and proteome quantification of a tumor model provides novel insights into post-transcriptional gene regulation. Genome Biol 14. https://doi.org/10.1186/GB-2013-14-11-R133

Kagi, J.H., Valee, B.L., 1960. Metallothionein: a cadmium- and zinc-containing protein from equine renal cortex. J Biol Chem 235, 3460–3465. https://doi.org/10.1016/s0021-9258(18)64490-4

Kalita, I., Iosub, I.A., McLaren, L., Goossens, L., Granneman, S., Karoui, M. El, 2024. An Hfq-dependent post-transcriptional mechanism fine tunes RecB expression in Escherichia coli. Elife 13. https://doi.org/10.7554/ELIFE.94918.1

Kawai, S., Suzuki, S., Mori, S., Murata, K., 2001. Molecular cloning and identification of UTR1 of a yeast Saccharomyces cerevisiae as a gene encoding an NAD kinase. FEMS Microbiol Lett 200, 181–184. https://doi.org/10.1111/J.1574-6968.2001.TB10712.X

Kayikci, Ö., Nielsen, J., 2015. Glucose repression in Saccharomyces cerevisiae. FEMS Yeast Res 15, 68. https://doi.org/10.1093/FEMSYR/FOV068

Kholmukhamedov, A., Schwartz, J.M., Lemasters, J.J., 2013. MitoTracker Probes and Mitochondrial Membrane Potential. Shock 39, 543. https://doi.org/10.1097/SHK.0B013E318292300D

Kim, H., Erickson, B., Luo, W., Seward, D., Graber, J.H., Pollock, D.D., Megee, P.C., Bentley, D.L., 2010. Gene-specific RNA polymerase II phosphorylation and the CTD code. Nature Structural & Molecular Biology 2010 17:10 17, 1279–1286. https://doi.org/10.1038/nsmb.1913

Kim, K.Y., Levin, D.E., 2011. Mpk1 MAPK association with the paf1 complex blocks sen1-mediated premature transcription termination. Cell 144, 745–756. https://doi.org/10.1016/J.CELL.2011.01.034/ATTACHMENT/91434CCD-0EC6-4F03-8A1E-D408DE255D60/MMC5.PDF

Kim, M., Ahn, S.H., Krogan, N.J., Greenblatt, J.F., Buratowski, S., 2004a. Transitions in RNA polymerase II elongation complexes at the 3′ ends of genes. EMBO J 23, 354. https://doi.org/10.1038/SJ.EMBOJ.7600053

Kim, M., Krogan, N.J., Vasiljeva, L., Rando, O.J., Nedea, E., Greenblatt, J.F., Buratowski, S., 2004b. The yeast Rat1 exonuclease promotes transcription termination by RNA polymerase II. Nature 432, 517–522. https://doi.org/10.1038/NATURE03041

King, M.S., Tavoulari, S., Mavridou, V., King, A.C., Mifsud, J., Kunji, E.R.S., 2020. A Single Cysteine Residue in the Translocation Pathway of the Mitosomal ADP/ATP Carrier from Cryptosporidium parvum Confers a Broad Nucleotide Specificity. International Journal of Molecular Sciences 2020, Vol. 21, Page 8971 21, 8971. https://doi.org/10.3390/IJMS21238971

Knight, S.A.B., Yoon, H., Pandey, A.K., Pain, J., Pain, D., Dancis, A., 2019. Splitting the functions of Rim2, a mitochondrial iron/pyrimidine carrier. Mitochondrion 47, 256–265. https://doi.org/10.1016/J.MITO.2018.12.005

Kojima, Y., Berger, C., Vallee, B.L., Kagi, J.H.R., 1976. Amino-acid sequence of equine renal metallothionein-1B. Proc Natl Acad Sci U S A 73, 3413–3417. https://doi.org/10.1073/PNAS.73.10.3413

Kolbe, H.V.J., Costello, D., Wong, A., 1984. Mitochondrial phosphate transport. Large scale isolation and characterization of the phosphate transport protein from beef heart mitochondria. Journal of Biological Chemistry 259, 9115–9120. https://doi.org/10.1016/S0021-9258(17)47273-5

König, J., Zarnack, K., Rot, G., Curk, T., Kayikci, M., Zupan, B., Turner, D.J., Luscombe, N.M., Ule, J., 2010. iCLIP reveals the function of hnRNP particles in splicing at individual nucleotide resolution. Nat Struct Mol Biol 17, 909–915.

Krakau, S., Richard, H., Marsico, A., 2017. PureCLIP: capturing target-specific protein-RNA interaction footprints from single-nucleotide CLIP-seq data. Genome Biol 18. https://doi.org/10.1186/S13059-017-1364-2

Krems, B., Charizanis, C., Entian, K.D., 1995. Mutants of Saccharomyces cerevisiae sensitive to oxidative and osmotic stress. Curr Genet 27, 427–434. https://doi.org/10.1007/BF00311211

Kristensen, A.R., Gsponer, J., Foster, L.J., 2013. Protein synthesis rate is the predominant regulator of protein expression during differentiation. Mol Syst Biol 9. https://doi.org/10.1038/MSB.2013.47

Kubicek, K., Cerna, H., Holub, P., Pasulka, J., Hrossova, D., Loehr, F., Hofr, C., Vanacova, S., Stefl, R., 2012. Serine phosphorylation and proline isomerization in RNAP II CTD control recruitment of Nrd1. Genes Dev 26, 1891–1896. https://doi.org/10.1101/GAD.192781.112

Kucukural, A., Özadam, H., Singh, G., Moore, M.J., Cenik, C., 2013. ASPeak: An abundance sensitive peak detection algorithm for RIP-Seq. Bioinformatics 29, 2485–2486. https://doi.org/10.1093/bioinformatics/btt428

Kuehner, J.N., Brow, D.A., 2008. Regulation of a Eukaryotic Gene by GTP-Dependent Start Site Selection and Transcription Attenuation. Mol Cell 31, 201–211. https://doi.org/10.1016/J.MOLCEL.2008.05.018

Kuehner, J.N., Pearson, E.L., Moore, C., 2011. Unravelling the means to an end: RNA polymerase II transcription termination. Nature Reviews Molecular Cell Biology 2011 12:5 12, 283–294. https://doi.org/10.1038/nrm3098

Kunji, E.R.S., Robinson, A.J., 2006. The conserved substrate binding site of mitochondrial carriers. Biochim Biophys Acta Bioenerg 1757, 1237–1248. https://doi.org/10.1016/j.bbabio.2006.03.021

Kwapisz, M., Wery, M., Després, D., Ghavi-Helm, Y., Soutourina, J., Thuriaux, P., Lacroute, F., 2008. Mutations of RNA polymerase II activate key genes of the nucleoside triphosphate biosynthetic pathways. EMBO J 27, 2411–2421. https://doi.org/10.1038/EMBOJ.2008.165

Kwong, J.Q., Davis, J., Baines, C.P., Sargent, M.A., Karch, J., Wang, X., Huang, T., Molkentin, J.D., 2014. Genetic deletion of the mitochondrial phosphate carrier desensitizes the mitochondrial permeability transition pore and causes cardiomyopathy. Cell Death & Differentiation 2014 21:8 21, 1209–1217. https://doi.org/10.1038/cdd.2014.36

LaCava, J., Houseley, J., Saveanu, C., Petfalski, E., Thompson, E., Jacquier, A., Tollervey, D., 2005. RNA degradation by the exosome is promoted by a nuclear polyadenylation complex. Cell 121, 713–724. https://doi.org/10.1016/j.cell.2005.04.029

Lan, P., Li, W., Schmidt, W., 2012. Complementary proteome and transcriptome profiling in phosphate-deficient Arabidopsis roots reveals multiple levels of gene regulation. Mol Cell Proteomics 11, 1156–1166. https://doi.org/10.1074/MCP.M112.020461

Lanz, M.C., Zatulovskiy, E., Swaffer, M.P., Zhang, L., Ilerten, I., Zhang, S., You, D.S., Marinov, G., McAlpine, P., Elias, J.E., Skotheim, J.M., 2022. Increasing cell size

remodels the proteome and promotes senescence. Mol Cell 82, 3255-3269.e8. https://doi.org/10.1016/j.molcel.2022.07.017

Larsson, C., Påhlman, I.L., Ansell, R., Rigoulet, M., Adler, L., Gustafsson, L., 1998. The importance of the glycerol 3-phosphate shuttle during aerobic growth of Saccharomyces cerevisiae. Yeast 14, 347–357. https://doi.org/10.1002/(SICI)1097-0061(19980315)14:4<347::AID-YEA226>3.0.CO;2-9

Leadsham, J.E., Gourlay, C.W., 2010. CAMP/PKA signaling balances respiratory activity with mitochondria dependent apoptosis via transcriptional regulation. BMC Cell Biol 11, 1–14. https://doi.org/10.1186/1471-2121-11-92/FIGURES/7

Leary, S.C., Kaufman, B.A., Pellecchia, G., Guercin, G.H., Mattman, A., Jaksch, M., Shoubridge, E.A., 2004. Human SCO1 and SCO2 have independent, cooperative functions in copper delivery to cytochrome c oxidase. Hum Mol Genet 13, 1839–1848. https://doi.org/10.1093/HMG/DDH197

Lee, F.C.Y., Ule, J., 2018. Advances in CLIP Technologies for Studies of Protein-RNA Interactions. Mol Cell 69, 354–369. https://doi.org/10.1016/J.MOLCEL.2018.01.005

Lee, M.V., Topper, S.E., Hubler, S.L., Hose, J., Wenger, C.D., Coon, J.J., Gasch, A.P., 2011. A dynamic model of proteome changes reveals new roles for transcript alteration in yeast. Mol Syst Biol 7. https://doi.org/10.1038/MSB.2011.48

Lee, T.I., Young, R.A., 2013. Transcriptional Regulation and Its Misregulation in Disease. Cell 152, 1237–1251. https://doi.org/10.1016/J.CELL.2013.02.014

Lemasters, J.J., Ramshesh, V.K., 2007. Imaging of mitochondrial polarization and depolarization with cationic fluorophores. Methods Cell Biol 80, 283–295. https://doi.org/10.1016/S0091-679X(06)80014-2

Lengefeld, J., Cheng, C.W., Maretich, P., Blair, M., Hagen, H., McReynolds, M.R., Sullivan, E., Majors, K., Roberts, C., Kang, J.H., Steiner, J.D., Miettinen, T.P., Manalis, S.R., Antebi, A., Morrison, S.J., Lees, J.A., Boyer, L.A., Yilmaz, Ö.H., Amon, A., 2021. Cell size is a determinant of stem cell potential during aging. Sci Adv 7, 271.

https://doi.org/10.1126/SCIADV.ABK0271/SUPPL_FILE/SCIADV.ABK0271_TABLES_S1_TO_S3.ZIP

Lin, J., Amir, A., 2018. Homeostasis of protein and mRNA concentrations in growing cells. Nature Communications 2018 9:1 9, 1–11. https://doi.org/10.1038/s41467-018-06714-z

Liu, X.D., Thiele, D.J., 1996. Oxidative stress induced heat shock factor phosphorylation and HSF-dependent activation of yeast metallothionein gene transcription. Genes Dev 10, 592–603. https://doi.org/10.1101/GAD.10.5.592

Loftus, T.M., Hall, L. V., Anderson, S.L., McAlister-Henn, L., 1994. Isolation, characterization, and disruption of the yeast gene encoding cytosolic NADP-specific isocitrate dehydrogenase. Biochemistry 33, 9661–9667. https://doi.org/10.1021/BI00198A035

Longtine, M.S., McKenzie, A., Demarini, D.J., Shah, N.G., Wach, A., Brachat, A., Philippsen, P., Pringle, J.R., 1998. Additional modules for versatile and economical PCR-based gene deletion and modification in Saccharomyces cerevisiae. Yeast 14, 953–961. https://doi.org/10.1002/(SICI)1097-0061(199807)14:10<953::AID-YEA293>3.0.CO;2-U

Lorenz, R., Bernhart, S.H., Höner zu Siederdissen, C., Tafer, H., Flamm, C., Stadler, P.F., Hofacker, I.L., 2011. ViennaRNA Package 2.0. Algorithms for Molecular Biology 6, 1–14. https://doi.org/10.1186/1748-7188-6-26

Lovci, M.T., Ghanem, D., Marr, H., Arnold, J., Gee, S., Parra, M., Liang, T.Y., Stark, T.J., Gehman, L.T., Hoon, S., Massirer, K.B., Pratt, G.A., Black, D.L., Gray, J.W., Conboy, J.G., Yeo, G.W., 2013. Rbfox proteins regulate alternative mRNA splicing through evolutionarily conserved RNA bridges. Nat Struct Mol Biol 20, 1434–1442. https://doi.org/10.1038/nsmb.2699

Love, M.I., Huber, W., Anders, S., 2014. Moderated estimation of fold change and dispersion for RNA-seq data with DESeq2. Genome Biol 15, 1–21. https://doi.org/10.1186/S13059-014-0550-8/FIGURES/9

Loya, T.J., O'Rourke, T.W., Degtyareva, N., Reines, D., 2013. A network of interdependent molecular interactions describes a higher order Nrd1-Nab3 complex involved in yeast transcription termination. Journal of Biological Chemistry 288, 34158–34167. https://doi.org/10.1074/jbc.M113.516765

Loya, T.J., O'Rourke, T.W., Simke, W.C., Kelley, J.B., Reines, D., 2018. Nab3's localization to a nuclear granule in response to nutrient deprivation is determined by its essential prion-like domain. PLoS One 13, 1–23. https://doi.org/10.1371/journal.pone.0209195

Lundberg, E., Fagerberg, L., Klevebring, D., Matic, I., Geiger, T., Cox, J., Älgenäs, C., Lundeberg, J., Mann, M., Uhlen, M., 2010. Defining the transcriptome and proteome in three functionally different human cell lines. Mol Syst Biol 6, 450. https://doi.org/10.1038/MSB.2010.106/SUPPL_FILE/MSB2010106-SUP-0004.XLS

Luo, M., Zhou, W., Patel, H., Srivastava, A.P., Symersky, J., Bonar, M.M., Faraldo-Gómez, J.D., Liao, M., Mueller, D.M., 2020. Bedaquiline inhibits the yeast and human mitochondrial ATP synthases. Commun Biol 3. https://doi.org/10.1038/S42003-020-01173-Z

Luo, W., Johnson, A.W., Bentley, D.L., 2006. The role of Rat1 in coupling mRNA 3′-end processing to transcription termination: implications for a unified allosteric–torpedo model. Genes Dev 20, 954. https://doi.org/10.1101/GAD.1409106

Luttik, M.A.H., Overkamp, K.M., Kötter, P., De Vries, S., van Dijken, J.P., Pronk, J.T., 1998. The Saccharomyces cerevisiae NDE1 and NDE2 genes encode separate mitochondrial NADH dehydrogenases catalyzing the oxidation of cytosolic NADH. Journal of Biological Chemistry 273, 24529–24534. https://doi.org/10.1074/jbc.273.38.24529

Mager, W.H., Moradas Ferreira, P., 1993. Stress response of yeast. Biochem J 290 (Pt 1), 1–13. https://doi.org/10.1042/BJ2900001

Maragkakis, M., Alexiou, P., Nakaya, T., Mourelatos, Z., 2016. CLIPSeqTools-a novel bioinformatics CLIP-seq analysis suite. RNA 22, 1–9. https://doi.org/10.1261/rna.052167.115

Marguerat, S., Bähler, J., 2012. Coordinating genome expression with cell size. Trends in Genetics 28, 560–565. https://doi.org/10.1016/j.tig.2012.07.003

Marguerat, S., Schmidt, A., Codlin, S., Chen, W., Aebersold, R., Bähler, J., 2012. Quantitative analysis of fission yeast transcriptomes and proteomes in proliferating and quiescent cells. Cell 151, 671–683. https://doi.org/10.1016/J.CELL.2012.09.019

Martins, D., Kathiresan, M., English, A.M., 2013. Cytochrome c peroxidase is a mitochondrial heme-based H2O2 sensor that modulates antioxidant defense. Free Radic Biol Med 65, 541–551. https://doi.org/10.1016/J.FREERADBIOMED.2013.06.037

Maticzka, D., Ilik, I.A., Aktas, T., Backofen, R., Akhtar, A., 2018. uvCLAP is a fast and non-radioactive method to identify in vivo targets of RNA-binding proteins. Nat Commun 9, 1142. https://doi.org/10.1038/s41467-018-03575-4

Mayer, A., Lidschreiber, M., Siebert, M., Leike, K., Söding, J., Cramer, P., 2010. Uniform transitions of the general RNA polymerase II transcription complex. Nature Structural & Molecular Biology 2010 17:10 17, 1272–1278. https://doi.org/10.1038/nsmb.1903

Mayr, J.A., Merkel, O., Kohlwein, S.D., Gebhardt, B.R., Böhles, H., Fötschl, U., Koch, J., Jaksch, M., Lochmüller, H., Horváth, R., Freisinger, P., Sperl, W., 2007. Mitochondrial Phosphate Carrier Deficiency: A Novel Disorder of Oxidative Phosphorylation. The American Journal of Human Genetics 80, 478–484. https://doi.org/10.1086/511788

Mayr, J.A., Zimmermann, F.A., Horváth, R., Schneider, H.-C., Schoser, B., Holinski-Feder, E., Czermin, B., Freisinger, P., Sperl, W., 2011. Deficiency of the mitochondrial phosphate carrier presenting as myopathy and cardiomyopathy in a family with three affected children. Neuromuscul Disord 21, 803–808. https://doi.org/10.1016/j.nmd.2011.06.005

McCann, C., Quinteros, M., Adelugba, I., Morgada, M.N., Castelblanco, A.R., Davis, E.J., Lanzirotti, A., Hainer, S.J., Vila, A.J., Navea, J.G., Padilla-Benavides, T., 2022. The mitochondrial Cu+ transporter PiC2 (SLC25A3) is a target of MTF1 and contributes to the development of skeletal muscle in vitro. Front Mol Biosci 9. https://doi.org/10.3389/fmolb.2022.1037941

McKellar, S.W., Ivanova, I., van Nues, R.W., Cordiner, R.A., Worboys, W., Langford, A., Jensen, T.H., Granneman, S., 2020. Monitoring Protein-RNA Interaction Dynamics in vivo at High Temporal Resolution using $χ$CRAC. J. Vis. Exp 61027.

McLain, A.L., Szweda, P.A., Szweda, L.I., 2011. α-Ketoglutarate dehydrogenase: a mitochondrial redox sensor. Free Radic Res 45, 29–36. https://doi.org/10.3109/10715762.2010.534163

Meaden, P.G., Dickinson, F.M., Mifsud, A., Tessier, W., Westwater, J., Bussey, H., Midgley, M., 1997. The ALD6 gene of saccharomyces cerevisiae encodes a cytosolic, Mg2+-activated acetaldehyde dehydrogenase. Yeast 13, 1319–1327. https://doi.org/10.1002/(SICI)1097-0061(199711)13:14<1319::AID-YEA183>3.0.CO;2-T

Miettinen, T.P., Björklund, M., 2016. Cellular Allometry of Mitochondrial Functionality Establishes the Optimal Cell Size. Dev Cell 39, 370–382. https://doi.org/10.1016/J.DEVCEL.2016.09.004

Minard, K.I., McAlister-Henn, L., 2001. Antioxidant function of cytosolic sources of NADPH in yeast. Free Radic Biol Med 31, 832–843. https://doi.org/10.1016/S0891-5849(01)00666-9

Mischo, H.E., Chun, Y., Harlen, K.M., Smalec, B.M., Dhir, S., Churchman, L.S., Buratowski, S., 2018. Cell-Cycle Modulation of Transcription Termination Factor Sen1. Mol Cell 70, 312-326.e7. https://doi.org/10.1016/j.molcel.2018.03.010

Mischo, H.E., Proudfoot, N.J., 2013. Disengaging polymerase: Terminating RNA polymerase II transcription in budding yeast. Biochimica et Biophysica Acta (BBA) - Gene Regulatory Mechanisms 1829, 174–185. https://doi.org/10.1016/J.BBAGRM.2012.10.003

Misra, R.R., Hochadel, J.F., Smith, G.T., Cook, J.C., Waalkes, M.P., Wink, D.A., 1996. Evidence that nitric oxide enhances cadmium toxicity by displacing the metal from metallothionein. Chem Res Toxicol 9, 326–332. https://doi.org/10.1021/TX950109Y

Mitchell, P., Petfalski, E., Shevchenko, A., Mann, M., Tollervey, D., 1997. The Exosome: A Conserved Eukaryotic RNA Processing Complex Containing Multiple 3′→5′ Exoribonucleases. Cell 91, 457–466. https://doi.org/10.1016/S0092-8674(00)80432-8

Mitchell, S.F., Jain, S., She, M., Parker, R., 2013. Global analysis of yeast mRNPs. Nat Struct Mol Biol 20, 127–133. https://doi.org/10.1038/nsmb.2468

Miyagi, H., Kawai, S., Murata, K., 2009. Two sources of mitochondrial NADPH in the yeast Saccharomyces cerevisiae. J Biol Chem 284, 7553–7560. https://doi.org/10.1074/JBC.M804100200

Monod, J., 1949. THE GROWTH OF BACTERIAL CULTURES. Annu Rev Microbiol 3, 371–394. https://doi.org/10.1146/ANNUREV.MI.03.100149.002103

Montaño-Gutierrez, L.F., Manzanaro Moreno, N., Farquhar, I.L., Huo, Y., Bandiera, L., Swain, P.S., 2022. Analysing and meta-analysing time-series data of microbial growth and gene expression from plate readers. https://doi.org/10.1371/journal.pcbi.1010138

Morgada, M.N., Abriata, L.A., Cefaro, C., Gajda, K., Banci, L., Vila, A.J., 2015. Loop recognition and copper-mediated disulfide reduction underpin metal site assembly of CuA in human cytochrome oxidase. Proc Natl Acad Sci U S A 112, 11771–11776. https://doi.org/10.1073/PNAS.1505056112/SUPPL_FILE/PNAS.201505056SI.PDF

Moyes, C.D., Mathieu-Costello, O.A., Tsuchiya, N., Filburn, C., Hansford, R.G., 1997. Mitochondrial biogenesis during cellular differentiation. https://doi.org/10.1152/ajpcell.1997.272.4.C1345 272. https://doi.org/10.1152/AJPCELL.1997.272.4.C1345

Mukhopadhyay, J., Das, K., Ismail, S., Koppstein, D., Jang, M., Hudson, B., Sarafianos, S., Tuske, S., Patel, J., Jansen, R., Irschik, H., Arnold, E., Ebright, R.H., 2008. The RNA Polymerase “Switch Region” Is a Target for Inhibitors. Cell 135, 295–307. https://doi.org/10.1016/j.cell.2008.09.033

Mundt, M., Anders, A., Murray, S.M., Sourjik, V., 2018. A System for Gene Expression Noise Control in Yeast. ACS Synth Biol 7, 2618–2626. https://doi.org/10.1021/ACSSYNBIO.8B00279/ASSET/IMAGES/MEDIUM/SB-2018-00279N_M017.GIF

Muñoz González, A.F., Wongprommoon, A., Swain, P.S., 2024. ALIBY (Analyser of Live-cell Imaging for Budding Yeast). GitLab repository: https://gitlab.com/aliby/aliby.

Neurohr, G.E., Terry, R.L., Lengefeld, J., Bonney, M., Brittingham, G.P., Moretto, F., Miettinen, T.P., Vaites, L.P., Soares, L.M., Paulo, J.A., Harper, J.W., Buratowski,

S., Manalis, S., van Werven, F.J., Holt, L.J., Amon, A., 2019. Excessive Cell Growth Causes Cytoplasm Dilution And Contributes to Senescence. Cell 176, 1083-1097.e18. https://doi.org/10.1016/j.cell.2019.01.018

Newman, J.R.S., Ghaemmaghami, S., Ihmels, J., Breslow, D.K., Noble, M., DeRisi, J.L., Weissman, J.S., 2006. Single-cell proteomic analysis of S. cerevisiae reveals the architecture of biological noise. Nature 2006 441:7095 441, 840–846. https://doi.org/10.1038/nature04785

Nicholls, D.G., 2004. Mitochondrial membrane potential and aging. Aging Cell 3, 35–40. https://doi.org/10.1111/J.1474-9728.2003.00079.X

Nogae, I., Johnston, M., 1990. Isolation and characterization of the ZWF1 gene of Saccharomyces cerevisiae, encoding glucose-6-phosphate dehydrogenase. Gene 96, 161–169. https://doi.org/10.1016/0378-1119(90)90248-P

Nosek, J., Fukuhara, H., 1994. NADH dehydrogenase subunit genes in the mitochondrial DNA of yeasts. J Bacteriol 176, 5622–5630. https://doi.org/10.1128/JB.176.18.5622-5630.1994

O'Brien, R.N., Shen, Z., Tachikawa, K., Lee, P.A., Briggs, S.P., 2010. Quantitative proteome analysis of pluripotent cells by iTRAQ mass tagging reveals post-transcriptional regulation of proteins required for ES cell self-renewal. Mol Cell Proteomics 9, 2238–2251. https://doi.org/10.1074/MCP.M110.000281

Oehler, V.G., Ka, Y.Y., Choi, Y.E., Bumgarner, R.E., Raftery, A.E., Radich, J.P., 2009. The derivation of diagnostic markers of chronic myeloid leukemia progression from microarray data. Blood 114, 3292–3298. https://doi.org/10.1182/blood-2009-03-212969

Olafson, R.W., McCubbin, W.D., Kay, C.M., 1988. Primary- and secondary-structural analysis of a unique prokaryotic metallothionein from a Synechococcus sp. cyanobacterium. Biochem J 251, 691–699. https://doi.org/10.1042/BJ2510691

O'Rourke, T.W., Reines, D., 2016. Determinants of amyloid formation for the yeast termination factor Nab3. PLoS One 11, 1–14. https://doi.org/10.1371/journal.pone.0150865

Outten, C.E., Culotta, V.C., 2003. A novel NADH kinase is the mitochondrial source of NADPH in Saccharomyces cerevisiae. EMBO J 22, 2015–2024. https://doi.org/10.1093/EMBOJ/CDG211

Overkamp, K.M., Bakker, B.M., Kötter, P., van Tuijl, A., De Vries, S., van Dijken, J.P., Pronk, J.T., 2000. In vivo analysis of the mechanisms for oxidation of cytosolic NADH by Saccharomyces cerevisiae mitochondria. J Bacteriol 182, 2823–2830. https://doi.org/10.1128/JB.182.10.2823-2830.2000/ASSET/45C57C3D-4E86-4FAB-9A23-4EEB9D034EE2/ASSETS/GRAPHIC/JB1001757004.JPEG

Padovan-Merhar, O., Nair, G.P., Biaesch, A.G., Mayer, A., Scarfone, S., Foley, S.W., Wu, A.R., Churchman, L.S., Singh, A., Raj, A., 2015. Single Mammalian Cells Compensate for Differences in Cellular Volume and DNA Copy Number through Independent Global Transcriptional Mechanisms. Mol Cell 58, 339–352. https://doi.org/10.1016/j.molcel.2015.03.005

Påhlman, A.K., Granath, K., Ansell, R., Hohmann, S., Adler, L., 2001. The Yeast Glycerol 3-Phosphatases Gpp1p and Gpp2p Are Required for Glycerol Biosynthesis and Differentially Involved in the Cellular Responses to Osmotic, Anaerobic, and Oxidative Stress. Journal of Biological Chemistry 276, 3555–3563. https://doi.org/10.1074/JBC.M007164200

Palmieri, L., Runswick, M.J., Fiermonte, G., Walker, J.E., Palmieri, F., 2000. Yeast mitochondrial carriers: Bacterial expression, biochemical identification and metabolic significance. J Bioenerg Biomembr 32, 67–77. https://doi.org/10.1023/A:1005564429242/METRICS

Pearson, E.L., Moore, C.L., 2013. Dismantling Promoter-driven RNA Polymerase II Transcription Complexes in Vitro by the Termination Factor Rat1. J Biol Chem 288, 19750. https://doi.org/10.1074/JBC.M112.434985

Pebay-Peyroula, E., cile Dahout-Gonzalez, C., Kahn, R., ronique Tré zé guet, V., J-M Lauquin, G., rard Brandolin, G., 2003. Structure of mitochondrial ADP/ATP carrier in complex with carboxyatractyloside.

Peoples, J.N., Ghazal, N., Duong, D.M., Hardin, K.R., Manning, J.R., Seyfried, N.T., Faundez, V., Kwong, J.Q., 2021. Loss of the mitochondrial phosphate carrier SLC25A3 induces remodeling of the cardiac mitochondrial protein acylome. Am

J Physiol Cell Physiol 321, C519–C534. https://doi.org/10.1152/AJPCELL.00156.2021

Perrone, G.G., Tan, S.X., Dawes, I.W., 2008. Reactive oxygen species and yeast apoptosis. Biochimica et Biophysica Acta (BBA) - Molecular Cell Research 1783, 1354–1368. https://doi.org/10.1016/J.BBAMCR.2008.01.023

Perry, S.W., Norman, J.P., Barbieri, J., Brown, E.B., Gelbard, H.A., 2011. Mitochondrial membrane potential probes and the proton gradient: a practical usage guide. Biotechniques 50, 98–115. https://doi.org/10.2144/000113610

Petrova, V.Y., Drescher, D., Kujumdzieva, A. V., Schmitt, M.J., 2004. Dual targeting of yeast catalase A to peroxisomes and mitochondria. Biochemical Journal 380, 393–400. https://doi.org/10.1042/BJ20040042

Phelps, A., Schobert, C.T., Wohlrab, H., 1991. Cloning and Characterization of the Mitochondrial Phosphate Transport Protein Gene from the Yeast Saccharomyces cerevisiae, Biochemistry.

Picault, N., Hodges, M., Palmieri, L., Palmieri, F., 2004. The growing family of mitochondrial carriers in Arabidopsis. Trends Plant Sci 9, 138–146. https://doi.org/10.1016/J.TPLANTS.2004.01.007

Pietsch, J.M.J., Mu, F., Adjavon, D.A., Farquhar, I., Ivan, B.N., Swain, P.S., 2023. Determining growth rates from bright-field images of budding cells through identifying overlaps. Elife.

Porrua, O., Hobor, F., Boulay, J., Kubicek, K., D'Aubenton-Carafa, Y., Gudipati, R.K., Stefl, R., Libri, D., 2012. In vivo SELEX reveals novel sequence and structural determinants of Nrd1-Nab3-Sen1-dependent transcription termination. EMBO Journal 31, 3935–3948. https://doi.org/10.1038/emboj.2012.237

Porrua, O., Libri, D., 2015. Transcription termination and the control of the transcriptome: why, where and how to stop. Nature Reviews Molecular Cell Biology 2015 16:3 16, 190–202. https://doi.org/10.1038/nrm3943

Porrua, O., Libri, D., 2013. A bacterial-like mechanism for transcription termination by the Sen1p helicase in budding yeast. Nature Structural & Molecular Biology 2013 20:7 20, 884–891. https://doi.org/10.1038/nsmb.2592

Preker, P., Nielsen, J., Kammler, S., Lykke-Andersen, S., Christensen, M.S., Mapendano, C.K., Schierup, M.H., Jensen, T.H., 2008. RNA exosome depletion reveals transcription upstream of active human promoters. Science (1979) 322, 1851–1854. https://doi.org/10.1126/SCIENCE.1164096/SUPPL_FILE/PREKER.SOM.PDF

Pronk, J.T., Steensma, H.Y., van Dijken, J.P., 1996. Pyruvate metabolism in Saccharomyces cerevisiae. Yeast. https://doi.org/10.1002/(SICI)1097-0061(199612)12:16<1607::AID-YEA70>3.0.CO;2-4

Quinlan, A.R., Hall, I.M., 2010. BEDTools: a flexible suite of utilities for comparing genomic features. Bioinformatics 26, 841–842. https://doi.org/10.1093/bioinformatics/btq033

Raj, A., Peskin, C.S., Tranchina, D., Vargas, D.Y., Tyagi, S., 2006. Stochastic mRNA synthesis in mammalian cells. PLoS Biol 4, 1707–1719. https://doi.org/10.1371/JOURNAL.PBIO.0040309

Raj, A., van Oudenaarden, A., 2009. Single-molecule approaches to stochastic gene expression. Annu Rev Biophys 38, 255–270. https://doi.org/10.1146/ANNUREV.BIOPHYS.37.032807.125928

Raj, A., van Oudenaarden, A., 2008. Nature, nurture, or chance: stochastic gene expression and its consequences. Cell 135, 216–226. https://doi.org/10.1016/J.CELL.2008.09.050

Rambout, X., Maquat, L.E., 2024. Nuclear mRNA decay: regulatory networks that control gene expression. Nat Rev Genet. https://doi.org/10.1038/s41576-024-00712-2

Randez-Gil, F., Sanz, P., Entian, K.-D., Prieto, J.A., 1998. Carbon Source-Dependent Phosphorylation of Hexokinase PII and Its Role in the Glucose-Signaling Response in Yeast. Mol Cell Biol 18, 2940. https://doi.org/10.1128/MCB.18.5.2940

Ransy, C., Vaz, C., Lombès, A., Bouillaud, F., 2020. Use of H2O2 to Cause Oxidative Stress, the Catalase Issue. Int J Mol Sci 21, 1–14. https://doi.org/10.3390/IJMS21239149

Raser, J.M., O'Shea, E.K., 2005. Noise in gene expression: Origins, consequences, and control. Science (1979) 309, 2010–2013. https://doi.org/10.1126/SCIENCE.1105891/SUPPL_FILE/RASER_SOM.PDF

Remels, A.H.V., Langen, R.C.J., Schrauwen, P., Schaart, G., Schols, A.M.W.J., Gosker, H.R., 2010. Regulation of mitochondrial biogenesis during myogenesis. Mol Cell Endocrinol 315, 113–120. https://doi.org/10.1016/J.MCE.2009.09.029

Robinson, A.J., Overy, C., Kunji, E.R.S., 2008. The mechanism of transport by mitochondrial carriers based on analysis of symmetry. Proc Natl Acad Sci U S A 105, 17766–17771. https://doi.org/10.1073/PNAS.0809580105

Robinson, M.D., McCarthy, D.J., Smyth, G.K., 2009. edgeR: A Bioconductor package for differential expression analysis of digital gene expression data. Bioinformatics 26, 139–140. https://doi.org/10.1093/bioinformatics/btp616

Robles, M.S., Cox, J., Mann, M., 2014. In-vivo quantitative proteomics reveals a key contribution of post-transcriptional mechanisms to the circadian regulation of liver metabolism. PLoS Genet 10. https://doi.org/10.1371/JOURNAL.PGEN.1004047

Rodrigues, F., Ludovico, P., Leão, C., 2006. Sugar Metabolism in Yeasts: an Overview of Aerobic and Anaerobic Glucose Catabolism. Biodiversity and Ecophysiology of Yeasts 101–121. https://doi.org/10.1007/3-540-30985-3_6

Rolland, F., Winderickx, J., Thevelein, J.M., 2002. Glucose-sensing and-signalling mechanisms in yeast. FEMS Yeast Res. 2, 183–201.

Rosenberg, M., Blum, R., Kesner, B., Maier, V.K., Szanto, A., Lee, J.T., 2017. Denaturing CLIP, dCLIP, Pipeline Identifies Discrete RNA Footprints on Chromatin-Associated Proteins and Reveals that CBX7 Targets 3′ UTRs to Regulate mRNA Expression. Cell Syst 5, 368-385.e15. https://doi.org/10.1016/J.CELS.2017.09.014

Runswick, M.J., Powell, S.J., Nyren, P., Walker, J.E., 1987. Sequence of the bovine mitochondrial phosphate carrier protein: structural relationship to ADP/ATP translocase and the brown fat mitochondria uncoupling protein. EMBO J 6, 1367–1373. https://doi.org/10.1002/J.1460-2075.1987.TB02377.X

Ruprecht, J.J., Kunji, E.R.S., 2020. The SLC25 Mitochondrial Carrier Family: Structure and Mechanism. Trends Biochem Sci 45, 244–258. https://doi.org/10.1016/J.TIBS.2019.11.001

Ruttkay-Nedecky, B., Nejdl, L., Gumulec, J., Zitka, O., Masarik, M., Eckschlager, T., Stiborova, M., Adam, V., Kizek, R., 2013. The role of metallothionein in oxidative stress. Int J Mol Sci 14, 6044–6066. https://doi.org/10.3390/IJMS14036044

Sadowski, M., Dichtl, B., Hübner, W., Keller, W., 2003. Independent functions of yeast Pcf11p in pre-mRNA 3′ end processing and in transcription termination. EMBO J 22, 2167. https://doi.org/10.1093/EMBOJ/CDG200

Sanchez, A., Golding, I., 2013. Genetic determinants and cellular constraints in noisy gene expression. Science 342, 1188–1193. https://doi.org/10.1126/SCIENCE.1242975

Saputra, F., Kishida, M., Hu, S.Y., 2024. Oxidative stress induced by hydrogen peroxide disrupts zebrafish visual development by altering apoptosis, antioxidant and estrogen related genes. Scientific Reports 2024 14:1 14, 1–14. https://doi.org/10.1038/s41598-024-64933-5

Schägger, H., Pfeiffer, K., 2000. Supercomplexes in the respiratory chains of yeast and mammalian mitochondria. EMBO J 19, 1777–1783. https://doi.org/10.1093/EMBOJ/19.8.1777

Schaughency, P., Merran, J., Corden, J.L., 2014. Genome-Wide Mapping of Yeast RNA Polymerase II Termination. PLoS Genet 10, 1004632. https://doi.org/10.1371/JOURNAL.PGEN.1004632

Schmelzle, T., Hall, M.N., 2000. TOR, a central controller of cell growth. Cell 103, 253–262. https://doi.org/10.1016/S0092-8674(00)00117-3

Schmid, M., Poulsen, M.B., Olszewski, P., Pelechano, V., Saguez, C., Gupta, I., Steinmetz, L.M., Moore, C., Jensen, T.H., 2012. Rrp6p Controls mRNA Poly(A) Tail Length and Its Decoration with Poly(A) Binding Proteins. Mol Cell 47, 267–280. https://doi.org/10.1016/j.molcel.2012.05.005

Schmidt, E.E., Schibler, U., 1995. Cell size regulation, a mechanism that controls cellular RNA accumulation: consequences on regulation of the ubiquitous

transcription factors Oct1 and NF-Y and the liver-enriched transcription factor DBP. J Cell Biol 128, 467–483. https://doi.org/10.1083/JCB.128.4.467

Schneider, C.A., Rasband, W.S., Eliceiri, K.W., 2012. NIH Image to ImageJ: 25 years of image analysis. Nature Methods 2012 9:7 9, 671–675. https://doi.org/10.1038/nmeth.2089

Schnoerr, D., Sanguinetti, G., Grima, R., 2017. Approximation and inference methods for stochastic biochemical kinetics—a tutorial review. J Phys A Math Theor 50, 093001. https://doi.org/10.1088/1751-8121/AA54D9

Schrödinger, L.& D.W., 2020. PyMOL.

Schulz, D., Schwalb, B., Kiesel, A., Baejen, C., Torkler, P., Gagneur, J., Soeding, J., Cramer, P., 2013. Transcriptome surveillance by selective termination of noncoding RNA synthesis. Cell 155, 1075. https://doi.org/10.1016/j.cell.2013.10.024

Seifert, E.L., Gál, A., Acoba, M.G., Li, Q., Anderson-Pullinger, L., Golenár, T., Moffat, C., Sondheimer, N., Claypool, S.M., Hajnóczky, G., 2016. Natural and induced mitochondrial phosphate carrier loss: Differential dependence of mitochondrial metabolism and dynamics and cell survival on the extent of depletion. Journal of Biological Chemistry 291, 26126–26137. https://doi.org/10.1074/jbc.M116.744714

Seifert, E.L., Ligeti, E., Mayr, J.A., Sondheimer, N., Hajnóczky, G., 2015. The mitochondrial phosphate carrier: Role in oxidative metabolism, calcium handling and mitochondrial disease. Biochem Biophys Res Commun 464, 369–375. https://doi.org/10.1016/J.BBRC.2015.06.031

Shi, F., Kawai, S., Mori, S., Kono, E., Murata, K., 2005. Identification of ATP-NADH kinase isozymes and their contribution to supply of NADP(H) in Saccharomyces cerevisiae. FEBS J 272, 3337–3349. https://doi.org/10.1111/J.1742-4658.2005.04749.X

Shino, S., Nasuno, R., Takagi, H., 2022. S-glutathionylation of fructose-1,6-bisphosphate aldolase confers nitrosative stress tolerance on yeast cells via a metabolic switch. Free Radic Biol Med 193, 319–329. https://doi.org/10.1016/J.FREERADBIOMED.2022.10.302

Siciliano, V., Garzilli, I., Fracassi, C., Criscuolo, S., Ventre, S., Di Bernardo, D., 2013. MiRNAs confer phenotypic robustness to gene networks by suppressing biological noise. Nat Commun 4. https://doi.org/10.1038/ncomms3364

Sies, H., Berndt, C., Jones, D.P., 2017. Oxidative Stress. https://doi.org/10.1146/annurev-biochem

Singh, S., Brocker, C., Koppaka, V., Chen, Y., Jackson, B.C., Matsumoto, A., Thompson, D.C., Vasiliou, V., 2013. Aldehyde dehydrogenases in cellular responses to oxidative/electrophilicstress. Free Radic Biol Med 56, 89–101. https://doi.org/10.1016/J.FREERADBIOMED.2012.11.010

Small, W.C., McAlister-Henn, L., 1998. Identification of a cytosolically directed NADH dehydrogenase in mitochondria of Saccharomyces cerevisiae. J Bacteriol 180, 4051–4055. https://doi.org/10.1128/JB.180.16.4051-4055.1998

Smith, M.C.A., Sumner, E.R., Avery, S. V., 2007. Glutathione and Gts1p drive beneficial variability in the cadmium resistances of individual yeast cells. Mol Microbiol 66, 699–712. https://doi.org/10.1111/j.1365-2958.2007.05951.x

Sohal, R.S., Mockett, R.J., Orr, W.C., 2002. Mechanisms of aging: an appraisal of the oxidative stress hypothesis,. Free Radic Biol Med 33, 575–586. https://doi.org/10.1016/S0891-5849(02)00886-9

Speakman, J.R., Garratt, M., 2014. Oxidative stress as a cost of reproduction: beyond the simplistic trade-off model. Bioessays 36, 93–106. https://doi.org/10.1002/BIES.201300108

Speakman, J.R., Talbot, D.A., Selman, C., Snart, S., McLaren, J.S., Redman, P., Krol, E., Jackson, D.M., Johnson, M.S., Brand, M.D., 2004. Uncoupled and surviving: individual mice with high metabolism have greater mitochondrial uncoupling and live longer. Aging Cell 3, 87–95. https://doi.org/10.1111/J.1474-9728.2004.00097.X

Steels, E.L., Learmonth, R.P., Watson, K., 1994. Stress tolerance and membrane lipid unsaturation in Saccharomyces cerevisiae grown aerobically or anaerobically. Microbiology (Reading) 140 (Pt 3), 569–576. https://doi.org/10.1099/00221287-140-3-569

Steinman, H.M., 1980. The amino acid sequence of copper-zinc superoxide dismutase from bakers' yeast. Journal of Biological Chemistry 255, 6758–6765. https://doi.org/10.1016/s0021-9258(18)43637-x

Steinmetz, E.J., Conrad, N.K., Brow, D.A., Corden, J.L., 2001. RNA-binding protein Nrd1 directs poly(A)-independent 3′-end formation of RNA polymerase II transcripts. Nature 413, 327–331. https://doi.org/10.1038/35095090

Steinmetz, E.J., Warren, C.L., Kuehner, J.N., Panbehi, B., Ansari, A.Z., Brow, D.A., 2006. Genome-Wide Distribution of Yeast RNA Polymerase II and Its Control by Sen1 Helicase. Mol Cell 24, 735–746. https://doi.org/10.1016/J.MOLCEL.2006.10.023

Strand, M.K., Stuart, G.R., Longley, M.J., Graziewicz, M.A., Dominick, O.C., Copeland, W.C., 2003. POS5 gene of Saccharomyces cerevisiae encodes a mitochondrial NADH kinase required for stability of mitochondrial DNA. Eukaryot Cell 2, 809–820. https://doi.org/10.1128/EC.2.4.809-820.2003/ASSET/B99DBC2E-8E6C-493C-A757-392BBCBDDE25/ASSETS/GRAPHIC/EK0430086007.JPEG

Sun, X.M., Bowman, A., Priestman, M., Bertaux, F., Martinez-Segura, A., Tang, W., Whilding, C., Dormann, D., Shahrezaei, V., Marguerat, S., 2020. Size-Dependent Increase in RNA Polymerase II Initiation Rates Mediates Gene Expression Scaling with Cell Size. Current Biology 30, 1217-1230.e7. https://doi.org/10.1016/J.CUB.2020.01.053/ATTACHMENT/F038265F-82A7-4E63-9DD8-68C3E611FACC/MMC6.XLSX

Suter, D.M., Molina, N., Gatfield, D., Schneider, K., Schibler, U., Naef, F., 2011. Mammalian genes are transcribed with widely different bursting kinetics. Science 332, 472–474. https://doi.org/10.1126/SCIENCE.1198817

Swaffer, M.P., Marinov, G.K., Zheng, H., Fuentes Valenzuela, L., Tsui, C.Y., Jones, A.W., Greenwood, J., Kundaje, A., Greenleaf, W.J., Reyes-Lamothe, R., Skotheim, J.M., 2023. RNA polymerase II dynamics and mRNA stability feedback scale mRNA amounts with cell size. Cell 186, 5254-5268.e26. https://doi.org/10.1016/j.cell.2023.10.012

Swain, P.S., Elowitz, M.B., Siggia, E.D., 2002. Intrinsic and extrinsic contributions to stochasticity in gene expression. Proc Natl Acad Sci U S A 99, 12795 LP – 12800. https://doi.org/10.1073/pnas.162041399

Swain, P.S., Stevenson, K., Leary, A., Montano-Gutierrez, L.F., Clark, I.B.N., Vogel, J., Pilizota, T., 2016. Inferring time derivatives including cell growth rates using Gaussian processes.

Swanson, W.H., Clifton, C.E., 1948. Growth and Assimilation in Cultures of Saccharomyces cerevisiae. J Bacteriol 56, 115–124. https://doi.org/10.1128/JB.56.1.115-124.1948

Takabatake, R., Siddique, A.B.M., Kouchi, H., Izui, K., Hata, S., 2001. Characterization of a Saccharomyces cerevisiae gene that encodes a mitochondrial phosphate transporter-like protein. J Biochem 129, 827–833. https://doi.org/10.1093/OXFORDJOURNALS.JBCHEM.A002926

Tan, B.L., Norhaizan, M.E., Liew, W.P.P., Rahman, H.S., 2018. Antioxidant and oxidative stress: A mutual interplay in age-related diseases. Front Pharmacol. https://doi.org/10.3389/fphar.2018.01162

Tessier, W.D., Meaden, P.G., Dickinson, F.M., Midgley, M., 1998. Identification and disruption of the gene encoding the K(+)-activated acetaldehyde dehydrogenase of Saccharomyces cerevisiae. FEMS Microbiol Lett 164, 29–34. https://doi.org/10.1111/J.1574-6968.1998.TB13063.X

Thattai, M., van Oudenaarden, A., 2004. Stochastic Gene Expression in Fluctuating Environments.

Thattai, M., van Oudenaarden, A., 2001. Intrinsic noise in gene regulatory networks. Proc Natl Acad Sci U S A 98, 8614–8619. https://doi.org/10.1073/PNAS.151588598/ASSET/296583DD-83EE-408D-8B96-34237EE6E852/ASSETS/GRAPHIC/PQ1515885005.JPEG

Thiebaut, M., Colin, J., Neil, H., Jacquier, A., Séraphin, B., Lacroute, F., Libri, D., 2008. Futile cycle of transcription initiation and termination modulates the response to nucleotide shortage in S. cerevisiae. Mol Cell 31, 671–682. https://doi.org/10.1016/j.molcel.2008.08.010

Thiebaut, M., Kisseleva-Romanova, E., Rougemaille, M., Boulay, J., Libri, D., 2006. Transcription Termination and Nuclear Degradation of Cryptic Unstable Transcripts: A Role for the Nrd1-Nab3 Pathway in Genome Surveillance. Mol Cell 23, 853–864. https://doi.org/10.1016/j.molcel.2006.07.029

Thomas, P.D., Mushayahama, T., 2022. PANTHER: Making genome-scale phylogenetics accessible to all. Protein Science 8–22. https://doi.org/10.1002/pro.4218

Thornalley, P.J., Vašák, M., 1985. Possible role for metallothionein in protection against radiation-induced oxidative stress. Kinetics and mechanism of its reaction with superoxide and hydroxyl radicals. Biochim Biophys Acta 827, 36–44. https://doi.org/10.1016/0167-4838(85)90098-6

Tietjen, J.R., Zhang, D.W., Rodríguez-Molina, J.B., White, B.E., Akhtar, M.S., Heidemann, M., Li, X., Chapman, R.D., Shokat, K., Keles, S., Eick, D., Ansari, A.Z., 2010. Chemical-genomic dissection of the CTD code. Nature Structural & Molecular Biology 2010 17:9 17, 1154–1161. https://doi.org/10.1038/nsmb.1900

Tribble, D.L., Jones, D.P., 1990. Oxygen dependence of oxidative stress. Rate of NADPH supply for maintaining the GSH pool during hypoxia. Biochem Pharmacol 39, 729–736. https://doi.org/10.1016/0006-2952(90)90152-B

Tudek, A., Porrua, O., Kabzinski, T., Lidschreiber, M., Kubicek, K., Fortova, A., Lacroute, F., Vanacova, S., Cramer, P., Stefl, R., Libri, D., 2014. Molecular basis for coordinating transcription termination with noncoding RNA degradation. Mol Cell 55, 467–481. https://doi.org/10.1016/j.molcel.2014.05.031

Turakainen, H., Aho, S., Korhola, M., 1993. MEL gene polymorphism in the genus Saccharomyces. Appl Environ Microbiol 59, 2622–2630. https://doi.org/10.1128/AEM.59.8.2622-2630.1993

Tyanova, S., Temu, T., Sinitcyn, P., Carlson, A., Hein, M.Y., Geiger, T., Mann, M., Cox, J., 2016. The Perseus computational platform for comprehensive analysis of (prote)omics data. Nat Methods 13, 731–740. https://doi.org/10.1038/nmeth.3901

Tzur, A., Kafri, R., LeBleu, V.S., Lahav, G., Kirschner, M.W., 2009. Cell growth and size homeostasis in proliferating animal cells. Science 325, 167–171. https://doi.org/10.1126/SCIENCE.1174294

Uhl, M., Houwaart, T., Corrado, G., Wright, P.R., Backofen, R., 2017. Computational analysis of CLIP-seq data. Methods. https://doi.org/10.1016/j.ymeth.2017.02.006

Ule, J., Jensen, K.B., Ruggiu, M., Mele, A., Ule, A., Darnell, R.B., 2003. CLIP Identifies Nova-Regulated RNA Networks in the Brain. Science (1979) 302, 1212 LP – 1215. https://doi.org/10.1126/science.1090095

Urdaneta, E.C., Beckmann, B.M., 2020. Fast and unbiased purification of RNA-protein complexes after UV cross-linking. Methods 178, 72–82. https://doi.org/10.1016/J.YMETH.2019.09.013

Uren, P.J., Bahrami-Samani, E., Burns, S.C., Qiao, M., Karginov, F. V., Hodges, E., Hannon, G.J., Sanford, J.R., Penalva, L.O.F., Smith, A.D., 2012. Site identification in high-throughput RNA-protein interaction data. Bioinformatics 28, 3013–3020. https://doi.org/10.1093/BIOINFORMATICS/BTS569

Vahalová, P., Červinková, K., Cifra, M., 2021. Biological autoluminescence for assessing oxidative processes in yeast cell cultures. Sci Rep 11. https://doi.org/10.1038/s41598-021-89753-9

van Dijken, J.P., Weusthuis, R.A., Pronk, J.T., 1993. Kinetics of growth and sugar consumption in yeasts. Antonie Van Leeuwenhoek 63, 343–352. https://doi.org/10.1007/BF00871229/METRICS

van Kampen, N.G., 2007. Stochastic Processes in Physics and Chemistry, Third Edition. Stochastic Processes in Physics and Chemistry, Third Edition 1–463. https://doi.org/10.1016/B978-0-444-52965-7.X5000-4

van Nostrand, E.L., Pratt, G.A., Shishkin, A.A., Gelboin-Burkhart, C., Fang, M.Y., Sundararaman, B., Blue, S.M., Nguyen, T.B., Surka, C., Elkins, K., Stanton, R., Rigo, F., Guttman, M., Yeo, G.W., 2016. Robust transcriptome-wide discovery of RNA-binding protein binding sites with enhanced CLIP (eCLIP). Nature Methods 2016 13:6 13, 508–514. https://doi.org/10.1038/nmeth.3810

van Nues, R., Schweikert, G., de Leau, E., Selega, A., Langford, A., Franklin, R., Iosub, I., Wadsworth, P., Sanguinetti, G., Granneman, S., 2017. Kinetic CRAC uncovers a role for Nab3 in determining gene expression profiles during stress. Nat Commun 8, 1–17. https://doi.org/10.1038/s41467-017-00025-5

Vaňáčová, Š., Wolf, J., Martin, G., Blank, D., Dettwiler, S., Friedlein, A., Langen, H., Keith, G., Keller, W., 2005. A new yeast poly(A) polymerase complex involved in RNA quality control. PLoS Biol 3, 0986–0997. https://doi.org/10.1371/journal.pbio.0030189

Vanlerberghe, G.C., McIntosh, L., 1997. Alternative Oxidase: From Gene to Function. Annu Rev Plant Biol 48, 703–734. https://doi.org/10.1146/ANNUREV.ARPLANT.48.1.703/CITE/REFWORKS

Vasiljeva, L., Buratowski, S., 2006. Nrd1 interacts with the nuclear exosome for 3′ processing of RNA polymerase II transcripts. Mol Cell 21, 239–248. https://doi.org/10.1016/j.molcel.2005.11.028

Vasiljeva, L., Kim, M., Mutschler, H., Buratowski, S., Meinhart, A., 2008. The Nrd1–Nab3–Sen1 termination complex interacts with the Ser5-phosphorylated RNA polymerase II C-terminal domain. Nature Structural & Molecular Biology 2008 15:8 15, 795–804. https://doi.org/10.1038/nsmb.1468

Vemuri, G.N., Eiteman, M.A., McEwen, J.E., Olsson, L., Nielsen, J., 2007. Increasing NADH oxidation reduces overflow metabolism in Saccharomyces cerevisiae. Proc Natl Acad Sci U S A 104, 2402–2407. https://doi.org/10.1073/PNAS.0607469104/ASSET/78972322-5DB0-421F-A806-D1CD7E99CA4E/ASSETS/GRAPHIC/ZPQ0020748230004.JPEG

Verduyn, C., Zomerdijk, T.P.L., van Dijken, J.P., Scheffers, W.A., 1984. Continuous measurement of ethanol production by aerobic yeast suspensions with an enzyme electrode. Appl Microbiol Biotechnol 19, 181–185. https://doi.org/10.1007/BF00256451

Vest, K.E., Leary, S.C., Winge, D.R., Cobine, P.A., 2013. Copper Import into the Mitochondrial Matrix in Saccharomyces cerevisiae Is Mediated by Pic2, a Mitochondrial Carrier Family Protein. Journal of Biological Chemistry 288, 23884–23892. https://doi.org/10.1074/jbc.M113.470674

Vest, K.E., Paskavitz, A.L., Lee, J.B., Padilla-Benavides, T., 2018. Dynamic changes in copper homeostasis and post-transcriptional regulation of: Atp7a during myogenic differentiation. Metallomics 10, 309–322. https://doi.org/10.1039/c7mt00324b

Villa, T., Barucco, M., Martin-Niclos, M.-J., Jacquier, A., Libri, D., 2020. Degradation of Non-coding RNAs Promotes Recycling of Termination Factors at Sites of Transcription. Cell Rep 32, 107942. https://doi.org/10.1016/j.celrep.2020.107942

Waldbauer, J.R., Rodrigue, S., Coleman, M.L., Chisholm, S.W., 2012. Transcriptome and proteome dynamics of a light-dark synchronized bacterial cell cycle. PLoS One 7. https://doi.org/10.1371/JOURNAL.PONE.0043432

Wallace, E., Haynes, S., 2021. The tidyqpcr R Package: Quantitative PCR analysis in the tidyverse. (Version 0.3.0). Github repository: https://github.com/ewallace/tidyqpcr.

Wang, X., Bai, Y., Ni, L., Weiner, H., 1997. Saccharomyces cerevisiae aldehyde dehydrogenases. Identification and expression. Adv Exp Med Biol 414, 277–280. https://doi.org/10.1007/978-1-4615-5871-2_32

Wang, X., Mann, C.J., Bai, Y., Ni, L., Weiner, H., 1998. Molecular cloning, characterization, and potential roles of cytosolic and mitochondrial aldehyde dehydrogenases in ethanol metabolism in Saccharomyces cerevisiae. J Bacteriol 180, 822–830. https://doi.org/10.1128/JB.180.4.822-830.1998

Wang, Z., Zhang, J., 2011. Impact of gene expression noise on organismal fitness and the efficacy of natural selection. Proc Natl Acad Sci U S A 108. https://doi.org/10.1073/PNAS.1100059108/-/DCSUPPLEMENTAL/PNAS.201100059SI.PDF

Waskom, M.L., 2021. seaborn: statistical data visualization. J Open Source Softw 6, 3021. https://doi.org/10.21105/JOSS.03021

Watanabe, N., Ishihara, T., Ohshima, Y., 2007. Mutants carrying two sma mutations are super small in the nematode C. elegans. Genes Cells 12, 603–609. https://doi.org/10.1111/J.1365-2443.2007.01077.X

Webb, S., Hector, R.D., Kudla, G., Granneman, S., 2014. PAR-CLIP data indicate that Nrd1-Nab3-dependent transcription termination regulates expression of hundreds of protein coding genes in yeast. Genome Biol 15, R8. https://doi.org/10.1186/gb-2014-15-1-r8

Wegner, S. V., Sun, F., Hernandez, N., He, C., 2011. The tightly regulated copper window in yeast. Chem Commun (Camb) 47, 2571–2573. https://doi.org/10.1039/C0CC04292G

West, S., Gromak, N., Proudfoot, N.J., 2004. Human 5’ --> 3’ exonuclease Xrn2 promotes transcription termination at co-transcriptional cleavage sites. Nature 432, 522–525. https://doi.org/10.1038/NATURE03035

Wickham, H., 2016. ggplot2: Elegant Graphics for Data Analysis, 2nd ed. Springer Publishing Company, Incorporated.

Williams, T.C., Espinosa, M.I., Nielsen, L.K., Vickers, C.E., 2015. Dynamic regulation of gene expression using sucrose responsive promoters and RNA interference in Saccharomyces cerevisiae. Microb Cell Fact 14, 1–10. https://doi.org/10.1186/S12934-015-0223-7/TABLES/3

Wlotzka, W., Kudla, G., Granneman, S., Tollervey, D., 2011. The nuclear RNA polymerase II surveillance system targets polymerase III transcripts. EMBO Journal 30, 1790–1803. https://doi.org/10.1038/emboj.2011.97

Wohlrab, H., 2006. The human mitochondrial transport/carrier protein family. Nonsynonymous single nucleotide polymorphisms (nsSNPs) and mutations that lead to human diseases. Biochim Biophys Acta Bioenerg. https://doi.org/10.1016/j.bbabio.2006.05.024

Wohlrab, H., Annese, V., Haefele, A., 2002. Single replacement constructs of all hydroxyl, basic, and acidic amino acids identify new function and structure-sensitive regions of the mitochondrial phosphate transport protein. Biochemistry 41, 3254–3261. https://doi.org/10.1021/BI0117551

Wohlrab, H., Kolbe, H.V.J., Collins, A., 1986. Isolation and reconstitution of the phosphate transport protein from mitochondria. Methods Enzymol 125, 697–705. https://doi.org/10.1016/S0076-6879(86)25057-0

Wolf, S.G., Mutsafi, Y., Dadosh, T., Ilani, T., Lansky, Z., Horowitz, B., Rubin, S., Elbaum, M., Fass, D., 2017. 3D visualization of mitochondrial solid-phase calcium stores in whole cells. Elife 6, 1–18. https://doi.org/10.7554/eLife.29929

Wu, C.Y., Alexander Rolfe, P., Gifford, D.K., Fink, G.R., 2010. Control of transcription by cell size. PLoS Biol 8. https://doi.org/10.1371/JOURNAL.PBIO.1000523

Wyers, F., Rougemaille, M., Badis, G., Rousselle, J.C., Dufour, M.E., Boulay, J., Régnault, B., Devaux, F., Namane, A., Séraphin, B., Libri, D., Jacquier, A., 2005. Cryptic pol II transcripts are degraded by a nuclear quality control pathway involving a new poly(A) polymerase. Cell 121, 725–737. https://doi.org/10.1016/J.CELL.2005.04.030

Xiang, K., Tong, L., Manley, J.L., 2014. Delineating the Structural Blueprint of the Pre-mRNA 3′-End Processing Machinery. Mol Cell Biol 34, 1894–1910. https://doi.org/10.1128/MCB.00084-14

Xie, S., Swaffer, M., Skotheim, J.M., 2022. Eukaryotic Cell Size Control and Its Relation to Biosynthesis and Senescence. Annu Rev Cell Dev Biol 38, 291–319. https://doi.org/10.1146/ANNUREV-CELLBIO-120219-040142/CITE/REFWORKS

Xu, Z., Wei, W., Gagneur, J., Perocchi, F., Clauder-Münster, S., Camblong, J., Guffanti, E., Stutz, F., Huber, W., Steinmetz, L.M., 2009. Bidirectional promoters generate pervasive transcription in yeast. Nature 457, 1033–1037. https://doi.org/10.1038/nature07728

Yang, Y., Sauve, A.A., 2016. NAD+ metabolism: Bioenergetics, signaling and manipulation for therapy. Biochim Biophys Acta Proteins Proteom. https://doi.org/10.1016/j.bbapap.2016.06.014

Zenklusen, D., Larson, D.R., Singer, R.H., 2008. Single-RNA counting reveals alternative modes of gene expression in yeast. Nat Struct Mol Biol 15, 1263–1271. https://doi.org/10.1038/NSMB.1514

Zhang, Z., Fu, J., Gilmour, D.S., 2005. CTD-dependent dismantling of the RNA polymerase II elongation complex by the pre-mRNA 3′-end processing factor, Pcf11. Genes Dev 19, 1572. https://doi.org/10.1101/GAD.1296305

Zhou, Y., Zhu, Y., Dai, L., Men, Y., Wu, J., Zhang, J., Sun, Y., 2017a. Efficiency Analysis and Mechanism Insight of that Whole-Cell Biocatalytic Production of Melibiose from Raffinose with Saccharomyces cerevisiae. Appl Biochem Biotechnol 181, 407–423. https://doi.org/10.1007/S12010-016-2220-7/FIGURES/7

Zhou, Y., Zhu, Y., Men, Y., Dong, C., Sun, Y., Zhang, J., 2017b. Construction of engineered Saccharomyces cerevisiae strain to improve that whole-cell

biocatalytic production of melibiose from raffinose. J Ind Microbiol Biotechnol 44, 489–501. https://doi.org/10.1007/S10295-017-1901-8

Zhu, X., Boulet, A., Buckley, K.M., Phillips, C.B., Gammon, M.G., Oldfather, L.E., Moore, S.A., Leary, S.C., Cobine, P.A., 2021. Mitochondrial copper and phosphate transporter specificity was defined early in the evolution of eukaryotes. Elife 10, 1–65. https://doi.org/10.7554/ELIFE.64690

Zhurinsky, J., Leonhard, K., Watt, S., Marguerat, S., Bähler, J., Nurse, P., 2010. A coordinated global control over cellular transcription. Current Biology 20, 2010–2015. https://doi.org/10.1016/j.cub.2010.10.002